United States
Environmental Protection
Agency

Industrial Environmental Research
Laboratory
Research Triangle Park NC 27711

EPA-600/7-78-110a
June 1978

EPA

Electrostatic Precipitator Technology Assessment: Visits in Japan, November 1977 - Appendices

Interagency Energy/Environment R&D Program Report

RESEARCH REPORTING SERIES

Research reports of the Office of Research and Development, U.S. Environmental Protection Agency, have been grouped into nine series. These nine broad categories were established to facilitate further development and application of environmental technology. Elimination of traditional grouping was consciously planned to foster technology transfer and a maximum interface in related fields. The nine series are:

1. Environmental Health Effects Research
2. Environmental Protection Technology
3. Ecological Research
4. Environmental Monitoring
5. Socioeconomic Environmental Studies
6. Scientific and Technical Assessment Reports (STAR)
7. Interagency Energy-Environment Research and Development
8. "Special" Reports
9. Miscellaneous Reports

This report has been assigned to the INTERAGENCY ENERGY-ENVIRONMENT RESEARCH AND DEVELOPMENT series. Reports in this series result from the effort funded under the 17-agency Federal Energy/Environment Research and Development Program. These studies relate to EPA's mission to protect the public health and welfare from adverse effects of pollutants associated with energy systems. The goal of the Program is to assure the rapid development of domestic energy supplies in an environmentally-compatible manner by providing the necessary environmental data and control technology. Investigations include analyses of the transport of energy-related pollutants and their health and ecological effects; assessments of, and development of, control technologies for energy systems; and integrated assessments of a wide range of energy-related environmental issues.

EPA REVIEW NOTICE

This report has been reviewed by the participating Federal Agencies, and approved for publication. Approval does not signify that the contents necessarily reflect the views and policies of the Government, nor does mention of trade names or commercial products constitute endorsement or recommendation for use.

This document is available to the public through the National Technical Information Service, Springfield, Virginia 22161.

EPA-600/7-78-110a

June 1978

Electrostatic Precipitator Technology Assessment: Visits in Japan, November 1977 - Appendices

by

Grady B. Nichols

Southern Research Institute
2000 Ninth Avenue, South
Birmingham, Alabama 35205

Contract No. 68-02-2610
W.A. 5
Program Element No. EHE624

EPA Project Officer: James H. Abbott

Industrial Environmental Research Laboratory
Office of Energy, Minerals, and Industry
Research Triangle Park, NC 27711

Prepared for

U.S. ENVIRONMENTAL PROTECTION AGENCY
Office of Research and Development
Washington, DC 20460

ABSTRACT

This volume of the two-volume report consists of appendices representing technical papers supplied to a team of U.S. investigators during a particulate control technology assessment visit to Japan. The visit included discussions with personnel from universities, industries, and major installations involved with particulate control. Significant research activities were noted in both the academic and industrial sectors related to particulate control and measurements.

The report proper, EPA-600/7-78-110, summarizes the results of the individual discussions, observations during the tours, and discussions of technical papers.

CONTENTS

CONTENTS (continued)

CONTENTS (continued)

CONTENTS (Continued)

CONTENTS (continued)

Appendix I (continued)

APPENDIX A

UNIVERSITY OF TOKYO

INITIATION CONDITION AND MODE OF BACK DISCHARGE

Senichi MASUDA, PhD.

Akira MIZUNO, MSc.

Department of Electrical Engineering
University of Tokyo
"

7-3-1, Hongo, Bunkyo-Ku, Tokyo,
Japan

Summary

Modes of back discharge occurring in the electrostatic precipitator were studied using, instead of a dust layer, the model samples of glass and mica plates with a pin-hole, and tissue papers. It was confirmed that back discharge started to occur when the apparent field strength in the sample layers exceeded its breakdown field strength. Back discharge became to be a streamer corona under atmospheric condition. It could be classified into space streamer mode, surface streamer mode and mixed streamer mode, depending upon the field distribution around the breakdown point in the sample layers. The first and the third modes occurred when the field strength in the air gap, Ea, exceeded about 5 kV/cm, and positive ions were generated in the whole gas space. The second mode appeared when Ea was lower than about 5 kV/cm, and ion generation was limited to the near surface region. Among the factors affective on the back discharge, the dust resistivity was the most essential. For low dust resistivity, space streamers tended to develop from the breakdown points when the applied voltage was raised. For high dust resistivity, on the other hand, the number of breakdown points increased and surface discharge was pronounced. Remarkable difference in modes was seen when using positive corona. Neither space streamer nor surface discharge occurred and the flashover voltage was higher than that with negative corona.

1. Introduction

Back discharge is one of the most difficult problems in electrostatic precipitators impairing their performance in many industrial plants.[1] This is an abnormal kind of discharge which is triggered by breakdown in a high resistivity dust layer deposited on the collecting electrode and which lowers the flashover voltage, reducing particle charge and causing a severe drop in collection efficiency. The nature of back discharge depends on many factors such as the electrical properties of the dust layer and the chemical properties of the particles themselves, and its form is very complicated. Therefore more intensive and basic investigations are required to solve the back discharge problem, and also to assess precipitator performance, when back discharge occurs.

Back discharge occurring when using negative corona can be classified into two major discharge modes. One is the streamer mode, occurring with high gas density, the other the glow corona mode, occurring with low gas density.

Normally streamers, formed at the breakdown point on the layer, proceed into the gas space towards the discharge electrode or to the accumulated charges on the dust surface, or in both directions, depending upon the field distribution around the starting point. It is appropriate to classify the streamer mode into three sub-modes; space streamer mode, surface streamer mode and mixed streamer mode. The third one appears in most of the practical cases.

In this paper, an experimental study on the back discharge of streamer mode carried out under atmospheric pressure and room temperature is reported. Studies on the back discharge of a glow corona mode will be reported separately.[2]

2. Initiation condition and initial mode of back discharge

At first the initiation condition and the initial mode of back discharge was studied using a needle to plane electrode system, located inside a thermostat where humidity could also be controlled. It was tested whether the initiation of back discharge was governed by the breakdown field strength of a layer, Eds, measured separately using parallel plane electrodes. In order to change Eds of a sample, two glass plates, each having a pinhole, were used on top of one another as the layer sample, as indicated in Fig.1. By altering the position of one plate and thus changing the distance between the holes, the value of Eds could be changed. The resistivity of the glass plate, ρ_d, was 6×10^{11} ohm-cm and the diameter of the pinhole was 0.5 mm. The thickness of one plate was 2.0 mm. An image intensifier tube (EMI, type 9912) was used at its maximum gain (about 10^6) to observe a back discharge glow at its initiation. Current pulse was observed at the same time by a cathode ray oscilloscope with a band width of 10 MHz.

The breakdown field strength of the layer in corona field at the initiation of back discharge, Eds', was estimated as follows.[3] Voltage-current density (V-J) curves with the layer for various values of Eds were measured, where J represents average current density at the measuring electrode. They are shown by solid curves 1, 2 and 3 in Fig.2 when the electrode gap was 60 mm. In the same figure, the air load V-J curve (without glass plates) was plotted by a dotted line, the plane electrode being raised to the position of the surface when the glass plates were present, i.e. a gap of 56 mm. The voltage across the glass plates, ΔV, is given by $\Delta V = V - V'$, where V and V' are the electrode

voltages corresponding to the same value of current density, J, with and without the glass plates, respectively. With the increase in applied voltage from zero, a Trichel pulse current appeared at the measuring electrode when corona started at the needle electrode. With the voltage further increased, repetition frequency of the Trichel pulse current increased and D.C. current component appeared as shown in Fig.3-a. This D.C. current component also increased when voltage was increased. When the point Ai (i = 1 ~ 3) (Fig.2) was reached, feeble but continuous glow appeared at the pinhole (Fig.3-b-2), leading to a slight non-linear increase in current. Breakdown of the layer at the pinhole occurred at this point. The current wave form at this point is shown in Fig.3-b-1. We took this point as the initiation point of back discharge. From the value of ΔV at this point, $(\Delta V)_o$, and the layer thickness, t, we get $Eds' = (\Delta V)_o / t$. The values of Eds' thus obtained at the points A_1 ~ A_3 in Fig.2 were compared with those of $\rho_d \times Jo$, where ρ_d is the layer resistivity and Jo the current density at the corresponding points. A good agreement could be seen between Eds' and $\rho_d \times Jo$ as indicated in Table 1. The values of Eds measured using parallel plane electrodes are also given. The values of Eds' agreed well with these values. This suggests that the breakdown of the layer occurred at a layer field strength nearly equal to Eds measured by a parallel plane electrode system. This continuous glow mode of back discharge at its initial stage should be considered as a kind of glow discharge. Hence this should be refered to as "onset-glow mode". It should be distinguished from the more intense "steady-glow mode" appearing under the conditions to be reported separately.[2]

With the further increase in voltage, a very small surface streamers

randomly appeared at the limited region around the upper edge of the pinhole (Fig.3-c-2) at point Bi (i = 1 ~ 3) in Fig.2, corresponding to $J = 0.5$ to 1.0×10^{-7} A/cm^2. (The expression of current density in A/cm^2 lost its sense here, since most of the current flew through the pinhole hereafter.) Fig.3-c-1 indicates current pulse of this streamer, which should be refered to as an "onset-streamer". The Trichel pulse current was still observed to exist. When the voltage was slightly raised above points Bi, space streamers and large surface streamers occurred from the pinhole at point |Ci (i = 1 ~ 3) in Fig.2 (see Fig.3-d-2), accompanied by large current pulses (Fig.3-d-1). A more intense rise in current occurred beyond these streamer starting voltages. It should therefore be noted that the criterion for occurence of the layer breakdown should be clearly distinguished from that for occurence of streamers which are the essential cause for rapid current increase. In the field measurements of V-J curves, only the initiation points of streamers could be detected because of much higher signal to noise ratio expected.

For glass plate with a pinhole described above, the onset-glow appeared at the layer breakdown voltage. However, when a sufficiently high resistivity layer, such as a mica plate with a pinhole ($\rho_d > 10^{15}$ ohm-cm), was used, a random breakdown occurred at first. With a slight increase in voltage, it was followed by a repetitive breakdown, as indicated in Fig.3-e. Then this was followed by a stable onset-glow. Hence, the layer breakdown voltage, Vb, was different from the starting voltage of the onset-glow, Vo, in this case. The streamer discharge in gas space is followed by a flashover occurring at a voltage much lower than that without back discharge. Thus there are four major critical voltages for back

discharge under atmospheric condition; layer breakdown voltage Vb, onset-glow starting voltage Vo, streamer starting voltage Vst and finally flashover voltage Vs. The random breakdown, onset-glow and onset-streamer constitute an initial stage of back discharge where the current rise remains still comparatively low. This stage should be refered to as "onset-stage".

3. Back discharge in streamer mode

With the increase in voltage beyond the point Ci in Fig.2, streamers are emitted either into gas space towards discharge electrode or along the surface of the layer, or in both directions. Hence, back discharge in this mode should be refered to as "streamer mode", more specifically space streamer mode, surface streamer mode and mixed streamer mode as a combination of the former two. When the voltage was further raised, space streamer proceeded towards the discharge electrode and it bridged across the electrode gap until it finally turned into flashover. It could be expected that the most essential factors deciding the respective mode of streamers would be the strengths of tangential and vertical field around the breakdown point of the layer as well as corona current. Thus, these effects were studied separately. The detailed mechanism of propagation for these streamers will be discussed in another paper.[4]

3.1 Effects of vertical field and current

Along with the study of the effect of vertical field, Ea, that of the corona current density, J, was also investigated. These two factors, Ea and J, are closely coupled to each other in an actual precipitator,

while their magnitudes at back discharge initiation largely differ from case to case, depending upon the dust layer resistivity as described in section 3.3. To investigate the effects of these two factors separately, a grid electrode was inserted between the needle and plane electrodes as shown in Fig.4. A transient fluctuation in the grid electrode potential was eliminated by using a condenser of 0.5 μF capacity connected paralled to its H.V.source. By the change in needle electrode voltage Va and grid electrode potential Vg, vertical field strength Ea and current density J could be varied independently. The value of Ea was calculated from the ratio Vg / (grid-to-plane spacing). In these experiments two glass plates each having a pinhole (0.5 mm in diameter) were used as before. The resistivity was 6×10^{11} ohm-cm and the breakdown field strength 20.7 kV/cm. Fig.5 shows curves of current density J plotted against voltage of needle electrode Va with the grid potential Vg being kept constant. The mode and current wave form of back discharge under atmospheric condition were observed with the aids of an image intensifier tube and a cathode ray oscilloscope. From these observations and the curves in Fig.5, the mode diagram of back discharge was depicted on Ea-J domain as shown in Fig.6-a. No back discharge occurred in region I because of low current density. When the current exceeded a certain value at which the layer breakdown condition described before was fulfilled, back discharge in the onset-glow mode occurred in region II (see Fig.3-b-2). The further increase in current resulted in the onset-streamers occurring around the edge of the pinhole in region III (see Fig.3-c-2). It should be noted that the critical current densities for the transitions between regions I, II and III were nearly constant respectively independent of

Ea, as is shown by the flat curves A and B. The two regions II and III should be refered to as "onset-stage" region. With the further increase in current beyond the other critical curves C and D, back discharge in the streamer modes (surface and mixed streamer modes) took place in region IV and V. The region IV, for lower value of Ea, is the surface streamer region where the surface streamer mode was predominant and space streamers were few (see Fig.6-b). In this region current density J saturated at curve E because of space charge limitation (see Fig.5), and no flashover could be resulted between the grid and the plane electrodes. Whereas in region V, when Ea exceeded 5 kV/cm, both the surface and space streamers occurred to form the mixed streamer mode (see Fig.7-b). Again the critical current density for the transition from the region III to IV and V was nearly constant, except for a corner area G. When J in the region V exceeded curve F, the streamer turned into a flashover. The critical value of the field strength between regions IV and V (curve H) was about 5 kV/cm under the atmospheric pressure and room temperature, which had been taken as a criterion for the occurence of streamer under these conditions. It should, however, be noted that the initiation and growth of space and surface streamers is also governed by current density J.

3.2 Effect of tangential field

In the present case where the surface resistivity of the layer is extremely high, the surface charge would be firmly bound to its original position. In this case the tangential field around the breakdown point will become a function of the surface charge density on the layer, σ_o, at the instant of breakdown at which the potential of the breakdown point

becomes almost zero. The value of σ_o in turn is given by εEds where ε is the dielectric constant of the layer. If σ_o is sufficiently high, the breakdown of the point will directly trigger the surface streamer. In the opposite case onset-glow appears prior to the occurence of surface streamer, so far as the vertical field strength in gas space is not sufficiently high for the space streamer to be triggered. Such a high vertical field strength does not normally exist at the initiation of back discharge, unless the layer resistivity is in the range of 5×10^{10} to 10^{11} ohm-cm as discussed later. Thus, the effect of σ_o on back discharge in streamer mode was studied. Two glass plates were used as before so that Eds and, hence, σ_o could be changed. Photographs of the back discharge for two values of breakdown strength are shown in Fig.7. When Eds was 13.8 kV/cm, a space streamer was dominant proceeding to the discharge electrode (Fig.7-a). When Eds was 33.8 kV/cm, the mixed streamer mode appeared where a remarkable surface streamer in the vicinity of the pinhole could be observed (Fig.7-b). This was because the tangential field strength became larger as σ_o increased. The surface discharge became especially dominant when the value of σ_o exceeded about 5×10^{-9} C/cm^2.

3.3 Effect of dust resistivity

A tissue paper was used as a sample in this experiment. This was because its apparent resistivity ρ_d could easily be changed from 10^8 to 10^{14} ohm-cm by adjusting the ambient humidity. Thus the effect of ρ_d on the back discharge mode under normal temperature was studied. Voltage-current density curves for different values of ρ_d, ranging from 6×10^9 to 2×10^{13} ohm-cm, are shown in Fig.8 where the electrode gap was kept at 60 mm. Photographs of the back discharge for three different values

of ρ_d are shown in Fig.9, where the values of J were in the same order.

When the resistivity was 6×10^9 ohm-cm (curve 1 in Fig.8), no back discharge occurred until flashover took place at V = 65 kV and J = 7.6 $\mu A/cm^2$. For the case of needle to plane electrode system and experimental conditions investigated, the initiation condition of back discharge, Eds = ρ_d x Jo, did not become to be fulfilled prior to the occurence of flashover when ρ_d was lower than about 5×10^{10} ohm-cm. In other words, the initiation voltage of back discharge was higher than the flashover voltage of the gap because of too low value of ρ_d. When the value of ρ_d slightly exceeded this critical value, space streamers occurred as soon as the layer broke down, owing to the large voltage drop across the gas space. For instance, when the resistivity was 0.9×10^{11} ohm-cm (curve 2), the streamer starting voltage Vst was about 27 kV. The number of breakdown points was less and streamers proceeded into space towards the discharge electrode, as shown in Fig.9-a. The occurence of space streamers lowered the flashover voltage Vs to a great extent. It was observed that, when ρ_d was between about 5×10^{10} and 0.9×10^{11} ohm-cm, excessive sparking tended to occur. In this range of ρ_d, Vst would be lowered with the increase in ρ_d, so that it finally becomes lower than Vs as in the case of curve 2 in Fig.8. A slight increase in voltage beyond Vst would cause flashover because Vst remained still close to Vs. For ρ_d higher than 10^{12} ohm-cm (curve 3 and 4), the back discharge streamers started to occur at a much lower voltage and current density. There was a larger interval between Vst and Vs so that the excessive sparking disappeared. There were more breakdown points with a general glow surrounding each point. In this case a surface glow dominated and space streamers were few. This tendency became

pronounced with the increase in ρ_d (Fig.9-c).

The different discharge modes were caused by the difference in the ratio of the voltage drop across the dust layer to that across the gas space. If the resistivity was high, the voltage drop across the dust layer was high even at a low current density on the initial stage of back discharge, whereas the voltage drop across the gas space was low. As a result, the development of a space streamer was suppressed, and a surface discharge occurred. In this case many weak points broke down and the current increased readily without excessive sparking. However, when voltage was raised, the space streamer occurred also in this case, taking the form of a general glow bridging across the gap. A more severe increase in current occurred at this later stage. It can be seen that flashover occurred almost at the same voltage inspite of a large difference in ρ_d, once back discharge occurred. This agrees well with the results of G.W. Penney,[5] i.e. the flashover voltage of back discharge was not affected by the value of resistivity. This flashover voltage was almost half the value of that under non-back discharge condition.

3.4 Charging efficiency in different regions

For negative corona, back discharge is a source of positive ions to produce a bipolar ion atmosphere in gas space. The effect on particle charging, however, is different depending on the mode of back discharge. In the surface streamer mode, the ion source is considered to be surface-like, but in the space or mixed streamer modes, ion generation in space may occur. These were confirmed by measuring particle charge using the electrode system as shown in Fig.10.[6] This system enabled the change

in back discharge mode by changing the field strength between grid and plane electrodes, Ea (see Fig.6). A steel ball, 3.0 mm in diameter, was dropped between plane and grid electrodes and its saturation charge was measured by a Faraday cage. Distance between plane and grid electrodes was 50 mm, grid to discharge electrodes 30 mm, and a mica plate having many pinholes was used as a layer. Fig.11 is an example of the results obtained, showing the saturation charge of a steel ball as a function of its position d from the plane electrode. The values indicated in the bracket represent the theoretical saturation charge due to monopolar ions, calculated from Pauthenier's equation.[7] In the surface streamer region (curve 1), the value of charge was about 90 % less than the theoretical value but the sign of particle charge remained the same as that of the discharge electrode. The value of charge decreased as the particle crossed nearer the plane electrode. This result indicates that the back discharge of this mode can be considered as a surface-like ion source so that the density of positive ions decreased into the space. In the mixed streamer region where space streamer was pronounced (curve 2), particle charge scattered largely around its average value which was a fairly high positive value and almost the same regardless of position. This result might indicate that positive ions were generated abundantly inside the whole space and took dominant role in particle charging. The effect of streamer tip to collide with a particle might also be a factor. The curve 3 represents the transition region between the foregoing two. In this case particle charges were also positive but as low as in the case of curve 1.

3.5 Back discharge with positive corona

It was observed that the mode of back discharge with positive corona at the needle was completely different, as shown in Fig.12. Tissue paper was used and the electrode gap was 60 mm. Voltage-current density curves are shown in Fig.13 for various values of ρ_d. In this case breakdown points were distributed uniformly on the surface, no space or surface streamers could be observed and the discharge mode was only glow mode independent on resistivity. The abnormal increase in current was small and the flashover voltage when back discharge occurred was approximately 1.5 times higher than that for back discharge with negative corona at the needle. The relationship between the flashover voltage of back discharge, Vs, and gap distance d is shown in Fig.14 for the positive and negative coronas. Vs of the positive corona was higher than that of the negative corona for gap distance range of 1.0 to 10.0 cm. The flashover voltage of the positive corona under back discharge condition was also higher than that without back discharge when the layer was removed (air load). The mechanism for this behavior is considered to be due to a stable nature of negative glow corona at the breakdown point and to the positive corona at the needle tip being converted to Hermstein's glow corona.[8] The latter may be resulted by copious negative ions fed to the needle electrode, from which electrons would be shedded to form a continuous and stable positive glow discharge at the needle tip.

4. Conclusions

From the experimental studies described above, using the model samples of tissue papers, glass and mica plate, the following results on the effects of apparent resistivity and breakdown field strength on back discharge were obtained.

(1) With the negative corona at the needle, the layer breakdown started to occur when Eds = ρ_d x J is fulfilled. It was followed by the onset-glow mode occurring with a slight increase in voltage. A rapid increase in current, however, occurred only when the streamers started to occur at a critical voltage Vst. Thus there are four major critical voltages for back discharge under atmospheric condition; layer breakdown voltage Vb, onset-glow starting voltage Vo, streamer starting voltage Vst and flashover voltage Vs. For the case of electrode system investigated, the initiation condition of back discharge may not be fulfilled prior to the occurence of flashover when ρ_d does not exceed about 5×10^{10} ohm-cm. When ρ_d is in the range of 5×10^{10} to 10^{11} ohm-cm, it becomes Vst $\geq$ Vs, so that excessive sparking occurs. When $\rho_d > 10^{12}$ ohm-cm, Vst becomes sufficiently lower than Vs so that excessive sparking disappears, but abnormal increase in current occurs.

(2) There are three sub-modes in the streamer mode; space streamer mode, surface streamer mode and mixed streamer mode, depending upon the field distribution around the breakdown point in the sample layers. This in turn is a function of ρ_d, Eds, Ea and J. In the space streamer mode, positive ion generation in space occurs and particle aquires a fairly high positive charge. Whereas in the surface streamer mode, positive ion generation is limited to the surface region and the sign of particle charge is the same

as that of the needle electrode. In most of the actual cases, however, the mixed streamer mode appears.

(3) With positive corona at the needle, back discharge mode is completely different. The flashover voltage is higher than that under back discharge condition with the negative corona.

Acknowledgements

This research was sponsored by the Ministry of Education, Japan, as its Special Research Project (I) (Project No.011914). The authors are gratefully indebted for its support. Thanks are also due to Mr. Masao Kuroda for his help given to a part of the experiments.

Nomenclature

ρ_d apparent dust resistivity

Eds breakdown field strength of the layer measured by parallel plane electrodes

Eds'breakdown field strength of the layer in corona field

σ_o surface charge density at the instant of breakdown

ε dielectric constant of the layer

Ea vertical field strength in the gap

Va discharge electrode voltage

Vg grid electrode potential

Vb layer breakdown voltage

Vo onset-glow starting voltage

Vst streamer starting voltage

Vs flashover voltage

J current density at the measuring electrode

Jo current density at the initiation of back discharge

References

1 S. Masuda, Recent Progress in Electrostatic Precipitation, Static Electrification 1975, Institute of Physics Conference Series, No.27, p. 154 (1975)

2 S. Masuda and A. Mizuno, Flashover Measurements of Back Discharge, J. Electrostatics (to be published)

3 S. Masuda, Reverse Ionisation Phenomena in Electrostatic Precipitator, J.I.E.E. Japan. 35-102 (1960) p. 1482

4 S. Masuda and A. Mizuno, Light Measurement of Back Discharge, J. Electrostatics (to be published)

5 G.W. Penney and S.E. Craig, Sparkover as Influenced by Surface Conditions in D.C. Corona, A.I.E.E. Trans. pt.1, vol. 79, May 1960, pp.112-18.

6 M. Kuroda, 1975 Graduation Thesis, Department of Electrical Engineering, University of Tokyo

7 M. Pauthenier, Moreau-Hanot, Rev. Gen. Elect., Tome XIV, No. 18 p. 583 (1932)

8 L.B. Loeb, Electrical Coronas, p.95 (1965) Univ. of California Press

Curve	Initiation point	ΔV (kV)	Jo (A/cm^2)	$Eds' = \Delta V/t$ (kV/cm)	$\rho d \times Jo$ (kV/cm)	Eds (kV/cm)
1	A_1	5.6	2.5×10^{-8}	14.0	15.0	15.7
2	A_2	9.2	4.1×10^{-8}	23.0	24.6	25.1
3	A_3	14.0	6.9×10^{-8}	35.0	41.4	39.0

Table 1 Comparison of Eds, Eds' and $\rho d \times Jo$

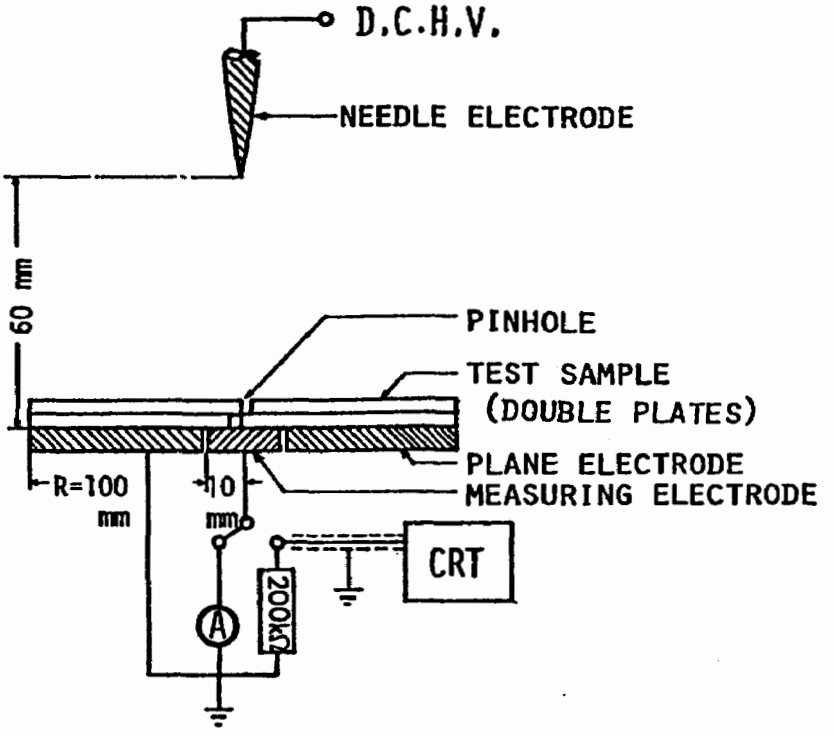
D.C.H.V.
NEEDLE ELECTRODE
60 mm
PINHOLE
TEST SAMPLE
(DOUBLE PLATES)
PLANE ELECTRODE
MEASURING ELECTRODE
R=100
mm
10
mm
CRT
200KΩ
A

Figure 1

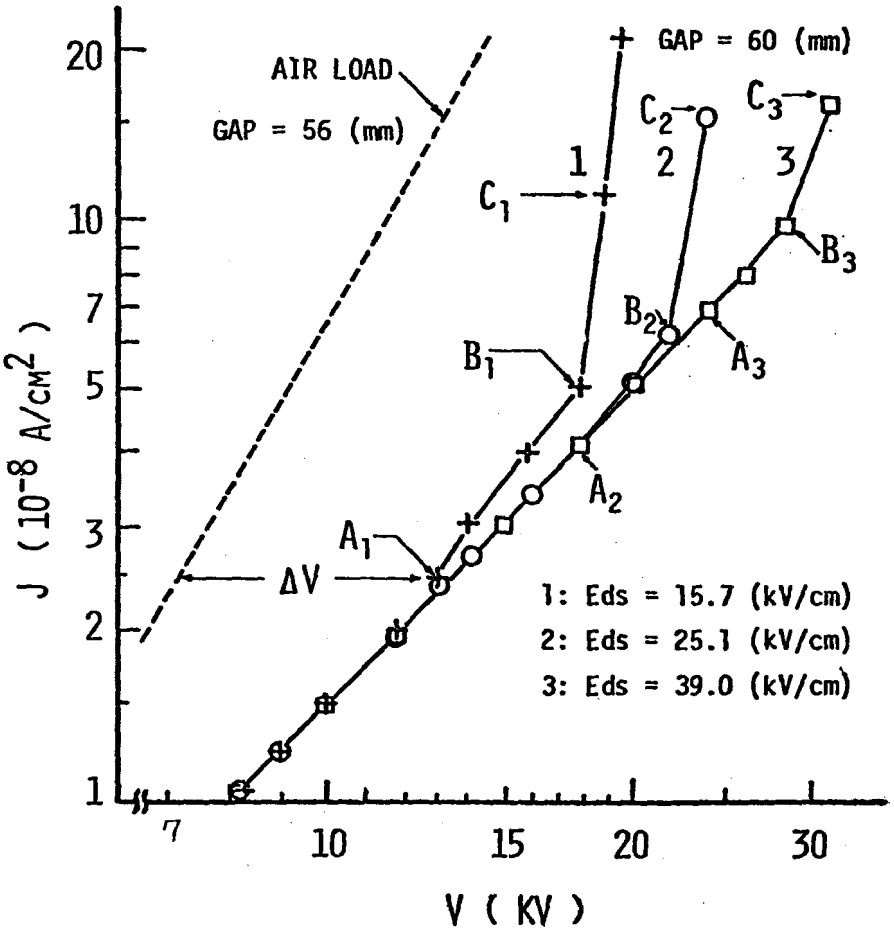
20
10
7
5
3
2
1
J (10⁻⁸ A/cm²)
AIR LOAD
GAP = 56 (mm)
GAP = 60 (mm)
C1
C2
C3
1
2
3
B1
B2
B3
A1
A2
A3
ΔV
1: Eds = 15.7 (kV/cm)
2: Eds = 25.1 (kV/cm)
3: Eds = 39.0 (kV/cm)
7
10
15
20
30
V (KV)

Figure 2

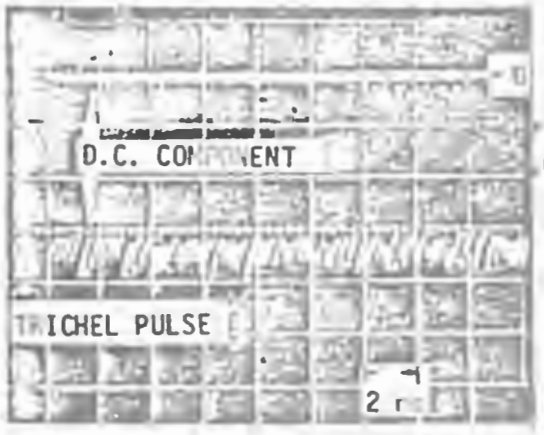

0.7 x 10^{-8} A/cm^2

(a) Trichel puls (12 kV, 2.0 x 10^{-8} A/cm^2)

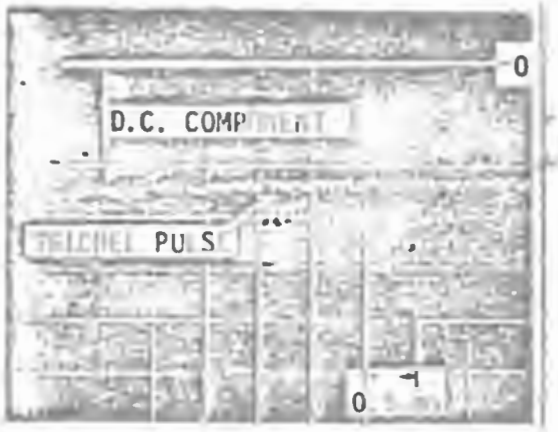

2 x 10^{-8} A/cm^2

(1) Cu nt

(2) Photograph obtained with intensifier

(b) Onset-glow (16 kV, 4.0 x 10^{-8} A/cm^2)

3 x 10^{-8} A/cm^2

(1) Current

(2) Photograph obtained with intensifier

(c) Onset-streamer (, 1.1 x 10^{-7} A/cm^2)

Figure 3a

1.5×10^{-7} A/cm^2

(1) Current

(2) Photograph obtained with intensifier

(d) Streamer (21 kV, 4.0×10^{-7} A/cm^2)

3×10^{-8} A/cm^2

(e) Repetitive breakdown (10 kV, 4.0×10^{-8} A/cm^2)
(Mica plate)

Figure 3b

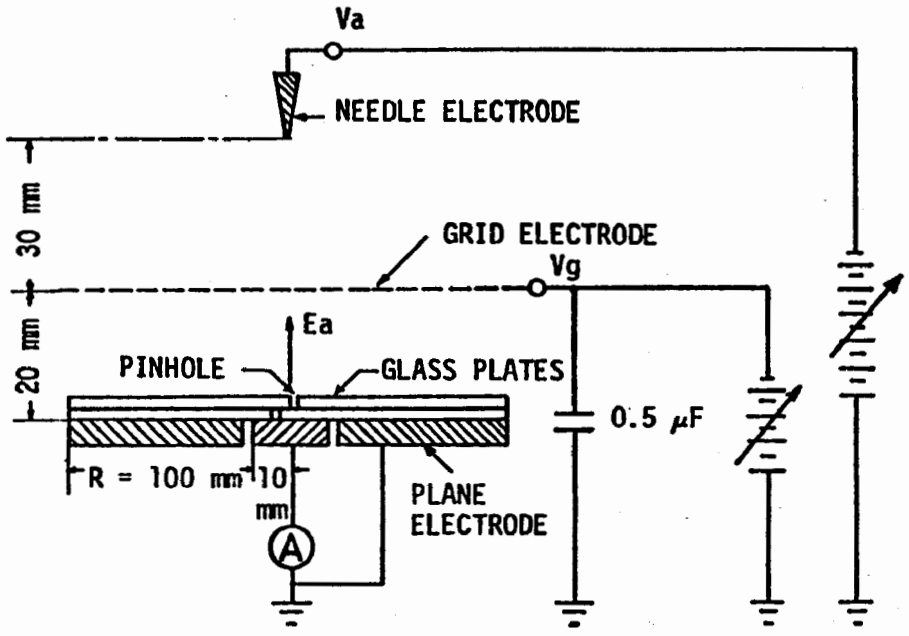

Figure 4 (modified)

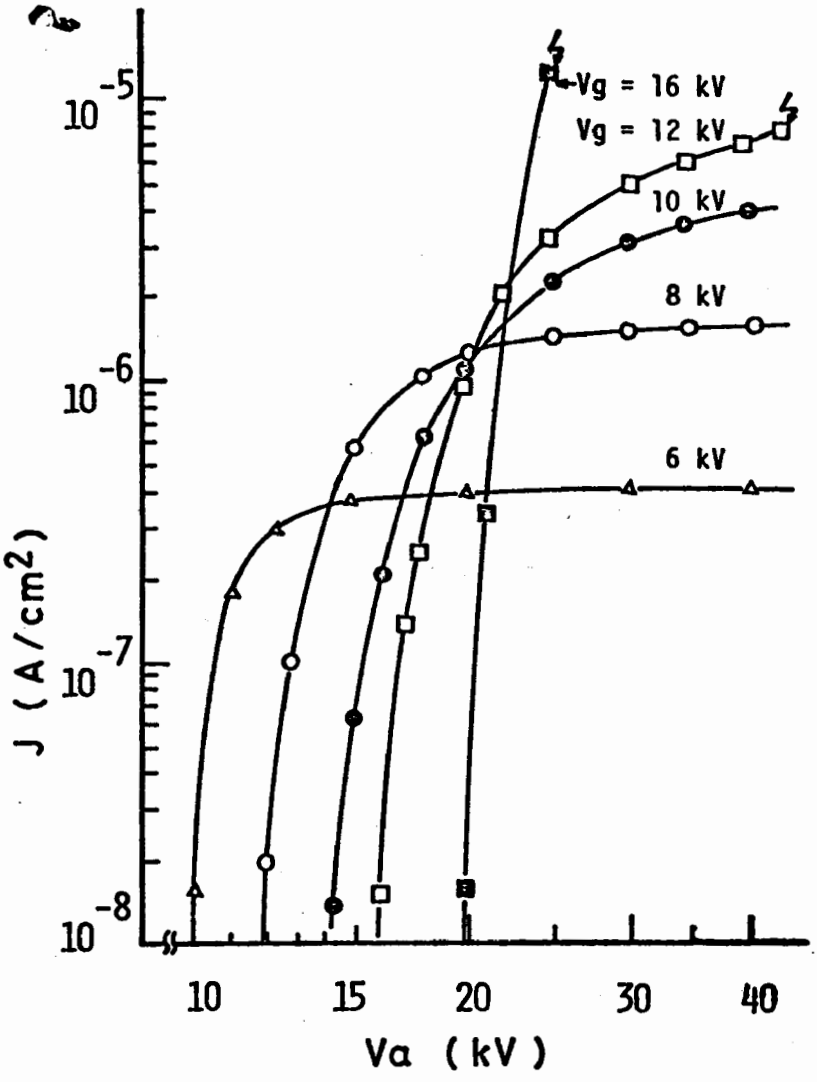
Vg = 16 kV
Vg = 12 kV
10 kV
8 kV
6 kV
J (A/cm2)
10-5
10-6
10-7
10-8
10
15
20
30
40
Va (kV)

Figure 5

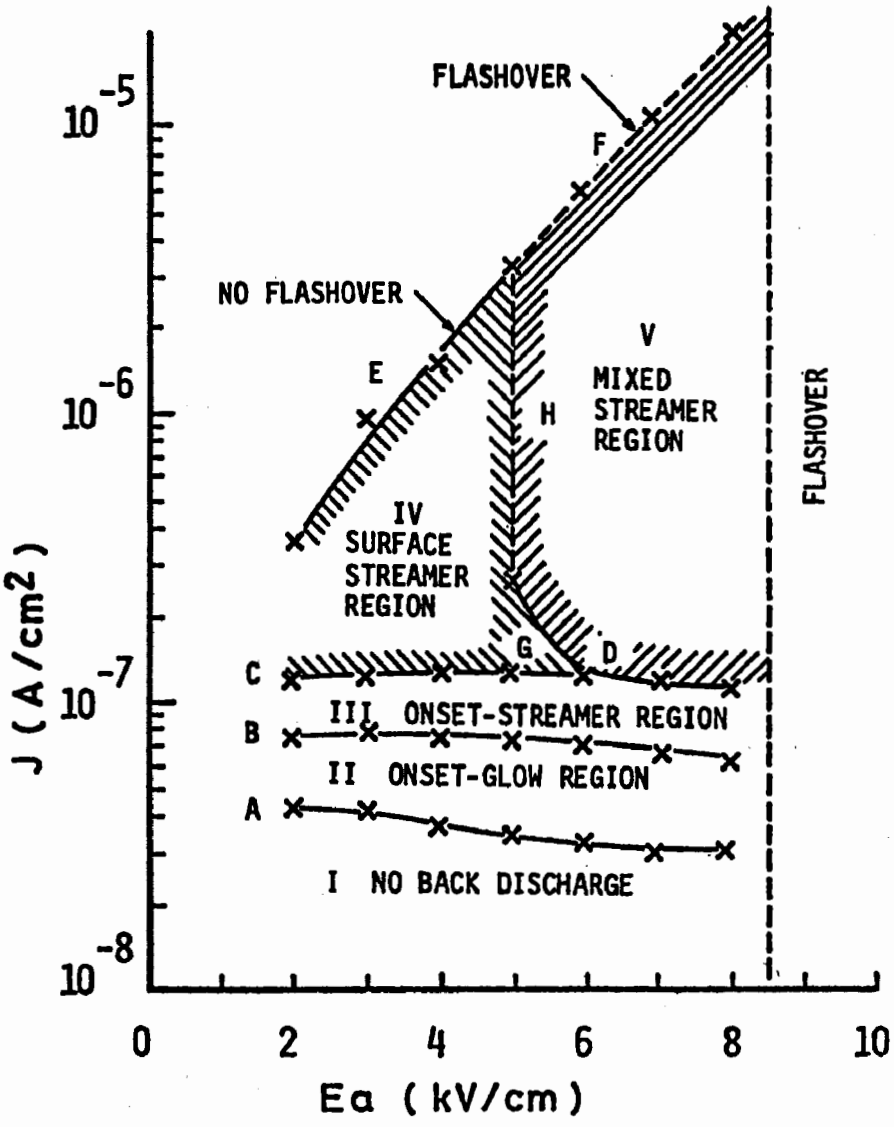
FLASHOVER
F
NO FLASHOVER
E
H
V
MIXED
STREAMER
REGION
FLASHOVER
IV
SURFACE
STREAMER
REGION
G
D
C
III ONSET-STREAMER REGION
B
II ONSET-GLOW REGION
A
I NO BACK DISCHARGE
10^{-5}
10^{-6}
10^{-7}
10^{-8}
J (A/cm^2)
0
2
4
6
8
10
Ea (kV/cm)

Figure 6a

Figure 6b
Photograph of back discharge in the surface streamer region [IV]
(Ea : 4.0 kV/cm, J : 5.0 x 10^{-7} A/cm^2)

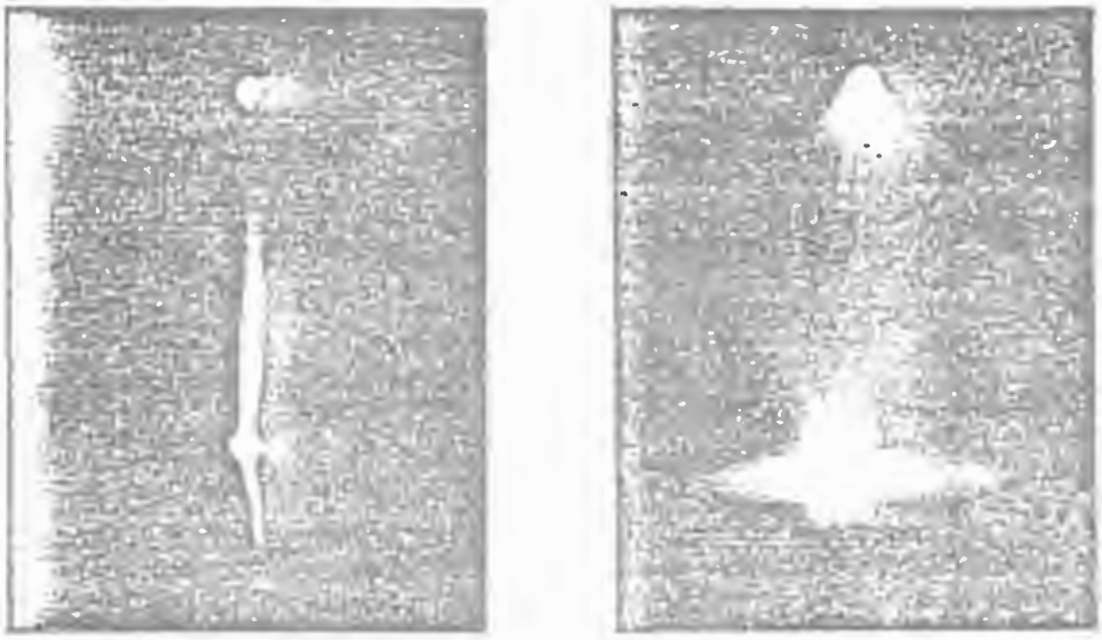

(a) Eds LOW

Eds - 13.8 (kV/cm)
V - 30 (kV)
I - 29 (μA)

(b) Eds HIGH

Eds - 33.8 (kV/cm)
V = 40 (kV)
I = 23 (μA)

Figure 7

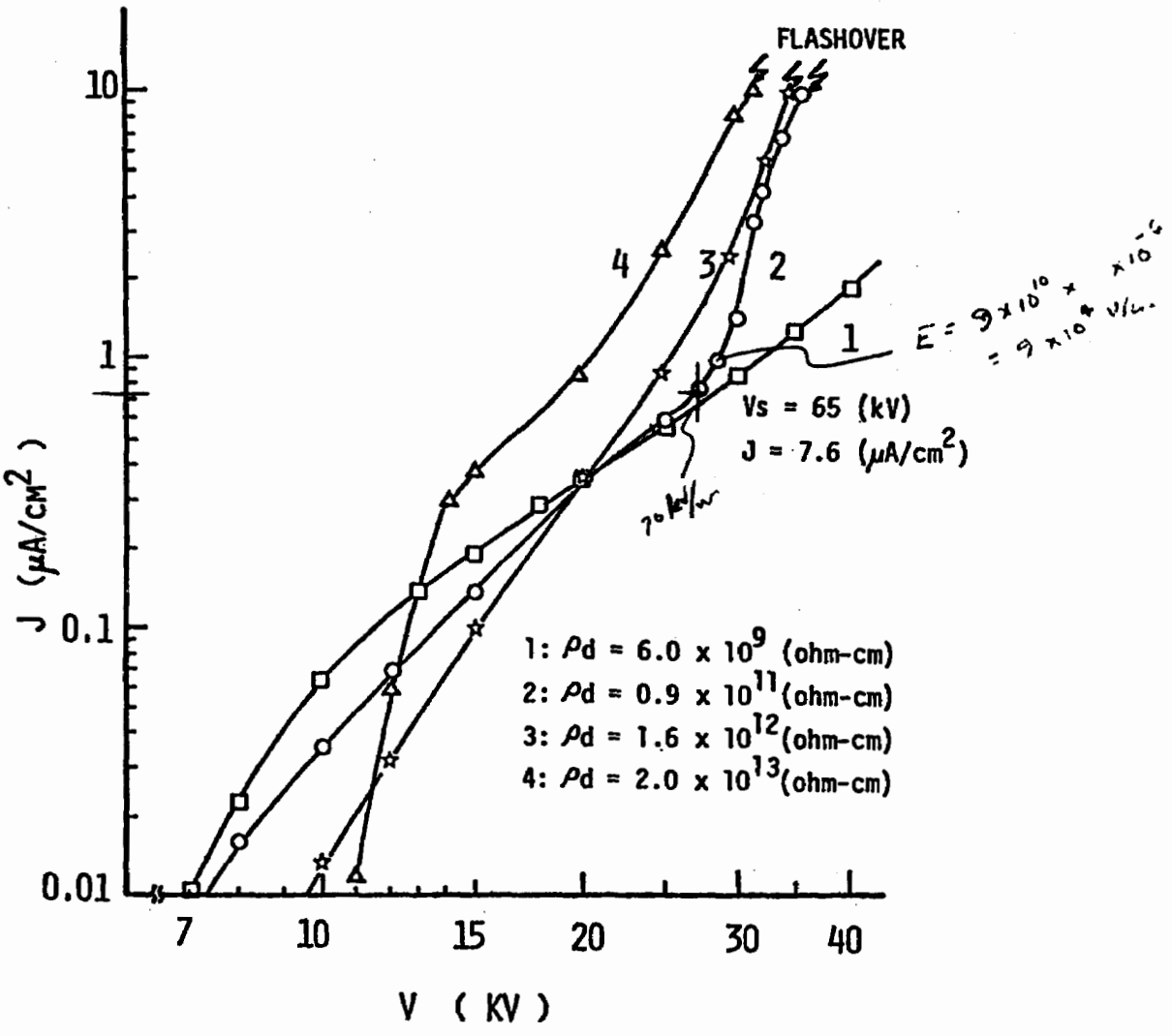
FLASHOVER
10
1
0.1
0.01
J (μA/cm²)
4
3
2
1
Vs = 65 (kV)
J = 7.6 (μA/cm²)
1: ρd = 6.0 x 10⁹ (ohm-cm)
2: ρd = 0.9 x 10¹¹ (ohm-cm)
3: ρd = 1.6 x 10¹² (ohm-cm)
4: ρd = 2.0 x 10¹³ (ohm-cm)
7
10
15
20
30
40
V (KV)

Figure 8

(a) $\rho_d = 0.9 \times 10^{11}$ (ohm-cm)
J = 3.2 ($\mu A/cm^2$)

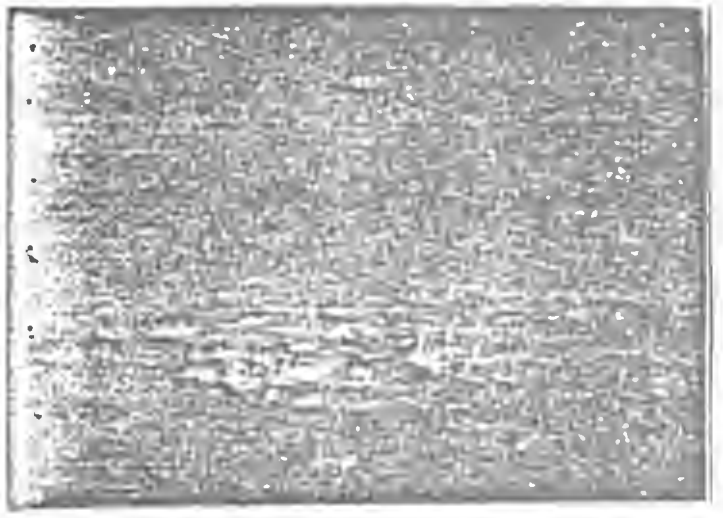

(b) $\rho_d = 1.6 \times 10^{12}$ (ohm-cm)
J = 5.5 ($\mu A/cm^2$)

(c) $\rho_d = 2.0 \times 10^{13}$ (ohm-cm)
J = 2.2 ($\mu A/cm^2$)

Figure 9

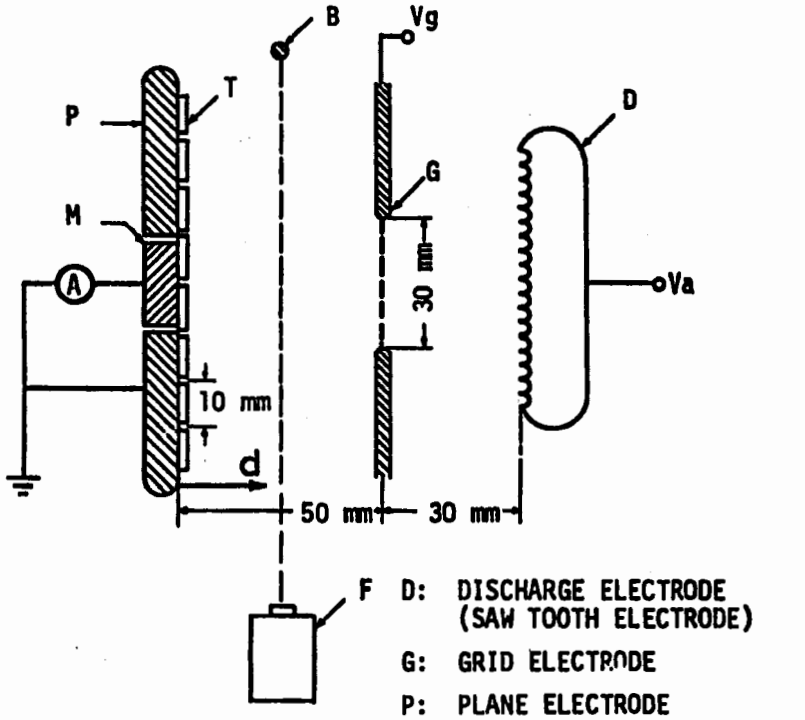

Figure 10 (modified)

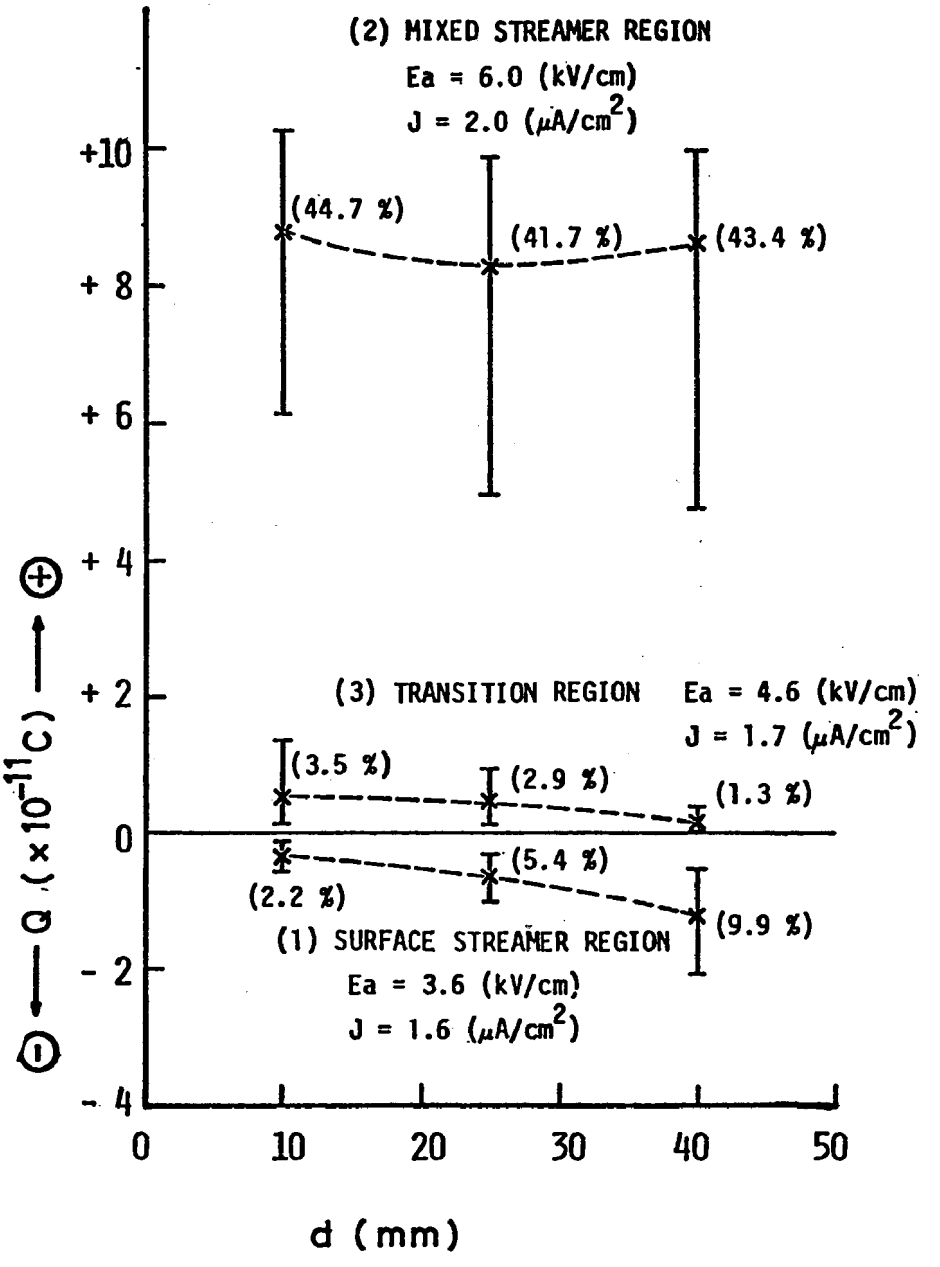
(2) MIXED STREAMER REGION
Ea = 6.0 (kV/cm)
J = 2.0 (μA/cm²)
(44.7 %)
(41.7 %)
(43.4 %)
(3) TRANSITION REGION
Ea = 4.6 (kV/cm)
J = 1.7 (μA/cm²)
(3.5 %)
(2.9 %)
(1.3 %)
(2.2 %)
(5.4 %)
(9.9 %)
(1) SURFACE STREAMER REGION
Ea = 3.6 (kV/cm)
J = 1.6 (μA/cm²)
+10
+ 8
+ 6
+ 4
+ 2
0
- 2
- 4
⊖ — Q (×10⁻¹¹C) — ⊕
①
0
10
20
30
40
50
d (mm)

Figure 11

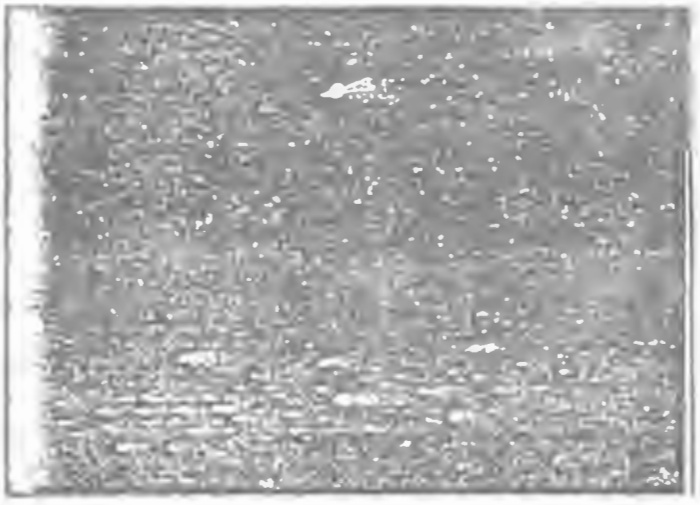

Figure 12

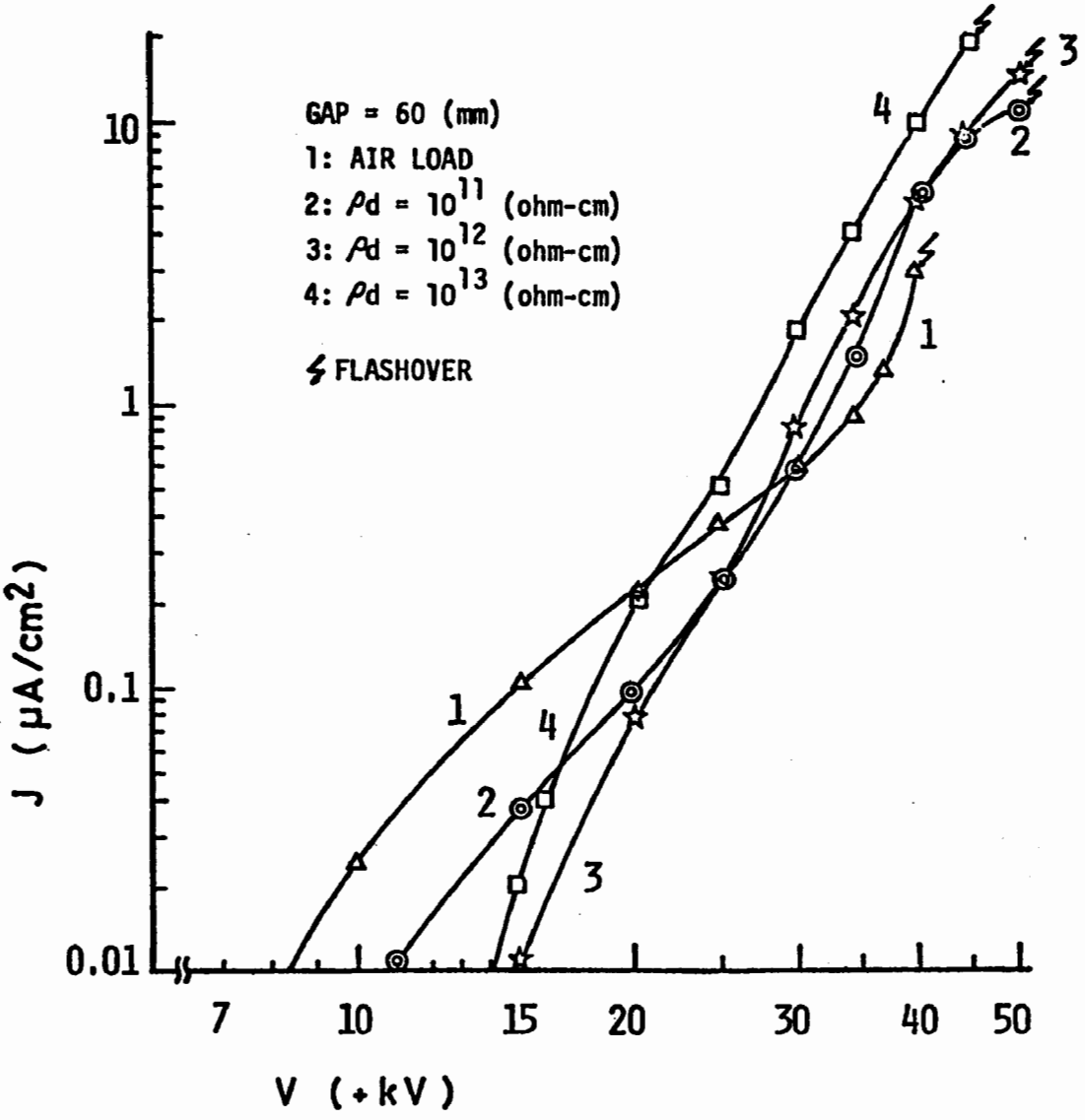
GAP = 60 (mm)
1: AIR LOAD
2: ρd = 10^11 (ohm-cm)
3: ρd = 10^12 (ohm-cm)
4: ρd = 10^13 (ohm-cm)
FLASHOVER
J (μA/cm²)
10
1
0.1
0.01
7
10
15
20
30
40
50
V (+kV)

Figure 13

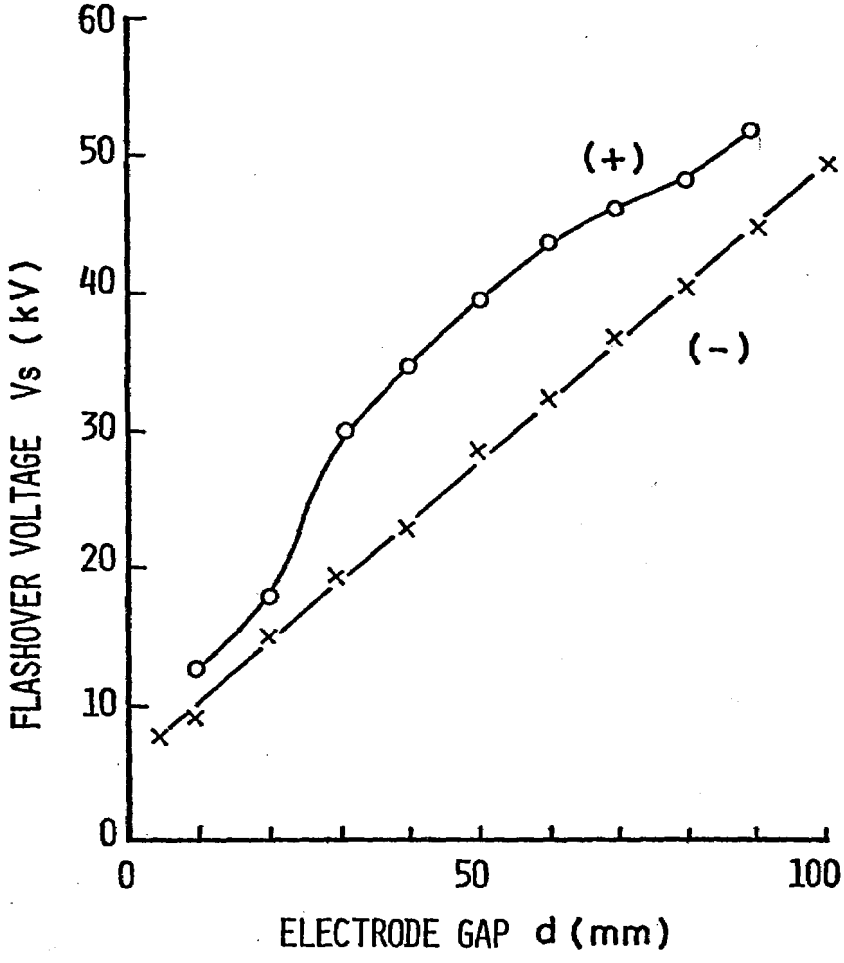
60
50
40
30
20
10
0
FLASHOVER VOLTAGE Vs (kV)
(+)
(-)
0
50
100
ELECTRODE GAP d (mm)

Figure 14

Figure caption

Fig.1 Electrode system for studying back discharge

Fig.2 Voltage-current curves under back discharge condition for different values of breakdown field strength
(A pair of glass plates, each having a single pinhole; sample resistivity $\rho_d = 6 \times 10^{11}$ ohm-cm)

Fig.3 Current wave forms and modes of back discharge

Fig.4 Electrode system for studying the effects of vertical field and current

Fig.5 Voltage-current density curves for different values of grid potential Vg (ref. Fig.4)

Fig.6 Effect of tangential field and current density on mode of back discharge
(a) Mode diagram in field-current domain
(b) Photograph of back discharge in surface streamer region (IV)
($Ea = 4.0$ kV/cm, $J = 5.0 \times 10^{-7}$ A/cm^2)

Fig.7 Effect of tangential field on back discharge in the mixed streamer mode
(A pair of glass plates, each having a single pinhole. Electrode gap = 50 mm)

Fig.8 Effect of dust resistivity ρ_d on voltage-current density curves under back discharge condition when negative corona is used
(Tissue paper, 1.0 mm in thickness)

Fig.9 Effect of dust resistivity on back discharge mode
(Tissue paper)

Fig.10 Electrode system for measuring particle charging

Fig.11 Saturation charge v.s. position d for different back discharge modes

Fig.12 Back discharge under positive corona point
(Tissue paper, V = +40 kV, $J = 2.8 \times 10^{-6}$ A/cm^2, $\rho_d = 10^{13}$ ohm-cm)

Fig.13 Voltage-current density curves under back discharge condition when positive corona is used
(Tissue paper, 1.0 mm in thickness)

Fig.14 Flashover voltage v.s. gap distance under back discharge condition with positive and negative coronas
(Tissue paper, $\rho_d = 1.2 \times 10^{11}$ ohm-cm, 1.0 mm in thickness)

Proc. 4th Int. Clean Air Congress
Paper No. V-52 (May 1977, Tokyo)

BACK DISCHARGE PHENOMENA IN BIAS CONTROLLED PULSE CHARGING SYSTEM

Phénomène de décharge de Back dans le système de chargement préventif à pulsations contrôlées

MASUDA, S. and DOI, I.
Department of Electrical Engineering, University of Tokyo
Tokyo, Japan

HATTORI, I. and SHIBUYA, A.
Ishikawajima-Harima Heavy Industries Company Limited
Tokyo, Japan

INTRODUCTION

Recently an emphasis is given in the field of electrostatic precipitation to the solution of back discharge. As is known, this phenomena occurs when the apparent dust resistivity of the deposited layer upon the collecting electrode exceeds about 5×10^{10} ohm-cm. When it occurs, many troublesome problems arise in the precipitation process, such as an excessive sparking hindering the increase of voltage and the decrease in particle charge owing to the ions of opposite polarity emitted from the back discharge points, hence reducing largely the collecting performance.

In principle, a technical solution lies in meeting the conditions to avoid the occurrence of back discharge phenomena, such that the apparent field strength E_d inside the dust layer given as the product of current density i_d and its dust layer resistivity ρ_d does not exceed its breakdown strength E_{ds}[1],

$$E_d = i_d \times \rho_d < E_{ds} \qquad (1)$$

The field strength E_{ds}, evidently is uncontrollable and the reduction of i_d, so far as the conventional electrode system is used, can only be realized by lowering of the main field strength E, which however, should be kept as high as possible to obtain the highest performance. Therefore, a solution of this problems with a purely electrical methods, requires to devise some means of controlling the current density i_d independently of E. Lüthi proposed one of such means by adding an additional third electrode near to the discharge electrode and applying a pulse voltage therebetween[2]. The authors improved this method by adding a dc bias voltage in series to the pulse voltage source, which was called "bias-controlled pulse charging system"[3]. In these systems, the intensity of the current density can be controlled by pulse width, repetition frequency, and the applied pulse height. Owing to a very high ion density from pulsive corona, the ion cloud expands very quickly during its migration towards a collecting electrode, so that the distribution of current there becomes uniform. The role of the dc bias voltage is to enable the use of an arbitrary electrode shape and a large discharge to third electrodes spacing, as well as to provide a wide flexibility for the fluctuation in operating conditions.

During the course of development of the author's system, it became clear that, apart from the theoretical initiation condition of back discharge given by unequality (1), the practical condition for starting of visible back discharge was also governed by E. This starting of visible back discharge can be assumed as the beginning of the true performance drop. Hence, the critical values of current and main voltage at the starting of visible back discharge in the pulse charging system were measured for dust resistivity range of 10^{11}—10^{14} ohm-cm. Secondly, the results obtained at a pilot plant were compared with those of laboratory measurements.

I. EXPERIMENTAL APPARATUS

The electrode system used in this experiment, having a construction similar to that used in the pilot plant, is shown in Fig. 1. It is constituted by two large grounded parallel plates serving as counter electrodes. A high dc voltage is applied between the third and counter electrodes to produces the main field. A barbed discharge electrode is located midst between a pair of third electrodes, and a pulse voltage is applied therebetween.

The whole electrode system is placed inside a large humidity controlled chamber. Instead of dust layer, a towel paper is attached on the counter electrode. The resistivity of the sample layer can very effectively be changed within a broad range of 10^{11}—10^{14} ohm-cm by controlling air relative humidity in this chamber.

The experiments are carried out under NTP.

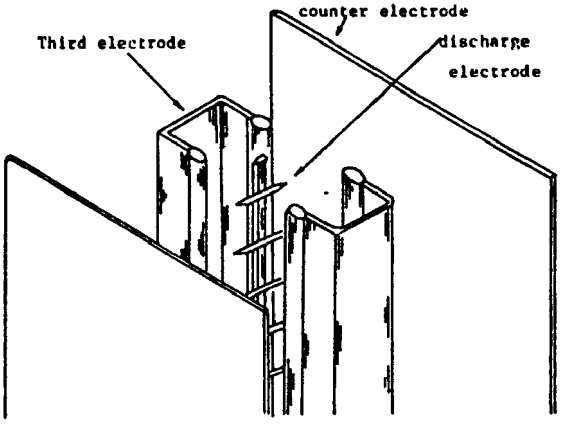

Fig. 1 Experimental apparatus for bias-controlled pulse charging system

II. SPECIALITIES IN BEHAVIOR OF BACK DISCHARGE

The start and mode of visible back discharge are governed by sample resistivity ρ_d, pulse width τ, pulse repetition frequency f, pulse height V_p, and main dc voltage V_c. The effect of E and i are contained implicitly in these results. It is found that behaviors of back discharge in the pulse charging system is largely different from those under a conventional electrode system. Hence, they are studied in detail.

2.1 Effect of Dust Resistivity

Among the effects of various factors described above, that of ρ_d is the most essential. In this pulse charging system, the visible back discharge does not occur normally unless ρ_d exceeds about 10^{13} ohm-cm, when $V_c \leq 100$ kv, $V_p \leq 30$ kv, and $f > 10$ Hz, duty cycle = 0.1. However, even in this range, random back discharge exceptionally occurs very rarely. It starts with the appearance of an unstable glow on the sample surface from which space streamers suddenly develop and turn to a flashover. When the frequency is high or pulse width large, the occurrence of back discharge becomes more frequent, but the starting condition becomes more obscure. The situation changes completely when the sample resistivity exceeds 10^{13} ohm-cm. In this case, with the initiation of back discharge, a very stable glow appears at first on the sample surface. With the increase in the dc voltage, a spot like glow points appear in the sample layer, their number increases, and finally, streamers occur toward the discharge electrode, bridging across the electrode gap. But these streamers are very hard to turn flashover in contrast to those under $\rho_d < 10^{13}$ ohm-cm. An interesting phenomena occurring in the resistivity range higher than 10^{13} ohm-cm is that streams jump from points to points over the whole sample surface. When the sample resistivity exceeds 10^{14} ohm-cm, a very noticeable phenomena starts to occur, such that back discharge also appears on the third electrode if it is covered by the layer. This back discharge appears only when the field strength E is sufficiently high so that breakdown of the layer on the third electrode can take place owing to the oncoming positive ions from the counter electrode. Also in the resistivity range beyond this order, if the main field strength E is sufficient enough, a feeble glow-like back discharge becomes possible to occur on the sample layer on counter electrode, even by the dark current, even without supply of pulse current.

2.2 Effects of Pulse Width and its Repetition Frequency

Pulse width and its repetition frequency have also an appreciable effect on the initiation and mode of back discharge. Back discharge becomes more active with the increase in pulse widths. The increase in pulse repetition frequency and pulse height have also the same effect, and these tendencies are observed in the whole range of sample resistivity investigated. For larger pulse widths or higher repetition frequencies more streamers develop toward the discharge electrode. These effects are most pronouncedly observable when pulse width is raised, followed by the increase in pulse repetition frequency, whereas the effect of pulse height was lowest among them.

III. CRITICAL VOLTAGE AND CURRENT FOR BACK DISCHARGE INITIATION

The visible back discharge starts, depending upon the sample resistivity ρ_d, at a certain critical current density i which, however, varies as the function of the main field strength E. The magnitude of i determines the charging rate, whereas that of E governs the particle saturation charge and Coulomb force. Hence, the utility limit of this charging system is to be judged from the critical values of i and E at which the visible back discharge initiates. Therefore the critical values of the main dc voltage and pulse current, V_{cc} and I_c, are measured for respective value of ρ_d, where the values of τ, f, and V_p are changed as parameters.

As described already, back discharge occurs very rarely when $\rho_d < 10^{13}$ ohm-cm. When the resistivity ρ_d is in the order of 10^{11} ohm-cm no appreciable difference is observed with the change of these parameters. In the Figs. 2(a) and (b) are shown the relationship between voltage V_{cc} and I_c for $\rho_d = (1.13 \sim 1.80) \times 10^{12}$ ohm-cm where f = 100 Hz, and V_p = 10 and 25 kv. A critical voltage V_{cc} as high as 50–80 kv can be attained for 20 cm spacing between discharge and counter electrodes, and zero bias voltage. It should be noted that the difference in the magnitude of V_p results in a large changes in $V_{cc}-I_c$ characteristics. This change occurs only when f>100 Hz. In general, the increase in ρ_d results in a decrease in V_{cc}. So

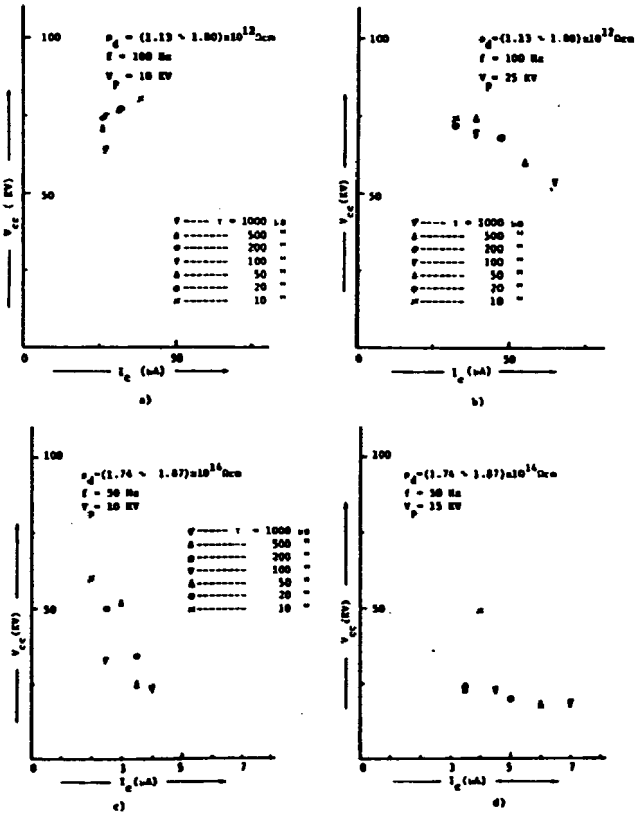

Fig. 2 Relationship between critical voltage V_{cc} and critical current I_c

far as f<100 Hz, the characteristic of Fig. 2(a) remains unchanged until ρ_d becomes about 10^{13} ohm-cm, although the magnitudes of each plot changes. If ρ_d exceeds about 10^{14} ohm-cm, back discharge becomes extremely easier to occur, and the drooping characteristics always appears independent of V_p and f, as shown in Figs. 2(c) and (d). The magnitudes of both V_{cc} and I_c become extremely low.

Generally the use of a narrow pulse width τ and a low pulse height V_p is preferable, because a high critical voltage V_{cc} is obtainable in this case. Under the conditions of this experiment, the highest value of V_{cc} is obtained when τ is reduced to its minimum of 10~20 μs. In this case V_{cc} = 50 kv is obtainable even when ρ_d is as high as 10^{14} ohm-cm.

It can be concluded that, with the use of the pulse charging system, back discharge can be very effectively avoided when a sufficiently narrow pulse width and low pulse height are used.

IV. RESULTS IN FIELD TEST

The above results were confirmed in a pilot plant test performed at the exit of an electrostatic precipitator located at an iron ore sintering furnace. The pilot plant consists of a combination of a pulse charging zone identical to that shown in Fig. 1 and a collecting zone out of the electrostatic screen, the details of which were reported elsewhere[3]. There were two stages of this combination in series, and the gas transit time through a single charging zone was about 0.4 sec. The dust consisted mainly of iron oxide (Fe_2O_3) particles and contained small amounts of salts of alkaline metals and alkaline earth metals, by several percents in total. The resistivity of the dust layer was very high, in the range of 10^{13}–10^{14} ohm-cm under operating conditions. The particle size of dust was extremely small, and more than 70 percents were in the range less than 1 μm in diameter. This was because most of the coaser particles had been collected in the preceding conventional precipitator. Instead of a pulse voltage a sinusoidal voltage was applied between the discharge and third electrodes, so that its equivalent pulse width τ_e was taken as a half period.

Fig. 3 shows the relationship between the peak voltage V_p and the current I flowing into the counter electrodes of one charging zone, where the main dc voltage V_c between the third and the counter electrodes was kept at 40 kv and the frequency of the ac voltage was either 62.5 or 50 Hz. The curves (1) and (2) show the V_p–I characteristics when the thickness of dust layer deposited on the counter electrodes was large. The equivalent pulse width τ_e for curve (1) is 10 ms, whereas that for curve (2) 1 ms. The sharp rise in curve (1) clearly shows the occurrence of a severe back discharge. This could, however, be amended to a great extent by reducing the equivalent pulse width τ_e to 1 ms as indicated by curve (2). The curves (3) and (4) indicate the characteristics when the dust layer thickness was kept very small. These two curves show a remarkable effect of decreasing the layer thickness as a counter measure to back discharge. The effect of decrease in pulse width can also be observed here. The characteristics of

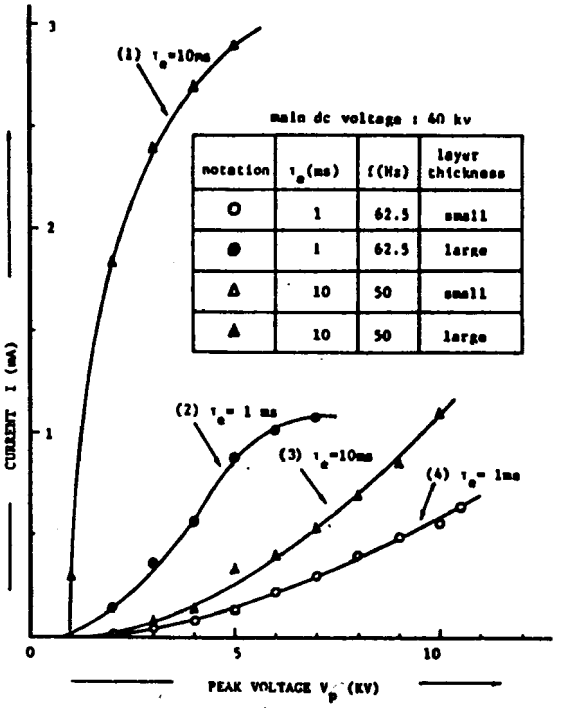

Fig. 3 Effect of peak voltage V_p and equivalent pulse width τ_e on current I

curve (4) is a normal one without back discharge.

The collection performance of 65–80 percent could be achieved, which exceeded the required level for an after collector to be installed. This performance level corresponds to a very satisfactory figure, if the extremely high resistivity and small size of dust as well as the very short treating time of about 1 s in total within active zones be taken into account.

ACKNOWLEDGEMENT

Fellowship of the Fundação de Amparo a Pesquisa do Estado de São Paulo (FAPESP), Brazil, given to one of the authors (Ioshiaki Doi) is highly appreciated.

REFERENCES

1) Masuda, S., Mizuno, A. & Akutsu, K., "Initiation and Mode of Back Discharge," J. Electrostatics (to be published).
2) Lüthi, J. E., Grundlagen Zur Elektrostatischen Abscheidung von hochohmigen Stauben, Dissertation ETH-Zurich, No. 3924 (1967).
3) Masuda, S., Doi, I., Aoyama, M. & Shibuya, A., "Bias-Controlled Pulse Charging System for Electrostatic Precipitator," Staub-Reihalt, *Luft* 36, 1, 19 (1976).

Reprinted from

Journal of Electrostatics, 2 (1976/1977) 375—396
© Elsevier Scientific Publishing Company, Amsterdam — Printed in The Netherlands
(Reprinted with permission)

LIGHT MEASUREMENT OF BACK DISCHARGE

SENICHI MASUDA and AKIRA MIZUNO

Department of Electrical Engineering, University of Tokyo, 7—3—1, Hongo, Bunkyo-Ku, Tokyo (Japan)

(Received January 19, 1977; in revised form April 7, 1977)

ELSEVIER SCIENTIFIC PUBLISHING COMPANY, AMSTERDAM

Journal of Electrostatics, 2 (1976/1977) 375—396
© Elsevier Scientific Publishing Company, Amsterdam — Printed in The Netherlands

LIGHT MEASUREMENT OF BACK DISCHARGE

SENICHI MASUDA and AKIRA MIZUNO

Department of Electrical Engineering, University of Tokyo, 7—3—1, Hongo, Bunkyo-Ku, Tokyo (Japan)

(Received January 19, 1977; in revised form April 7, 1977)

Summary

Light measurements of back discharge are made under negative d.c. high voltage and negative pulse high voltage application, with the aid of a photomultiplier tube and an image convertor camera connected to an image intensifier. The light signal of back discharge in the mixed streamer mode indicates that it consists of two parts, the primary light wave rising very rapidly, and the secondary light wave rising more slowly. The former proceeds into space while the latter proceeds along the layer surface. In the space streamer mode, the primary light wave is dominant and the secondary light wave is very weak. When a sufficiently high pulse voltage is applied under lower pressure, back discharge is triggered by free electrons supplied from the needle electrode. As the pressure is increased, an abrupt change in the triggering carriers occurs from electrons to negative ions.

1. Introduction

Back discharge is a phenomenon which impairs the collection performance of electrostatic precipitators. It is an abnormal discharge starting from the dust layer deposited on the collecting electrode and triggered by its breakdown. The authors studied the initiation condition and mode of back discharge as well as its flashover voltage, and clarified the effects of various parameters affecting them, as reported separately [1,2]. Studies were further made on the propagation of back discharge in the streamer mode and its triggering process by the use of a light measurement technique. As reported separately [3], particles are ejected at back discharge points from the layer, so that, after a short transient period of time, pinholes are formed in the layer. Hence, through these studies, the precipitated layer was modelled by the insulating discs having a 0.5 mm pinhole backed by a metal electrode.

2. Experimental apparatus

2.1 Electrode system

A needle-to-plane electrode system is used with a gap d of 50 mm or 20 mm, as shown in Fig. 1. A glass plate, having resistivity ρ_d of 6×10^{11} ohm.cm, 2.0-mm thickness, and a pinhole of 0.5-mm diameter, is located on the plane electrode as a test layer. This is to improve reproducibility of the phenomena.

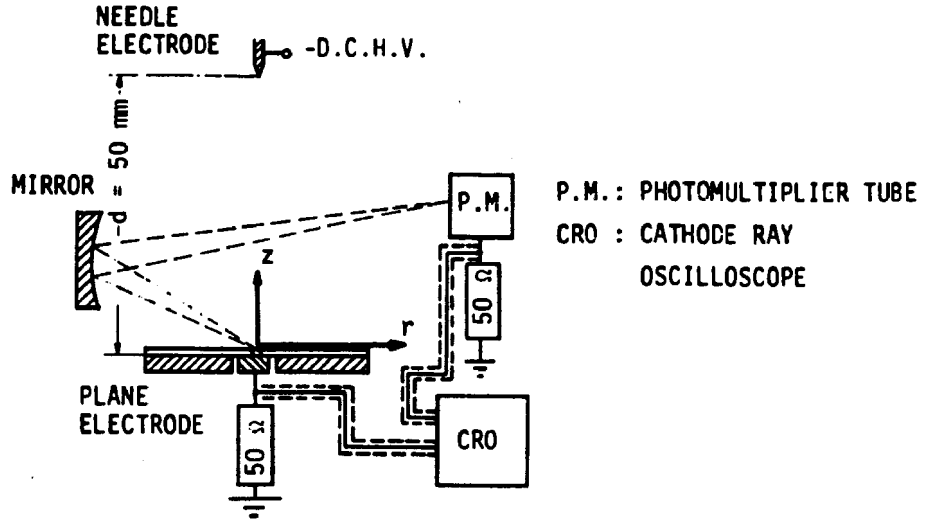

(a) MEASURING SYSTEM FOR STUDYING
BACK DISCHARGE STREAMER PROPAGATION

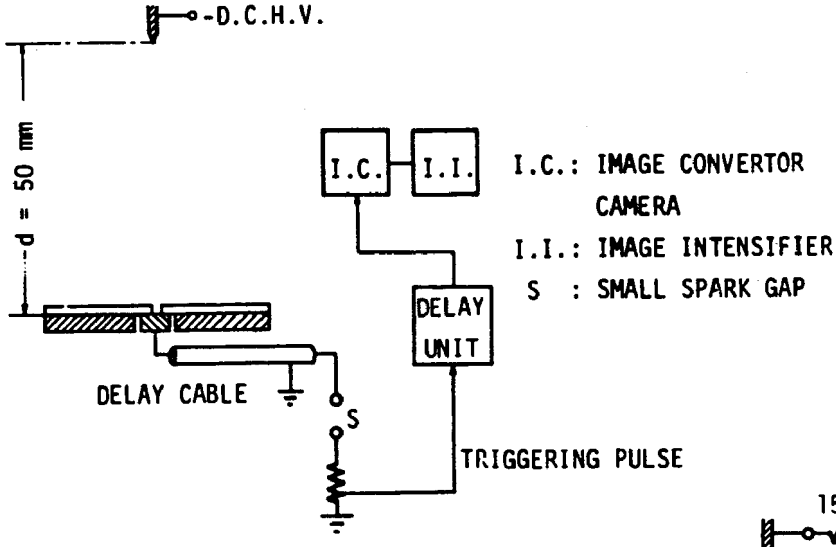

(b) TRIGGERING CIRCUIT FOR IMAGE
CONVERTOR CAMERA

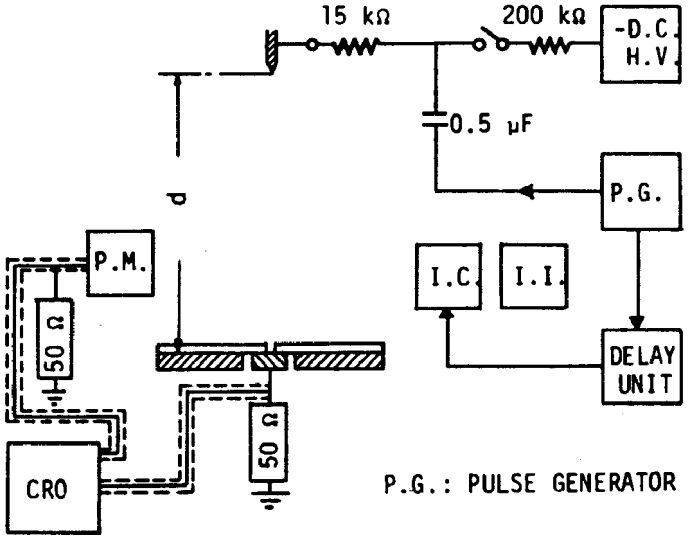

(c) TRIGGERING CIRCUIT FOR IMAGE

Fig.1. Experimental apparatus.

A mica plate, having ρ_d greater than 10^{15} ohm.cm, 0.20-mm thickness, and a pinhole of 0.5-mm diameter, is also used for the measurement with pulse high voltage. As reported separately, difference in sample resistivity does not affect the discharge in the gas space to be studied [2]. The plane electrode consists of measuring and guard electrodes.

2.2 Photomultiplier measurements

The light signal from a point inside the back discharge streamer is measured simultaneously with current. The light is focussed onto a slit in front of a photomultiplier tube, using a concave mirror as shown in Fig. 1(a). An area of 0.5-mm square at the measured point can be resolved. The measured point can be traversed by altering the position of the photomultiplier. The output resistance of the photomultiplier tube and the resistance for current waveform detection are 50 ohm, equal to the characteristic impedance of the cable used, so that distortion in wave-form is avoided. The input resistance of the dual beam oscilloscope (Tektronics 7844) is 50 ohm, and rise time of the measuring circuit is about 2 ns. The needle electrode is applied with a negative d.c. high voltage in this measurement. The effect of surface resistivity of the sample is studied by locating the electrode system inside a thermostat in which the humidity can also be controlled.

2.3 Streak photograph measurement

Propagation of the back discharge streamer is also measured by a streak photograph method using an image convertor camera (John Hadland, Ima—Con) combined with an image intensifier tube (EMI, type 9912) having a maximum gain of 10^6. Fluctuation in the period between successive back discharge pulses, especially when d.c. high voltage is used, is very large (of the order of 100 μs) compared to the duration of the phenomenon (shorter than 1 μs). Therefore, two different triggering circuits are used to synchronize the image convertor camera accurately to the start of the back discharge to be observed. Figure 1 (b) shows the one which is used when d.c. high voltage is applied to the needle electrode. The measuring electrode is connected to one end of a delay cable, and its other end is grounded through a small spark gap. Then, the spark in the gap, caused by the increase in voltage at the measuring electrode, results in an earth potential appearing at the electrode after a certain delay time, so that back discharge is triggered. This spark signal is also fed to the image convertor camera so that it is completely synchronized to the phenomenon. In this measurement, the electrode system is located inside the thermostat. Figure 1(c) shows the second triggering circuit. A negative d.c. high voltage is applied so that a negative corona occurs at the needle electrode and a faint onset-glow [1] occurs at the sample. Then, a single or periodic negative pulse high voltage is applied superimposed to the negative d.c. voltage. After a certain formation time, the back discharge is triggered. The pulse signal is also fed to the image convertor camera. In order to study the triggering mechanism in more detail, the measurement is performed under

vacuum, using a pulsed high voltage alone. The circuit shown in Fig.1(c) is used also in this case, and the electrode system is located inside a vacuum chamber.

3. Results obtained

3.1 Negative d.c. high voltage application

Measurements are performed using a negative d.c. high voltage to be applied to the needle electrode, with the glass plate sample on the plane electrode.

3.1.1 Mixed streamer mode

The authors reported that back discharge in the form of surface streamer becomes dominant when the sample surface has a charge density σ_0 higher than about 5×10^{-9} C/cm^2 at the instant of breakdown, and a sufficiently high surface resistivity [1]. In the present experiment, the value of $\sigma_0 = \epsilon E_{ds}$ of the sample used is about 5×10^{-9} C/cm^2, where ϵ is the dielectric con-

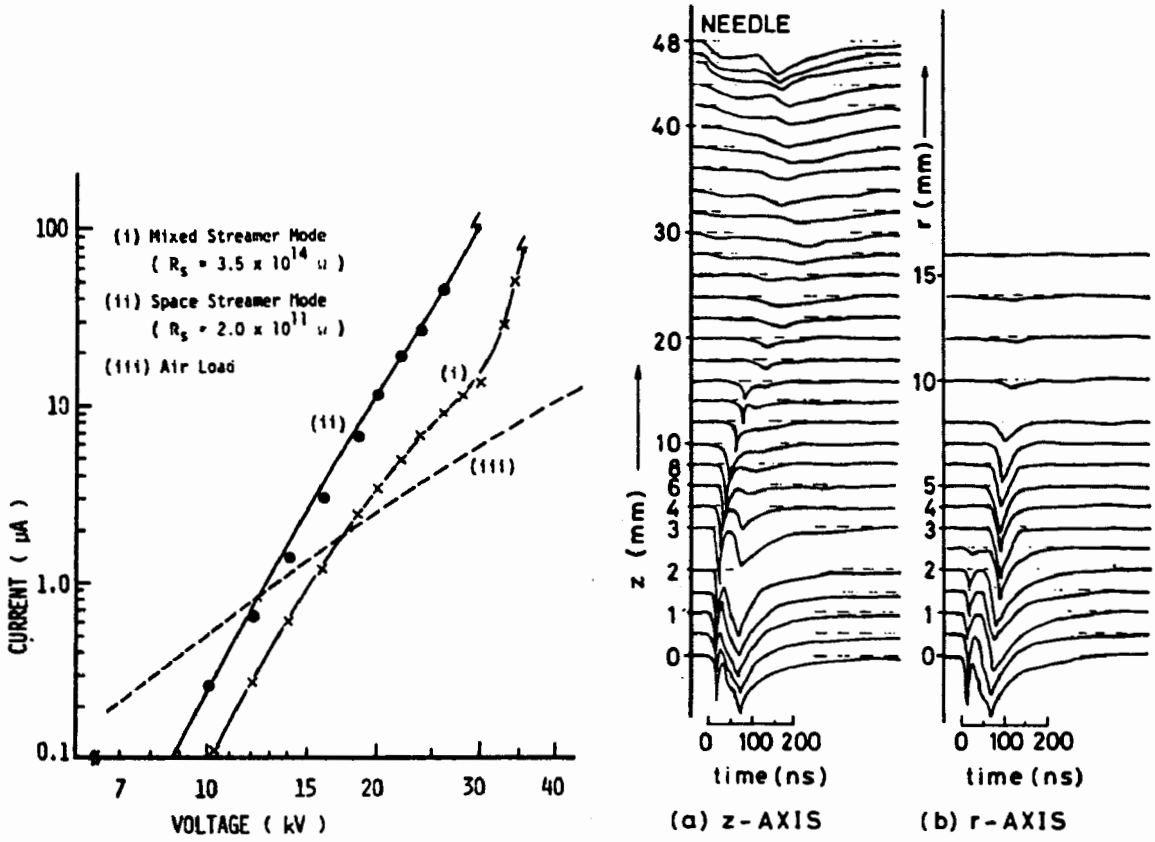

Fig.2. Voltage–current curves of back discharge for different modes. Sample: glass plate with a pinhole.

Fig.3. Change in light signal of back discharge in space (see Fig. 1(a)).

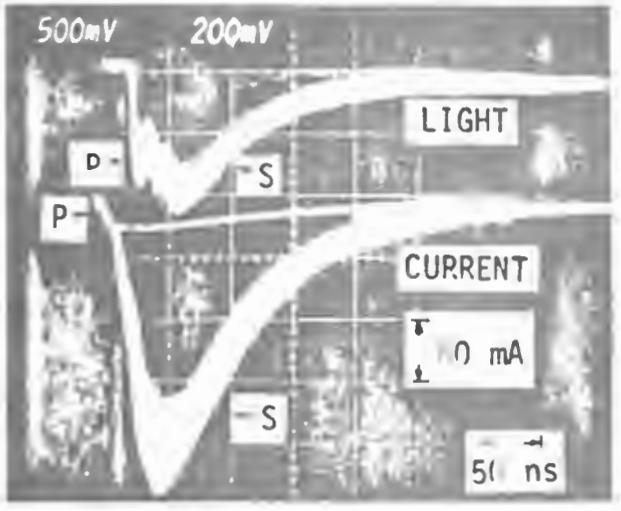

(a) LIGHT SIGNAL AT THE BREAKDOWN POINT
(z = 0, r = 0) AND CURRENT WAVEFORM
(V = -28 kV, I = 13 A)

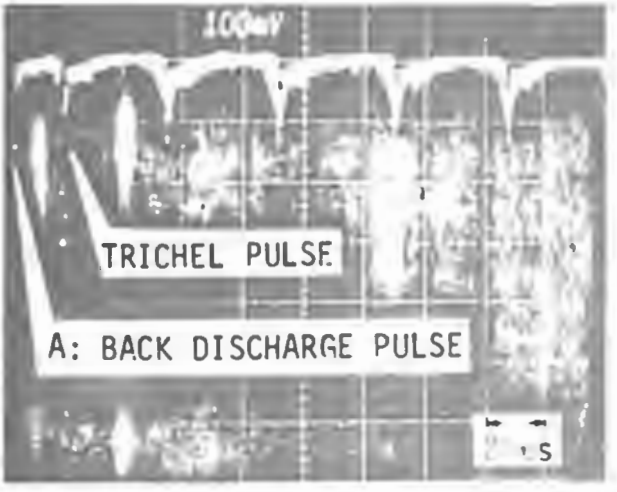

(b) LIGHT SIGNAL AT THE TIP OF THE
NEEDLE ELECTRODE (z = 48 mm)

Fig.4. Light and current waveform of d harge in the mixed streamer mode.

stant of the sample. When the surface resistivity R_s is set to 3.5×10^{14} ohm by reducing ambient humidity (R.H. = 20%, T = 40°C), both surface and space streamers occur to form the mixed streamer mode [1]. The following measurements are performed under these conditions of humidity, temperature and atmospheric pressure inside the thermostat.

A voltage—current characteristic in this case is shown by curve (i) in Fig.2. The light measurements described below are performed for the back discharge occurring when the applied voltage is −26 kV. The change in light signal in the normal direction z and in the tangential direction r are shown in Fig.3 (see Fig. 1(a)). The light signal at the breakdown point ($z = 0$, $r = 0$) shows that the back discharge pulse in the mixed streamer mode consists of two parts. There is a "primary light wave" which rises very rapidly and lasts about 20 ns, followed by a "secondary light wave" which rises more slowly and lasts about 200 ns. The former proceeds in the z-direction and the latter in the r-direction. The interval between the primary and secondary light waves, however, varies widely, depending upon the value of applied voltage and surface resistivity. It can be seen that the primary light wave advances towards the needle electrode with a speed of about 4×10^7 cm/s, while the secondary light wave propagates along the sample surface with a speed of about 2.5×10^7 cm/s. Figure 4(a) shows an example of the typical light and current waveforms of back discharge in the mixed streamer mode. The primary light wave corresponds to the first rise in current waveforms, as indicated by P in Fig.4(a), having a small pulse height and a charge content of $1—2 \times 10^{-9}$ C/pulse, as described in Section 3.1.2. The secondary light wave corresponds to the second rise in current, as indicated by S in Fig.4(a) which has a much larger pulse height and a charge content of $2—4 \times 10^{-8}$ C/pulse. Table 1 shows the charge content per pulse in this mode for various applied voltages. The charge content per pulse remains almost the same even when the applied voltage is changed, so that the change in current results from the change in the average repetition frequency of the back discharge pulse.

The light signal at the tip of the discharge electrode is shown in Fig.4 (b). The first pulse, indicated by A, occurs at the same instant as that for a back

TABLE 1

Charge per single back discharge pulse (mixed streamer mode)

Voltage (kV)	Q (C)	T_a (ms)	$I = Q/T_a$ (A)	I measured (A)
16	2.0×10^{-8}	60	0.34×10^{-6}	1.3×10^{-6}
18	2.0×10^{-8}	34—36	0.6×10^{-6}	2.5×10^{-6}
22	2.8×10^{-8}	12	2.4×10^{-6}	4.4×10^{-6}
25	3.0×10^{-8}	6.5	4.6×10^{-6}	8.0×10^{-6}
28	$2.8—3.6 \times 10^{-8}$	3.2—3.5	1.08×10^{-5}	1.3×10^{-5}

T_a: average pulse repetition period

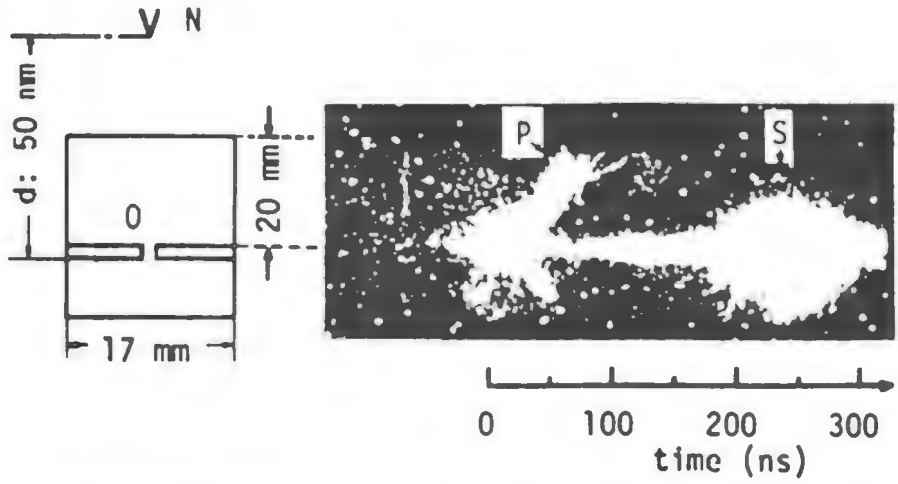

(a) STREAK PHOTOGRAPH OF PRIMARY AND SECONDARY LIGHT WAVES
(P:760 Torr, V:-28 kV, I:13 μA) (see Fig.1-b)

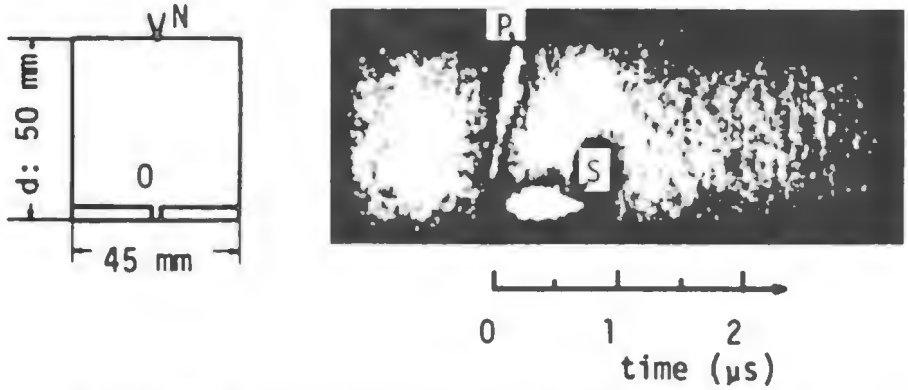

(b) BACK DISCHARGE TRIGGERED BY APPLYING PULSE HIGH VOLTAGE IN ADDITION TO -D.C. VOLTAGE
(P:410 Torr, Vp:-10 kV, τ_p:10 μs, D.C.:-15 kV)
(see Fig.1-c)

Fig.5. Streak photograph of back discharge in the mixed streamer mode. N: needle electrode, O: breakdown point, P: primary light wave, S: secondary light wave.

discharge pulse and has the same shape as the light signal shown in Fig.3 at z = 48 mm when the time scale is magnified. The other pulses in Fig.4(b) have an entirely different waveform which corresponds to that of the Trichel pulse.

Streak photographs taken by the method described in Section 2.3 are shown in Fig.5. Figure 5(a) is a side view obtained by the method in Fig.1(b). This photograph clearly shows the development of primary and secondary

light waves. Figure 5(b) is also a side view obtained by the method in Fig. 1(c) where pulsed high voltage is applied to the d.c. high voltage. In this case, the measurement is performed under P = 410 torr, because the triggering proves to be difficult under atmospheric pressure. Dry air is used inside a vacuum chamber so that the surface resistivity can be kept sufficiently high and the mixed streamer mode appears. These photographs indicate that, once the onset-glow mode has turned into the streamer mode, the continuous glow disappears and the streamers are triggered each time by the layer breakdown. The reproducibility can be much improved by the method of Fig. 1(c). As a result, it is found that secondary light wave appears at the instant when the primary light wave nears the discharge electrode. It should also be pointed out that the pulse repetition period in the mixed streamer mode is about two orders of magnitude larger than that in the space streamer mode to be described later.

3.1.2 Space streamer mode

As reported separately, back discharge in the space streamer mode appears when the vertical field strength exceeds about 5 kV/cm and the value of $\sigma_0 = \epsilon E_{ds}$ is comparatively small [1]. In this experiment, however, it is found that, as long as the surface resistivity R_s is low, the space streamer mode occurs even though the value of σ_0 exceeds about 5×10^{-9} C/cm^2. The voltage—current characteristic in this case when $R_s = 2 \times 10^{11}$ ohm is shown by curve (ii) in Fig.2 and the light signal from the breakdown point, and current waveform, are shown in Fig. 6(a).

In this mode, the secondary light emitting spot is very weak and occurs randomly so that it cannot clearly be observed by the photomultiplier. The charge content per single current pulse is about 10^{-9} C/pulse. The repetition period, however, is much smaller (50—300 μs) than that in the mixed streamer mode, and hence the current is several times higher than that in the latter mode (see Fig.2). Figure 6(b) shows a streak photograph of back discharge in side view in the space streamer mode, which is taken under P = 410 torr. The light under atmospheric pressure is too weak to be seen even with the aid of the image intensifier, unless the applied d.c. high voltage is excessively high. This high d.c. voltage causes an instability in the streamer which results in random sparking. In addition, its repetition period under atmospheric pressure becomes larger than the time frame of the streak camera. All these problems can be solved when the pressure is lowered to the value used of 410 torr. In this case, room air (R.H. = 76%, T = 20°C) is also used in the vacuum chamber so that a sufficiently low value of R_s is obtained. Three successive back discharge glows are seen in the photograph. It should be noted that glow at the needle electrode does not appear at the time when back discharge glow disappears. It can be seen on the sample side that the space streamers occur at first, followed by a faint glow at the breakdown point which corresponds to the weak secondary light wave described above.

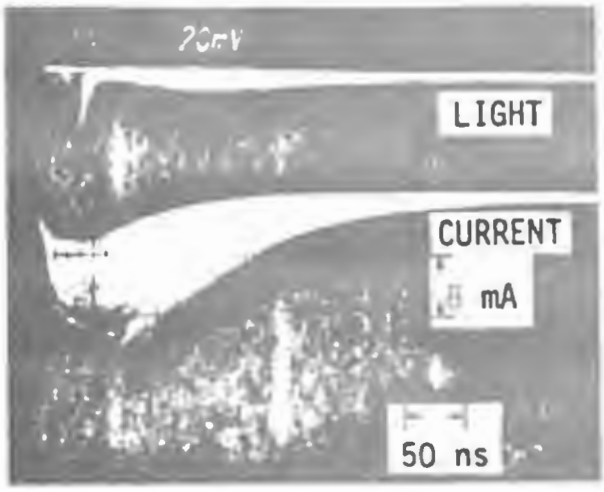

(a) LIGHT SIGNAL FROM THE BREAKDOWN POINT
AND CURRENT WAVEFORM
(P: 760 Torr, V: -22 kV, I: 12 μA)

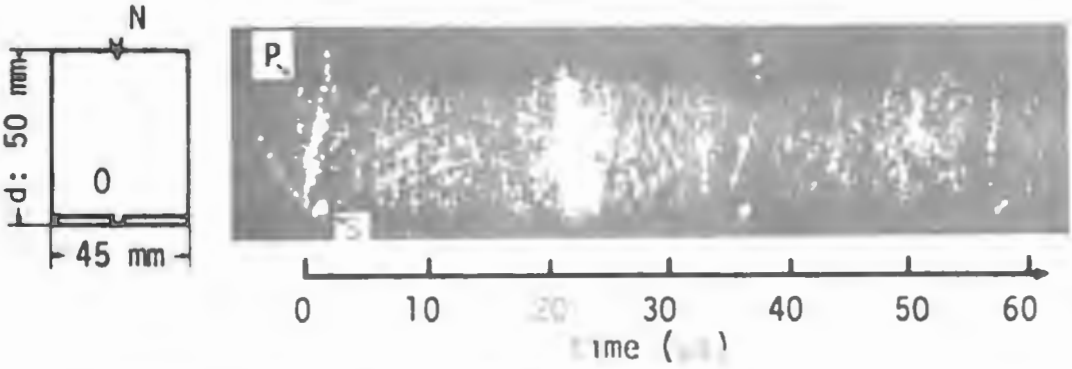

(b) STREAK PHOTOGRAPH FROM SIDE VIEW
(P: 410 Torr, V: -10 kV)

Fig.6. Light and current pulse and streak photograph of back discharge in the space streamer mode

3.1.3 Flashover

The flashover from back discharge to the streamer mode is studied by the streak photograph method described in Fig.1(c), where pulsed high voltage (V_p = −10 kV, τ_p = 1.0 ms) is applied to the discharge voltage of −10 kV. Room air (R.H. – 76%, T = 20°C) is used inside the vacuum chamber as before. The light signal at the breakdown point and current waveform are shown in Fig. 7(a). There are two stages, A and B, the former corresponding to the back discharge pulse at its initial stage, the latter to those at its final

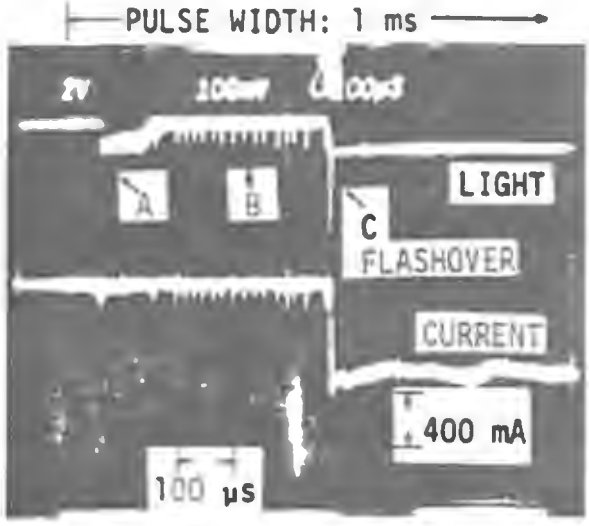

(a) LIGHT AND CURRENT SIGNALS AT FLASHOVER
(P: 410 Torr, Vp: -10 kV, τ_p: 1 ms, D.C.: -15 kV)

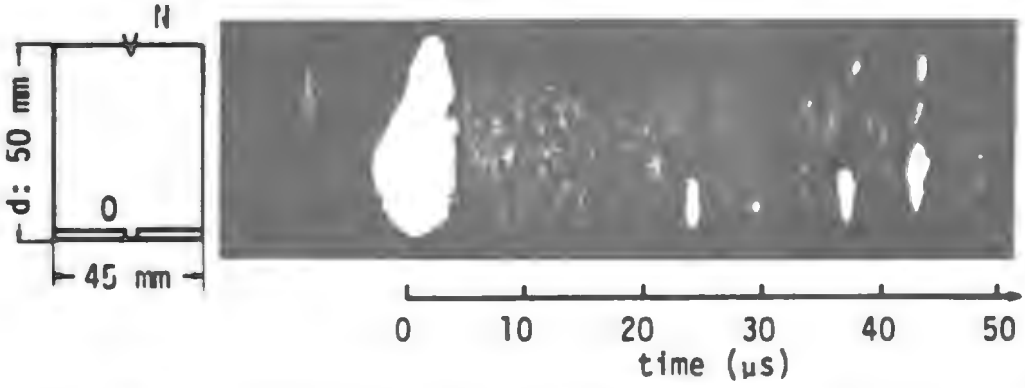

(b) BACK DISCHARGE TRIGGERED BY APPLYING PULSE HIGH VOLTAGE

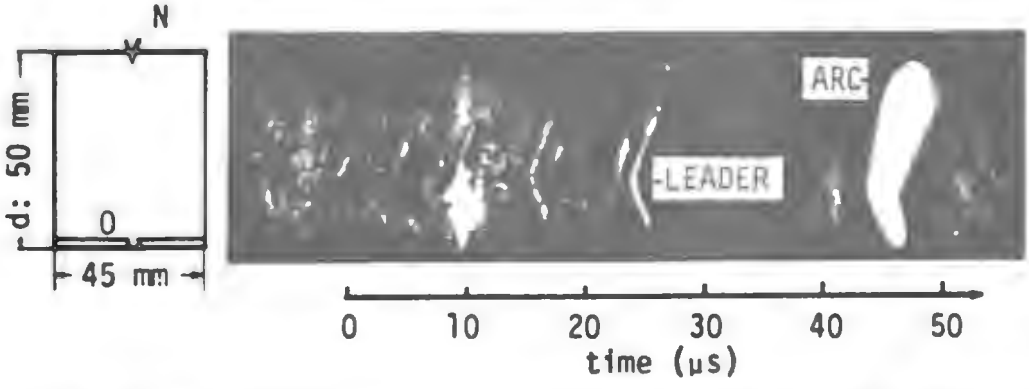

(c) STREAK PHOTOGRAPH OF FLASHOVER CAUSED BY BACK DISCHARGE FROM SIDE VIEW

Fig.7. Flashover caused by back discharge (see Fig. 1(c)).

stage. The large and continuous light signal in stage A is due to a saturation in the photomultiplier tube used. The streak photographs in stages A and B are shown in Fig.7(b) and (c), respectively, where the light intensity in the latter is reduced to one half of the former by an iris. When the pulsed voltage is applied, the back discharge in the space streamer mode is triggered after a certain formation time of about 50—100 μs. It should be noted that the first streamer is highly luminous owing to the full voltage appearing between two electrodes. This streamer disappears when the voltage stored in the capacitance between the electrodes falls. The following streamers are much weaker because the triggering of the streamers — the sample breakdown — could happen before the electrodes have been charged up to the source voltage. However, during the course of repeated streamer discharge, the streamer channel could be sufficiently heated up and localized to form a "leader" [4]. The leader proceeds along the streamer channel towards the discharge electrode, and finally turns into a flashover at point C, which should be taken as the high voltage arc in this case.

3.2 Negative pulse high voltage application

3.2.1 Streak photograph of back discharge

Streak photographs of back discharge are taken when a periodic negative pulsed high voltage having a square waveform is applied. The method described in Fig. 1(c) is used where the d.c. high voltage source is removed. Figure 8(a)(i) indicates the waveform of the pulse voltage used, and Fig. 8(a) (ii) its initial part. The pulse rise time is 0.5 μs, its height V_p is −25 kV, and its width τ_p (10 μs) is much longer than the time-scale of the phenomena observed. The electrode gap is 50 mm. A mica plate with a pinhole of 0.5-mm diameter and 0.2-mm thickness is used as the test layer. Figures 8(b)(i) and (ii) indicate the results obtained where the time-scale is changed. A corona glow appears at first at the needle electrode at least 500 ns after the application of the pulse voltage. Hence, the needle is applied with the full pulse voltage when the corona glow occurs. This glow lasts for about 100 ns, emitting electrons which will be attached to electro-negative gas molecules to form a dense negative space charge around the needle tip. The negative corona is thus quickly choked. After a delay time of 400—800 ns, the primary light wave of back discharge starts to occur, triggered by the accumulated negative charge on the sample layer. This delay time, which may be the transit time of the carriers from the needle to the sample layer, is too short to be explained by ion transit time, suggesting the role of electrons for triggering carriers in this case of pulse voltage application, as described in the next section. The propagation speed of the primary light wave is about 5×10^7 cm/s, and the secondary light wave appears again when the primary light wave approaches the needle electrode. Once the primary light wave reaches the needle electrode, a continuous second glow corona appears at its tip. Figure 8 (b) (ii) shows the photograph taken with a much lower

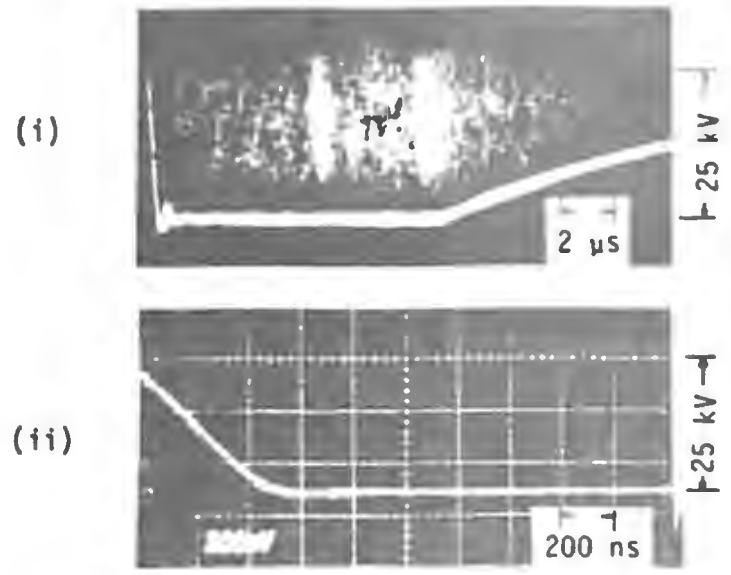

(a) WAVE FORM OF APPLIED PULSE HIGH VOLTAGE

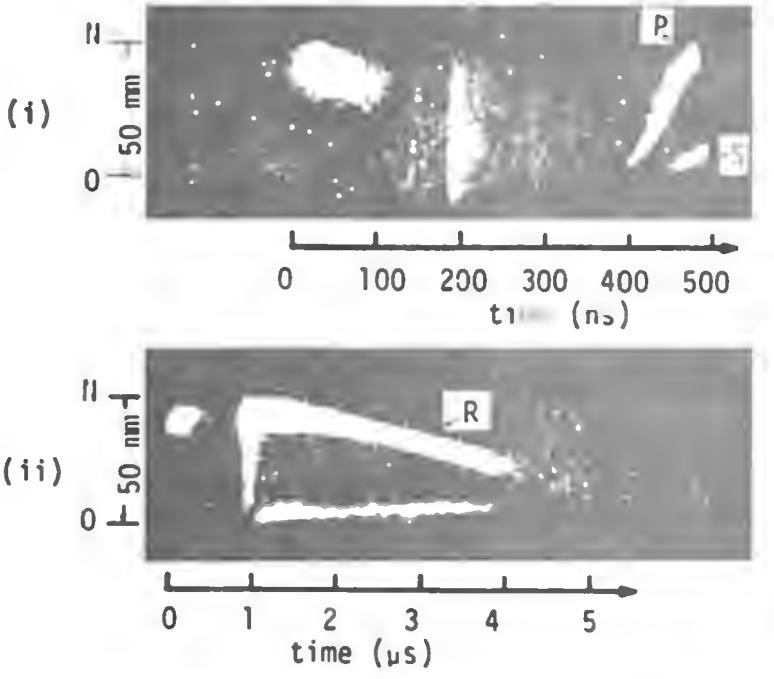

(b) STREAK PHOTOGRAPHS OF BACK DISCHARGE WITH PULSE HIGH VOLTAGE (see Fig.1-c)
(d: 50 mm, P: 170 Torr, Vp: -[illegible] kV, t_p: 10 μs, f: 10 Hz, mica plate with a pinhole)

Fig.8. Back discharge with pulse high voltage application P primary light wave, S: secondary light wave, R return light wave

streak speed. The second glow appearing at the needle electrode moves gradually towards the plane electrode with a speed of about 0.7×10^7 cm/s. This glow should be referred to as the "return light wave" [5]. When the voltage is further raised, both the secondary light wave and return light wave proceed into space to form an intensive glow in the middle of the gap and cause flashover as described later. The propagation velocity of the primary light wave and the intensity of the secondary light wave vary with the change in the pulse voltage as shown in Fig.9. The velocity of the primary light wave is about 5×10^7 cm/s for $V_p = -25$ kV, 3×10^7 cm/s for $V_p = -20$ kV, and 2×10^7 cm/s for $V_p = -15$ kV. The velocity of the primary light wave, as well as the intensity of the secondary light wave, increase as the voltage is raised. It should also be noted that the secondary glow at the needle tip disappears when the voltage is lowered.

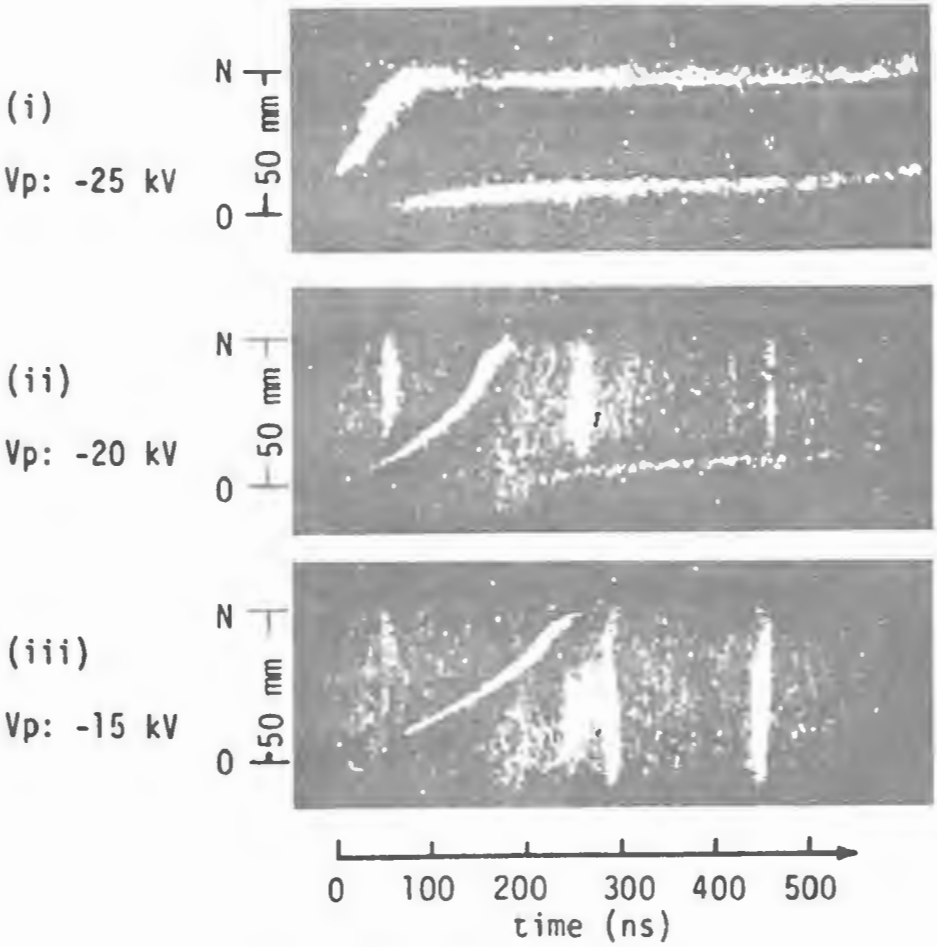

Fig.9. Streak photographs of back discharge with pulse. P: 160 torr, τ_p 10 μs, f: 10 Hz, sample: mica plate with a pinhole

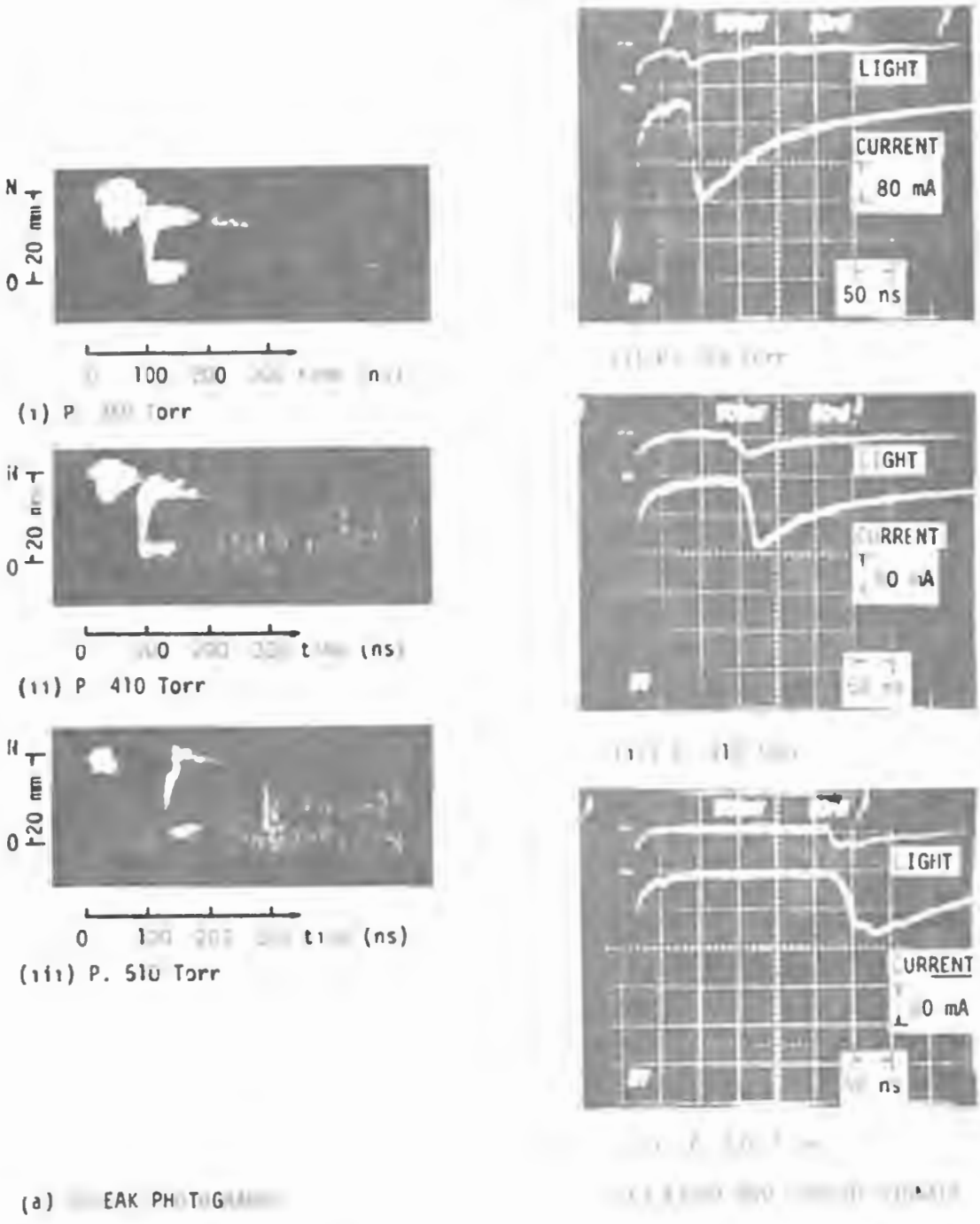

Fig.10 Change in t... time V_p — 20 kV ... mic... plate with a pinhol...

3.2.2 Triggering delay of back discharge and triggering carriers

There exists a triggering delay time τ_d from the first glow at the needle electrode to the initiation of back discharge. During this delay time, carriers are considered to migrate across the gap. Carriers are considered to be electrons because of an extremely high velocity estimated from d/τ_d. This value, estimated from Fig. 8(b), is 0.6—1.2 × 10^7 cm/s, which is about three orders of magnitude higher than that for negative ions [6]. The velocity of electrons is given in [7] as a function of E/P. Taking the average field intensity $\overline{E} = V_p/d$, we get $\overline{E}/P = 31.0$ V/cm.torr in this case, giving an approximate value of electron velocity of about 1.2 × 10^7cm/s.

In order to confirm the carriers to be electrons, the triggering delay time is measured using streak photographs as well as oscillograms of the current waveform, and is compared with the carrier transit time measured separately. Figure 10(a) shows the streak photographs obtained under different pressures, where the electrode gap is 20 mm, and the mica plate with a pinhole is used. It is checked every time that the corona glow appears at the needle tip after the pulse has reached its peak voltage. In this measurement, room air (R.H. = 61%, T = 17°C) is used inside the vacuum chamber as before. Figure 10(b) shows current waveforms and light signals from the whole gap, measured under the same conditions but not simultaneously with the streak photograph. The first rise in current corresponds to the glow at the needle tip, while the second rise corresponds to the occurrence of back discharge streamer. These waveforms enable more accurate evaluations of τ_d which agree very well with those estimated from the streak photographs.

The values of τ_d obtained from these measurements are plotted in Fig.11

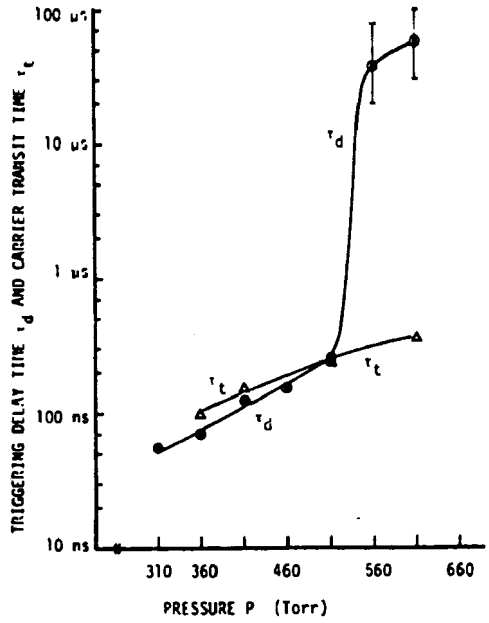

Fig.11. Triggering delay time and carrier transit time as a function of pressure.

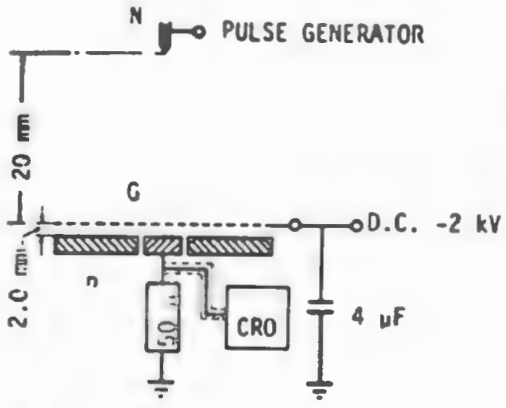

H: NEEDLE ELECTRODE
G: GRID ELECTRODE
P: PLANE ELECTRODE
CRO: CATHODE RAY OSCILLOSCOPE
(Vp: -22 kV, τ_p: 10 μs, f: 10 Hz)

(a) MEASURING SYSTEM

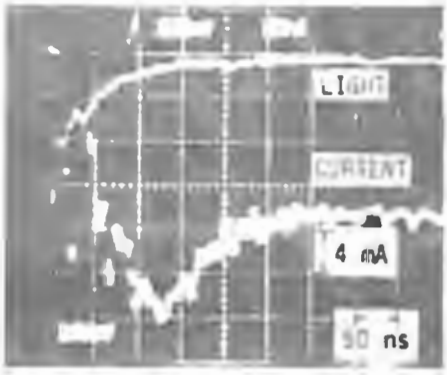

(i) P. 360 Torr

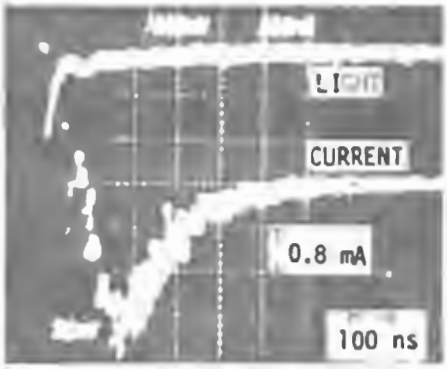

(ii) P. 410 Torr

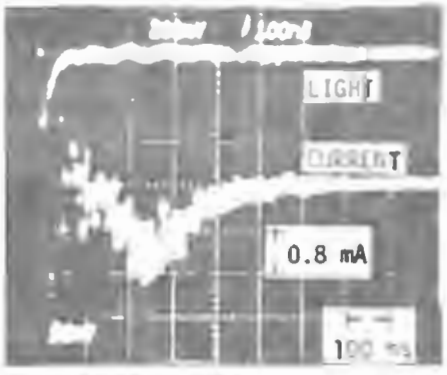

(iii) P. 510 Torr

Fig.12. Carrier transit time measurement.

as a function of pressure P. An abrupt increase in τ_d, more than two orders of magnitude, occurs at $P = 560$ torr, and suggests a sudden decrease in carrier mobility. The width of the pulse voltage is raised to 100 μs above this pressure. It is expected that, with the decrease in gas mean-free-path, the range of free electrons emitted from the needle tip is lowered, and finally becomes shorter than the electrode gap at $P > 510$ torr. Above this critical pressure, the mobility of ions produced by electron attachment may govern the value of τ_d.

Figure 12(a) indicates the electrode system for measuring the carrier transit time τ_t. In order to suppress the disturbing effect of the displacement current caused by the movement of carrier space-charge, a grid electrode with 0.5-mm-square mesh is located near the plane electrode to cover its whole surface. The distance between the plane and the grid electrodes is 2.0 mm. The gap between the needle and the grid electrodes is 20 mm, equal to that in Fig.10. A d.c. voltage of -2.0 kV is applied to the grid electrode to drive the incoming carriers to the plane electrode and a capacitor with 4.0 μF capacitance is connected in parallel to eliminate the effect of transient fluctuation in grid potential. In this measurement, the mica plate is removed, and a pulse voltage with $V_p = -22$ kV, $\tau_p = 10$ μs, $f = 10$ Hz, is applied to the needle electrode. The pulse voltage appearing between the needle and grid electrodes is -20 kV, equal to that between the needle and the plane electrodes in Fig.10.

Figure 12(b) shows the current signal obtained at the plane electrode under different pressures. These signals should correspond to the arrival of the carriers. Light signals from the needle electrode are also indicated as the time origin. The time elapsed from this origin to the peak of the current signal may be taken as the carrier transit time, τ_t. The values of τ_t obtained are plotted against pressure P in Fig.11. A fairly good coincidence can be seen between τ_d and τ_t in the pressure range lower than 510 torr. At $P = 610$ torr, a very large discrepancy appeared between τ_d and τ_t. It should, however, be noted in Fig.12(b) (iv) that the peak value of current in this case becomes very small. This suggests that the number of incoming fast carriers becomes too small to trigger the back discharge in the case of τ_d measurement. It is expected that the second peak may appear in Fig.12(b)(iv) at a much longer time delay beyond the frame, corresponding to the ion transit time.

Figure 13 indicates the values of d/τ_d for $P < 510$ torr and d/τ_t obtained from Fig.12, the approximate values of the carrier velocity, as functions of $\overline{E}/P$. The electron velocity taken from [7] is also indicated. The very good agreement between these values confirms that the fast carriers triggering back discharge in the low pressure range are electrons. The pressure, above which electrons cannot trigger back discharge, should be referred to as the critical pressure P_c. In this case, P_c is 510 torr. It should also be added that free electrons, smaller in number, also arrive at the plane electrode in the pressure range higher than P_c, although the triggering may be effected by ions in this range.

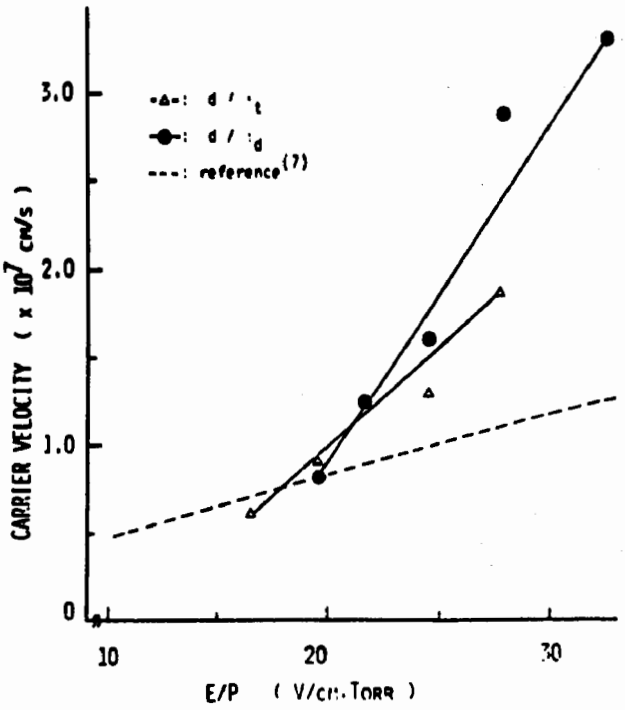

Fig.13. Carrier velocity as a function of $\bar{E}/P$.

3.2.3 Back discharge in N_2 and SF_6 gases

The results described so far clearly indicate the importance of electron affinity of gas molecules encountered to determine the critical pressure P_c. In addition, it is known that streamer propagation is also strongly affected by the gas electron affinity. These effects are studied in more detail using N_2 having no electron affinity and SF_6 gas with a very high electron affinity. A streak photograph of back discharge in N_2 gas, when the pulse voltage is applied, is shown in Fig.14(a). In this case, the chamber is evacuated at first to about 1 torr, and, thereafter, N_2 gas (99.99%) is introduced up to P = 310 torr. It is observed that the triggering delay in this case is 200 ns, much higher than that for air, but still indicating the carriers to be electrons. A faint glow continues to exist at the needle tip after the initial strong glow. There exists a certain delay from the pinhole breakdown to the initiation of the back discharge streamer, whereas no delay time exists between the primary and the secondary light waves in contrast to the case in air.

The streak photograph of back discharge occurring in SF_6 gas is shown in Fig.14(b). SF_6 gas is introduced into the vacuum chamber in the same way as in the case of N_2 gas. Even at a low pressure of P = 160 torr, the triggering delay amounts to 4 μs, much larger than the expected value for electrons. It is expected that the critical pressure P_c lies at a much lower value than 160 torr in this gas with a very strong electron affinity. The small value of 4 μs triggering delay may be attributed to the increase in ion mobil-

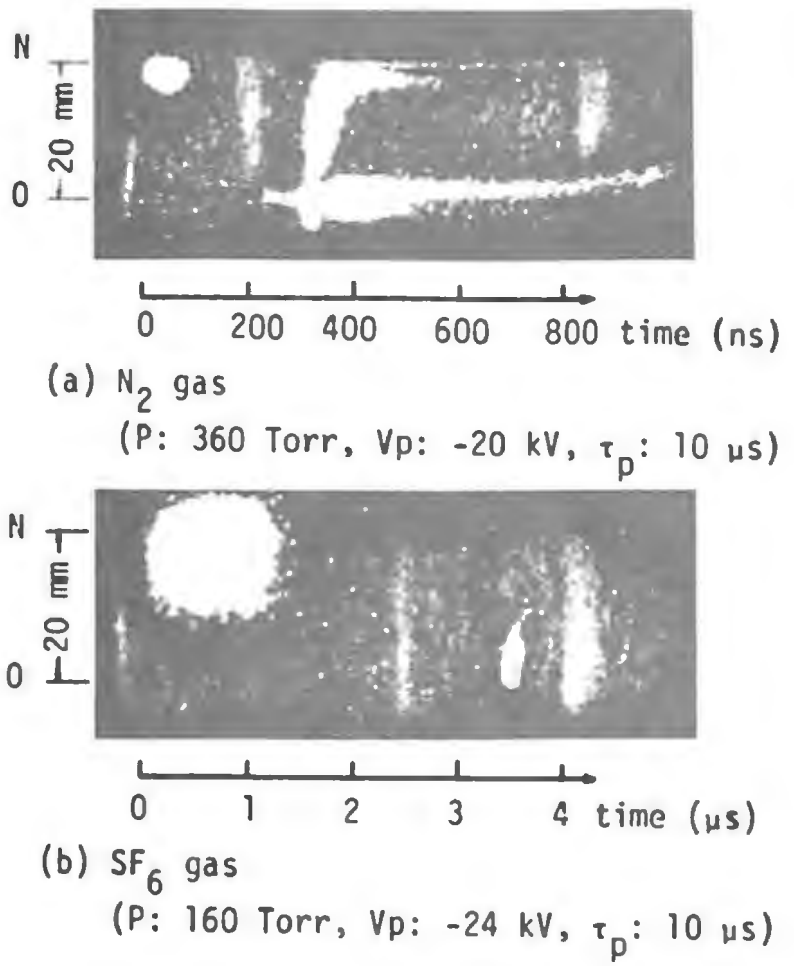

Fig. 14. Back discharge with pulse under N_2 and SF_6 gas Sample: mica plate with a pinhole.

ity at the reduced pressure of P = 160 torr. It should be noted that the streamer propagation into space is highly suppressed, and the secondary light wave completely disappears.

3.2.4 Flashover

The streak photographs of flashover occurring in air and N_2, when a single pulse voltage is applied, are shown, respectively, in Fig. 15(a) and (b). There is no remarkable difference in character of the two pictures, although the former is blurred by a strong halation. After the glow at the needle tip, the back discharge streamer is triggered from the pinhole. At the instant the streamer nears the tip, the second streamers are launched from both sides to meet at the middle point and finally to turn into a highly luminous channel of a flashover.

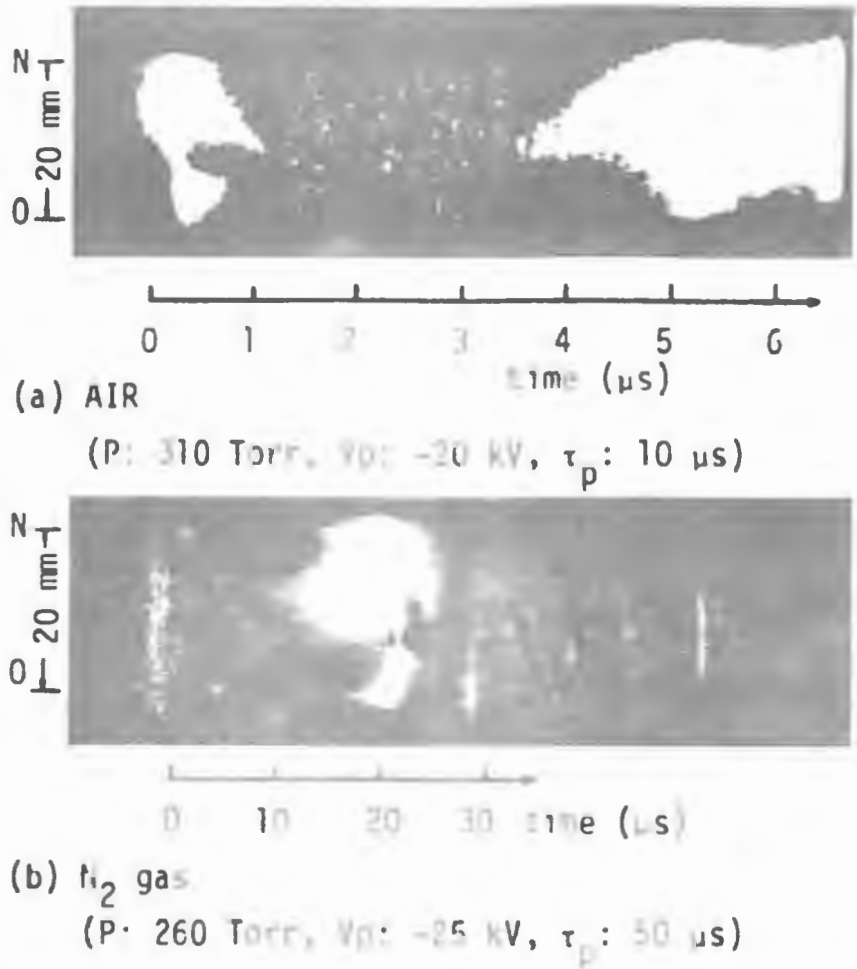

Fig 14. Flashover caused by back discharge with pulse Sampler wire plate with a pinhole

4. Conclusions

The following conclusions are obtained from the light measurements of back discharge:

(1) In the mixed streamer mode occurring in air under atmospheric pressure, the light signal consists of primary and secondary waves. The primary light wave corresponds to a space streamer and the secondary light wave to a surface streamer, each resulting in a different current pulse. The former has a charge content of 1—2 × 10^{-4} C/pulse, while that of the latter is 2—4 × 10^{-4} C/pulse, both remaining almost constant, independent of applied voltage. The period of successive back discharge pulses, however, becomes smaller as the voltage is raised. The mode of back discharge occurring under atmospheric air is considered to be triggered by negative ions supplied from the discharge electrode.

(2) In the space streamer mode, the primary light wave is dominant, while

the secondary light wave is extremely weak. The charge per single current pulse is about $1—2 \times 10^{-9}$ C/pulse. The pulse repetition frequency in this mode, however, is one or two orders of magnitude larger than that in the mixed streamer mode, so that total current in the former mode becomes larger than that in the latter under equal applied voltage.

(3) Flashover seems to be caused by the leader developing along the channel left by the preceding streamers when d.c. voltage is applied.

(4) When a sufficiently high pulse voltage is applied under lower pressure, back discharge is triggered by free electrons supplied from the needle electrode. As the pressure is increased, an abrupt change in the triggering carriers occurs from electrons to negative ions. The electron affinity of gas molecules is a major factor in this process.

Acknowledgement

This research was sponsored by the Ministry of Education, Japan, as its Special Research Project (I) (Project No. 011914). The authors are gratefully indebted for its support.

Nomenclature

d	electrode gap
E_{ds}	breakdown field strength of the layer
$\bar{E}$	average field strength of the gap (V_p/d)
f	frequency of pulse
P	pressure
P_c	critical pressure for the change in the triggering carrier
R.H.	relative humidity
R_s	surface resistivity of the layer
T	temperature
T_a	average pulse repetition period
V_p	peak value of pulse voltage
ϵ	dielectric constant of the layer
ρ_d	apparent resistivity of the layer
σ_0	surface charge density at the instant of layer breakdown
τ_d	triggering delay time
τ_p	width of pulse voltage
τ_t	carrier transit time
N	needle electrode
O	breakdown point
P	primary light wave
R	return light wave
S	secondary light wave

References

1 S. Masuda and A. Mizuno, Initiation condition and mode of back discharge, J. Electrostatics, to be published.

2 S. Masuda and A. Mizuno, Flashover measurements of back discharge, J. Electrostatics, to be published.

3 S. Masuda, A. Mizuno and K. Akutsu, Initiation condition and mode of back discharge for extremely high-resistivity powders, to be presented at the 1977 Annual Meeting of IEEE IAS, Los Angeles, October 1977.
4 I. Tsuneyasu, Observations of air breakdown in positive point to plane gaps under impulse voltage and its mechanisms, J. Inst. Electr. Eng. Jpn., 96B (1976) 63.
5 N. Ikuta, T. Ushita and Y. Ishiguro, Positive streamer corona and its propagation mechanism, J. Inst. Electr. Eng. Jpn., 90 (1970) 1816.
6 E.W. McDaniel and M.R.C. McDowell, Low-field mobilities of the negative ions in oxygen, sulfur hexafluoride, sulfur dioxide, and hydrogen chloride, Phys. Rev., 114 (1959) 1028.
7 H. Ryzko, Drift velocity of electrons and ions in dry and humid air and in water vapour, Proc. Phys. Soc., 85 (1965) 1283.

INITIATION CONDITION AND MODE OF BACK DISCHARGE FOR EXTREMELY HIGH RESISTIVITY POWDERS

Senichi MASUDA, Akira MIZUNO and Kensuke AKUTSU

Department of Electrical Engineering, Univereity
of Tokyo, 7-3-1, Hongo, Bunkyo-Ku, Tokyo, JAPAN

Summary

Initiation condition of back discharge occurring in case of extremely high resistivity powders, including the case of electrostatic powder coating, is calculated, considering space charge field inside the deposited powder layer. The mixmum field strength occurs at the layer-electrode interface, and its value rises with the increase in the layer thickness. When it exceeds the breakdown value, back discharge starts to occur and the growth of thickness stops, resulting in the so-called "thickness limiting phenomena". The theoretical initiation condition provides the estimation of the limiting thickness, which agrees fairly well with the measured value. The mode of back discharge in this case is that of onset glow occurring at a number of breakdown points in the layer, and taking the form of general glow.

1. INTRODUCTION

It is well known that back discharge lowers the collection performance of electrostatic precipitators to a great extent.(1,2) In case of electrostatic powder coating, it has recently been discovered by Bassett et al that the back discharge results in a limiting of the coat thickness and causes the so-called "craters" or "orange peels" over the finished coat.(3) The back discharge is a kind of gaseous discharge appearing on the surface of the powder layer deposited, and it is triggered by breakdown of the layer. It is therefore expected to occur when the apparent field strength inside the layer exceeds its breakdown threshold E_{ds}. Thus, in the field of electrostatic precipitation, when the resistivity of the deposited layer, ρ_d, is comparatively low, less than about 10^{13} Ωcm, the initiation condition of back discharge has long been considered as

$$E_d = i_d \rho_d \geq E_{ds} \qquad (1)$$

where i_d = current density in dust layer and ρ_d = apparent resistivity of the dust layer. The authors studied the mode of back discharge under various conditions, and found that there are two different modes, one being the glow mode and the other the streamer mode.(4,5) They further confirmed that the layer breakdown is governed by the condition of Eq.(1) when $\rho_d < 10^{13}$ Ωcm. However, it was considered that the initiation condition might become entirely different because of the layer space charge when the ρ_d-value becomes extremely high and exceeds the level of 10^{14} - 10^{15} Ωcm. The appearence of limiting thickness itself means that, in spite of a very high ρ_d-value, the back discharge does not occur until a certain layer thickness is exceeded, suggesting the thickness to be another factor. The authors observed on the other hand that in case of very high ρ_d-value the back discharge could be resulted even in the absence of i_d supplied by ionic current,(6) which is to be described in the next section. According to the authors' observation, the mode of back discharge in this case was also somewhat different from those in the case of electrostatic precipitation. Hence, the initiation condition and mode of back discharge were studied for the case of extremely high resistivity powders.(6)

2. PRELIMINALY OBSERVATIONS

It is studied at first whether back discharge can take place without the aid of ionic current when the ρ_d-value becomes extremely high. Fig.1 shows the experimental apparatus.(7) In order to reject all the possibility of ionic current to be supplied, two sphere electrodes with 14 cm diameter are used inside a shielding chamber (1m × 1m × 1m). The total stray current can be kept below 0.1 - 0.3 nA under the applied voltage of 50 kV. Polyethylene powder with $\rho_d \approx 10^{15}$ Ωcm is negatively charged by tribo-electrification and fed with the aid of air flow from a plastics nozzle onto the surface of the lower electrode B, where both electrodes are grounded. After the powder supply is stopped, the electrode B is connected to either a negative or a positive high voltage source. When it is connected to a positive H.V.source, the powder adheres to the electrode surface. At a certain voltage, back discharge is detected with an image intensifier tube (EMI, type 9912), and it turns into a spark at +40 kV. When a negative voltage is applied to the electrode B, all the powder violently jumps up to deposit on the surface of the opposite electrode A. These phenomena can occur after several hours of powder deposition, but completely disappear after 40 hours.

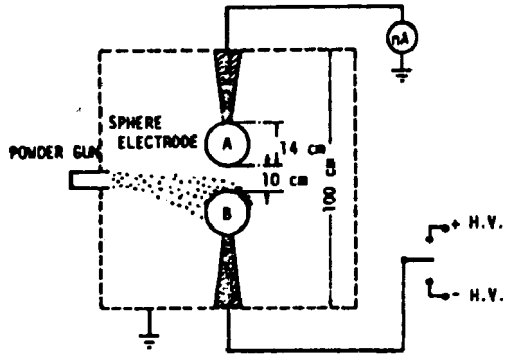

Fig.1 Experimental Apparatus (I) for Preliminary Observation

Another experiment is performed to examine these phenomena in more detail, using the apparatus shown in Fig.2. The powder, negatively charged by tribo-electrification, is fed into a space between two parallel electrodes applied with a dc high voltage. The powder is separated in the field to deposit on the surfaces of both electrodes. This is because a minority portion of the powder is charged positively, although the net powdar charge is negative. After several 10 seconds back discharge starts to occur at the upper area of the positive electrode at which the amount of deposition is maximum. It triggers a new back discharge to occur at the opposite area on the negative electrode, owing to the copious ions supplied from the initial back discharge point. These back discharges propagate gradually downwards on both electrodes towards the lower areas. This phenomenon, named "back discharge propagation" by the authors, also occurs in electrostatic precipitators when the ρ_d-value exceeds 10^{14} Ωcm.(8)

It is observed that the layer thickness at the initiation of back discharge is much larger in the [illegible]

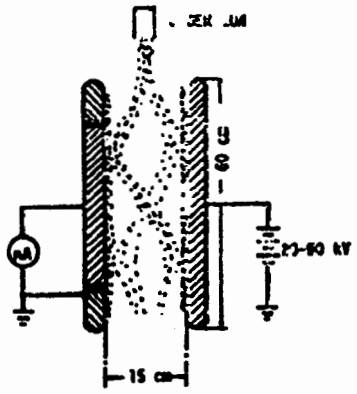

Fig.2 Experimental Apparatus (II) for Preliminary Observation

two cases compared with the usual case of powder coating with ionic current supplied.

These two experiments clearly indicate that back discharge can take place without the aid of ionic current when the ρ_d-value exceeds the level of 10^{15} Ωcm and a sufficiently high external field is applied in a favourable direction. This suggests the necessity of formulating its initiation condition on a more general basis.

3. THEORETICAL CONDITION OF BACK DISCHARGE INITIATION

We assume the continuous and uniform flows of charged powder particles and ions coming from a gas space perpendicular onto a grounded plane electrode to form a uniform powder layer on it (Fig.3). The layer thickness is growing with a constant rate b (m/s). We calculate the field distribution inside the layer, starting from the following fundamental equations in one-dimensional case:

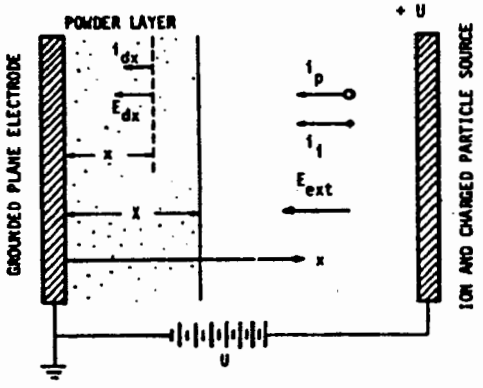

Fig.3 One-Dimensional Model of Powder Deposition Process

i) Continuity equation:

$$-\mathrm{div}\,\vec{i}_d = \partial i_{dx}/\partial x = \partial q_d/\partial t \qquad (2)$$

ii) Poisson's equation:

$$\mathrm{div}\,\varepsilon_d\vec{E}_d = -\varepsilon_d \partial E_{dx}/\partial x = q_d \qquad (3)$$

iii) Ohm's law:

$$i_{dx} = E_{dx}/\rho_d \qquad (4)$$

where q_d = charge density inside the layer, ε_d = apparent dielectric constant of the layer, and i_{dx} and E_{dx} are the x-components of current density $\vec{i}_d$ and field intensity $\vec{E}_d$ inside the layer respectively, taken positive to the left direction.

We take the following boundary conditions;

(I) Boundary between the layer and gas space:

a) Position of the boundary:

$$X = bt \quad (m) \qquad (5)$$

b) Current density at the boundary: (outside the layer)

$$i_o = i_i + i_p = i_i + 3\phi b q_p/4\pi a^3 = \text{constant} \quad (A/m^2) \qquad (6)$$

(inside the layer)

$$i_{dx}(X) = E_{dx}/\rho_d \quad (A/m^2) \qquad (7)$$

c) Field intensity at the boundary:

$$E_{dx}(X) = E_{ext} = \text{constant} \quad (V/m) \qquad (8)$$

(II) Boundary between the layer and the plane electrode:

d) Potential at the boundary:

$$U_d(0) = 0 \quad (V) \qquad (9)$$

where t = time, i_i = ionic current density, i_p = particle current density, i_o = total current density, q_p = charge of a single particle, a = particle radius, ϕ = packing ratio of the layer, E_{ext} = externally applied field, $U_d(x)$ = potential inside the layer. The condition (8) may be plausible if we assume the layer thickness to be adequately small compared with the inter-electrode distance.

Continuity equation (2) at the boundary between the layer and the gas space can be written as:

$$i_o - E_{dx}(X)/\rho_d = q_d(X)b \qquad (10)$$

or

$$q_d(X) = (i_o - E_{dx}(X)/\rho_d)/b = q_o - E_{ext}/b\rho_d = q_d \text{ (constant)} \qquad (11)$$

where

$$q_o = i_o/b = (i_i + i_p)/b = (i_i + 3\phi b q_p/4\pi a^3)/b \qquad (12)$$

From Eq.(2) ~ (4), we get

$$\partial q_d/\partial t = -\tau_d q_d \qquad (13)$$

where $\tau_d = \varepsilon_d\rho_d$ = relaxation time of the layer (14)

Integrating Eq.(13) under the condition

$$q_d(x,t) = q_o \quad \text{at} \quad t = x/b \qquad (15)$$

we get for $x \leq bt$, or $x \leq X$

$$q_d(x,t) = q_o\exp(-(t-x/b)/\tau_d) \qquad (16)$$

$$= q_o\exp(-(X-x)/L_d) \qquad (17)$$

where $L_d = b\tau_d$ = relaxation length (18)

Putting Eq.(16) into Eq.(3), and integrating from x to X, we get

$$-\varepsilon_d E_{ext} + \varepsilon_d E_{dx}(x,t) = q_o L_d(1 - \exp(-(X-x)/L_d)) \qquad (19)$$

Considering Eq.(11), we get finally the field distribution as

$$E_{dx}(x,t) = E_{ext} + (i_o\rho_d - E_{ext})(1 - \exp(-(X-x)/L_d)) \qquad (20)$$

$$= E_{ext} + (i_o\rho_d - E_{ext})(1 - \exp(-(t-x/b)/\tau_d)) \qquad (21)$$

$$= E_{ext}\exp(-(X-x)/L_d) + (i_o\rho_d - E_{ext})(1 - \exp(-(X-x)/L_d)) \qquad (22)$$

Eq.(22) indicates that the relaxation length L_d represents the penetration depth of the external field into inside the layer.

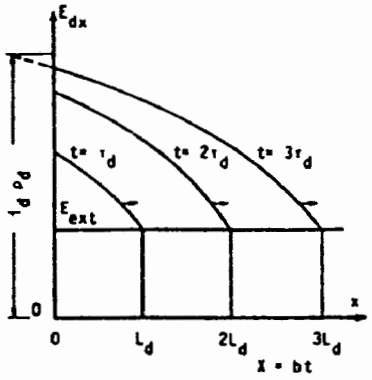

Fig.4 Field Distribution inside a Deposited Layer (general case; $X_o \sim L_d$, $t_o \sim \tau_d$)

Fig.4 depicts the field distribution inside the layer at the instant $t = \tau_d$, $2\tau_d$ and $3\tau_d$ respectively. It can be seen that the field distribution is an exponential function of time and depth, propagating with a velocity b in the x-direction. The maximum field strength occurs at x = 0 (the boundary between the layer and the plane electrode). It is therefore expected that back discharge may start from this boundary when this maximum field strength E_{max} exceeds the breakdown threshold value E_{ds}. Hence the general form of initiation condition of back discharge should be

$$E_{max} = E_{ext} + (i_o\rho_d - E_{ext})(1 - \exp(-X_o/L_d)) \geq E_{ds} \quad (23)$$

or

$$E_{max} = E_{ext} + (i_o\rho_d - E_{ext})(1 - \exp(-t_o/\tau_d) \geq E_{ds} \quad (24)$$

which clearly indicate the existence of the critical thickness X_o and critical time t_o at which back discharge occurs. This thickness may be considered approximately equal to the limiting thickness. From these equations, the approximate values of limiting thickness and time, X_o and t_o, can be obtained as

$$X_o/L_d = t_o/\tau_d = \ln((i_o\rho_d - E_{ext})/(i_o\rho_d - E_{ds})) \quad (25)$$

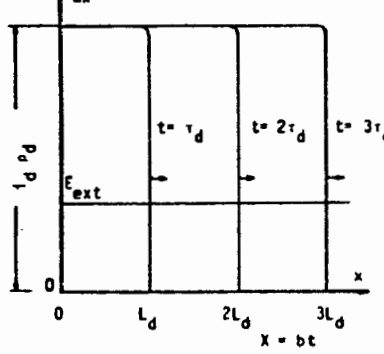

Fig.5 Field Distribution inside a Deposited Layer (low resistivity case - Case(I); $X_o \gg L_d$, $t_o \gg \tau_d$)

Two different cases may be of special interest. One is the Case(I) where the ρ_d-value is comparatively low as in the case of electrostatic precipitation. The other is the Case(II) where the ρ_d-value is extremely high as in the case of electrostatic powder coating.

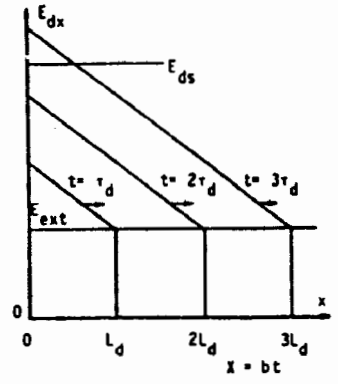

Fig.6 Field Distribution inside a Deposited Layer (high resistivity case - Case(II); $X_o \ll L_d$, $t_o \ll \tau_d$)

Case (I): In this case, the value of L_d becomes very small and conditions $X_o \gg L_d$ and $t_o \gg \tau_d$ are fulfilled, so that Eq.(23) and (24) reduce to Eq.(1) where the effect of layer thickness disappears. The field distribution in this case is shown in Fig.5, which indicates the effects of the layer space charge and external field to be negligibly small.

Case (II): In this case, the condition $X_o \ll L_d$ and $t_o \ll \tau_d$ are fulfilled, so that we get from Eq.(23) and (24)

$$E_{max} = E_{ext} + (i_o\rho_d - E_{ext})(X_o/L_d) = E_{ext} + (i_o\rho_d - E_{ext})(t_o/\tau_d) \geq E_{ds} \quad (26)$$

$$X_o/L_d = t_o/\tau_d = (E_{ds} - E_{ext})/(i_o\rho_d - E_{ext}) \quad (27)$$

when $i_o\rho_d \gg E_{ext}$ as in most practical cases, Eq.(26) and (27) are further simplified to

$$E_{max} = E_{ext} + (i_o/\epsilon_d)t_o \geq E_{ds} \quad (28)$$

$$X_o = bt_o = \epsilon_d b(E_{ds} - E_{ext})/i_o \quad (29)$$

When, contrary to the assumption made, i_o changes during deposition process, Eq.(28) should be modified to

$$E_{max} = E_{ext} + \int_o^{t_o}\{i_o(t)/\epsilon_d\}dt \geq E_{ds} \quad (30)$$

Eq.(29) suggests that the limiting thickness X_o becomes inversely proportional to the total current density i_o or q_o/b which is the space charge density in this case (see Eq.(12)). Hence, the limiting thickness X_o can be controlled by changing the total source current i_o. Here, the particle charge q_p should be kept as high as possible for the best deposition performance to be obtained. It should be noted that the higher the layer space charge density q_o, the larger becomes the adhesion force of the layer. This suggests that the thickness and adhesion ability of the layer may not be compatible. In this case of an extremely high ρ_d-value, the conduction current E_{dx}/ρ_d in the layer becomes negligible compared with the displacement current. Eq.(30) suggests that, if the value of E_{ds} is known, the occurence of back discharge could be predicted by measuring $\int_o^{t_o}\{i_o(t)/\epsilon_d\}dt$. On the contrary, if the value of this integral at the initiation of back discharge is measured, we could estimate the value of E_{ds}, the breakdown field strength of a limited area adjacent to the plane electrode. Since $i_o(t)$ is equal to the current passing from the unit area of the plane electrode to the ground, this integral can be estimated by the use of a series capacitor connected between the plane

electrode and the ground.

It should finally be pointed out that Eq.(25) and (27) also suggest the back discharge to occur even without the supply of ionic current i_i when the layer thickness X becomes sufficiently large. It is expected that the layer space charge $q_o = i_o/b$ in this case may be fairly low so that, unless the particle charge q_p is kept sufficiently high, the adhesion of the layer may be lower.

The field distribution in this case is depicted in Fig.6. The higher the total source current density i_o compared with the powder daposition rate b, the steeper becomes the slope of the curves, this being $i_o/\varepsilon_d b$ when $i_o \rho_d \gg E_{ext}$.

4. EXPERIMENTAL VERIFICATION

In the case of $\tau_d \gg t_o$, an experimental verification of Eq.(23) and (24) are made by comparing the experimental value of E_{max} from Eq.(30) at the initiation of back discharge with the value of E_{ds} measured separately using parallel plane electrodes. This verification is made intentionally for the extreme case where the ionic current i_i is kept negligibly small compared with the particle current i_p so that we can assume $i_o \doteq i_p$. Fig.7 shows the experimental apparatus which meets this requirement and allows an independent control of E_{ext} and i_o ($\doteq i_p$). The value of E_{ext} can be changed by the grid potential V_g, while the value of i_o by changing the discharge electrode voltage V_a of powder gun as well as the powder feeding rate W_p. The value of $\int_o^{t_o}(i_o(t)/\varepsilon_d)dt$ is measured by recording the capacitor voltage V_c, where

$$V_c = S\int_o^{t_o}(i_o(t)/\varepsilon_d)/C \qquad (31)$$

where C = capacity = 10^{-8} F and S = surface area of the measuring electrode. The epoxy-resin powder, having a ρ_d-value of 2×10^{16} Ωcm and a specific dielectric constant $\varepsilon_s = 2.5$ is used. The size of the powder particle is in the range of 0.01 ~ 0.05 mm. The experiment is conducted under a constant temperature and relative humidity (20 C° and 40 %). For the powder sample used, we get $\tau_d \doteq 2 \times 10^3$ s, so that the condition for Case (II) ($\tau_d \gg t_o$) is satisfied. The start of back discharge is detected by its accompanying light emission using the image intensifier tube (EMI, type 9912)

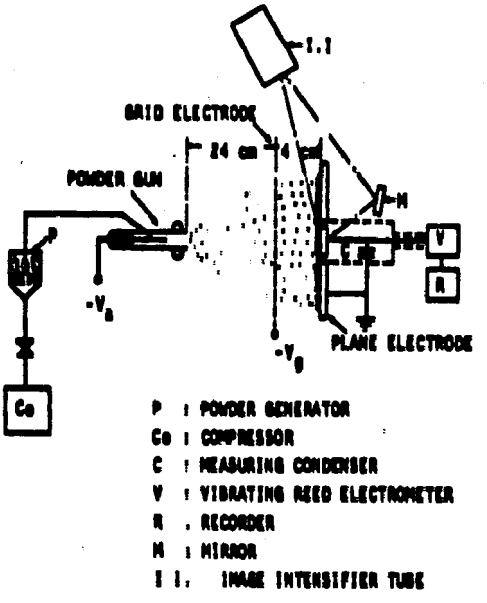

Fig.7 Electrostatic Powder Deposition Apparatus for Experimental Verification of Back Discharge Initiation Condition

The values of the capacitor voltage V_c and the layer thickness X at the initiation of back discharge, denoted by $(V_c)_o$ and X_o respectively, are measured for various values of i_o, thereby changing the layer space charge density q_o. From the value of $(V_c)_o$ and E_{ext}, the value of E_{max} at the initiation of back discharge, $(E_{max})_o$, is calculated using Eq.(30). The measurement of X_o is made by cutting the layer and observing its cross-section with a microscope.

The relationship between $(E_{max})_o$ and X_o measured in the wide range of $i_o = 10^{-10} \sim 10^{-8}$ A/cm² and powder feeding rate $W_p = 10 \sim 80$ g/min is plotted in Fig.8. The value of E_{ds} measured by parallel plane electrodes, denoted by $\overline{E_{ds}}$, is also given, which decreases with layer thickness. It can be seen that, in spite of such a wide variation in q_o made in this experiment, the value of $(E_{max})_o$ remains almost constant in the thickness range between 0.3 and 1.0 mm investigated, and further that its value agrees very well with the value of $\overline{E_{ds}}$ at a small thickness of about 0.1 mm. This supports the theoretical conclusion that back discharge should initiate from the limited area adjacent to the plane electrode.

The experiment in the smaller thickness range is omitted because of its difficulty. When the ionic current is made negligibly small, no back discharge can be resulted with the powder sample used in the thickness range lower than 0.25 mm. If the ionic current is supplied, a fairly large error cannot be avoided because of by-pass current to flow directly to the plane electrode at the start of powder deposition and the limiting time t_o to become very short.

However, the results so far obtained seem to provide a sufficient support for the validity of the theoretical initiation condition of back discharge described in the preceding section.

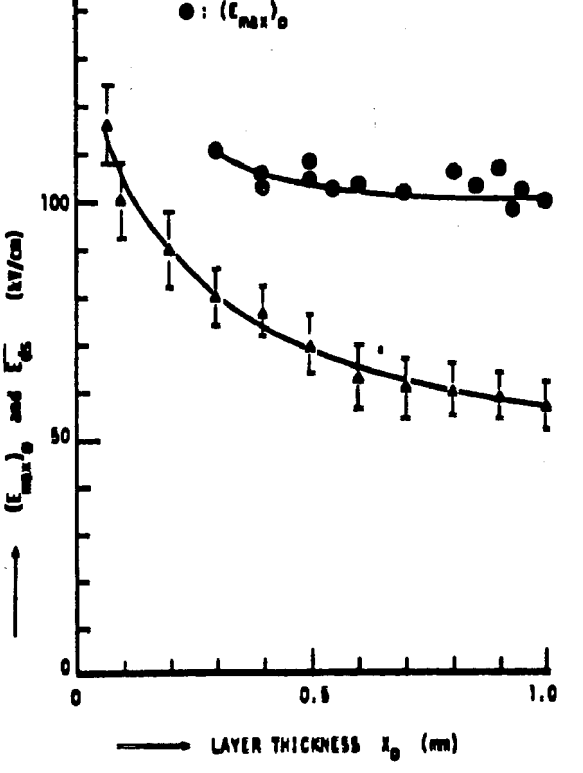

Fig.8 Comparison between $(E_{max})_o$ and $\overline{E_{ds}}$

5. MODE OF BACK DISCHARGE

The mode of back discharage for extremely high resistivity powders is observed using an electrostatic powder deposition apparatus shown in Fig.7. The negative corona is primarily used. In order to observe the light emission at the boundary between the plane electrode and the powder layer, the measuring electrode is made of a conductive glass plate as is reported by Ting and Hughes.[9] The image intensifier tube is also used with its maximum gain of about 10^6.

5.1 Back discharge at very low ionic current

Under the condition of negligibly small ionic current (lower than about 10^{-12} A/cm^2) as described before, the thickness of the layer can grow sufficiently large. But, finally the back discharge takes place, resulting in craters. Fig.9-a shows a photograph of light emissions during the course of powder deposition, taken from both the front and the back side at the beggining stage of back discharge (image intensifier, exposure time = 5.0 s). The layer thickness at this time is about 0.5 mm. The back discharge occurs at discrete points, and fairly large craters are produced. The light emissions are pulsive and move randomly around the layer so far as the deposition is continued. The intensity of light emission is stronger at the boundary than on the surface. This does not change even if the positive corona is used. When the powder feed is stopped, the light emission disappears. However, when the grid voltage is sufficiently raised to enable a spontaneous back discharge, or a sufficient amount of ionic current is supplied from an external source, the light emission appears again in a form of fixed and stable glows. Fig.9-b shows the craters appeared on the layer surface.

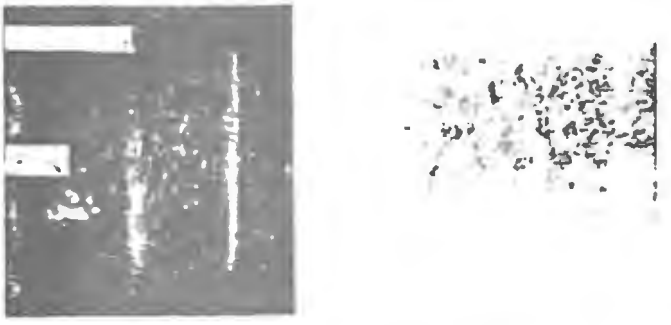

(a) light emission (b) craters

Fig.9 Back Discharge and Craters at Very Low Ionic Current (i_i = 10^{-12} A/cm^2)

5.2 Back discharge at higher ionic current

When a sufficiently large ionic current is supplied, back discharge can occur at a lower thickness, less than 0.25 mm, but its intensity is so low that it can hardly be detected visually. When observed with the image intensifier tube, it can be seen that the back discharge takes a form of general glow, the whole surface glowing uniformly and no glow spot being detected. Fig.10-a shows a photograph of such glow taken from the front and the back side simultaneously with the powder being fed, when i_o = 5 × 10^{-7} A/cm^2 and X = 0.15 mm (image intensifier tube, exposure time 2.0 s). The intensity of the general glow is stronger at the boundary than on the surface, when the negative corona is used. This reverses when the positive corona is used. The craters cannot be detected visually.

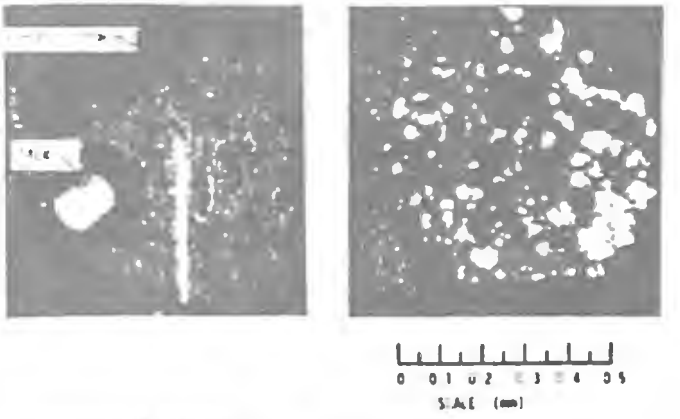

(a) normal photograph (b) microscopic photograph

Fig.10 Back Discharge at High Current Density (i_i = 5 × 10^{-7} A/cm^2)

5.3 Microscopic observation of general glow

In order to study the structure of the general glow in more detail, an observation is made using a microscope coupled with the image intensifier tube. When the electrode becomes almost covered by powder, light emission in the form of general glow starts to occur. Fig.10-b is a photograph of this light emission taken from the back side (exposure time = 3.0 s). This shows the existence of many discrete glow points, scattered with a distance in the order of particle size. As in the case of very low ionic current, the light emissions occur randomly at many points, moving around the layer when the powder is being fed. A number of small voids are formed at the same time, and they also move around along the boundary. It should be noted that, in spite of this general glow appearing, the powder can continue to deposit up to a certain value of thickness, about 0.25 mm. The reason for this powder penetration will be discussed later. When the powder feed is stopped with ionic current being supplied, the fixed glow points appear also in this case, so far as the layer thickness is larger than 0.1 mm. Fig.11-a and b are the photographs of the layer back side with back discharge which clearly indicate these fixed glows to appear at the voids.

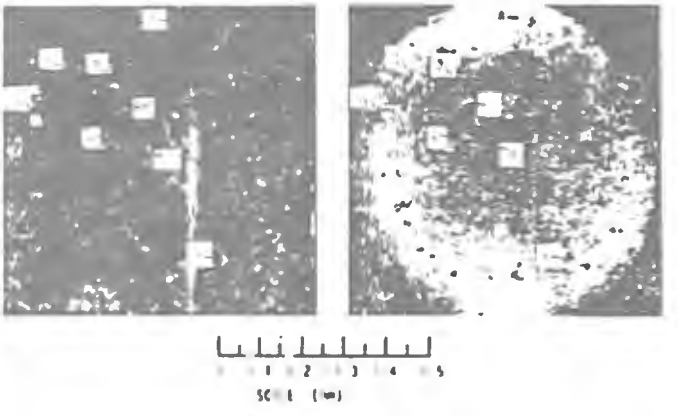

(a) fixed glow points (b) voids

Fig.11 Microscopic Observation of General Glow

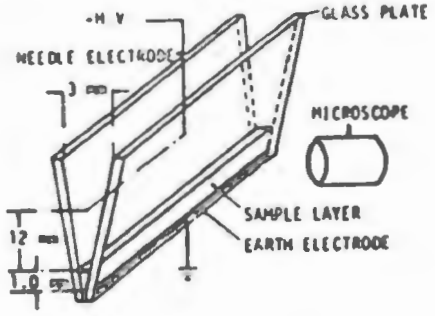

Fig.12 Experimental Apparatus for Observation of Breakdown Channels inside the Powder Layer

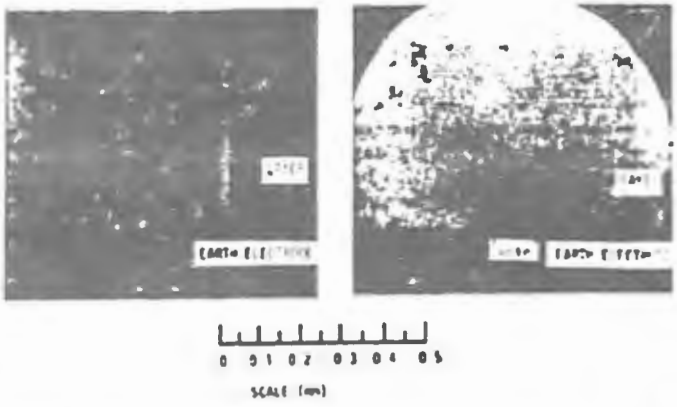

(a) breakdown channel (b) cross-section

Fig.13 Microscopic Observation of Breakdown Channels inside the Powder Layer

Breakdown channels inside the powder layer is also observed using an apparatus shown in Fig.12, where the image intensifier tube is also used. Fig.13-a and b are the photographs of the layer cross-section with and without back discharge. These indicate the breakdown channels stemming from the bright glow points at the voids on the boundary and penetrating into the inside of layer.

5.4 Microscopic observation of craters

No change is visually detected in the smoothness of the layer surface after the occurence of general glow. Hence, a more detailed examination is made by microscopic observation.

Fig.14-a and b indicate the microscopic photographs of the layer surface with and without the general glow. The thickness of the layer is 0.2 mm. It is clearly shown in Fig.14-b that a number of very small craters are formed by the general glow, which is named "micro-craters". The size of the micro-crater is almost equal to particle size. These micro-craters can be observed within the thickness range between 0.1 and 0.25 mm for the powder used. In the range less than 0.1 mm, they become undistinguishable from the irregularities of the deposited surface. In the thickness range larger than 0.25 mm, they turn into the much larger craters usually observed.

Fig.15 is a photograph of the usual craters which occur under a fairly low ionic current at a larger layer thickness (X = 0.5 mm). The crater size is much larger compared with the micro-crater. In most of such craters, several large particles are observed to be remaining on the bottom with a loose packing, which may allow the plasma column of a continuous glow to be maintained therebetween.

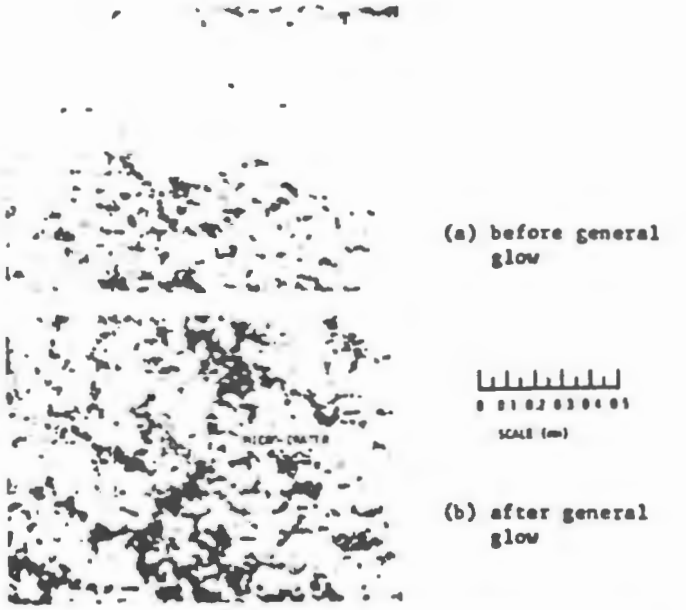

(a) before general glow

(b) after general glow

Fig.14 Microscopic Observation of Micro-Craters

Fig.15 Microscopic Observation of Normal Craters

5.5 Current wave form of back discharge and formation of craters

Fig.16-a shows a current wave form of back discharge in the case of very low ionic current when the larger craters are being formed at the thickness of 0.5 mm. In this case, i_i and i_p are so small ($i_i = 10^{-12}$ A/cm^2, $i_p = 10^{-9}$ A/cm^2) that the current consists mainly of back discharge pulses at the craters. Fig.16-b indicates a current wave form of back discharge of general glow type when the powder supply is stopped and many fixed glow points are existing ($i_o = 7 \times 10^{-7}$ A/cm^2). In this case, current consists of dc component alone. This suggests that the general glow is the back discharge in the glow mode already reported,[5] occurring at many breakdown points (micro-craters).

An experiment is made to study the formation process of craters in more detail. A mica plate having a pinhole with 1.0 mm diameter and 1.5 mm thickness is used on a plane electrode of a needle-plane electrode system as a layer sample (Fig.17). The epoxy-resin powder is filled in the pinhole. A negative high voltage is applied to the needle electrode, and back discharge is produced at the pinhole. At this instant, the powder ejection is resulted, as shown in Fig.18-a. When a crater is completed inside the pinhole the powder ejection stops, and back discharge turns from a pulsive breakdown into a stable glow of the onset-glow mode.[4] Fig.18-b indicates the current wave form during and after this process. At the initial stage when the powder ejection is being made, back discharge is pulsive consisting of repetitive breakdowns. Then, it turns into a non-pulsive glow when the crater is completed.

(a) very

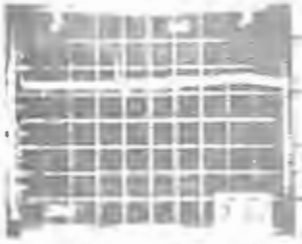

(b) higher

Fig 1

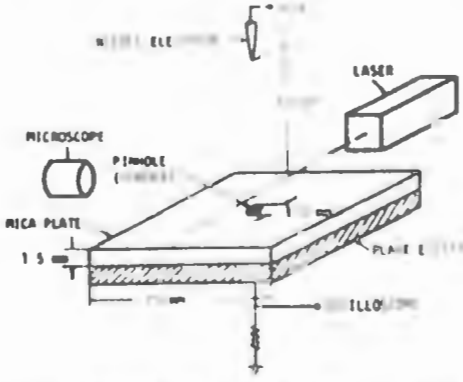

Fig.17 Experimental Apparatus for Observation of Powder Electron

(a) powder electron

(b) current

Fig.18

X_o, can be estimated from the theory using the value of E_{ds}.

(2) In case the ionic current is negligibly small, the limiting thickness, X_o, can become high and the large craters can be formed. In this case, pulsive light emissions take place during the course of powder deposition when back discharge started.

(3) In case the higher ionic current is supplied, the value of X_o becomes smaller and back discharge takes a form of general glow. This consists of a number of very small glow spots. In this case, micro-craters are formed.

(4) So far as the negative corona is used, the light emission is stronger at the powder-electrode boundary than the powder surface.

ACKNOWLEDGEMENT

The authors are very grateful to Prof. A.W.Bright of the Southampton University for the very valuable discussions which stimulated and helped this work. They also thanks Mr. Toshiyuki Saito for his help in doing a part of the experimental works.

REFERENCES

1. H.J.White, Industrial Electrostatic Precipitation, Addison Wesley, 1963
2. S.Masuda, Recent Progress in Electrostatic Precipitation, Static Electrification 1975, Institute of Physics Conference Series No.27, p.154 (1975)
3. J.D.Bassett, R.P.Corbett and J.Cross, Institute of Physics Conference Series, No.27, p.221 (1975)
4. S.Masuda, A.Mizuno and K.Akutsu, Initiation Condition and Mode of Back Discharge, J. of Electrostatics (to be published)
5. S.Masuda, A.Mizuno, Flashover Measurements of Back Discharge, J. of Electrostatics (to be published)
6. S.Masuda, A.Mizuno and K.Akutsu, Proc. of 3rd Int. Conf. on Static Electricity, 24-a (Grenoble, April, 1977)
7. S.Masuda, K.Akutsu and T.Saito, Proc. 1976 Annual Conference of I.E.E.Japan, No.470 (1976)
8. S.Masuda, I.Doi, I.Hattori and A.Shibuya, Utility Limit and Mode of Back Discharge in Bias-Controlled Pulse Charging System (to be presented to 1977 Annual Conf. of IAS, IEEE, Los Angels)
9. Yui-Cheong Ting, J.F.Hughes, Proc. of 3rd International Congress on Static Electricity, 27-a, (Grenoble, April, 1977)

Errata

(A) Boundary condition c) [Eq.(8)] should be corrected as

c) Field intensity at the boundary:

$$(\varepsilon_d/\varepsilon_o)E_{dx}(X) = E_{ext} = \text{constant (V/m)} \qquad (8)$$

According to this correction, $[E_{ext}]$ should be replaced with $[E'_{ext}]$ in the following equations (20) ~ (30), where

$$E'_{ext} = (\varepsilon_o/\varepsilon_d)E_{ext}$$

(B) Eqs.(11) and (15) should be corrected as

$$q_d(X) = (i_o - E_{dx}(X)/\rho_d)/b$$
$$= q_o - E'_{ext}/b\rho_d = q_{do} \text{ (constant)} \qquad (11)$$

$$q_d(x,t) = q_{do} \quad \text{at} \quad t = X/b \qquad (15)$$

Thus,

$$q_d(x,t) = q_{do}\exp(-(t-x/b)/\tau_d) \qquad (16)$$
$$= q_{do}\exp(-(X-x)/L_d) \qquad (17)$$

Then, Eq.(19) should be

$$-\varepsilon_o E_{ext} + \varepsilon_d E_{dx}(x,t) = q_{do}L_d(1 - \exp(-(X-x)/L_d)) \qquad (19)$$

(C) Eq.(31) should be

$$V_c = S\int_o^{t_o}\{i_o(t)\}dt/C \qquad (31)$$

(D) Figures (4), (5), (6) and (8) should be modified as follows, according to the correction (A).

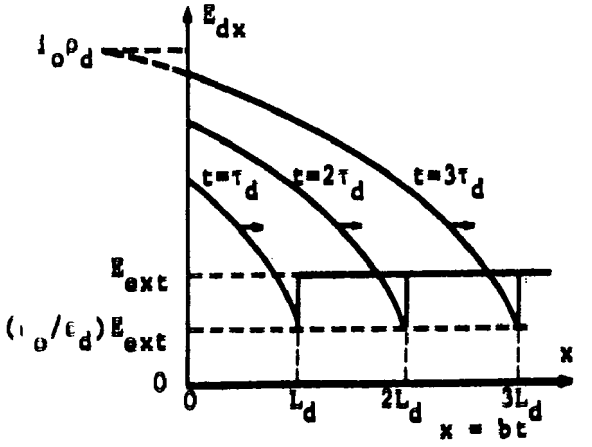

Fig.4 Field Distribution inside a Deposited Layer (general case; $X_o = L_d$, $t_o = \tau_d$)

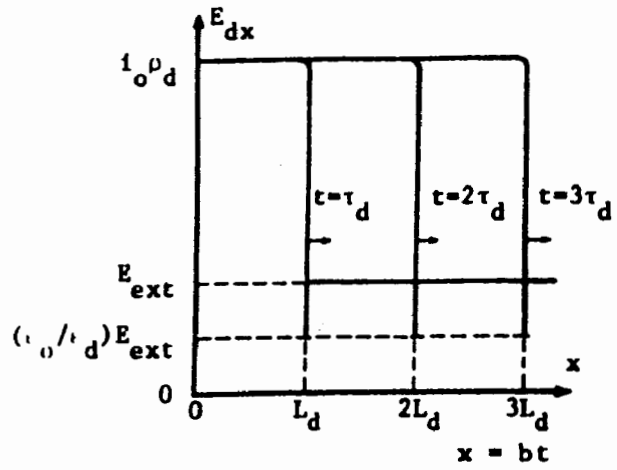

Fig.5 Field Distribution inside a Deposited Layer (low resistivity case - Case(I); $X_o \gg L_d$, $t_o \gg \tau_d$)

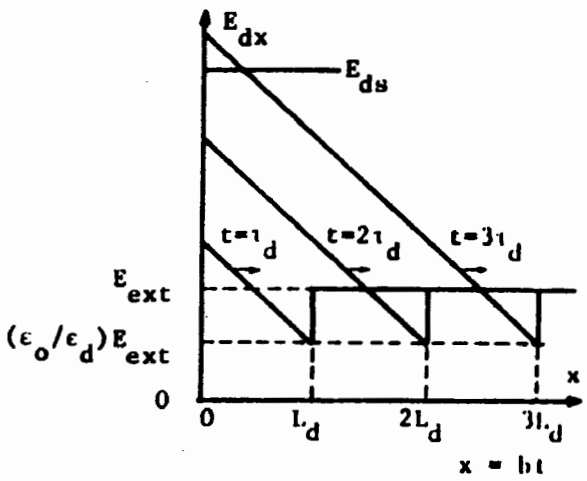

Fig.6 Field Distribution inside a Deposited Layer (high resistivity case - Case (II); $X_o \ll L_d$, $t_o \ll \tau_d$)

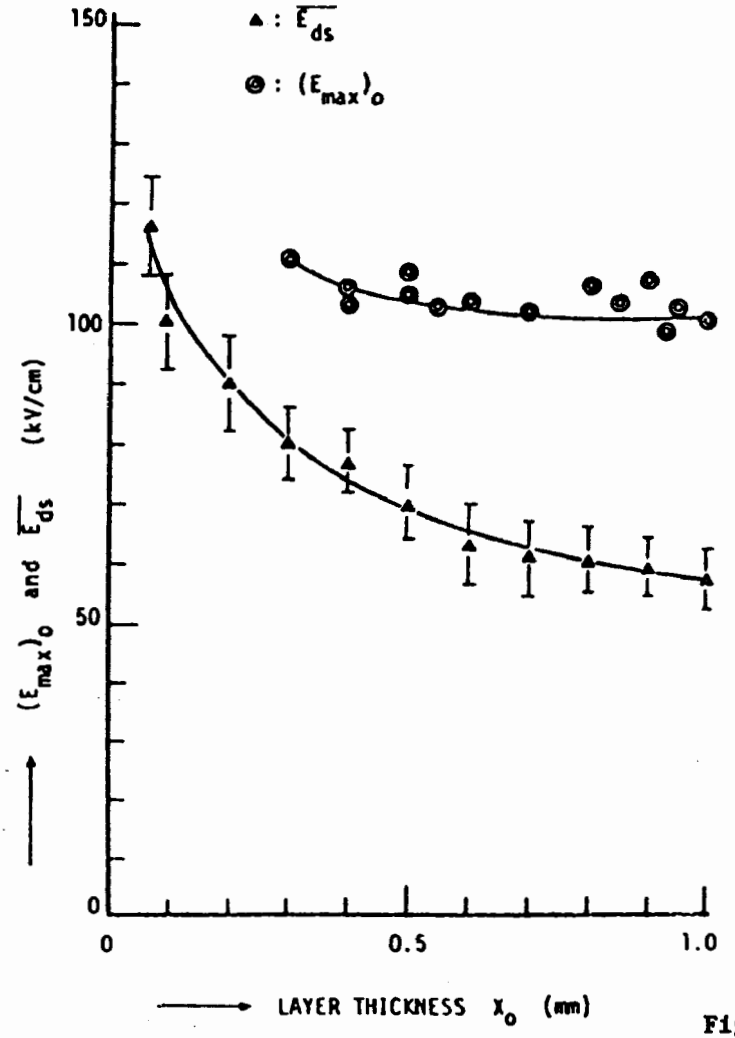

Fig.8 Comparison between $(E_{max})_o$ and $\overline{E_{ds}}$

UTILITY LIMIT AND MODE OF BACK DISCHARGE IN BIAS-CONTROLLED PULSE CHARGING SYSTEM

Senichi MASUDA, PhD. — Department of Electrical Engineering, University of Tokyo, 7-3-1, Hongo, Bunkyo-ku, Tokyo, Japan.

Ioshiaki DOI, PhD. — "

Ichiro HATTORI, PhD. — Ishikawajima-Harima Heavy Industries, 3-2-16, Toyosu, Koto-Ku, Tokyo, Japan.

Akira SHIBUYA, BSc. — "

Summary

Back discharge is investigated in the bias-controlled pulse charging system to be used in an electrostatic precipitator, and its practical utility limit is established in terms of critical main dc voltage V_{cc} and critical current I_c at which the visible back discharge initiates. Among the factors affecting this utility limit, the apparent resistivity of sample layer, ρ_d, has the most essential effect. The width and height of pulse voltage are the second important factors. When $\rho_d < 10^{13}$ ohm-cm, the occurence of visible back discharge is very seldom in this pulse charging system. When ρ_d exceeds 10^{13} ohm-cm, it becomes necessary to decrease the width and height of pulse voltage to improve the loss of the utility limit. When $\rho_d \geq 10^{14}$ ohm-cm, a large reduction appears in both V_{cc} and I_c, which, however, can be amended to some extent by using a very narrow pulse width and a low pulse height.

1. INTRODUCTION

Back discharge, one of the major troubles in electrostatic precipitators, is an abnormal corona discharge occurring on the surface of dust layer deposited on the collecting electrode when the apparent resistivity of the layer exceeds the threshold of about 5×10^{10} ohm-cm. In this case the potential drop across the layer becomes so high that breakdown takes place in the layer and triggers back discharge. Hence, its initiation condition is given by the layer breakdown condition, which, in case of electrostatic precipitators, takes the form[1]:

$$\rho_d \, i_d \geq E_{ds} \qquad (1)$$

where i_d = apparent current density in dust layer, and E_{ds} = breakdown field strength of the dust layer. It is evident from Eq.(1) that the solution of back discharge trouble will be enabled by reducing either ρ_d or i_d without decreasing the main field strength in corona space. Lüthi proposed a method to reduce i_d independent of the main field strength, which is indicated in Fig.1 (a)[2]. The third electrodes are arranged to the vicinity of the discharge electrode, and a periodical pulse discharge is applied therebetween. A dc high voltage is applied between the third and collecting electrodes to maintain the main field. This method proved to have an excellent performance for suppression of back discharge in laboratory tests, but in its practical application the following essential difficulties remained to be solved:

1) The difficulty in suppressing dc corona to occur in the pulseless period when the distance between the third and discharge electrodes is increased to the level of 10 cm, necessary for scale-up, and the gas and dust conditions fluctuate. This dc corona deteriorates the control performance of this method.
2) The prohibitively high initial and running costs of the pulse voltage source to be used.

A practical solution to these difficulties was provided by the authors by inserting a dc bias-voltage in series to the pulse voltage, as shown in Fig.1 (b), which is called the "bias-controlled pulse charging system"[3]. Through the control of maximum field strength at the discharge electrode, this bias-voltage can not only insure the choking of the dc corona to occur in the pulseless period, but also enables the use of ac or halfwave voltages instead of the very expensive sharp pulse voltage.

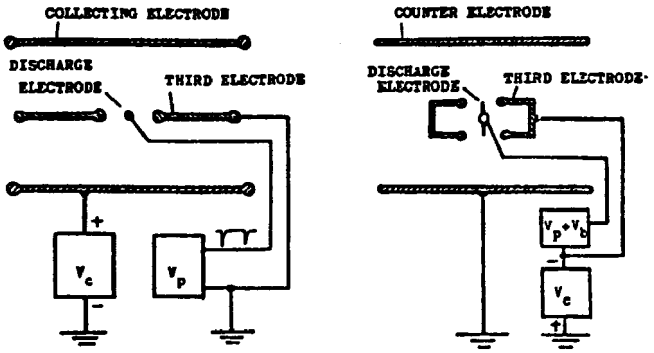

Fig.1 Pulse charging system

A problem arised, however, in the course of its development that the initiation of visible back discharge, which better represents the actual performance drop than the initiation of dust layer breakdown according to Eq.(1), is not only affected by ρ_d and i_d, but also by the strength of the main corona field. This means that the practical utility limit of this system for each value of ρ_d should be judged from the critical values of main dc voltage V_{cc} and current I_c at which the visible back discharge initiates. As is known, these two quantities are the most essential parameters determining the collection performence, since the saturation charge imparted to dust particles in corona field is proportional to the main field strength while the charging time constant is inversely proportional to the ratio of ionic current density to field strength. Furthermore, it also became clear that behaviours of back discharge in the pulse charging system are largely different from those observed in the conventional twin-electrode system.

Thus, the utility limit of this system and the mode of back discharge were studied in the ρ_d-range of $10^{11} - 10^{14}$ ohm-cm.

2. EXPERIMENTAL APPARATUS

The electrode system used in the present laboratory tests has an identical construction to those used in the pilot-plant tests described later, and is shown in Fig.1 (b) and Fig.2. The total surface area of the two counter (collecting) electrodes is 1 m^2, and the discance between the third and counter electrodes is 20 cm. The whole electrode system is placed inside a humidity controlled chamber, in which air humidity can be changed in a wide range under normal temperature and press-

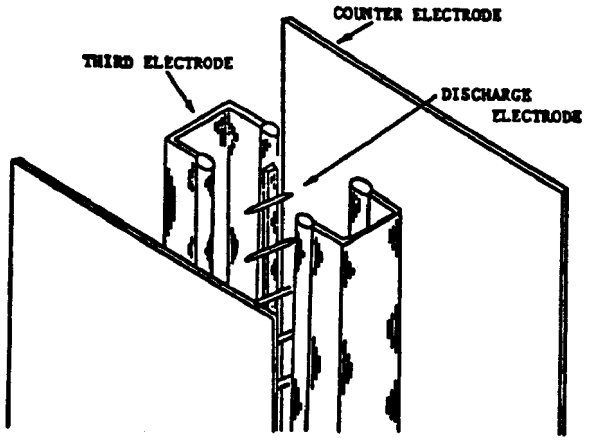

Counter to third electrode distance = 20cm

discharge to third electrode distance = 5cm

Fig.2 Electrode system used in laboratory and pilot-plant tests

ure. Instead of dust layer, paper towels are attached onto the surfaces of the counter and third electrodes, because their ρ_d-value can easily be changed within a broad range of 10^{11} - 10^{14} ohm-cm by controlling the air relative humidity.

The ρ_d-value of the paper towel is very sensitive to pressure so that it cannot successfully be measured by the parallel electrodes commonly used. The probe method, shown in Fig.3, is used throughout the present experiments, since it proved to provide very satisfactory results for the soft materials such as a paper towel[4]. The potential of the very light probe electrode, V_d, is measured by a zero method such that V_2 is adjusted to give $I_2 = 0$. At this point, we get:

$$V_2 \triangleq V_d = i_d \rho_d d \qquad (2)$$

where d = sample thickness. Hence, the ρ_d-value can be obtained from the relation

$$\rho_d \triangleq V_2 S / I_1 d \qquad (3)$$

where S = area of measuring electrode, and I_1 = current from measuring electrode. A protecting circuit consisting of r, L, R and C is provided to the high sensibility current meter I_2 for the purpose of preventing a damage to occur when a sparking takes place either between the plate and probe electrodes or between the needle and probe electrodes.

The pulse voltage source used in the present laboratory tests provides a periodical square-wave pulse with a rise time of 1 μs and a minimum duty cycle of 0.1, where the parameters can be changed in the range: pulse height = 0 - 30 kV, pulse width = 10μs - 10 ms, and pulse repetition frequency = 0 - 1 kHz. Throughout the laboratory tests the dc bias-voltage is omitted.

3. OBSERVATION OF BACK DISCHARGE

The initiation and mode of the visible back discharge are affected by the apparent resistivity of the sample layer ρ_d, pulse width τ, pulse repetition frequency f, pulse height V_p, and the main dc voltage V_c. The effects of field strength and current density in the gas and sample layer are contained implicitly in the effects of the above parameters.

3.1 Effect of ρ_d

Among the effects of the parameters described above, that of ρ_d is the most essential. In this system the visible back discharge occurs only scarcely

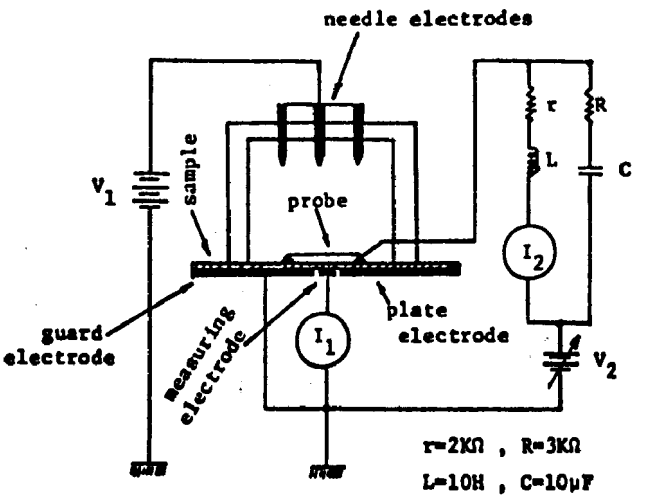

Fig.3 Probe method for measuring sample resistivity

in the resistivity range of $\rho_d < 10^{13}$ ohm-cm, when $V_c \leq$ 100 kV, $V_p \leq 30$ kV (negative polality), f > 10 Hz, and duty cycle ≤ 0.1. Once it appears, it takes the form of an unstable glow, from which a streamer suddenly develope toward the discharge electrode and turns into a flashover. When the frequency, f, or pulse width, τ, is raised, the occurence of the visible back discharge becomes more frequent, while its starting condition becomes more obscure.

The situation changes completely when the ρ_d-value exceeds 10^{13} ohm-cm. The visible back discharge appears in the form of a stable diffuse glow. With the increase in the main dc voltage V_c, the spot-like glow points appear on the sample surface with increasing number, as shown in Fig.4 (a) and (b). When V_c is further increased, the streamers develop from the glow points toward the discharge electrode, and finally bridge across the gap between the counter and discharge electrodes. A remarkable difference of these streamers from those occurring under $\rho_d < 10^{13}$ ohm-cm is that they very hardly turn into flashover. Another interesting behaviour of back discharge in the ρ_d-range higher than 10^{13} ohm-cm is that the glow spots jump around from point to point over the whole sample surface.

When the ρ_d-value exceeds 10^{14} ohm-cm, the visible back discharge also appears on the layer attached to the third electrodes if the main dc voltage V_c is kept sufficiently high. It is triggered by the positive ions coming from the back discharge spots on the collecting electrode, and disappears when these spots disappear. Another interesting phenomenon to be noticed in this extremely high resistivity range is that, even without the aid of negative ionic current, a feeble glow-like back discharge can occur only by dark current when V_c is kept sufficiently high.

3.2 Effects of V_c, V_p, f and τ

The effects of V_c, V_p, f and τ are indicated in the pictures of back discharge shown in Fig.4 (a) - (e). The values of parameters are indicated in the attached table in which the values of third electrode current, I_t, and counter electrode current, I_c, are also given. The comparison is made by changing one of the parameters, underlined in each line, the other parameters being kept almost equal. Fig.4 (a) and (b) clearly indicate the effect of V_c to activate the glow spots into streamer mode. A marked effect of increase in pulse width is indicated in (b) and (c). The increase in frequency, f, also results in an activity increase in back discharge, as shown in (a) and (d). (b) and (e) indicate that V_p has the same effect as V_c. Although these pictures are taken under an extremely high value

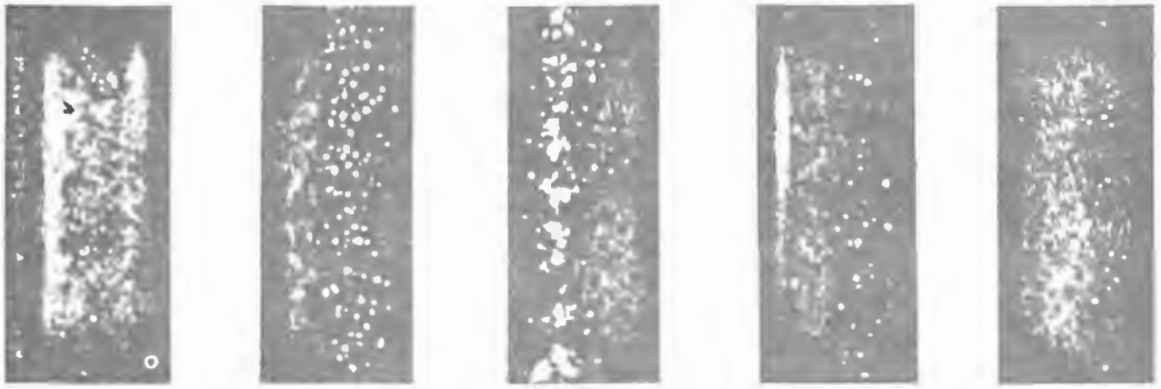

(a) (b) (c) (d) (e)

parameters	(a)	(b)	(c)	(d)	(e)
ρ_d (ohm-cm)	(1.2-4.4) x 10^{14}	"	"	"	"
V_c (kV)	45	58	60	35	54
V_p (kV)	- 20	- 20	- 20	- 20	- 10
f (Hz)	100	100	100	1,000	100
τ (μs)	100	100	1,000	100	100
I_t (μA)	100	300	254	100	100
I_c (μA)	55	175	164	60	100

Fig.4 Effects of V_c, V_p, f and τ on activity of back discharge

of ρ_d, the tendencies described above are observed in the whole range of ρ_d. It is felt that the effect of pulse width, τ, is the most essential, and next to it come those of V_c and V_p, and finally that of f.

4. UTILITY LIMIT

The utility limit of this system expressed in terms of the critical dc main voltage V_{cc} and critical average pulse current I_c is measured under various values of parameters ρ_d, V_p, and τ, with the value of f being kept at 100 or 200 Hz. The results obtained for the ρ_d-values of about 10^{11}, 10^{12}, 10^{13} and 10^{14} ohm-cm are shown in Fig.5 - 8 respectively. The utility limit giving the highest possible values of V_{cc} and I_c corresponds to the best collection performance.

In conformity with the fact that visible back discharge hardly occurs in the ρ_d value range $< 10^{13}$ ohm-cm, the utility limit as high as (V_c = 80 - 6[illegible] kV, I_c = 50 - 30 μA) is attainable in this range, as shown in Fig.5 and 6. The effects of τ and V_p are small except for cases of a very high V_p-value, as in Fig.5 (d) and Fig.6 (c), (d), where drooping characteristics with the increase in τ appear. A detailed examination shows that a slight loss in the utility limit occurs with the increase in the ρ_d-value from about 10^{11} to 10^{12} ohm-cm.

A remarkable loss in the utility limit appears when ρ_d exceeds 10^{13} ohm-cm, as shown in Fig.7. The decrease in I_c occurs in common, and that in V_{cc} also takes place for larger values of V_p and τ.

When ρ_d finally exceeds the threshold of 10^{14} ohm-cm, a very large reduction both in V_{cc} and I_c appears, as shown in Fig.8. However, it should be noted that the use of a very narrow pulse width of about 10 μS and a sufficiently low pulse height of about -10 kV provides a substantial improvement. The merit of a narrow pulse width and a low pulse height is also clearly observed in Fig.7.

From the results obtained it may be concluded that the most favourable ρ_d-range for this system to solve back discharge trouble will be that lower than 10^{13} ohm-cm, while a slight difficulty may appear in the range of ρ_d = 10^{13} - 10^{14} ohm-cm and the use of a narrow pulse width will become necessary. The range of ρ_d = 10^{14} seems to provide the upper limit for this system, where only the use of a very narrow pulse width could save the performance drop to some extent.

5. PILOT-PLANT TEST

The predictions obtained from the laboratory tests are examined at a pilot-plant located at an iron ore sintering furnace in connection to the exit of a conventional type electrostatic precipitator. This pilot-plant consists of a charging zone identical to that shown in Fig.1 (b) and Fig.2 and a collecting zone out of zig-zag arranged negative and positive channal electrodes, as shown in Fig.9. The gas transit time through a single charging zone is about 0.4 s. The dust consists mainly of Fe_2O_3 particles and contains small amounts of salts of alkaline metals as well as alkaline-earth metals by several percents in total. Its particle size is extremely small, and more than 70 % are in the range of sub-micron diameter. This is because most of the coarser particles has been collected in the preceding precipitator. The ρ_d-value of the dust is as high as 10^{13} - 10^{14} ohm-cm under operating conditions. In this test, a half-wave voltage with f = 50 and 625 Hz, produced by rectification of sinusoidal

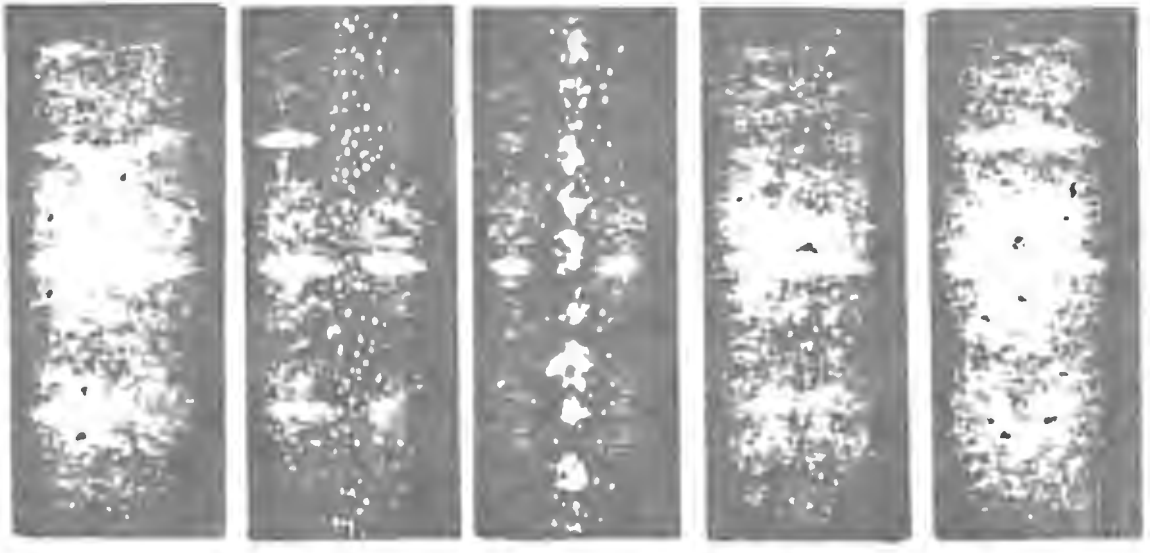

parameters	(a)	(b)	(c)	(d)	(e)
ρ_d (ohm-cm)	(1.2-4.4) x 10^{14}	〃	〃	〃	〃
V_c (KV)	45	58	60	33	34
V_p (KV)	- 20	-20	-20	- 20	-10
f (Hz)	100	100	100	1,000	100
τ (μs)	100	100	1,000	100	100
I_t (μA)	100	300	~~254~~ 294	100	100
I_c (μA)	55	175	164	60	~~100~~ 52

Fig.4 Effects of V_c, V_p, f and τ on activity of back discharge

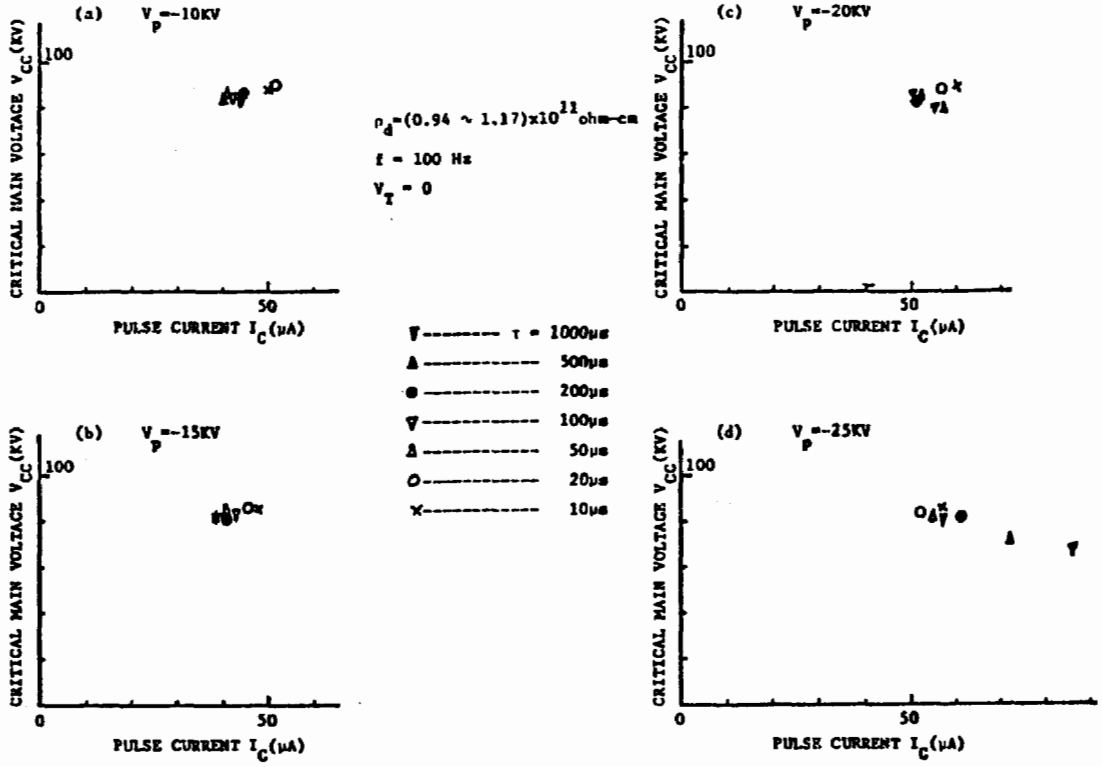

Fig.5 Utility limit - 1 ($\rho_d \doteq 10^{11}$ ohm-cm)

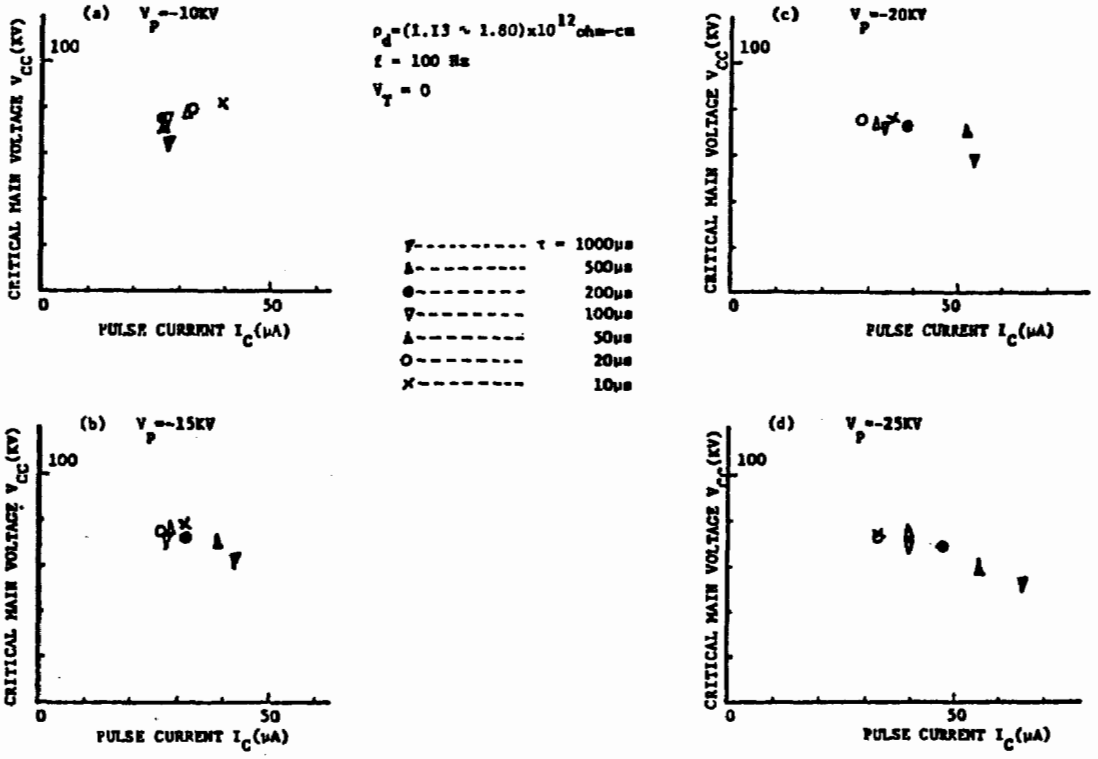

Fig.6 Utility limit - 2 ($\rho_d \doteq 10^{12}$ ohm-cm)

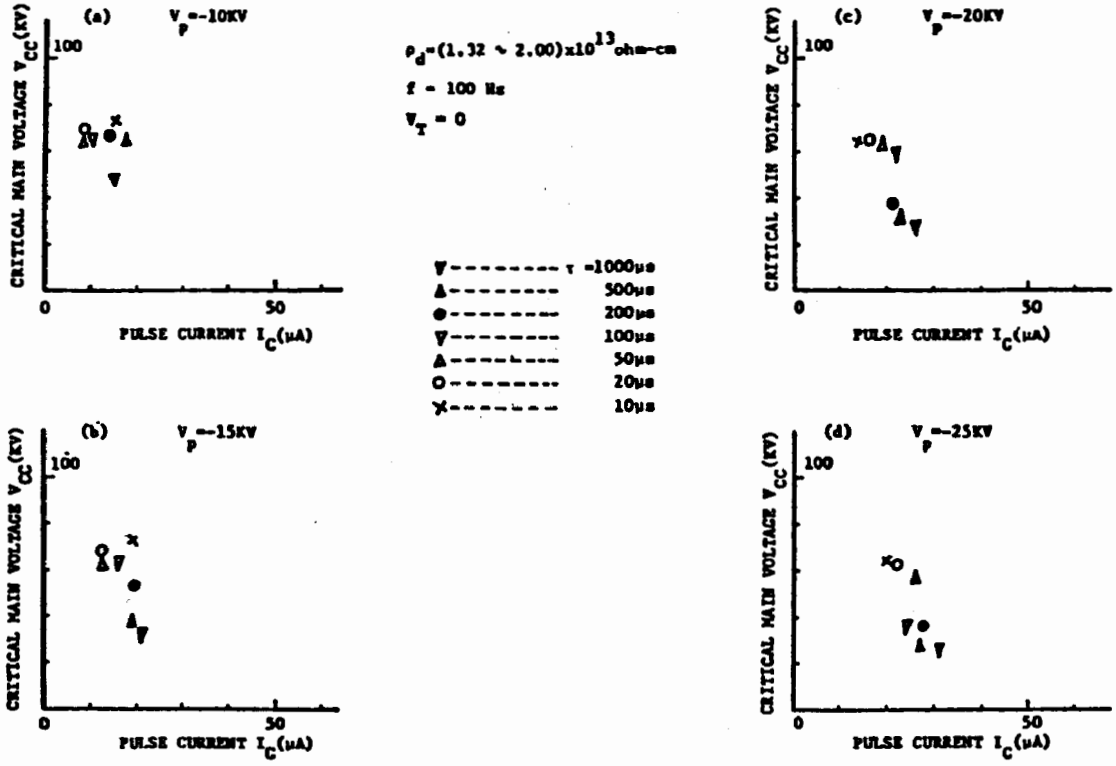

Fig.7 Utility limit - 3 ($\rho_d \doteq 10^{13}$ ohm-cm)

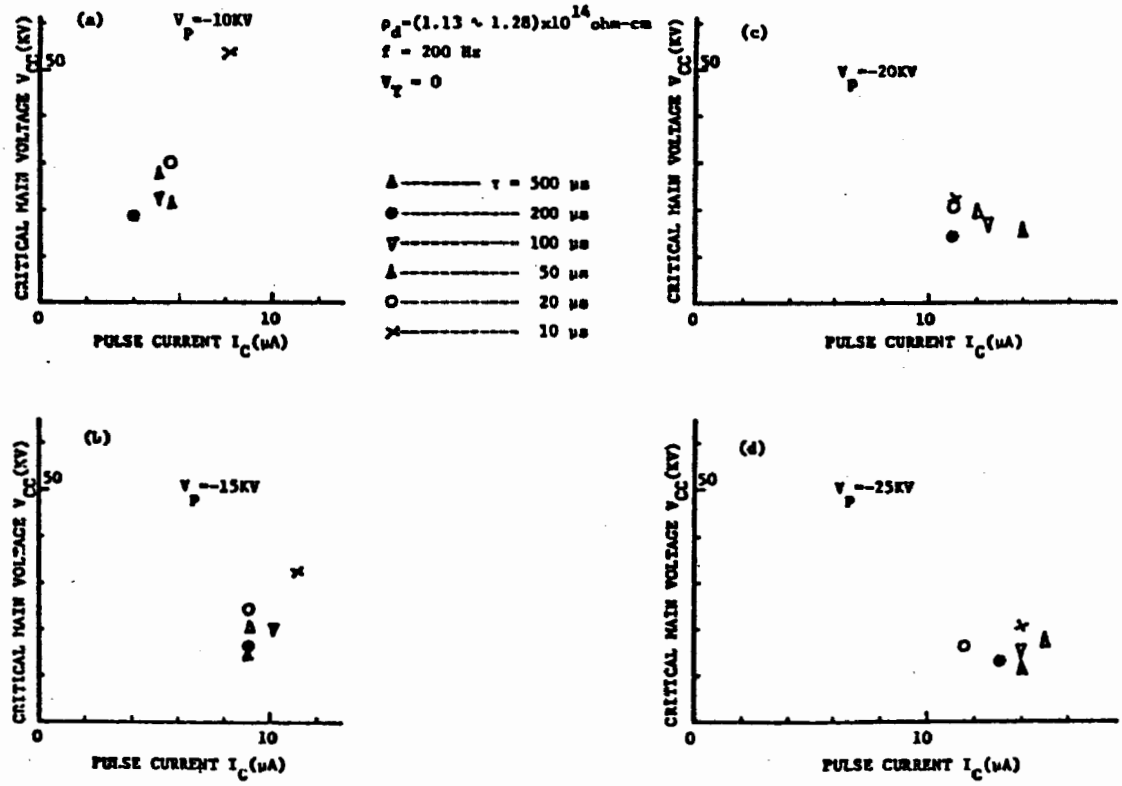

Fig.8 Utility limit - 4 ($\rho_d \doteq 10^{14}$ ohm-cm)

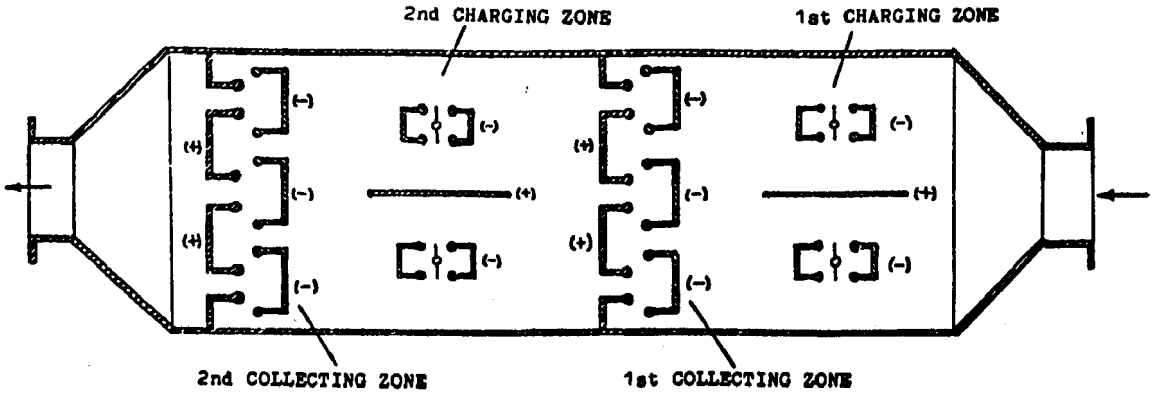

Fig.9 Construction of pilot-plant precipitator (PAC-ES type)

ac voltage, is used instead of a sharp pulse voltage. Hence, its equivalent pulse width τ_e can be assumed to be approximately 10 ms or 1 ms.

Fig.10 shows the relationship between the peak voltage V_p and the current I flowing into the counter electrodes of the first charging zone, where V_c is kept at 40 kV. The curve (4) indicates the normal V_p - I characteristics without back discharge. It can be seen from the curves (1) and (2) that back discharge, represented by abnormal increase in current I, is enhanced by the growth of thickness of dust layer. A remarkable improvement is observed to occur when an electrode rapping with sufficient strength and frequency is provided so that the layer thickness becomes small. The curves also clearly indicate the merit of using a narrow pulse width.

The collection performance of 65 - 85 % can be achieved under the optimum condition of curve (4), which exceeds the requirement set forth to the after-collector to be installed. This performance level represents a very satisfactory figure, considering the extremely high ρ_d-value, small particle size, and a very short treatment time.

It is concluded from this test that this system can provide a solution to back discharge occurring under $\rho_d = 10^{13} - 10^{14}$ ohm-cm when a half-wave voltage with $\tau_e \leq 1$ ms is used in combination to an effective electrode rapping (see Fig.7 (a)).

6. CONCLUSION

The following conclusions are obtained from the foregoing studies:

1) The bias-controlled pulse charging system and pulse charging system can provide an effective technical solution to the back discharge trouble up to the ρ_d -value of about 10^{14} ohm-cm.
2) The most favourable range of ρ_d for these systems is up to 10^{13} ohm-cm.
3) A slight difficulty appears in the range $\rho_d = 10^{13} - 10^{14}$ ohm-cm, where the use of a narrow pulse width becomes necessary for improving the performance loss.
4) The ρ_d-value of 10^{14} seems to provide an upper limit for these systems, where back discharge starts to occur also on the third electrode when V_c is raised sufficiently high. At this resistivity level back discharge can occur on the counter electrode even by a dark current when V_c is raised beyond a certain value.
5) The use of an extremely narrow pulse width in the order of 10 μs and a low pulse height may provide a possibility of improving a large performance drop to occur at $\rho_d > 10^{14}$ ohm-cm.

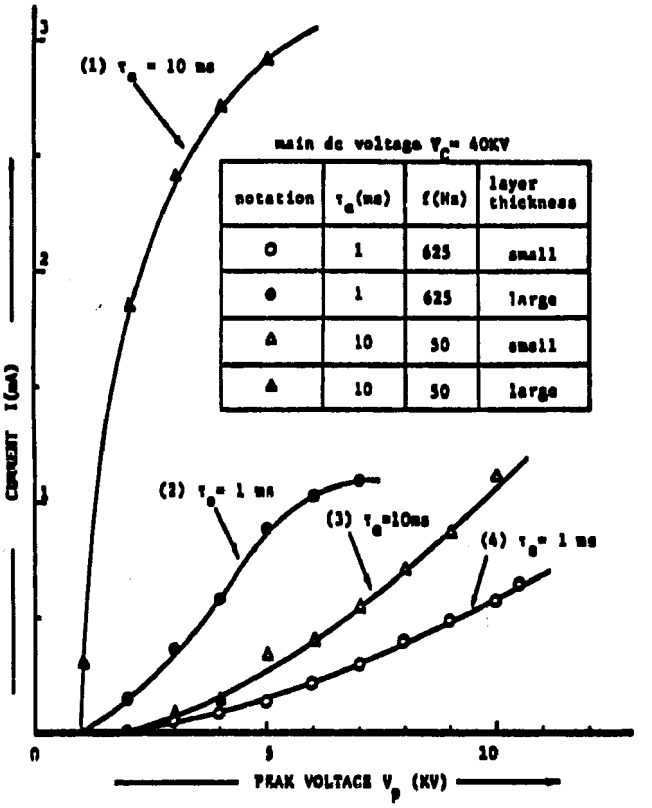

Fig.10 Relationship between counter electrode current I and peak voltage V_p (first charging zone; V_c = 40 kV, bias-voltage V_t = 0)

Acknowledgement

The authors wish to express their gratitude to the co-workers for their supports and assistances given to this work. Also one of the authors (Ioshiaki Doi) wishes to acknowledge the followship grants given by Japanese Ministry of Education and by Fundação de Amparo a Pesquisa do Estado de São Paulo (FAPESP), Brasil (Fis. 75/659).

References

(1) S.Masuda and A.Mizumo: Proc. 3rd Int. Conf. Static Electricity, 24-a (April, 1977 in Grenoble in France)

(2) J.E.Lüthi: Dissertation ETH-Zürich, No.3924 (1967)

(3) S.Masuda, I.Doi, M.Aoyama and A.Shibuya: Staub-Reinhalt. Luft, Bd.36, S.19 (1976)

(4) S.Masuda and S.Obata: Proc. 1975-Gen. Conf. of Inst. Elect. Engrs. Japan, Paper No.906 (1975)

THE ANALYSIS OF ELECTRIC WIND IN ELECTROSTATIC PRECIPITATOR (BY LASER DOPPLER VELOCIMETER)

S. Masuda, K. Akutsu, K. Aihara
Department of Engineering
University of Tokyo

Introduction

The electrostatic precipitator charges dust particles to remove them electrostatically, but the effect of electrical wind (ion wind) in precipitating process of particles cannot be ignored. In the electrostatic precipitator, there is a negative electrical wind from a discharging electrode and a reverse electrical wind due to inverse ionization phenomena. The velocities of these winds are at least several m/sec. On the other hand, the electrical moving velocity of the charged dust particle in the electrical field of 5 kV/cm is about 0.1 ∿ 1.0 m/sec for the particle with diameters ranging from 1 to 10 μm and at most 10 cm/sec for the submicron particle with diameter of about 0.1 ∿ 1.0 μm, Therefore, you have to treat the precipitating process of particles with diameter of less than 10 μm as, so called, EHD process which considers hydrodynamic field as well as electrical field.

Here, in this experiment, we have analyzed the electrical wind using the Laser Doppler Velocimeter. First, we have analyzed the negative electrical wind from the needle-point in point-to-plane electrodes. Secondly, we have generated inverse ionization by placing a mica plate with a hole on the plate electrode instead of dust particles and have analyzed the negative ionization electrical wind. Finally, we have investigated the behavior of submicron particles in the vicinity of a boundary layer near the plate electrode when there is a current parallel to the plate.

Measurement Method

The Laser Doppler Velocimeter is designed to measure the velocity of particles, which move at the same speed as current, by measuring the Doppler shift of scattered light from the particles. As scattering particles, we have used the D.O.P. particles [DOP Di-Octil-Phtalic Acid, average particle diameter of 0.3 μm]. An experimental apparatus is shown in Figure 1. In order to distinguish Vn and V'n in Figure 1, we have used the frequency shift system which shift the frequency of the other beam by 40 MHz. The size of measuring region is 116 μm wide, 1138.8 μm long and 0.008 mm^3 volume.

Experimental Results

Negative Electrical Wind

Velocity distributions of negative electrical wind (ion wind) in a perpendicular direction and in a parallel direction to the plate are shown in Figures 2 and 3. Figure 4 shows the velocity changes of the negative electrical wind which is perpendicular to the plate by applying various amounts of negative voltage to the needle-point. In the immediate vicinity of the plate, the negative wind velocity is proportional to the square of the voltage.

Reverse Ionization Electrical Wind

We have used the mica plate which has a pin-hole with a diameter of 0.5 mm instead of a dust particle. Figure 5 shows the measurement of velocity distributions of inverse ionization electrical wind in a perpendicular direction to the plate in the area above pin-hole. Figure 6 shows velocity changes in r direction. In the range of the voltage (15 kV $\sim$ 20 kV) and the electrical current 1 μA $\sim$ 10 μA), the increase in voltage and electrical current will increase the velocity of inverse ionization electrical wind in a perpendicular direction to the plate, however when the voltage and the electrical current exceed above range and when the streamers can be visually identified, the velocity will not be dependent on the voltage and electrical current and will be around 10 m/sec. A similar amount of inverse ionization electrical wind can be obtained by increasing the number of pin-holes and by superposing the influencing ranges of wrecking points. Also the negative electrical wind from the needle point was increased in about 0.5 m/sec (however, voltage = 25 kV).

Behavior of D.O.P. Particles in Vicinity of Bounday Layer

Figure 7 presents the behavior of D.O.P. particles near the plate when there is a parallel current r* direction in Figure 1) to the plate.

Conclusion

Since a negative electrical wind maintains a fairly high velocity [4 m/sec in 5 kV/cm and $6.4 \times 10^{-4} A/m^2$] as far as immediately before the plate, we think that most of the particles will be carried to the vicinity of precipitating point. The vicinity of precipitating point with a boundary layer and an eddy of about 30 cm/sec will be created just outside of this boundary layer. Also, since the inverse ionization electrical wind will exist in the area of several millimeters located a 1 cm in front of a wrecking point and have a high velocity of maximum 12 $\sim$ 13 m/sec, most of the particles in this area will probably be blown away.

Acknowledgment

We would express our sincere appreciation to beneficial suggestions given by Professor Toshimitsu Asakura, Hokkaido University concerning the Laser Doppler Velocimeter.

References

1. Mishina, Asakura: Application to the Measurements of Light Heterodine—Doppler Velocimeter—Applied Physics, Volume 42, Edition 6 (1973), 560.

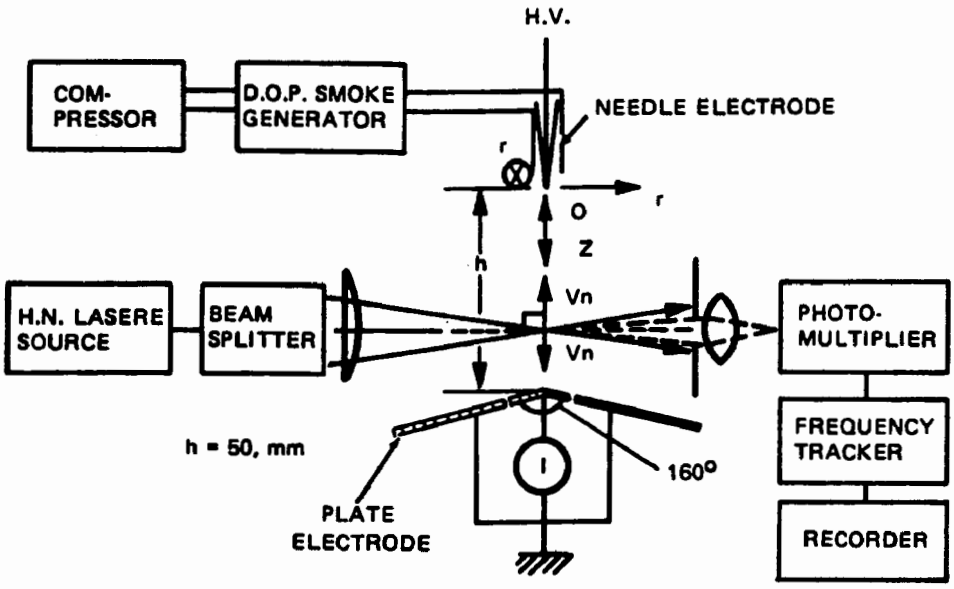

Figure 1. Schematic diagram of experimental apparatus.

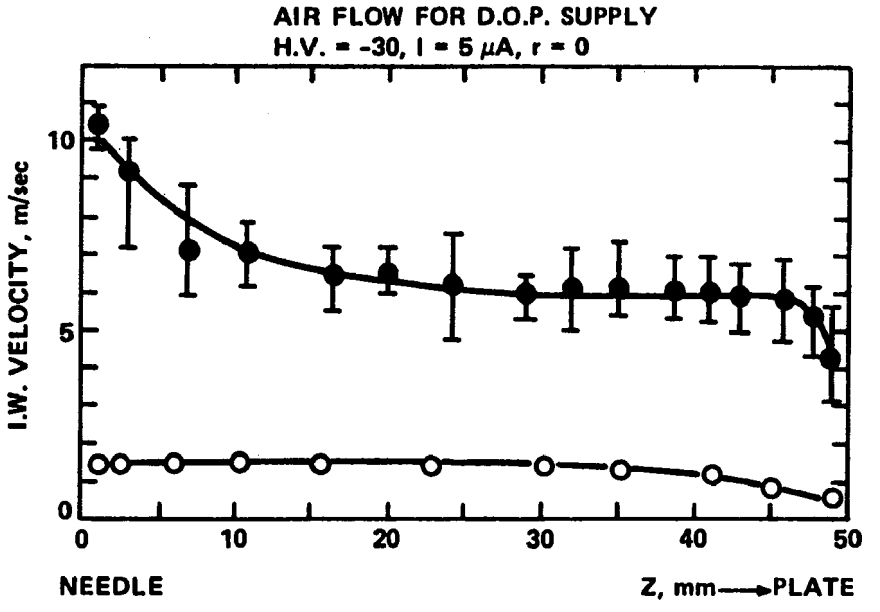

Figure 2. Negative I.W. distribution.

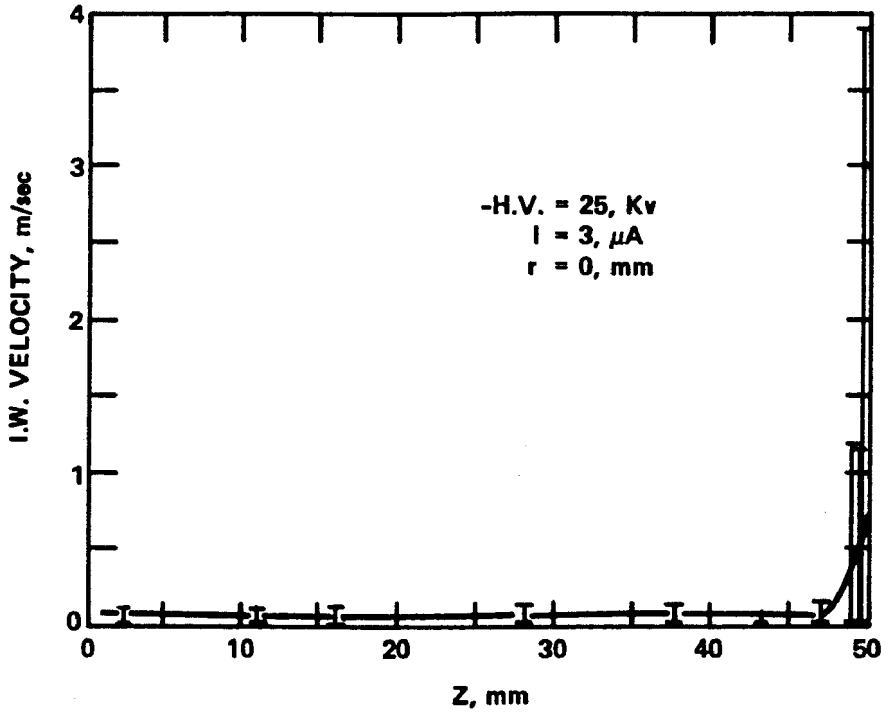

Figure 3. Distribution of negative I.W (Z direction).

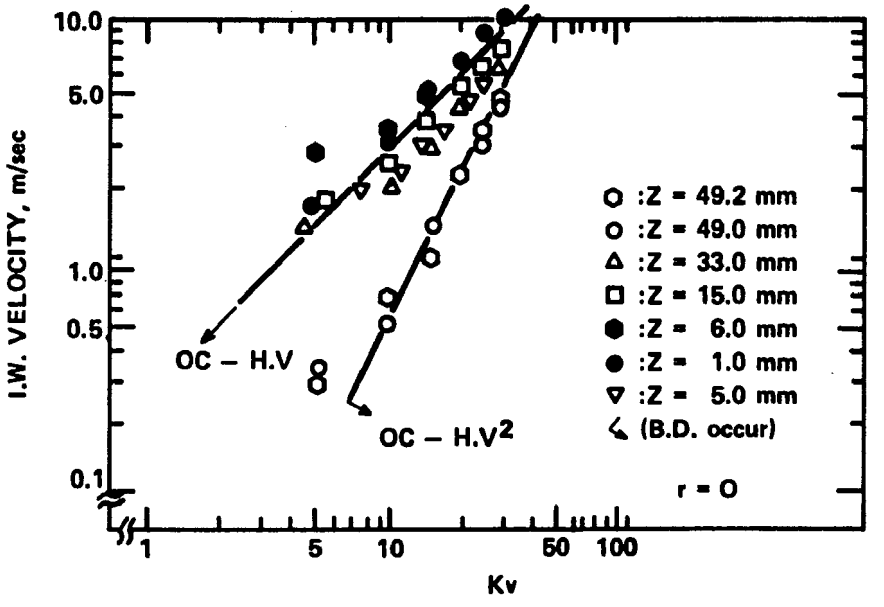

Figure 4. Negative I.W. (Z direction) vs. -H.V.

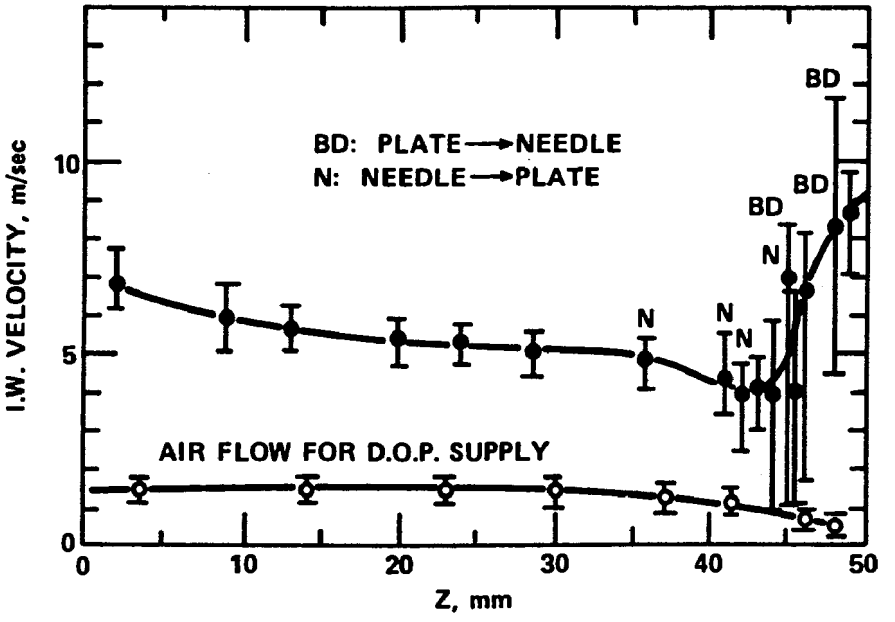

Figure 5. I.W. distribution (Back Discharge Occur).

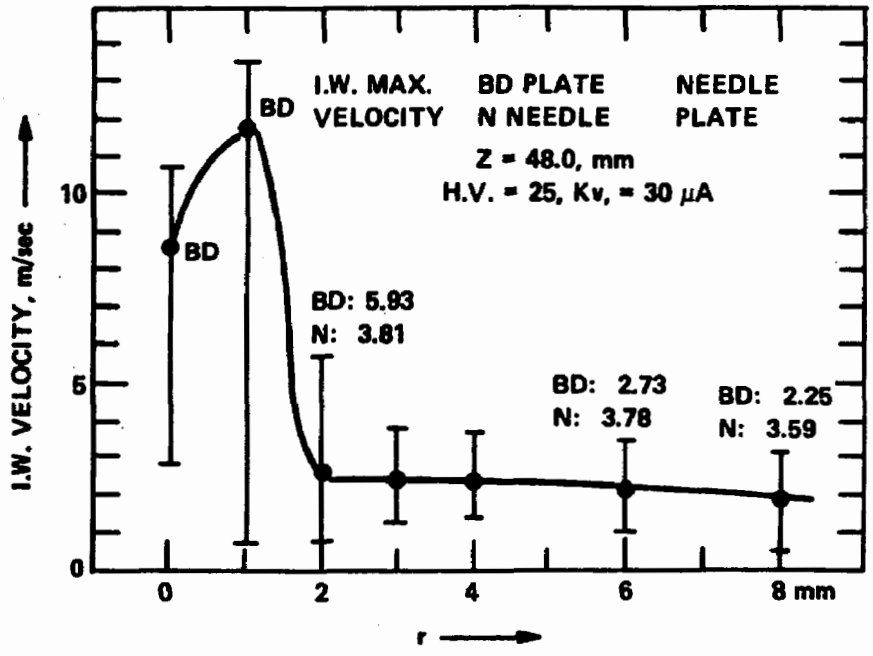

Figure 6. I.W. distribution of r direction (Z = 48.0 mm)

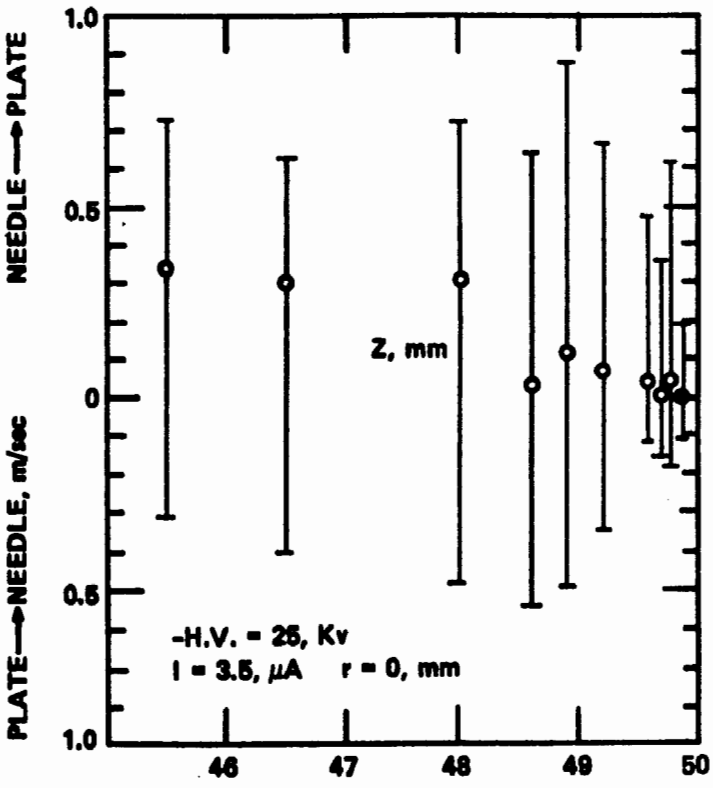

Figure 7. Submicron particles velocity nearby boundary layer.

FUNDAMENTAL ANALYSIS OF ELECTRON BEAM GAS ELIMINATION

S. Masuda, K. Akutsu, and M. Hirano

Introduction

Presently, the most effective method considered for eliminating NO_X (mainly NO) in the burned exhaust gas is the electron beam denitrate method. This is the radiological chemical method in which N_2 or H_2O in exhaust gas is activated by a high energy electron beam which was accelerated to 1~2 MeV and it will oxidize NO and then nitrate it. Therefore, this method requires neither special catalytic agent and oxidation agent nor reheating or pressurizing exhaust gases. Also, by added NH_3 in the electron beam injecting space, it will have solid nitrate aerosol and will prevent corrosion of equipment by nitric acid as well as possible precipitation. Most of all, this process can desulphurate as well as denitrate and the resulting product of this process ($3NH_4NO_3 \cdot (NH_4)_2SO_4$) can be utilized as a fertilizer.

As explained above, the electron beam denitrate method is a very epoch-making process, but initial and operating costs of the electron beam generating equipment is very high. In order to overcome this, it is planned to combine the electron beam injection into the electrostatic precipitator, namely to install the precipitating electrode in the beam injection space. This change can make an overall system compact, reduce the installing space and cost, but it is necessary to analyze how the electrical field generated in the electron beam injection space will affect denitrate reaction. This paper here has analyzed it experimentally.

Experiment Apparatus and Method

Gas Flow System (see Figure 1)

The electro-magnetic valves are located at the entrance and the exit of reaction cell to control a flow of sample. As a sample, a constant flow rate of (1 1/30 sec) N_2 is used as a carrier and small amounts of NO and NH_3 are supplied through capillary tubes. The concentration of sample is controlled by measuring pressure with manometer. Valves V_1 and V_2 are closed during experiment to have a stand-still condition.

Optical Measurement System (see Figure 2)

The measurement of NO was done by Infrared-Ray Molecule Extinction Method which uses a luminescence source of NO itself. This is based on the fact that only NO can absorb the luminescence (5.3 μm) which is produced when NO in a vibration excitation state returns to a stable state. The removal of NO under the electron beam application can be measured with high sensitivity-

Figure 1

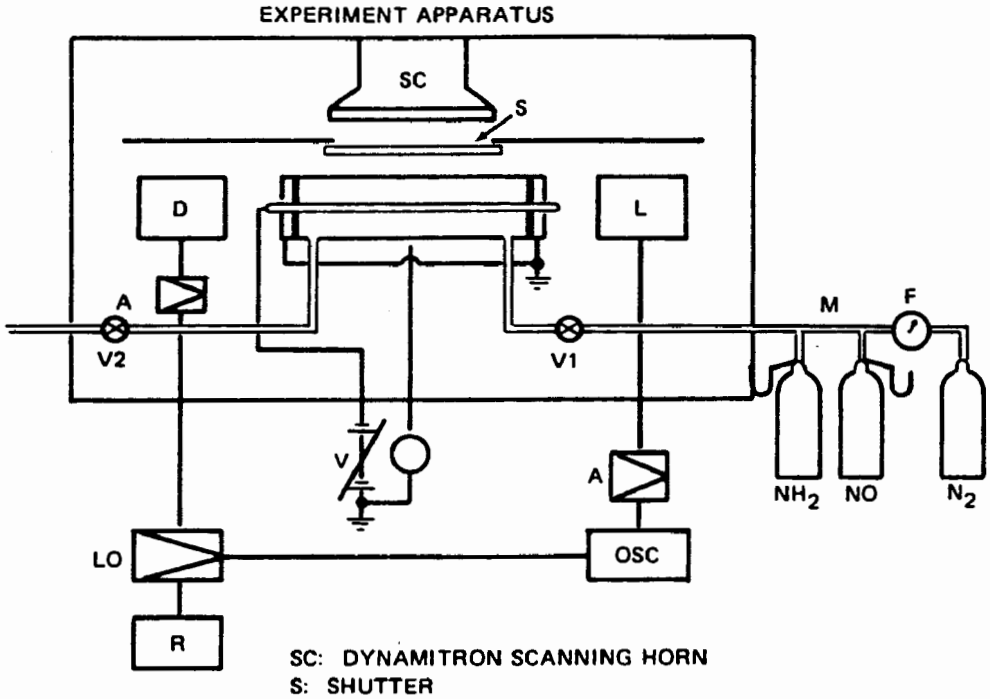

SC: DYNAMITRON SCANNING HORN
S: SHUTTER
L: NO-LAMP
D: InSb-DETECTOR
A: AMPLIFIER
LO: LOCK-IN AMPLIFIER
R: CHART RECORDER
OSC: RC-OSCILLATOR
M: MANOMETER
F: FLOWMETER
V1, V2: ELECTRO-MAGNETIC VALVES

Figure 2

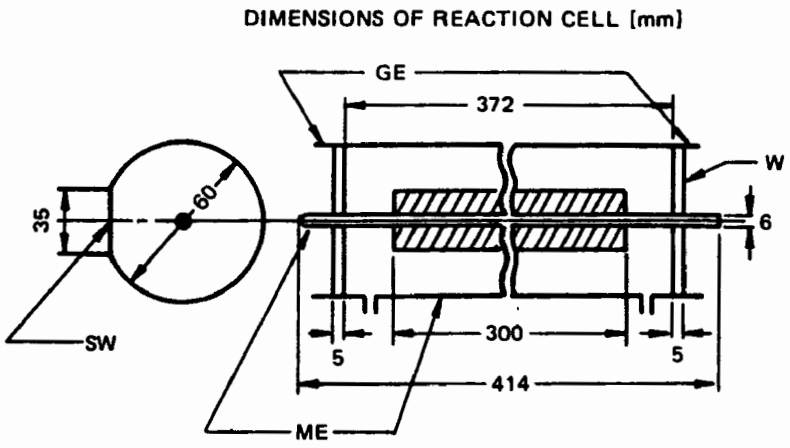

W: CaF_2 WINDOW
GE: GUARD ELECTRODE
ME: MAIN ELECTRODE
SW: STAINLESS STEEL WINDOW

high-speed-sequential-measurement in a real time. This technique has negligible interfernece by coexisting materials (H_2O, N_2, aerosols, etc.). Also, in order to have a better signal to noise ratio, the RC oscillator is used as a power source to modulate at Hz and the frequency composition of 120 Hz is extracted by the lock-in-amplifier.

Beam Application System

The dynamitron in University of Tokyo-Nuclear Research General Center was used as an electron beam application source. The application of beam is done by opening or closing the shutter and the beam will be scanned horizontally at 10 Hz to cover a sample entirely.

High Voltage System and Reaction Cell

The reaction cell has a same axis cylinder type main electrode and a negative high voltage is applied to the inside cylinder part. The outside cylinder has a separate guard electrode which is grounded and the electric current is measured between the main electrode and the ground. The cell has a CaF_2 window and a stainless steel window for the infrared ray and the electron beam, respectively.

Experiment Results

Figure 3 presents the relationship between beam application time and NO concentration when approximately 800 ppm of NO and 2000 ppm of NH_3 are supplied (about 1000 ppm of H_2O are possibly included because of system configuration) at the electron beam acceleration energy of 1.2 MeV and at the beam electric current of 97 μA. This figure shows that the existence of electrical field will promote denitrate reaction. Here the relationship between the reaction velocity (gradient of Figure 3 curve) and the applied voltage. On the other hand, the voltage-current characteristics in beam application space is linear as shown in Figure 5 and this satisfies the Ohm's law. Thus, the relationship between the denitrate reaction velocity and the electric current between electrodes will be similar to Figure 4. Here, in order to analyze how much the existence of electrical field contributes to the denitrate reaction, the relationship between the electric current and the 1/nth power of $(Vr-225)/225$ for the reaction velocity Vr are obtained (note; i vs $\underline{n}/\overline{(Vr-225)/225)}$ and Figure 6 shows this relationship for n = 2, 3, and 4.

Conclusion

1. In a mixed gas of N_2, NH_3 and H_2O, NO concentration decreases proportionally to the beam application time and the reaction amount is independent from NO concentration unlike ordinary chemical reactions. This means that the denitrate

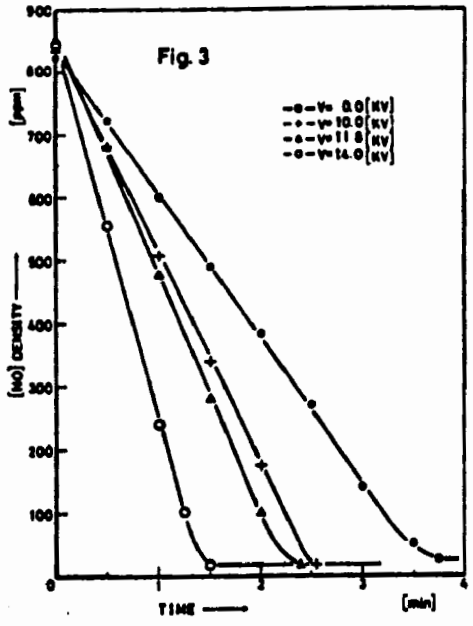
Fig. 3
[ppm]
[NO] DENSITY
TIME
[min]
0
100
200
300
400
500
600
700
800
900
1
2
3
4

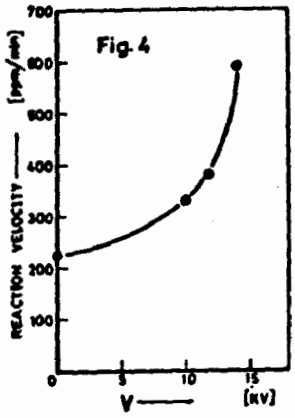

Fig. 4

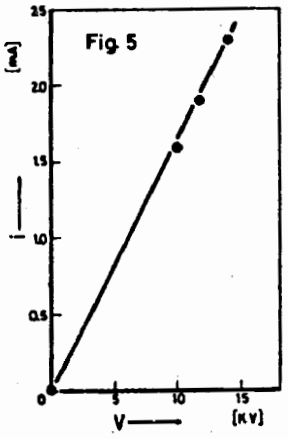
Fig. 5
25
20
1.5
1.0
0.5
0
i [mA]
5
10
15
V [KV]

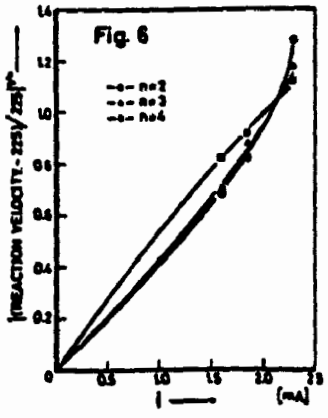
Fig. 6
n=2
n=3
n=4
1.4
1.2
1.0
0.8
0.6
0.4
0.2
0
0.5
1.0
1.5
2.0
I
[mA]

reaction is done in proportion to the number of emitted electrons (supplied from a source), thus it is expected that the denitrate reaction velocity is proportion to the number of emitted electrons (supplied from a point source), thus it is expected that the denitrate reaction velocity is proportional to the beam electric current. This was actually verified by the preparatory experiment done before this experiment.

2. The electrical field added to the application space extensively promote the denitrate reaction. It was confirmed that the electrical field and the electrical current contribute to the decrease reaction velocity of NO with the order of about third power and have a good effect in a speedy elimination of the aerosole product as well as a denitrate reaction, whatever the cause of this effect will be.

3. In the beam application space, the voltage is proportional to the current thus the applied electric power contributes to the denitrate reaction velocity with a power of 1.5th.

4. For the most effective denitrate case which is the 14 Kv and 2.3 mA, its average electrical field strength (3.68 Kv/cm) is about the same as that of ordinary electrostatic precipitator (3 Kv/cm). But the beam application space is abundant with various ions and electrons which give a high conductivity and the average current density will be 6.28×10^{-5} A/cm^2 which is larger than 100 times that of ordinary electrostatic precipitator (2×10^{-8} A/cm^2) and also the average electric power density will be 2.34×10^{-2} W/cm^3 which again is larger than 100 times that of ordinary one. Since the conductivity in the application space has a close relationship with the application amount rate (is proportional to the square root of the application amount rate), it is necessary to place the electrode in the application space which has the best denitrate rate (= denitrate amount/applied energy) in the actual plant. It will be a future project to obtain these conditions.

Motion of a Microcharge Particle Within Electrohydrodynamic Field

Electrical Engineering in Japan, Vol. 94, No. 6, 1974

Translated from Denki Gakkai Ronbunshi, Vol. 94A, No. 12, December 1974, pp. 515-522

S. MASUDA and Y. MATSUMOTO
Faculty of Engineering, University of Tokyo

Electrical Engineering in Japan, Vol. 94, No. 6, 1974

Translated from Denki Gakkai Ronbunshi, Vol. 94A, No. 12, December 1974, pp. 515-522

Motion of a Microcharge Particle Within Electrohydrodynamic Field

S. MASUDA and Y. MATSUMOTO
Faculty of Engineering, University of Tokyo

1. Introduction

Recently the study of the motion of microcharged particles (particle size 0.1 to 100 μm) in the EHD (electrohydrodynamic) field has become important in connection with the design of electrostatic precipitators and electrostatic painting. This study is reduced to the solution of equations of the motion of charged particles in the EHD field under given boundary and initial conditions. However, the analysis is very difficult if the boundary conditions are complicated and many problems still remain unsolved.

Steinbigler [1] proposed a charge substitution method which enables one to obtain approximate solutions for two-dimensional and symmetrical three-dimensional electric fields under complicated boundary conditions [2-6]. Using this method, we analyzed two-dimensional steady potential field of perfect flow under complicated boundary conditions [7]. In this paper, we analyze the motion of microcharged particles in EHD field by means of charge substitution and present a method of calculating collection efficiency of two-stage electrostatic precipitator (EP-ES type electrostatic precipitator [8]).

2. Equation for Motion of Microcharged Particles in EHD Field

The motion of microcharged particles in EHD field is described by

$$m\frac{d^2\boldsymbol{r}}{dt^2}+6\pi\eta a\left(\frac{d\boldsymbol{r}}{dt}-\boldsymbol{V}(\boldsymbol{r})\right)=q\boldsymbol{E}(\boldsymbol{r}) \tag{1}$$

where $\boldsymbol{r}$ is the positional vector of the particle, m is the particle mass, a is the particle radius; q is the particle charge, η is the viscosity coefficient of the medium, $\boldsymbol{V}(\boldsymbol{r})$ is the velocity vector of the medium at $\boldsymbol{r}$ and $\boldsymbol{E}(\boldsymbol{r})$ is the electric field at $\boldsymbol{r}$. It is assumed that Stokes' equation holds for the viscosity of the medium for Reynolds number $Re < 0.5$.

In the viscous flow, it is difficult to determine $\boldsymbol{V}(\boldsymbol{r})$ under complicated boundary conditions in both laminated flow and turbulence. Therefore, $\boldsymbol{V}(\boldsymbol{r})$ is approximated by the velocity distribution in the steady-state potential flow. Since both $\boldsymbol{V}(\boldsymbol{r})$ and $\boldsymbol{E}(\boldsymbol{r})$ are vectors in the potential fields, Eq. (1) is rewritten as

$$m\frac{d^2\boldsymbol{r}}{dt^2}+6\pi\eta a\frac{d\boldsymbol{r}}{dt}=-\operatorname{grad}\varphi_{EHD}(\boldsymbol{r}) \tag{2}$$

$$\varphi_{EHD}(\boldsymbol{r})=-\int_0^{\boldsymbol{r}}\{6\pi\eta a\boldsymbol{V}(\boldsymbol{r})+q\boldsymbol{E}(\boldsymbol{r})\}\,d\boldsymbol{r} \tag{3}$$

$$=6\pi\eta a\varphi_f(\boldsymbol{r})+q\varphi_e(\boldsymbol{r}) \tag{4}$$

where φ_f and φ_e are the velocity potential and electric potential with the origin O as a reference. In Eqs. (3) and (4), φ_{EHD} is called EHD potential and the resultant force $\boldsymbol{f}_{EHD}=-\operatorname{grad}\varphi_{EHD}$ at the right-hand side of Eq. (2) is called EHD force.

Under similar boundary conditions (duct walls or electrodes), the flow field and electric field are similar. Therefore, the distance is normalized to the suitable length (such as the electrode

surface distance) b

$$\phi_e(r) = -\int_0^r \boldsymbol{E}(r)\,dr = bE_0\phi_e(r/b) \tag{6}$$

$$\phi_f(r/b) = -\int_0^{r/b} \frac{\boldsymbol{V}(r/b)}{V_0}\,d(r/b) \tag{7}$$

$$\phi_e(r/b) = -\int_0^{r/b} \frac{\boldsymbol{E}(r/b)}{E_0}\,d(r/b) \tag{8}$$

V_0 and E_0 are the average flow rate and average electric field intensity in the region under consideration; φ_f and φ_e are the velocity potential and electric potential normalized to the average flow rate V_0 and average electric field E_0 in dimensionless space. These are called normalized velocity potential and normalized electric potential, respectively. Substituting Eqs. (5) and (6) into Eq. (4), we obtain

$$\begin{aligned}\varphi_{EHD}(r) &= C\{\phi_f(r/b) + K\phi_e(r/b)\} \\ &= C\phi_{EHD}(r/b)\end{aligned} \tag{9}$$

where

$$C = 6\pi\eta ab V_0$$

$$K = qE_0/6\pi\eta a V_0 = qU/6\pi\eta ab V_0 \tag{10}$$

$$\phi_{EHD}(r/b) = \phi_f(r/b) + K\phi_e(r/b) \tag{11}$$

where $U = bE_0$ is the applied voltage between electrodes; $\phi_{EHD}(r/b)$ is called normalized EHD potential in the dimensionless space and K is called electric field factor.

In the dimensionless coordinate normalized to b, the equation of motion (2) is rewritten as

$$\begin{aligned}mb\frac{d^2(r/b)}{dt^2} + 6\pi\eta ab\frac{d(r/b)}{dt} \\ = -\frac{C}{b}(\mathrm{grad})_b\phi_{EHD}(r/b)\end{aligned} \tag{12}$$

where $(\mathrm{grad})_b$ is a gradient operator in the dimensionless coordinate system. Further, we normalize the time by

$$\theta = \sqrt{mb^2/C} = \sqrt{mb/6\pi\eta a V_0} = \sqrt{T\tau} \tag{13}$$

where $\tau = m/b\pi\eta a$ is the relaxation time of the particle motion, and $T = b/V_0$ is the duration that the medium stays in the region under consideration. From Eq. (12), we obtain*

$$\frac{d^2(r/b)}{d(t/\theta)^2} + \zeta\frac{d(r/b)}{d(t/\theta)} = -(\mathrm{grad})_b\phi_{EHD}(r/b) \tag{14}$$

where

$$\zeta = \frac{6\pi\eta a}{m}\theta = \sqrt{\frac{6\pi\eta ab}{mV_0}} = \sqrt{\frac{T}{\tau}} \tag{15}$$

*Since θ contains a and m, there is no time scale common to all particles. Therefore, Eq. (14) must be used carefully in the study except for the analysis of particle trajectories.

3. Modes of Particle Motion

As seen in Eq. (14), modes of particle motion in the dimensionless space are determined by the distribution of normalized EHD potential $\phi_{EHD}(r/b)$ and dimensionless parameter

3.1 Effect of $\phi_{EHD}(r/b)$

In the EHD field with similar boundary conditions (duct shape, electrode shape, etc.), the distributions of normalized velocity potential $\phi_f(r/b)$ and normalized electric potential $\phi_e(r/b)$ and their magnitudes are independent of the structural size, average flow rate V_0 and average electric field E_0. Specifically, $\phi_f(r/b)$ and $\phi_e(r/b)$ are pattern functions representing geometrical patterns of flow field and electric field. However, normalized EHD potential $\phi_{EHD}(r/b)$ which is a linear combination of $\phi_f(r/b)$ and $\phi_e(r/b)$ is dependent on the value of K even under similar boundary conditions.

As seen in Eq. (10), K is a ratio between average electric force acting on particles and average viscosity force (with respect to stationary particles) and represents the effect of physical parameters other than the patterns of the flow field and electric field. The larger the value of K, the more the electrodynamic force is dominant over the hydrodynamic force.

(i) When $K \ll 1$, we have $\phi_{EHD} \approx \phi_f$ and the particle motion depends on the flow field only.

(ii) When $K \gg 1$, we have $\phi_{EHD} \approx K\phi_e$ and the particle motion depends on electric field only.

(iii) When $K \sim 1$, the particle motion depends on both flow field and electric field, and is of the EHD motion.

3.2 Effect of ζ

As seeb in Eq. (14), ζ represents the effect of viscosity on inertia in the motion and is called the viscosity factor

(i) When $\zeta \ll 1$, the inertia term is effective and the particle motion becomes ballistic. Specifically, the initial conditions affect greatly the particle motion and the EHD potential wall becomes soft, resulting in weakening its constraint force.

(ii) When $\zeta \gg 1$, the viscosity term is effective and the particle motion becomes viscous. Particles move along the gradient of the EHD potential and its lines of force coincide with the particle trajectories. The initial conditions are less effective and the EHD potential wall becomes hard, resulting in strengthening of its constraint force.

(iii) When $\zeta \sim 1$, the particle motion is affected by both inertia and viscosity.

In case of (i) and (iii), particle loci can be obtained by solving Eq. (14). In practice, however, the condition of $\zeta \gg 1$ in (ii) holds. In such cases, the particle loci can be determined from the lines of force in the EHD field.

4. Examples of Particle Motion

As described in the previous section, the particle motion is analyzed by obtaining the normalized EHD potential ϕ_{EHD} in the dimensionless space under the given boundary conditions. For this purpose, we draw the flow path and electrodes in the coordinate system with b as unit length, and obtain ϕ_f and ϕ_e, i.e., the velocity potential and electric potential in the flow field with unit flow rate and with unit electric potential applied to the electrodes, respectively. It is not necessary to take the coordinate origin as a reference point; a point where the flow rate distribution is uniform is taken as a reference point for ϕ_f and one of electrodes is taken as a reference point for ϕ_e. In obtaining ϕ_f and ϕ_e under complicated boundary conditions, the charge substitution method is most effective; sufficiently accurate result can be obtained within a short time by a computer with small memory capacity. In the following we obtain ϕ_f and ϕ_e by means of charge substitution for 2-stage electric participator and analyze the particle motion with ϕ_{EHD} for various values of K. For deriving ϕ_f and ϕ_e by means of charge substitution, refer to [1-6, 7].

4.1 Parallel arrays of cylindrical electrodes arranged in a zigzag fashion in a uniform flow

We consider two parallel arrays of cylindrical electrodes (diameter d) arranged in a zigzag fashion. Particles start to flow downward from points 0, 1, ... 10 which equally divide the surface interval between upstream electrodes. They have the initial velocity identical to the flow rate in the y-direction and have the charge of the same polarity as the upstream electrodes. The electric field factor is assumed to be K = 2.

Figure 2(a) shows the EHD lines of force passing through 0, 1, ... 5, which were calculated by means of charge substitution. Figures 2(a)-(g) show the loci of particle motion for the value of ζ in the range of $10 \sim 0.1$ which were obtained by calculating Eq. (14) by computer. As the value of ζ increases, the particle motion becomes viscous and their trajectories coincide with EHD lines of force. Inversely, as the value of ζ decreases, the particle motion becomes ballistic, and the initial conditions become more effective and the loci of particle motion deviate from the EHD lines of force.

Figure 3 shows the loci of motion of particles which starts from point 0; the dotted line represents the EHD line of force which passes the

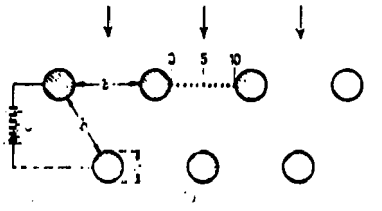

Fig. 1. Parallel cylinder electrodes arranged in a zigzag fashion in a uniform flow.

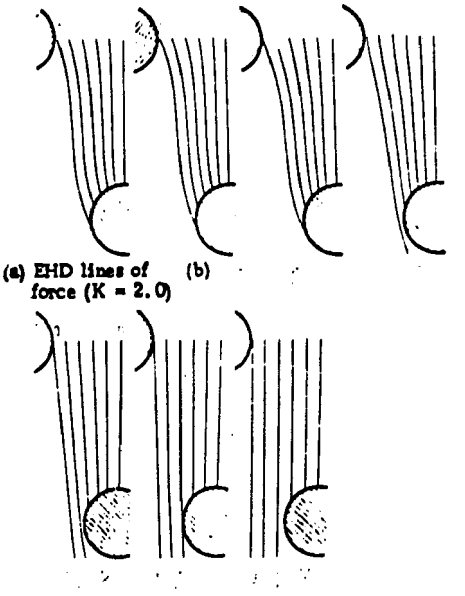

Fig. 2. EHD lines of force and loci of particle motion for the case of Fig. 1.

point 0. As seen in this figure, the loci of particle motion can be estimated from the EHD lines of force in the range of $\zeta \geq 5$. For $\zeta \geq 10$, they can be estimated with high accuracy. It is seen from Eq. (15) that the loci of particle motion can be estimated from the EHD lines of force if the particle radius is

$$a_c \leq \left(\frac{3}{5} \sim \frac{3}{10}\right)\sqrt{\frac{\eta b}{2\rho V_0}} \qquad (16)$$

Figure 4 shows the relation between a_c and V_c for a case of $\rho = 2.5 \times 10^3$ kg/m^3, b = 5 cm, $= 1.83 \times 10^{-5}$ Ns/m^2 (20°C in air) and $\eta = 2.39 \times 10^{-5}$ Ns/m^2 (150°C in air). In electrostatic precipitator, the average gas flow rate is $V_0 \simeq 1$ m/s. Substituting $\zeta < 5$ into Eq. (16), we obtain $a_c \geq 9$ μm. Inversely, the electrostatic precipitator can correct particles of radius $a \leq 5$ μm. Therefore the loci of particle motion can be estimated from the EHD lines of force with sufficient accuracy. Theoretical collection efficiency can be estimated from a rate of the lines of force which terminate at the downstream electrode

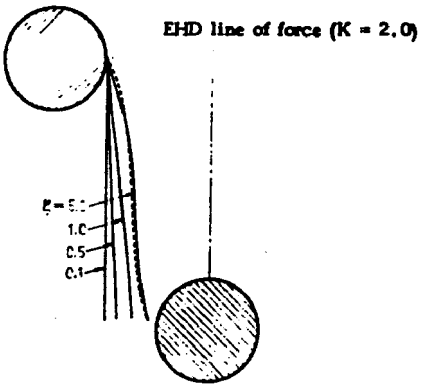

Fig. 3. EHD line of force and loci of particle motion starting from the point O for the case of Fig. 1.

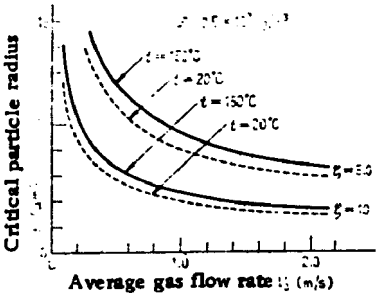

Fig. 4. Critical particle radius a_C for locus estimation by EHD lines of force vs. average flow velocity V_0 for the case of air flow.

(collecting electrode) to those which start from points 0, 1 ... 5.

When particles are charged by corona discharge, their theoretical saturated charge is given [9] by

$$q_{in} = 4\pi\varepsilon_0 \frac{3\varepsilon_s}{\varepsilon_s+2} a^2 E_c \qquad (17)$$

when ε_S is specific dielectric constant of particle, ε_0 is dielectric constant of vacuum, and E_C is the field intensity in corona space. Substituting Eq. (17) into Eq. (10), we obtain electric field factor

$$K = 2\varepsilon_0\varepsilon_s a E_c E_0 / \eta V_0(\varepsilon_s+2) \qquad (18)$$

Letting $\varepsilon_S = 2.5$, $E_C = E_0 = 5$ kV/cm and $\varepsilon = 2.39 \times 10^{-5}$ Ns/m^2 (150°C in air) and expressing a and V_0 in terms of [μm] and [m/s], respectively, we obtain $K \simeq 0.1\,(a/V_0)$. Therefore, as the particle radius a increases and as the flow rate V_0 decreases, the electric field factor K increases. For the condition $K \geq 1$ under which the particle motion is effectively controlled by electric field in the EHD field, we have a [μm] $\geq 10\,V_0$ [m/s]. Therefore, it is difficult to collect extremely small particles by electrostatic precipitator unless the value of V_0 is reduced below 1 m/s.

4.2 Parallel arrays of channel electrodes arranged in a zigzag fashion with their openings facing each other in a uniform flow

We consider a case (Fig. 5) where channel electrodes are arranged in a zigzag fashion with their openings facing each other; the charge has the same polarity as the upstream electrode and cylinders are attached at the edges of channel electrodes. These electrodes are used as a particle collector of 2-stage electrostatic precipitator; an electric charger by means of corona discharge is installed at the upstream side. In this electrode arrangement, openings between the upstream channel electrodes work as a nozzle to absorb particles and electric field in a space between the upstream and downstream channel electrodes force particles to enter openings of the downstream electrodes.

Assuming that the particle radius is sufficiently small with the condition of $\zeta \geq 5$, we estimate the particle collection coefficient from the distribution of the EHD lines of force.

Figure 6 shows the distribution of the EHD lines of force for K = 0 ~ 3.0 which was obtained by means of charge substitution. It is assumed that the lines of force start from points which divide the interval between two upstream electrodes equally by 20. In the field calculation, the charge to be substituted was not placed behind the downstream channel electrodes. Therefore, electric lines of force and EHD lines of force did not terminate at the downstream electrode and the interior of the channel electrodes. However, electric field inside the channel electrodes is so small that the errors can be neglected in the estimation of the lines of force and collecting efficiency. The collecting efficiency can be expressed in terms of a ratio of the number of the lines of force terminating at the downstream electrodes to that of the lines of force entering the openings. When K = 0 (Fig. 6(a)), the EHD lines of force coincide with the stream lines and collecting efficiency is zero. As the value of K increases the distribution of the EHD lines of force approaches that of electric lines of force and particles are forced to enter the interior of electrodes, resulting in an increase of collecting efficiency.

Figure 7 shows the relation between collection efficiency and electric field factor; particles whose loci correspond to lines of force terminating at the downstream channel electrodes inner than point P were counted. In this electrode arrangement, the 100% collection coefficient can be obtained for $K \geq 1.95$.

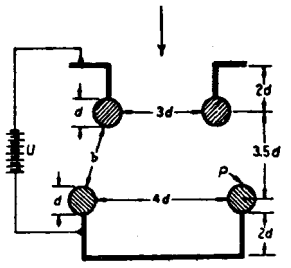

Fig. 5. Parallel channel-electrodes arranged in a zigzag fashion with their openings facing against each other.

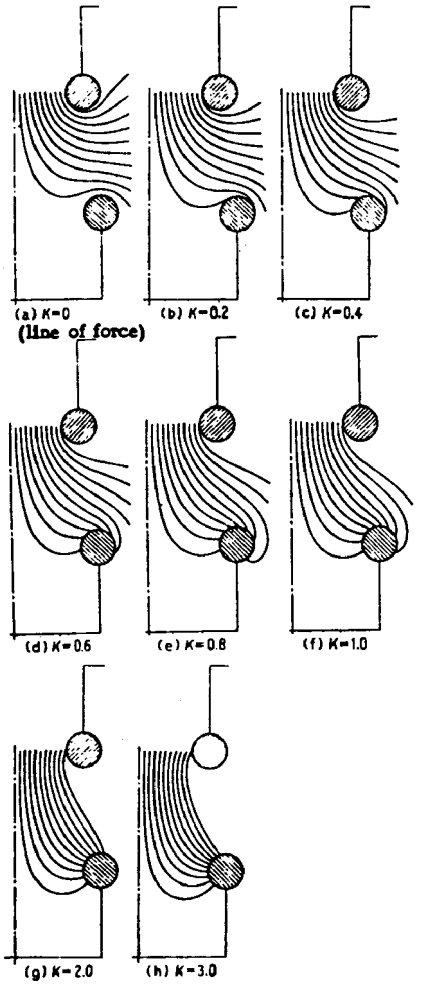

Fig. 6. Distribution of EHD lines of force (case of Fig. 5).

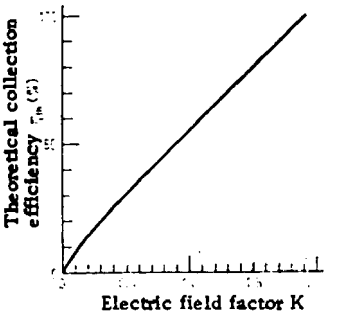

Fig. 7. Theoretical collection efficiency ηth vs. electrical field factor K for the case of Fig. 5.

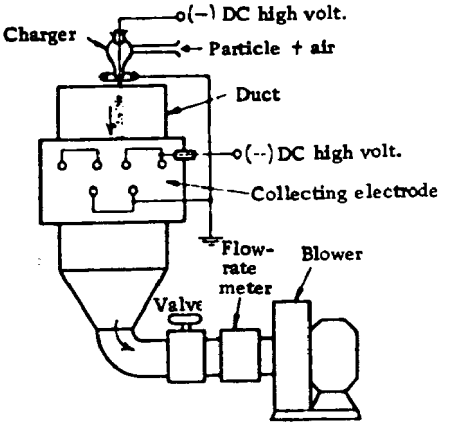

(a) Experimental setup

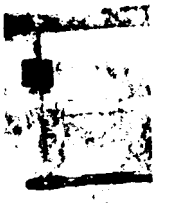

(b) Electric charger

Fig. 8. Experimental apparatus.

5. Observation of Loci of Particle Motion

We have observed the loci of particle motion using the electrodes shown in Fig. 5 with d = 2.17 cm and measured electric charge.

Figure 8(a) and (b) show the experimental setup and electric charger, respectively. Lycopodium particles ($\bar{a} \simeq 15\ \mu$m, $\bar{m} = 1.5 \times 10^{-11}$ kg) which are almost spherical were used as test particles. Their electric charge varies around the average $\bar{q} = 1.1 \times 10^{-14}$ C. The average air flowrate was $V_0 = 20$ cm/s which allows particles to move in a viscous mode with the condition of $\zeta > 5$.

Figure 9 shows the loci of particle motion for $K_1 = 0 \sim 4.0$.

Figure 9(a') shows the flow of cigarette smoke. The collection efficiency in this case is higher than that estimated from the EHD lines of force. This may be (1) because eddys occur below the upstream electrodes and absorb particles into the interior of the downstream electrodes, and (2) because the

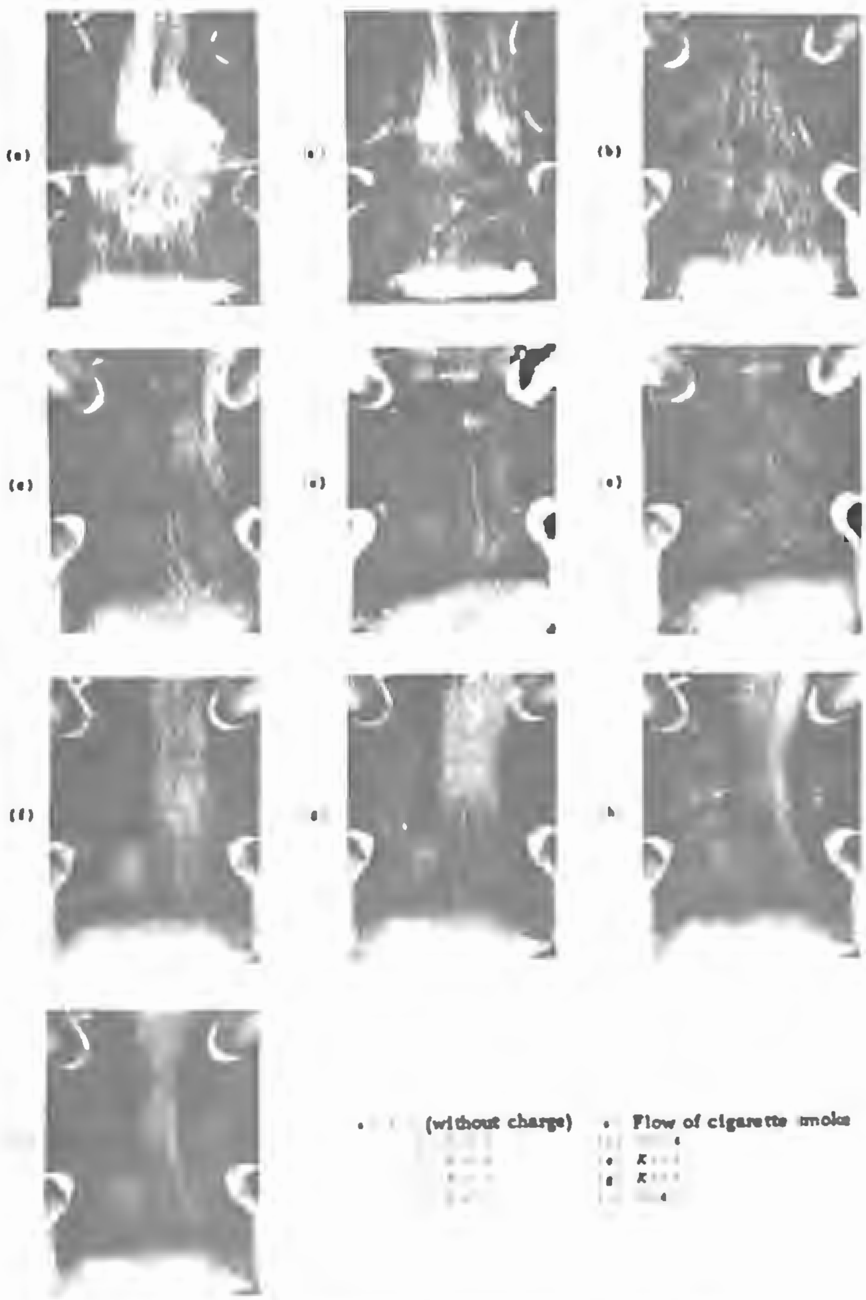

Fig. 9. Pictures of particle loci (see Fig. 6).

particle motion becomes balli[illegible]tic in a region b[illegible]low the upstream channel [illegible]lectro[illegible]s wher[illegible] th[illegible] average flowrate is 3 V_0.

To examine the above results in more detail, we observed the amplitude of particle motion in the ac field and measured electric charge q(c) of lycopodium particles which escape from the downstream electrodes. Figure 10 shows the relation between q_{max} and E_0 [illegible] U/b where U(V) is the applied electric field. In this electrode arrangement an interval between two adjacent upstream chann[illegible]l electrodes was identical to an interval of the downstream channel electrodes 4 d (d [illegible] 2.17 cm) and V_0 [illegible] 20 cm/s. As seen in Fig. 11, when $K_c > 1.4$, particles do not escape from the downstream channel electrodes. From Eq. (10), the theoretical maximum electric charge of particles which escape from the downstream channel electrode is given by

$$[illegible] \doteq 4 \times \frac{6\pi\eta a V_0}{E_0} \qquad (19)$$

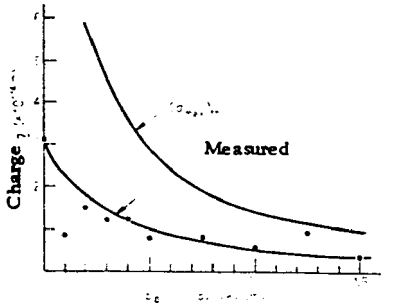

Fig. 10. Comparison of the maximum charge q_{max} of uncollected particles with its theoretical value $(q_{max})_{th}$ (see Fig. 11).

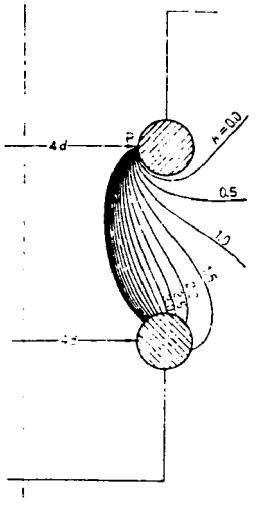

Fig. 11. EHD line of force starting from the point P (see Fig. 10).

In Fig. 10, the solid curves represent the measured relation between $(q_{max})_{th}$ and E_0 for a = 15 x 10^{-6} m, η = 1.83 x 10^{-5} Ns/m^2 and V_0 = 0.2 m/s. The maximum of q is dependent on the electric charger and is about 3 x 10^{-14} C which corresponds to E_0 = 0. Accordingly, the measured q_{max} is much lower than the calculated value, and the measured collection efficiency is higher than the collection efficiency estimated from the EHD lines of force.

6. Conclusions

The motion of microcharged particles in the EHD field has been analyzed and the performance of two-stage electrostatic precipitator has been discussed. The result obtained in this research is summarized as follows.

(1) The analysis of particle motion can be simplified by use of EHD potential, and the loci of particle motion can be studied in terms of normalized time and space.

(2) The EHD potential can readily be calculated by means of charge substitution.

(3) In an electrostatic precipitator, the viscosity factor ζ is always larger than 1, and the mode of particle motion is viscous. The loci of particle motion coincide with the EHD lines of force from which collection efficiency can be estimated.

(4) When K $\geq$ 1, the particle motion can be controlled by electric field.

(5) In practice, the collection efficiency is lower than that estimated from the EHD lines of force because of the generation of eddys and ballistic region.

The analysis method described above is applicable to not only electrostatic precipitator but also other fields relating to the motion of microcharged particles in the EHD field.

REFERENCES

1. H. Steinbigler. Dissertation, T.H. München, 1969.
2. H. Singer. Ibid., 1969.
3. P. Weiss. Ibid., 1972.
4. Masuda, Mitsumoto. Trans. I.E.E., Japan, Vol. 93-A, 305, July 1973.
5. Masuda, Matsumoto and Uemura. 1971 Tokyo Branch Meeting, I.E.E., Japan, No. 372.
6. Takechi, Masuda, Matsumoto, Nioka. 1973 Nat'l Conv. I.E.E., Japan, No. 842.
7. Masuda, Matsumoto. To be published in Trans. I.E.E., Japan.
8. Shibuya, Masuda. To be reported at the 1975 Nat'l Conv., I.E.E., Japan.
9. H.J. White. AEEE Trans., Vol. 70, 1186, 1951.

Submitted July 1, 1974

Journal of Electrostatics, 3 (1977) 311—325
© Elsevier Scientific Publishing Company, Amsterdam — Printed in The Netherlands
(Reprinted with permission)

A PRELIMINARY STUDY OF RE-ENTRAINMENT IN AN ELECTROSTATIC PRECIPITATOR

J.D. BASSETT, K. AKUTSU and S. MASUDA

Department of Electrical Engineering, University of Tokyo (Japan)

(Received November 11, 1976; in revised form March 25, 1977)

Summary

Observations were made of re-entrained particles which were deposited electrostatically in a laboratory model precipitator. Photographs of particle trajectories were obtained, the mean gas flow at which re-entrainment occurred, and the structure of the flow near the collecting electrode, were measured.

A distinct difference between trajectories of particles was noted depending upon whether or not 'back discharge' was occurring. Consideration of adhesion and removal forces was consistent with mean flow measurements at which re-entrainment occurred, and the shape of observed particle trajectories could be explained by a combination of electrical, gravitational and flow forces. Flow measurements indicated a velocity gradient in the laminar boundary layer sufficient to explain particle removal, although significant differences in the velocity gradient for different mean flow velocities could not be observed.

1. Introduction

This paper describes an investigation to observe the processes causing dust re-entrainment in an elecrostatic precipitator. It was the initial stage of a study into the overall electrofluiddynamic (EFD) nature of the precipitation process, including particle motion both before and after being first collected.

Fourteen years ago, White [1] devoted two chapters in his book on industrial precipitation to gas flow and re-entrainment effects. He quotes an example where poor gas flow reduced a possible efficiency of 95% to 60-70% because of re-entrainment and poor particle collection. Recently considerable interest has arisen in the study of the interaction of fluid and electric fields in precipitators. Studies of the effect of turbulence on the particle concentration profile [2] or the effect of ionic wind [3] on the precipitation process show that EFD phenomena are attracting more attention as precipitators have to become more efficient.

The experiments to be described can be divided into three parts. Particles were deposited electrostatically on the collecting electrode of a laboratory model precipitator. Firstly, the re-entrained particle motion was observed. Secondly, the mean gas flow velocity threshold was measured at which re-

entrainment occurred. Thirdly, an attempt to measure the structure of the gas flow near the collecting electrode was made. The re-entrained particle trajectories, with and without back discharge occurring, will be discussed as well as the relative importance of the forces causing (or allowing) re-entrainment to occur. Finally, the flow measurements in the duct will be discussed, and the main conclusions of the investigation given.

2. Experimental work

Observations of re-entrainment, and determination of the re-entrainment threshold gas flow, both involved photographic recording of the particles. Flow measurements were undertaken using a laser Doppler anemometer. All experiments were conducted using the same laboratory model precipitator.

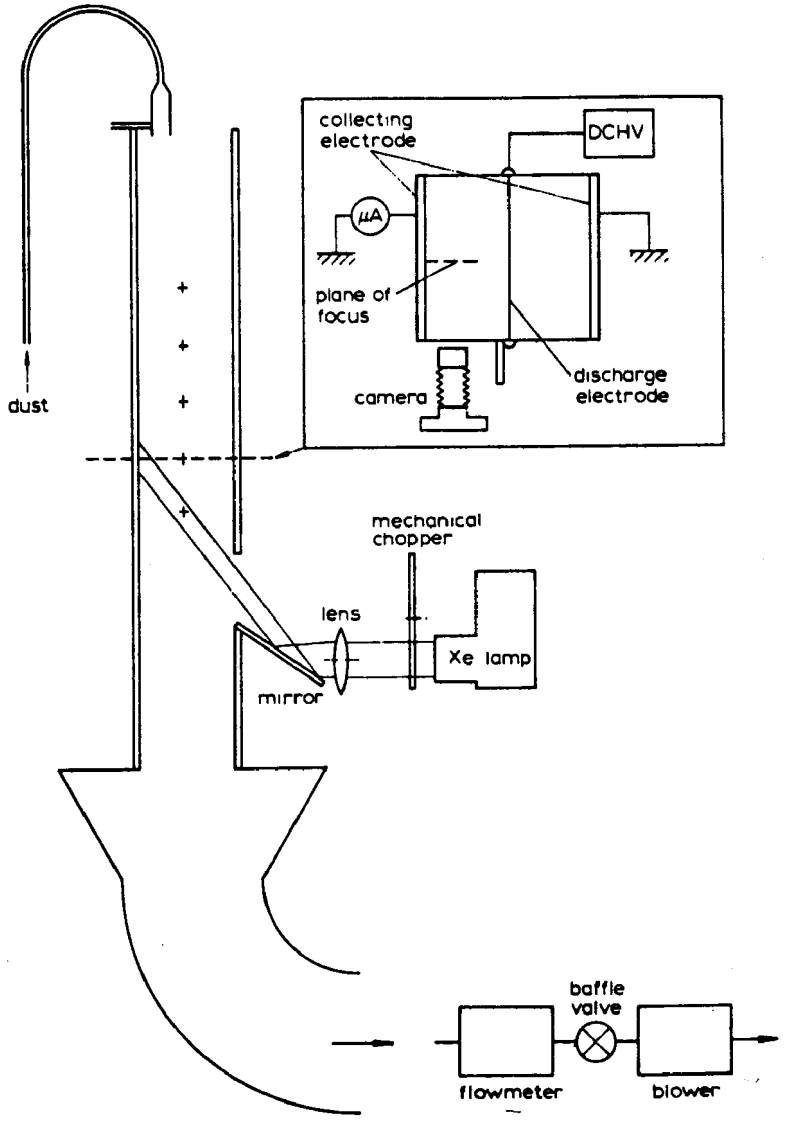

Fig. 1. Experimental apparatus.

2.1 Apparatus

A model of a precipitator was constructed as illustrated in Fig. 1. It consisted of a duct, 18-cm square in section and 1.4-m high. The duct was constructed of acrylite plate (1-cm thick) with collecting electrodes on two sides. Five discharge electrodes, made of 1-mm diameter piano wire, were positioned at the centre of the duct, 12 cm apart. These were connected to a Ransberg 150 kV negative DC source, with a digital kV-meter for voltage monitoring. One collecting electrode was connected through a microammeter to earth, the other directly to earth. The base of the duct was connected to a blower through a flow-meter and baffle valve, as shown in the figure. The volume flow rate available was 4.5 m^3 min^{-1}, giving a maximum value of mean velocity in the duct of 2.3 m s^{-1}, and a Reynolds number of ~34,000. Dust particles could be introduced into the duct by a simple powder-feed system, consisting of a vibrating fluidised bed, the powder cloud being transported by air flow. A deposit was formed by precipitating the particles on the collecting electrode under a low air flow velocity.

2.2 Observations of the occurrence of re-entrainment

These initial experiments involved photographic observation of re-entrainment. An area of the collecting electrode was illuminated by a 2-mm wide slit of intense white light from a xenon lamp. A mechanical chopping disc could be used if intermittent lighting were required. The period of chopping used was either 3·7 or 1·8 ms. This slit of light was introduced into the duct with a lens and mirror system, as shown in Fig. 1. Photographs were taken using a Nikon camera with bellows and a 105 mm lens giving a linear magnification of 1·2—1·4 times. The exposure times used ranged from 1/15—1/125 s. Kodak Tri-X film was used and, as no contrast was required, was force developed to give maximum speed.

2.3 Determination of re-entrainment threshold

In order to determine the flow rate or mean gas velocity at which re-entrainment started to occur, photographic observation was also used. The lighting system was as described above (without chopping) and a fixed exposure time of 1/1000 s was used. Using a mechanical film transport, 8—10 photographs were taken at the rate of about two per second, after a layer of particles had been deposited electrostatically. The precipitator voltage was kept constant and several minutes were allowed to elapse between deposition and flow application. This was to ensure that the layer had reached a 'steady state' condition. The number of particles in the gas was counted from the film record for each value of flow rate. As these results could not be normalised by the total number deposited, although this was kept as constant as possible, the re-entrained number was expressed as a number per

photograph, i.e., it was assumed that the series of short exposure photographs provided a system of random sampling.

2.4 Flow measurements

The method used for flow measurement was a laser anemometer system (marketed by Nippon Kagaku Co.). An anemometer provides a voltage which is directly proportional to the velocity of particles passing through the crossing point of two laser beams. The particles used for these flow measurements were dioctyl phthalate (DOP), 0·3 μm in diameter. The voltage could be recorded as a function of time and thus give information on velocity fluctuations and turbulence. Velocity measurements were made for three values of mean flow rate and at 8 positions in the duct. Electrode geometry did not allow measurement closer than 2 mm from the collecting electrode. Two methods of analysing the velocity—time signal were attempted. The first involved using a 'real time' correlation and probability analyser together with a Fourier transform analyser. The second used an F.M. tape recorder to store the velocity—time signal, complete with DC component, on magnetic tape. The recording time used for each set was 20 s. This was then analysed using an A/D converter and conventional digital computer. The second method yielded more useful results. The mean velocity, the standard deviation, the probability histogram (and calculated distribution curve) and the power spectrum could be obtained for one data set simultaneously.

3. Experimental results

3.1 Observations of re-entrainment

For these initial experiments, observations of re-entrainment caused by air flow alone were sought. However, some interesting results were obtained when electrical effects also played a part. The first dust to be used in these

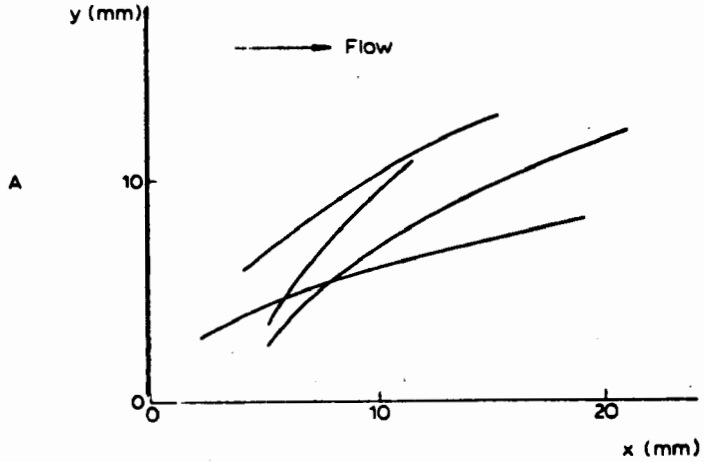

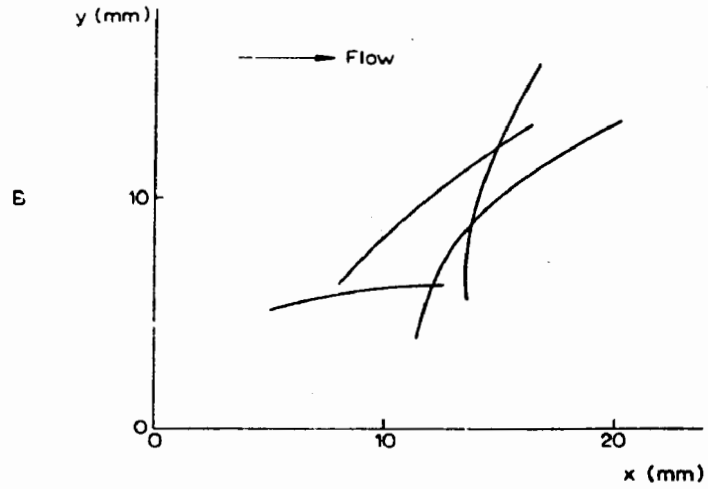

Fig. 2. Trajectories of re-entrained calcium carbonate particles at a mean flow velocity of 2.3 m s^{-1}. (A) 21 kV on discharge electrode — initial current 13 μA. (B) 25 kV on discharge electrode — initial current 40 μA.

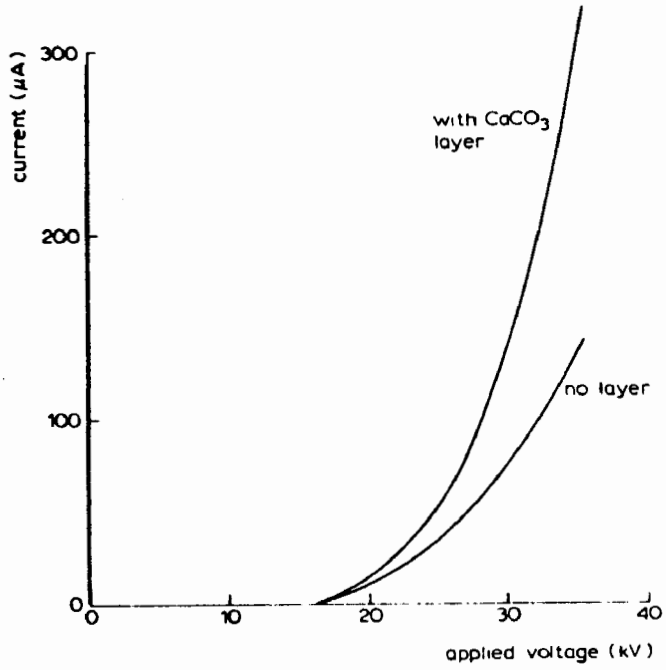

Fig. 3. Voltage—current characteristics when using calcium carbonate powder.

experiments was calcium carbonate powder. The diameter of the particles was between 50 μm and 130 μm. The trajectories of re-entrained particles are shown in Fig. 2. The voltage—current curves shown in Fig. 3 for this case, and the very uneven appearance of the layer, indicated that back discharge was occurring. Similar results to $CaCO_3$ were obtained when lycopodium and nylon powders were used. Finally, a sample of glass powder was tried. The diameter was 60—70 μm and the particles were spherical. Although adhesion was low, back discharge did not occur. The *V—I* characteristic with and without a layer corresponded to the 'no layer' curve of Fig. 3. Trajectories of re-entrained glass particles are shown in Fig. 4.

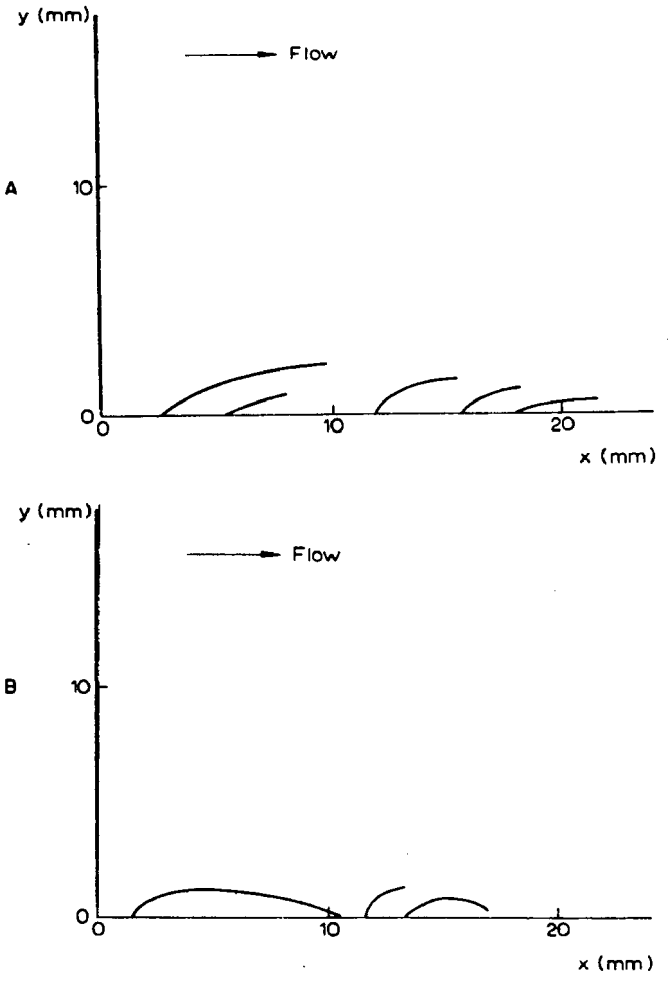

Fig. 4. Trajectories of re-entrained glass particles at a mean flow velocity of 2·3 m s^{-1}. (A) 21 kV on discharge electrode — current 14 μA. (B) 25 kV on discharge electrode — — current 40 μA.

3.2 Measurement of re-entrainment threshold

The glass powder described above was used for these measurements. As mentioned in Section 2.3, the layer was allowed to stabilise for a few minutes before measurements were made. A total of over 1800 re-entrained particles were counted to give the graph shown in Fig. 5. The mean velocity across the duct at which these particles were not dislodged by the gas flow can be seen to be approximately 1·5 m s^{-1}, regardless of applied voltage.

3.3 Flow measurements

Having established a mean flow velocity at which these particular glass particles were re-entrained, an attempt was made to measure the properties of the gas flow which caused re-entrainment to occur. The time-mean velocity profile in the duct, starting 2 mm away from the collecting electrode towards the duct centre, is shown in Fig. 6. The turbulent intensity, equivalent

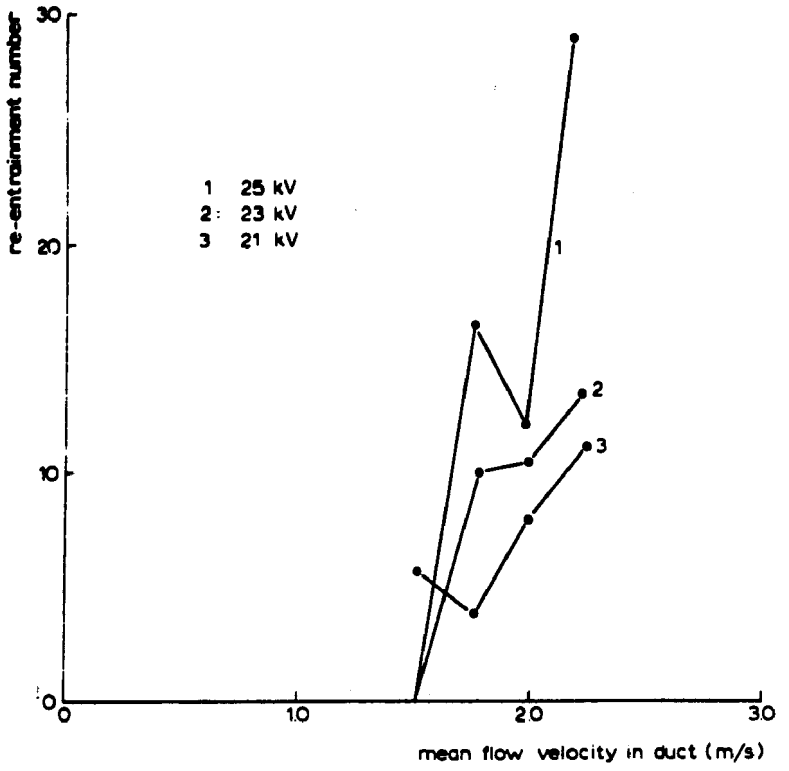

Fig. 5. Re-entrainment threshold maesurements at: (1) 25 kV, 40 μA. (2) 23 kV, 20 μA. (3) 21 kV, 13 μA.

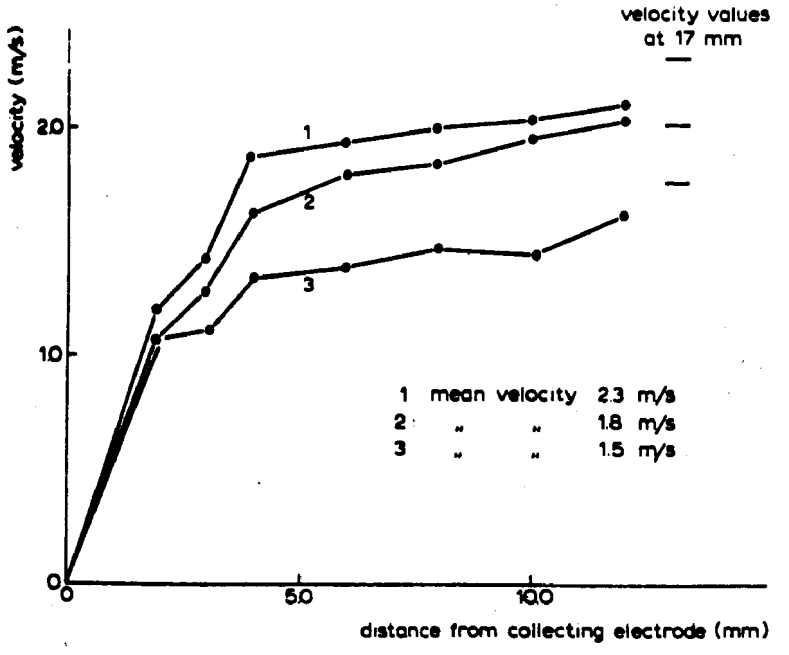

Fig. 6. Velocity profiles in model precipitator at three values of mean flow velocity.

to the standard deviation of the velocity signal divided by the overall mean velocity, is plotted in Fig. 7.

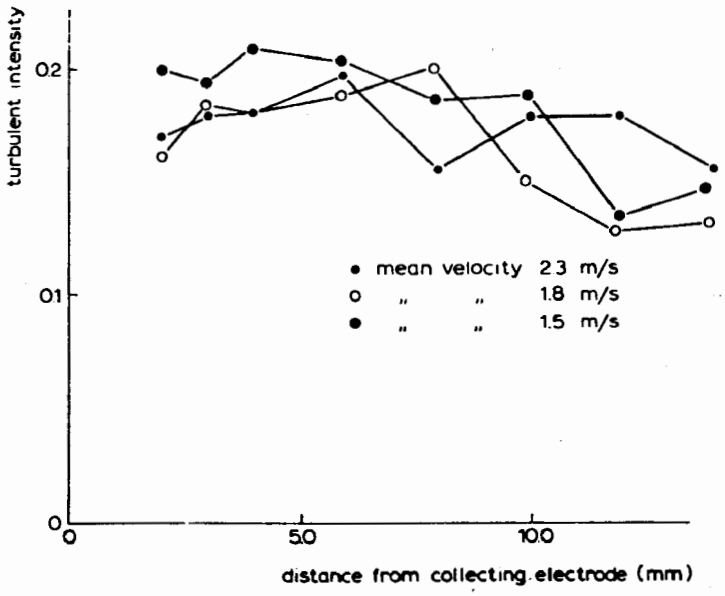

Fig. 7. Turbulent intensity against distance from collecting electrode at three values of mean flow velocity.

4. Discussion

The behaviour of particles in a precipitator has to be described by a combination of electric and fluid fields. Recently more and more attention has been paid to this part of the precipitation process. Examples of this are the work of Masuda and Matsumoto [4], on improving particle collection by the use of an electrofluid-dynamic approach, the paper by Adachi [3] discussing the role of ionic wind, considerable velocities being generated from this source, and the paper by Cooperman [2] in which consideration of the gas flow is shown to lead to a more generally applicable theoretical equation to predict precipitator efficiency. The specific problem of re-entrainment in the gas requires a consideration of the balance between particle adhesion forces and the removal force caused by the flow.

4.1 Particle removal by air flow

The removal of dust particles by an air flow has been discussed by Zimon [5]. The conditions for detachment of a particle from a horizontal surface are given as:

$$F_f > \mu(F_{ad} + P - F_l) \tag{4.1}$$

where F_f is the frontal force acting on the particle, μ is the coefficient of friction, F_{ad} the adhesion force, P the weight and F_l the lift force. For a

vertical surface this equation will become:

$$F_f > \mu(F_{ad} - F_l) - P \tag{4.2}$$

The discussion up to now has only accounted for mechanical forces, but in the precipitator problem, electrical forces also play an important part. For conducting particles, the charge induced on a particle on a plane surface was given by Felici [6] as:

$$q = 1{\cdot}5 \times 10^{-10} E a^2 \tag{4.3}$$

Where E is the electric field applied (undisturbed by the particle) and a the particle radius. Thus, the electrical force of removal, which will tend to reduce the adhesion force, F_{ad}, is given by :

$$F_r = 1{\cdot}5 \times 10^{-10} E^2 a^2 \tag{4.4}$$

A rough estimate of values of the forces described above, as applied to the spherical glass particles used in the experiments, will now be given. Zimon [5] quotes a value for the adhesion force F_{ad} of glass spheres on a steel plate as $2{\cdot}3 \times 10^{-8}$ N for 40—60 μm diameter particles for 97 % relative humidity, allowing two hours for capillary forces to stabilise. This is therefore to be considered a maximum value as particles were normally deposited for a period of a few minutes. Particle weight, assuming a density of $2{\cdot}5 \times 10^3$ kg m^{-3} is $2{\cdot}8 \times 10^{-9}$ N, and the coefficient of friction for glass spheres on steel, again given by Zimon, is 0·6. The resistivity of the dust used was measured and found to be $1{\cdot}7 \times 10^7$ Ωm, i.e. relatively conducting. The maximum applied voltage used in the experiments was 25 kV giving a maximum electric field of $2{\cdot}8 \times 10^5$ Vm^{-1}. The removal force, because of this field, calculated from eqn. (4.4), was 10^{-8} N. Thus, F_{ad} would range from $2{\cdot}3 \times 10^{-8}$ N with no applied field to $1{\cdot}3 \times 10^{-8}$ N with maximum field. However, the maximum value of adhesion force was given above. Its minimum value can be estimated from

$$F_{ad} > \frac{P}{\mu} \tag{4.5}$$

giving $F_{ad} = 4{\cdot}6 \times 10^{-9}$ N. It is worth noting that there is only a factor of 5 between the maximum and minimum values of this adhesion force. Thus, the maximum value of frontal force, F_f, can be calculated, if the lift force, F_l, is neglected:

$$F_f > 0{\cdot}6\,(2{\cdot}3 \times 10^{-8} - 1{\cdot}6 \times 10^{-17} V^2) - 2{\cdot}75 \times 10^{-9} \tag{4.6}$$

Values of F_f calculated from eqn. (4.6) are tabulated in the second column of Table 1 below, using the maximum adhesion force. If the minimum adhesion force is used, of course F_f is zero.

At each value of mean flow rate a certain frontal force is applied to the particles on the electrode. It is reasonable to assume that the re-entrained number (N) of particles is an increasing function of the difference between the applied force (F_a) and that required for removal (F_f) as calculated above, i.e.,

$$N = f(F_a - F_f) \tag{4.7}$$

where N increases as $(F_a - F_f)$ increases, and F_a is assumed proportional to flow velocity. The results shown in Table 1, taken from the measured values of re-entrained particles (Fig. 5), are in reasonable agreement with this.

TABLE 1

		Re-entrainment number (from Fig. 5)		
V (kV)	F_f (× 10^{-8} N)	2·3 m s^{-1}	2·0 m s^{-1}	1·75 m s^{-1}
0	11.0	0	0	0
21	6.8	11	8	4
23	6.0	13	10	10
25	5.1	29	12	16

4.2 Particle trajectories after removal

For large particles, as used in these experiments, once removal has occurred, the motion can be described by a combination of electrical and flow forces, as discussed below.

The x-direction is assumed parallel to the flow and the y-direction perpendicular to the flow, as shown in Fig. 8. It is assumed that once the flow force, F_f, has overcome the adhesion force, F_{ad}, electrical forces dominate particle motion in the y-direction, and flow forces dominate motion in the x-direction. Velocity fluctuation due to turbulence in these directions is neglected because of the large particle size. For smaller particles this should be considered.

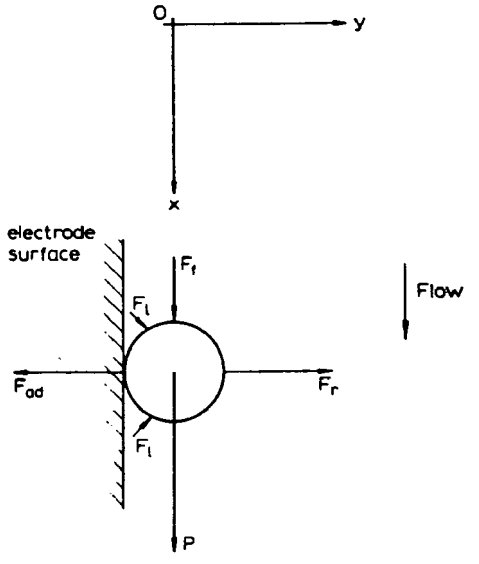

Fig. 8. Coordinates used for calculation of particle trajectories.

4.2.1 Electrical force

The maximum initial electrical force on the particle will be given by the charge calculated from eqn. (4.3) multiplied by the electric field. However, the particle is always being subjected to the corona-ion current flowing to the collecting electrode. This will result in a lower value of initial charge and also, once re-entrained, a decrease of particle charge with time, through zero, to a value of opposite sign so that it will be deposited again. Thus, the particle charge at time t, calculated using the equation of Pauthenier and Moreau-Hanot [7], is given by:

$$q(t) = q_i - (q_i + q_0)\ \frac{t}{t+\tau} \tag{4.8}$$

where q_i is the initial charge, q_0 the saturation charge (eqn. 4.9) and τ the charging-time constant (eqn. 4.10). For relatively conducting particles, such as glass

$$q_0 = 12\pi\epsilon_0 a^2 E \tag{4.9}$$

where ϵ_0 is the permittivity of free space, a the particle radius and E the undisturbed electric field where the particle is being charged.

$$\tau = \frac{4\epsilon_0 E}{J} \tag{4.10}$$

where J is the current density.

The equation of motion in the y-direction is given by:

$$m\ \frac{dV_y}{dt} = q(t)E - 6\pi\eta a V_y \tag{4.11}$$

where m is the particle mass, the field E is assumed constant in the region of particle motion, η is the air viscosity and V_y the velocity. This velocity was calculated numerically for a time increment of 1 ms. The position value, y, was calculated from the velocity difference:

$$y = \frac{V_i + V_{i+1}}{2} \times 10^{-3} \tag{4.12}$$

4.2.2 Gravitational and flow forces

The equation of motion in this case is given by:

$$m\ \frac{dV_x}{dt} = m\,g + 6\pi\eta a(V_f(y) - V_x) \tag{4.13}$$

where g is the gravitational constant, and $V_f(y)$ is the flow velocity value at y at the same time increment for which V_x is being calculated.

As no flow data were available when these calculations were made, eqn. (4.13) was solved for $V_f = 0$.

4.2.3 Particle trajectories and the influence of back discharge

Particle trajectories calculated by the above method for initial charge values of 50, 60 and 70 % of that calculated by eqn. (4.3) are shown in Fig. 9. These compare well with the trajectories of glass particles during deposition, where only gravitational forces were acting. They are similar to the trajectories of re-entrained glass particles as shown in Fig. 4.

The trajectories of re-entrained $CaCO_3$ particles shown in Fig. 2 clearly show the difference when back discharge is occurring. Instead of particles remaining within a millimetre or two of the collecting electrode surface and re-deposition occurring, they are ejected to several millimetres (up to 16 mm), and in the time interval of the photographs often showed no sign of re-depositing. Work on particle charging during back discharge by Mizuno [8] has shown that a dust layer, when back discharge is occurring, can act as a surface source of ions of the opposite sign. Thus, particles would be expected to move further from the electrode, as re-charging would not immediately commence. It would appear that the effect of back discharge on precipitator performance is not only reduced collection efficiency, but also detrimental if re-entrainment occurs, as particles are removed into the full flow

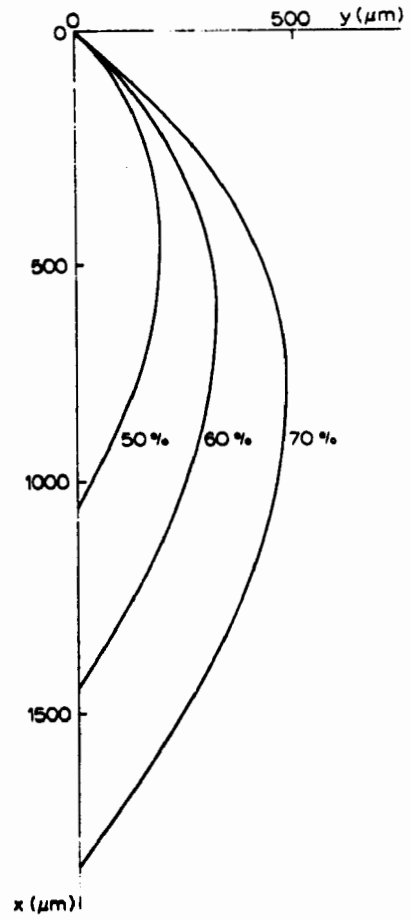

Fig. 9. Calculated particle trajectories.

of the gas stream, instead of staying close to the collecting electrodes. The observed trajectories also show an extremely high velocity perpendicular to the flow. This might be explained by ionic wind occurring from the back-discharge points. This kind of ionic wind has been observed by Adachi [9].

The particles used in these experiments were considerably bigger than those normally precipitated. Domination of particle motion away from the collecting electrode by electrical forces would probably not occur with smaller particles and flow forces would also have to be considered in this direction. However, when small particles are electrostatically precipitated, strong coagulation occurs so that the agglomerates actually re-entrained probably have a size of several tens of microns. Thus these experiments using large $CaCO_3$ and glass particles should serve well for predicting how re-entrainment occurs in practical precipitators.

4.3 Structure of the flow

During the earlier stages of these experiments, it was hoped that a back-scatter detection laser anemometer could be used. This would enable the flow very close to the collecting electrode to be measured either parallel or (almost) perpendicular to the electrode. As mentioned in Section 2.4, the particles used to seed the flow for laser Doppler measurement were DOP, 0.3 μm mean diameter, and it was found that the back-scattered intensity was not sufficient for measurement. The sampling rate of the burst signal was less than 100 s^{-1}, giving a frequency response of the order of tens of Hz. Thus, a forward scatter system, as mentioned earlier, was used to give the results shown in Figs. 6 and 7, and this is the reason for measurements only beginning 2 mm away from the electrode.

From Fig. 6 it can be seen that the thickness of the boundary layer is several millimetres, and Fig. 7 shows that at all positions the flow was fluctuating. It can be seen from Fig. 6 that the velocity gradient in the boundary layer close to the collecting electrode was almost the same regardless of the main flow velocity. A calculation of the frontal force, F_f, as discussed in Section 4.1 assuming a laminar boundary layer, is given by Schlichting [10]:

$$F_f = \frac{6\pi\eta\, V_b a}{\delta} \tag{4.14}$$

where V_b is laminar boundary layer velocity and δ is the thickness of the laminar boundary layer. It is unlikely that this model could explain the significant differences of re-entrainment observed as shown in Fig. 5, as the flow data would indicate values of F_f not significantly different for the various values of mean velocity. However, the value of F_f calculated from eqn. (4.14) gives $1{\cdot}2 \times 10^{-9}$ N, for 60 μm diameter particles and a velocity gradient of 500 s^{-1}, which is of the right order given that the assumptions in section 4.1 are correct. Flow measurements closer to the electrode are re-

quired before more accurate calculations from eqn. (4.14) can be usefully employed.

It can be seen that the values of turbulent intensity at different flow rates were all approximately the same. In fact the value 2 mm from the collecting electrode for the lowest flow rate was highest. The mean value of turbulent intensity for 1.5 m s^{-1} applied velocity was 0.16, for 1.8 m s^{-1} it was 0.11 and for 2·3 m s^{-1}, 0·10. The order of error of the velocity measurement system was assumed to be 10 %. When the turbulent intensity results were re-plotted, after subtracting 10 % of the mean value from the standard deviation, the same order of results occurred — highest for the lowest flow rate. Unless a constant value of error was occurring, allowing a fixed amount to be subtracted from the velocity standard deviation, the turbulent intensity measured appears to be slightly higher for the lowest value of applied flow rate.

The power spectra indicated that energy was contained up to higher frequencies at higher flow rates. The maximum frequency for a fixed power-spectrum value was taken from all the spectra (for the eight values of distance into the duct). The mean value of this maximum frequency for a 1·5 m s^{-1} applied velocity was 17·3 Hz, for 1·8 m s^{-1} it was 20·2 Hz and 2·3 m s^{-1} it was 28·4 Hz. These values are more reasonable than the turbulent intensity measurements, possibly because the method of obtaining the power spectrum analyses the shape of the whole velocity—time signal, whereas calculations of standard deviation can be influenced by spurious voltage fluctuations which might have occurred as no filtering was used before the signal was input to the A/D converter.

5. Conclusions

Observations of re-entrainment occurring showed that the motion of the glass particles away from the collecting electrode was not influenced by the flow once they had become dislodged. Electrical forces perpendicular to the electrode could explain the observed trajectories. The smaller particles normally precipitated would be expected to be affected by flow forces perpendicular to the collecting electrode. However, electrostatically precipitated particles often coagulate on collection, the agglomerates having a size of several tens of microns, similar to the particles used in these experiments.

Considerations of the adhesion and removal forces acting on a particle were in agreement with experimental measurements of the number of re-entrained particles plotted against the applied flow velocity.

The influence of back discharge on re-entrainment was observed. This showed that loss of efficiency when re-entrainment occurs is likely to be far worse if back discharge is occurring as well, because particles would be ejected into the full flow of the gas stream instead of staying close to the collecting electrode.

Acknowledgements

Dr. Bassett would like to acknowledge gratefully the support of the Royal Society for a 10-month fellowship in Japan, and to thank his co-authors for their kindness and hospitality during his stay.

References

1 H.J. White, Industrial Electrostatic Precipitation, Addison-Wesley, 1963, Chaps. 8 and 10.
2 P. Cooperman, Nondeuschian phenomena in electrostatic precipitation 69th Annual Meeting of the Air Pollution Control Association, Paper No. 76-42.2, Portland, Oregon, June 27—July 1 1976.
3 T. Adachi, Ionic wind in the electrostatic precipitator, J. Res. Assoc. Powder Tech., Jpn, 12 (3) (1975) 146.
4 S. Masuda and Y. Matsumoto, Motion of a microcharge particle within electrohydrodynamic field, Electr. Engi. in Jpn, 94 (6) (1974) 20.
5 A.D. Zimon, in M. Corn (Ed.), Adhesion of Dust and Powder, Plenum Press, New York, 1969.
6 N.J. Felici, The forces and charges on small objects in contact with an electrode in an electric field, Rev. Gen. Electri. 75 (1966) 1145.
7 M.M. Pauthenier and M. Moreau-Hanot, The charge acquired by spherical particles in an ionised atmosphere and an electric field, J. Phys. Radium, 3 (1932) 590.
8 A. Mizuno, Studies of back discharge phenomena, J. Electrostat. (to be published).
9 T. Adachi, Ionic wind in the electrostatic precipitator — experimental treatment by the Schlieren method, Trans. I.E.E., Jpn, 93-B. (7) (1973) 273.
10 H. Schlichting, Boundary Layer Theory, J. Kestin (Trans.), McGraw Hill, New York, 1968.

Inst. Phys. Conf. Ser. No. 27 © 1975: Chapter 3
(Reprinted with permission)

Recent progress in electrostatic precipitation

Senichi Masuda
Department of Electrical Engineering, University of Tokyo, Tokyo, Japan

Abstract. Recent progress in the field of electrostatic precipitation, which is one of the most important applications of electrostatic forces, is reviewed. A description of the construction and general principles of precipitators is given. This is followed by an account of the progress achieved in both the technical developments and the scientific understanding of precipitator performance. Finally, the inherent difficulty in the design of precipitators is explained.

1. Introduction

Electrostatic precipitators play a major role in the emission control of particulate pollutants, especially when the emphasis is on the removal of very fine particles of less than 3 μm diameter. These fine particles are important factors in the visibility of stack emissions, water drop nucleations, the carriage of gaseous pollutants into lungs and they are a general health hazard. Although both the principles and the construction of electrostatic precipitators are extremely simple, the actual operation is complicated by many factors which impair the efficiency. As a result, in spite of many research achievements, precipitator design has long been considered an art rather than an engineering science. This situation, however, is being improved by increased efforts in research and development.

2. Principle and construction

The principle of electrostatic precipitation is explained by the system of concentric cylinder electrodes shown in figure 1. Particles charged by collision with unipolar ions emitted from the discharge electrode are driven by the coulombic force on to the collecting electrode, where they are precipitated. The layer of particles is dislodged by mechanical rapping of the collecting electrode and they fall into a hopper. Meanwhile the cleaned gas is taken from the outlet to a stack. In practice, a duct-type precipitator with parallel-plate collecting electrodes and a horizontal gas flow is usually used for treating large volumes of gas. This is because of its simple and economical construction and uniform gas distribution. A negative corona is usually used for emission control because of its higher spark voltage, whereas the positive corona is chosen for the purpose of air cleaning when the supression of harmful ozone becomes a major factor. In the latter case a two-stage structure is common in which the charging and collection is performed in different stages. For the voltage sources, only one reference is cited (Hall 1975) and a discussion of this subject is omitted.

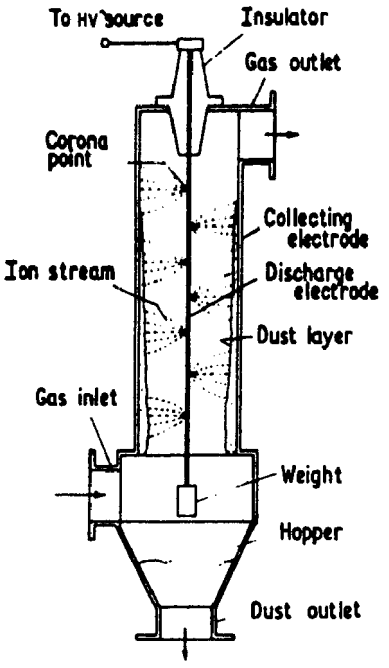

Figure 1. Principle of electrostatic precipitation.

The corona field inside a precipitator having both ion and dust space charges is not easy to calculate except for the simple case of figure 1. The field at a distance r from the axis is approximately given (Pauthenier and Moreau-Hanot 1932) by

$$E(r) = \left[\frac{I}{2\pi\epsilon_0\mu}\left(1 + \frac{2\epsilon_s}{\epsilon_s + 2}S_r\right) + \left(\frac{E_0 r_0}{r}\right)^2\right]^{1/2}\left(\frac{V}{m}\right) \qquad (1)$$

for the case when the total surface area of particles, $S(m^2/m^3)$, per unit volume is not very large. Here, I = current per unit length of wire (A m^{-1}); ϵ_0 = permittivity of free space; ϵ_s = relative permittivity of particulate material; μ = ion mobility (m^2 V^{-1} s^{-1}); E_0 = breakdown field strength of the gas at the wire surface (V m^{-1}).

If the applied voltage is kept constant, the dust space charge causes an increase in E adjacent to the collecting electrode and a decrease in the vicinity of the discharge electrode, thus lowering the charging current I. This last effect is called 'corona quenching'. The effect of this quenching on the precipitator is two-fold. Firstly, the charge on a particle decreases as a result of the drop in charging rate, and thus there is a decline in efficiency. Secondly, the increase in the collection field strength causes an increase in efficiency. It was discovered recently by Awad and Castle (1975), that if the initial corona current was low, the latter effect was more than counteracted by the former effect and therefore there was a resultant decrease in collection efficiency.

The particles entering the corona field are charged by ion collision by two mechanisms. One is the effect (called field bombardment) of the external field driving ions towards the particle surface and the other is the thermal diffusion mechanism, in which collisions result from the thermal motion of the ions, without the aid of an external field. The theoretical charge acquired by a spherical particle by field bombardment is expressed (Pauthenier and Moreau-Hanot 1932) by

$$q_f = q_\infty \frac{t/\tau}{1 + t/\tau} \text{ (C)} \qquad (2)$$

where

$$q_\infty = 4\pi\epsilon_0 \frac{3\epsilon_s}{\epsilon_s + 2} a^2 E_c = \text{saturation charge (C)} \tag{3}$$

and

$$\tau = \frac{4\epsilon_0}{\mu\rho_i} = \frac{4\epsilon_0 E_c}{i} = \text{charging time constant (s)} \tag{4}$$

where t = time (s); a = particle radius (m); E_c = charging field strength (V m^{-1}); ρ_i = density of ionic space charge (C m^{-3}) and i = ion-current density (A m^{-2}). Equation (3) indicates the importance of the field strength E_c in determining the saturation charge on the particle, whereas equation (4) shows that the current i governs the charging rate. We may assume $t_0 = 3\tau$ to 10τ as the necessary charging time, because 75% and 91% of the saturation charge are obtained after 3τ and 10τ, respectively. If we take the typical values of $E_c = 5 \times 10^5$ V m^{-1} and $i = 2 \times 10^{-4}$ A m^{-2}, we obtain $\tau = 0{\cdot}088$, in other words the necessary charging time t_0 in this case is between 0·26 and 0·88 s. The theoretical charge imparted to a spherical particle by thermal diffusion is (White 1951):

$$q_{th} = q^* \ln(1 + t/\tau^*) \text{ (C)} \tag{5}$$

where

$$q^* = \frac{4\pi\epsilon_0 akT}{e} = \text{charge constant (C)} \tag{6}$$

$$\tau^* = \frac{4\pi\epsilon_0 kT}{aCN_0 e^2} = \text{charging time constant (s)} \tag{7}$$

k = Boltzmann's constant = $1{\cdot}38 \times 10^{-23}$ (J K^{-1}); T = absolute temperature (K); e = electronic charge = $1{\cdot}602 \times 10^{-19}$ (C); C = RMS value of the ionic thermal velocity = $(3kT/m)^{1/2}$ (m s^{-1}), m = ionic mass (kg); N_0 = number of ions per unit volume (m^{-3}) and the assumption is made that $a \gg \lambda$ where λ = ionic mean free path. According to equation (5) the charge q initially rises very quickly to become $q = 6q^*$ at $t = 402\tau^*$, thereafter rising very slowly so that it can be assumed to remain approximately constant. Hence, we may take $q_\infty = 6q^*$ as the quasi-saturation charge with charging by thermal diffusion and $t_0 = 402\tau^*$ as the necessary charging time. For $T = 150$ °C; $a = 0{\cdot}1\,\mu$m; $m = 5{\cdot}313 \times 10^{-26}$ kg (for O_2^- ion) and $N_0 = 5 \times 10^{13}$ m^{-3} we get $t_0 = 1{\cdot}13$ s. These are typical values for industrial precipitations.

If a was as small as 0·01 μm the necessary charging time becomes the large value of 1 1 3 s. Numerical calculations show that the field bombardment charging is predominant for particles larger than 2 μm, whereas thermal diffusion charging dominates for particles smaller than 0·2 μm. In the intermediate range, the sum of the charges calculated independently by equations (2) and (5) gives a good approximation (Hewitt

1957). There are many detailed studies on particle charging (see Penny and Lynch 1957, Murphy *et al* 1959, Smith and Penny 1961, Liu *et al* 1967, Liu and Yeh 1968, Smith and McDonald 1975).

The charged particles migrate under the action of the coulombic forces towards the collecting electrode. Assuming that the viscous resistance acting against the particle motion is of the Stokes form, then the theoretical migration velocity within a gas at rest is

$$w = \frac{qE_p}{6\pi\eta a} \text{ (m s}^{-1}\text{)} \tag{8}$$

where E_p = collecting field strength (V m^{-1}) and η = gas viscosity (N s m^{-2}). For very fine particles below 1 μm in diameter the theoretical migration velocity must be modified by multiplying by the Cunningham correction factor $(1 + A\lambda/a)$, in other words w increases with decreasing particle size. For air at NTP, $A = 0{\cdot}86$ and $\lambda = 0{\cdot}1$ μm (White 1962). The curve A in figure 2 represents the theoretical migration velocity, w, as a function of particle radius, a, under typical precipitator conditions. It is assumed that

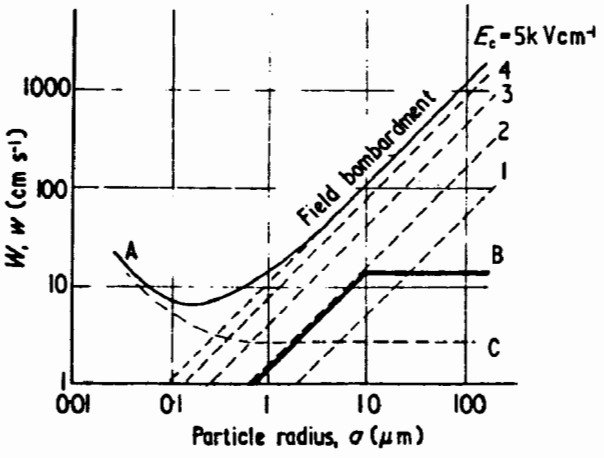

Figure 2. Theoretical particle migration velocity w (curve A) and apparent migration velocity W (curve B) against particle radius a. Curve C is thermal diffusion.

the charge imparted by ionic thermal diffusion is $q_\infty = 6q^*$. The curve clearly indicates that if sufficient charging time is available, w becomes a minimum when a is between 0·1 and 1·0 μm; this was verified by Hewitt (1957) experimentally and in field tests by McCain *et al* (1975). The remarkable increase in the necessary charging time, t_0, required for particles with a less than 0·1 μm should be noted, since the available charging time in practice is normally limited to 5 to 10 s. The theoretical migration velocity given by equation (8) cannot usually be used to estimate the collection efficiency η_c because of too many disturbing factors. These include turbulence, which is enhanced by the electric wind; the partial re-entrainment of precipitated dust, etc. A first order approximation of η_c can be obtained by using the very crude assumption that, because of the mixing effect of the turbulence, the particle concentration is uniform over an arbitrary cross section perpendicular to the gas flow, and that the collection rate is governed by a single parameter called the 'apparent migration velocity', W, for all particles, regardless of size, throughout the whole collecting region. We then obtain the well known Deutsch equation:

$$\eta_c = 1 - e^{-WF} \tag{9}$$

where $F = S_c/Q$ = specific collection surface (s m^{-1}) where Q = total gas flow rate (m^3 s^{-1}) and S_c = total surface area of the collecting electrodes (m^2). Equation (9), because of its simplicity, is widely used for design purposes in either its original or a modified form. W is to be considered a design parameter representing all the process factors except the precipitator dimensions, and should be determined using equation (9) by experimentally measuring the collection efficiency. The curve B in figure 2 represents an average value of W calculated from the fractional collection efficiencies measured in different industrial precipitators. The difference between curves A and B probably result from the fact that the larger particles tend to re-entrain more easily because of their less effective adhesion compared to smaller particles (Heinrich 1961). The factors affecting W are many in number and usually difficult to estimate in advance. As a result precipitator design requires a lot of experience which is obtained from analysing data on similar precipitators already in operation. The data often differs, however, from plant to plant. This situation means that the prediction of precipitator performance is probabilistic in nature, especially when sufficient safety allowances cannot be included (Masuda 1966). Another difficulty in the concept of 'apparent migration velocity' has been raised recently because of results from 'large-spacing type' precipitators. These have much larger electrode spacings than conventional precipitators and yet the two types have comparable collection efficiencies even when they are of equivalent sizes and operate under nearly identical plant conditions. This comparibility was also observed even in a pilot plant of a wet-type precipitator where no back discharge or dust re-entrainment occurred (Ago *et al* 1975). It seems under suitable conditions that the 'apparent migration velocity' increases in proportion to the electrode spacing. This effect cannot be fully explained, even considering the increased stability of operation which is a feature of the large-spacing type, and thus there is a need for more detailed studies on the precipitation process itself.

In the following section, some of the recent progress achieved in understanding the precipitation process is described.

3. Ion curtain patterns and their effect on charging efficiencies

It is well known that the negative corona appears on a wire electrode at several points, from which ion currents in the form of tufts start towards the collection electrode. Hence in the region near the wire, ion dead spaces occur between the tufts and in these spaces the ion concentration is so small that particles passing through them may not be charged; in other words the charging time constant of equation (4) or (7) becomes exceedingly large. The decrease in charging efficiency in the dead spaces was confirmed experimentally (Masuda *et al* 1973b) and this led to more detailed studies on the ion curtain patterns. It was discovered that there was a similarity between the ion curtain pattern and the electrode configuration. Figure 3 shows that the distribution of ion current upon the collecting electrode follows a similar pattern to that of the electrode system (Niioka 1974, Masuda and Niioka 1974). It was also observed that in cases where there were dead spaces on the collecting electrode, back discharging and re-entrainment took place and that, for some particles a number of fibre-like pearl chains protruded from the surface of a dust layer in a dead space. These chains could jump into space and split into sections (Masuda *et al* 1973a).

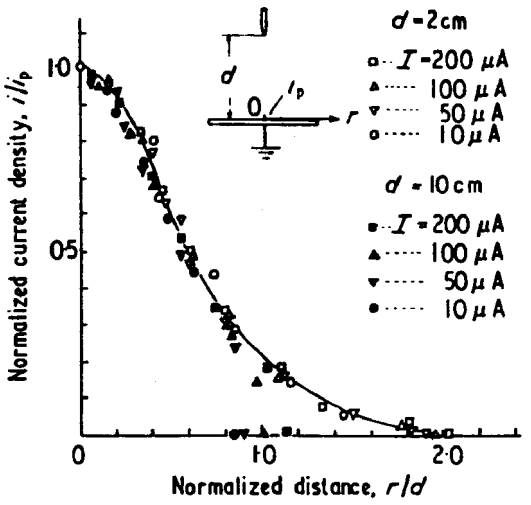

Figure 3. Normalized current density on plate electrode (i/i_p) against normalized distance (r/d).

The problem of dead spaces may be solved by the use of a special type of positive corona called 'Hermstein's glow'. This glow occurs uniformly along the wire but still has a greatly increased spark voltage; sometimes higher than that of a negative corona (Hermstein 1960). Hermstein's glow occurs when the field strength and its gradient in the vicinity of the discharge electrode are so high that the shedding of electrons from negative ions can occur in this restricted region. These electrons diffuse over the electrode surface to form an electron sheath capable of suppressing streamer formation. Hence, the formation of Herstein's glow is encouraged by supplying the discharge electrode with a small number of negative ions (Hermstein 1960). A remarkable increase in the average charge on a particle could be obtained by using Hermstein's glow, produced by knife-edge electrodes, compared to the charge obtained from using a negative corona from identical electrodes (Niioka 1974, Masuda and Niioka 1973).

4. Electro-fluid dynamic phenomena and particle motion inside precipitators

There are two kinds of phenomena to be studied in more detail from the EFD point of view; these are electric winds and particle motion and in both the effects of electric and fluid fields have to be considered. Figure 4(*a*) is a Schlieren photograph at the core of an electric wind, taken with a horizontal gas flow with a velocity of 1·25 m s^{-1}. An approximate estimate of the electric wind velocity obtained from the curvature of the curve is about 20 m s^{-1} in the vicinity of the needle point, and the average value is in the range of several m s^{-1}. This is much higher than expected (Adachi *et al* 1974). It follows, therefore, that particles of less than 10 μm diameter may be transported towards the vicinity of the collecting electrode by the vortex motion of the gas flow which is enhanced by the electric wind (see figure 2). At the collecting electrode, the flow must reverse and only the particles impinging on the boundary layer, either because of the electric force or the random motion of the particles, may be collected. Therefore, the motion of charged particles, especially small ones, can only be correctly understood using the EFD approach, in which the mode of the motion can be approximately estimated by the dimensionless factor

$$K = \frac{w_0}{V_0} = \frac{qE_0}{6\pi\eta a V_0} \tag{10}$$

(*a*) (*b*)

Figure 4. Schlieren photographs of electric wind. (*a*) Core of electric wind (d = 3 cm V = 18 kV, v = 1·25 m s^{-1}; (*b*) electric wind by back-discharge (d = 6 cm, V = 30 kV)

where w_0 represents the theoretical migration velocity under the average electric field between the electrodes, E_0, and V_0 represents the RMS value of vortex velocity. The effect of the electric field will become predominant for particle transport for $K > 10$, while the effect of turbulence will play a major role when $K < 0{\cdot}1$. More detailed information is being collected both concerning the coupling of the vortex motion and the electric wind, and the structure of the boundary layer under actual conditions. For example, figure 4 shows a picture of the electric wind produced by a back discharge (Masuda and Adachi 1975).

When no vortex motion exists, as in the case of the collecting part of a special two stage precipitator shown in figure 5 (Masuda *et al* 1974b, Shibuya and Masuda 1975), the problem can be simplified by approximating the fluid flow to the theoretical flow of an ideal fluid. In this case, both electric and fluid fields can easily be calculated by the use of the charge-substituting method (Steinbigler 1969) and its modification (Matsumoto 1974, Masuda and Matsumoto 1974a), even with complicated boundary

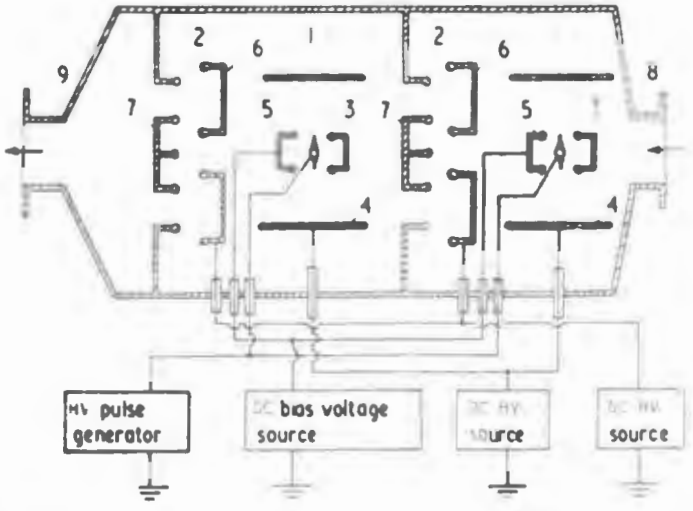

Figure 5. A new two-stage type electrostatic precipitator with the bias-controlled pulse charging system for the charging parts and the channel electrodes for the collecting parts. 1. Charging part, 2. collecting part, 3. discharge electrode, 4. counter electrode, 5. third electrode, 6. driving electrode, 7. collecting electrode, 8. gas inlet, 9. gas outlet.

conditions. The particle motion can be analysed using this method by using the concept of the EFD potential, in which the equation of motion is expressed in the form

$$\frac{md^2\mathbf{R}}{dt^2} + \frac{6\pi\eta a d\mathbf{R}}{dt} = -\text{grad}\ \psi_{\text{EFD}}(\mathbf{R}) \tag{11}$$

where

$$\psi_{\text{EFD}}(\mathbf{R}) = -\int_0^{\mathbf{R}} (6\pi\eta a\mathbf{V}(\mathbf{R}) + q\mathbf{E}(\mathbf{R})).\, d\mathbf{R}$$

$$= \text{EFD potential} \tag{12}$$

where $\mathbf{R}$ = position vector, m = particle mass, $\mathbf{V}(\mathbf{R})$ = velocity vector of fluid flow. Whether the particle motion is by the ballistic or viscous mode is determined by a parameter $\zeta = (6\pi\eta ab/m\bar{V})^{1/2}$, where b = electrode distance and V = average gas velocity. When $\zeta \gg 1$, as in the case in most practical systems, the inertia term in equation (11) can be neglected compared to the viscous term, the motion becoming 'viscous' in nature and follows the EFD lines of force drawn inside the EFD potential field. Figure 6 shows the EFD lines of force inside the collecting region in figure 5 (Matsumoto 1974, Masuda and Matsumodo 1974b). With this motion the effectiveness of the electric force compared to that of the fluid force is governed by the dimensionless factor $K = q\bar{E}/6\pi\eta a\bar{V}$ where $\bar{E}$ is the average electric field between the electrodes. One would achieve a 100% collection efficiency with $K \geqslant 1{\cdot}95$. Figure 6(*a*) indicates the stream lines of the fluid field when $K = 0$.

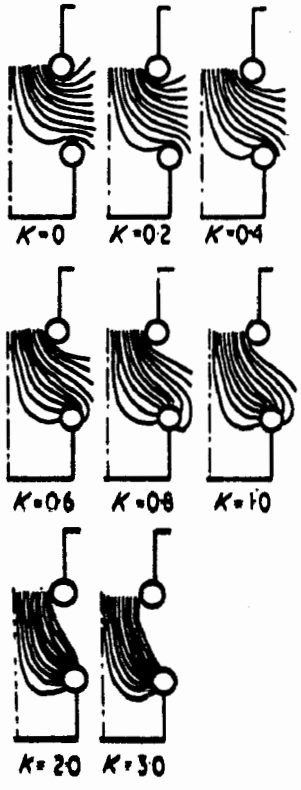

Figure 6. EFD lines of force inside the collecting parts of the precipitator shown in figure 5.

5. Adhesion of particles and dust re-entrainment

The pre-requisite conditions for effective dust collection are both the existence of enough adhesion between particles and sufficient adhesion between the particles and the collecting electrode. This allows the build-up of a firm layer, which on rapping can be dislodged to fall into the hopper without disintegrating and being carried out by the gas stream. In this sense, an electrostatic precipitator should act as an effective dust coagulating device in which electrical adhesion plays a major role for particles with a resistivity $\rho_d > 10^{10}\,\Omega$ cm (Dalmon and Tidy 1972a). This force is caused by the potential difference between particles in contact and is proportional to both the apparent resistivity of the dust layer, ρ_d, and the apparent current density within the dust layer, i_a (Simm 1962). Another possible cause of adhesion of an electrical origin is that produced through contact electrification (Penny 1975). Low-resistivity particles ($\rho_d < 10^4$ Ω cm) arriving at the collection electrode are 'inversely' charged by induction even though they are also bombarded by ions, and pulled back into the gas stream, in other words there is an abnormal dust re-entrainment of these particles unless the non-induction adhesion forces are powerful enough to overcome the induction effect. Van der Waals (London) forces are also involved in adhesion; their effect on coagulation increases with decreasing particle size (Lowe and Lucas 1953). At comparatively low temperatures, when the relative humidity is high enough, the capillary condensation of water molecules on to nucleation centres, may also be an important parameter in adhesion. It was recently reported that a remarkable increase in collection efficiency for fly ash could be obtained by enhancing dust adhesion through injecting small amounts of suitable additive compounds such as triethylamine (Tassiker 1975) or ammonia (Dismukes 1975). (This ammonia injection is also used to solve the SO_3 corrosion problem in boilers burning heavy oil.) It is found that very fine fumes of ammonium sulphate or ammonium bisulphate are produced in considerable quantities and that this often results in corona quenching (Dismukes 1975).

6. Back discharge (back corona)

The back discharge is one of the most difficult problems impairing precipitator performance in many large scale industrial plants. The plants affected include ore sintering furnaces in the steel industry; rotary kilns and clinker coolers in the cement industry; smelter furnaces in the metal industry and especially boilers in thermal power plants burning low sulphur coal (these produce high resistivity, mainly metal oxide, dusts). The effects of the back discharging depend on the value of ρ_d. There are two major ones: one is the excessive sparking that occurs when the resistivity is between 5×10^{10} and $10^{12}\,\Omega$ cm. This causes a decrease in the collection efficiency because of the impairment of the collection process. The other is the increase in current which occurs when $\rho_d > 10^{12}\,\Omega$ cm. A copious number of ions are emitted from a number of corona points occurring over the whole surface of the dust layer on the collecting electrodes, and these ions neutralize the useful charge on the particles so that often no particles are collected. These phenomena occur as a result of the breakdown of the dust layer because

of its high apparent resistivity, ρ_d, when the following field condition is locally satisfied at the layer's weak points:

$$E_d = i_d \times \rho_d > E_{ds} \tag{13}$$

where E_d = apparent field strength in the dust layer and E_{ds} is the layer's breakdown strength. Normally the breakdown of the dust triggers streamers in the gas space which, depending on the field distribution around the breakdown point, proceed either towards the discharge electrode, or to the space charge accumulated around the breakdown point, or in both directions. These streamers cause large amounts of carrier multiplication and photon emission; these processes supplying a copious number of positive ions which cannot only neutralize the particle charge but also the negative ion space charge. After the extinction of a streamer, the surface charge is restored by negative ions supplied either from the discharge electrode or from the residual gas plasma, and thus the cycle can once again be triggered, each cycle causing a pulse discharge. Figure 7 indicates the effect of the current, I, and the average field strength in the gas space, normal to the sample layer, E_{gn} ($E_{gn} = V_g/d$) upon the mode of back discharge. Both I and E_{gn} could be changed independently and a mica plate, with a 0·5 mm diameter pin hole, was used as the sample layer (Mizuno 1975, Masuda and Mizuno 1975a). It is shown that a breakdown at the pin hole triggers a surface discharge when $E_{gn} > 3{\cdot}3$ kV cm^{-1} and a streamer in the gas space when $E_{gn} > 5{\cdot}1$ kV cm^{-1}. These discharges become sparks if a certain limit of I is exceeded, even with a constant E_{gn}.

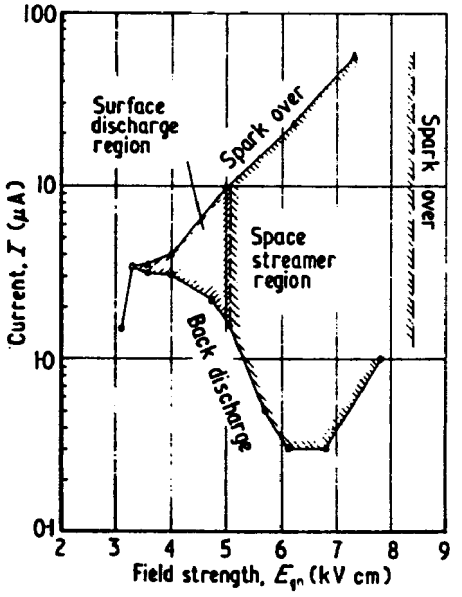

Figure 7. Effects of the normal field strength, E_{gn}, and the total current, I, upon the mode of back discharge (E_{ds} = 15·6 kV cm^{-1}).

When $E_{gn} > 8{\cdot}4$ kV cm^{-1} a streamer becomes a spark. Figure 8 shows pictures of back discharges which indicate the effects of tangential fields. These fields are caused by the surface charge of density $\sigma_d = \epsilon_d \times E_{ds}$ and in the figure the value of E_{ds} was changed by using two parallel glass plates with pin holes and changing the distance between the pin holes. This varies E_{ds} and thus σ_d (Mizuno 1975, Masuda *et al* 1974a). Figure 8 clearly shows that the surface discharge is largely increased by an increase in σ_d. The results in figure 7 seem to explain the reason why the two completely different modes,

(a)

Figure 8. Effect of the tangential field strength upon the mode of back discharge (a) E_{ds} = 22.2 kV m^{-1}, 19 kV, 40 μA; (b) E_{ds} = 36.7 kV m^{-1}, 19 kV, 30 μA

excessive sparking and abnormal rise in current occur with different values of the apparent dust resistivity ρ_d. Consider the difference in voltage drops across the gas region and dust layer that occur with different ρ_d. For low ρ_d, when the applied voltage is raised, E_d in the dust layer will remain small, while E_{gs} in the gas region will sharply rise causing a rapid growth of streamers and thus excessive sparking. When, on the other hand, ρ_d is high, the situation will be reversed in that while no sparking will occur in the gas region, but there will be breakdown at numerous weak points in the dust layer because of the rapid rise in E_d. This will result in a sharp rise in the total current. Figure 9 shows an oscillogram of a typical current waveform of a back discharge pulse along with the accompanying light emission. Figure 10 shows the variation of light emission at various points in space as well across the surface layer. A glass plate with a pin hole was used as the sample layer and the spot resolution was 0.1 mm (Mizuno 1975, Masuda and Mizuno 1975b). The light signals at the graph origins show that the back discharge pulse consists of two parts: the primary wave rises very rapidly and lasts about 20 ns; the secondary wave rises more slowly and lasts about 200 ns. The former effect corresponds to the first rise in the current waveform which has a small pulse height and consists of a charge of 1.2×10^{-9} C pulse (shown in figure 9). The second-

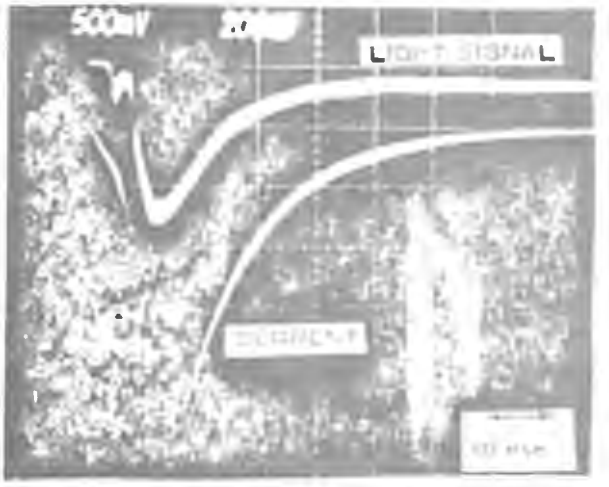

Figure 9. Waveforms of current and light signal of back discharge pulse

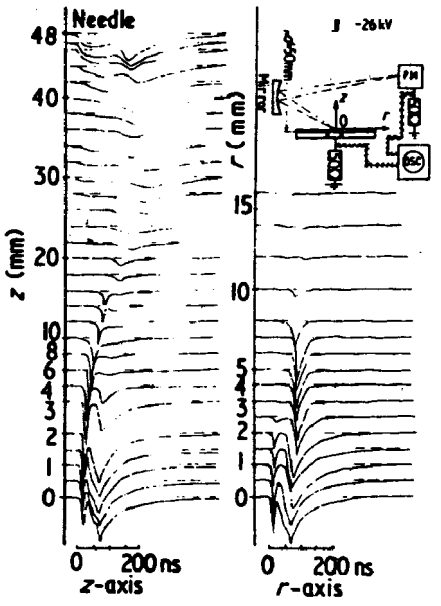

Figure 10. Waveforms of light signals of back discharge measured at various positions taken along the z- and r-axes.

ary wave corresponds to the second rise in current which has a much larger pulse height and a charge content of $2-4 \times 10^{-8}$ C per pulse. It was confirmed that the primary corresponds to a streamer advancing into the gas region with a speed of 4×10^{7} cm s^{-1} and the secondary to the surface discharges which cause much greater charge multiplication. It was observed that when the applied voltage was increased the charge per pulse remained the same in both cases whilst the average repetition frequency increased. The repetition frequency was found to be lower for the surface discharge mode than the space streamer mode, so that, as far as one breakdown point is concerned, the current rise becomes steeper for the latter mode in spite of its smaller charge emission per pulse. Figure 10 also shows that the light signal from the needle point starts almost simultaneously with that from the pin hole and that there is a second rise in emission at the needle with the arrival of the steamer. Figure 11 shows a schematic representation of the streamer propagation calculated from the waveform in figure 10. Figure 12 illustrates a picture of the back discharge which occurs when a positive potential is applied to the discharge electrode. This shows a completely different mode in which discharges occur from points uniformly distributed over the dust layer. As the applied voltage is increased *no* streamers are produced, either from the needle point or from the back discharge

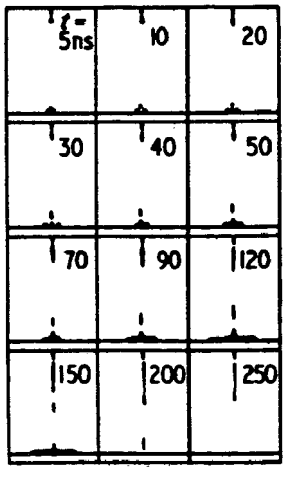

Figure 11. Propagation of back discharge streamers (schematic representation).

Figure 12. Back discharge under positive discharge electrode.

points, but a spark discharge suddenly occurs. The steamer corona at the positive needle point is fully suppressed, presumably because of negative ions supplied from the back discharge points (as in the case of Hermstein's glow). As a result, the spark-over voltage is increased compared to the case when the dust layer is removed (Mizuno 1975, Masuda and Mizuno 1975a).

7. Particle charging

In addition to the theoretical and experimental works already cited, a detailed examination of Pauthenier's equations (2)–(4) was conducted in which the field strength E_c, corona current density i, and the charging time t could be changed independently (Masuda and Akutsu 1975). With spherical conducting particles a very good agreement of the measured value of charge with that calculated from equation (2) was obtained while, for particles such as teflon, with high surface and volume resistivities, the saturation charge always remained about half as much as that given by equation (3), except when the particles were subjected to rotational motion. This discrepancy is evidently the result of the fact that the charges imparted to the insulating particles by the ion bombardment cannot be instantly uniformly distributed over the particle surface, this was an important assumption in the derivation of equations (2)–(4). In the case of moderately resistive particles (i.e. glass) where the dielectric and surface conductivity relaxation times, τ_m, are negligibly small compared to the charging time constant, τ, of equation (4), then there is good agreement between the measured values of acquired charge with those calculated from equations (2)–(4) for conducting particles of the same radius ($\epsilon_s \to \infty$). It is evident that in this case the particles behave like conducting particles because the distribution time for the charge (from ion bombardment and polarization) is the short time taken for the internal field to disappear. Hence the term $3\epsilon_s/(\epsilon_s + 2)$ in equation (3), expressing the effect of the dielectric constant, loses its meaning. This is due to the contradicting assumptions that the distribution of polarization charge has the time constant for a dielectric particle and that the distribution of imparted charge has the time constant for a conducting particle. Under normal

precipitator conditions we can assume that particles having a volume resistivity of below 10^{11} Ω cm (this implies $\rho_d < 10^{13}$ Ω cm (Masuda 1965)) to be quasi-conducting particles (Masuda and Akutsu 1975).

The particle charge imparted by bipolar ions was also measured under back-discharge conditions. The distribution of positive and negative ion densities, ρ_+ and ρ_-, were calculated by using the data obtained in the relation derived by Pauthenier (1961). It could be shown that even a weak back discharge could cause a remarkable decrease of the particle charge to 10% of its normal value. This was predicted by Pauthenier (1961). In some cases a polarity change even occurred. It was also observed that, in the space streamer mode, ρ_+ and ρ_- became nearly equal and almost constant through the luminous region, which suggests that the carrier production takes place in a fairly wide region of the gas space. In contrast with the surface discharge mode, ρ_+ and ρ_- showed an exponential decay in space from both sides. However, their rates of decay with distance were very low so that a long extension of the positive ion cloud to the discharge electrode region was observed.

As a novel method of particle charging, the use of gamma rays has been proposed. The bipolar ions produced by the high-energy electrons are separated by a transverse electric field, and used to charge the particles which are then collected on to the electrodes (Heinsohn *et al* 1975).

8. Dust resistivity

Figure 13 exemplifies the effect of ρ_d upon the precipitator performance, expressed in terms of the apparent migration velocity, W. It is clearly indicated that the preferable range for electrostatic precipitation is for particles with ρ_d between 10^4 and 10^{10} Ω cm and that the efficiency is limited by dust re-entrainment and back discharge. The

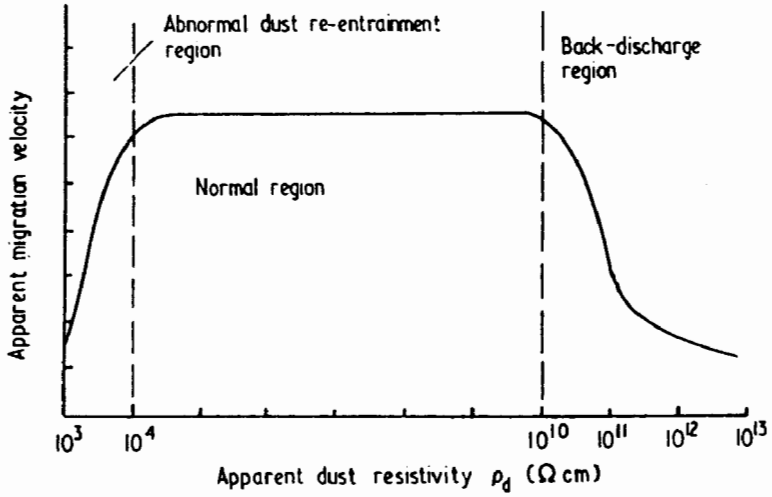

Figure 13. Effect of dust resistivity, ρ_d, upon the apparent migration velocity, W.

value of the apparent resistivity, ρ_d, for a high-resistivity dust layer depends, as is illustrated in figure 14, upon the temperature and humidity of the ambient gas. It is also affected by its chemical composition and the presence of impurities in the gas (e.g. SO_3). At low temperatures the resistivity is determined by the surface conduction which is usually governed by the absorption of water molecules. At higher temperatures the

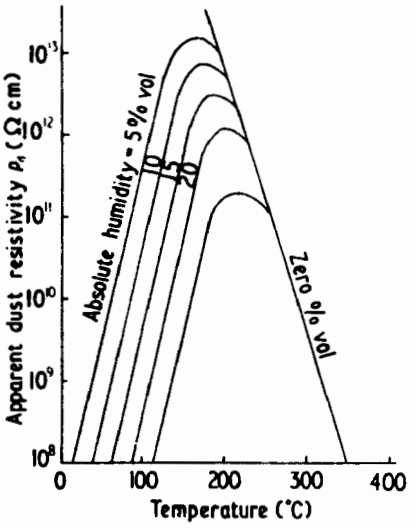

Figure 14. Effects of temperature and humidity of ambient gas upon the apparent resistivity of high-resistivity dust.

resistivity will be determined by bulk conduction. Current constrictions at the contact points between the particles will also effect the resistivity (Masuda 1965). The resistivity has a maximum at a temperature between 100 and 200 °C which unfortunately is the temperature range of exit gases in most industrial emission sources. Therefore, back-discharge troubles often occur. It was recently discovered that alkali metal ions served as charge carriers in both surface and volume conduction in layers of fly ash (Bickelhaupt 1975).

9. Technical progress and new development

The large-spacing precipitator with an electrode spacing of 20–50 cm, described previously, has proved to be successful in many of its applications. This includes cases with high-resistivity dust where in some cases a cost reduction of approximately 20% has been obtained. The roof-top type of precipitator is in increasing use. It is installed on the roof of a plant building from which one has severe dust emission, for example from an electric furnace. A large hot mass of gas rises to the ceiling where it enters the precipitator and then passes through it by free convection and is emitted directly into the open air. Often conductive plastics are used for the collection electrodes because of their low weight.

The wet-type of precipitator is attracting increased attention because of its very good performance. It is entirely free from dust re-entrainment and back discharges and also performs the additional function of removing gaseous pollutants such as SO_2, HF, etc. The problems with this type have been the necessity of irrigation water, the treatment of the emitted slurry and the reheating of the cool gas at the outlet in order to recover gaseous lift. These problems can be solved effectively in the hybrid-type of precipitator in which the dry and wet types of precipitators were integrated inside a common casing to make an optimized system (Ago *et al* 1973, 1975). The major portion of the incoming dust was collected in the dry stage and the remaining very fine dust was effectively removed in a fairly small wet stage. This meant that a large reduction in the amount of irrigation water, the slurry emission and the temperature drop, could be achieved. The slurry, after concentration, could be dried by the use of the

heat contained either in the inlet gas or in the collected dust in the dry stage. The merit of this system has been found to be emphasised when very high degrees of emission control for particulate and gaseous pollutants have to be achieved.

As regards the solution of the back-discharge problem, the conditioning of the inlet gas by use of a water spray has long been used to reduce the value of ρ_d below about $5 \times 10^{10}\ \Omega$ cm. In this case the rapid and perfect evaporation of atomized water has to be obtained (Masuda and Saito 1966). The so-called 'chemical conditioning' using suitable additives (Dalmon and Tidy 1972b) has also proved to have been effective in some applications. For instance, the injection of SO_3 into the inlet gas is widely used for the fly ash of low-sulphur coal in order to prevent back discharging (Busby and Darby 1963, Darby and Heinrich 1966, Cook 1975). The possibility of conditioning fly ash by the addition of a sodium compound such as Na_2CO_3 to low-sulphur coal, as it is being burned, was also recently proposed (White 1975). Another solution to back discharging is the use of the so-called 'hot-side' precipitator in which collection is made at higher temperatures (300–400 °C) (see figure 14). The key factor in this system is the consideration of the structural thermal-expansion properties (Walker 1975).

Purely electrical solutions have also been studied. Figure 15 shows one such approach, where pulse charging is used in conjunction with a third electrode (Lüthi 1967). The remarkable features of this method are that the current density can be

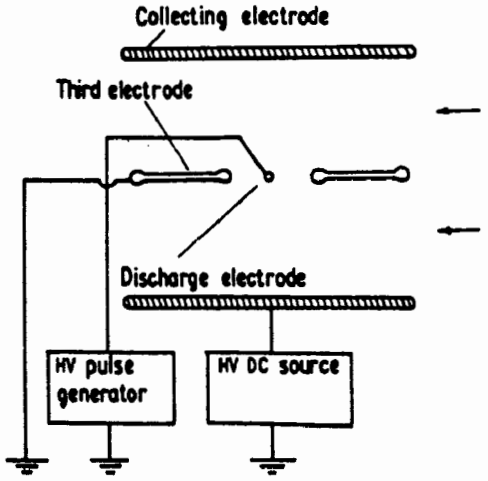

Figure 15. Pulse-charging system with the third electrode (Lüthi 1967).

adjusted independently of the main field strength by changing the magnitude or repetition frequency of the pulse voltage, and that a very uniform current density is obtained over the complete surface of the collection electrode because of the expansion of the dense ion cloud that is produced by the pulses. Thus the condition necessary for the avoidance of back discharging, $i_d \times \rho_d < E_{ds}$, can be met over the dust surface whilst the main field strength is always kept at its maximum. A further study revealed that it is desirable to put an additional DC bias voltage in series with the pulse voltage (see figure 5). This ensures the suppression of the DC corona during the pulse-free period, regardless of fluctuations in the plant conditions (i.e. gas temperature and dust concentration), especially when the distance between the discharge electrode and the third electrode has to be increased to meet design requirements (Masuda *et al* 1974b). It could be shown in the pilot plant tests that the precipitator shown in figure 5, equipped

with the bias-controlled pulse-charging system, exhibited an increase in collection efficiency from 63% to 93% for dust with the very high apparent resistivity of $10^{13}\,\Omega$ cm (Masuda *et al* 1974b). It was also observed that this method might provide an effective solution for corona quenching because, with the aid of the third electrode, a sufficient number of ions could be pulled from the discharge electrode, regardless of the dust space charge existing in the main field. Instead of a pulsed field, an AC voltage could be used in series with the bias voltage. Another very effective electrical approach to the solution of the back-discharging problem is to use an AC voltage in conjunction with an insulating film over the collecting electrode (Krug 1971). The practicability of this method will depend on progress in the field of insulator materials.

The investigation of EFD motion of charged particles led to a new two-stage precipitator of the type shown in figure 5, in which the charged particles coagulate in the charging section and are led into the inside of downstream channels by the action of the gas flow and the use of electric fields, where they are then electrically precipitated (Shibuya and Masuda 1975). A remarkable reduction in precipitator size could be achieved by this method under suitable conditions.

10. Conclusions

The recent progress in electrostatic precipitation has been reviewed. The major difficulty lies in the inherent problem of a multi-variable system, where the many process variables which affect the overall performance have to be considered together. The gap between scientific understanding of the elementary processes and the design procedure has thus been inevitably large. In order to lessen this gap, more detailed studies are needed of not only the physical phenomena but also the ability of the theories to correlate the major process variables with the overall precipitator performance.

References

Adachi T, Suyama T, Shimoda M and Masuda S 1974 *Proc. Gen. Conf. Inst. Elect. Engrs. Japan* No718

Ago S, Itoh T, Saito H, Furuya N and Masuda S 1973 *Proc. Gen. Conf. Inst. Elect. Engrs. Japan* No838

Ago S, Itoh T, Saito H, Furuya N and Masuda S 1975 *Proc. Gen. Conf. Inst. Elect. Engrs. Japan* No921

Awad M B and Castle G S P 1975 *J. Air Pollution Control Assoc.* 25 172

Bickelhaupt R E 1975 *J. Air Pollution Control Assoc.* 25 148

Busby H G T and Darby K 1963 *J. Inst. Fuel* 36 184

Cook R E 1975 *J. Air Pollution Control Assoc.* 25 156

Dalmon J and Tidy D 1972a *Atmos. Env.* 6 81

Dalmon J and Tidy D 1972b *Atmos. Env.* 6 721

Darby K and Heinrich D O 1966 *Staub-Reinhalt. Luft* 26 464

Dismukes E B 1975 *J. Air Pollution Control Assoc.* 25 152

Hall H J 1975 *J. Air Pollution Control Assoc.* 25 132

Heinrich D O 1961 *Trans. Inst. Chem. Engrs.* 39 145

Heinsohn R J, Levine S H, Fjeld R J and Malamud G W 1975 *J. Air Pollution Control Assoc.* 25 179

Hermstein W 1960 *Archiv für Elektrotechnik* 45 209, 279

Hewitt G W 1957 *AIEE Trans.* part I 76 300

Kuroda M 1975 *Graduation Thesis* Department of Electrical Engineering, University of Tokyo
Krug H 1971 *Dissertation* TU Karlsruhe
Liu B Y H, Whitby K T and Yu H H S 1967 *J. Appl. Phys.* **38(4)** 1952
Liu B Y H and Yeh H C 1968 *J. Appl. Phys.* **39(3)** 1396
Lowe H J and Lucas D H 1953 *Brit. J. Appl. Phys.* (suppl) 2 40
Lüthi J E 1967 *Dissertation* ETH-Zürich No3924
Masuda S 1965 *Staub* **25** 175
—— 1966 *Staub-Reinhalt. Luft* **26** 459
Masuda S and Adachi Y 1975 *Trans. Inst. Elect. Engrs. Japan* to be published
Masuda S and Akutsu K 1975 *Proc. Gen. Conf. Inst. Elect. Engrs. Japan* No909
Masuda S, Akutsu K and Mizuno A 1974a *Proc. Gen. Conf. Inst. Elect. Engrs. Japan* No723
Masuda S, Aoyama M, Shimozono S, Hattori J and Shibuya A 1974b *Proc. 19th Ann. Meeting Static Electrification Group Japan* (Inst. Polym. Sci. Japan) p35
Masuda S and Matsumoto Y 1974a *Proc. Gen. Conf. Inst. Elect. Engrs. Japan* No722
—— 1974b *Trans. Inst. Elect. Engrs. Japan* **94-A** 515
Masuda S, Matsumoto Y and Ohba Y 1973a *Proc. Gen. Conf. Inst. Elect. Engrs. Japan* No839
Masuda S and Mizuno A 1975a *Proc. Gen. Conf. Inst. Elect. Engrs. Japan* No924
—— 1975b *Proc. Gen. Conf. Inst. Elect. Engrs. Japan* No923
Masuda S and Niioka M 1973 *Proc. Gen. Conf. Inst. Elect. Engrs. Japan* No847
—— 1974 *Proc. Gen. Conf. Inst. Elect. Engrs. Japan* No719
Masuda S and Saito H 1966 *I and E C Process Design and Development* **5** 135
Masuda S, Shibuya A and Ikeno E 1973b *Proc. Gen. Conf. Inst. Elect. Engrs. Japan* No844
Matsumoto Y 1974 *Dissertation* Department of Electrical Engineering, University of Tokyo
McCain J D, Gooch J P and Smith W B 1975 *J. Air Pollution Control Assoc.* **25** 117
Mizuno A 1975 *Dissertation* Department of Electrical Engineering, University of Tokyo
Murphy A T, Adler F T and Penny G W 1959 *AIEE Trans.* part 1 **78** 318
Niioka M 1974 *Dissertation* Department of Electrical Engineering, University of Tokyo
Pauthenier M 1961 *La Physique des Forces électrostatiques et leurs Application* (Centre National de la Recherche Scientifique) p279
Pauthenier M and Moreau-Hanot M 1932 *J. Phys. Radium* **3** 590
Penny G W 1975 *J. Air Pollution Control Assoc.* **25** 113
Penny G W and Lynch R D 1957 *AIEE Trans.* part 1 **76** 294
Shibuya A and Masuda S 1975 *Proc. Gen. Conf. Inst. Elect. Engrs. Japan* No920
Simm W 1962 *Staub* **22** 463
Smith P L and Penny G W 1961 *AIEE Trans.* part 1 **80** 340
Smith W B and McDonald J R 1975 *J. Air Pollution Control Assoc.* **25** 168
Steinbigler H 1969 *Dissertation* TH München
Tassicker O J 1975 *J. Air Pollution Control Assoc.* **25** 122
White H J 1951 *AIEE Trans.* part 2 **70** 1186
—— 1962 *Industrial Electrostatic Precipitation* (New York: Addison-Wesley) p157
—— 1975 *J. Air Pollution Control Assoc.* **25** 102
Walker A B 1975 *J. Air Pollution Control Assoc.* **25** 143

Discussion

Mr W E G Plumtree (Rank Xerox)

Particularly with respect to the results in figure 7 (back-discharge plot), how much dust was present in the system?

Professor Masuda

Instead of a dust layer we used a mica plate with a 0·5 mm diameter pin hole. The thickness of the plate was 1 mm.

Senichi Masuda

Mr R Hours (CEA)

About two years ago American authors proposed the use of γ-rays to charge (and thereby remove) very fine particles from the flue gases of coal-fired power stations. Scientifically, this idea is interesting, but due to the very low yield of γ-ray ionization, powerful – and therefore dangerous – radioactive sources are necessary. Consequently the system appears uneconomical compared with those based on corona charging. What is your opinion about that?

Professor Masuda

I don't think that the use of γ-rays in particle charging will find a wide practical application in the field of electrostatic precipitation, because of the problems you pointed out. I comment, however, that a high energy electron beam (0·75–1·5 MeV, 100 mA) might be effectively used for the removal of NO_x and SO_x from the exit gases out of large-scale industrial furnaces (ore-sintering furnaces, thermal power plants, etc). It was discovered that these gaseous pollutants are effectively converted by the electron beam irradiation into aerosol particles within about 1 second. These particles may be collected by an electrostatic precipitator. Large-scale development work is now going on in Japan by a research group from the steel industries. It is expected that a very high initial investment in this method may be balanced by the benefits of a very small pressure drop and the ease of operation where no catalyst is used.

Dr J C Gibbings (Liverpool University)

The design of electrostatic precipitation is a good example of electrostatics being very much an inter-disciplinary study in that the study of the electric field must go hand-in-hand with the fluid mechanics study of the flow pattern for real progress to be made. Professor Masuda pointed out that his field calculations for $K = 0$ gave flux lines identical to the streamlines; but these streamlines are for the potential flow and no real flow in ducts would correspond to these streamlines. In the past, the design of precipitators has been spoilt by lack of concern with analysis and knowledge of the flow. For example, the electric wind from an electrode will convey a particle towards a surface, but unless centrifugal and electrostatic forces remove it from the flow on to the surface, then the return flow, which continuity insists must exist, will equally convey it away again: in principle this is why the presence of turbulence in the flow is of such significance in effectively greatly increasing the diffusion coefficient.

FLASHOVER MEASUREMENTS OF BACK DISCHARGE

Senichi MASUDA, PhD

Akira MIZUNO, ME

Department of Electrical Engeneering,
University of Tokyo

7-3-1, Hongo, Bunkyo-Ku, Tokyo,
Japan

Summary

The mode change and flashover voltage of back discharge under different gaseous conditions were studied with a special attention to the effects of dust layer thickness and alkaline components contained in dust. It was found that back discharge took either streamer or steady-glow mode depending upon gas mean free path. These modes have their own characteristic flashover voltage as a function of gas mean free path, where its value for the former mode is much lower than that for the latter. Thickness of the dust layer and existence of the alkaline components also govern the initiation of streamer so that the flashover voltage is largely affected by these factors.

1. Introduction

Back discharge has long been one of the unsolved problems in electrostatic precipitation. This is an abnormal discharge caused by breakdown of high resistivity dust layer deposited on collecting electrode. The mode and effect of back discharge differ largely, depending upon the polarity of corona discharge used. In this paper, however, we restrict ourselves to the case of negative polarity which has been in common use because of its higher flashover voltage under normal operating conditions. If back discharge takes place, flashover voltage falls to about half the value of that under normal operation, and particle charge will be neutralized. When the field strength inside the dust layer exceeds its breakdown value, the initiation of back discharge takes place. A random or repetitive breakdown appears at the breakdown point, owing to the continuous ion supply from corona discharge. With a slight increase in

voltage, it turns to a feeble but continuous spot-like onset-glow, refered to as "onset-glow mode". The current wave form contains that of Trichel pulse superimposed on a D.C.component. With the further increase in voltage, this onset-glow either triggers the streamer discharge in gas space or along the layer surface, or it turns to a pulseless point-like glow with increased intensity. The former mode should be refered to as "streamer mode", while the latter as "steady-glow mode". Thus, the mode of back discharge after onset stage can be classified into streamer and steady-glow modes, as described separately.[1] When gas mean free path is large, the transition occurs from the streamer mode to the steady-glow mode with an increase in voltage beyond a certain critical voltage. This mode transition is reversible and affected not only by the gas mean free path but also by the thickness of dust layer and its chemical composition. When the thickness is small, streamer mode does not occur and the flashover voltage is high. Among the effects of chemical composition, the most remarkable is that of alkaline metal compounds which lowers the flashover voltage of back discharge to a great extent. In this case streamer propagation becomes very pronounced so that it easily turns to a flashover.

In this paper, the effects of mean free path, dust layer thickness and alkaline content in dusts on back discharge mode and flashover voltage are reported.

2. Experimental apparatus

The effects of mean free path on the flashover voltage and mode of back discharge were studied by changing the pressure P under room temperature or by changing the temperature T under atmospheric pressure. A needle to plane electrode system with a gap of 50 mm was used inside a thermostat or vacuum chamber as shown in Fig.1. A mica plate having a pinhole of 0.5 mm in diameter, tissue paper and dust samples of various chemical compositions were used as test layer samples to be located on the plane electrode. As a most important parameter, the resistivity of the test layer was measured before each experiment. The change of the resistivity under vacuum condition was enabled by drying the layer by heat during evacuation to about 1 torr, and thereafter adding dry air, so that a desired air pressure could be obtained. By this method, the value of resistivity could be maintained constant at least during each experiment. However, its value was delicately dependent upon the drying condition. Hence, its measurement at a position separate from the centre area using a fixed counter electrode on the layer surface should be excluded. Thus, before each measurement, a counter electrode was set on a centre position facing to a measuring electrode and removed therefrom after the experiment, with the aid of a remote-controlled crane model. In the case of resistivity measurement under elevated temperature inside the thermostat, a separate measuring cell was used, because the resistivity value in this case was a unique function of the thermostat temperature, so far as the equilibrium condition was reached. An image intensifier tube (EMI, type 9912) was used to observe a faint glow of back discharge at its initial stage and to investigate the difference in discharge modes in detail.

3. Effect of mean free path

A mica plate with a pinhole of 0.5 mm in diameter and 0.45 mm thickness was used as the test layer. The flashover voltage Vs was plotted against the normalized mean free path $\lambda/\lambda o$, as shown in Fig.2, where λo is the mean free path at NTP. The solid curves represent the results obtained by changing P under room temperature (20 °C) while the dotted curves indicate those obtained by changing T under atmospheric pressure (760 torr). The scales for these P and T are also given. It can be seen that the curves measured by changing T or P agree well with each other. It should be noted that there exist two different curves for flashover (curve I and II), each covering the different range of $\lambda/\lambda o$. In the area under the curve I, the onset-glow mode was followed by the streamer mode with the increase in voltage, while the steady-glow mode occurred in the area under the curve II. As a result there are three different regions in $\lambda/\lambda o$, A, B and C as indicated in the figure, each corresponding to different mode changes. In region A, back discharge in the streamer mode followed the onset-glow mode and turned to flashover on curve I. In region C, back discharge in the steady-glow mode followed the onset-glow mode and no streamers appeared until flashover took place on curve II. Region B is a transition region between A and C. Fig.3 shows the photographs indicating the mode transition in this region. The onset-glow mode appeared at first at the pinhole (Fig.3-a). With the increase in applied voltage, it turned into streamer mode (Fig.3-b), bridged across the gap and finally turned to random sparking on the curve I (Fig.3-c). In region B, the random sparking tended more easily to occur at smaller value of $\lambda/\lambda o$. Slightly above the curve I, streamers suddenly disappeared to turn to a stable steady-glow (Fig.3-d). This lasted

until flashover occurred on curve II. The voltage-current characteristics in this region were further studied with the use of X-Y recorder, where the electrode voltage V and the current from the measuring electrode, I, were recorded. The result obtained with no additional output impedance is shown in Fig.4-a where the output impedance was only that of the source (Ro = 15 M ohm) so that it was comparatively small. From the onset-glow at the pinhole, the space streamer appeared at point A. With the increase in voltage, it bridged across the gap, resulting in a transition from point B to C. When the source voltage was further increased, the space streamer became more luminous and current I increased, the electrode voltage, however, remaining almost constant (curve ii). Fluctuations of the current and voltage were large. Around the point D, random sparking took place. With the source voltage slightly increased from point D, the transition of the streamer to the steady-glow mode occurred, accompanied by the transition of the curve from point D' to B' where D' and B' were very close to D and B respectively. Thereafter, the voltage and current followed the curve (i') until flashover occurred at a point beyond E. Then, when the voltage was lowered, the voltage and current followed the identical curve E-B' until point F was reached. The inverse transition from the steady-glow to streamer mode occurred at point F, resulting in the transition of the curve from F to C. With the further decrease in voltage, the streamer mode lasted following curve (ii') until point G was reached where it turned to the onset-glow mode again. Thereafter the voltage and current followed the initial curve (i). Thus, it can be seen that voltage-current characteristics consists of two curves (i)-(i') and (ii)-(ii'), the former corresponding

to the glow mode, and the latter to the streamer mode. The curve (i)-(i') is subdivided into part (i) and (i'), the former includes the onset-glow mode while the latter corresponds to the steady-glow mode. It was observed that these transitions of mode and V-I characteristics were governed by the output impedance of the high voltage source, as indicated in Fig.4-b and c. In the case of Fig.4-b, the additional resistance of R = 27 M ohm was inserted in series to the output circuit, while in the case of Fig.4-c, that of R = 55 M ohm was used. In Fig.4-b, B' was fairly apart from B, and C' was somewhat apart from C. The transition from F to C' was unstable, and the inverse transition easily took place, even when the source voltage was kept constant. But, when the voltage was further decreased, the streamer mode became stable and the voltage and current followed the curve (ii'). When the output impedance was excessively high, as in the case of Fig.4-c (R = 55 M ohm), neither random sparking nor transition took place at point D'' where the source voltage was its upper limit, 50 kV. With the decrease in voltage, the curve followed (ii) and (ii'). The current wave form in region B in Fig.2 is shown in Fig.5. As the onset-glow started, Trichel pulses superimposed to a small D.C. current were observed (Fig.5-a), and with the increase in voltage, random pulses having much larger pulse height appeared, which corresponds to space streamers (Fig.5-b). Finally pulseless D.C. current appeared with the transition from streamer to steady-glow mode (Fig.5-c). No Trichel pulse could be observed in this mode. This suggests the mechanism of electron emission from discharge electrode to have changed from that for the onset-glow mode.

4. Effect of dust layer thickness

The effect of thickness of the layer was studied using three mica plates with different thickness, each having a pinhole with 0.5 mm in diameter, and three tissue papers with different lamination number. The resistivity of the mica plates were higher than 10^{15} ohm-cm, while that of the tissue papers were about 10^{12} ohm-cm. Fig.6 and 7 show the values of flahsover voltage obtained for the mica plates and the tissue papers respectively, plotted against pressure P with the $\lambda/\lambda o$ scale identical to that in Fig.2. It can be seen in Fig.6 that, with the decrease in the mica plate thickness t, the transition pressure P_{bc} from the region B to C shifted towards the side of higher pressure range (lower mean free path). P_{bc} finally exceeded 760 torr before t = 47μm was reached. When t was 47μm, streamers did not appear and the flashover voltage was given only by curve 3, which agreed well with the curve II in Fig.2. The curves 1 and 2 also agreed to the curves I and II in Fig.2 except for their ranges.

For tissue papers having a number of weak points, when t was 2.6 mm, the two curves I and II coalesced into one transition curve in the region B as indicated by curve 1 in Fig.7. This was because the transition from the streamer to the steady-glow mode occurred at first at the centre region of the layer and propagated towards the peripheral region with the increase in applied voltage. The flashover occurred not from the steady-glow points but from the streamers stemming from the distant breakdown points so that flashover voltage in the region B took the value between curves I and II. When t was 0.6 and 0.06 mm, only the steady-glow mode appeared and flashover occurred at curves 2 and 3 which corresponded to

the curve 3 in Fig.6. The curves 2 and 3 in Fig.7 also roughly agreed with the curve II in Fig.2. It was concluded that the decrease in the layer thickness shifted the transition pressure between resions B and C, P_{bc}, towards the side of higher pressure range, resulting in the dominance of the steady-glow mode and the increase in flashover voltage.

5. Effect of chemical composition of dust

In an electrostatic precipitator, flashover must usually be dominated by streamer mechanism since the values of both pressure and gap distance are large. It is considered, therefore, that the existence of alkaline components may help streamer development because of their low ionisation energy so that the flashover voltage under back discharge condition may become lower. For example, the exhaust gas from an iron ore sintering furnace contains fairly high content of alkaline metal compounds, especially that of potassium, and it has been found that the collection performance drops as its content increases.

The flashover voltage Vs of a needle to plane electrode system (gap 50 mm) was measured, with various kinds of dust layers (thickness 2.0 mm) on the plane electrode. The samples used were the first class agents and shown in Table 1. The experiments were conducted in a thermostat or vacuum chamber, and the change of dust resistivity was enabled using the methods described in section 2.

The flashover voltage Vs and the apparent resistivity ρ_d for each dust layer plotted against temperature T are shown in Fig.8 and 9 respectively. In this case measurement was made under atmospheric pressure. The scale of the temperature in Fig.8 is the same as that in Fig.2. The abrupt

rise in Vs in curves 2, 3 and 5 in Fig.8 were due to the disappearence of back discharge resulted by the decrease in dust resistivity with the increased temperature (Fig.9). Curves 1 and 2 in Fig.8 roughly agree with the curve II in Fig.2, while curve 3, 4 and 5 with the curve I. For $CaCO_3$ and Fe_2O_3 dusts (curve 1 and 2), back discharge after the onset-glow stage was at first of streamer mode, but it changed into the s steady-glow mode when craters had been formed at the breakdown point and Vs became high. In these dusts particles were easily ejected from the area around the back discharge point so that conical craters tended to be formed. Hence, it was probable that the effective thickness of the layer at the crater bottom became so small that no streamer could occur. On the other hand, for K_2SO_4, KCl and NaCl dusts (curve 3, 4 and 5), all containing alkaline metals, the streamer mode always dominated so that Vs was lower.

The flashover voltage under room temperature plotted against pressure P is shown in Fig.10 where the scale of P is also the same as that in Fig.2. The apparent resistivity ρ_d could be kept constant inspite of a large change in pressure by using dry air. It was confirmed that the Vs curves of various dusts could be classified into curves I, II and III. Curves I and II agreed with the curves I and II in Fig.2. Curve III was a transition curve between the curves I and II, like the curve 1 in the region B in Fig.7. In the dusts corresponding to curve III, pinholes were easily formed at the breakdown points.

The classification of dusts by their Vs curves is shown in Table 1. These results show that alkaline dusts are included in Group I (curve I), non-alkaline dust tending easily to form conical craters in Group II (curve II)

and dusts in which pinholes easily appear are classified in Group III (curve III). With the existence of alkaline compound, only curve I appeared and no transition to the steady-glow mode occurred, the streamer mode lasting until flashover took place, at least within the range of T, P and the layer thickness investigated. The lack of curve II for alkaline compounds might be a result of the fact that the transition pressure P_{ab} between regions A and B was shifted towards the low pressure side beyond the range investigated. On the contrary, the lack of curve I for non-alkaline dust investigated might be caused by the shift of the transition pressure P_{bc} between regions B and C towards the high pressure side beyond the range studied. The characteristics of curve III might be explained by the propagation model of mode transition assumed for curve 1 in Fig.7.

The effect of alkaline compounds on voltage-current characteristics under back discharge with a single breakdown point was studied. In this experiment the thickness of the layer must be kept constant so that its effect could be excluded. For that purpose a mica plate having a pinhole (0.5 mm in diameter) was again used, and its surface was painted by water solution of K_2SO_4 (10 % in weight) and thereafter dried. Fig.11-a and b show the difference in voltage-current curves with and without K_2SO_4 film under the pressure P = 360 torr, where no additional output resistance was used. An X-Y recorder was used also for these measurements. Fig.11-a shows the identical characteristics as those in Fig.4-a. In Fig.11-b, when K_2SO_4 film existed on the surface, a streamer appeared at a lower voltage. With the voltage increased, it bridged across the electrodes and flashover occurred. In this case the transition to the steady-glow mode did not take place, except for a transient one appearing rarely at the instant of flashover.

6. Discussions

6.1 Summary of back discharge phenomena

The phenomenological behaviors of back discharge so far described can be summarized as follows. Back discharge starts with the breakdown of a weak point or pinhole in the layer, when the condition $\rho d \times J \geq Eds$ is fulfilled.[1] This breakdown, occurring randomly at first, becomes more or less periodical when the voltage is raised. With the voltage further increased, it turns to a feeble spot-like onset-glow. When the layer resistivity is comparatively low, less than about 10^{12} ohm-cm, where a sufficient negative ion current is being supplied from the discharge electrode at the instant of breakdown, the layer breakdown directly triggers the onset-glow. With the further increase in voltage, the onset-glow turns either to the streamers (surface and/or space streamers) or to the more luminous steady-glow. In some cases, a small sized onset-streamer is observed to appear around the upper edge of the pinhole prior to the occurence of the well developed streamers. The difference between the onset-glow and steady-glow lies in the magnitude and wave form of current, the former current being lower (less than about 50 μA/point) and containing both D.C. and Trichel pulse component, while the latter being higher (more than about 50 μA/point) and completely non-pulsive. This difference suggests the change in corona mechanism occurring at the discharge electrode. The D.C. current component in the onset-glow increases with the increase in voltage. In the region A where gas mean free path λ is small, flashover occurs directly from the space streamer, while in region C where λ is large, steady-glow turns to flashover without occurence of streamer.

In the intermediate region B, the onset-glow is followed by the streamers, which bridge the electrode gap and cause random sparking. The random sparking tends more easily to occur at a smaller λ/λ_0 side in region B. The streamers, however, disappear at a certain critical voltage to turn to the steady-glow. Flashover occurs from the steady-glow in this region. The decrease in the layer thickness shifts the boundary value of P_{bc} between the regions B and C towards the smaller side of λ. The existence of compounds having low ionisation potential shifts the boundary value of P_{ab} between the regions A and B to the larger side of λ. In case of the layer having many weak points or pinholes, the mode transition between the streamer and steady-glow modes takes place from one point to another so that flashover curves in the region B coalesce into a single curve.

6.2 Mechanism of back discharge

There are three discharge districts in back discharge to be considered separately (Fig.12): (1) the breakdown point in the layer, (2) the layer surface and gas space, and (3) the corona point at discharge electrode. The discharge mechanism in these three districts may be different, but closely connected to each other to characterize the over-all behavior of back discharge.

After a pre-onset stage, a spot-like glow discharge at the breakdown point remains to exist either in the form of the onset-glow or in the form of the steady-glow, so far as the streamers do not occur. When the streamers occur, the spots glow repetitively only at the instant of streamer occurence. Judging from the magnitude of current density, the onset-glow and the steady-glow should be taken as a kind of glow discharge having a structure

as shown in Fig.12. A most remarkable feature of these glow discharges at the breakdown point is that they lack a cathode electrode as a source of electrons which maintain the discharges themselves. There must exist some origin of electrons at the location S near the top of the glow spot. The only possible source of electrons may be the negative ions, supplied from the discharge electrode, from which electrons will be sheded. The electron shedding, however, requires a value of field strength to pressure ratio higher than about 20 V/cm-torr.[2] This field may only be formed by space charge of highly concentrated positive ions accumulated at the location P under the shedding zone S. The electrons, shedded from negative ions, will be strongly accerelated by the positive ion space charge field to ionize gas molecules at the area G under the region P. This ionizing region G may correspond to the negative glow in a usual glow discharge and provide a sufficient quantity of positive ions to the region P. This positive ion space charge region P may correspond to the cathode darkspace.[3]

In region A where gas mean free path λ is sufficiently small, the number of collision for unit length becomes large, while the diffusion of produced plasma will be largely suppressed. Hence, the positive ion density could become so high that the condition for streamer initiation[4]

$$\int_0^L (\alpha - \eta)\, dl = K \quad , \quad K = 10 \sim 20 \qquad (1)$$

may be fulfilled. Here α is the first Townsend coefficient and η the attachment coefficient of electrons to neutral molecules. The integration should be performed from the origin O, through the breakdown channel and along the optimum field line in gas space to the position L where $\alpha = \eta$. The streamer propagate either into gas space towards the discharge electrode or along the layer surface, or the both directions. With the increase in voltage the space streamer finally reaches at the discharge

electrode to cause a mighty flashover capable of turning into arc in this case.

In region B where the gas mean free path λ becomes larger, the plasma density in streamer channel cannot become sufficiently high so that it cannot trigger the mighty flashover when it bridges over the electrode gap, or even when it triggers a random sparking, so far as the output impedance of the source is not sufficiently low. In this case the transition from the streamer mode to the steady-glow mode occurs at the bridge-over stage of the streamer, but not at the instant of sparking. At this stage copious positive and negative ions are produced in the gas space. As a result a strong positive ion space charge accumulates in front of the discharge electrode resulting in an enhanced electron emission from its surface because of gamma action (electron emission by positive ion bombardment). The electron space charge can effectively compensated by the strong positive ion space charge so that no periodical choking of electron avalanche occurs. Hence, the Trichel pulse disappears and a sufficient quantity of negative ion current can now be supplied from the pulseless negative glow corona. In the meantime, a strong negative ion sheath is formed near the region S to enhance the positive ion supply from the layer breakdown point. The highly increased densities of positive and negative ions in gas space may reduce the field in the gap so that streamer cannot be maintained. This might be the situation causing the transition from the streamer to steady-glow mode. The mighty flashover takes place from the steady-glow only when the voltage is sufficiently raised.

In region C where the gas mean free path λ is very large, the streamer initiation condition (1) cannot be fulfilled owing to the decrease in collision number and the increase in diffusion of plasma. With the increase in voltage, the positive ion accumulation in front of the discharge electrode also increases so that D.C. current component due to gamma action of the positive ion collision also increases. Finally, when the choking effect of negative ions from the discharge electrode is offset by the positive ion space charge, the Tirchel pulse may completely disappear so that the onset-glow mode turns to the steady-glow mode. The sufficient increase in voltage results in the mighty flashover to occur directly from the steady-glow. Hence, it is expected that the boundaries between the regions A, B and C may also be governed by the output impedance of the source.

The existence of two flashover voltage represented by curves I and II clearly suggests that, once back discharge occurred, the flashover becomes solely governed by the mode of the preceding discharge and is not affected by dust resistivity, ρd, although ρd has an essential effect on the initiation of back discharge itself.

6.3 Effect of layer thickness and ionisation potential of dust

The essential part in the integration in equation (1) seems to exist inside the pinhole itself so that the product (pressure P) x (layer thickness t) should play a major role in the streamer initiation. Thus it can be understood that, with the decrease in layer thickness t, the boundary pressure P_{bc}' between the regions B and C shifted towards the side of higher pressure. In Fig.5, the values of P x t at the boundary

pressure between B and C are 35.7 torr-mm for t = 115μm and 22.8 torr-mm for t = 60μm respectively. Whereas, in case of t = 47μm, no streamers appeared at P = 760 torr. This may suggest that streamer will not occur if the value of P x t is smaller than about 20 torr-mm.

The effective value of α in equation (1) may become larger if the layer contains components with low ionisation potential such as alkaline metal compounds. Such compounds may emit their molecules inside the breakdown point or even into gas space. The lack of region B and C for these compounds suggests that equation (1) for streamer initiation could be fulfilled even at a lower value of P so that the boundary pressure P_{ab} between A and B may be shifted to the side of lower P beyond its range investigated. Therefore, the streamer initiation condition becomes easily to be fulfilled inside the breakdown point in this case. There may exist these components also in gas space, ejected from the breakdown point. Then, the streamer propagation may be enhanced also in gas space.

7. Conclusions

From the results of flashover measurements under back discharge condition, following conclusions were obtained.

(1) There are three different regions in the mode change of back discharge. These regions are mainly determined by the mean free path of gas. Properties of back discharge were almost the same under various values of pressure or temperature investigated so far as the value of mean free path was the same. As described in section 3, back discharge takes streamer mode in region A, whereas in region C, steady-glow mode occurs. In region B, transition from streamer mode to steady-glow mode occurs.

(2) Flashover voltage under back discharge condition is also determined by the gas mean free path. There are two curves of flashover voltage. The lower one corresponds to the streamer mode (curve I), while the higher one to the steady-glow mode (curve II).

(3) If the layer thickness is very small, streamer mode cannot occur so that flashover voltage becomes high.

(4) If alkaline dusts are present, streamer causes flashover before the transition to the steady-glow mode occurs so that flashover voltage is largely reduced.

Acknowledgements

This research was sponsored by the Ministry of Education, Japan, as its Special Research Project (I) (Project No.011914). Prof. Y. Miyoshi is gratefully acknowledged for his helpful discussions about the mechanisms of back discharge mode. Thanks are also due to Mr. R. Shimoda for his help given to a part of the experiments.

Nomenclature

λ gas man free path

λ_o gas mean free path at NTP

T gas temperature

P gas pressure

Vs flashover voltage

α first Townsend coefficient

η electron attachment coeffecient

ρ_d apparent resistivity of dust layer

t layer thickness

References

1. S. Masuda and A. Mizuno, Initiation Condition and Mode of Back Discharge, J. of Electrostatics (to be published)

2. Q. Vuhuu and R.P Comsa, Influence of Gap Length on Wire-Plane Corona, IEEE Trans. PAS 88 p. 1462 (1969)

3. J.D. Cobine, Gaseous Conductors, p 213, Dover Edition, 1958

4. T. Takuma, Discharge Characteristics of Gases, Part 1, Central Reserch Institute of Electric Power Industry Technical Report No. 69015, (1969)

I	II	III
$KMnO_4$	$CaCO_3$	mica plate
K_2SO_4	Fe_2O_3	sulphur
$Sr(NO_3)_2$	Al_2O_3	SiO_2
$(NH_4)_2SO_4$	Cr_2O_3	
$NaNO_3$	MgO	
NaCl		

Table 1

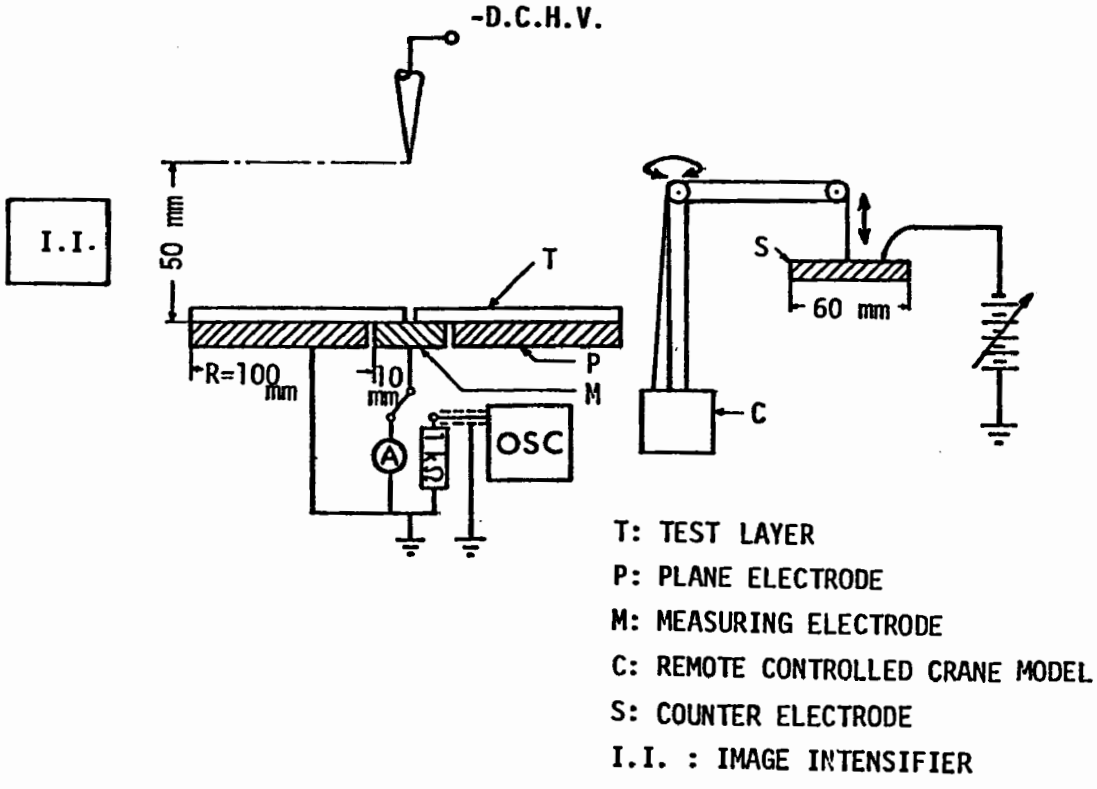
-D.C.H.V.
I.I.
50 mm
T
S
60 mm
R=100 mm
10 mm
P
M
C
OSC
T: TEST LAYER
P: PLANE ELECTRODE
M: MEASURING ELECTRODE
C: REMOTE CONTROLLED CRANE MODEL
S: COUNTER ELECTRODE
I.I. : IMAGE INTENSIFIER

Figure 1

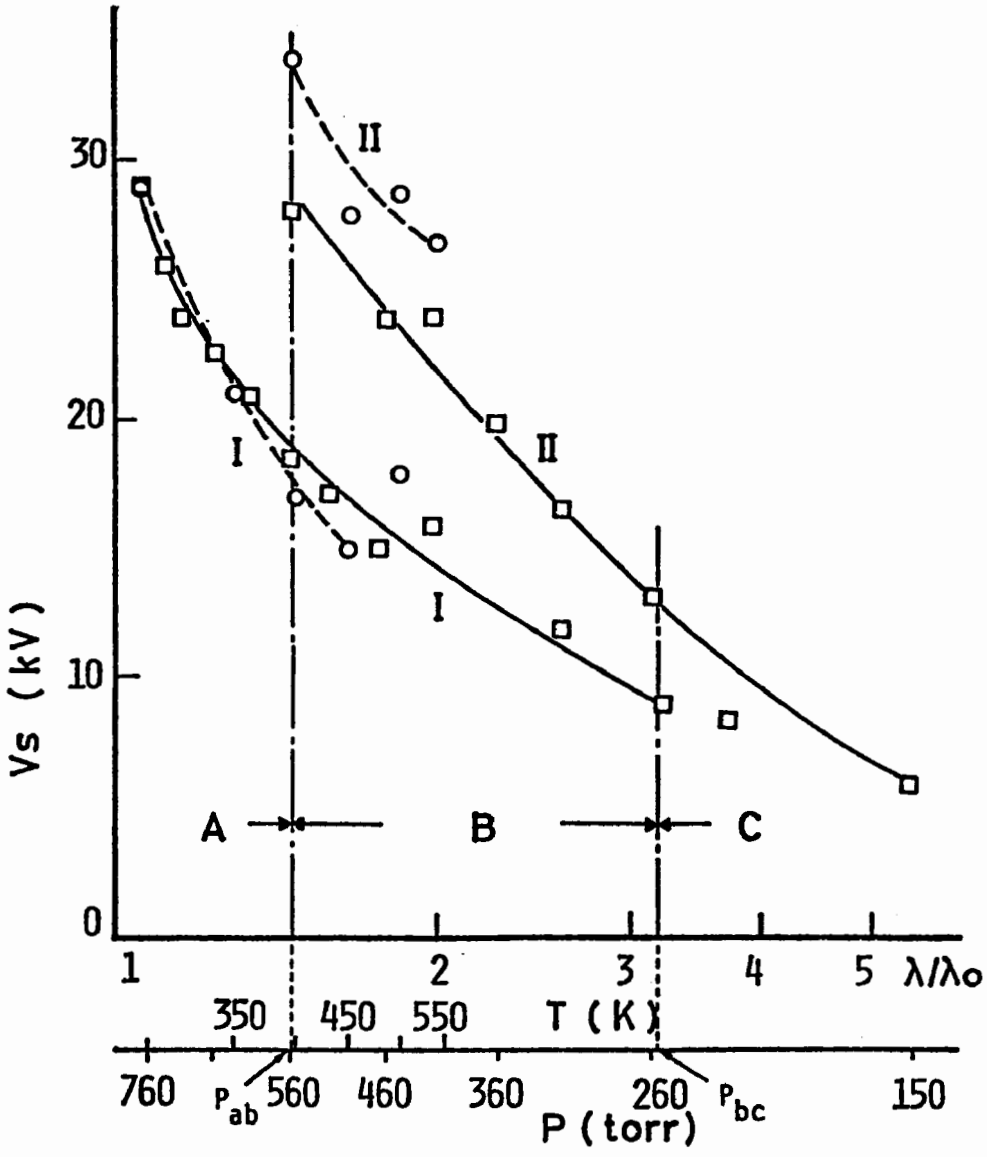
30
20
10
0
Vs (kV)
II
I
II
I
A
B
C
1
2
3
4
5
λ/λo
350
450
550
T (K)
760
P_{ab}
560
460
360
260
P_{bc}
150
P (torr)

Figure 2

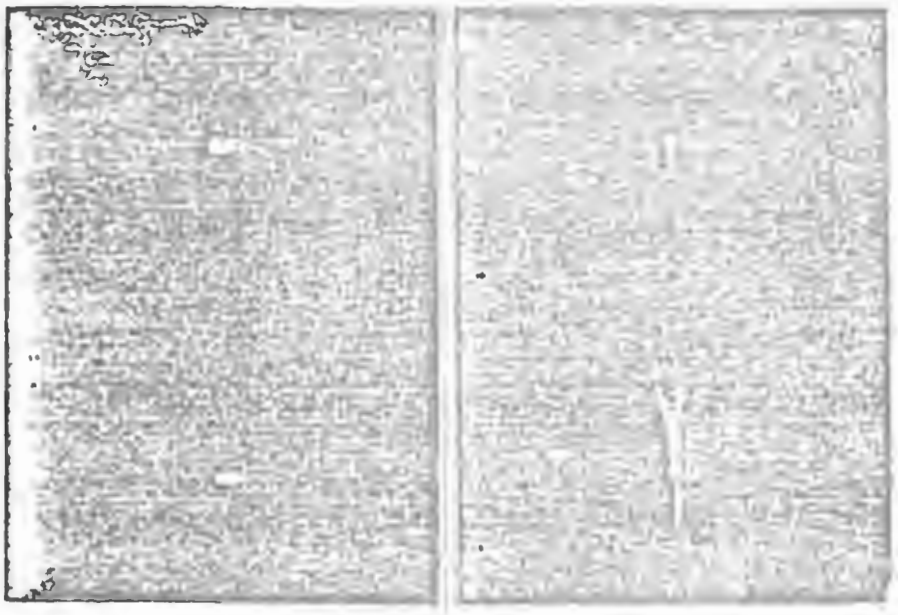

(a) ONSET-GLOW
V - 12 kV

(b) SP E R
(on curve I)

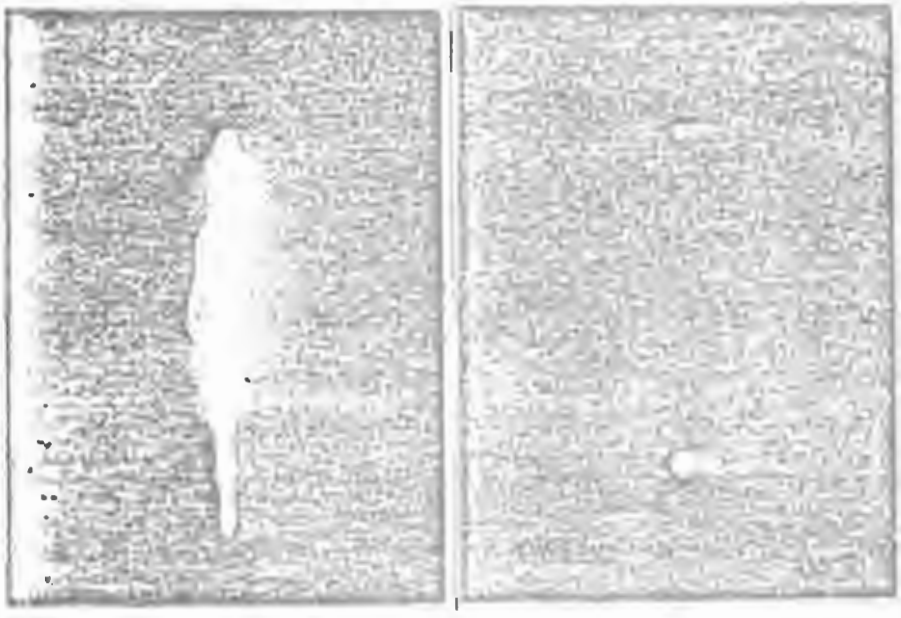

(c) RANDOM SPA I
V - 18 kV
(on curve I)

( ) STEADY-
(on curve I nd II)

Figure

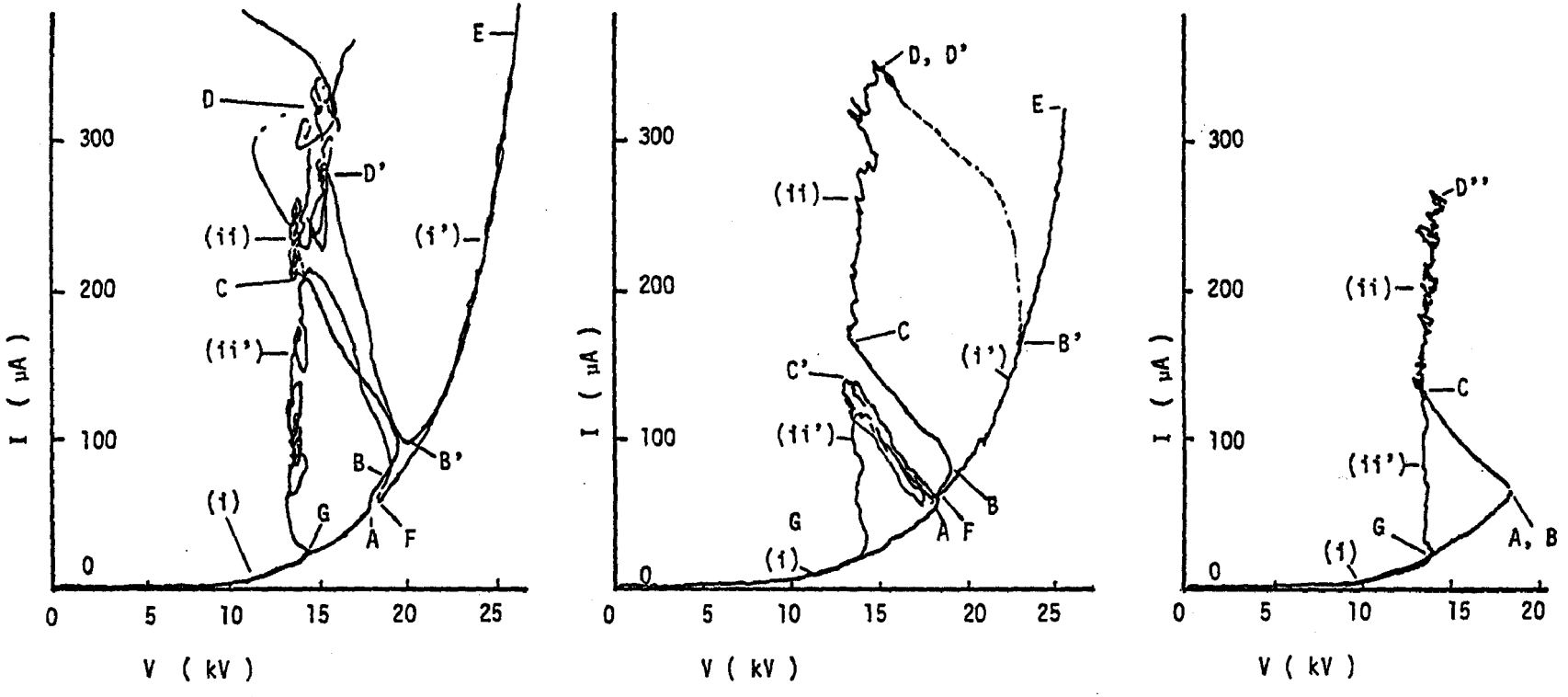
I (μA)
V (kV)
D
D'
E
(ii)
(i')
C
(ii')
B
B'
(i)
G
A
F
0
100
200
300
5
10
15
20
25
D, D'
C'
A, B
(a) R = 0
(b) R = 27 MΩ
(c) R = 55 MΩ

Figure 4

(a) Onset-Glow Mode

(V = 12 kV, I = 2.5 μA
20 μA/div., 20 μs/div.)

(b) Streamer Mode

(V = 14 kV,
2 mA/div., 20 μs/div.)

(c) Steady-Glow Mode

(V = 18 kV, I = 85 μA,
20 μA/div., 20 μs/div.)

Figure 5

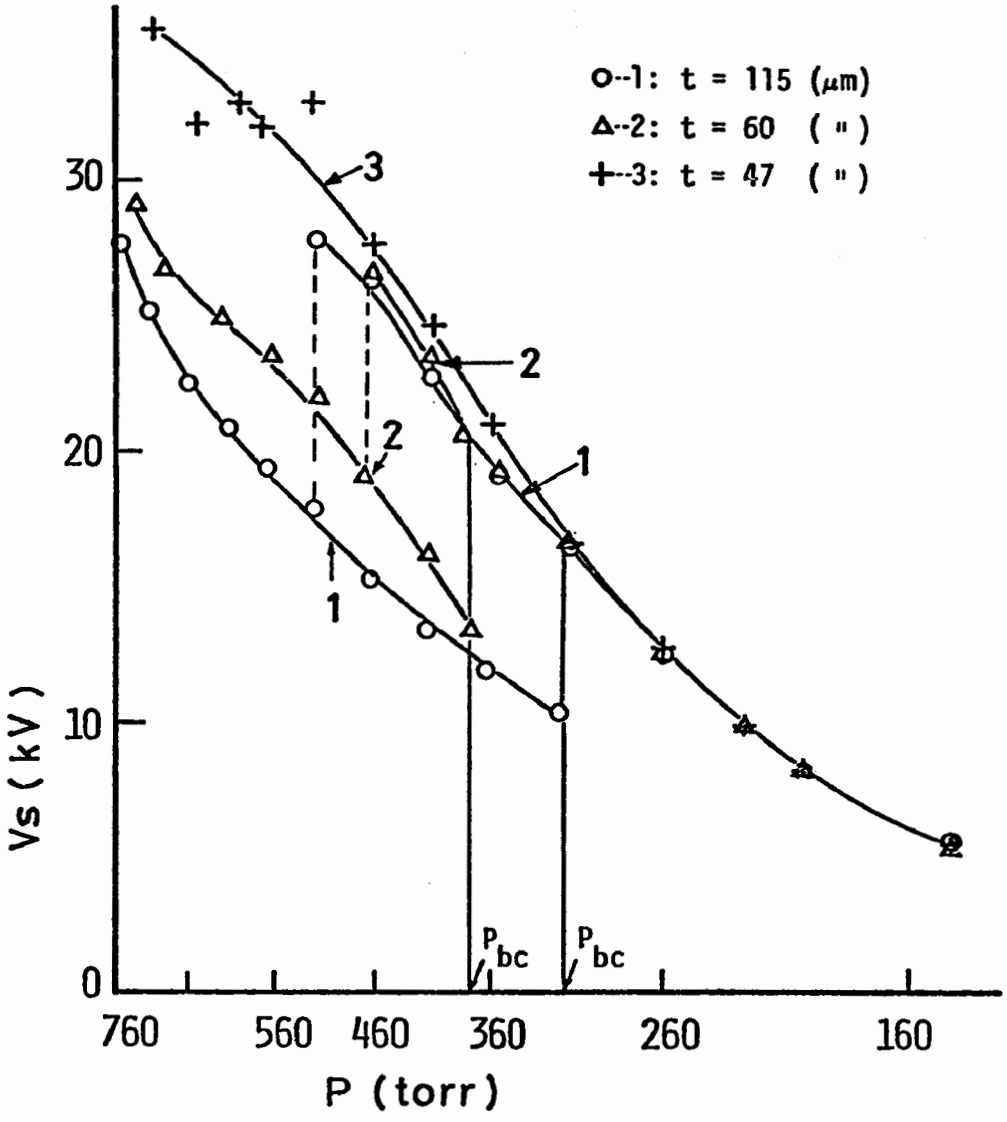
o--1: t = 115 (μm)
Δ--2: t = 60 (")
+--3: t = 47 (")
30
20
10
0
Vs (kV)
760
560
460
360
260
160
P (torr)
P bc
P bc
1
2
3

Figure 6

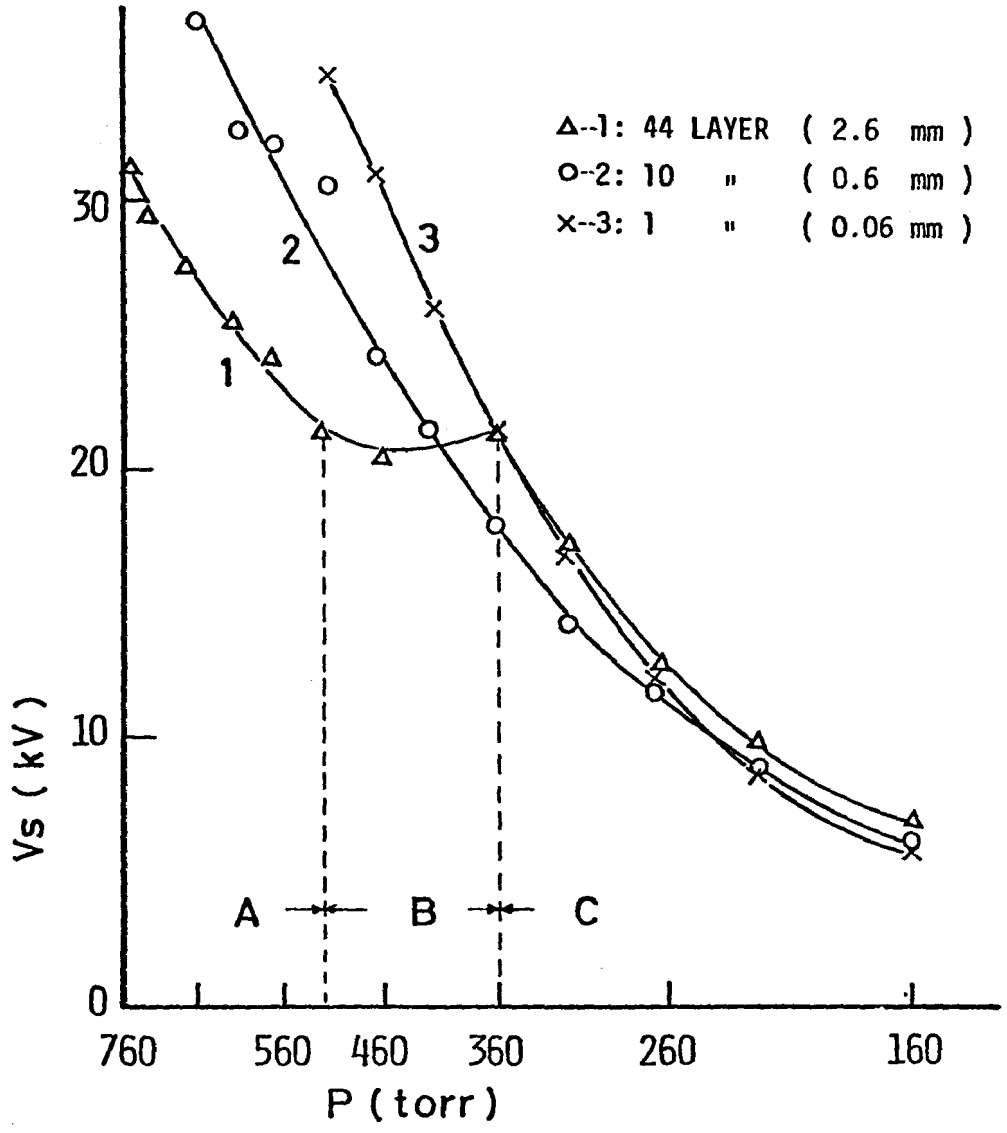
△--1: 44 LAYER (2.6 mm)
○--2: 10 " (0.6 mm)
×--3: 1 " (0.06 mm)
Vs (kV)
30
20
10
0
1
2
3
A
B
C
760
560
460
360
260
160
P (torr)

Figure 7

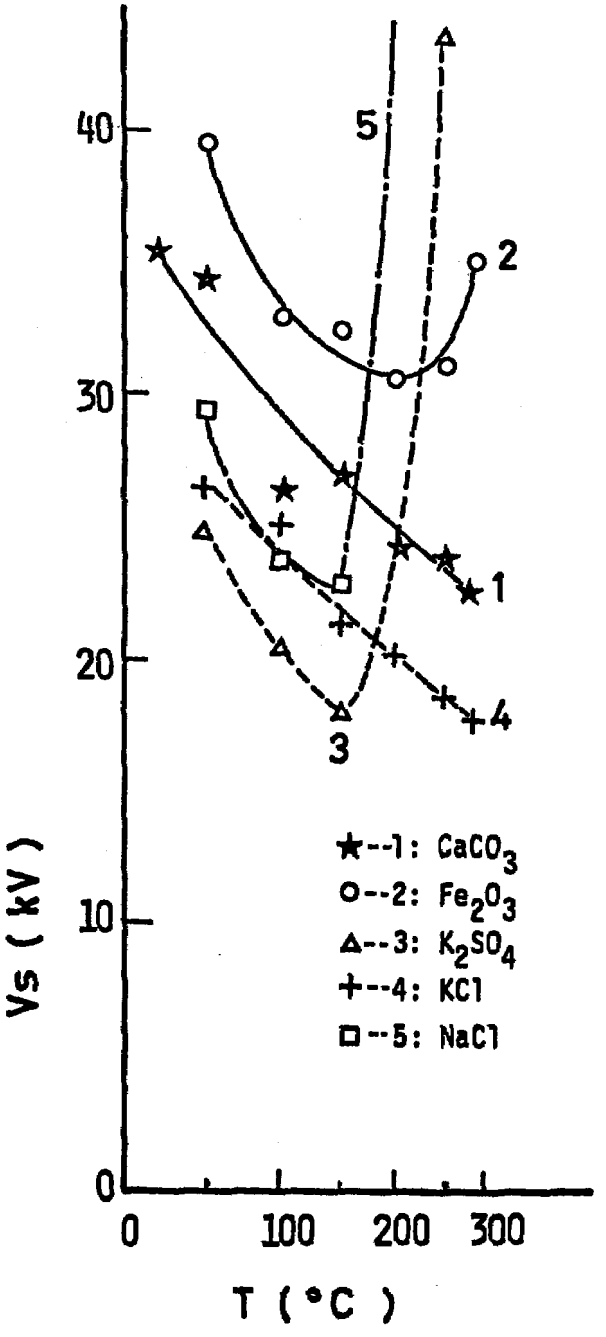
40
30
20
10
0
Vs (kV)
0
100
200
300
T (°C)
5
2
1
4
3
★--1: CaCO3
○--2: Fe2O3
△--3: K2SO4
+--4: KCl
□--5: NaCl

Figure 8

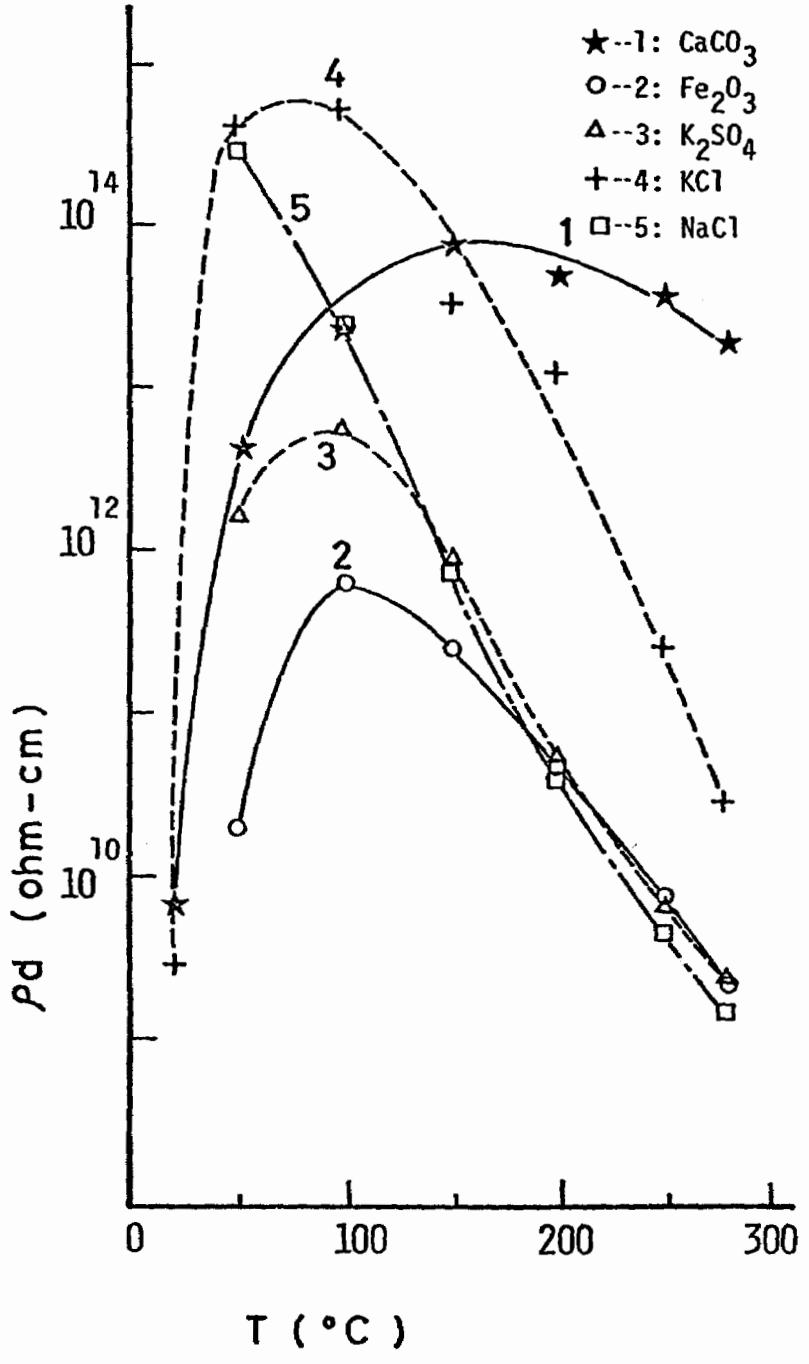
★--1: $CaCO_3$
○--2: Fe_2O_3
△--3: K_2SO_4
+--4: KCl
□--5: NaCl
10^{14}
10^{12}
10^{10}
ρd (ohm-cm)
0
100
200
300
T (°C)

Figure 9

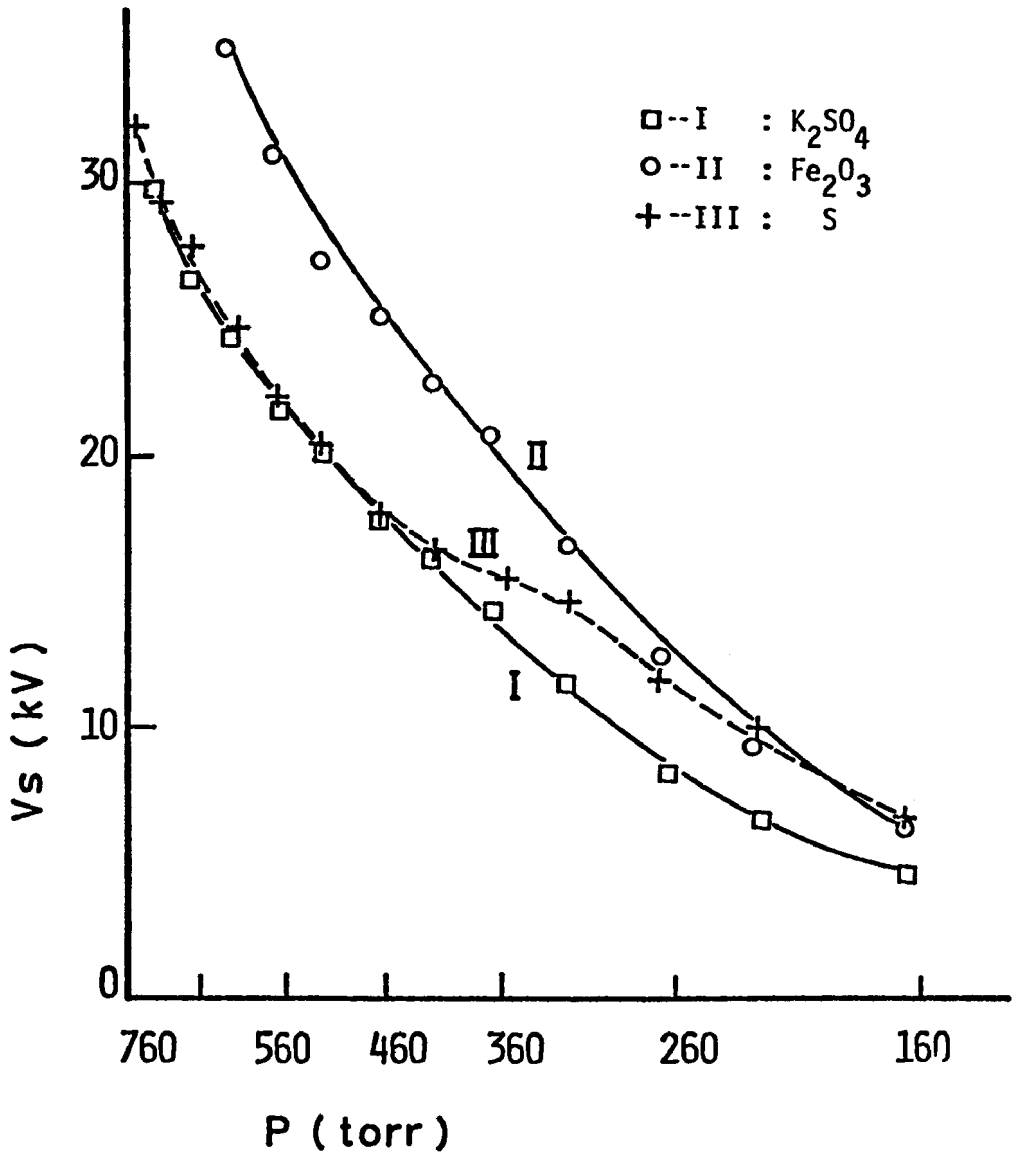
□--I : K_2SO_4
○--II : Fe_2O_3
+--III : S
30
20
10
0
Vs (kV)
760
560
460
360
260
160
P (torr)
I
II
III

Figure 10

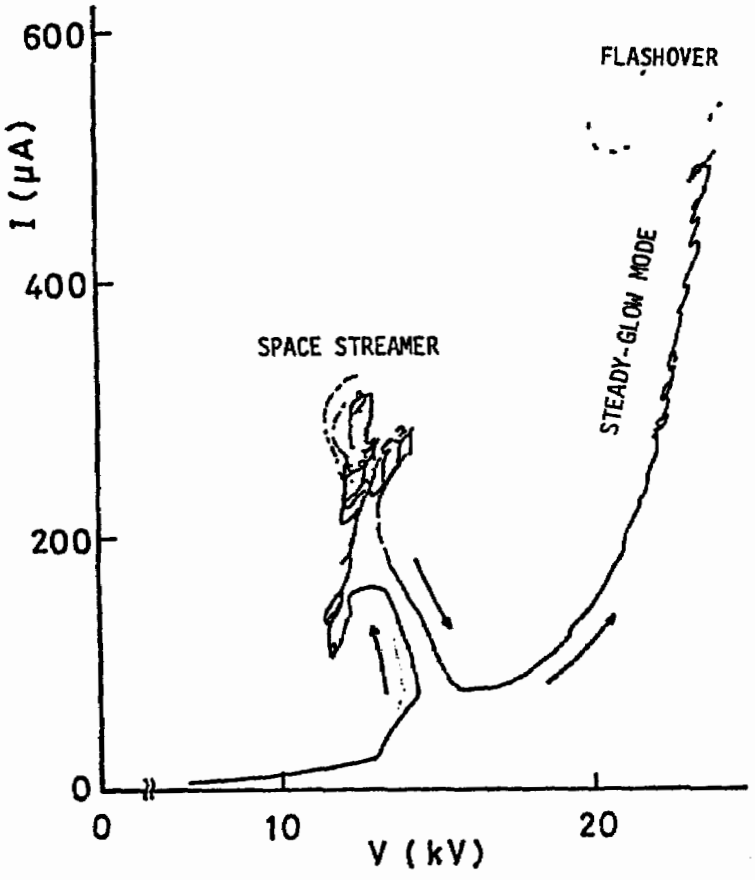

(a) Mica Plate with No Coating

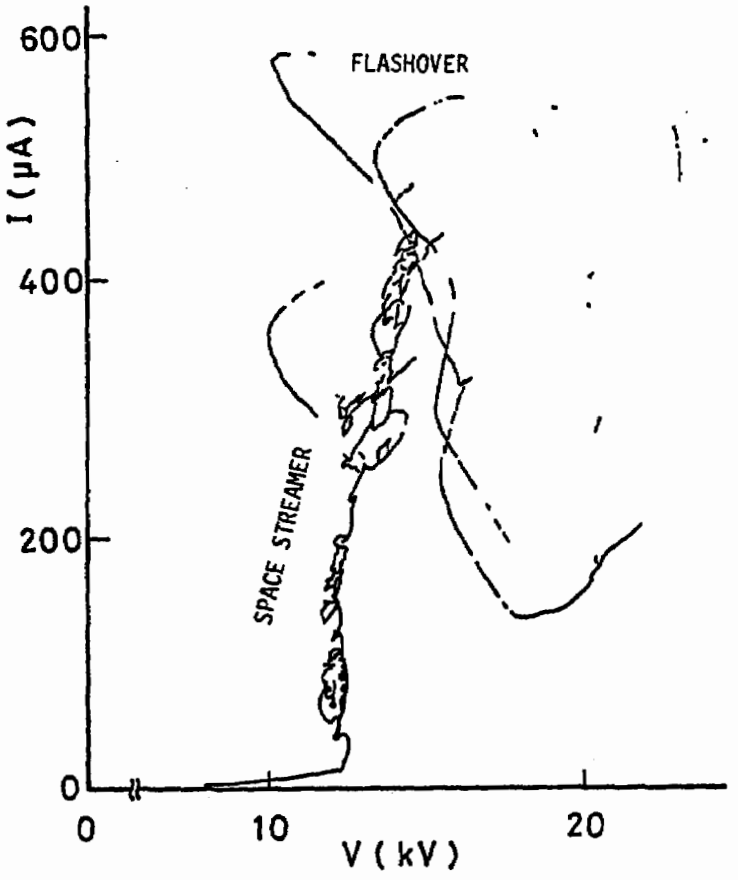

(b) Mica Plate with K_2SO_4 Coating

Figure 11

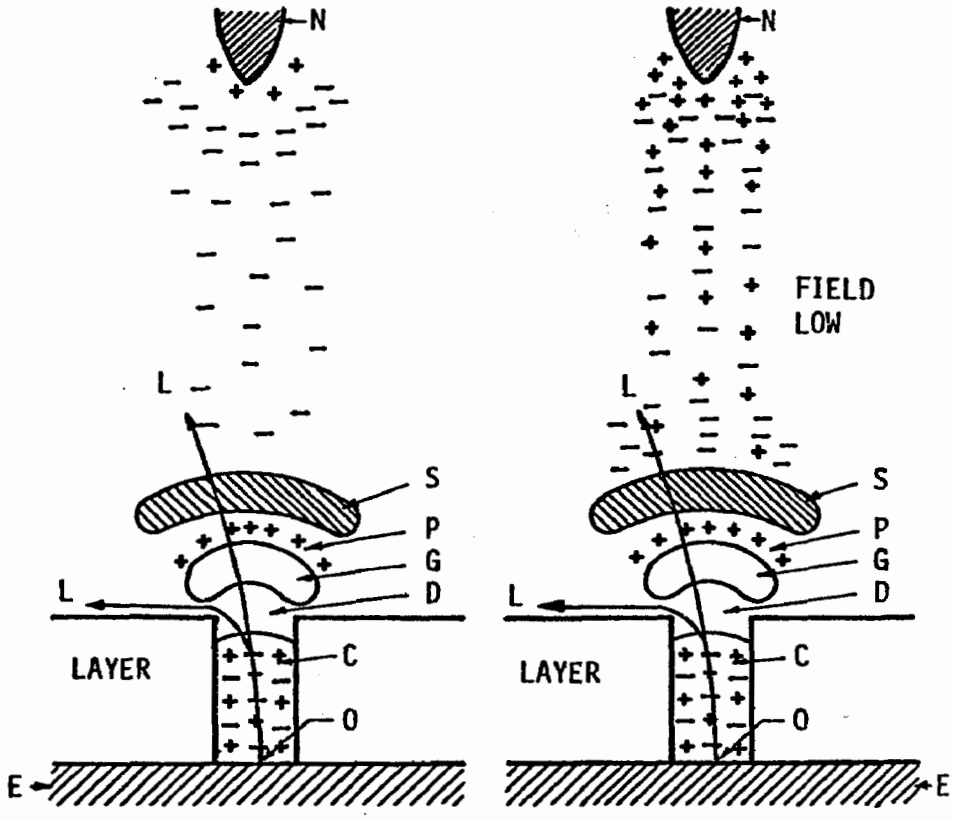

(a) ONSET-GLOW (Trichel Pulse)

(b) STEADY-GLOW

S: electron shedding zone

P: accumulate zone of positive ion

G: negative glow

D: dark space

C: positive column

N: needle electrode

E: plane electrode

Figure 12

Figure Caption

Table 1 CLASSIFICATION OF DUST

Fig.1 ELECTRODE SYSTEM FOR MEASURING FLASHOVER VOLTAGE OF BACK DISCHARGE

Fig.2 FLASHOVER VOLTAGE v.s. TEMPERATURE AND PRESSURE

Fig.3 TRANSITION OF BACK DISCHARGE MODE IN REGION B (T = 450 K, mica plate with a pinhole)

Fig.4 VOLTAGE-CURRENT CHARACTERISTICS WITH DIFFERENT OUTPUT IMPEDANCE

Fig.5 CURRENT WAVE FORM OF BACK DISCHARGE IN REGION B (P = 360 torr, mica plate with a pinhole)

Fig.6 EFFECT OF LAYER THICKNESS ON P- Vs CHARACTERISTICS (mica plate with a pinhole)

Fig.7 EFFECT OF LAYER THICKNESS ON P-Vs CHARACTERISTICS (tissue paper)

Fig.8 EFFECT OF TEMPERATURE ON FLASHOVER VOLTAGE (atmospheric pressure)

Fig.9 APPARENT DUST RESISTIVITY v.s. TEMPERATURE

Fig.10 EFFECT OF ALKALINE COMPOUND ON FLASHOVER VOLTAGE (T = 20 °C)

Fig.11 VOLTAGE-CURRENT CURVES WITH AND WITHOUT K_2SO_4 FILM ON THE SURFACE OF MICA PLATE WITH A PINHOLE (thickness: 0.2 mm, P = 360 torr, T = 20 °C)

Fig.12 SCHEMATIC REPRESENTATION OF BACK DISCHARGE IN THE GLOW MODES

Proc. 4th Int. Clean Air Congress
Paper No. V-47 (May 1977, Tokyo)

BASIC STUDIES ON BACK DISCHARGE MODE AND STREAMER PROPAGATION

Etudes fondamentales sur le mode de déversement inversé et la propagation en courant

[illegible] S and MIZUNO A.
Faculty of Engineering, Tokyo University
Tokyo, Japan

INTRODUCTION

[illegible] of the [illegible] in electrostatic precipitation. This is an abnormal discharge caused by breakdown of high resistivity dust layer deposited on collecting electrode. The mode and effect of back discharge differ largely, depending upon the polarity of corona discharge used. In this paper, however, we restrict [illegible] negative [illegible] [illegible] under normal operating conditions. If back discharge [illegible] [illegible] falls to about half the value of that under [illegible] [illegible] neutralized. When the field strength inside the dust layer exceeds its breakdown value, the initiation of back discharge [illegible] [illegible] point. With the further increase in voltage, this [illegible] either trigger the streamer [illegible] along the layer surface [illegible] like glow [illegible] latter [illegible] which [illegible] pletely [illegible] Under [illegible] [illegible]

I. BACK DISCHARGE IN THE STREAMER MODE

[illegible] and mixed streamer mode [illegible] two is shown in Fig. [illegible] essential factors [illegible] is the [illegible]

around the breakdown point as well as corona current density J. Ea and J, however, are closely coupled to each other. Thus, the effect of Ea and J must be studied separately by using a grid electrode inserted between a needle to plane electrode system. By the change of needle electrode voltage and grid electrode voltage, J and Ea can be varied independently. The electrode gap is 50mm and the distance between grid and plane electrode 20mm. A pair of glass plates each having a pinhole are used on top of [illegible] as the layer located on the plane electrode. The resistivity of the glass plate used is 6 x 10^{11} [illegible] and the diameter of the pinhole is 0.[illegible] mm, the thickness of one [illegible]. The breakdown field strength [illegible] of the [illegible] can be changed by changing the distance of the [illegible]

From the observation of back discharge mode with the [illegible]

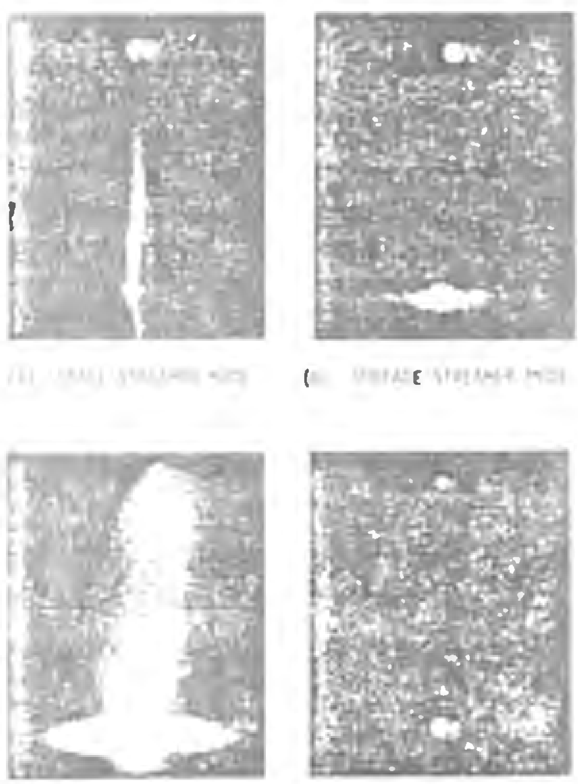

(a) [illegible] STREAMER MODE (b) [illegible] STREAMER MODE
(c) [illegible] MODE (d) [illegible] MODE

Fig. 1. [illegible] of back discharge in different modes

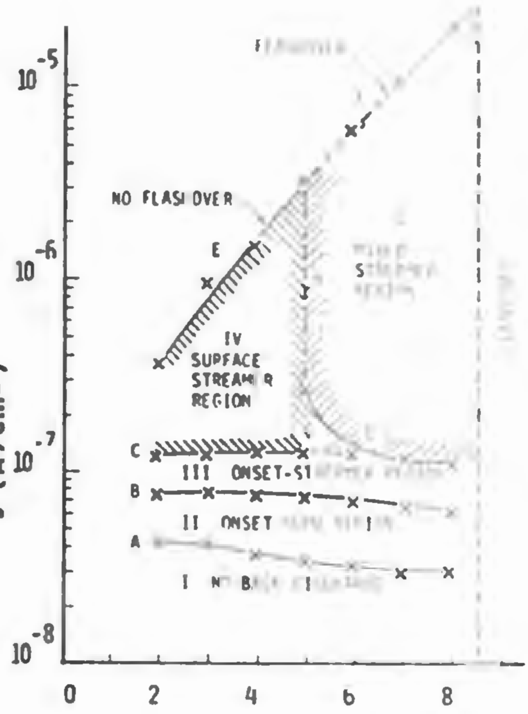

Fig. 2 Mode diagram of back [illegible]

aid of on image intensifier tube and curren[illegible] the mode diagram of back discharge [illegible] depi[illegible] domain as shown in Fig. 2, where Ed[illegible] = 20 [illegible] kV/cm. With the increase in current, the layer bre[illegible], Eds < ρd x J, is fulfilled on curve A, and onset [illegible] occurs in region II. The further incre[illegible] in current [illegible] in the streamers occurring around the upper [illegible] pinhole in region III. It should be noted that the [illegible] current densities for the transition between re[illegible] I, II and III are nearly constant respectively, [illegible] flat curves A and B. With the [illegible] beyond the other critical curves [illegible] in the streamer mode takes place in region IV [illegible] region IV, for lower value of [illegible] region where the surface streamer [illegible] n[illegible] and space streamers [illegible] few [illegible] exceeds about 5 kV/cm, [illegible] streamer occur to form [illegible] the critical current density for [illegible] gion III to IV and V is nearly c[illegible] area G. The critical value of the [illegible] region IV and V (curve H) is about [illegible] pheric condition. This value has [illegible] value for the occurrence of streamers.

The tangential field around the [illegible] become a function of the surface charge density [illegible] layer at the instant of breakdown. The value of σ, in turn, is given by ϵEds where ϵ is the [illegible] Eds the breakdown field strength of the layer. Fig. 1-a shows the pictures of back discharge [illegible] kV/cm, while Fig. 1-c is for Eds = 33 [illegible] kV/cm. [illegible] streamer becomes especially dominant [illegible] σ_0 exceeds about 5 x 10[illegible] C/cm²

Charging efficiency in [illegible] IV and V are measured and it is confirmed that the positive ion source is considered to be [illegible] the surface streamer region, but [illegible] in the [illegible] mixed streamer region.

In an actual precipitator, [illegible] Et [illegible] and J, are closely coupled to each other, depending upon the dust resistivity ρd. The effect of ρd is studied by using [illegible] in which ρd can easily [illegible] by changing the [illegible] about 5 x 10^{10} and 0.9 x 10^{11} Ωcm, number of breakdown points is less and streamers pr[illegible] into gas space. In this range of ρd, [illegible] the streamer starting voltage [illegible] voltage V[illegible]. For ρd higher than 10^{11} Ωcm, the back discharge streampers start to [illegible] er voltage and current density. In this [illegible] large interval between V[illegible] and V[illegible] [illegible] disappears but [illegible] in[illegible] dominant. There are more breakdown [illegible] with a general glow surrounding each point.

II. PROPAGATION OF STREAMER

Propagation [illegible] is measured by using photomultiplier tube [illegible] the propagation of light emission [illegible] the normal direction [illegible] space), and in the tangential direction (layer surface), respectively. The light signal [illegible] that the back discharge streamer [illegible] about [illegible] n[illegible]

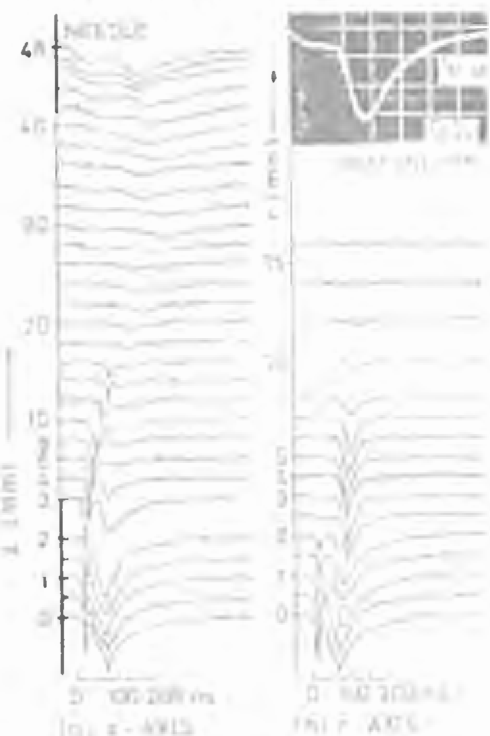

Fig. 3 [illegible]

slowly and lasts about 200 ns. The former proceeds in the z direction and the latter in the r direction. The primary wave corresponds to the first rise in the current wave and the secondary wave to the second rise in current which has a much larger pulse height and a charge of $2-4 \times 10^{-8}$ C/pulse. The value of charge per pulse remains nearly constant until just before flashover takes place, while the period of each succesive pulse decreased with the increase in current.

III. MODE TRANSITION OF BACK DISCHARGE[3]

The effects of mean free path on the flashover voltage and mode of back discharge are studied. A mica plate having a pinhole of 0.5mm in diameter and 0.45mm thickness is used as a layer. The flashoever voltage Vs is plotted against the normalized mean free path as shown in Fig. 4, where λo is the mean free path at NTP. The solid curves represent the results obtained by changing P under room temperature while the dotted curves indicate those obtained by changing T under atmospheric pressure. The scales for these P and T are also given. It can be seen that the curves measured by changing T or P agree well with each other. It should be noted that there exist two different curves for flashover (curve I and II), each covering the different range of $\lambda/\lambda o$. In the area under the curve I, the onset-glow mode is followed by the streamer mode with the increase in voltage, while the steady-glow mode occurs in the area under the curve II. As a result there are three different regions of $\lambda/\lambda o$, A, B and C as indicated in the figure, each corresponding to different mode changes. In region A, back discharge in the streamer mode follows the onset-glow mode and turns to flashover on curve I. In region C, back discharge in the steady-glow mode follows the onset-glow mode and no streamer appears until flashover takes place on curve II. Region B is a transition region between A and C. The onset-glow mode appears at first at the pinhole. With the increase in applied voltage, it turns into streamer mode, bridges across the gap and finally turns to random sparking on the curve I. Slightly above the curve I, streamers studdenly disappers to turn to a stable steadyglow mode (Fig. 1-d). This lasts until flashover occurs on curve II. The current wave form in region B at the onset-glow consists of Trichel pulses superimposed to a small D.C. current component, and with the increase in voltage, random pulses having much larger pulse height appears corresponding to space streamers. Finally pulseless D.C. current appears with the transition from streamer to steady-glow mode, no Trichel pulse being observed in this mode.

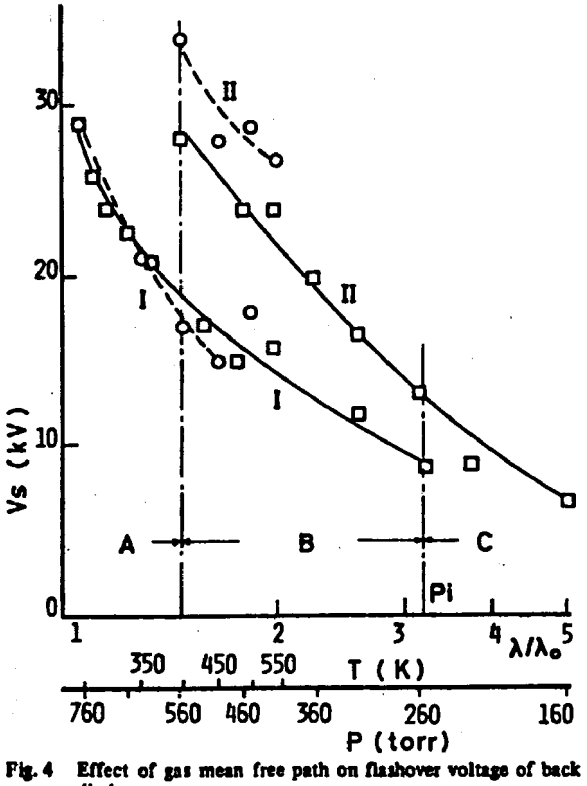

Fig. 4 Effect of gas mean free path on flashover voltage of back discharge

It is observed that no streamer occurs when the thickness of the layer, t, is 47μm even under P = 760 toor. The boundary pressure Pi between regions B and C shifts towards the side of smaller $\lambda/\lambda o$ when t decreases, and the value of Pi x t lines in the range between 18.6 and 35.7 torr-mm. It also is observed that, when the dust layer contains alkaline compounds having low ionisation potential, the region A covers the whole $\lambda/\lambda o$ range investigated, so that Vs becomes lower and is given only by the curve I in Fig. 4. Namely, the existence of alkaline compounds shifts the boundary pressure between regions A and B towards the lower pressure side.

REFERENCES

1) Masuda, S. & Mizuno A., "Initiation condition and mode of back discharge," *J. of Electrostatics* (to be published).
2) Masuda, S., Recent Progress in Electrostatic Precipitation, Static Electrification 1975, Institute of Physics Conference Series, No. 27 p. 154.
3) Masuda, S. & Mizuno A., "Flashover measurements of back discharge," *J. of Electrostatics* (to be published).

Senichi Masuda (Tokyo University). The Present Status of Electrostatic Precipitator Technology. Presented at the Electrotechnical Colloquium of the Technical University of Munich, May 4, 1977.

1. Introduction

The control of atmospheric pollution has become one of the most important social goals of today, with the effective removal of very fine particles (< 3 μm) from waste gases being especially emphasized. These fine particles are present in smoke emissions and are the nuclei for the formation of fog and clouds. Because of their high specific surface, they act as carriers of harmful gases into the depths of the lungs, and so they are harmful to health. For this reason, the electrostatic precipitator, which was born at the beginning of this century, has been given an important task today. Although the principle and the construction of an electrostatic precipitator are very simple, its practical use is often very complicated, because of many interfering effects that can be avoided only with difficulty. As a result, electrostatic precipitator technology has for a long time been considered an art. However, this situation is today slowly experiencing a change as the result of intensive research and development.

2. Principle and Construction in General

The principle and construction of an electrostatic precipitator can be explained by reference to the tubular design in Fig. 1. It consists of a grounded tubular electrode (collecting electrode) and insulated wire electrode (discharge electrode), between which a high potential is applied. On the discharge electrode there appears a corona discharge, which supplies a unipolar ion current to the inner wall of the tube. The suspended particles, along with the exhaust gas, enter the tube from below and pass up through the tube, in which they are strongly charged with a unipolar charge by ion impact. They are then driven by the coulombic force to the inner surface of the tube and deposited there, where they form a dust layer. This layer is dislodged by mechanical rapping of the tube and falls into a hopper below. The cleaned gas is led out the upper end to the stack.

In practical application, instead of the tubular type, the so-called plate precipitator is mostly used. It is equipped with parallel plate collection electrodes. The plate design has a simpler structure, in which uniform gas distribution is more easily achieved, especially with larger gas volumes. The corona in industrial precipitators is usually negative, since its sparking voltage is higher than for a positive corona. In air cleaning,

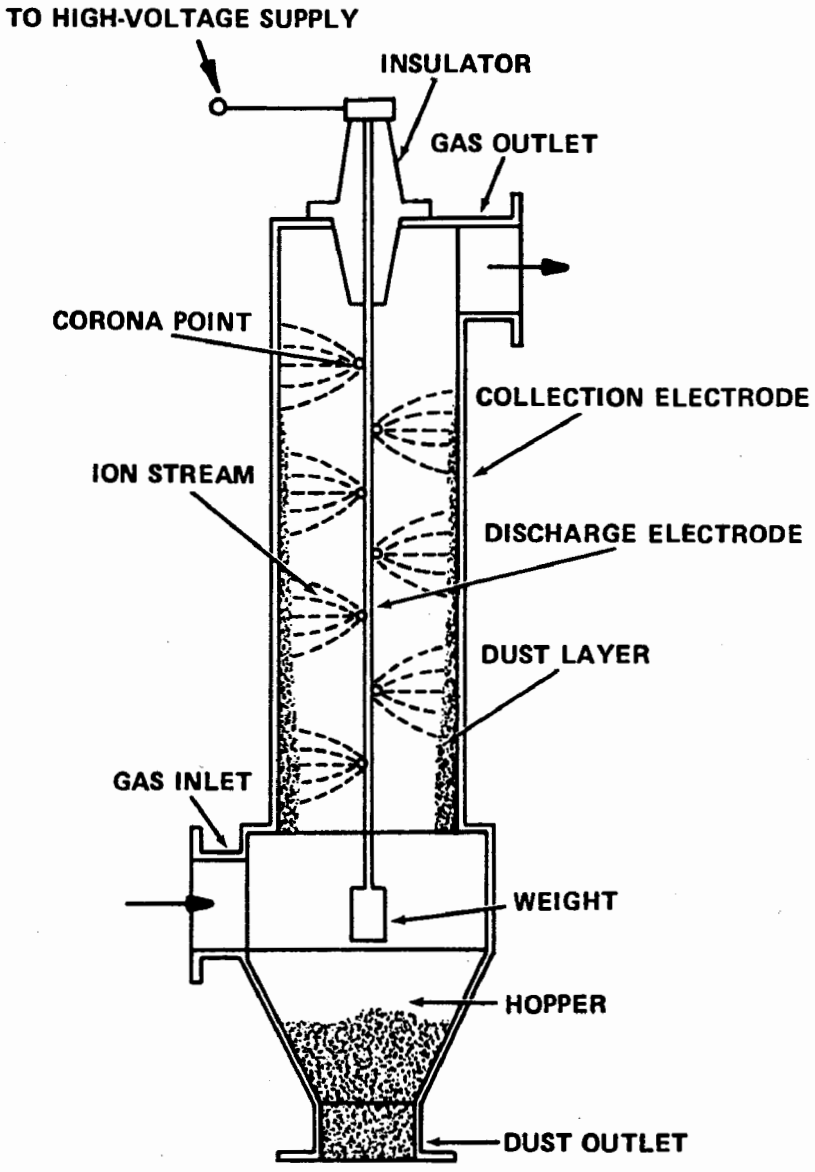

Figure 1. Principle of electrostatic precipitator (tube type).

a positive corona with appreciably less ozone production is used, because of the harmful effects on health of ozone. In this application, a two-stage construction with separate charging and collection zones is mostly used (Fig. 2).

In order to achieve the highest collection capacity, the precipitator must be operated with the highest voltage possible; the operation is also, however, determined by the continuous fluctuation of the sparking voltage with changes in the operating conditions. This requires two functions of the high voltage supply. One is the suppression of transition from sparking to arcing and the rapid rebuilding of the normal operating voltage, which is achieved with the aid of a thyrister circuit. The other is the automatic monitoring of the optimum operating voltage. Hence the spark rate is measured, for example, and the voltage is so regulated that this rate is kept at a preselected value. Also the power supply must have a static voltage-current characteristic, which guarantees stable operation of the precipitator.

3. Collection Process

3.1 Equations of motion of charged particles

The collection process in an electrostatic precipitator is based on the following expression for the motion of the charged particles in the electrical and fluid-dynamic fields (electrohydrodynamic or EHD fields):

$$m(d^2R/dt^2) + 6\pi\eta a(dR/dt) = qE + 6\pi\eta aV \qquad (1)$$

where m = particle mass, kg

a = particle radius, m

q = particle charge, coul

μ = gas viscosity, Nsec/m^2

E = field strength vector, V/m

V = gas velocity vector, m/s

R = position vector of particle, m

For extremely small particles with $a < 1$ μm, the viscosity η must be divided by the Cunningham correction factor $(1 + A\lambda/a)$ in consideration of the ion slip effect, where λ = free path of the ion and A = constant. For atmospheric air, $A = 0.866$ and $\lambda = 0.1$ μm [1]. Eq. 1 shows that the particle motion in the electrostatic precipitator is strongly influenced by the coulombic force and by the viscous drag force of the gas flow $6\pi\eta aV$, in which,

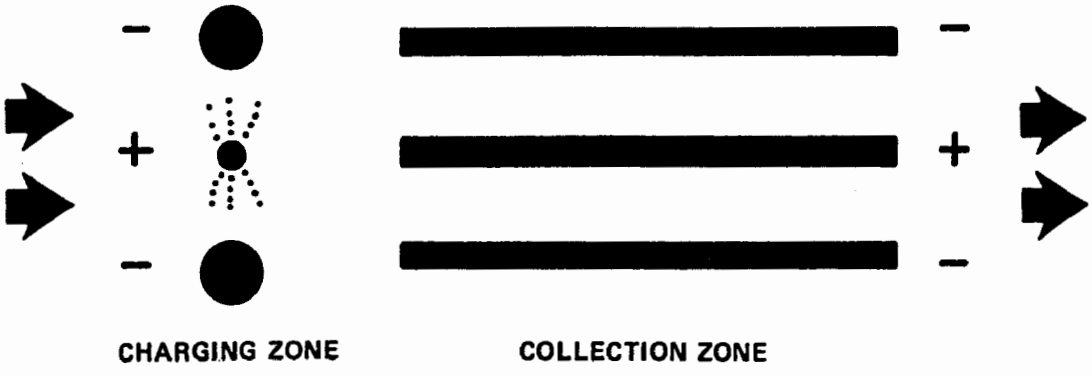

Figure 2. Two-stage construction.

as will be explained later, the corona wind plays a large role [2]. The saturation charge, which the particle reaches in the corona field, is proportional to a^2. The relation of the coulombic force to the fluid dynamic force is:

$$K_o = q\,E/\,6\pi\eta a\,V = [12\pi\varepsilon_s\varepsilon_o E\,a^2/(\varepsilon_s + 2)]/6\pi\eta\,V\,a$$

$$= [2\,\varepsilon_o\varepsilon_s E/(\varepsilon_s+2)\eta V]\,a \qquad (2)$$

Therefore, this relation is proportional to a. This means that the coulombic force will predominate for the larger particles with $a \geq$ several tenths of μm. Then the particle velocity may be calculated with the resulting "theoretical migration velocity" =

$$W_{th} = qE/6\pi\eta a \quad m/sec \qquad (3)$$

For the smaller particles with $a \leq$ several μm, on the other hand, the fluid-dynamic force $6\pi\eta a$ plays the decisive role in the collection process. Thereby the result is that the particle path in the electrostatic precipitator must in general always take place with consideration of these two forces, i.e., from the EHD point of view.

In the following, the magnitude of each factor in Eq. 1 is considered more closely.

3.2 Corona field strength

The electric field in an electrostatic precipitator is encumbered by the strong space charge of ions and charged aerosol particles, so its analytical calculation generally is achieved only with difficulty. An exception is the concentric cylinder such as in Fig. 1. For it the field strength was represented by Pauthenier and Moreau-Hanot [3] by the following approximation:

$$E(r) = \left[\frac{I}{2\pi\varepsilon_o\mu}\left(1 + \frac{2\varepsilon_s}{\varepsilon_s+2}\,S_r\right) + \left(\frac{E_o r_o}{r}\right)^2\right]^{1/2} \quad V/m \qquad (4)$$

where I = ion current per unit length of wire, A/m

ε_o = permittivity of a vacuum = 8.842×10^{-12} F/m

μ = ion mobility, m^2/Vsec

ε_s = specific dielectric constant of the particle material

S = total surface of the aerosol particles in unit gas volume, m^{-1}

r_0 = wire radius, m

E_0 = breakdown field strength of the gas at the wire surface, V/m.

For plate precipitators one can obtain a rough estimate of the voltage-current characteristic from Eq. 1.

In this equation the effect of particle space charge is represented by the value of S, which is determined by both the particle concentration and the particle size. The higher both these values are, the more significant the particle space charge effect. As a result, the field strength increases near the inner wall of the tube, while it decreases at the wire surface. The former effect gives rise to sparking, so the sparking voltage is sharply reduced several fold. The latter effect leads to a reduction of the corona current, which again with an increase in the particle charging time decreases the effective value of the achievable particle charge with limited residence time. This effect is called the "corona quenching effect". Both the effects mentioned above can, therefore, generally lower the collection capability of the precipitator. It has, however, recently been shown that the increase in the field near the plate can accelerate the particle collection [4].

3.3 Particle charging

The magnitude of the particle charge plays the decisive role in the electrostatic precipitator, as it does in all other applications of electrostatic force. The particles are hit and charged in the corona field by the neighboring ions through their thermal motion. Thus a deficiency of ions occurs in this immediate neighborhood, so a continuous supply is required for further charging of the particles. Two separate mechanisms for ion transport operate. One is the field effect, in which the coulombic force drives the ions from the outer regions to the inner regions (Fig. 3 (a)). The other is the diffusion effect, in which the ions are transported, as the result of concentration differences, to the inner regions by their thermal movement (Fig. 3 (b)). The former mechanism is called "field charging" and the latter "diffusion charging". Under practical operating conditions for electrostatic precipitators, field charging is determinative for the larger particles with $a > 1$ µm, while for very small particles with $a < 0.1$ µm diffusion charging is decisive. The charge for particles with intermediate sizes is well approximated by the sum of both charges [5].

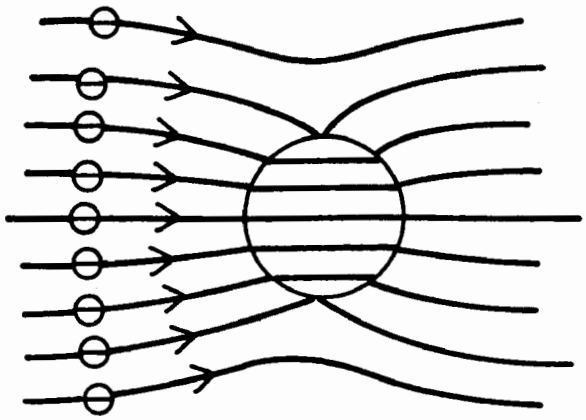

(a) FIELD CHARGING

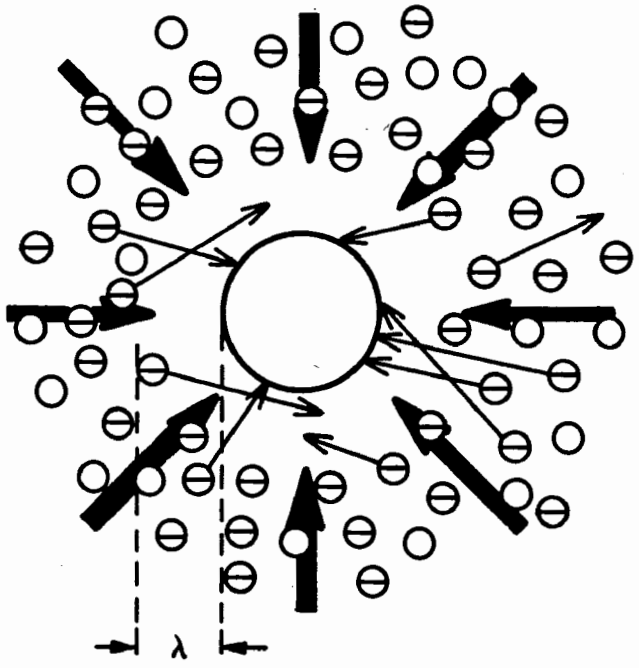

(b) DIFFUSION CHARGING

Figure 3. Charging mechanisms in corona field.

3.3.1 Field charging

The quantity of charge Q_f that is imparted to one particle in field charging is, according to Pauthenier [3]:

$$Q_f = Q_\infty \, [t/(t + \tau)] \quad \text{coul} \tag{5}$$

in which

$$Q_\infty = 4\pi\varepsilon_0 \frac{3\varepsilon_s}{\varepsilon_s+2} a^2 E_c = \text{saturation charge, coul} \tag{6}$$

$$\tau = \frac{4\varepsilon_0}{\mu\rho i} = \frac{4\varepsilon_0 E_c}{i} = \text{charging time constant, sec} \tag{7}$$

where t = charging time, sec

E_c = charging field strength, V/m

ρ_i = ion space charge density, coul/m^3

i = ion current density, A/m^2

The particle charge increased with time t, finally reaching the saturation charge Q_∞ (Fig. 4(a)). This final condition is limited in that the increased potential of the charged particle repels all the field lines. After the charging time $t = 10\,\tau$ sec the particle charge Q_f reaches 91% of the saturation value, so one can assume as the charging time $T = 10\,\tau$ sec. According to Eq. 6, the saturation charge is proportional to the field strength E_c, while the charging time according to Eq. 7 is inversely proportional to the ion current i and independent of E_c. Hence under practical conditions, with a restricted residence time t, the magnitude of the particle charge Q_f depends not only on E_c, but also on the ion current density i. At $E_c = 3 \times 10^5$ V/m and $i = 2 \times 10^{-4}$ A/m^2 the value of the charging time constant $\tau = 0.053$ sec.

3.3.2 Diffusion charging

The quantity of charge Q_d by diffusion charging according to White [6] is:

$$Q_d = Q^* \ln(+ t/\tau^*) \quad \text{coul} \tag{8}$$

where $$Q^* = \frac{4\pi\varepsilon_0 akT}{e} = \text{specific charge, coul} \tag{9}$$

$$\tau^* = \frac{4\pi\varepsilon_0 kT}{aCN_0e^2} = \text{charging time constant, sec} \tag{10}$$

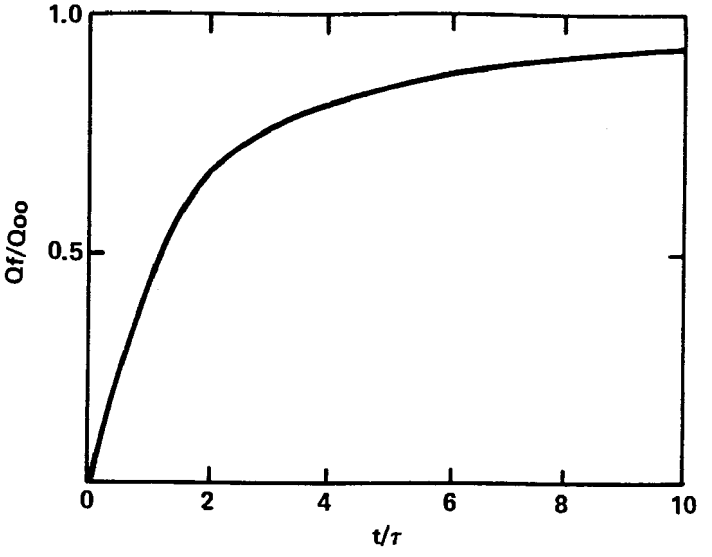

(a) FIELD CHARGING

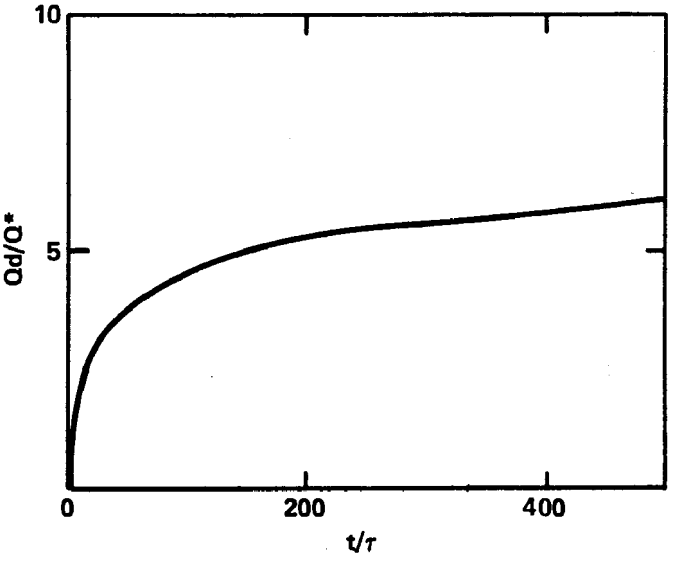

(b) DIFFUSION CHARGING

Figure 4. Increase of particle charge with time (normalized).

where k = Boltzmann constant = 1.38×10^{-23} J/K

T = absolute temperature, °K

e = elementary charge = 1.602×10^{-19} coul

C = r.m.s. value of thermal ion velocity = $(3kT/m)^{\frac{1}{2}}$ m/sec

m = ion mass, kg

N_o = no. of ions/m^3

$a \gg \lambda$ assumed

According to Eq. 8 the charge increases very rapidly at first, and reaches 6 Q* at time $t = 402\ \tau^*$. Then it increases appreciably slower, so in a practical sense it remains almost constant (Fig. 4(b)). Hence one can assume for diffusion charging 6 Q* as a quasi-saturation charge and $t = 402\ \tau^*$ as the charging time constant. Under typical application conditions of T = 150°C, $a = 0.1$ μm, $m = 5.3 \times 10^{-26}$ kg (for O_2^- ion) and $N_o = 5 \times 10^{13}$/m^3, one obtains, e.g., a charging time t = 1.13 sec. For yet smaller particles with a = 0.01 μm the charging time t is as large as 11.3 sec.

3.4 Migration velocity of particles and collection efficiency of precipitator.

From Eq. 3 and the above-mentioned saturation charge Q_∞ or 6 Q* one can evaluate the theoretical migration velocity. Curve A in Fig. 5 represents the change of this value W_{th} as a function of particle radius a, with the assumption of corona field strength $E = E_c = (1\text{-}5) \times 10^5$ V/m and the above-mentioned operating conditions. It is noticeable that W_{th} has a minimum value of ca 0.1 m/sec in the range of 0.1 - 1.0 μm radius. These statements have been verified both in laboratory trials as well as in practical installations [5,7]. The increase in the curve for the even smaller radius region is attributed to the effect of ion slippage. In practical installations the high migration velocities for very small particles are almost unobtainable because of the accompanying increase in charging time, since the residence time in the precipitator is usually restricted to 5 - 10 sec.

As was already mentioned, these W_{th} values represent only the electrical effect in the collection process, so they indicate in no way the basis of collection efficiency, on account of the numerous interferences that operate. Such interferences include primarily gas flow turbulence, which is greatly increased by the corona wind. They include the reentrainment of the deposited dust layer on the collecting electrode, which arises

especially on rapping of the electrodes, and reverse ionization, which represents the abnormal corona on the collecting electrodes and which occurs with very high resistivity dust. This strong gas turbulence produces a uniform distribution of the dust concentration on a plane perpendicular to the direction of the gas flow. From this consideration Deutsch derived the following formula for collection efficiency:

$$\text{Collection efficiency} = 1 - \exp(-wf) \tag{11}$$

where $F = S_a/G$ = specific collection area, sec/m

S_a = total surface of the collection electrode, m^2

G = gas flow, m^3/sec

w has the dimensions of velocity and is termed the "effective migration velocity" or "w value"

This formula has a very simple form and has proved useful in practical installations as an approximation applicable at least for the same type of dust and operating conditions. Therefore, it can be used for precipitator design when the w value is considered only as a measure of collection efficiency in operation.

This w value represents a design parameter that includes the effects of all the process factors, including dust properties and operating conditions, as well as type of gas. Curve B in Fig. 5 represents the mean value of w for many installations for removing fly ash as a function of the particle radius a [8]. The flattening of the curve in the large particle size range is surprising, and is explained by the tendency for reentrainment of the larger particles. There are so many influencing factors that determine the w value that they in no way allow the design variables to be based on theory. As the result, in the design of precipitators many examples are required, which are to be had only by the evaluation of collection efficiency in many practical installations. It must be emphasized, however, that such practical data from installations with similar w values sometimes differ, giving the precipitator design more or less of a statistical character [9]. Another puzzling w value is found with the so-called large-spacing type, which has an appreciably larger electrode separation distance [10]. It has been found that the collection efficiency at a constant gas volume remains almost constant, up to a certain limit, with increasing electrode separation distance. This means that with an increase in electrode separation the w value must increase proportionately. This effect was confirmed not only in dry precipitators, but also in wet precipitators, in which neither dust reentrainment nor reverse discharge occurs. The basis for this effect cannot be properly explained even considering the higher stability of the large-spacing precipitator, and further investigation is required.

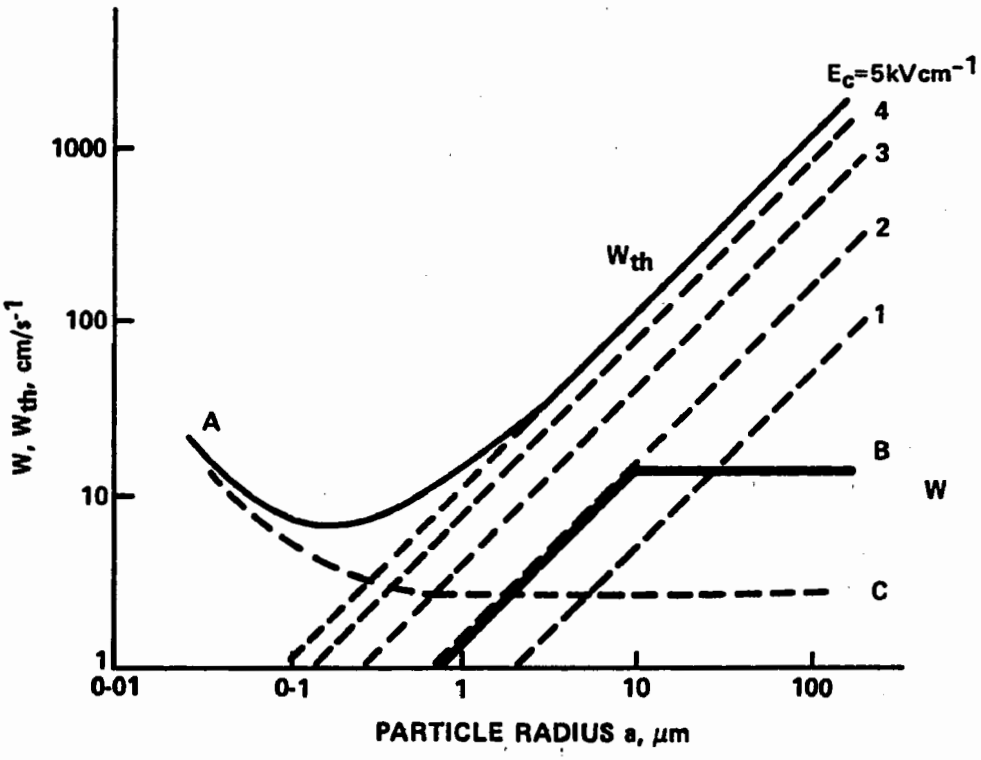

Figure 5. Theoretical and effective migration velocities as functions of particle radius a.

4. Distribution of Ion Current and Charging Efficiency

For the most rapid and uniform charging of the particle, not only the magnitude of the ion current density, but also its distribution, plays a decisive role. As is known, the negative corona on the wire electrode appears in the form of scattered corona points, from which the tufts of ion flow spread out in the direction of the collection electrodes. Between these streamers there are ion dead spaces, in which the charging time constant is large, because of limited current density, and the charging efficiency of the particles is sharply reduced. This effect was confirmed experimentally [11] and gave rise to a detailed study of current distribution. It was found [12] that the law of similarity applies to current distribution at the collection electrode. Figure 6 shows an example. It was further observed that when such a dead space is formed, dust reentrainment and reverse discharge can also be present; with the former a zero current region occurs; with the latter an increased current region. For resolving these dead space questions, "Hermstein corona" with positive corona, which is distributed uniformly over the wire electrode and which has an appreciably higher sparking voltage offers a possibility [12]. The conditions for this corona are that the field strength and its gradient near the corona electrode are sufficiently high. The former results in electron stripping from negative ions; the separated electrons spread out with a higher mobility over the electrode surface and there form an electron sheath suppressing the "streamers". The latter also retards the development of streamers. Thus, the formation of the Hermstein corona is accelerated by supplying a small number of negative ions to the positive electrode [13]. The Hermstein corona has been used to increase the particle charging efficiency, although interfering effects of moisture and dust load have been recognized [14]. Hence, its applicability under practical conditions is still an open question.

5. EHD Processes

There are two processes in an electrostatic precipitator that must be considered from the EHD point of view. One is the collection process itself, in which, as has already been explained, the interfering field of the corona wind plays a decisive role. The other is the corona wind, which is the result of momentum exchange between the electrically accelerated ions and the neutral molecules on impact. In principle this flow field can be determined by the Navier-Stokes equation, but as another force the coulombic force density, which acts as a motive force per unit gas volume is drawn in play

$$F = \rho_i E \ N/m \tag{12}$$

for which as an ancillary condition the continuity equation of the gas flow must be considered. The distribution of the ion

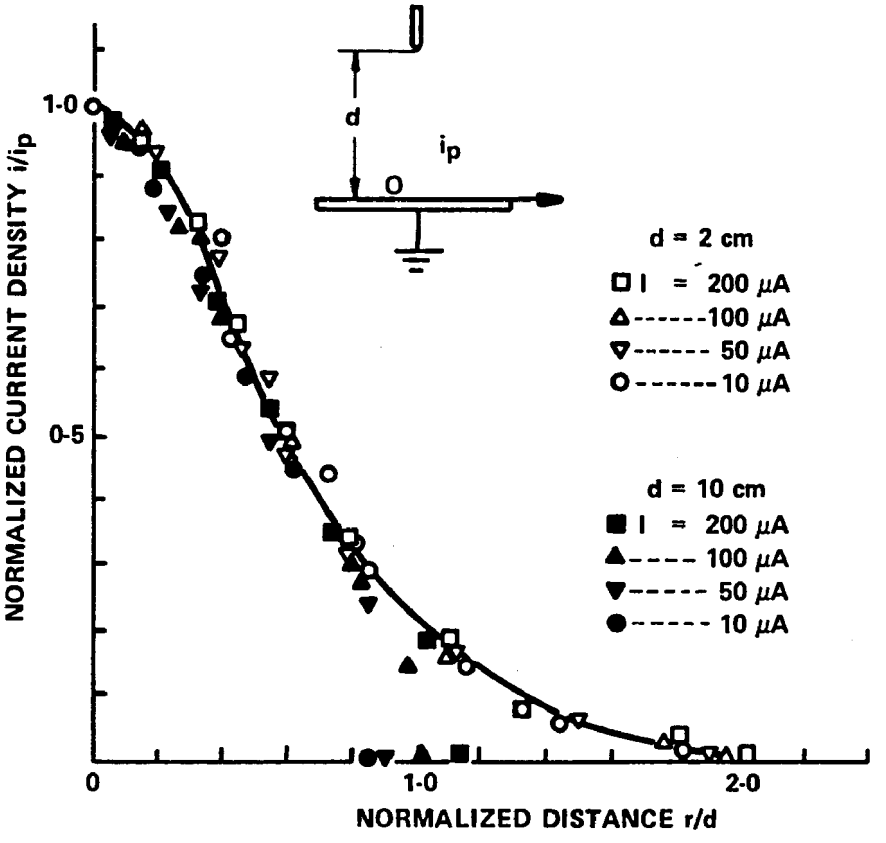

Figure 6. Normalized distribution of ion current density on plate electrode.

space charge density ρ_i can be calculated from the Poisson equation and the continuity equation of the ion flow. For the point-plane electrode this corona wind field can be determined analytically [16] but for complicated conditions its mathematical solution is still open.

On the other hand, many experimental studies of the corona wind have been made with the aid of laser-doppler velocity measurements and schlieren photography. Fig. 7(a) shows, e.g., a schlieren photograph of corona wind on which a horizontal gas flow has been superimposed [17]. The figure shows clearly the presence of a kind of jet stream with a higher velocity. Figs. 8 and 9 show the velocity components oriented perpendicular and parallel to the plate along the axis of the point-plane electrode without superimposition of another gas flow, which was measured with the use of a laser-doppler measurement instrument up to a very close distance to the surface (0.05 mm) [18]. In the main part of the corona field along the axis, there is a perpendicular velocity of as much as 6-7 m/sec. It is astonishing that this perpendicular component extremely near to the plate has as high a value of 4-5 m/sec. and that then its direction of flow changes suddenly by 90° and it flows along the plate with an equally high velocity. This remarkable effect can be attributed to the special character of the ion driving force which acts up to the surface of the plate. By diluting the boundary layer, this effect can also produce a significant increase in the gas/plate heat exchange (corona cooling). Fig. 10 shows the fluctuation of the perpendicular velocity component inside the boundary layer with superimposition of the corona wind and the gas flow parallel to the plate [18]. Outside the very near vicinity of the plate surface, the fluctuation of the velocity in the positive and negative directions is very large, although the average velocity is positive (in the direction of the surface). This means that in the main part of the boundary layer of ca 5 mm thickness, gas turbulence is present with a velocity of about 0.5 m/sec. As was already explained in Fig. 7(a), there predominates in the corona field a kind of jet stream with a significantly higher gas velocity than the theoretical particle migration velocity according to Eq. 3, also shown clearly in Fig. 8. Thus, most of the particles < 10 µm are first transported to the vicinity of the plate by this jet stream, where the gas stream must change its direction. There only the larger particles can be collected, those that with the aid of electrical and inertial forces can overcome the turbulence (Fig. 10) predominating in the boundary layer and finally reach the plate. The smaller particles, especially in the size range of 0.1 - 1.0 µm, are captured only with difficulty, except for the very small particles that reach the plate as the result of gas turbulence. The main part will flow along the plate with the parallel flow and again return to the main field. The velocity of this reverse flow is of course essentially less than that of the corona wind.

Figure 4
A Schlieren Photograph of Corona Wind

(did not reproduce)

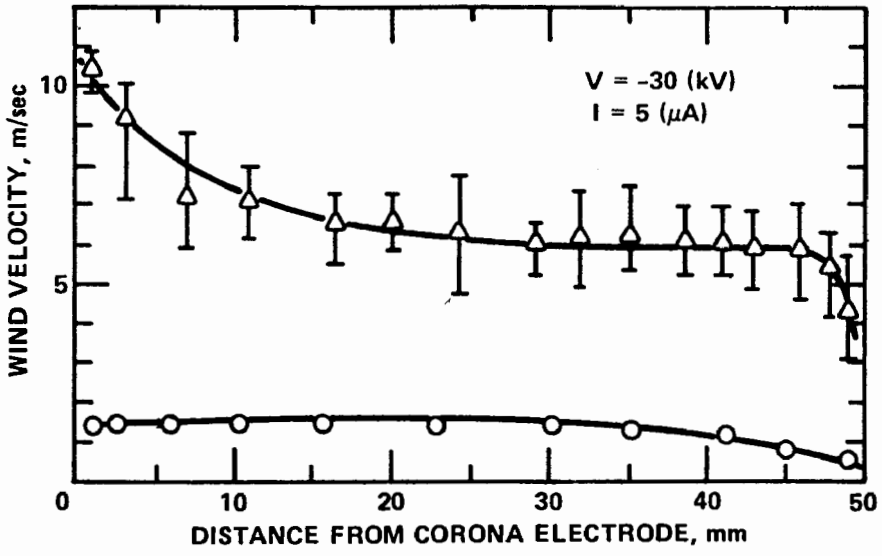

Figure 8. Distribution of perpendicular component of corona wind velocity along axis (point-plate; DOP particle 0.03 μm).

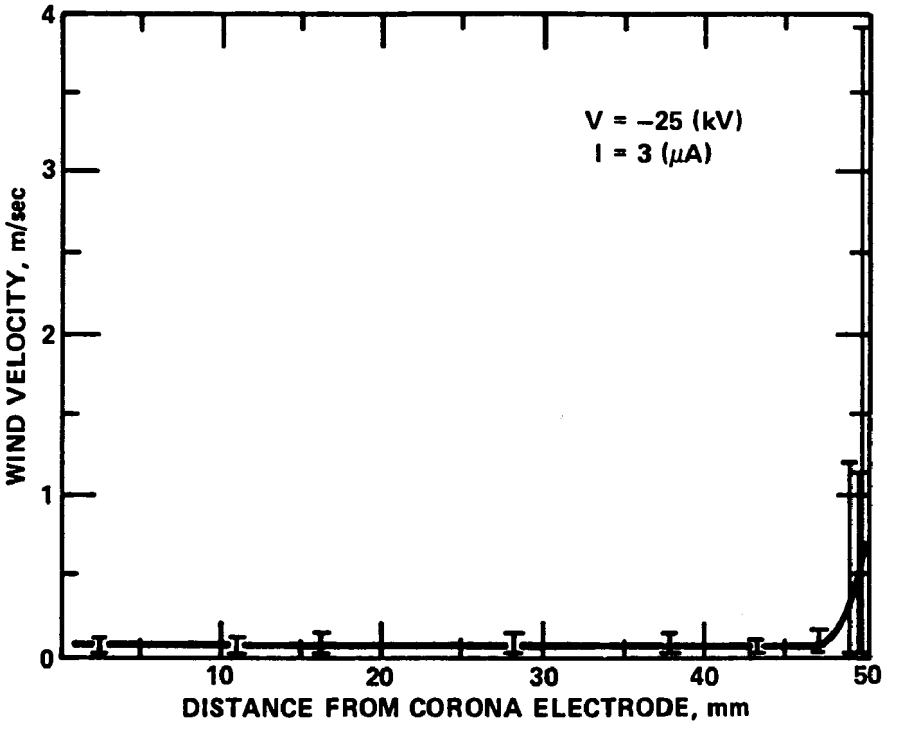

Figure 9. Distribution of parallel component of corona wind velocity along axis (point-plate; DOP particle 0.03 μm).

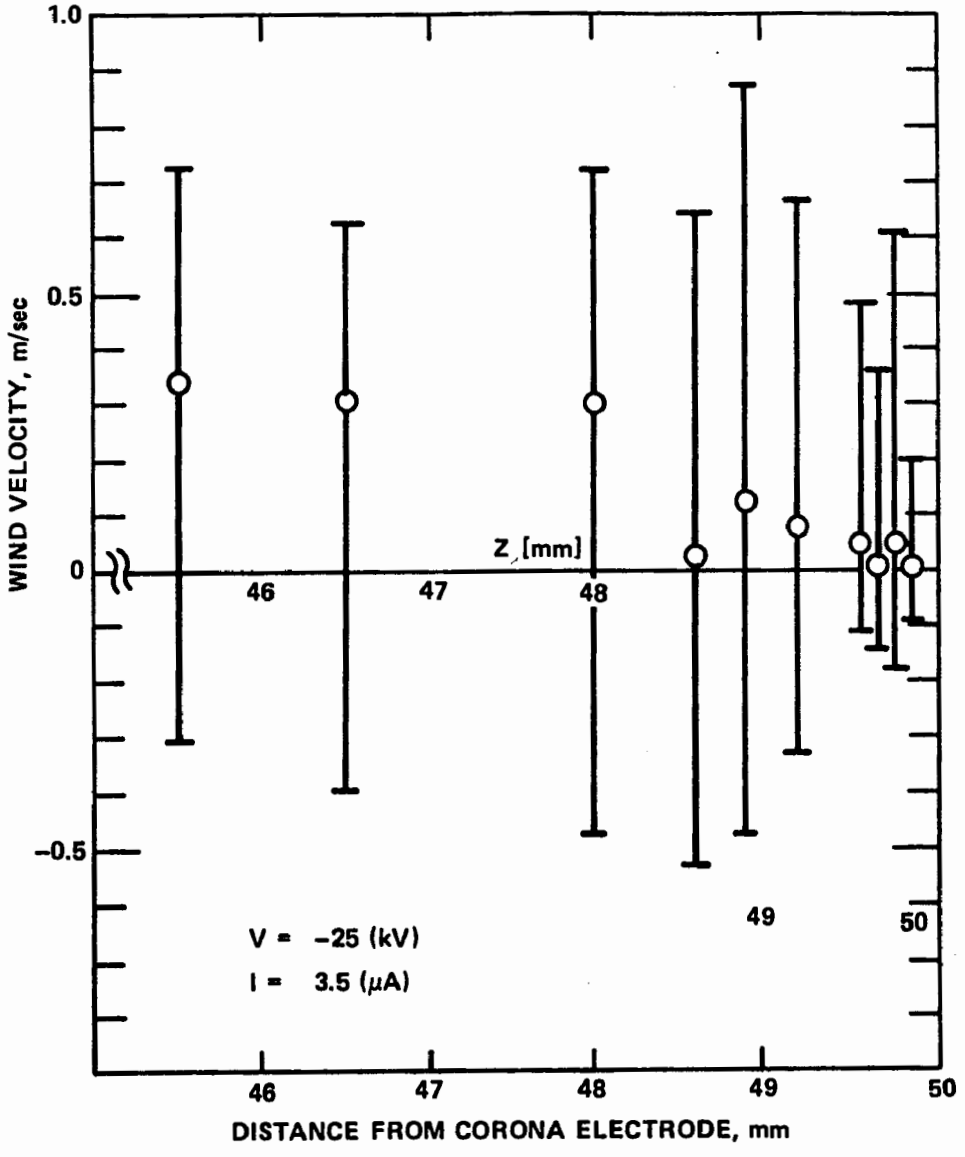

Figure 10. Variation in perpendicular current velocity in boundary layer (corona wind + parallel gas flow).

The collectability of the particles in the turbulent boundary layer can be divided into two parts, which represent the relationship of the electrical and inertial forces to the turbulent force:

$$K_1 = W_{th}/V_o = q\ E_c/6\pi\eta a V_o \tag{13}$$

$$K_2 = W_m/V_o = [(1/2)(MV_k^2)/\delta]/6\pi\eta a V_o \tag{14}$$

where V_o = r.m.s. of turbulent velocity, m/sec

W_m = mean inertial velocity in boundary layer, m/sec

V_k = vertical component of initial viscosity of particle on entry to the boundary layer, m/sec

M = particle mass, kg

δ = thickness of turbulent boundary layer, m

The value of V_o can be obtained by computer evaluation of the velocity fluctuations measured with the laser-doppler instrument. For particles with values of K_1 or K_2 larger than about 10 one can calculate collection in the usual way.

The very high parallel velocity of the corona wind after impact on the plate surface indicates that it can produce a considerable amount of dust reentrainment. It was established with the laser-doppler measuring instrument that dust reentrainment mostly can occur at mean gas velocities above 1-2 m/sec [19]. Apparently one must find the correct compromise between the above-mentioned positive and negative effects of the corona wind to fit the adhesion characteristics of the individual dust. In this connection the voltage characteristic of the corona wind velocity in the main field and in the region near the surface is useful (Fig. 11). The difference between the curves indicates a possibility that one could well use the transport effect of the corona wind and a smaller voltage reduction without any considerable interference by dust reentrainment. Since according to Eq. 12 the motive force for the corona wind is directly proportional to the ion current, one can regulate the corona wind effect by correct choice of the voltage-current characteristic. This requires also a correct choice of the corona electrode type or the application of a special current-regulating charging system, as in Fig. 13.

Fig. 7(b) represents a schlieren photograph of the corona wind, which arises in reverse discharge. The wind direction is perpendicular to each reverse discharge point from above. Fig. 12 shows the distribution of the perpendicular component of the corona wind velocity along the axis of the point-plate electrode system under conditions of reverse discharge, where its absolute value is represented. The wind directed toward the plate by

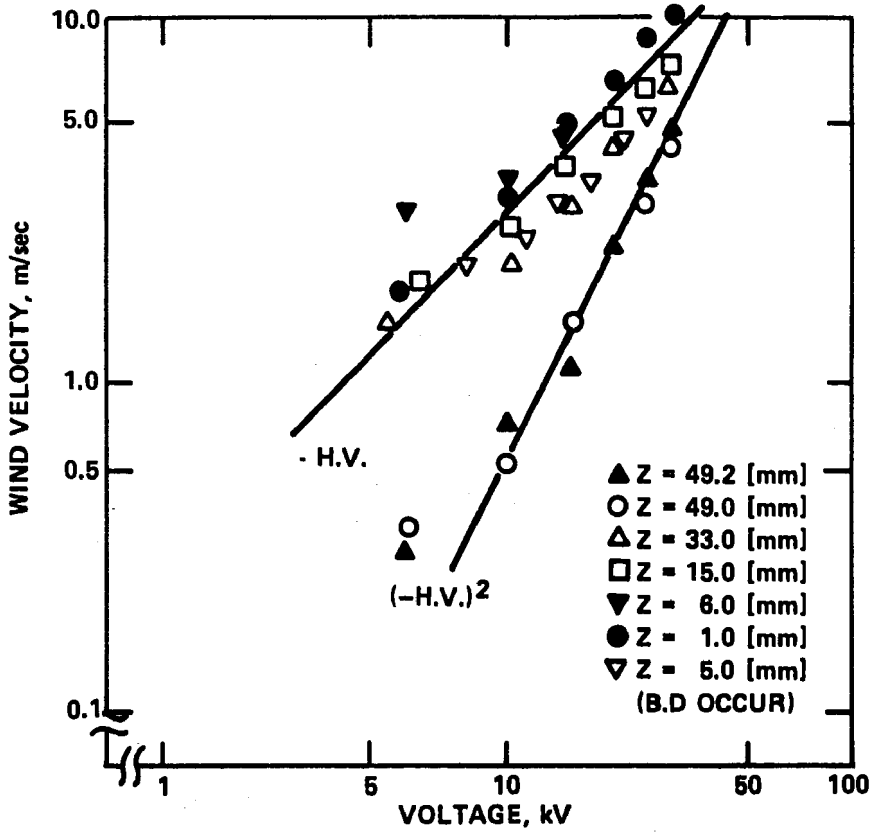

Figure 11. Perpendicular component of the corona wind velocity as a function of voltage.

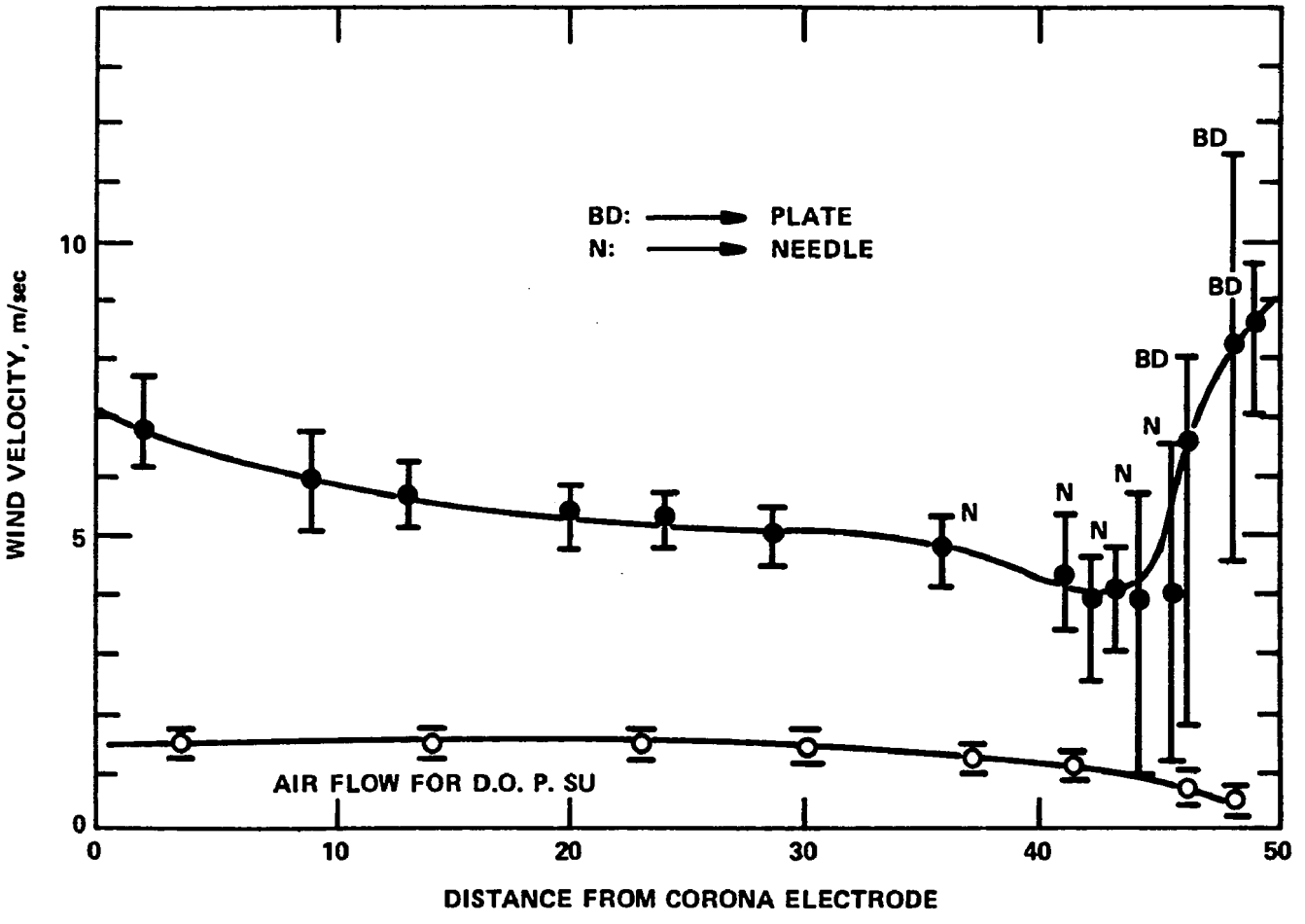

Figure 12. Distribution of perpendiuclar component of corona wind velocity along axis under conditions of reverse discharge.

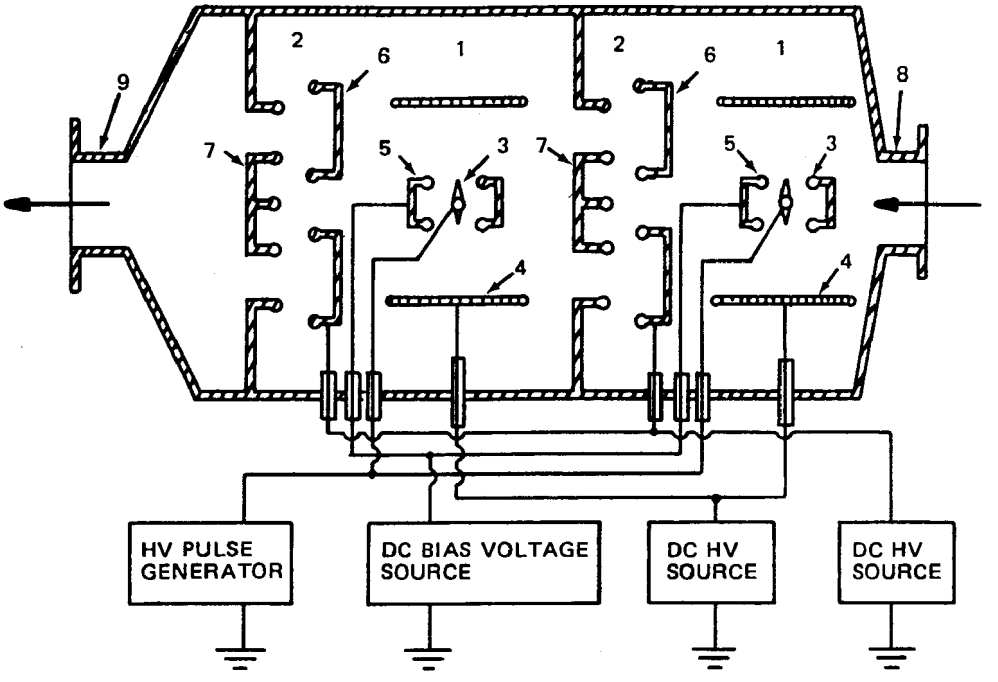

Figure 13. New type of two-stage precipitator with bias-controlled pulse charging system and electrical screen.

negative ions is indicated by "N", while the reversed wind direction by the reverse discharge ions (positive ions) is marked "BD". Although the region of the reverse corona wind is relatively restricted (ca 5 mm), its velocity is astonishingly large, 5-10 m/sec. Experimentally it was established that this strong reverse discharge corona wind not only can repel the oncoming particles back to the main field, but also can tear particles from the dust layer and can enter the main field with a high velocity even up to 5-10 cm distance [19].

With reference to the EHD treatment of particle motion we must consider the application of the EHD potential [21] which is defined as:

$$\frac{md^2R}{dt^2} + \frac{6\pi\eta a dR}{dt} = -\text{grad}\ \psi_{EHD}(R) \qquad (15)$$

from which

$$\psi_{EHD}(R) = -\int_0^R (6\pi\eta a V(R) + qE(R)\ dR = \text{EHD potential, J} \qquad (16)$$

Eq. 15 represents the equation of motion of the charged particle in the EHD field, in which the gas flow field is assumed to be that for an ideal gas. The mode of the particle motion changes according to the parameter:

$$\zeta = (6\pi\eta ab/m\bar{V})^{\frac{1}{2}} \qquad (17)$$

where b = electrode separation, m

$\bar{V}$ = mean gas velocity, m/sec

If $\zeta >> 1$, as in the case of the smaller particles that are being considered in an electrostatic precipitator, the particle motion is "viscous", in that the first term in Eq. 15, compared to the second term (viscosity term), is negligible. In this case the particle moves along the lines of force of the EHD potential field, so the particle collection efficiency is obtained as the result of these lines of force. This calculation can be arrived at easily with the aid of the charge-substitution method combined with a computer [22,23]. Fig. 14 represents the distribution of the EHD lines of force in the collection zone of the 2-stage electrostatic precipitator shown in Fig. 13 [21]. This distribution of lines of force varies according to the relationship of the electrical force to the hydrodynamic force, as can be seen from Fig. 14.

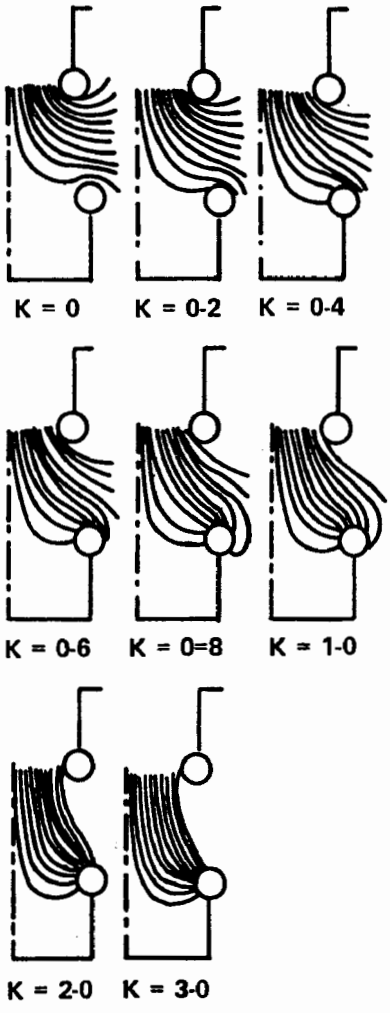

Figure 14. EHD lines of force.

$$K_3 = q\bar{E}/6\pi\eta aV \qquad (18)$$

where $\bar{E}$ = mean field strength between the two electrodes, m/sec. If $K_3 = 0$, the distribution coincides with the streamline distribution, while with an increase in the K_3 value, the lines of force which terminate on the collection electrode increase, and finally at $K_3 = 1.95$ give a 100% collection efficiency. Actually one cannot directly estimate the collection efficiency from the calculation of EHD lines of force in many instances, because the effects of the moving mass and the viscosity of the jet stream that is formed and the turbulence operate on the particle motion, usually in a positive direction.

6. Adhesion and Reentrainment of Dust

One of the most important factors in the effective collection of dust is the strong adhesion between dust particles and between the dust layer and the collection electrode. This allows the formation of a sufficiently strong dust layer that on electrode rapping will fall into the hopper below without disintegration and reentrainment. In this sense the electrostatic precipitator must function as an effective dust coagulator. In this respect, with high-resistivity dust, which has a specific layer resistivity of $\rho_d > 10^{10}$ ohm-cm, the so-called electrical adhesion plays an important role [24]. This force arises from the potential difference at individual particle contacts. It is proportional to the ρ_d value and the current density i_d in the dust layer [25]. Apparently the roles of the contact charge and electret formation in the dust layer under the action of the electric field also come into question [26]. Experimentally it has been established that an electrically deposited dust layer has a 30-60 times s stronger adhesion force that one deposited mechanically.

As was already explained, the gas flow causes dust reentrainment if the average velocity exceeds 1-2 m/sec [19]. This limits the usable gas velocity in a precipitator and results in a large size for the installation. For air filters, which are used under atmospheric conditions, the dust layer has a sufficiently high adhesive force, as the result of absorbed water molecules, so a relatively high air flow, about 8 m/sec, is usable.

For low-resistivity dust, with $\rho_d < 10^4$ ohm-cm, another kind of dust reentrainment can occur completely on an electrical basis. In this instance, the particle on reaching the plate immediately gives up its charge and finally, despite the arriving ion jet, becomes strongly positively charged by induction. Then it is immediately returned to the main field. As a result, an abnormal dust reentrainment is produced, insofar as it is not overcome by other kinds of adhesive action. In addition to electrical adhesion forces, there is also the van der Waals force, which

acts more effectively with decreasing particle size [27]. Under atmospheric conditions in which relatively high moisture is predominant, water adsorption in capillaries of the particles plays an important role (capillary condensation). Recently it has been found that one can increase the collection efficiency by increasing the adhesion action by injecting small amounts of triethylamine [28] or ammonia [29] into gas. Ammonia injection is already used to protect against corrosion by SO_3 in oil-fired steam power plants. The corona-quenching effect is due to the formation of extremely fine particles of ammonium sulfate and bisulfate [29].

7. Reverse Discharge Processes

For very highly resistive dusts with $\rho_d = 5 \times 10^{10}$ ohm-cm, mostly metal oxides, electrical breakdown occurs due to a high voltage drop which then leads to a reverse discharge abnormal corona in the dust layer. This process has long presented one of the most difficult problems in electrostatic precipitator technology; in many industrial installations it results in an appreciable hindrance to precipitator collection efficiency, e.g., in ore sintering plants of the steel industry, rotating kilns and clinker coolers in the cement industry, melting furnaces in metal foundries, and coal-fired steam power plants. The fly ash from coal with a low sulfur content, which is required for lowering the SO_x content in the stack gas, has an especially high ρ_d value, so its removal in an electrostatic precipitator presents great difficulties with reverse discharge. Depending on the magnitude of the ρ_d value, there are two forms of reverse discharge. In the region between 5×10^{10} and ca 10^{11} ohm-cm, there is an extremely strong tendency to spark (excessive sparking), which upsets the stable precipitator operation, and as a result more or less degrades the collection efficiency. In an even higher ρ_d value region, above 10^{12}-10^{13} ohm-cm, the sparking tendency disappears, and there arises over the entire dust layer surface a sheet-like glow corona, often with streamer coronas developing toward the main field, and with an associated strong increase in the corona current (abnormal current increase). This current increase is associated with a supply of positive ions from the reverse discharge points. These positive ions not only neutralize the useful negative charge of the particles but also charge them positively so the particles are repelled and are completely removed from the collection process.

Since, as was explained above, the reverse discharge is caused by the breakdown of the dust layer, its initial conditions can be formulated as:

$$i_d \rho_d \geq E_{ds} \quad \text{V/m} \tag{19}$$

where i_d = current density inside the dust layer, A/m^2

E_{ds} = breakdown field strength of the dust layer, V/m

Impulse-like breakdown occurs repeatedly in the dust layer, by which the particles are ejected from breakdown point into the gas space one after the other, and finally a pinhole is formed in the dust layer. This pinhole allows the formation of a stable initial glow corona in it. With an increase in the electrode voltage the discharge goes over an initial streamer corona in impulse-like streamer corona, which, depending on the field distribution, develops either at the corona electrode or along the dust layer surface, or in both directions. The first is a "space streamer", the second a "surface streamer", and the third a "mixed streamer" [30]. Fig. 15 is a diagram of the reverse discharge in atmospheric air, which takes the form of reverse corona as a function of the field component E_a perpendicular to the surface and the ion current density i. Thus, one sees that the space streamer arises first at a higher field strength $E_a > 5$ kV/cm, which agrees with the development conditions of the streamers. In the mixed streamer region, and in the outer surface streamer the space streamer is also present; the occurrence of sparking is determined only by the ion current density i. Since the amount of charge associated with a streamer impulse remains almost constant, the ion current is proportional to the streamer frequency.

With increase in the ion current, the period between two streamers decreases and finally reaches the order of magnitude of a plasma life time, when sparking can appear. In the region of $E_a < 5$kV/cm, only the surface streamer occurs, and no sparking takes place. In this region the ion current depends on its space charge and is related to the main field strength. As a result there is in this region an upper limit to the current, which represents the saturation current. It is notable also that the breakdown in the dust layer directly goes over into sparking, if the main field strength exceeds 8.4 kV/cm. The effect of the tangential field component on the form of the reverse discharge is shown in Fig. 16. This component E_t is mainly determined by the density of the surface discharge on the dust surface σ_{ds} at the moment of breakdown, and further the magnitude of σ_{ds} is connected to the breakdown field strength of the dust layer in the following way:

$$\sigma_{as} = \varepsilon_d E_{ds} \quad coul/m^2 \tag{20}$$

where ε_d represents the dielectric constant of the dust layer. In Fig. 16 an experimental layer was applied on two glass plates, one on top of the other, with pinholes, whereby its breakdown field strength E_{ds} could be regulated by changing the distance separating the two pinholes [30]. By increasing the E_{ds} value

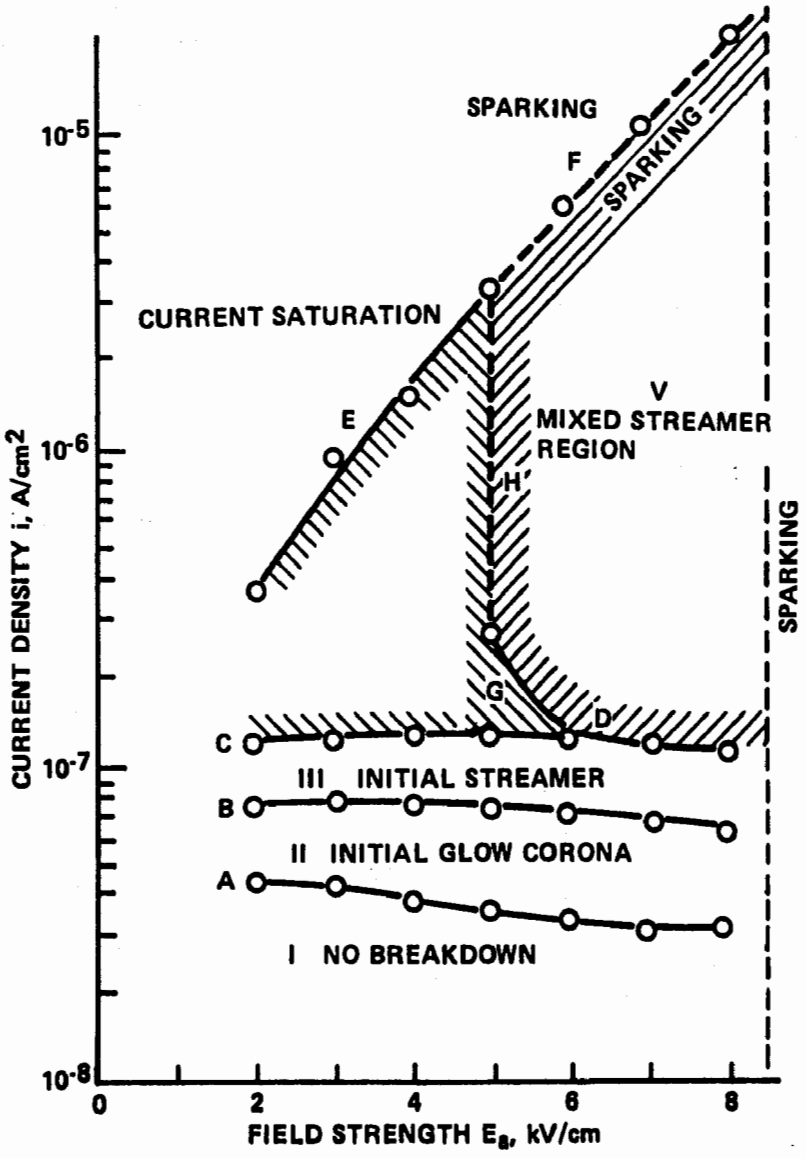

Figure 15. Reverse discharge diagram.

Figure 16
Photograph of Corona From High Resistivity Layer

(did not reproduce)

the development of the surface streamers could be greatly accelerated. It was established that the conditions for development of the surface streamers are the presence of a sufficiently large surface charge density, greater than ca 5 x 10^{-9} coul/cm^2, as well as a sufficiently high surface resistivity of the dust layer. Fig. 15 explains partly the basis for the difference in appearance of the reverse discharge which occurs with change in the dust layer resistivity. This change leads to a corresponding variation in the division of potential between gas field and dust layer. If the ρ_d value is low, the field strength in the gas space E_a increases with increase in the voltage, while the field strength in the dust layer E_d remains relatively low. The development of the space streamer is greatly accelerated, which leads to excessive sparking. If on the other hand, the ρ_d value is high, the situation is reversed, so no sparks occur in the gas space, while in the dust layer on account of a rapid increase in the field strength breakdown occurs at many points one after the other, before sparking occurs. Thus, the abnormal current increase described above.

Fig. 17 shows a typical oscillogram of the impulse current and the accompanying light emission occurring on reverse discharge. The spatial change in the light emission oscillogram is represented in Fig. 18, in which the measurements were made along the electrode axis and the surface of the layer. The spatial resolution of the measurements was 0.3 mm, and a glass plate with a pinhole was used as a test layer [31]. From the light emitted signal at the original point it may be seen that the reverse discharge impulse consisted of a primary and a secondary wave. The former represents the first increase in the current impulse and rises very rapidly. It lasts very briefly (about 20 nsec) and has a small impulse height. The current impulse connected with this primary wave has a charge of 1-2 x 10^{-9} coul/impulse. The secondary wave corresponds to the second current impulse, which has an appreciably greater impulse height with a charge of 2-4 x 10^{-8} coul/impulse and a long duration (ca 200 nsec). With the aid of an "image converter camera" combined with an "image intensifier", it was established that the primary wave represents a space streamer, which develops with a velocity of ca 4 x 10^7 cm/sec at the corona electrode. The secondary wave represents the surface streamer, which has a velocity of ca 2.5 x 10^7 cm/sec and an appreciably higher charge. If the surface resistivity of the layer is smaller, the surface streamer disappears, and the space streamer is present. With both the primary wave and the secondary wave the related charge per impulse remains constant independent of the voltage, while the impulse frequency changes when the voltage changes. In general, the impulse frequency of the surface streamer is appreciably smaller than that of the space streamer, so the space streamer, despite its smaller charge per impulse, has a greater influence on the increase in current. Fig. 19 shows the reverse discharge for a positive corona electrode, which has a completely different appearance. In this case

Figure 17

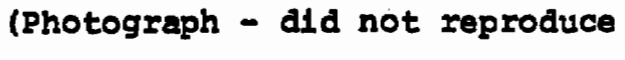
(Photograph - did not reproduce

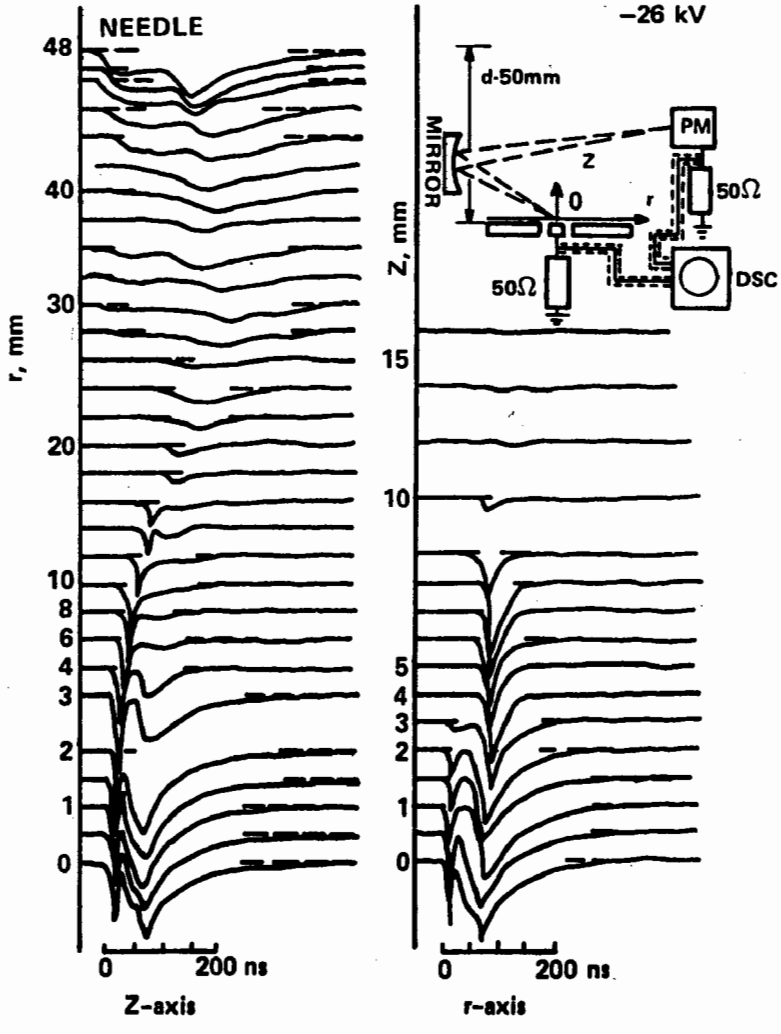

Figure 18. Wave form of light signal measured along z- and r- axes.

Figure 19

(Photograph - did not reproduce)

numerous glow points are uniformly distributed over the dust layer surface. From neither the discharge points nor the positive corona electrode is there a streamer, but sparking occurs suddenly. The usual streamer from a positive corona is completely suppressed, presumably on the same basis as with the Hermstein glow corona, namely because of negative ions supplied from the reverse discharge points. Experimentally it was established that the sparking voltage in this case is higher than that without a dust layer [30].

Fig. 20 shows the sparking voltage at reverse discharge as a function of the mean free path of the ions λ [31]. As a test layer was used a mica plate with a small hole, and the magnitude of λ was varied by changing either the temperature or pressure. Outside the higher temperature region, where no reverse discharge takes place, the sparking voltage is determined only by the magnitude of the λ value, quite independent of variation in temperature or pressure. The sparking voltage is represented by two curves I and II, the validity regions of which agree in Region B but not in Regions A and C, above and below. Curve I represents the voltage at which the sparking develops over the space streamer, while curve II represents the voltage at which the sparking takes place directly from the glow reverse corona. In Region C with a higher value of λ no streamer occurs, and the glow reverse corona is present up to Curve II, at which sparking suddenly occurs. In Region A with a smaller value of λ, which also corresponds to atmospheric conditions according to Ref. 15, there appears after the already explained initial glow corona the space streamer, which goes over to sparking at Curve I. On the other hand, in Region B the sparking that sometimes takes place on Curve I disappears, if the voltage exceeds only slightly Curve I, and suddenly goes over to impulse-free stable glow reverse corona. In this case a stronger sparking finally appears at an appreciably higher voltage on Curve II. The boundaries between A and B or B and C can be shifted according to the magnitudes of dust layer thickness, alkali content of the dust, etc., which determine streamer development. E.g., boundary B/C is shifted to the left for a decrease in the dust layer thickness, to finally appear outside the region being considered, so no streamer will occur in atmospheric air. On the other hand boundary A/B is shifted to the right for an alkali-containing dust, so sparking in the total region will be controlled by Curve I at an appreciably lower sparking voltage. This fact may be the basis for the observation that in an electrostatic precipitator for dust removal from an iron ore sintering furnace gas, in which high-resistivity dust with a high potassium content is encountered, the collection capability against the strongly abnormal increase in current and the related lower operating voltage is usually unsatisfactory. Fig. 21 shows schematically the structure of the initial glow corona and stable glow jet corona in the developed

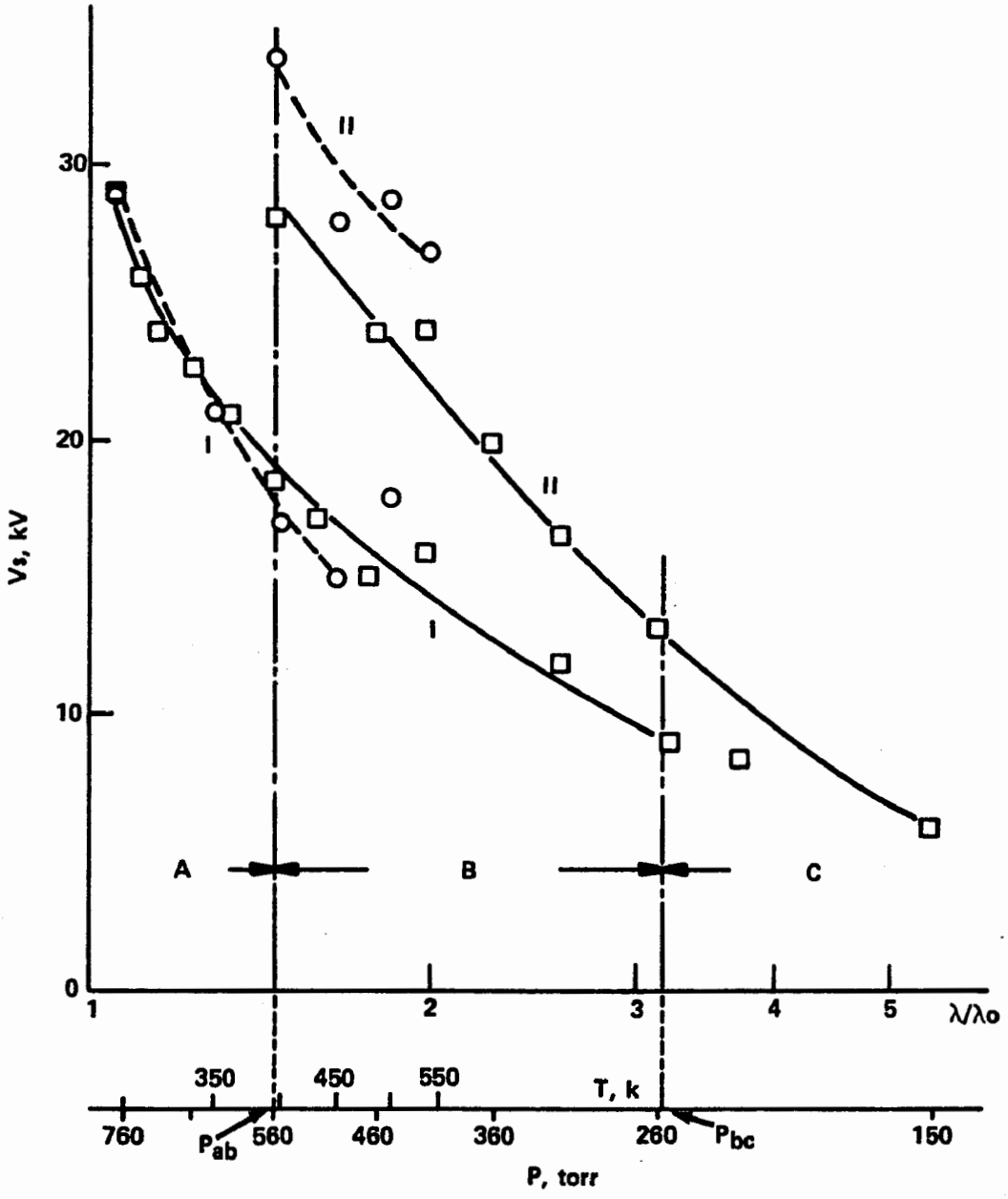

Figure 20. Sparking voltage V_S with reverse discharge as a function of mean free path of ions.

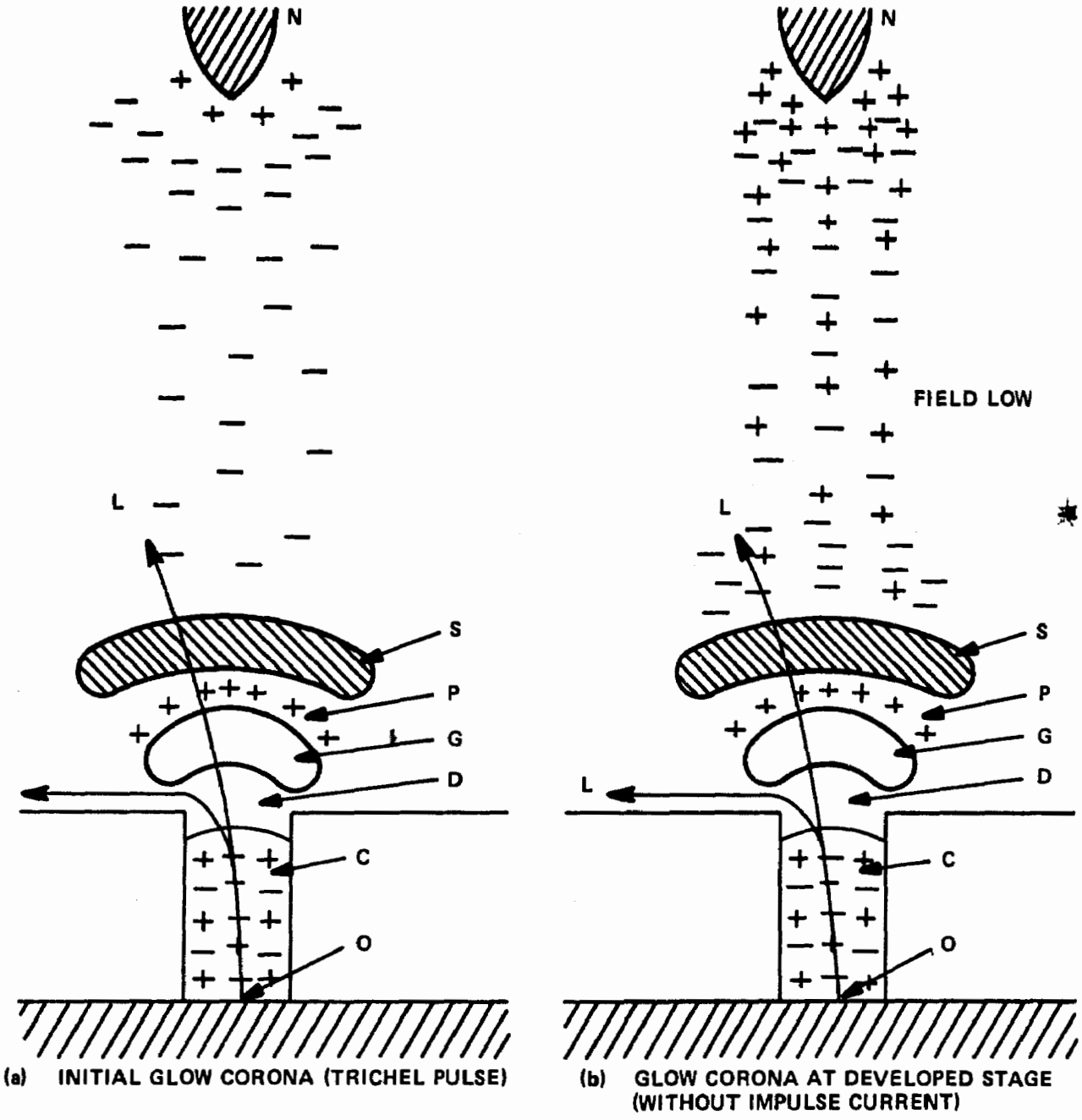

N: NEGATIVE ELECTRODE
S: REGION OF STRIPPING ELECTRONS FROM IONS
P: REGION OF ACCUMULATION OF POSITIVE IONS
G: NEGATIVE GLOW
D: DARK ZONE
C: POSITIVE POST
E: PLATE ELECTRODE

Figure 21. Mechanism of glow corona in reverse discharge.

stage (without impulse current) which occurs in Region C and in the zone between I and II of Region B. In these special glow corona, which have no negative electrode as electron sources, the electrons in Region S, which with the aid of strong space charge field were stripped from the negative ions and produced the positive ions accumulated in P, must have been supplied to the glow corona.

Fig. 22 shows the streak photos of the space streamer, which were taken under a low pressure of 170 Torr on applying the impulse voltage [32]. After applying the impulse voltage there first appears a short-lived light emission at the corona electrode. About 400 nsec later begin the light emission of the space streamers from the reverse discharge points back to the corona electrode. It was established that the dead time between the two light appearances corresponds exactly to time for passage of the electrons between two electrodes (d = 50 mm) [32]. With an increase in the pressure of the air this dead time increases slowly at first, and at a certain pressure of about 470 Torr there is a discontinuous increase in the dead time. Finally there occurs once more a slow increase in the dead time with pressure. This indicates that at this critical pressure there has been a change in the charge carriers causing the reverse discharge from electrons despite their higher concentration to ions, and because of their high electron attachment probability, to electronegative molecules.

8. Particle Charging

Experimentally it has been established that the Pauthenier formula for field charging, Eq. 5 - 7, applies very well, at least for spheres of conducting materials. It must be emphasized, however, that the "conducting materials" in this instance include not only "conductors" in the normal sense, but also such materials, the relaxation time $\varepsilon\rho$ (ε = dielectric constant, ρ = specific resistivity) for which is appreciably less than the charging time constant in Eq. 7. In the course of the charging process, the charges on the sphere are distributed in the same way as they exist on a true conductor. Since high-resistivity dusts have a specific layer resistivity generally 100 - 1000 times higher than their specific volume resistivity [33], a dust with a specific layer resistivity $< 10^{13}$ ohm-cm can be considered as a quasi-conducting dust because of its relaxation time constant of 1-10 msec. For insulator spheres, the measured value of their saturation charges is always only about half of the theoretical value in Eq. 6 [34]. If an insulator sphere is reversed by passage through the corona field, its saturation charge becomes almost equal to the theoretical value. This is attributed to two contradictory assumptions derived from Eq. 5 - 7. Namely, for calculation of the external field of the sphere it was assumed that the sphere is made of insulating material, and that nevertheless the charge given to the sphere is distributed over its surface, as though the sphere were a conductor.

Figure 22

(Photograph - did not reproduce)

Pauthenier has also derived the formula for charging a spheres by bipolar ions [35,36], which allows an evaluation of the particle charging under reverse discharge conditions, so far as the concentrations of positive and negative ions are known. According to this formula, the particle charge on larger masses is reduced due to the combined action of small amounts of false ions (positive ions), which has been experimentally confirmed [34]. Further, it was established that the surface streamer as a source of false ions acts as a source of surface ions, while the space streamer acts as a source of volume ions, and so ions of both polarities are produced in the field volume. Thus, the dust particle can under conditions of space streamers often be strongly positively charged. It is remarkable that the recombination probabilities of both ions under the operating conditions of the electrostatic precipitator are so low that a considerable quantity of positive ions can reach the corona electrode. Extremely high dust resistivities of $\rho_d > 10^{13}$ ohm-cm can cause a reverse discharge from the corona electrode to the dust layer deposited on it. In this way the so-called propagation of the reverse discharge takes place along both electrodes.

Gas ionization by irradiation with gamma rays or high-energy electron beams can be considered as a new charging method [37,38]. An electric field must be applied to the ionization field, by introducing parallel electrodes. The positive and negative ions are electrically separated in order to form at each electrode a zone of a multitude of ions with a given polarity. There the dust particles can be effectively charged by the ion multitude and collected on the appropriate electrode with a high collection efficiency. These methods have been found to be a very useful aid in electronic experiments for removal of NO_x and SO_x from exhaust gases [38]. The gaseous impurities (NO_x and SO_x) are converted by high-energy electrons and with the aid of NH_3 additions to solid aerosols, the particles of which are then captured with the aid of an applied electric field. It has been established also that these radiochemical reactions are accelerated by the action of an electric field [39].

9. Dust Resistivity

Fig. 23 represents the effective migration velocity w (as a measure of collection capability) of an electrostatic precipitator as a function of the ρ_d value of the dust layer. The precipitator usually shows its highest capability in the ρ_d-region of 10^4-10^{10} ohm-cm. In the low-ρ_d region the collection capability falls off due to the occurrence of abnormal amounts of dust reentrainment, while in the high-ρ_d region it falls off due to reverse discharge. The specific resistivity of high-resistivity dust layers is very sensitive to effects of temperature, gas moisture, and also the presence of small amounts of special substances, such as SO_3. Fig. 24 represents schematically the

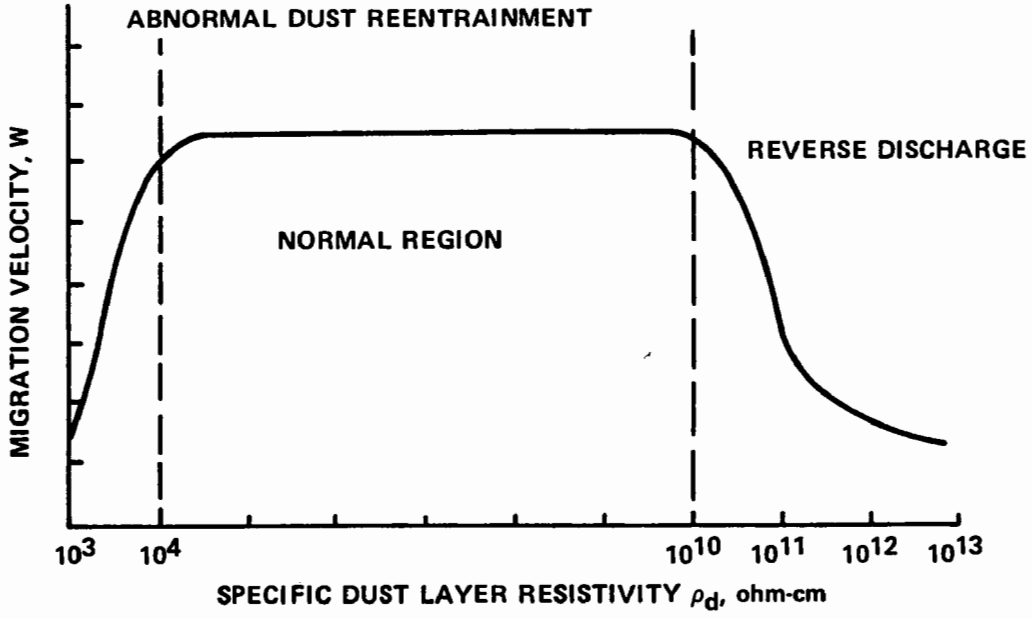

Figure 23. Change in effective migration velocity W as function of specific dust layer reistivity.

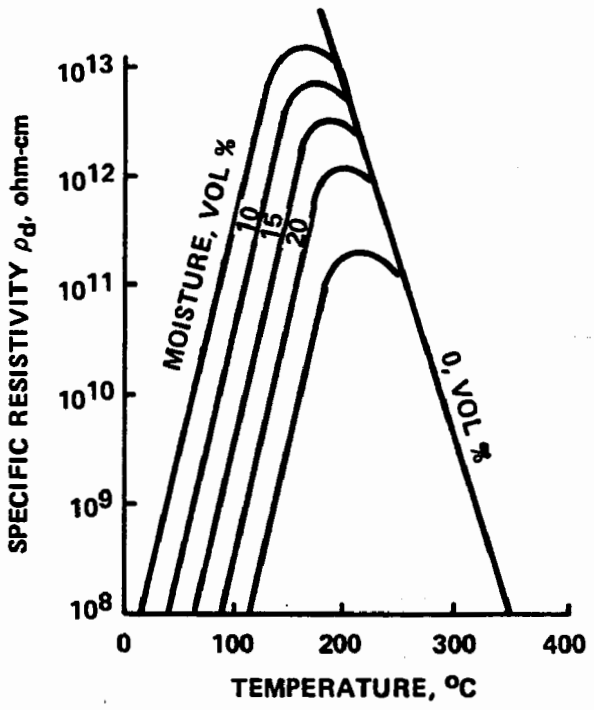

Figure 24. Effect of temperature and moisture on the specific dust layer resistivity ρ_d of high-resistivity dust.

effects of temperature and gas moisture content on the ρ_d value of a high-resistivity dust layer. The electrical conductivity of the dust layer results in general from surface conduction and volume conduction of the particles, and the conducting path is also affected by the way in which the layer is formed [33]. In the low-temperature region, where the relative gas humidity is sufficiently high and the amount of water absorbed on the dust surface is sufficiently large, surface conduction predominates. In the higher temperature region, volume conduction predominates, and it increases with increase in temperature. As a result of the equilibrium between the two conduction mechanisms, there is a maximum in the ρ_d value at 100-200°C, which corresponds to the operating temperature of many industrial waste gases. Thus, it is not seldom in many large industrial installations that interference by reverse discharge results.

Recently it has been found that alkali metal ions in fly ash from coal play an important role as current carriers [40].

10. Technical Advances and Developmental Results

The so-called "large-spacing electrostatic precipitators" with an appreciably larger electrode distance, up to 20-50 cm, has found more and more applications in Japan in many branches of industry, including use with high-resistivity dust, usually with good results. In many instances a reduction in capital cost of about 20% has been achieved. Fig. 26 shows a "roof-type electrostatic precipitator" which has been built on the roof of a factory building, from which there is a heavy dust emission. A large volume of hot, dust-laden gas rises, e.g., from an electric furnace and enters directly into the electrostatic precipitator. It flows without the use of blowers, only by free convection, through the precipitator, and enters the atmosphere directly after dust removal. To decrease the weight of the collection electrodes, they are made from a conducting plastic [40], and they are cooled with trickling water. The wet electrostatic precipitator has found much interest because of its advantages--high collection capability without dust reentrainment or reverse discharge, plus the added action of effective gas absorption (SO_2, HCl, HF, etc.). The high gas absorption capacity in this instance is related to the already explained dilution of the boundary layer by the corona wind. In the practical application of wet electrostatic precipitators questions arise as to the large amount of irrigation water required, the generation of waste water that must be treated, and the lowering of the gas temperature that hinder the buoyancy of the stack plume. One of the solutions for these difficulties is the so-called "hybrid electrostatic precipitator", in which the dry stage and the wet stage are installed in series in a common housing. The main part of the dust (about 90%) is first removed in the dry stage with relatively

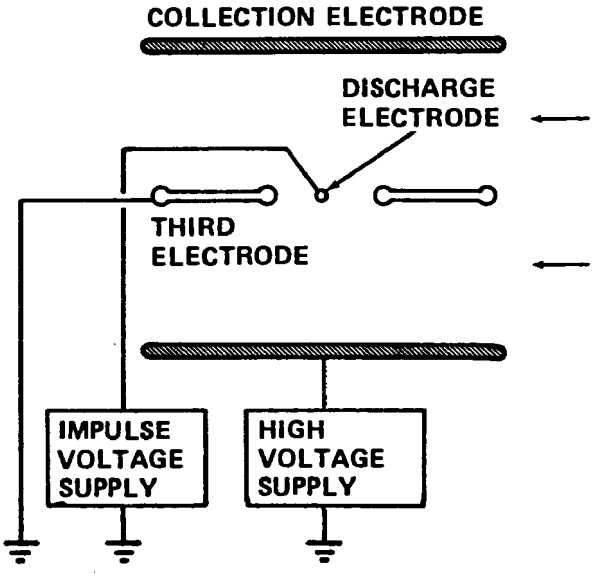

Figure 25. Impulse charging system according to Luthi.

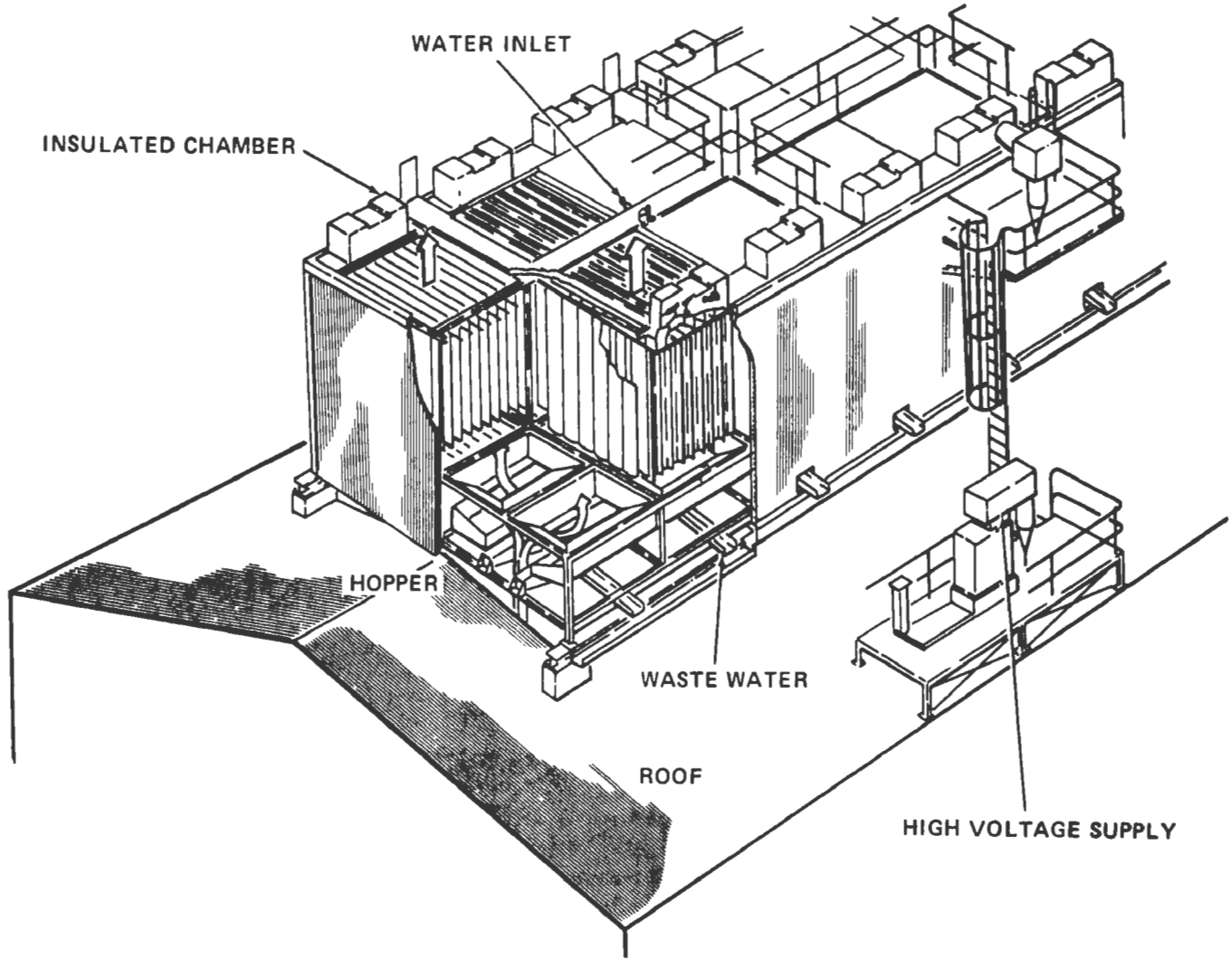

Figure 26. Roof-mounted electrostatic precipitator with plastic collection electrodes (Sumitomo Heavy Ind.).

small dimensions, and then the remainder with a very small particle size can be effectively captured in the wet stage with a very high collection performance. Most of the waste water is recirculated to the irrigation after removal of sludge. This system allows large reductions in the amount of irrigation water used and sludge generated, with less gas cooling, while simultaneously a higher collection performance and proportionally smaller dimensions of the precipitator are achieved. The advantages of this process are especially worthy if a very high collection efficiency for dust and simultaneous gas absorption are involved.

Concerning the technical solution of interference by reverse discharge, humidifying the gas with a water spray at the entry to the precipitator has been used for a long time; the ρ_d value of the dust layer is reduced to about 10^{10} ohm-cm by humidifying the gas and by lowering its temperature. The most important question here is to insure the rapid and complete evaporation of the water spray [43]. In some applications the injection of a suitable chemical means for lowering the ρ_d value has been found to be a very effective method [44]. So, for example, the injection of small amounts of SO_3 (several tens of ppm) into the entering gas with a high-resistivity fly ash, which arises in the combustion of coal with an extremely low sulfur content, has been applied with great success [45,46,47]. Recently it has been proposed to mix sodium salts, e.g., Na_2CO_3 with the coal to be burned [48]. Another solution to the reverse discharge problem is to operate the precipitator at an appreciably higher temperature, about 300-400°C, "hot-side operation". This is done by installing the precipitator ahead of the air preheater in the power plant. It is clear that the ρ_d value is greatly reduced thereby (cf. Fig. 24). In designing the unit the thermal expansion properties of the construction material must be considered.

In addition to the above-mentioned operating precautions for preventing reverse discharge, purely electro-technical methods can be used. Fig. 25 represents one according to Lüthi [49], in which a third electrode is installed near the corona electrode and a pulse voltage is applied across them. Thus, there is between the third electrode and the collection electrode a high voltage by which the field is formed. By varying the magnitude or repetition frequency of the voltage pulse, one can regulate the magnitude of the ion current quite independently of the main field strength, which allows the removal of the reverse discharge according to Eq. 19 at the highest attainable main voltage. The highly concentrated negative ion cloud is produced. Because of the strong propagating force, in the course of migrating to the collection electrode, the cloud expands to provide at the collection electrode a homogenerous distribution of ion current density. This is one of the most important conditions for avoiding reverse discharge. In the practical application of this

method, one must increase the distance between the third electrode and the corona electrode to at least about 10 cm, in order to avoid undesirable variations in construction. However, this makes the screening of the corona electrode by the third electrode during the pulse-free time period very difficult, which represents the condition required for avoiding current injection from the corona electrode during the pulse-free period and the formation of pulsed corona charging. Also fluctuations in gas and dust properties cause trouble with screening. One solution is offered by the application of a uniform voltage, which is superimposed on the pulse voltage and brings the potential of the corona electrode in the pulse-free time down under the corona potential. Such a system is used in the charging zone of the two-stage precipitator in Fig. 13 and is termed the "bias-controlled pulse charging system" [20]. It was established in an experimental precipitator like that in Fig. 13 that with this charging system one can increase the collection efficiency from 63% to 93% for an extremely high-resistivity dust with $\rho_d \sim 10^{13}$ ohm-cm. Further, it has been established in many other installations that this system, at least up to a ρ_d value $< 10^{14}$ ohm-cm, is one of the effective precautions. Beyond this ρ_d limit the above-mentioned propagation of the reverse discharge effect also takes place on the third electrode, and also when no pulse current is furnished. It has been established that in application of this system in the region of $\rho_d = 10^{13}$-10^{14} ohm-cm, consideration must also be given to the main field strength and the pulse breadth [50].

The application of an a.c. voltage combined with an insulating film on the collection electrode has also proved to be effective in avoiding the reverse discharge effect [51]. One problem with that approach is the material for the insulating film, which must be trouble-free for long time periods at high temperature.

The investigation of EHD particle migration in the electrostatic precipitators has led to new kinds of two-stage precipitator shown in Fig. 13. This system has enabled a substantial reduction of the precipitator volume [52].

11. Conclusions

An overview of the present condition of science and practice of electrostatic precipitators was prepared. In it was recognized the special character of the collection process, on which numerous factors operate simultaneously. Each presents its own difficulties to precipitator practice and the investigation of separate elementary processes can not completely provide an understanding of collection as a whole. The gap between science and practice in electrostatic precipitator technology remains very large. Considering the present and future needs for even cleaner air in the environment, increased activity on research and development in this boundary region of practice is very desirable.

Literature

1. H.J. White: Industrial Electrostatic Precipitation, p. 157, Addison-Wesley, New York (1962).
2. S. Masuda: Recent Progress in Electrostatic Precipitation, Inst. Phys. Conf. Ser. No. 27, p. 154, Inst. Phys. London (1975).
3. M. Pauthenier and M. Moreau-Hanot: J. Phys. Radium, Vol. 3, p. 590 (1932).
4. M.B. Awad and G.S.P. Castle: J. Air Pollution Control Assoc., Vol. 25, p. 172 (1975).
5. G.W. Hewitt: AIEE Trans. Pt. 1, Vol. 76, p. 300 (1957).
6. H.J. White: AIEE Trans. Pt. 2, Vol. 70, p. 1186 (1951).
7. J.D. McCain, J.P. Gooch, and W.B. Smith: J. Air Pollution Control Assoc., Vol. 25, p. 117 (1975).
8. D.D. Heinrich: Trans. Inst. Chem. Engrs., Vol. 39, p. 145 (1961).
9. S. Masuda: Staub-Reinhalt. Luft, Vol. 26, p. 459 (1966).
10. S. Ago, T. Itoh, H. Saito, N. Furuya, and S. Masuda: Proc. 1975 - Gen. Conf. Inst. Elect. Engrs. Japan, Paper No. 921 (1975).
11. S. Masuda, A. Shibuya, and E. Ikeno: Proc. 1973 - Gen. Conf. Inst. Elect. Engrs. Japan, Paper No. 844 (1973).
12. S. Masuda and M. Niioka: Trans. Inst. Elect. Engrs. Japan, Vol. A-96, No. 9, p. 411 (1976).
13. W. Hermstein: Archiv f. Elektrotech., Vol. 45, pp 209 and 279 (1960).
14. S. Masuda and M. Niioka: Trans. Inst. Elect. Engrs. Japan, Vol. 8-95, No. 9, p. 423 (1976).
15. M. Robinson: Trans. AIEE, Vol. 80, p. 143 (1961).
16. T. Adachi, S. Masuda, and K. Akutsu: Velocity Distribution of Negative Ionic Wind in A Point-to-Plane Corona Discharge, Journal of Electrostatics, in press, Elsevier, Amsterdam.
17. T. Adachi, T. Shimoda, M. Suyama, and S. Masuda: Proc. 1974 - Gen. Conf. Inst. Elect. Engrs. Japan, Paper No. 718 (1974).
18. S. Masuda, K. Akutsu, and K. Aihara: Proc. 1977 - Gen. Conf. Inst. Elect. Engrs. Japan (1977).
19. J.D. Bassett, K. Akutsu, and S. Masuda: Preliminary Study on Dust-Reentrainment in Electrostatic Precipitators, Journal of Electrostatics, in press, Elsevier, Amsterdam.
20. S. Masuda, Y. Doi, M. Aoyama, and A. Shibuya: Staub-Reinhalt, Luft, Vol. 36, No. 1, p. 19 (1976).
21. S. Masuda and Y. Matsumoto: Trans. Inst. Elect. Engrs. Japan, Vol. A-94, p. 515 (1974).
22. H. Steinbigler: Dissertation, T.U. München (1969).
23. S. Masuda and Y. Matsumoto: Trans. Inst. Elect. Engrs. Japan, Vol. A-96, p. 1 (1976).
24. J. Dalmon and D. Tidy: Atmos. Env., Vol. 6, p. 81 (1972).
25. W. Simm: Staub, Vol. 22, p. 463 (1962).

26. G.W. Penny: J. Air Pollution Control Assoc., Vol. 25, p. 113 (1975).
27. H.J. Lowe and D.H. Lucas: Brit. J. Appl. Phys. (suppl.) No. 2, p. 40 (1953).
28. D.J. Tassicker: Air Pollution Control Assoc., Vol. 25, p. 122 (1975).
29. E.B. Dismukes: ibid., p. 152 (1975).
30. S. Masuda and A. Mizuno: Initiation Condition and Mode of Back Discharge, Journal of Electrostatics, in press, Elsevier, Amsterdam.
31. S. Masuda and A. Mizuno: Flashover Measurement of Back Discharge, ibid., in press, Elsevier, Amsterdam.
32. S. Masuda and A. Mizuno: Light Measurement of Back Discharge, ibid., in press, Elsevier, Amsterdam.
33. S. Masuda: Staub, Vol. 25, No. 5, p. 175 (1965).
34. S. Masuda and K. Akutsu: Proc. 1975 - Gen. Conf. Inst. Elect. Engrs. Japan, Paper No. 90' (1975).
35. M. Pauthenier: La physique des Forces electrostatique et leurs application (Centre National de la Recherche Scientifique) p. 279 (1961).
36. N. Ishiga: Master-Dissertation, Dept. E.E., Univ. Tokyo (1976).
37. R.J. Heinsohn, S.H. Levine, R.J. Fjeld, and G.W. Malamud: J. Air Pollution Control Assoc., Vol. 25, p. 179 (1975).
38. S. Masuda, N. Ishiga, and K. Akutsu: Proc. 69 Annual Meeting of APCA, Paper No. 76-71.11 (1976).
39. S. Masuda, K. Akutsu, and Hirano: Proc. 1977 - Gen. Conf. Inst. Elect. Engrs. Japan, - (1977).
40. R.E. Bickelhaupt: J. Air Pollution Control Assoc., Vol. 25, p. 148 (1975).
41. Inst. Elect. Engrs. Japan: Technical Report "Present and Future of Electrostatic Precipitator Technology" (1976).
42. S. Masuda, S. Ago, T. Itoh, H. Saitou, and N. Furuya: Proc. 69 Annual Meeting of APCA, Paper No. 76-42.1 (1976).
43. S. Masuda: I & EC - Process Design and Development, Vol. 5, No. 2, p. 135 (1966).
44. J. Dalmon and D. Tidy: Atmos. Env., Vol 6, p. 721 (1972).
45. H.G.T. Busby, and K. Darby: J. Inst. Fuel, Vol. 36, p. 184 (1963).
46. K. Darby and D.D. Heinrich: Staub-Reinhalt. Luft, Vol. 26, p. 464 (1966).
47. R.E. Cook: J. Air Pollution Control Assoc., Vol. 25, p. 156 (1975).
48. H.J. White: ibid., p. 102 (1975).
49. J.E. Lüthi: Dissertation ETH-Zürich, No. 3924 (1976).
50. S. Masuda, Y. Doi, A. Shibuya, and I. Hattori: Performance of Bias-Controlled Pulse Charging System, Proc. 4th Clean Air Congress (May 1977, Tokyo) (1977).
51. H. Krug: Dissertation, TU Karlsruhe (1971).
52. A. Shibuya and S. Masuda: Proc. 1975 - Gen. Conf. Inst. Elect. Engrs. Japan, Paper No. 920 (1975).

APPENDIX B

ISHIKAWAJIMA-HARIMA HEAVY INDUSTRIES

Ishikawajima-Harima Heavy Industries Co., Ltd.

Oct. 1977

Technical Information

IHI's
NEW PRECIPITATION TECHNIQUES
PAC AND ES

Air Pollution Control Engineering Department

Environment Control Equipment Division

Ishikawajima-Harima Heavy Industries Co., Ltd.

Tokyo Japan

IHI PAC and ES TYPE ELECTROSTATIC PRECIPITATOR

Ushers in a new era of dry-type electrostatic precipitation.

Wide Range of Application

Through successful prevention from back discharge and reentrainment which are caused by high resistivity dust and low resistivity dust respectively, the PAC makes it possible to collect the dust in a range which can not be covered by conventional techniques of electrostatic precipitators (EP).

High Efficiency

The PAC and ES an achievement of IHI's new engineering techniques, has been developed to satisfy the stringent demand for air pollution control.
It can technically hold the outlet dust concentration to 10 mg/Nm^3 or below.
This value is virtually difficult of attaining by the conventional dry-type EP to precipitate the high and low resistivity dust.

Compact

In case of treating too high resistivity dust, the PAC can be installed at a small or elevated place.

Energy Saving

Electric power consumption is in no vain to effectively collecting the dust and the draft loss is almost the same as the EP.

Easy Maintenance

Unlike the EP, electrodes of the PAC are readily accessible.

Stable Performance

In the EP, changes in gas conditions can exert a significant influence on its performance. But in the PAC, the main electric field and corona current are singly controllable at its charging stage to accord with gas changes.
This ensures stable performance of the PAC at all times.

Patents are applied for

Japanese and foreign patents are being applied for, and some have already been granted.

1) Particle charging device for use in an electric dust collecting apparatus U.S. Patent No. 4018577.

CONSTRUCTION AND PRINCIPLE

A unit of the PAC consists of a discharge electrodes, control electrodes and collector electrodes.

Making full use of the electrodes' functions, the PAC has over-come such drawbacks to conventional electric precipitators as the back charge, the reentrainment and the corona suppression.

A strong electric field is generated between the collector and control electrodes by an electric source (1).

* Negative corona ions which are intermittently generated from the discharge electrode by an electric source (2) are led to the space between the collector electrode and the control electrode to provide the maximum charge to the dust in exhaust gas.

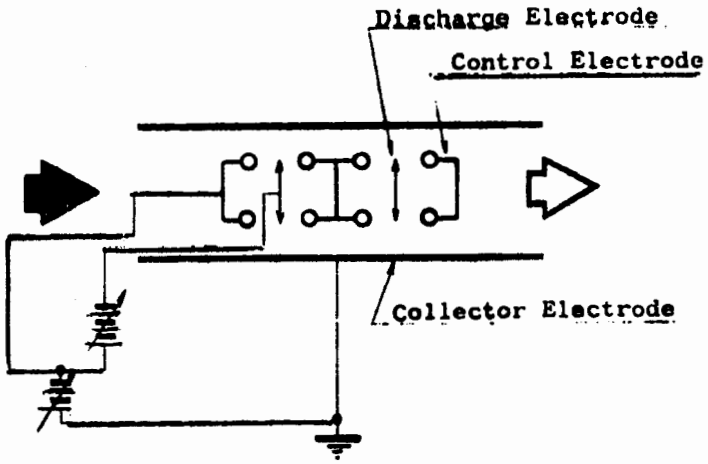

FUNCTION

Charging Dust Particles

Intermittently generated ionic clouds are led through a strong electric field, which has been preset by the control electrode, to the collector electrode as they are diffusing.

This method successfully prevents corona quenching and back discharge and permits dust particles to be charged at a rate far beyond that achieved by conventional EP's.

In the EP, an electric field is generated partially close to the discharge electrode. As a result, the electric field is not adequate and the rate of charging is limited.

In the PAC, independent control of the control electrode and the discharge electrode is available by individual electric sources which allow each electrode to operate efficiently with fluctuations of gas temperature, dust concentration, humidity, electrical resistivity of dust, etc.

Because of its construction, EP's voltage and current are in a fixed, functional relation and cannot be controlled independently. In contrast, the PAC can control voltage and current independently according to gas conditions, and consequently can precipitate all kinds of dust.

Gas Temperature Characteristics

As gas temperature rises, the electric field strength against breaking at the needle of the discharge electrode will be reduced and spark discharge will readily occur. To cope with this condition, the electrode voltage of the PAC is adjustable for controlling the electric field at the needle of the discharge electrode. Thus stable operation is maintained.

Unit Characteristics

The electrostatic screen created in the collecting stage prevents effects of ionic wind and permits dust particles to grow larger and coarser by electrostatic condensation.

As a result, in contrast to the EP, the PAC maintains constant high efficiency at each unit.

ES in progress of IHI's development techniques

In accordance with a conventional precipitation theory, IHI's engineering groups are developing the dust collection stage of ES type.

This stage consists of many pairs of guiding electrode and a collector electrode facing each other at right angles to the gas flow. While negative high voltage is applied to the guiding electrodes, the collector electrodes are grounded.

Between a pair of the electrodes a direct current electric field and a flow field of fluid dynamics are generated. The former moves the charged dust toward the pockets of collector electrodes and the latter keeps the dust inside the electric field and forces it into the pockets.

The electric field and the flow field combine to create an electrostatic screen (electro-fluid dynamics) for effective precipitation.

The dust thus adhered and accumulated in the pockets is dropped into a hopper by rapping.

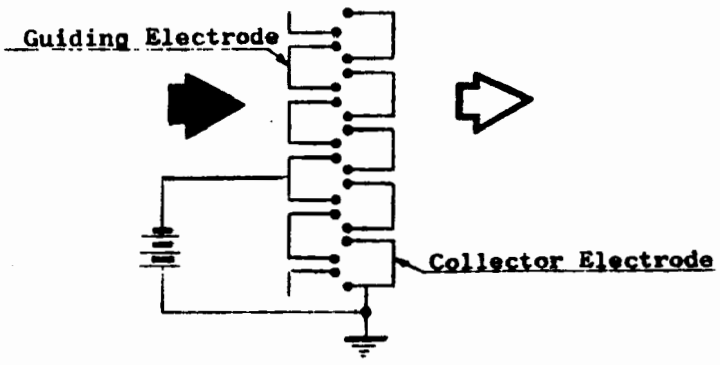

Portable test model of the PAC-ES

IHI has produced a large, portable test model of the PAC-ES and carried out testing with actual exhaust gases from iron and steel productions (gases from coolers of sintering plants and their environmental gases) and heavy oil boilers. In these tests the model was proved satisfactory.

"Table 1" shows the performance record of the portable test model.

Table 1 One example of data of performance test

Gas tested	Exhaust gas from cooler of sintering plant (cooler flue gas)		Exhaust gas from boiler (C heavy oil)	
Gas temp. ^{o}C	115 ~ 170		116 ~ 160	
Moist in gas %	0		9.9 ~ 12.3	
Gas Quantity m^3/min	48	78	40	60
Dust cont. (inlet) g/Nm^3	2.074	1.803	0.034	0.034
Dust cont. (outlet) g/Nm^3	0.0037	0.0083	0.0023	0.0034

APPENDIX C

HITACHI LTD.

HIGH TEMPERATURE ELECTROSTATIC PRECIPITATOR FOR COAL FIRED BOILER

H. Imanishi, Y. Oataki, K. Ootsuka,
and K. Watanabe

Introduction

The coal fired steam plants have been replaced with the oil fired ones since late 1950's and currently most of the steam plants utilize crude oil or gas. This is considered to be an appropriate consequence in the standpoint of fuel security, combustion restrictions and prevention of air pollution due to flyash. On the other hand, due to the protective policy for coal industry, some coal fired steam plants are still operating and some more plants are being planned. Also, the oil crisis which hit the world in late 1973 had a great impact to our country (Japan) and the reconsideration of fuel was strongly required. Therefore, the utilization of coal as fuel to the steam plants are reviewed seriously.

Because the coal fired boilers produce a great deal of ($10 \sim 30$ g/Nm^3) flyash, it is necessary to install a high efficiency electrostatic precipitator for the prevention of air pollution. However, the apparent resistivity of this flyash varies significantly due to the quality of coal this will effect the performance of electrostatic precipitators. Especially in the temperature range of $120 \sim 150$°C such as at the exit of air heater (A/H), the apparent characteristic resistance of dust is so high that is is sometimes hard to maintain a stable performance. This tendency is more obvious for a lower sulphur content in the coal.

Recently, in order to prevent an air pollution due to SO_x, there are very many steam plants, especially in the United States, which utilize coals with low sulphur content and the high temperature ESP is often considered for this purpose. Namely, the apparent characteristic resistance of fly ash is almost independent of the quality of coal and will be the value for a normal operating range of the ESP in a high temperature range between 350°C and 400°C. Thus, it is possible that the high temperature ESP will demonstrate a better performance than the low temperature ESP.

Here, we have confirmed a feasibility of the high temperature electrostatic precipitator by grasping the characteristics of dust in the coal fired boiler exhaust gases and the characteristics of precipitating rate. Based on this study, we have performed a model test at the pilot plant which use the coal fired exhaust gases. Following is the description of the high temperature ESP for coal fired boilers.

1. Principle of Electrostatic Precipitator

In order to separate and collect effectively those extremely tiny flyashes in gas, it is most sufficient to apply the electrostatic precipitator which utilizes the corona discharge. Figure 1 shows the principle of electrostatic precipitator. Normally a negative high voltage DC is applied to a discharging electrode and a precipitating electrode is connected to a ground.

Figure 1

PRINCIPLE OF ELECTROSTATIC PRECIPITATOR

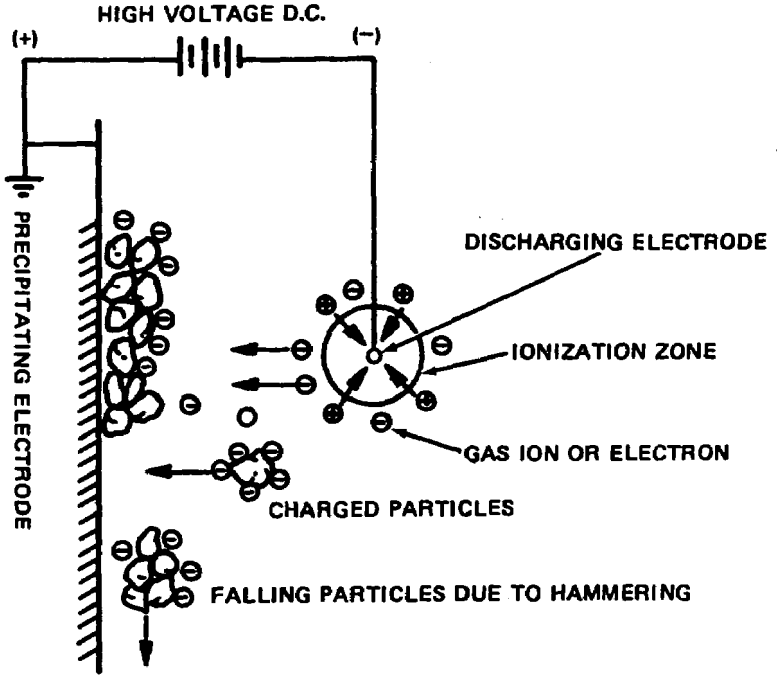

A discharging electrode uses a wire with a small curvature radius and negative ions are generated in this vicinity by producing a partial insulation break off, then the corona electrical current will move to the precipitating electrode. Drifting dusts will be charged by colliding with these negative ions and will be carried to the precipitating electrode by coulomb force and be accumulated on its surface.

The migration velocity of dust to the precipitating electrode is, as shown in Equation 1, proportional to the particle diameter (d) and square of the electrical field strength. Therefore unlike the case for mechanical precipitator, the precipitating rate does not decrease drastically for tiny dusts, and even extreme tiny dusts can be collected with a high precipitating rate in conjunction with precipitating process by Coulomb force. The precipitating rate can be expressed by Deutsch's equation Equation 2).

$$w = kdE_o^2 \qquad (1)$$

$$\eta = 1 - \exp\,[-Kw\tau] \qquad (2)$$

where w = particle migration velocity

d = dust diameter

E_o = electric field strength

k = constant

η = precipitating rate

τ = charging time

k = electrode constant

Based on these equations, a long charging time and a high electrical field strength are necessary to improve the precipitating rate. Also, it is necessary to apply appropriate size and type of discharging electrode and precipitating electrode, and any past experience was fully incorporated in this aspect. The characteristics of dusts and gases need to be reviewed in detail in the following apsects.

2. Dust Characteristics and Precipitating Efficiency

There are some factors, such as the concentration, particle size, precipitation, adhesiveness (adsorption) and apparent characteristic resistivity of the dusts in boiler exhaust gases, which will affect the efficiency of EP. These factors vary significantly depending on the fuel used in the boiler, boiler firing method and the operating temperature of EP. Table 1 shows the dust characteristics of boiler exhaust gas for the coal-fired boiler and the crude oil-fired boiler.

2.1 Effect of The Contained Ash Concentrations

The higher the contained ash concentrations are, the lower the corona electrical current is for a constant charging voltage. Thus it is necessary to make a charging voltage high in order to maintain a constant corona electrical current. When the same corona electrical current is maintained the precipitating rate will increase accordingly with dust concentrations, because the specific

Table 1. Boiler Exhaust Gas Dust Characteristics

Item	Item	Coal fired	Crude oil fired
Amount of ashes	g/Nm^3	17~25	0.05~0.2
Average particle size	μ	20~30	10~12
Dust composition			
SiO_2	%	50~55	Ashes 15~20
Al_2O_3	%	27~30	
SO_3	%	0.3~0.7	25~35
C	%	0.3~1.0	50~60
Apparent characteristic resistivity	Ω-cm	$1x10^{12-13}$	$1x10^{3-5}$

area of the dust contained per unit gas volume will become larger and the electrical field strength in the precipitating region will increase. However, when the electrical field strength exceeds a certain limit, there will be strong sparks and a stable charging cannot be maintained.

2.2 Effects of Particle Size and Physical Characteristics

The smaller the particle size is, the smaller the electrical charges and the migration velocity of the precipitating electrode are. On the other hand, since smaller particles have more active movements and different size particles collide with the relative velocities due to different amount of charges, it is easy to precipitate them. Actually it is possible to precipitate extremely small particles such as fume with high efficiency. This precipitating function can be promoted by the particle's moisture absorbent characteristics. The precipitation characteristics extensively depend on dust composition and particle size, but this has not been totally analyzed yet.

A Region ---- Low voltage, large current, stable charge, low function region

B Region ---- Normal Region

C Region ---- High voltage, low current, decreasing η region

D Region ---- Unstable charge, decreasing η region

E Region ---- Low voltage, large current, stable charge, low function region

Anyway, small particles promote to extend precipitations and help the electrostatic precipitator improve its efficiency. On the other hand since tiny particles have strong adsorption which will cause a problem to adhere to precipitating electrodes and will be a cause of decreasing efficiency of electrostatic precipitating, it is necessary to be careful in handling. The adsorption of dusts decrease with high temperature and the mobility of dusts increase.

2.3 Dust Apparent Characteristic Resistivity and Behavior of EP

The apparent characteristic resistivity is the most important factor among those which affect EP performance. Normally the values of apparent characteristic resistivity with which EP can maintain a stable performance are, as shown in Figure 2, in the region of 10^4~10^{11} Ω-cm and it is difficult to precipitate particles outside of region. In A Region (less than 10^4 Ω-cm) of Figure 2, the dust whose main composition is carbon such as the crude oil-fired boiler exhaust gas dust may escape without being effectively precipitated because of the low apparent characteristic resistivity causes the reentraining phenomena. In regions C, D, and E, tiny dusts whose main composition is silica such as fly-ashes, cement dusts and fine particle emissions from metal refinery will cause an inverse ionization phenomena (the voltage between the surface and the inside of dust layer over the electrode will increase, and an electrical breakdown will be created to neutralize electrons from discharging electrode and the discharging

Figure 2. Precipitator Operating Characteristics As a Function of Particulate Resistivity

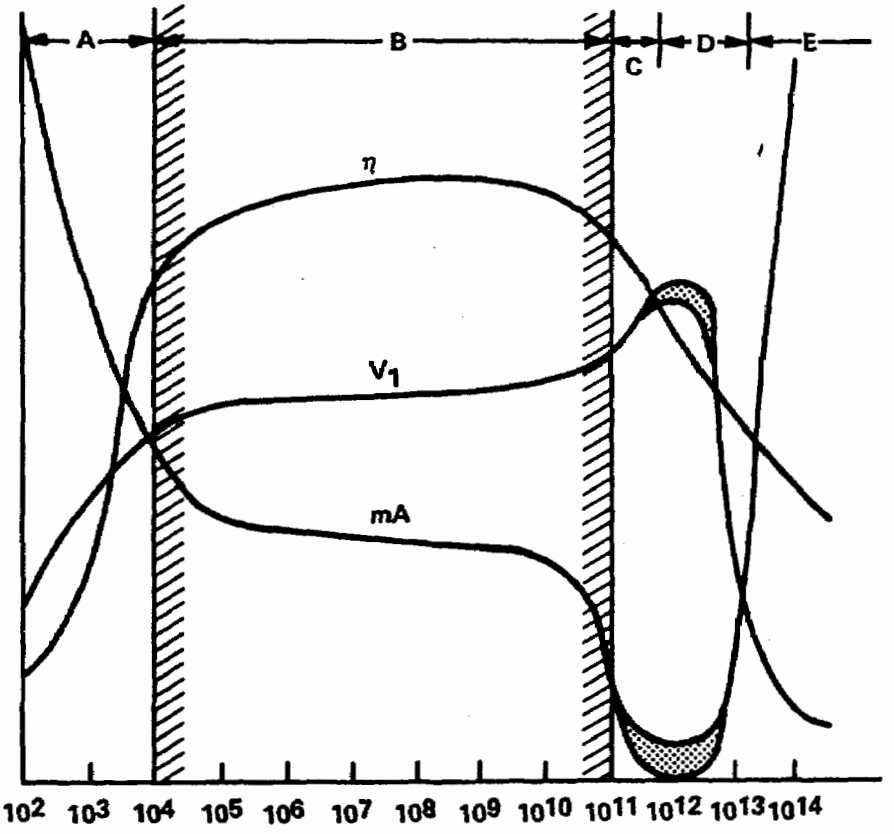

condition will be unstable), and the precipitating performance will be considerably decreased.

Also this apparent characteristic resistivity depends on a sulphur content of the fuel used in the boiler and a temperature and it will decrease with higher sulphur content and higher exhaust gas temperature as shown in Figure 3. Table 2 shows one example of the apparent characteristic resistivity of coal-fired boiler exhaust gas dusts.

Table 2. Apparent Characteristic Resistivity of Coal-Fired Boiler Exhaust Gas Dusts

Temperature	Sulphur content in fuel	Apparent characteristic resistivity	EP precipitation degree
Low temperature region (120~130°C)	1.0~2.0%	10^{10}~$10^{11}\Omega$-cm	Easy
Air preheater exit	less than 1%	10^{12}~$10^{13}\Omega$-cm	Difficult
High temperature region (300~400°C)	1.0~2.0%	10^{9}~$10^{10}\Omega$-cm	Easy
Coal saver exit	less than 1%		

When the EP is used in the low-temperature region, it is possible to have a normal precipitation for high-sulphur-content coal dusts. But it is difficult to have a normal precipitation for low-sulphur-content coal dusts because the apparent characteristic resistivity is as high as 10^{12}~$10^{13}\Omega$-cm and an inverse ionization phenomena are created. On the other hand, in the high-temperature region, since even the low-sulphur-content coal dusts are affected by the temperature and the apparent

Figure 3. Dust Apparent Characteristic Resistivity and Temperature

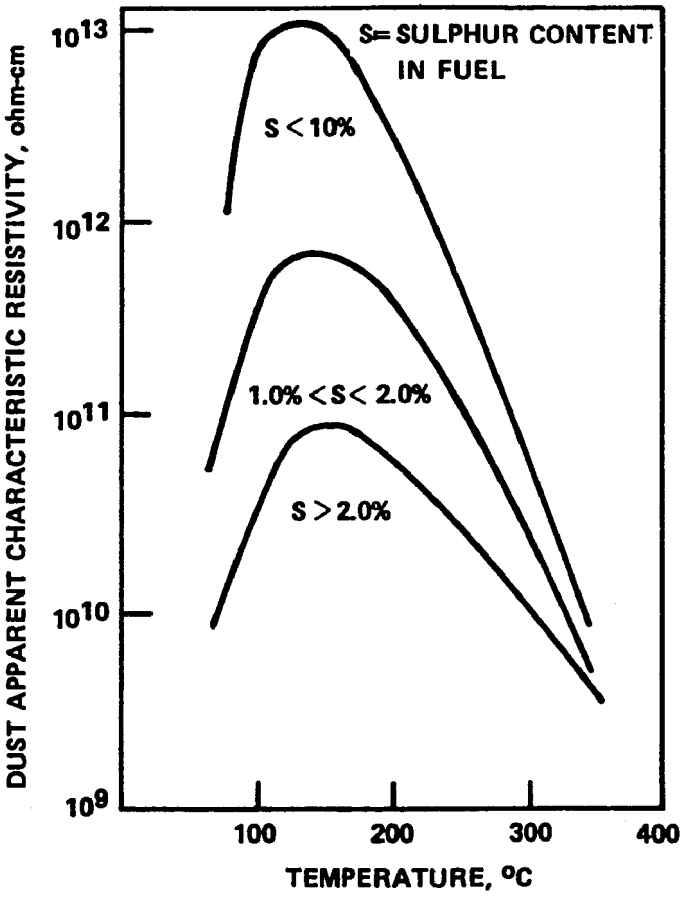

characteristic resistivity is decreased as low as 10^9~$10^{10}\Omega$-cm, it is possible to have a normal precipitation. Therefore in high temperature region, it is possible to have a constant precipitation with high efficiency for any quality of coal.

Thus, as shown in Figure 4, the size of EP due to the sulphur content of coal varies significantly at 150°C depending on the sulphur content while it is constant at 320°C. It is therefore advantageous to apply high temperature EP in order to obtain a high efficiency constantly regardless with the quality of coals.

3. Characteristics of High Temperature EP

As a purification purpose of coal-fired boiler exhaust gas, high temperature EP has the following advantages as compared with ordinary low temperature EP.

1) High performance can be obtained regardless with quality and sulphur content of coal.
2) It is easy to fall off dusts by hammering and it is seldom to degrade its performance by dust adsorption to precipitating electrode and discharging electrode.
3) It has better dust mobility in hopper and has less trouble with ash stuck.
4) It is possible to keep the A/H in a clean condition longer than usual and to have less decrease of A/H performance and require less frequent use of the sort blower.

Figure 4. Sulphur Content in Coal and and Size of Precipitator

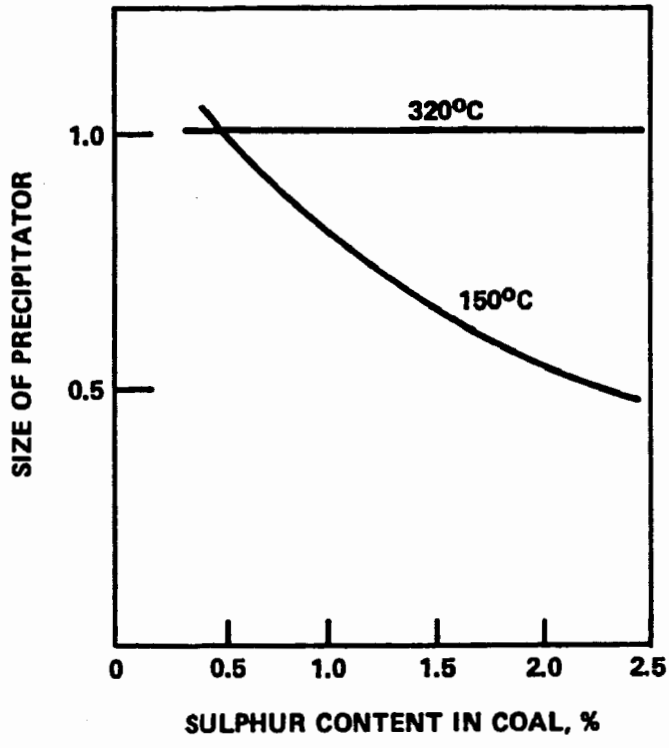

Including the above characteristics, Table 3 shows a comparison of high-temperature EP and low-temperature EP for high resistivity dusts. As an environmental integrity standpoint and in order to decrease extensively the fly ashes from the low-sulphur-content coal-fired generating plant, it is most certain (promising) to use the high-temperature EP which can maintain high efficiency without affected by coal quality.

4. Experience of High-Temperature EP

Generally in our country, since the standard limit of fly ash exhaust with EP was high and domestic coals with relatively high sulphur content were used, only low-temperature EP was used in stand alone or in combination with multi-cyclon (MC) and we have hardly had an experience with high-temperature EP for coal-fired boilers. But recently in the United States, since the low-sulphur-content coals have been used more often for larger volume of boilers and ordinary low temperature can no longer maintain high performance for these boilers, the application of high-temperature EP has been widely accepted in order to prevent the degradation of EP performance for low-sulphur-content coal and its technology has been well established. According to our survey, more than 70 units of high-temperature EPs (including thos under constructions) have been installed. Especially in the West of the United States where great amounts of low-sulphur-content coals are obtained, about 60% of constructed generating plants use high-temperature EPs. Figure 5 presents installations of high-temperature EPs in the United States (including presently

Table 3. Comparison of EP Concept for High Resistive Dusts

Item	Low temperature EP (140°C)	High temperature EP (350°C)
Performance		
Real gas amount	Base	About 1.5 times
Gas viscosity	Base	About 1.4 times
Dust apparent characteristic resistivity	10^{11}~10^{13}	$<10^{11}$
Dust moving velocity	Small	Large
Precipitation performance	Fair	Excellent
Performance for coal quality variation	Fair	Excellent
Re-scattering	Large	Small
Maintenance		
Air heater ash adsorption	Large	Small
Hopper ash stuck	Medium	Small
Ash mobility	Small	Large
Anti-corrision	Not necessary	Not necessary
Thermal expansion	Small	Large
Economy		
EP volume	Small	Large
Composing material quality	Ordinary steel	Ordinary steel
Width for heat insulation	30-50 mm	100-200 mm

Figure 5. Installations of High Temperature EP for Coal Fired Generating Plants in the U.S. (Including ones under construction)

under construction or under planning). Table 4 is an example of the operating experiences and as you can see good results have been achieved.

4.2 Experience in Ordinary Industrial Application

For ordinary industrial plants which create ashes, the ash compositions and characteristics vary depending on the used main raw material, the used sub-raw material, kind of fuel and amount of fuel. The temperature range in which EP is used is fairly wide and some system (plant) requires to be processed as high as at 400°C due to its characteristic. There have been some ordinary industrial high-temperature EPs installed in our country and their main applications are for exhaust gas purification of such as cement kiln, metal refinery, and city garbage-burning boiler. Among these EPs, those EPs such as the former ones require to be processed at a high temperature in order to return the collected dusts to production process for a re-utilization of raw materials, but the main reason for high temperature application is that the apparent characteristic resistivity is too high at low temperature and that the applicable region of electrostatic precipitator is exceeded. Table 5 shows some of these operating experiences.

5. Coal-Fired Boiler High-Temperature EP Model Test at Ebetsu Generating Plant

The purpose of this model test was to verify precipitation characteristics and fundamental data for actual system design at high-temperature regions, and as a result the original objectives

Table 4. High Temperature EP Operating Experiences in the United States

Generating Plant	A		B		C		D		
Fuel (Coal)									
S Content	0.2 1.2%		1.3%		0.24 0.65%		0.5% (Average)		
Ash Content	6 15%		18.3%		3.4 22%		7.9% (Average)		
Heat	5,277 kcal/kg		6,138 kcal/kg		4,555 kcal/kg		6,000 kcal/kg (Average)		
Unit No.	1	2	1	2	1	2	1	2	3
Specifications									
Capacity	105 MW	120 MW	350 MW	←	447 MW	←	750 MW	←	←
Gas Amount	999,260 m^3/h	1,138,440 m^3/h	2,948,000 m^3/h	←	5,012,640 m^3/h	←	6,698,000 m^3/h	←	←
	(430,960 Nm^3/h)	(478,145 Nm^3/h)	(1,249,695 Nm^3/h)	←	(2,079,712 Nm^3/h)	←	(2,839,000 Nm^3/h	←	←
Gas Temperature	360°C	377°C	371°C	←	385°C	←	371°C	←	←
Entering Ash Amount	1.5 g/Nm^3	1.1 g/Nm^3			1.3 g/Nm^3	←	9.2 g/Nm^3	←	←
Precipitating Rate	97.9%	97.9%	99.5%	←	Design Value 99.9%	←	99.5%	←	←
Initial Operation	'76.4	'75.10	Under construction	'73	Under construction		'74.5	'75.3	

Sketches Related to Table 4

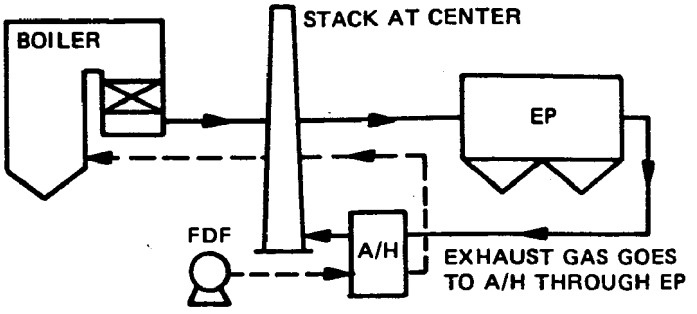

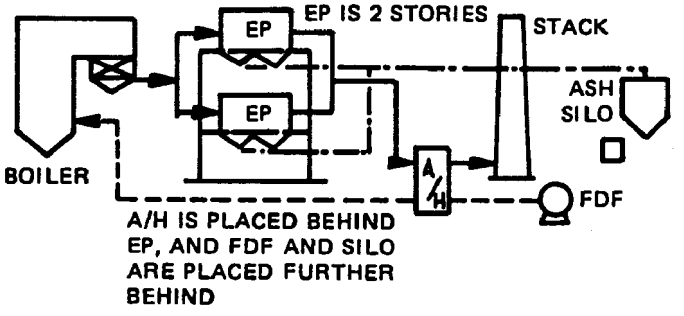

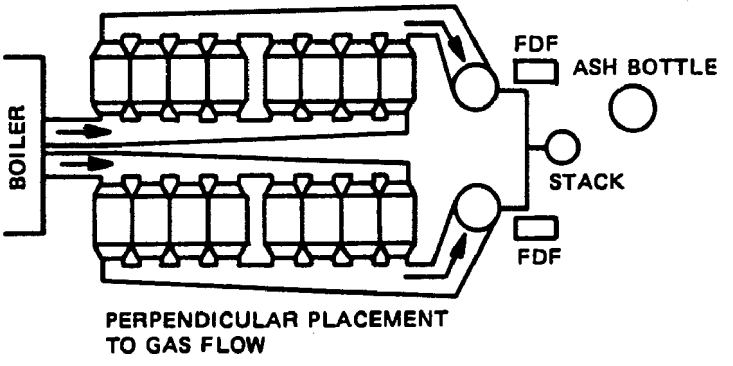

Table 5. Ordinary Industrial High Temperature EP Operating Experiences in Japan

	Gas Amount	Gas Temp.	Precipitating Rate	Initial Operation
Cement Clinker Cooler	775,000	248	99.97	'73.9
Cement Clinker Cooler	536,300	295	90.4	'74.5
Cement Clinker Cooler	462,300	237	99.51	'70.9
Metal Refinery Sulphur Metal Burning Boiler	89,200	334	99.5	'68.2
Metal Refinery Copper Self Burning Boiler	131,800	285	99.6	'73.8
Sulphate Production Zinc Metal Burning Boiler	45,600	319	99.92	'67.3
City Garbage Burning Boiler	81,300	360	98.1	'72.3
City Garbage Burning Boiler	79,000	328	99.7	'73.11
City Garbage Burning Boiler	110,900	302	99.88	'73.3
City Garbage Burning Boiler	88,000	285	99.1	'72.7

have been achieved and the precipitation characteristics have been grasped as well as various findamental data have been verified. The following is the general description of this test.

5.1 Design Specification and Test Condition

Table 6 shows the design specifications for this test. This test utilized the No. 3 boiler (specifications shown in Table 7) and coals as fuel (S content 0.2~0.5%) with a normal burning condition (O_2% in exhaust gas and etc.) of boiler, and we have verified dust characteristics (fly ash amounts, apparent characteristic resistivity, etc.) as well as precipitation characteristics due to coal quality. Figure 6 shows the flow-sheet of the pilot plant and Figure 7 shows its exterior view.

5,2 Test Results

1) Entering Fly Ash Amounts and Precipitating Rate

Even when the entering fly ash amounts varied from 15 g/Nm^3 to 35 g/Nm^3, the precipitating rate did hardly change. Figure 8 shows the result of measurements.

2) Gas Temperature and Precipitating Rate

When the gas temperature is at 300~365°C, the apparent characteristic resistivity of dusts is about 10^8~10^9Ω-cm which has no effect to precipitating rate. Actually there was hardly any change in precipitating rate. Figure 9 shows this result of measurement.

Table 6. Design Specifications

Item	Specification
Process gas amount	2,000 Nm^3/h
Process gas temperature	350°C
Entering fly ash amount	20 g/Nm^3
Exiting fly ash amount	0.04 g/Nm^3
Precipitating rate	>99.8%
High temperature EP	
- Type	SO-HP_{12} (steel plate and frame outside type, horizontal gas flow 1 chamber 2 sections)
- Precipitating electrode	
Type	Angular wave type precipitating electrode plate
Distance	300 mm
- Discharging electrode	
Type	Frame composing type
Size	4 mm angular
- Charging facility	
Power level	DC 60 Kv DC 60 mA
Unit	2 units

Table 7. Specifications of Tested Boiler

Item	Specification
Power	125 MW
Boiler type	B&W, reheat single body emitter type
Ventilation system	Balance ventilation
Burner system	Circular burner
Burning system	Tiny powder coal burning, crude oil mixed burning
Air preheater	Ljunstrom type

Figure 6

FLOW SHEET FOR THE PILOT PLANT

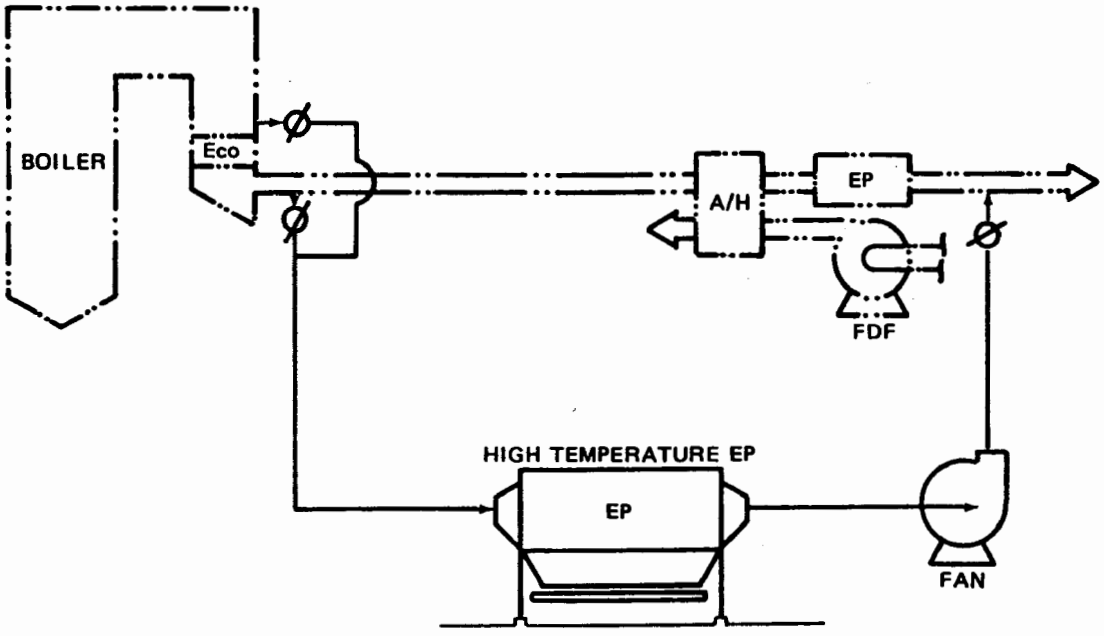

Figure 7. Photograph of Exterior View

(not reproducible)

Figure 8

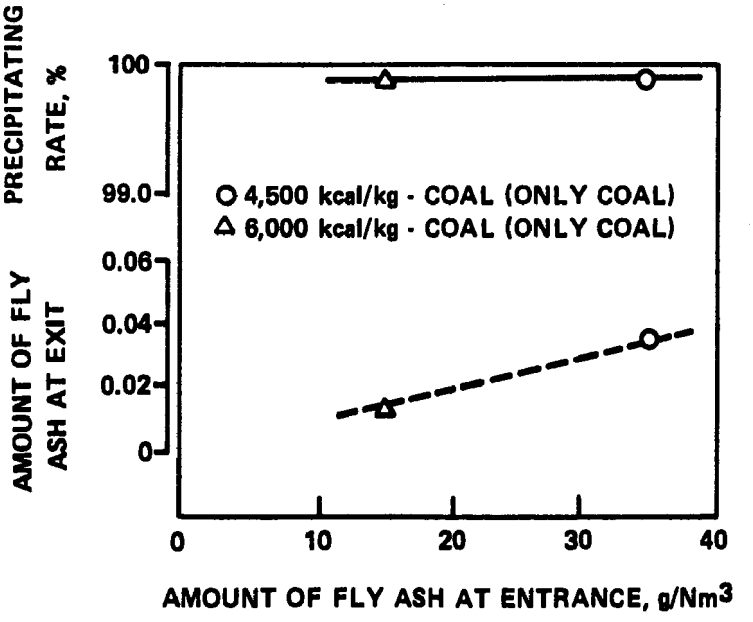

AMOUNT OF FLY ASH AT ENTRANCE
VS. PRECIPITATING RATE

Figure 9
Gas Temperature Vs. Precipitating Rate

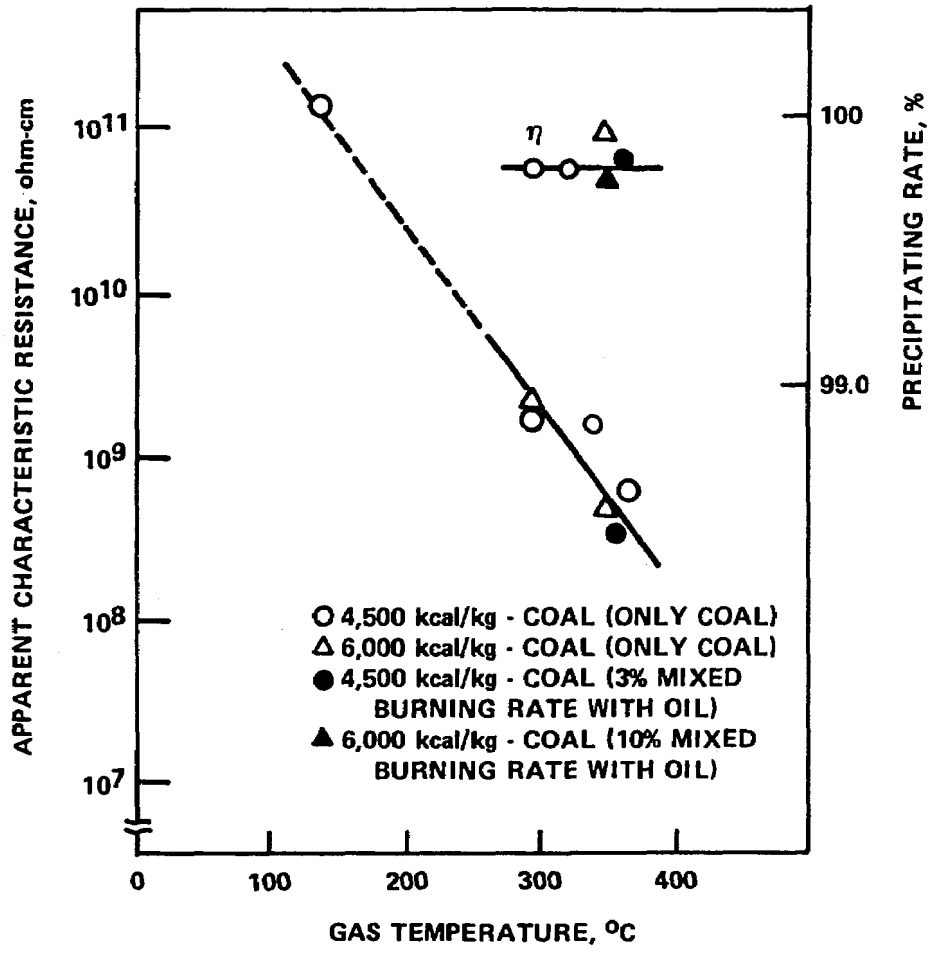

3) Process Gas Amount and Precipitating Rate

In order to verify the relationship between the performance and the process gas amount which is the important factor to determine the size of EP, we have done the gas amount variance test. Its result is shown in Figure 10.

Also, in order to investigate the effect of gas velocity in the EP to the precipitating performance, we have done tests by changing duct numbers (passing cross-section) of the pilot EP. But there was no re-scattering phenomena of dusts due to gas velocity increases and the expected precipitating performance was obtained as planned.

4) Charged Voltage and Precipitating Rate

As shown in Equation (1), the relationship between charged voltage and precipitating rate is that the square of charged voltage contributes to the performance. The result of this measurement is shown in Figure 11. It was determined from this figure that the charged voltage should be more than 35 Kv but that the charged voltage more than 40 Kv did have little effect in performance.

Based on these results, it was concluded that the high temperature EP is the most effective one for coal-fired boiler exhaust gas fly ashes.

Also, this pilot EP had operated continuously for about 7,000 hours and had always maintained stable performances during this test period.

Figure 10
Process Gas Vs. Precipitating Rate

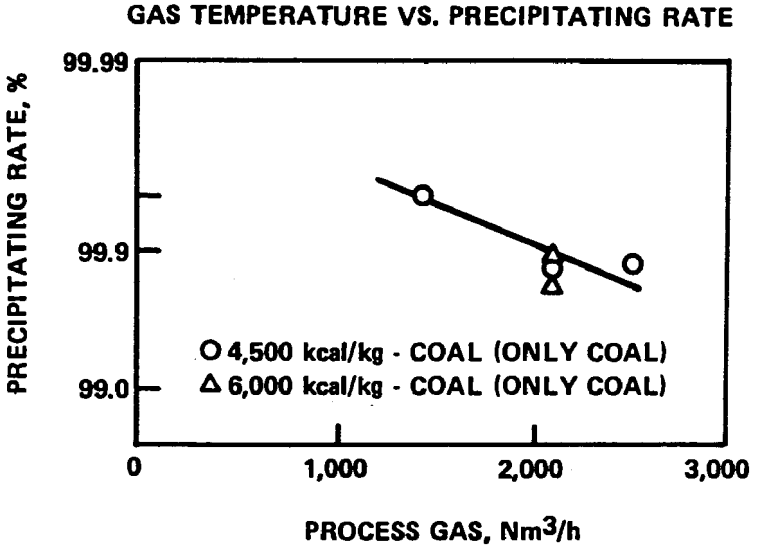

Figure 10
Process Gas Vs. Precipitating Rate

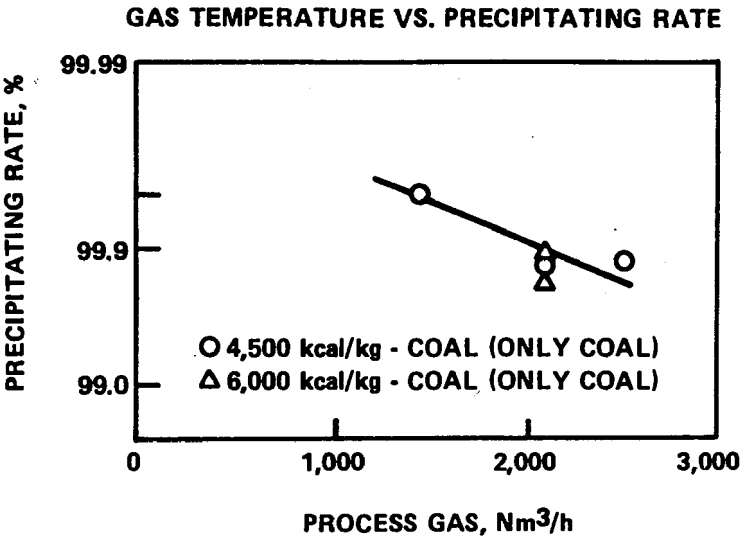

Figure 11

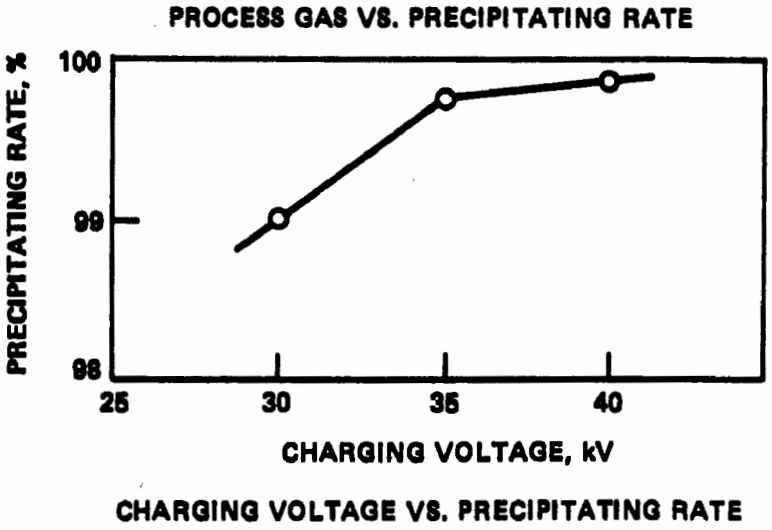

CHARGING VOLTAGE VS. PRECIPITATING RATE

6. Problem Area and Counter Plan for High Temperature ESP

Although a high temperature electrostatic precipitator is very effective for the boiler which utilizes coals of a low sulfur content, there are following problems when compared with a low temperature ESP:

(1) Since it is operated at high temperature, real quantity of gas will be huge.

(2) Placement space including ESP is larger and the duct work is somewhat complicated.

(3) Amount of heat diffusion from external surface of ESP is larger.

(4) Thermal expansion and decrease in material strength is larger

It is possible to cope with items (1) and (2) by reviewing the overall placement including boiler in the planning stage. Enough heat insulation will be required for item (3). It is also possible to cope with item (4) based on the design of experienced industrial high temperature ESP (for cement, metal refinery and normal city dusts etc.). Table 8 shows a comparison between high temperature electrostatic precipitators and low temperature electrostatic precipitators in configuration.

CONCLUSION

This paper has presented a principle of high temperature ESP and a part of experimental results at the Ebetsu Generating Plant. This experiment has confirmed the feasibility of designing 350 MW size high temperature electrostatic precipitators.

We would express our deep appreciation to the following parties for various assistances and helps in testing the pilot plant: Mr. Okizaki, Manager, Department of Steam Plant, Hokkaido Electric Power Co.; Mr. Kobayashi, Plant Manager, Ebetsu Generating Plant; Mr. Ikemi, Manager, Department of Environmental Technology, Hitachi, Ltd.; Mr. Arikawa, Hitachi Laboratory; Mr. Kawaike, Manager, Precipitator Planning, Hitachi Plant Engineering and Construction.

Also we would appreciate all the assistance given by the Babcock Hitachi Co.

Table 8

Comparison between High Temperature ESP and Low Temperature ESP in Configuration

	Item	High Temperature ESP	Low Temperature ESP (Usual)
(1)	Steel frame chamber	Separate steel frame (holder) from precipitating chamber and apply sliding mechanism.	Steel frame (holder) and precipitating chamber are combined.
(2)	Pitch between electrodes	Apply 300 mm after considering decreases in spark voltage and strain due to temperature.	250 mm
(3)	Electrode plate	Apply special angular wave type electrode plate, thermal strain less than 5 mm at 350°C (experimental value).	Strain about 10 mm
(4)	Discharging electrode	Use discharging wire of 4mm with frame type	Same as left
(5)	Glass tube chamber	Glass is made of Almina and seal air is put in for anti-stain.	Glass is white ceramic. Seal air is put in.
(6)	Precipitating Electrode (Plate) Hammer	Hammer is set considering expansion of electrode plate.	No special consideration.
(7)	Discharging Electrode (Plate) Hammer	Hammer is a vertical shaft type attached to the discharging frame, and the overall system is hung from the top.	Same as left
(8)	Position determining beam.	Not supported by casing, but placed on the electrode (plate) and hung from above.	Supported by casing.

References

(1) Hashimoto, Taniguchi: "Principle and Application of Electrostatic Precipitator", Denki Shoin (1965-10)

(2) Society of Electrical Engineering (Electricity), "Electrical Technology Special Committee Report of Anti-Pollution" 2nd Edition No. 45 (1976-9)

HIGH TEMPERATURE ELECTROSTATIC PRECIPITATOR FOR COAL FIRED BOILER

Y. Oataki, K. Ootsuka, and K. Watanabe

(1) Introduction

One of the factors which affect the precipitating efficiency of the electrostatic precipitators (EP) is a apparent characteristic resistivity (ρ) of dusts. This ρ varies depending on a dust composition and a gas temperature. Especially the fly ash dusts produced in the coal fired boilers are affected strongly by the sulphur content in coal and sometimes cannot be precipitated in a stable manner due to high ρ at the exit of air heater whose gas temperature is 130 - 150°C.

Recently, re-evaluation of fuel have been strongly required and the coal fired boiler is being reconsidered. In this case, the low sulphur content coals will probably be the main source due to the standpoint of anti-pollution from SO_x. Especially in the United States, there are very many steam plants which utilize coals with low sulphur content and the high temperature Electrostatic Precipitators the important part for processing dusts. This is based on the fact that ρ decreases and is independent of the coal quality at high gas temperatures as shown in Figure 1, and the precipitation is done within a high gas temperature region of 350 - 400°C by placing the EP at the economizer exit of the boiler.

However, because we have not had any experience with high temperature EP for boilers in our country, we have developed a pilot plant with a real gas (2000 Nm^3/h) and evaluated the operating efficiency of the high temperature EP.

Figure 1. Sulphur Content, Temperature and Electrical Resistance

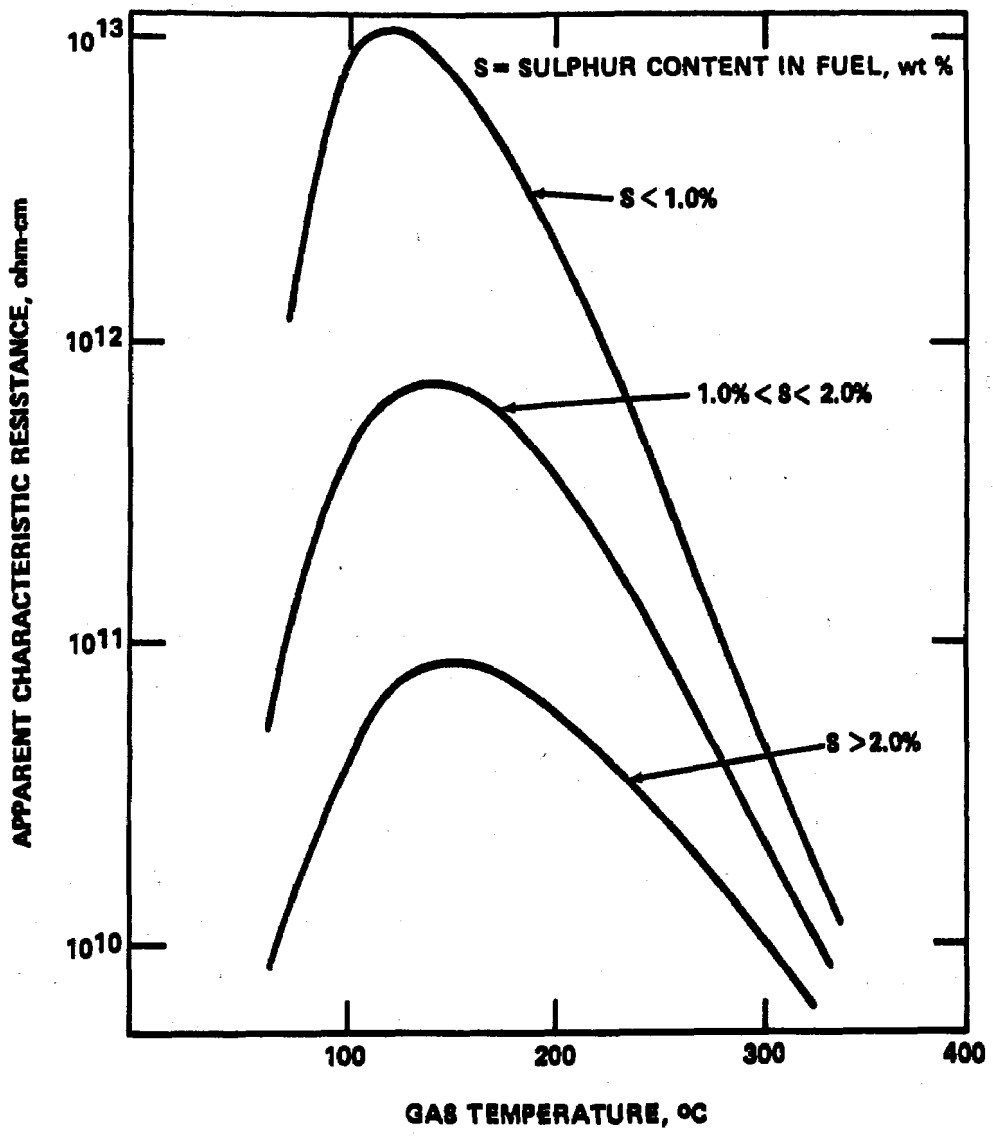

(2) General Description of Pilot Plant

A test was performed by installing experimental apparatuses shown in Table 1 at the Ebetse Generating Plant Unit No. 3 (125 MW), and the expected performance was experienced. Figure 2 is its flow sheet. Table 2 shows a composition of coals used for this test.

(3) Description of Operating Results

3-1 Voltage - Current Characteristics

When gas temperature increases, there will be more electrical current because a relative density ∂ of gas decreases and a molecular movement becomes active.

$$\partial = \frac{273 + 20}{273 + t} \cdot \frac{P}{760} \qquad (1)$$

As a result of this, a spark voltage decreases and it will be difficult to maintain a high electrical field strength. Also when a dust concentration becomes high, a total surface area of fly ashes per a unit gas volume becomes larger and an electrical current will be restricted. Figure 3 presents a voltage-current characteristic of gases for air load and at high temperature. Since section 2 has a lower dust concentration than Section 1, it will be easier to have an electrical current.

3-2 Gas Temperature and Precipitating Rate

We have changed a gas temperature and investigated a relationship between the apparent characteristic resistivity (ρ) of dust and the precipitating rate. Figure 4 shows its result. ρ changed from 1.8×10^9 Ω-cm (at Tg = 300°C) to 8×10^8 Ω-cm (Tg = 365°C) but the precipitating rate did not almost change. We also have compared the quality of coal between 4500 kcal/kg and 6000 kcal/kg, there was no difference due coal quality at a high temperature region. We further have investigated the case of mixed burning with crude oil but there was no effect in performance.

Table 1. Design Specifications

Items	Specifications
Gas Flow Rate	2,000 Nm^3/h
Process Gas Temperature	350°C
Type	$SO\text{-}HP_{1.2}$
Precipitating Electrode	
Type	Angular Wave Type Precipitating Electrode Plate
Gap	300 mm
Discharge Electrode	
Type	Frame Composition
Width	Angular Wire
Charging System	
Power	DC 60 kv, 60 ma
Unit No.	(2 units)

Figure 2. A Flow Sheet of Pilot Plant

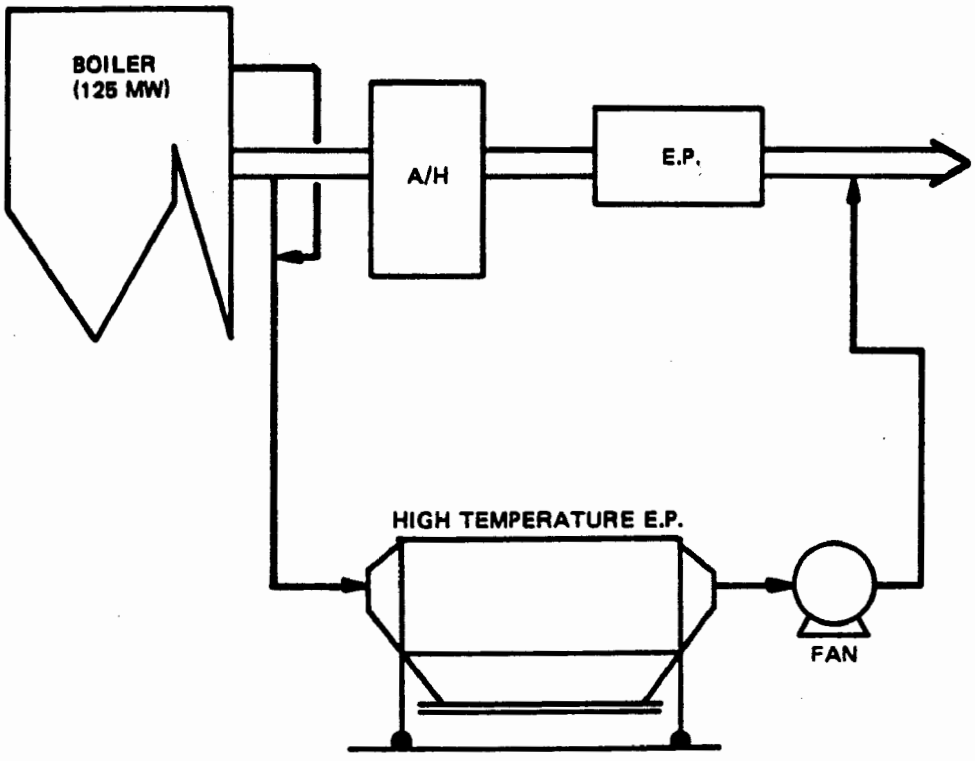

Table 2. Coal Compositions

Heat	4500 kcal/kg	6000 kcal/kg
Sulphur Content	0.43%	0.26%
Ash Content	36.6%	17.6%

Figure 3. Voltage-Current Characteristics

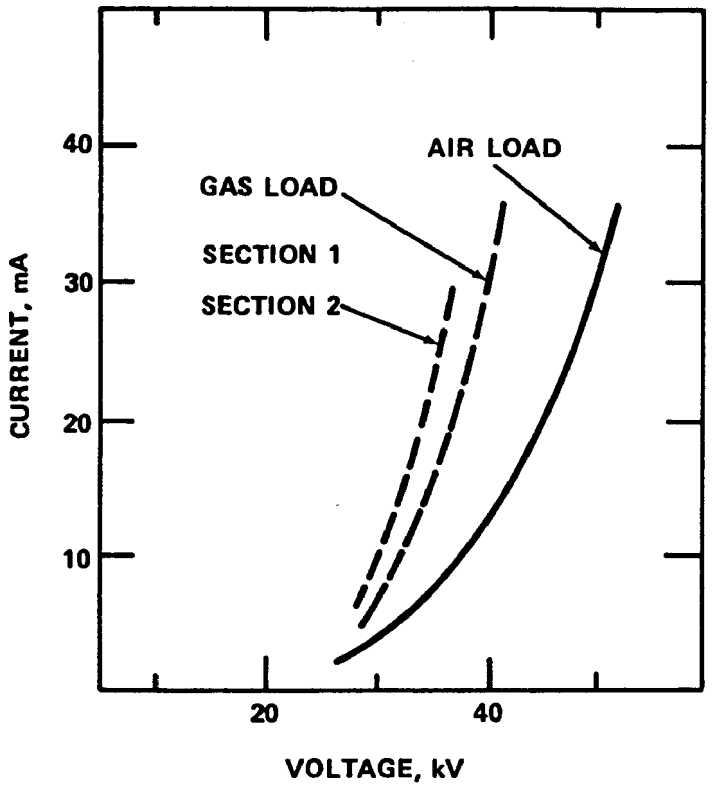

Figure 4. Gas Temperature Vs. Precipitating Rate

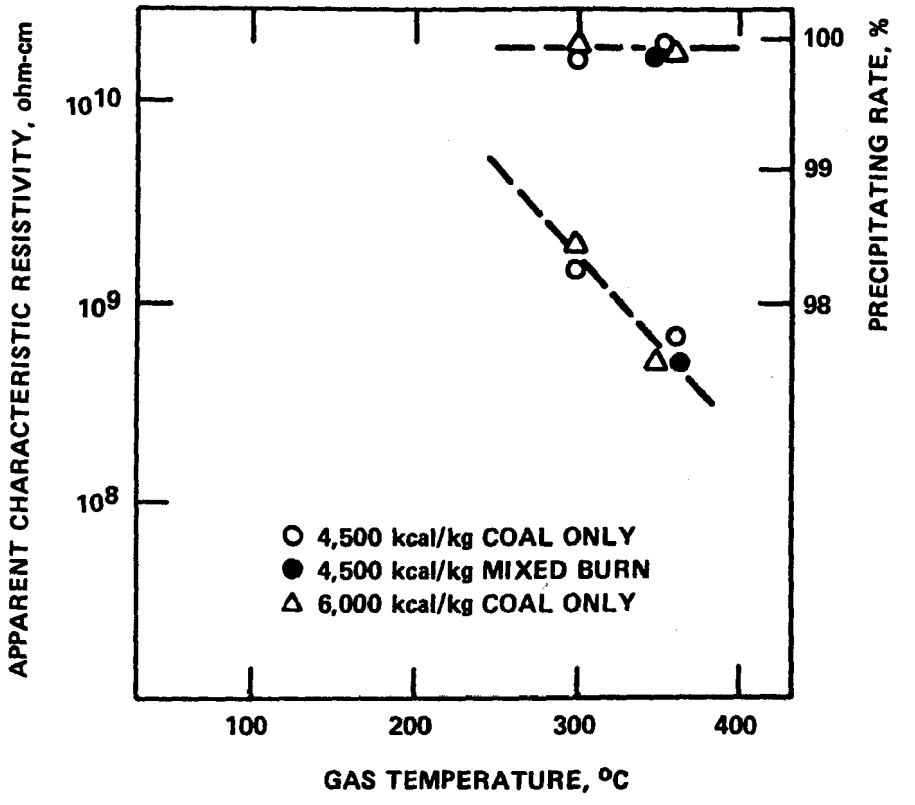

3-3 Performance of High Temperature Electrostatic Precipitator

In order to confirm the relationship between a performance of EP and a scale factor which is the major factor to determine the size of EP, we have performed tests by changing the quantities of process gas. As shown in Figure 5, the result better than the planned precipitating rate was obtained for the planned gas amount (2000 Nm^3/h). Also as stated before, it was confirmed that there was no effect by the quality of coal.

(4) Conclusion

We have grasped the performance of high temperature EP by using the pilot plant and confirmed that the expected performance can be obtained regardless of coal quality.

(5) References

1) Hashimoto, Tanignchi: Principle and Practice of Electrostatic Precipitator, Denkishoin

2) Society of Electronics: Anti-Pollution Electrical Technology Special Committee Report: 2nd Edition Volume 45 (1976-9)

Figure 5. Scale Factor Vs. Precipitating Rate

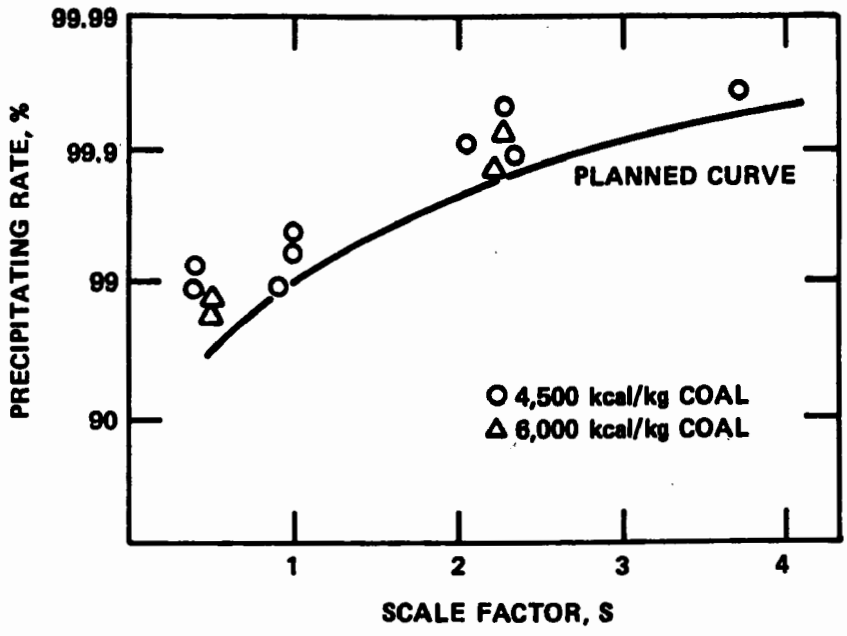

ELECTRIC FIELD DISTRIBUTION IN WIDE PLATE SPACING ELECTROSATIC PRECIPITATOR

T. Misaka, S. Matsubara,
and K. Fujibayaski

This paper discusses the results of an experimental investigation to map the electric field as a function of position for a variety of corona to collection electrode spacings. The electric field values were determined by the use of conducting spheres dropped through a corona discharge into a Faraday cage. The field distribution measured follows closely to that expected from theoretical conditions used in the E.P.A.-SRI computer systems model.

1) Since it is known that the precipitating rate does not decrease with expanding the precipitating electrode space in the electrostatic precipitator (EP), the EPs with wider precipitating electrode space than ordinary ones are used. This is contrary to the result of Deutch's equations. We think that a reason to this is associated with the distribution of electrical field strength in the EP and have analyzed the relationship between precipitating electrode space and electrical field strength distribution.

2) Experimental Apparatus and Experimental Method

In order to measure the electrical field strength in the EP, we have used the steel ball drop method since it is considered to be the best method. Figure 1 shows the experimental apparatus. A flat plate was used as the precipitating electrode and the precipitating electrode space was made to be changeable from 250 mm to 750 mm. A 4 mm angular wire was placed in the discharging electrode with 200 mm space. A measurement was done in the area indicated in Figure 1.

3) Experimental Results and Review

Since the precipitating electrode spacings are different, a comparison of the electrical field strength distribution was done with a same average electrical field strength (Changing voltage and distance between discharging and precipitating electrodes). Figure 2 shows the experimental results. In the region of 100 mm from the discharge electrodes, the electrical field strength has a same tendency and is independent of precipitating electrode space. When a distance from the discharging electrodes becomes larger than that, the electrical field strength will gradually increase as it approaches the precipitating electrodes. The electrical field strength in the vicinity of the precipitating electrodes is about 1.47 times (for 500 mm) and 1.02 times (for 750 mm) that of the precipitating electrode spaces with 250 mm.

Figure 1. Experimental Apparatus

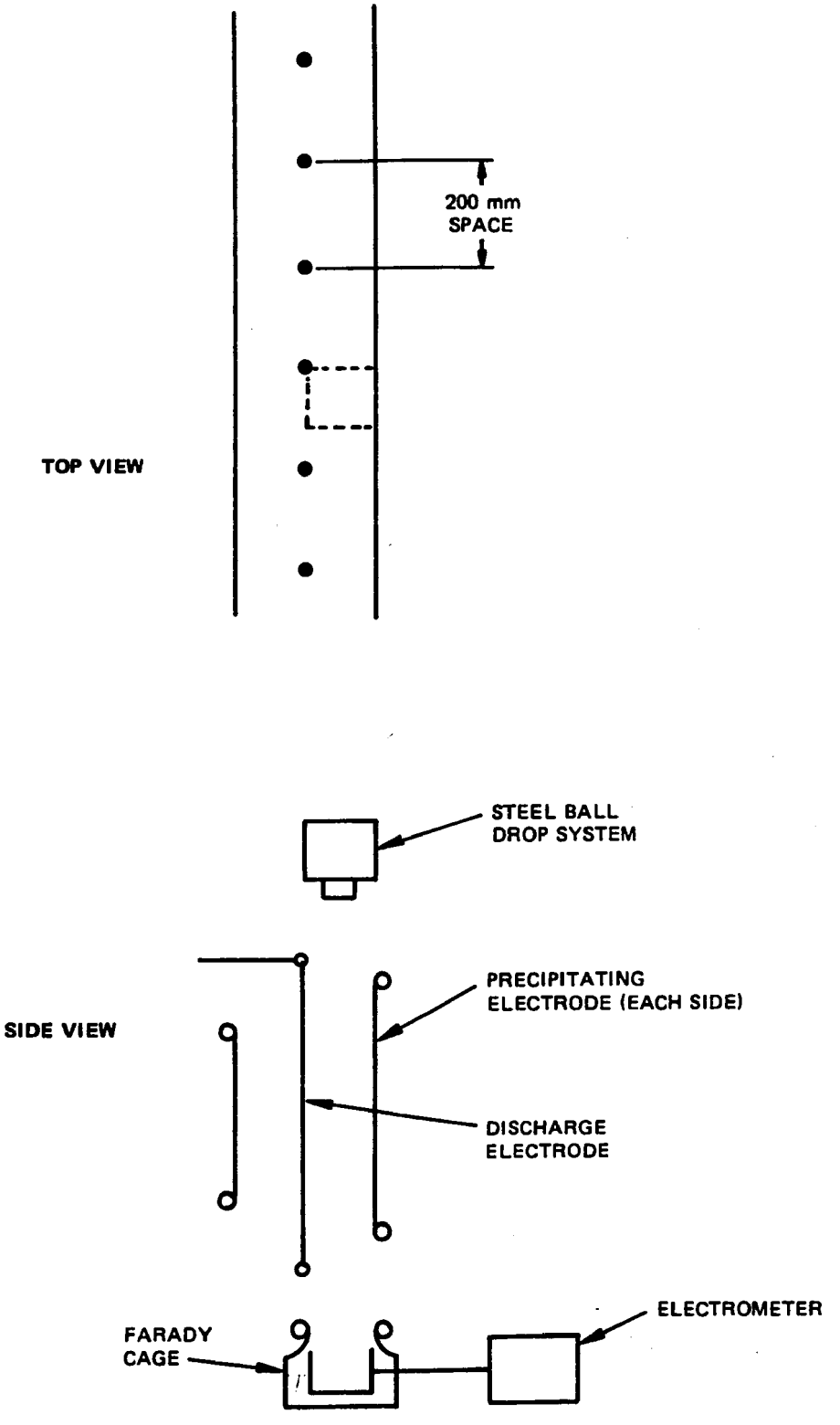

Figure 2. Electrical Field Strength Distributions in Precipitating Space 250, 500 and 750 mm

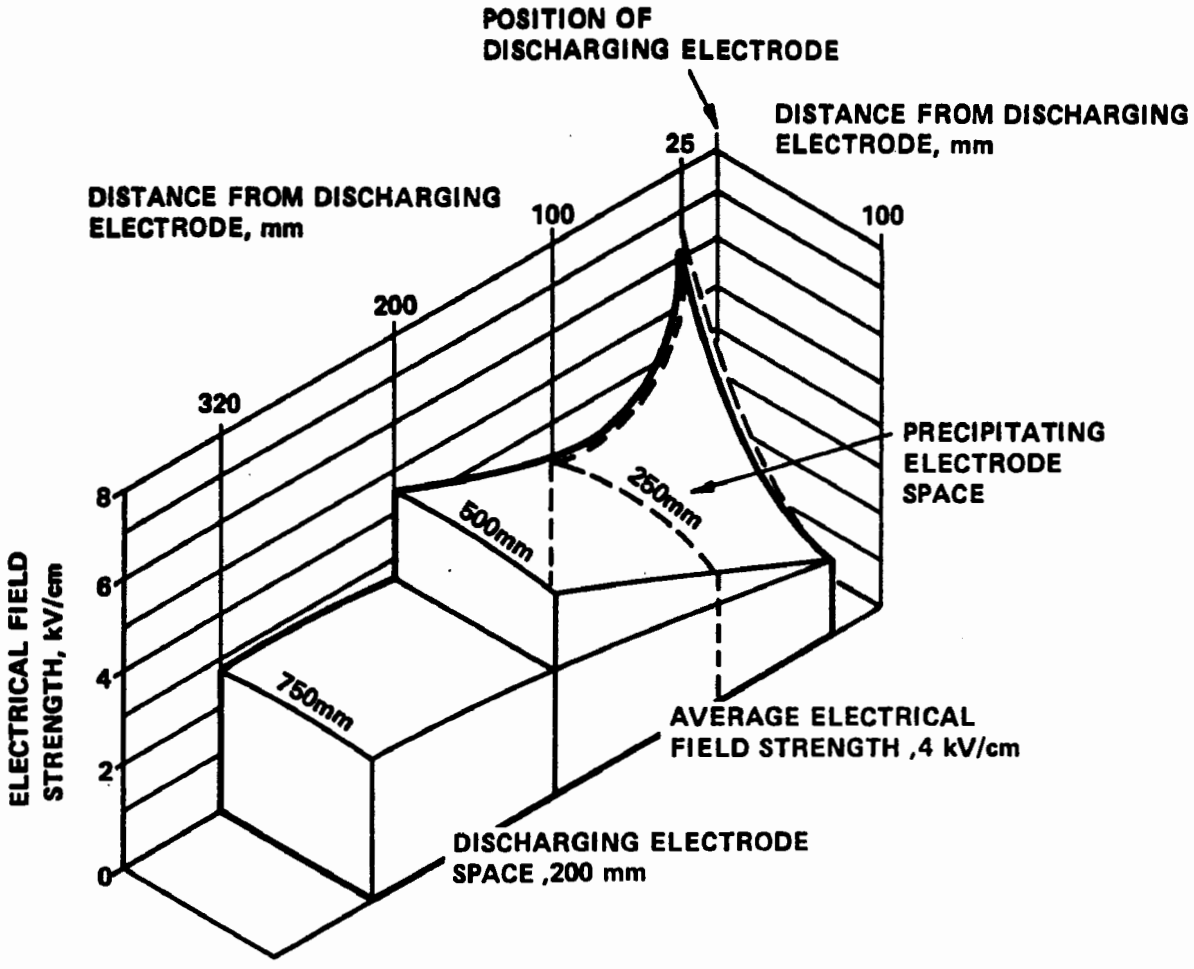

The reason why the electrical field strength increases as it approaches the precipitating electrode is considered to be due to a space charge by corona discharge. Also, if the measured value of the electrical field strength is applied to the Deutch equation, the precipitating rate is about the same for 500 mm and is lower for 750 mm as compared with the case of 250 mm precipitating electrode space.

ELIMINATION OF SO_2 AND NO IN A CORONA DISCHARGE FIELD

Keizoo Ootsuka, Tsugita Yukitake, Makoto Shimoda

Hitachi, Ltd.

Introduction

It is known that in the electrostatic precipitators, negative ions are produced due to corona discharge, and ion wind and ozone (O_3) will be created. We are analyzing the removal of sulphurous acid gas (SO_2) and nitrogen oxides (mainly nitrogen mono-oxide) as well as the elimination of ashes using wet collection type ESP.

Principle

1) Elimination of SO_2 - Application of Gas Agitation by Ionic Wind[1,2] promotes contacts between SO_2 in gas and absorbent liquid. This turbulence enhances the elimination of SO_2 according to reactions 1) or 2)

$$SO_2 + H_2O \longrightarrow H_2SO_3- \quad (1)$$

$$SO_2 + 2NaOH \longrightarrow Na_2SO_3 + H_2O \quad (2)$$

2) Elimination of NO - Application of Oxidization Process by Ozone (O_3)

Since NO is insoluble, NO will be transferred to a soluble NO_2 or N_2O_5 by applying oxidization by ozone (O_3) and eliminated by absorbent liquid. These reactions are shown as follows:

$$NO + O_3 \longrightarrow NO_2 + O_2 \quad (3)$$

$$2NO + O_3 \longrightarrow N_2O_5 \quad (4)$$

$$2NO + H_2O \longrightarrow HNO_3 + HNO_2 \quad (5)$$

$$N_2O_5 + H_2O \longrightarrow 2HNO_3 \quad (6)$$

Experimental Apparatus and Experimental Method

Figure 1 is a flow-sheet of experimental apparatus. A mixed gas which was arranged to have a similar composition as oil fired boiler exhaust gas is injected into the wet electrode type ESP and the concentrations of SO_2 and NO are measured at the exit of the ESP. A negative high voltage DC is charged to the moisture type ESP. The temperature of exhaust gas is 55°C.

Experimental Results

Figure 2 shows one example of sulphur elimination characteristics. Once a discharge is begun, the sulphur elimination rate is improved by increasing the consumption of electric power. Figure 3 shows the oxidization characteristics of NO. The oxidation rate of NO is improved also by increasing the consumption of electric power. Also it was verified that the oxidized NO can be absorbed by H_2O or NaOH.

Conclusion

It was confirmed that the elimination of SO_2 and NO is feasible by using the wet electrode type ESP.

References

1) Uchigasaki and others: The Chemical Engineering 31 878 ('67).

2) Adachi: Engineering Laboratory Journal, Yamaguchi University 19, 81 ('67).

Figure 1. Experimental Apparatus Flow Sheet

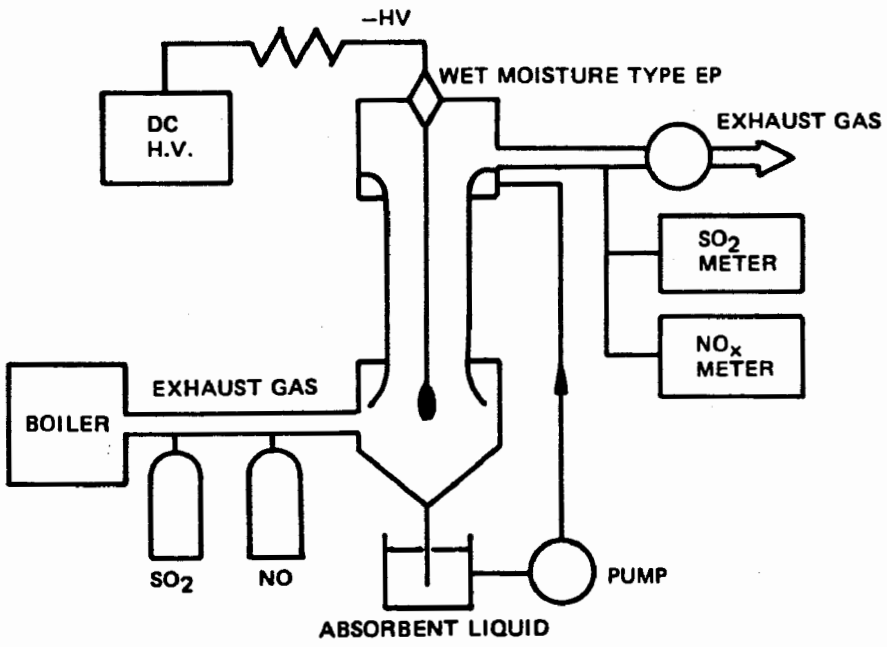

Figure 2. SO_2 Removal Rate as a Function of Power Consumption

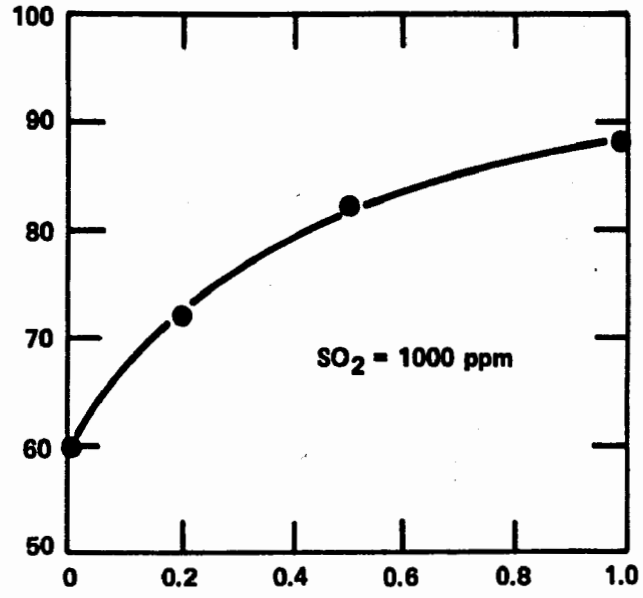

Figure 3. NO Removal Rate as a Function of Power Consumption

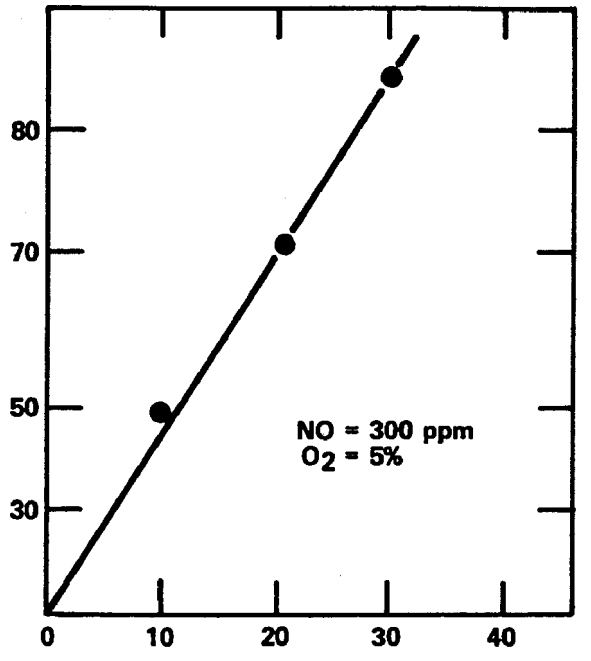

HITACHI EP-SB TYPE ELECTROSTATIC PRECIPITATOR (EP)

1. Principles and Characteristics

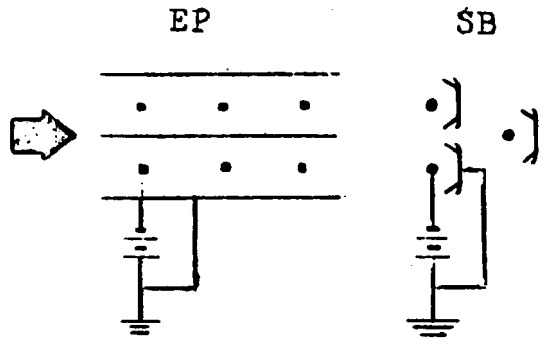

Dust sucked from the inlet receives electric charge at EP. Dust of large particle size will be collected there, while fine articles with electric charge are concentrated together and fed to SB(Shoot Buffle).

SB can collect charged fine particles with high efficiency making use of a resultant force of electrostatic collecting force under high electric field formed in two stages and mechanical collecting force caused by collision of dust against the shoot buffle.

(HITACHI PATENT 404109)

[Characteristics]

1 The space can be saved by 20 - 25 % to obtain the same collecting efficiency of EP only.

2 By using a discharge wire for SB to control corona discharge, power supply for unit processing gas quantity can be reduced by 40 % as compared to EP only.

3 The shoot buffle with a special form is located vertically to gas flow, which will hardly cause performance drop due to re-entrainment.

2. Example in Cement Plant

	Specifications	
Quantity of processing gas	350,000 m^3N/H	
Inlet gas contents	18 g/m^3N	
Outlet gas contents	0.03 g/m^3N	
Collecting efficiency	99.8 %	
Collecting capacity rate	EP-SB system 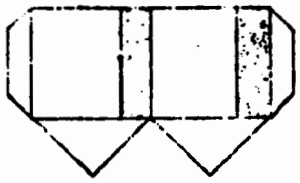 75 %	EP system 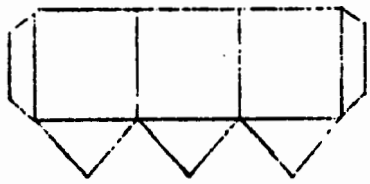 100 %

3. Application

(1) Cement plant

(2) Trash burner

(3) Improvement of performance of the existing Electrostatic Precipitator (SB only)

MEASUREMENT OF SUSPENDED PARTICULATES

Mesure des particules en suspension

OOTSUKA, K., TSUJI, S. and ARIKAWA, Y.
Hitachi Research Laboratory of Hitachi, Ltd.
Hitachi, Ibaragi, Japan

INTRODUCTION

Emission standards for particulates in a stack gas have been established to control air pollution. In Japan, the concentration of particulates must be less than 50 mg/Nm^3 for a large scale oil-fired boilers, i.e., the volume of stack gas of 40,000 Nm^3/h or more.

A standard method for the particulate measurement is he dust tube and filter paper method. They are based on manual gravimetric procedures, making a continuous measurement impossible.

A continuous monitor, therefore, is strongly desired for controlling the operating conditions of boilers and dust collectors.

Particulates can be detected continuously and automatically using light beam. The number and size of particulates can be measured by the scattered light from the dust particles, which has been applied to air pollution monitoring.

A monitor of particulates in a stack gas by the light scattering method has not been used until now, because it is difficult to sample a hot and moist gas of high particulate concentrations.

We have developed a new stack dust monitor, which continuously measures mass concentration and particle size distribution of particulates in a stack gas.

I. DESIGN AND DEVELOPMENT OF THE STACK DUST MONITOR

A schematic diagram of the new stack dust monitor is shown in Fig. 1. It consists of an iso-kinetic sampler, direct and diluent sampler, optical system, particle size analyzer and number-to-weight calculator.

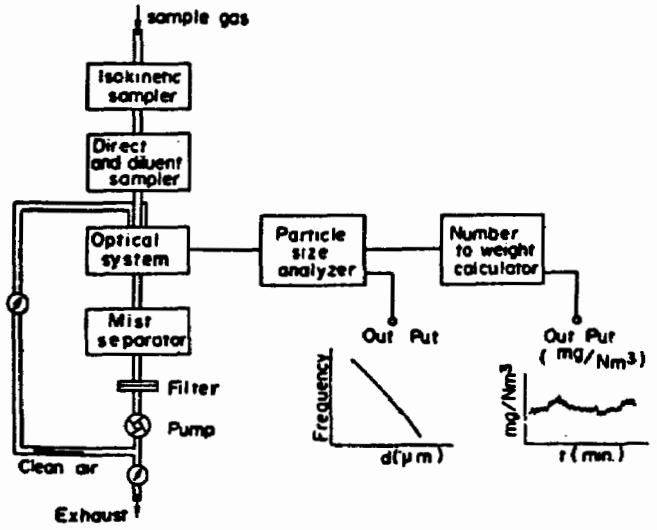

Fig. 1 Schematic diagram of stack dust monitor

1.1 Optical System

Fig. 2 shows the principle of the forward light scattering optical system.

With the aid of an incandescent lamp, several pairs of lenses and a slit, a bright focus (illuminated volume) is formed. The main beam is intercepted by a light stop and a light trap. When dust particles in sample gas pass through this focus, the scattered light in the forward direction is reached photo-multiplier. The sample gas is surrounded by a clean air curtain to prevent deposition of the dust particles on the surface of the lenses.

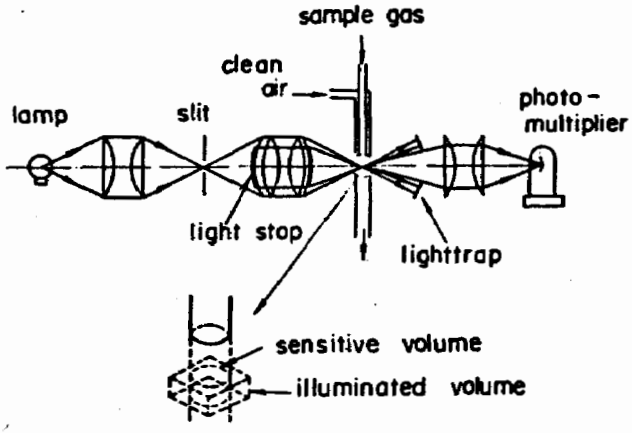

Fig. 2 Optical system of forward light scattering

The output from the photo-multiplier is an electrical pulse. The number and height of the pulse correspond to the number and size of particles, respectively. Therefore, the concentration and size of particulates are measured simultaneously by this instrument.

And then, depending on the results of the analysis of the particle size with the pulse height, the volume concentration of mean particle size is obtained for the different size classes of particles, and thus the total volume concentration is obtained.

Multiplying this total volume concentration with a coefficient (mean density of dust particles), the relative mass concentration of the dust will be obtained.

The relationship between number of particles and counting errors is calculated theoretically. The counting error increases with the particle concentration. In order to obtain 5 percent or less of the counting error, the particle concentration must be less than 3.2 x 10^8 particles/m^3. For a sample of higher concentrations of particulates, the

sample gas should be diluted with clean air.

In order to lead a hot and moist sample gas directly in the optical system, the protection of the apparatus, especially the lenses, against temperature rise and mist formation is necessary.

1.2 Sampling Apparatus

We have developed a new sampling apparatus shown in Fig. 3. A stack gas is sampled by the ejection effect. Clean air is supplied to the ejector of the sampling probe from the outside of the stack. This sampler is set in the stack.

Only a small fraction of the gas which enters to the probe is introduced to the optical system, most of the fraction being returned to the main stream of the stack gas with the clean air.

The sampling flow rate is proportional to the flow rate of the clean air supplied to the sampler.

When the mass concentration is less than 10 mg/Nm^3, the sample gas is led directly to the optical system (Fig. 3a). When the mass concentration is higher than 10 mg/Nm^3, the sample gas is diluted with the clean air supplied to the sampler, and then led to the optical system (Fig. 3b).

1.3 Calculation

The calibration of particle size is carried out using monodisperse polystyrene latex (PSL) aerosols, obtained by nebulizing aqueous suspensions of uniform latex spheres. (Dow Chemical Co., Midland, Mich.)

Fig. 4 shows the calibration curve, giving the height of electrical pulses (e) as a function of the particle diameter (d). The coefficient is found to be between 0.9 and 1.1, and the pulse height proportional to the particle size.

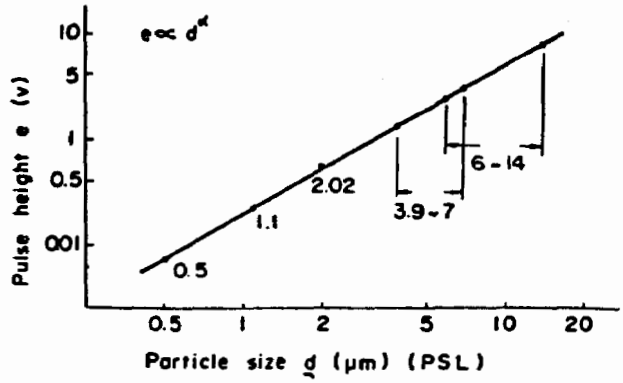

Fig. 4 Calibration curve for stack dust monitor

II. APPLICATION

Particles in a stack gas is usually distributed from 1 μm to 100 μm and properties of dust are variable in each plant.

This new stack dust monitor can be used for various kinds of emission sources, such as oil-fired boilers, coal-fired boilers, kraft recovery and hogged fuel-fired boilers, incinerators, cement kilns, sintering furnaces, cokes ovens, gas turbines, glass furnaces, blast furnaces and so on.

Several application data are shown in Fig. 5. A is coal-fired fly-ash dust, B cement dust, C oil-fired carbon dust, D coke and E an Al_2O_3 particle. Samples of various sizes are prepared by a sieving and sedimentation method. The nature of these test particles is as follows: A is a spherical, white particle, B an irregular shaped, gray particle, C a spherical, black particle, D an irregular shaped, black particle, and E an irregular shaped, white particle. F is a spherical, white, standard particle.

From the data, it is clear that there exists an obvious quantitative relation between the pulse height and the

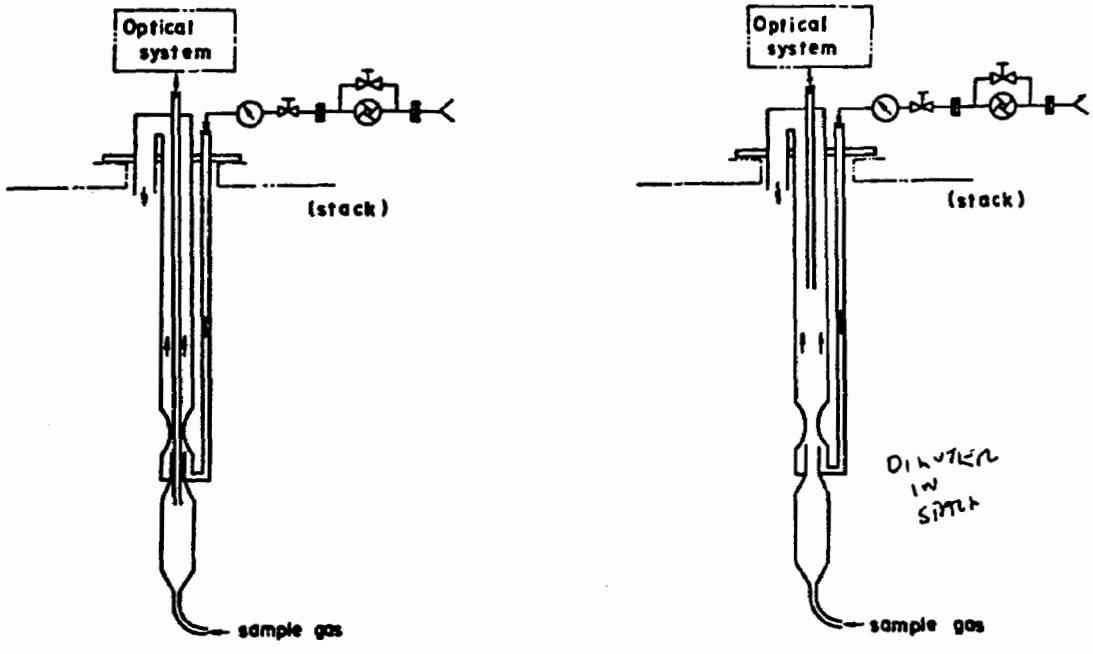

Fig. 3 Sampling apparatus of stack gas

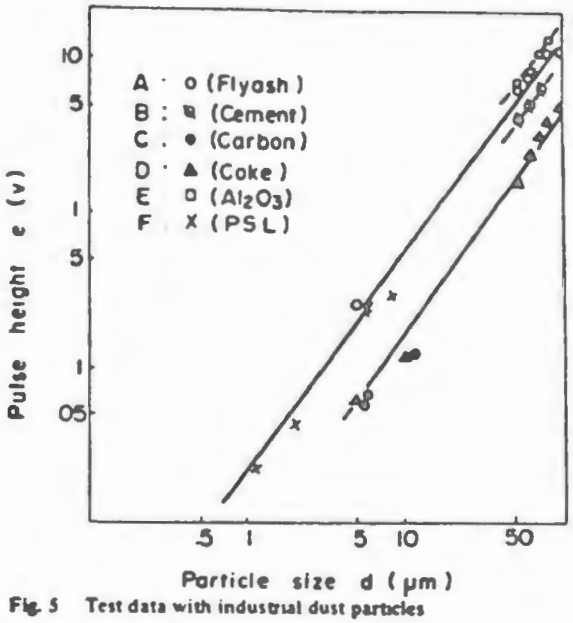

Fig. 5 Test data with industrial dust particles

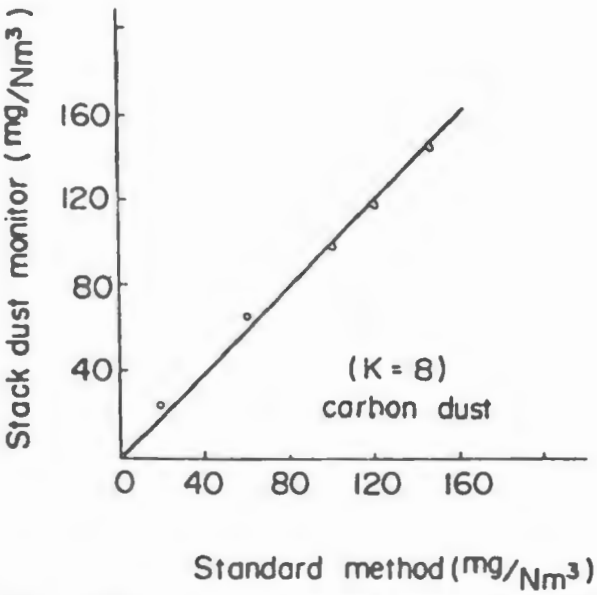

Fig. 6 Relationship between stack dust monitor and standard method

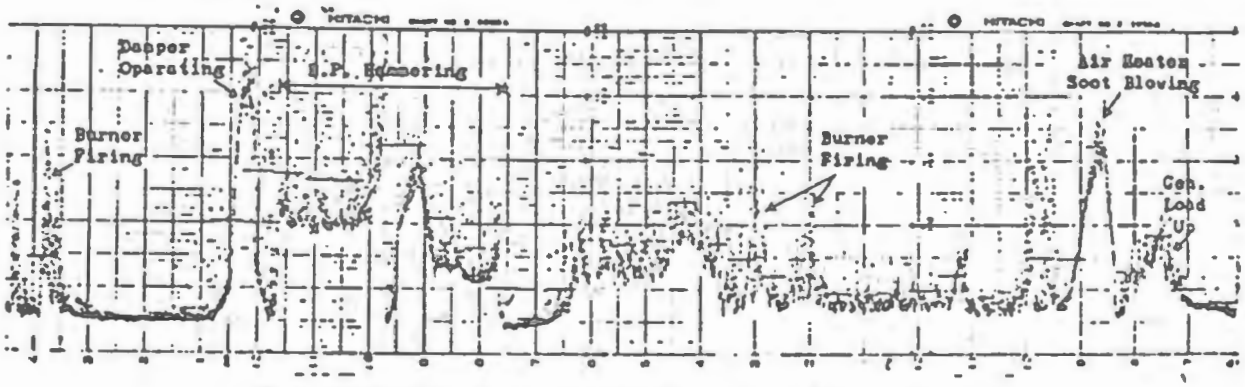

Fig. 7 Operating data of stack dust monitor (Emission from oil-fired power boiler)

particle size, and that the pulse height is very much affected by the optical properties of the particles. The optical properties will vary considerably in accordance with the type of fuel and combustion conditions.

In order to determine the absolute mass concentration of particulates, calibration curve must be prepared for each sample by simultaneous measurement with the manual standard method.

The linear relationship between mass concentration measured with the stack dust monitor and the filter paper method is obtained as shown in Fig. 6. The constant, K, is a conversion coefficient for the absolute mass concentration.

Fig. 7 shows the continuous operating data with a oil-fired boiler at the outlet of the Electrostatic Precipitator. It shows a wide variation of dust particles in the stack gas with the change of operational conditions of the boiler It is also shown that when the load of the boiler rises, the soot sticked at air heater is blown out and the collecting plates of electrostatic precipitator are hammered, the dust concentration increases instantaneously.

Hitachi Dust Collection Equipment and Systems

September, 1977

Hitachi, Ltd.

Hitachi Plant Engineering & Construction Co., Ltd.

Contents

1. Preface

Hitachi has been manufacturing dust collection equipment since 1924 and has a very old history as a manufacturer of electrostatic precipitators in Japan.

Hitachi's supply record of electrostatic precipitators reached to more than one thousand in the field of thermal power plants, iron industries, non-ferrous metal refining industries, and so forth, and the total treated gas volume amounted to more than 150,000,000 Nm^3/h, including the Japanese record in throughput capacity of 4,260,000 Nm^3/h /unit for a 1000MW oil fired thermal power plant.

It is said that design of dust collection equipment, especially electrostatic precipitators, require abundant experiences on the characteristic analysis of dust, such as particle size, shape, electric resistivity, etc., and on the nature of gases. Hitachi, today, can furnish the optimum design and engineering of dust collection equipment and systems through his experiences.

In addition to such experiences, our researchers have been proceeding with many improvements on performance from the view point of engineering and economy. And main theme of Hitachi now are as follows,

1) improvement of dust removal efficiency
2) energy saving
3) cost reduction

This brochure explains of our recent results in the development of electrostatic precipitators.

2. Industries and applied dust collection systems

Based on its abundant experiences and sophisticated engineering capability, Hitachi has been manufacturing and furnishing superior dust collection equipment and systems for various industries.

Table 1. shows the relation between typical industries and type of dust collection equipment applied.

The following explanations are the outline of dust collection systems for some typical industries.

1) EP for thermal power plants

Dust collection systems for pulverized coal fired boilers and oil fired boilers slightly differ from each other.

In the former case, the dry type EP or the combination of the multi-cyclone and the dry type EP is adopted, because the exhaust gas from the boiler contains much dust. The main components of the dust ~~is fly ash~~ are SiO_2, Al_2O_3 and so forth.

The dust has sometimes the character of high electrical resistivity depending on the kinds of coal. As such high electrical resistivity may cause the phenoma of back ionization. The following technological considerations to reduce the electrical resistivity are paid;

a. mixfiring with high sulfur coal or heavy oil

b. injection of SO_3 into the exhaust gas

c. control of gas temperature

In the latter case, the exhaust gas contains rather less dust which mainly consists of low electrical resistive free carbon. And the gas also contains comparatively much sulfur trioxide which sometimes produces corrosive and adhesive snow fume.

In consideration of such character of the gas and the dust, the dry type EP adopting ammonia injection is applied.

The ammonia injection produces ammonium sulfate which prevents snow fume and raises the resistivity of dust to optimum value.

2) EP for an iron industry (Fig 2)

Iron industry has various sources of exhaust gases such as, the coke oven,

the sintering machine, the blast furnace, the converter, the open hearth furnace, the electric furnace, the scarfer, and so forth.

The dust contained in these gases mainly consists of iron sulfide. Character of gas and dust differs from each other, so that most suitable system should be selected to meet each source. Therefor in planning of dust collection system for iron industy, much attention should be paid to gather gas effectively, to prevent corrosion and errosion, to give effective rapping, to make adequate washing and so forth.

For instance, in case of the blast furnace gas, the venturi scrubber and the wet type EP are used considering prevention of explosion and high efficiency for the gas from the converter or the open hearth furnace, the combination of the stabilizer and the wet type EP is used considering the high resistivity of dust contained.

As an inside-shop dust collection system for the blast furnace, the converter, the open hearth furnace, and so forth, a bag filter system has been used hitherto, but recently a roof mounted EPis attracting attention because of its many advantages like power saving.

3) EP for a cement industry (Fug 3)

In cement industry, there is a lot of gas sources such as raw material mill dryer, kilns (Lepor method kiln, dry method kiln which includes suspension pre-heater and so on), clinker cooler and product mill etc.

The exhausted gases usually contains much volume of dust, and its electric resistivity is high. To prevent back ionization phenomena, which disturbe dust collecting operation, it is required to reduce the electric resistivity of the dust by adding moisture in a stabilizer installed before EP or by treating the gas in relatively high temperature condition. Another method to get high dust removal efficiency is to apply the constant current control with thyristor which contributes to make charging stable. The structure of the electrostatic precipitator is designed not to cause strain of electrodes and casing in high temperature condition. And the stabilizer with special spray nozzles is adopted to reduce drainage.

4) EP for sulfuric acid plants (Fig.4)

- The operation of iron sulfide calcination and other operations such as drying, sintering and melting of copper, zinc, lead and so on, produce large volume of gas which is rich in sulfur oxides. And this gas is used as raw material to produce sulfusic acid.
- Because of high content of dust, this gas is pretreated with a cyclone and finally fine dust is removed with an electrostatic precipitator. Mist electrostatic precipitator removes sulfuric acid mist in high efficiency, which is produced in gas cooling process.
- In designing the dust collection systems of sulfuric acid plants, it is very important to consider the prevention of corrosion and air leakage, the thermal expansion and the insulation effect etc.

Table 1. Industies and Supplied Dust Collection Systems

Item / Industry	Gas source	Applied system	Remark
Thermal Power Plant	pulverized coal fired boiler	MC-Dry EP. Dry EP	· treatment of high resistive dust and high content dust.
	heavy oil fired boiler	Dry EP-MC, Dry EP	· treatment of fine and low ~~electric~~ resistive dust.
Iron Industry	Blast Furnace (main)	VS-Wet EP	· Prevention of gas explosion. · High efficiency gas cleaning
	Blast Furnace (inside -shop gas)	Wet EP, Open BF Roof EP	· Advanced gas gathering technology.
	Coke Oven	Wet EP, SP-Wet EP	· prevention of CO gas explosion and adhesion of tar
	Sintering machine	Dry EP	· treatment of high electrical resistive dust
	Converter(direct gas)	ST-Dry EP	· treatment of fine and high electrical resistive dust
	Converter(inside-shop gas)	ST-Dry EP	· advanced gas gathering technology
	Electric Furnace (direct gas)	closed BF ST-Dry EP	· control for variation of gas volume and temperature. · provention of CO gas explosion.
	Electric Furnace (inside-shop gas)	open BF,Roof EP	. advanced gas gathering technology.
	Open Hearth Furnace (direct gas)	ST-Dry EP	· treatment of fine and high electlical resistive dust.
	Open Hearth Furnace (inside shop gas)	Dry EP, Open BF Roof EP	· advanced gas gathering technology.
	Hot Scarfer	Wet EP	· prevention of adhesion of dust.
	Cold Scarfer	SP-Wet EP Closed BF	· gas gathering system for moving gas source.

Item / Industry	Gas Source	Applied system	Remark
Oil & Chemical Industry	Fluid Catalytic Conveter	Dry EP	• treatment of hard and high electrical resistive dust.
	Oil Gas Generator	Wet EP	• prevention of adhesion of tar.
Cement & Ceramic Industry	Suspension Preheater Kiln	ST-Dry EP	• treatment of high electrical resistive dust.
	Lepor Kiln	Dry EP	• prevention of corrosion.
	Limestone Dryer	Dry EP	• prevention of corrosion.
	Clinker Cooler	MC-Dry EP, Dry EP	• Treatment of high electrical resistive dust and high content dust.
	Melting Furnace of Sodium Glass	ST-Dry EP	• prevention of corrosion and adhesion of acid dust.
	Carbon Electrod Calcinating Furnace	Wet EP	• treatment of adhesive tar and deposited material.
Pulp Industry	Lime Kiln	Dry EP	• treatment of high electrical resistive dust.
	Soda Recovery Boiler	Dry EP	. prevention of corrosion and adhesion of tar.
Non-ferrous Metal Refinery & Subfuric Acid Industry	Copper Self-melting Furnace	Dry EP	. prevention of adhesion of dust.
	Copper Converter	Dry EP	. "
	Iron Sulfide Ore Calcinating Furnace	Dry EP	. "
	Zinc Ore Calcinating Furnace	Dry EP	. "
	Sulfic Asid Plant	Wet EP	. prevention of corrosion.
	Almina Calcinating Kiln	MC-Dry EP	. Treatment of high content dust, prevention of errosion.
	Al-Electrolysis	Dry EP	. prevention of burning of carbon dust and CO gas.

Item / Industry	Gas Source	Applied system	Remark
Non-ferrous Metal Refinery & Sulfuric Acid Industry	Al-Smelter	ST-Dry EP, Wet EP Closed BF	. treatment of high electric resistive dust.
	Nickel Kiln	MC-Dry EP, Wet EP	. "
	Chromite Kiln	Dry EP	. "
Municipal	Solid Waste Incinerator	Dry EP, Wet EP	. variety in composition of gas to be treated.

Note: Dry EP: Dry type Electrostatic Precipitator,

Wet EP: Wey type EP

Roof EP: Roof-mounted EP

Open BF: Open type Bag Filter,

Closed BF: closed type Bag-Filter

MC: Multi Cyclone

VS: Venturi Scrubber

ST: Stabilizer

SP: Spray Tower

Fig.1 EP for thermal power plants

Dust collector for 600 MW oil fired boiler
Gas volume 2,510,000 m³ h
Temperature 141°C

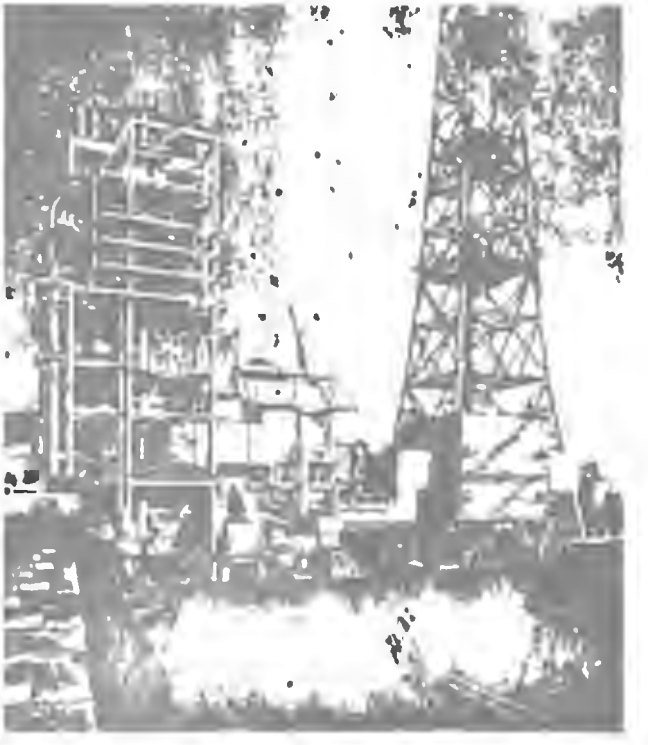

Dust collector for 220 MW oil fired boiler
Gas volume 937,000 m³,h
Temperature 141°C

Fig. 2 EP for iron industry

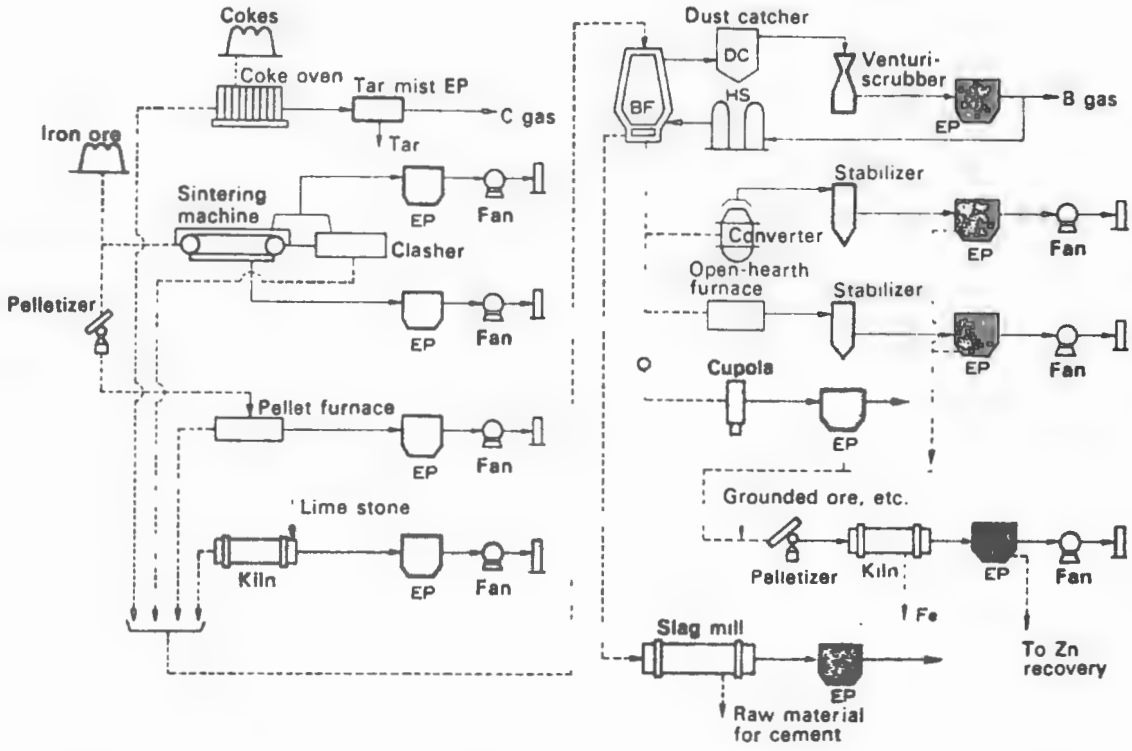

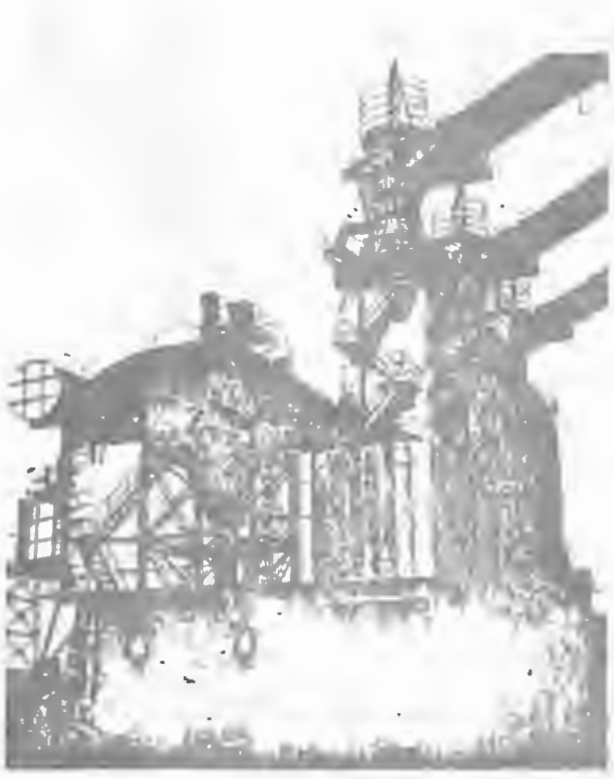

ST-EP dust collector for converter gas

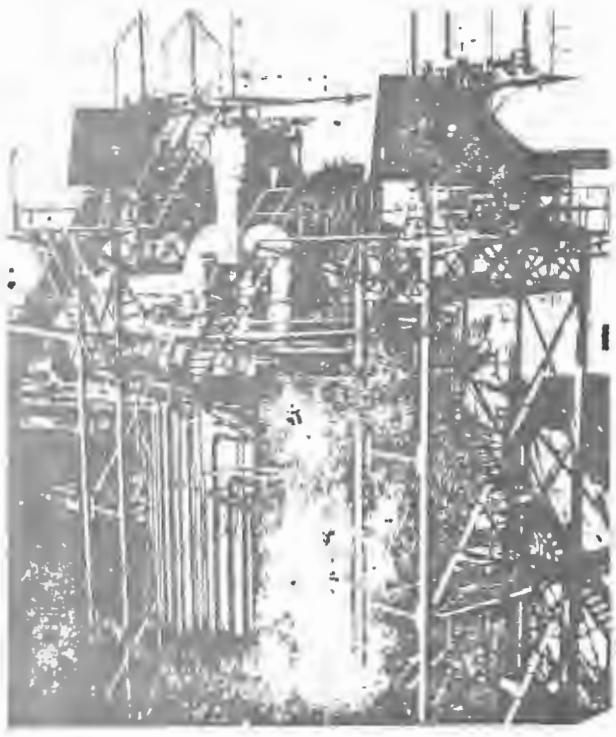

Wet-type EP for blast furnace gas

Fig.3 EP for cement industry

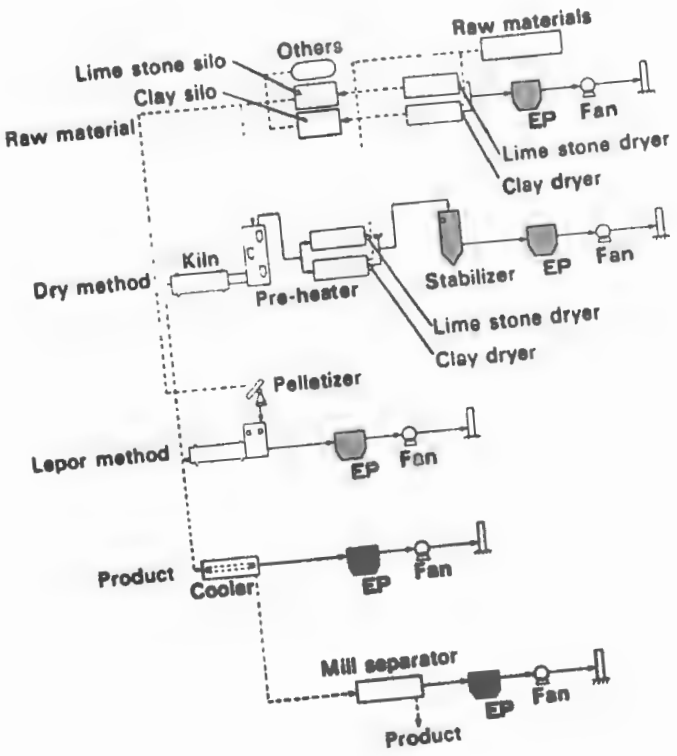

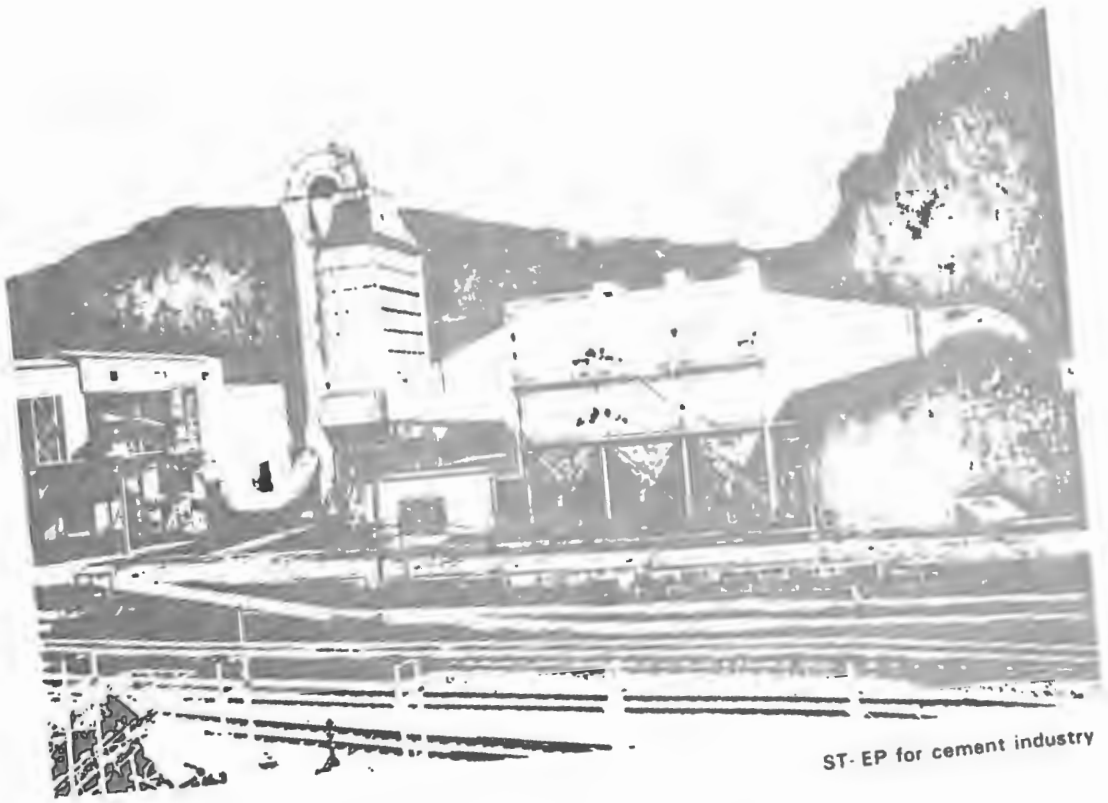

ST- EP for cement industry

Fig.4 EP for sulfuric acid plants

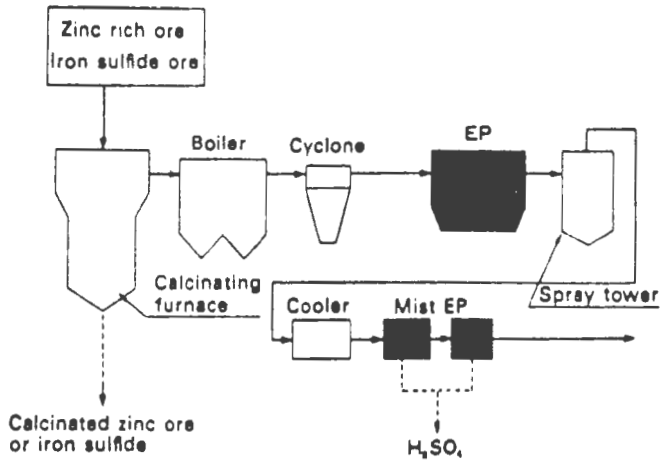

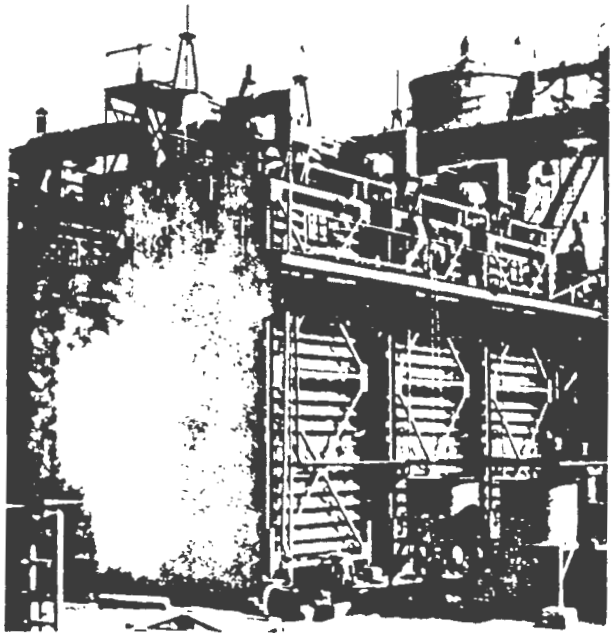

EP for sulfuric acid mist

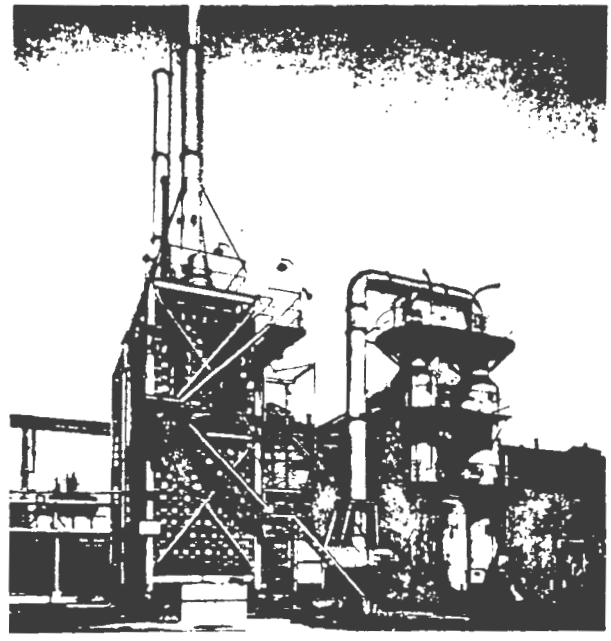

EP for gas from waste acid concentration plant

3. Features of Hitachi Electrostatic Precipitators

Recently Hitachi has carried out remarkable improvement on performance, manufacturing technology as well as economy. As a result, the cost of a new model EP became about 83 % of the coventional one.

The typical improvements are outlined below and illustrated in Figure 5.

1) High Performance Collecting Electrode (Pressed Type Electrode)

The collecting electrode is one of most principal elements consisting an electrostatic precipitator. A newly developed pressed type electrode gives higher dust removal efficiency than the coventional electrode manufactured by rolling does. The outline of the pressed type electrode is illustrated in Fig. 6.

Moreover, this electrode has feature of small strain at high temperature condition.

2) High Performance Discharging Electrode

Improvement has been given for the frame on which descharging electrodes are fixed. As the new frame is constructed by pipes and clamps and there is technical consideration to reduce strain at high temperature condition, the new frame contributes to keep the position of discharging electrodes at the initiated position. Furthermore, another technical consideration to protect discharging electrodes from breaking.

Fig. 7 shows the outline of the new type frame.

The combination of low strain collecting electrodes and discharging electrodes assures high dust removal efficiency because the distance between two electrodes is kept constant. Hitachi successed in reducing the equipment size from ten to twenty percent through the above improvement on electrodes.

3) Improvement of gas flow uniformity

The outlet dust concentration is regulated severer year by year, and the requied efficiency of EP becomes higher.

To improve the efficiency of EP, we can not neglect the dicrease in efficiency caused by ununiformity of gas flow.

Through earnest research and test we established technology of improving the uniformity of gas flow in EP.

We are introducing some examples of test results.

Figure 8B shows the relation between open area ratio of gas flow distribution plate and deviation of gas velocity.

Figure 8A shows the relation between deviation of gas velocity and dust collecting efficiency.

Applying these test results, we can improve efficiency of EP resulting about 10 per cent reduction of size.

4) Saving Energy Type Insulator Chamber.

Since the insulator is one of the most important parts in the EP, it should keep up the sufficient insulating function under any operation conditions.

Fig. 9 shows the outline of the newly developed saving energy type insulator chamber which secures the above mentioned function.
As the insulator is tightly covered with a small and light shelter which isolates the insulator from the atmosphere and prevents from contaminations.

The inside of the insulator is kept clean with the seal air which prevents the treating gas from coming into the inside, because the seal air is introduced into the inside then is exhausted into the EP through the specially designed guard stool. Dewing on the insulator is prevented with a small capacity heater derectly installed on the insulator. As the seal air flow in this new type makes 60 per cent decrease and the heater capacity 85 ~ 90 per cent decrease, electric power consumption of the whole EP results in 10 ~ 30 per cent decrease.

5) Adoption of Parts Manufacturing with Press Method

Adoption of pressed manufactured parts such as electrodes, casings, rotary valves and so on improved the quality and reliability of EP, with the effect of mass production.

Fig. 5 Features of Hitachi Electrostatic Precipitators

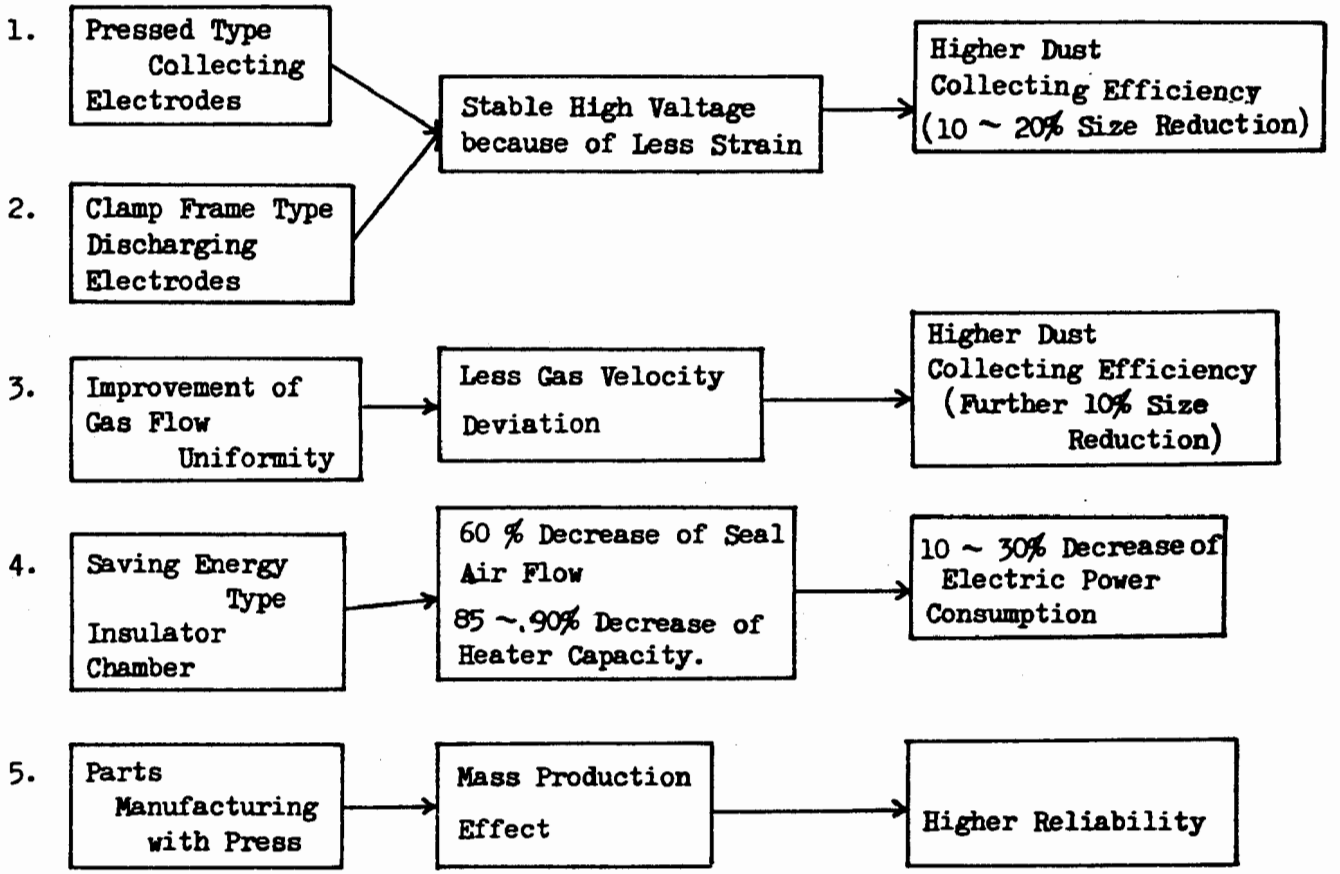

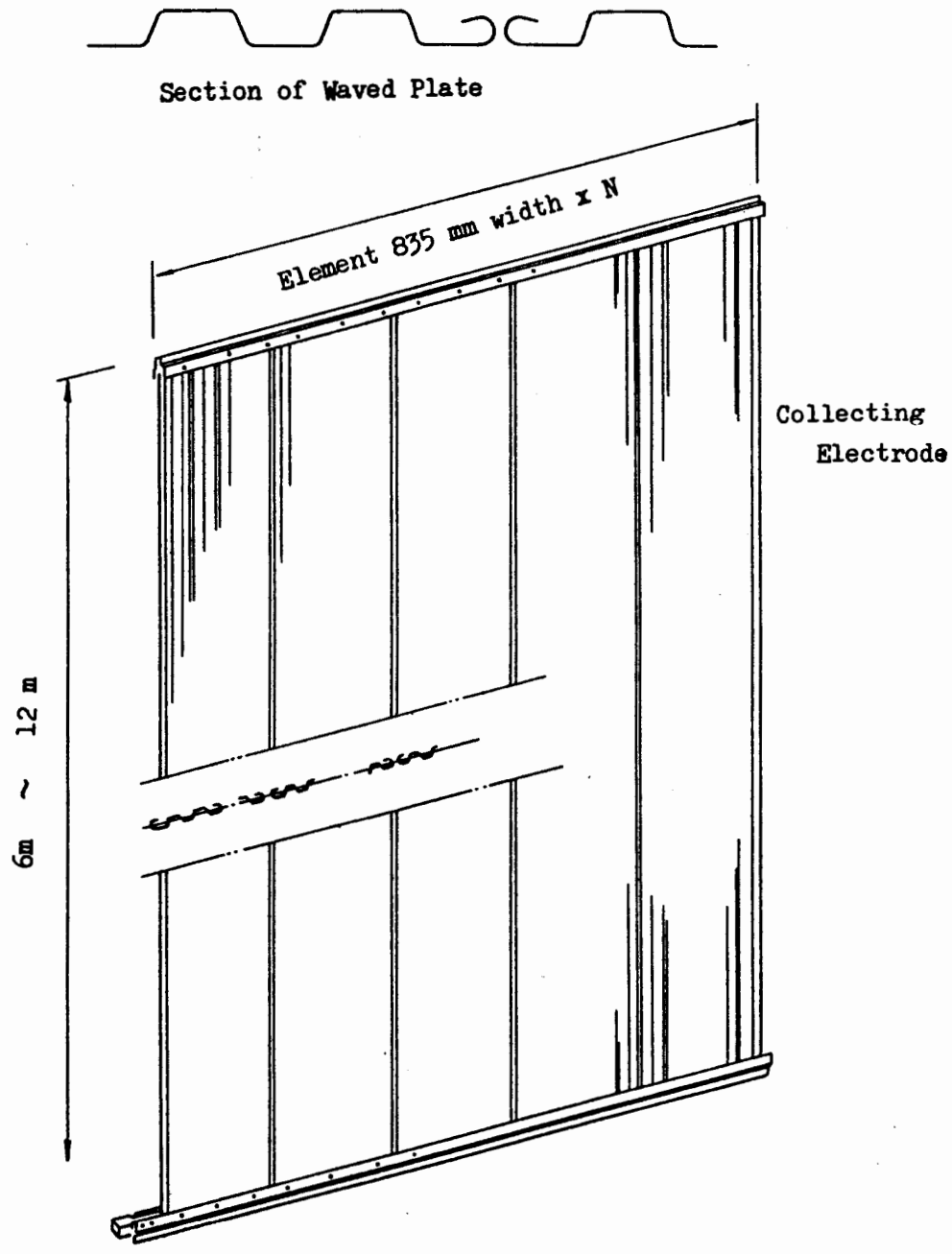

Fig 6. Outline of High Performance Collecting Electrode

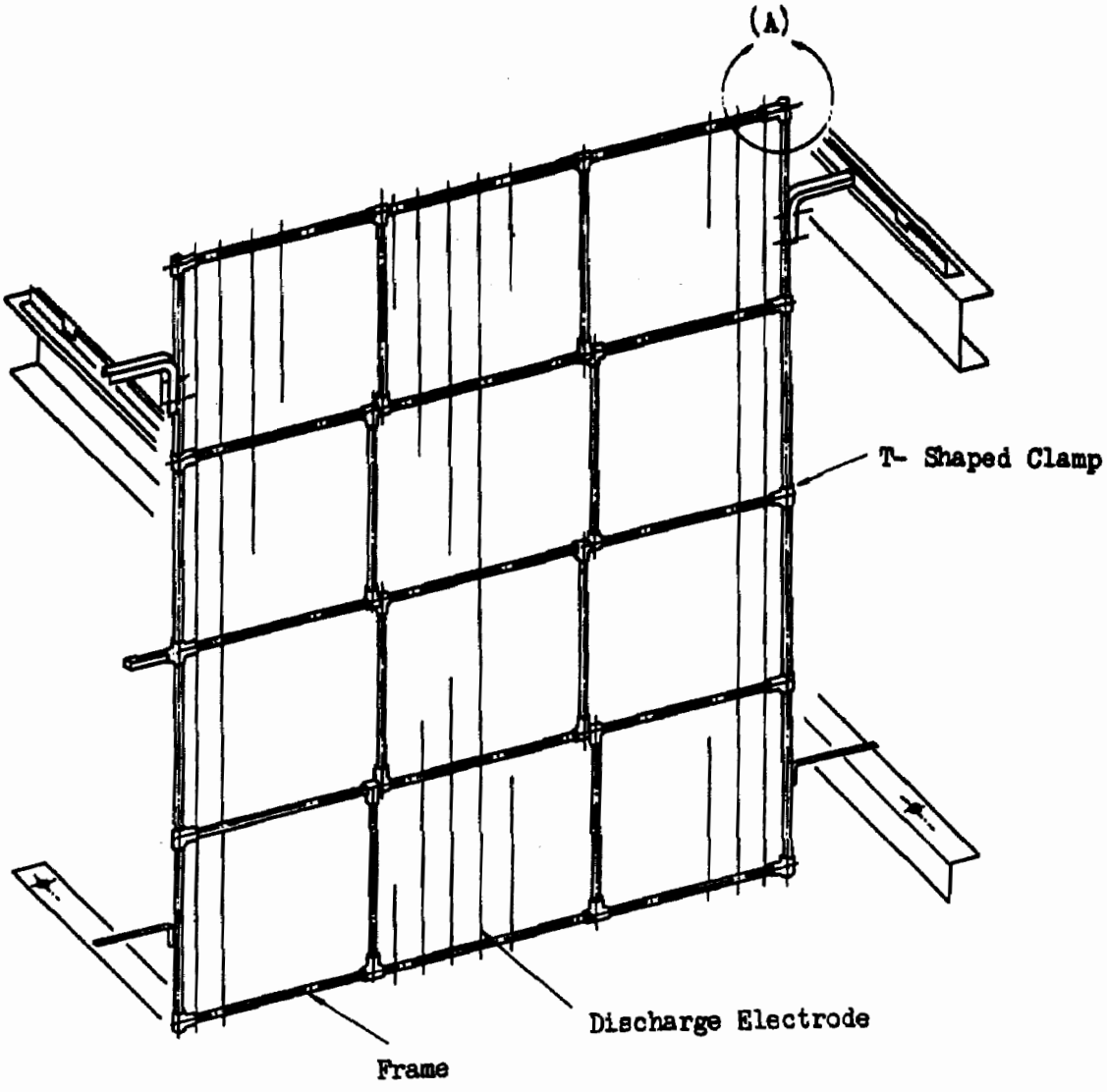

Fig 7. Outline of High Performance Electrode

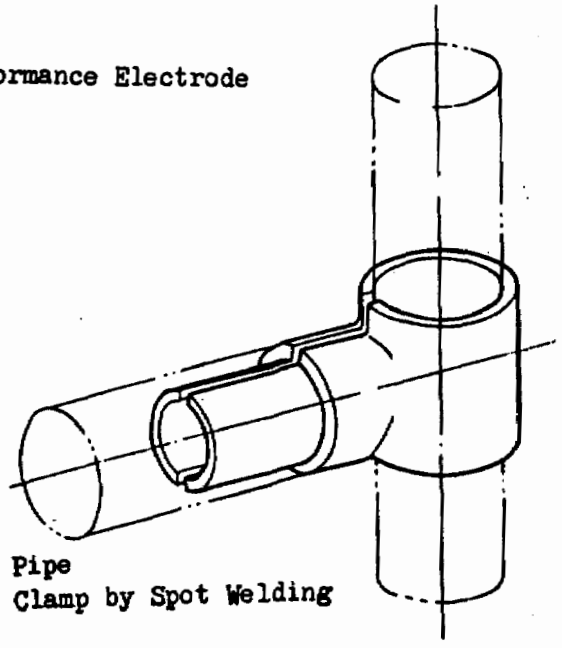

Fig 7. (A) Frame Pipe
Fixed to Clamp by Spot Welding

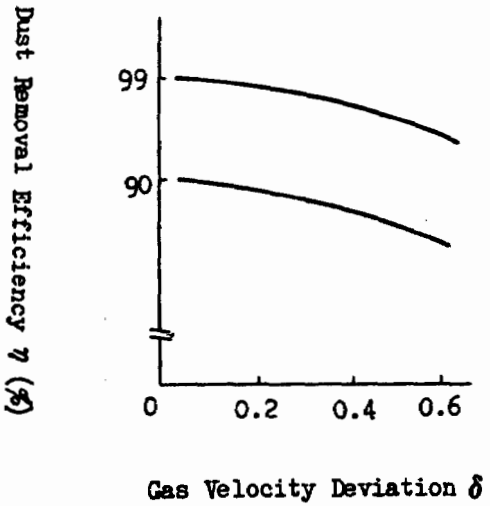

A. Relation between Gas Velocity Deviation and Dust Removal Efficiency

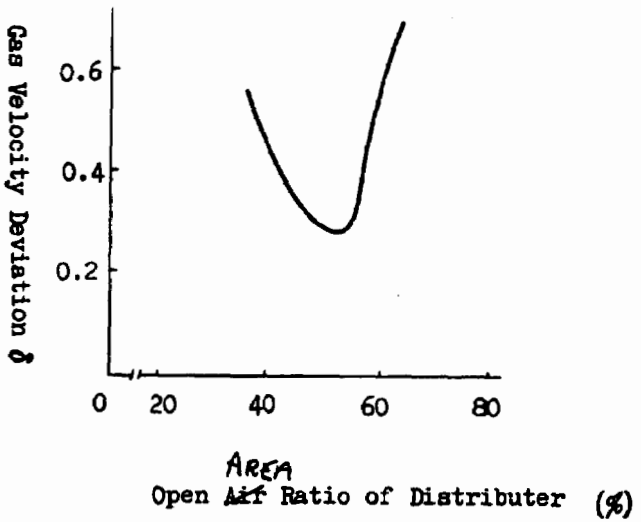

B. Relation between Open Area Ratio of Distributer and Gas Velocity Deviation

Fig 8. Gas flow uniformity and Dust removal efficiency

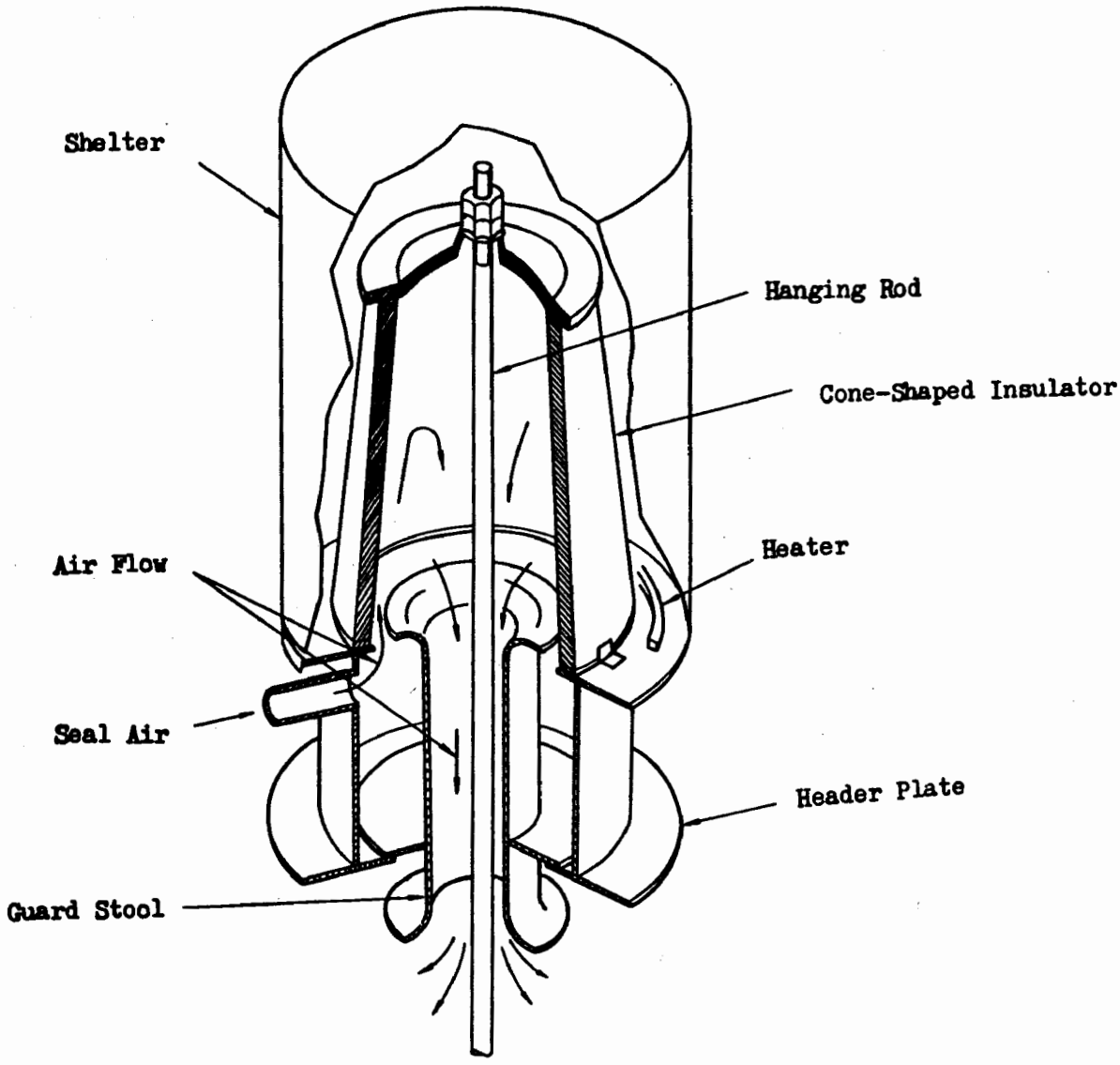

Fig 9. Outline of the Saving Energy Type Insulator Chamber

4. Wide-pitch Electrostatic Precipitator

A wide-pitch electrostatic precipitator (hereinafter refer to EP) stands for an EP having wide distance between a collecting electrode and a discharge electrode more than 200mm. The distance of the conventional EP is about 125mm.

In spite of some expected advantages, such as reduction of investment cost, easy maintenance, reduction of total weight and so forth, the idea of the wide-pitch EP had not appeared until Hitachi's development because there was lack of sufficient theory on collecting mechanism in the wide-pitch EP.

Fundamental study of the driving force observed in a space of EP and charging cheracter of dust has been carried out with a Schlieren device and some kinds of pilot plants. The study gave us enough information on the mechanism of dust collection in the wide-pitch EP to start design of a Hitachi wide-pitch EP.

1) Principle

It is said that dust removal efficiency (η) is given using the following Deutsch's equation.

$$\eta = 1 - e^{-K\frac{Ve \cdot t}{P}}$$

where Ve: migration velocity of dust

t : charging time

p : distance between a collecting electrode and a discharge electrode

This equation shows the narrower P brings the higher η . On the other hand, our testing results show the increase of the distance P in a certain range gives rather higher efficiency. The above phenomena could be explained by introducing the idea of ion wind.

Hitachi considers;

(1) The driving force to move charged dust to the collecting electrode might consist of not only the Coulomb's force, but also the force of ion wind.

(2) In a narrow-pitch EP, the force of ion wind is too strong to scatter dust accumulated on the collecting electrode resulting in low efficiency.

On the other hand, in the case of a wider-pitch EP having the distance of more than about 600^{mm}, the contribution of the force of ion wind decreaces.
These data means that is the optimum distance of the two electrode.
It is required to raise applied voltage propartionally to the distance of two electrodes.

2) Structure

Fig. 10 showes a conceptual figure of the wide-pitch EP in contrast with the conventional one. The former has only half the total number of the latter's elements (collecting and discharging electrodes, etc.), though the former's size is much the same with the latter's one. On the other hand, the applied voltage to the former would be as high again as one to the latter.

3) Features

On the performance

(1) [High efficiency is obtainable] even for the gas containing small amount of dust or fine dust because scattring of accumulated dust does not occur in the wide-pitch EP.

(2) [Stable charging is maintainable] because the effect of strain of electrodes is smaller than that of the conventional EP even for hot gas.

On the economy

(3) [Cost reduction is obtainable] because number of collecting electrodes and discharge electrodes are reduced.

(4) [Cost of civil work is reducible] because the weight of the wide-pitch EP becomes lighter than that of the conventional EP.

On the running and maintenance fee

(5) In case of the wet type wide-pitch EP, [the consumption of washing water is reducible] because the total surface area of the collecting electrode is small.

(6) [Inspection of the interior is easy] because the distance of the two electrodes is wide.

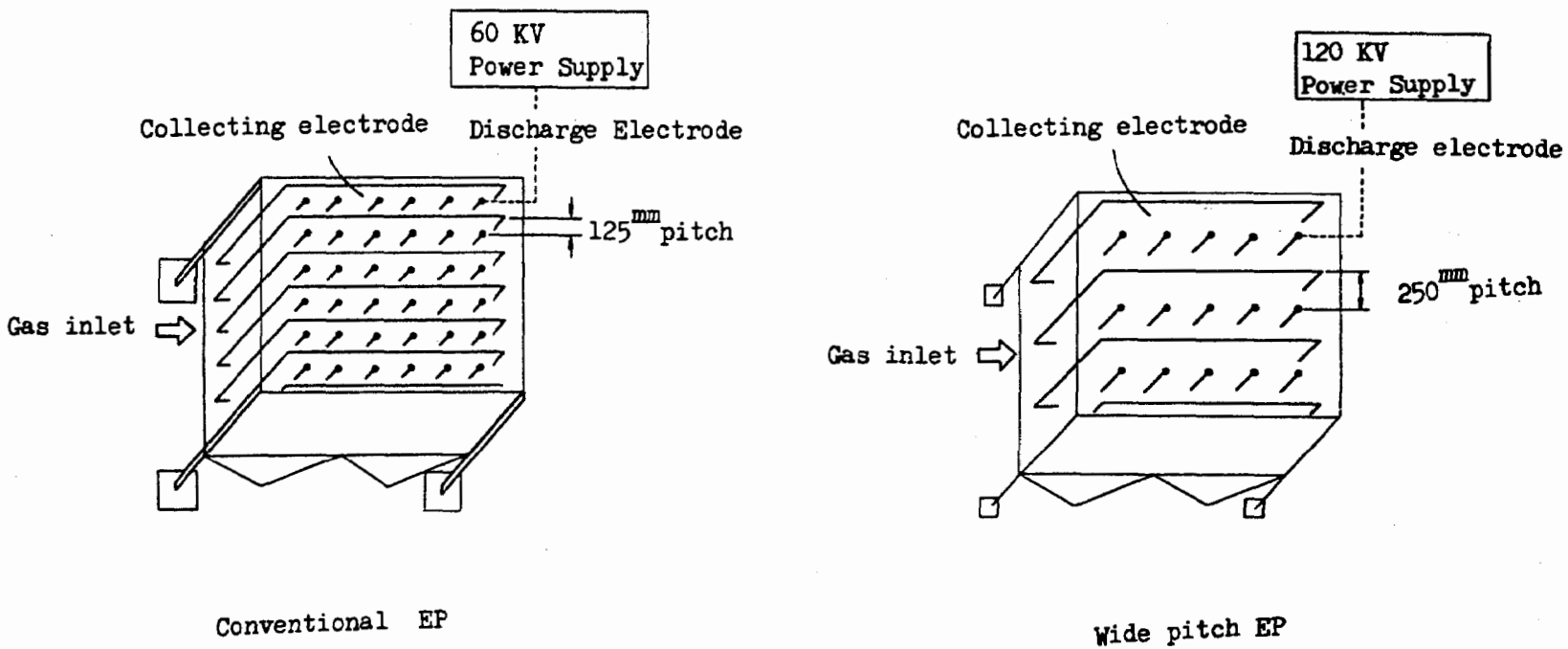

Fig 10. Conceptual Figure of Conventional EP and Wide Pitch EP

5. Roof Mounted EP

In iron industry, exhausted gases from converters and electric furnaces are spread in the shop and are discharged from ventilator.

In order to keep the working environment clean, bag filter system has been used, which needs large capacity fan and long ducts.

We have developed roof mounted EP aiming at saving of electric power consumption. We have two types: one is dry type, and the other is wet type.
The roof mounted EP is based on following technology.

(1) abundant experiences of gas gathering technology

(2) wide pitch EP having high efficiency

1) Principle

The dust containing exhausted gas from the furnace is gathered effectively, with specially designed hood, and then introduced into the roof mounted EP.

By planning of effective gas gathering system, working environment in the shop are free from contamination, without using a fan.

2) Structure

Fig.11 shows outside views of dry and wet type EP#, which have a gas gathering hood at the bottom.

3) Features

(1) Features in Performance

a. Both wet and dry type are applicable depending on the operating conditions. In the case of low electric resistive dust or in the case of installation on the remote roof from the source, we recommend dry type.

On the other hand, in the case of high electric resistive dust or in the case of wet gas, we recommend wet type.

b. Effective gas gathering hoods is combined.

Ascending gas from the source are gathered effectively with hoods to be introduced into the EP.

c. Wide pitch EP is adopted.

Adoption of the wide pitch EP enables the reduction of load on the shop structure and the easiness of maintenance.

d. Standardized units are adopted.

Planning is simplified and Construction is made easy.

(2) Features in Operation and Maintenance

a. Cost of Equipment

The cost of equipment is decreased compared with that of the bag filter which requires a large capacity fan and long ducts.

b. Cost of Operation

The consumption of electric power is over 70 per cent less than that of the bag filter.

c. Maintenance

The maintenance of equipment is easy. The roof mounted EP has no filters, which requires troublesome maintenance.

d. Other Features

The roof mounted EP does not require any space on the ground, resulting in compact layout.

(3) Appliance

The roof mounted EP is applied for following facilities in various fields of industry, such as iron industry, non-ferrous metal refinery plants, mechanical industry and so on.

Blast furnace
Converter
Open hearth furnace
Electric furnace
Others (Coke Oven, cement plant, etc.)

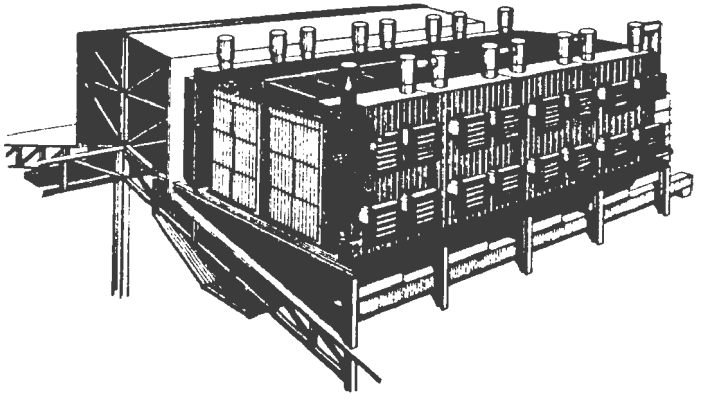

Dry Type

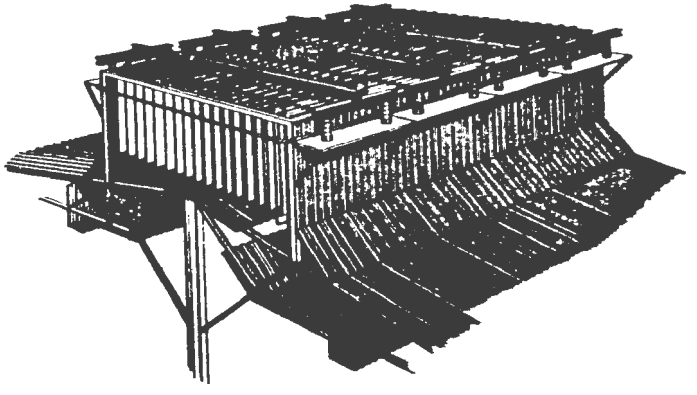

Wet Type

Fig 11. Hitachi Roof Mounted EP

Large Capacity and Special Application List of Hitachi Electrostatic Precipitator

NOV, 1, 1977

Hitachi Plant Engineering and Construction

	Application	Client	Site location & Plant NO.	Capacity Nm^3/h	Applied Temp C	Outlet dust Content g/Nm^3	Collecting efficiency %	Year of Completion
1	Thermal Electric power Generation							
	oil fired boilor	Tokyo Electric Power Co, Inc.	Kashima Power Station No,6unit (1000MW)	2,820,000	140	23	82	1973
		Kyushu Electric Power Co, Inc	Buzen Power Station No,1unit (500MW)	1,500,000	145	12	88	1977
	Coal fired boilor	Tokyo Elictric Power Co, Inc	Yokosuka Power Station No,1,2unit (265MW)	845,000	128	1.2	96	1960
		Kansai Electric Power Co, Inc	Amahigashi Power Ststion No,1,2unit (156MW)	481,000	130	0.6	98.	1963
2	Cement Industry							
	Suspension Preheater Kiln (Dopole Kiln)	Osaka Cement Co, Ltd.	Kochi No,7 plant	420,000	170	0.05	99.8	1973
	Air quenching Cooler	Osaka Cement Co, Ltd.	Kochi No,7 plant	400,000	180	0.05	99.8	1973
3	Iron and Steel Industry							
	L.D Converter	Nippon Steel Corp	Muroran	250,000	720	0.1	99.7	1969
	sintering machine	Nippon steel Corp	Muroran No,5 plant	400,000	80	0.1	98.6	1969

	scarfing machine	Sanyo Special Steel Co,Ltd	Himeji	72,500	44-66	0.05	98.75	1972
4	Nonferrous Metal Industry							
	Copper flash Smelter	Nippon Mining Co,Ltd	Hitachi	99,000	350	0.2	99.2	1972
	Copper Converter	Nippon Mining Co,Ltd	Hitachi	45,000	400	0.2	87.5	1972
	Copper Pyrite Bed Roaster	Nippon Mining Co, Ltd	Hitachi	48,250	350	0.2	94	1972
	Zink fluid Bed Roaster	Nippon Mining Co, Ltd	Tsuruga	34,300	350	0.2	99	1968
5	Municipal Incinerator							
		Tokyo Metropolitan Office	Adachi	102,000	300	0.03	99.4	1977
	Wide space EP	Maebashi City	Maebashi	75,600	250	0.1	94.2	1976
6	Petroleum Industry							
	Fluideric Catalytic Cracking	Koa Oil Co,Ltd	Osaka	289,6000	200	0.05	75	1973
7	Glass Industry							
	Glass smelting furnace	Nihon Taisan Bin Kogyo Co,Ltd	Oogaki No,3 plant	23,000	250	0.02	99	1974
8	Gas Industry							
	Coke oven environment (plate type wet EP)	Tokyo Gas Co,Ltd	Turumi	300,000	40	0.02	99.3	1969

APPENDIX D

SUMITOMO HEAVY INDUSTRIES, LTD.

R. Ep

ROOF-MOUNTED ELECTROSTATIC PRECIPITATOR

1977, Oct.

SUMITOMO HEAVY INDUSTRIES, LTD.

INTRODUCTION

Recently, it is believed that the most important matter in planning a production facilities is how to make a energy saving program.

Meanwhile as for the dust collecting system of buildings the Bag Filter Type systems, consuming such a large amount of electric power for forced suction as used in a blooming mill, have been applied so far in many cases. However, our Electric Building Dust Collector, which we are going to explain now, is an completely different type of building dust collector. Namely, it is Roof-mounted Electrostatic Precipitator (hereinafter called R-EP.) mounted a compact and light electric dust collecting system directly on the upper part of building which collects dust contained gas rising by natural ventilation. The present machines have been adapted, since we put on sale on 1973, to many equipment such as converters, electric furnance, blast furnace pouring places, foundry shops, etc., and are enjoying good reputation.

We believe it will greatly contribute to energy saving of your company. We wish to explain here general characteristics and matters to be kept in mind in planning, especially, about R-EP for steel making convetor and a comparison to other types of building dust collecting system.

1. Workshop dust collection system

The systems and their general appraisals are as shown in the following table.

Table 1 Merits and demerits of various workshop dust collection systems

	(1) Canopy hood System	(2) Closed workshop system	(3) Close workshop system with opening-closing type monitor	(4) Canopy hood and closed workshop combined system	(5) R - EP
Dust collection systems	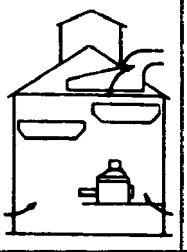	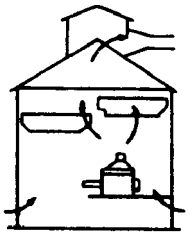	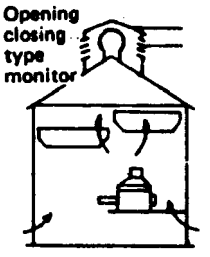	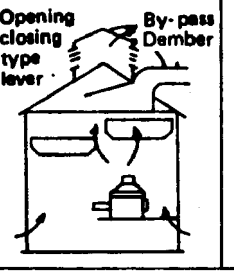	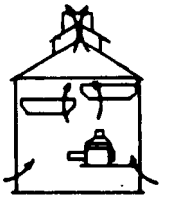

	Merits	Demerits
(1) Conopy hood system	(1) The collection efficiency of dark colored gas is good. (2) The working environment is good by the combind use of the monitor.	(1) Those which cannot be collected by the hood leak into the open air. (The effect on open air distrurbance is great.) (2) Due to installation of a great remodeling becomes necessary from the aspect of structure and strength of the workshop top. (3) A great amount of treating air capacity is necessary.
(2) Closed workshop	(1) There is a gas storage effect. (2) Cost of installation is cheap (Will do with a small amount of trating air capacity.) (3) There are hardly any colored gas leaks.	(1) The gas will originate an inversion phenomenon when the balance of the storage capacity and the suction capacity is offset and there lies a fear of harming the working environment.

	Merits	Demerits
(3) Closed workshop system with opening-closing type monitor	(1) The gas storage effect can be utilized. (2) Since it is of an opening-closing type of monitor, the working environment is good.	(1) Cost of installation is expensive. (2) Inspection and maintenance of the monitor part are necessary.
(4) Canopy hood and closed work-shop combained system	(1) The collection efficiency of dark colored gas is good and there is also a strage effect. (2) Since it is of an opening-closing type monitor, the working environment is good.	(1) Cost of installation is expensive (2) Due to installation of hood, a great remodeling becomes necessary from the aspects of structure and strength of the workshop top. (3) Inspection and maintenance of the monitor part are necessary.
(5) R-EP	(1) Installation areas of by-pass, etc., become unnecessary. (2) Operating and installation costs are cheaper in comparison to the bag-filter. (3) Pressure loss can be extremely minimized.	(1) A problem point exists on the dust collection efficiency. (2) Actual results of this system for electric arc funances are presently very scarce.

In the smoke collectkng system of workshop precipitators, there are presently 5 systems undertaken.

1) Canopy hood system

This system is a method where a canopy hood is attached to a position which does not interfere with the crane operation, etc., and the generating dusts are instantaneosly suctioned by the hood. In order to suction and treat the dusts generating from

the furnace intactly, a large capacity exhaust blower which corresponds to the momentary maximum value of the generating dusts is necessary. Since the natural ventilation monitor of the workshop is left opened, the hot air and steam of the heating device, heated lumps, etc., within the plant are discharged in their condition from the monitor. In case the dusts generating from the furnace are of mass volume and the treating air capacity is small, the dust and hot air leaking from the hood will be discharged from the exhaust monitor and it will not be favorable from the point of environmental pollution prevention, however, cases of extremely deteriorating the environment within the workshop are nil.

2) Closed workshop system

This most widely adopted system stores the dusts generating from the electric furnace at the top of the closed workshop and performs gradual exhaustion within a fixed period. Since the top of the workshop is used as a smoke stop, the capacity of about 1/2 - 1/3 of the momentary maximum dust volume will be sufficient as the treating air capacity of the precipitator even when a great volume of dust is generated.

If the airtightness is perfect, there is no fear of the dust leaking from the workshop, however, in case the treating air capacity is too little in quantity, there lies a fear of the dust flowing within the workshop and deteriorating the working environment. Particularly, there are heat sources such as ladle, dryer, etc., within the closed workshop and when this hot air remains at the

top of the workshop, the low temperature dusts will hand over in the workshop so it becomes necessary to consider extra treating air capacity. Moreover, in case the storage capacity becomes insufficient due to the balance offset of the workshop closed capacity and the treating air capacity of the precipitator, the dust descending phenomenon will originate and the environment within the factory will be deteriorated.

Generally, when determing the treating air capacity of this system, factors of ventilation time, storage capacity, fixed ascending current, maximum dust generating time and ascending speed are considered.

3) Closed workshop system with opening-closing type monitor

This is an interim system of the above 1) and 2) systems and in case there are no generating dusts or in case of dust-free hot air, natural ventilation is performed by using the workshop monitor and in case of mass volume dust generation, the workshop monitor is closed and the stored dust is suctioned and this operation is repeated. However, there remain problems on the opening-closing mechanism, operation and reliability of the monitor. Since this system is of the monitor opening-closing type, the working environment is superior in comparison to other systems.

4) Canopy hood and closed workshop combined system

Similarly as in system 3) above, this is an interim system of the above 1) and 2) systems and a canopy hood is provided directly on top of the electric furnace and the opening-closing of the work-

shop monitor is made possible. In case the generating dusts are few, they are suctioned by the canopy hood and natural ventilation is performed with the workshop monitor left opened and in case of large volume dust generation, the monitor is closed and suction is performed from the canopy hood and it is a system where suction and treatment are made upon temporarily storing the leaked dusts within the workshop. Similarly as in system 3) above, there remain problems such as reliability, intricacy, etc., of the mechanism in this system also.

5) R-EP

The electrostatic precipitator is an equipment which provides electric charge to particles within the dusts and separately collects them to the collecting electrodes and this system is a method in which this electrostatic precipitator is mounted on top of the workshop and dust collection is performed.

In comparison to the bag filter, it does not necessitate installation spaces of a precipitator, exhaust blower, etc., and the operating cost is cheap.

2. Electrostatic precipitator on the top of workshops

1) Characteristic of general electrostatic precipitators

As well-known, the principle of the electrostatic precipitator is based upon generating a corona discharge between the discharge electrode and the collecting electrode and charging the suspended dusts within the gas with electricity by means of negative corona discharge, collecting the charged dusts to the collecting electrodes by the Coulomb's force, releasing the collected dusts by means of hammering, washing, etc., and collecting at the bottom part and removing out from the vessel.

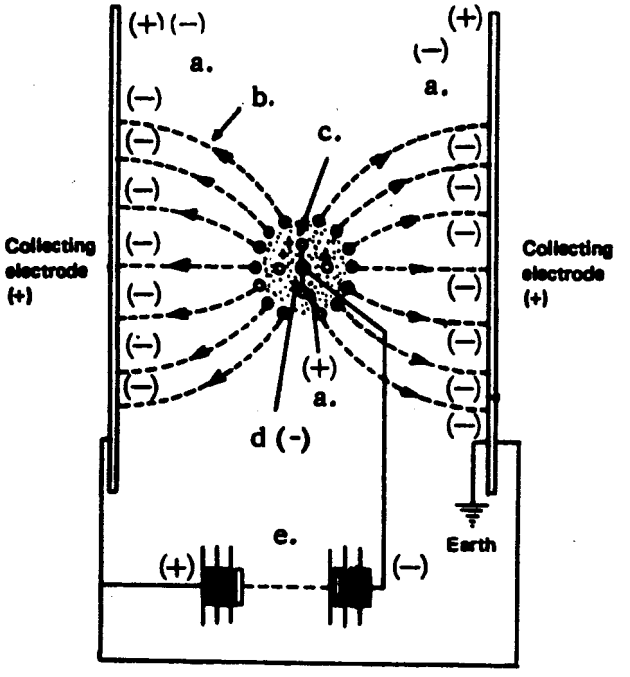

a. Electric charge layer
b. Locus of particles
c. Ionization sphere
d. Discharge electrode
e. High voltage DC power source

Fig. 1 Principles of electrostatic precipitator

(1) High collecting efficiency

The dusts are almost instantaneously electric charged by the numerous negative ions, electrons, etc., between the electrodes and by means of the high voltage power source which has the electric charging capacity of about 100 each for those of about 1 micron size and about several ten each for those of 0.1 micron being applied to the charging and discharge electrodes, the dusts are powerfully collected to the collecting electrodes by the Coulomb's force.

In this case, the dust is to move while receiving a resistance due to viscosity of the gas, however, in comparison to coarse dust, it is found that the finer the dust, the greater the charge and since the viscosity resistance is small, they can be adequately collected. Resultantly, since the electrostatic precipitator is capable collecting coarse dust as well as fine dust, a high collecting efficiency can be obtained. It is common that a collecting efficiency of 99.99% is obtained in the wet type and that of 99.9% is obtained in the dry type.

(2) Operating cost is cheap

The Coulomb's force works on the dust as aforementioned but since it does not practically work on the gas, only a slight ionic wind is originated. Since the inner part contains only the discharge and collecting electrodes and is free from other obstacles, etc., the gas pressure loss is extremely small and even when including the perforated gas distribution plate which

is provided so that the dust is uniformly distributed flow, there is only a loss of 10 - 20 mmAq and resultantly, the capacity of the exhaust blower which suctions the gas can be made small..

Moreover, electricity consumption amount will vary according to applications, however, it is about 0.05 - 0.5 KWH/1000m^3.

(3) The maintenance fee is cheap

There are hardly any movable parts in the inner part so when it is used under an ordinary good condition, it is practically maintenance-free.

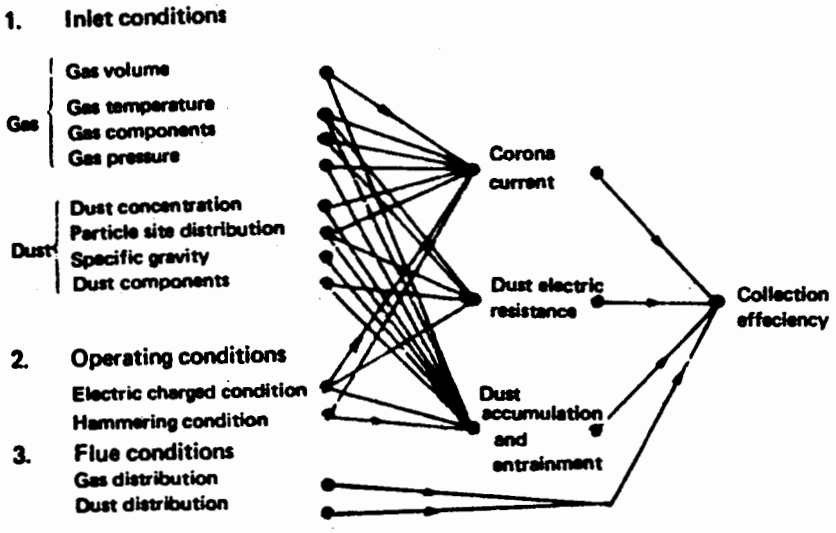

Fig. 2 Performance factorial diagram of electrostatic precipitator

On the factors which the electrostatic dust collecting action has, there are many factors which provide influence to the collection efficiency, however, the following 5 items are resultantly important.

(1) Control of voltage and current

It lies in how great a voltage is placed, how great a corona current is flown and how great the Coulomb's force is made so it is necessary to provide sufficient care in the controlling method. There are the following control methods which are currently employed.

Saturable reactor system

Thyristor system

(2) Invesed ionization phenomenon

This is a phenomenon in which electric discharge is made from the surface of the dust which has been collected and accumulated at the collecting electrode in case of a dry type and as causes, the specific resistance of the dust is dominant. Generally, it generates at the value of more than 10^{11} - 10^{12} Ω - cm and results as shown in the figure below.

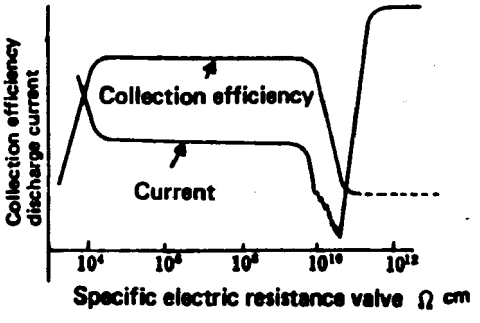

Fig. 3 Relations among the specific electric resistance value and the collection efficiency and discharge current

The collection efficiency will drop by about 10 - 20% and an extremely great amount of current will flow and moreover, the voltage will drop up to 20 - 40% of the normal voltage.

Since there are various studies made by many persons on the elucidation of this phenomenon, details will be omitted here, however, it is believed that under the present state, there are no remedy means on the current dry type precipitator, itself. Therefore, the method of varying the gas conditions at the precibitator inlet and lowering the resistance value of the dust, itself, has been employed.

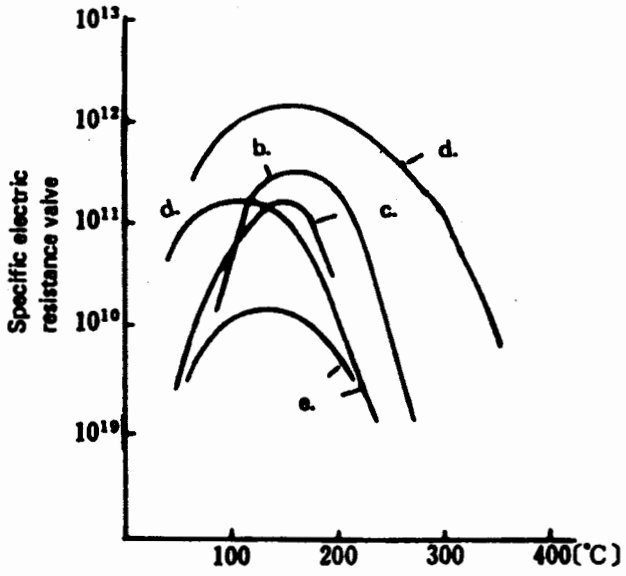

a. Limestone kiln moisture 10%
b. Generating boiler moisture 3%
c. Sintered dust-proof moisture 3%
d. Sintering machine main exhaust moisture 5%
e. Sintering machine main exhaust moisture 10%

Fig. 4 Relations among the specific electric resistance value and temperature, moisture, etc.

As shown in the above diagram, there are the raising and lowering of the gas temperature, increase of moisture in the gas, addition of sulfuric acid, etc. It has recently been described that the ultra high-voltage wide pole pitch type, field screen type, etc., are types in which inversed ionization is difficult to generate, however, the actual results and details are unknown.

(3) Re-entrainment of dust

The re-entrainment of dust also originates on the dry type and in this case, the phenomenon occurs when the electric resistance of the dust is less than the value of 10^4 Ω - cm. Under the present condition, there are no progress on the remedies for this case and it is approximately the same as mentioned for the preceding item (2).

In case of heavy and special boiler dusts, the addition of ammonia is performed as the additive into the gas for combining it with SO_3 in the gas and forming ammonium sulfate and raising the resistance value up to above 10^4 Ω - cm. Moreover, on the rapping method of the rapping device, that is, on the strength, frequency, rapping pieces of collecting electrodes, etc., the method with the least re-entrainment is being studied and on the strength too, the actual necessary gravitational acceleration (g) is being measured and efforts are exerted for grasping the suitable value.

Furthermore, upon considering that re-entrainment is unavoidable, there is also the method of providing a damper at the back of the rapping section and intercepting the gas flow during the period. The effect of re-entrainment due to rapping of the front chamber, etc., is descreased by minutely separating the gas flowing direction chambers or lowering the height of the collecting electrode.

(4) Flow regulation of gas and dust

It is necessary to prevent the drift of the gas and dust within the precipitator. Normally, there is a drift of about 30 - 40%, however, this has been fairly improved by preparing a model prior to designing and preliminarily installing it in a suitable position through testings. Moreover, with the development of the measuring technology, actual measurement by an actual machine and labor adjustment have become possible.

In case this drift is great, the effect placed on the efficiency is great and there are times when the reentrainment increases, the adhesion amount of dust to the collecting electrode is biased and the outlet dust concentration increases by about 10 - 20%.

2) Points which have been considered at development

(1) Inversed ionization phenomenon

The electric resistance value of the dust to be handled by the workshop precipitator is about 10^9 - 10^{13} Ω - cm and high so there lies a danger of originating this phenomenon.

(2) Weight reduction

As measures for obtaining a lightweight body, plasticization of the collecting electrode, the strength reduction due to removal of the rapping device and removal of the rain entering prevention roof have been performed and a great weight reduction has been made,

(3) Re-entrainment prevention

The prevention of re-entrainment of collected dust since they are mainly less than 100 μ.

(4) Explosion

Since there lies a danger of coal dust and carbon monoxide explosions, make it an opened type to extent possible and avoid an airtight structure.

The semi-wet type (intermittent cleaning) electrostatic precipitator on the top of wrkshops has been developed upon providing considerations on the abovementioned points.

3) Characteristics

(1) Simplification of facilities

By directly mounting the electrostatic precipitator on top of the workshop, the hood, duct, blower, motor, chimney and foundation work are not necessary.

(2) Extremely cheap running cost

Treatment by natural outflow of the exhaust gas eliminates the necessity of a large capacity blower so treatment can be made by extremely cheap running cost.

(3) Purges noises

Noises do not practically originate as a blower is not necessary.

(4) Economizes on installation space

No installation space is necessary for the precipitator, blower, etc.

(5) Inspection and maintenance are simple

Since movable parts such as the rapping device, blower, motor, etc., are few in number, not only are inspection and maintanance simple but their frequency is less.

(6) Highly stabilized collection efficiency

A high collection efficiency can be maintained as an electrostatic precipitator is employed.

(7) Dust removal system is semi-wet type

Removal of dust is done by an intermitted washing system that to separate the R-EP into many small blocks and wash dust away block by block.

Washing of 1 block takes only about 10 minutes a day, and the quantity of water required is only about 600 l/min.

As it is a semi-wet system, there is no tear for back colona effected even for the dust of high resistivity further, it is effective for re-scattering.

In addition, as there is no such equipment as rapping system, dust valve, screw conveyor, etc., the building is not subject to any vibration, and maintenance is easy.

(8) Natural ventilation type

As R-EP utilizing hot air and building draft, the building shall not be filled with gas even in case of power failute, thus, there will be no trouble for ventilation.

4) Structure and function

Construction of R—EP

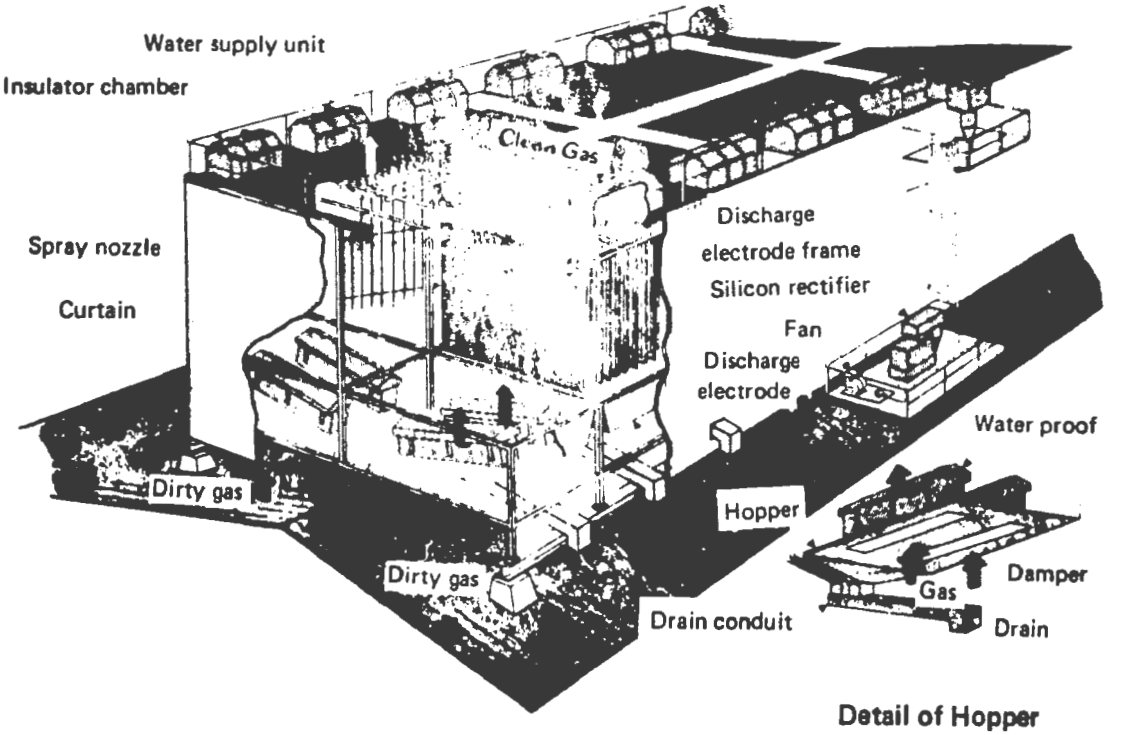

Detail of Hopper

(1) Gas flow

The dusty gas ascends by the heat current and the draft effect of the workshop, however, when the resistance increases and the ascending current is obstructed by installing a precipitator and the dusty gas remains within the workshop, the working environment will become unfavorable. Thereforce, it is necessary to select a brand which has possibly small resistance and is capable of collecting minute particle dust when installing a precipitator on top of workshops.

This equipment employs the electrostatic precipitator with a small resistance and which is capable of collecting minute particles and the hopper and louver possess a flow regulation effect so that the dusty gas volume uniformly flows within the electrostatic precipitator.

(2) Shell

By drastically employing special lightweight steels, the structure of the workshop beams are those which require minimum reinforcement.

(3) Collecting electrode

Although practically all collecting electrodes of conventional electrostatic precipitators are of steel plate property, it is necessary to use material quality with a small specific gravity for weight reduction.

The temperature of the gas flow within the workshop is practically all below 80°C and by using conductive synthetic

resins with heat resisting and corrosion resisting properties, the problem of weight reduction is solved.

(4) Discharge electrode

In this equipment, the gas temperature is below 80°C and the heat distortion is comparatively small and the frame structure which does not necessitate rapping due to adoption of the intermittent spraying system proves to be extremely convenient for installation, centering, adjustment, etc., and it is also a great merit construction aspect.

(5) Dust shaking systems

In the dust shaking system (rapping system) of dry type electrostatic precipitators, there are 3 systems; the pneumatic, electromagnetic and the machine systems.

All systems shake off the dust by means of impacts and vibrations. In the electrostatic precipitator on the top of workshops system, however, upon considering reasons such as maintenance of movable parts being troublesome, it would be undesirable to apply vibrations to the workshop, the collected dust is extemely fine, etc., the intermittent spraying system was employed.

For determining the spraying conditions which indicate the maximum removal efficiency under minimum water volume during intermittent spray, experiments were performed on the configuration of the spray nozzle, spraying hydraulic pressure, spraying angle, nozzle pitch, etc., and the optimum spraying condition was discovered.

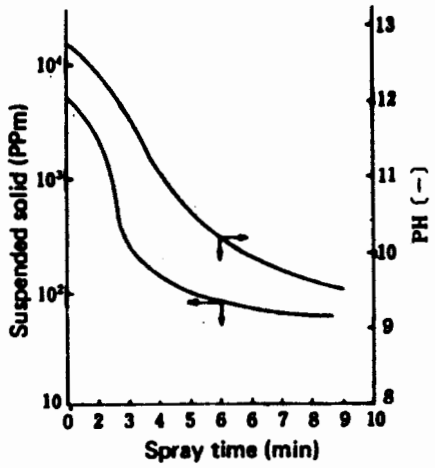

Fig. 6 Variations of suspended solid and pH in waste water by spray time

(6) Waste water treatment method

The dust collected at the collecting plate is water washed and removed by intermittent spraying and become slurry. This slurry passes through the louver hopper and is guided to the waste water treatment installation by the drainage gutter.

As an example, variations by time of suspended solid and pH in sprayed waste water in a converter plant is shown in Fig. 6 above.

In can be understood from the chart that the suspended solid and pH are extremely great immediately after spray commencement but several minutes later, they have considerably declined. Thus, the setting of the spray time is facilitated by this curve.

The waste water treatment installation differs according to the slurry composition, treatment object (Determined by the waste

water disposal standard), waste water volume, etc.

An example of the waste water treatment method is shown in Fig. 7 below. In the diagram, the sprayed waste water is sent to the settling tank after being lowered up to the prescribed pH at the storage and neutralization dual-purpose tank and after the clear water in the settling tank is further adjusted to the stipulated pH, a portion of it is reused as the intermittent spray liquid and the remainder is discharged as final effluent. On the other hand, the sludge is sent to the hydroextractor via the sludge storage tank and here it is hydroextracted and discharged as cakes.

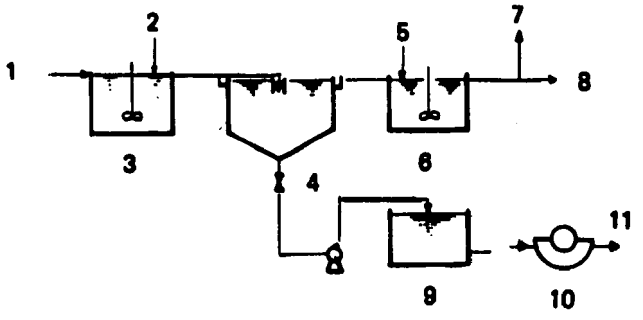

1	Sprayed waste water	2	Chemical addition
3	Storage and neutralization both-purpose tank	4	Sedimentiation (Settling) tank
5	Chemical addition	6	Neutralization tank
7	To spray equipment (Recycling)	8	Final effluent
9	Sludge storage tank	10	Hydroextractor
11	Cake		

Fig. 7 Example of waste water treatment

5) Consideration points on installation of R-EP

It is necessary to provide care on the following points when planning the installation of the electrostatic precipitator on the top of work-shops.

(1) Generating gas volume

Since the ascending current from the high temperature dust generating source is a heat current which ascends while mixing the ambient air, it can be considered that the ascending speed will differ according to the degree of the gas temperature. Therefore, it decreases in proportion to the distance from the high temperature dust generating source and at the top of the workshop, it lies in a tendency of becoming relatively uniform.

a) In case to install on an existing building

It is safer to make an plan based on the results of measurement of discharge gas before hand at the monitor position of existing building.

b) In case to install on a new building

Find out the theoretical amount of gas to be generated using the following formulas and determin the amount based on the resulting value after including the value of our experience.

Amount of gas generated from convertor (Qz)
(Design standard of hood)

$Qz = 1.95\ Z^{3/2} \times \sqrt[3]{H'}\ H'$ (Theoretical amount of gas)

$H' = \frac{1.45}{60}\ As\ (\triangle t)^{4/3}$

$Q = (1.5 \sim 2.5)\ qz$

(Generated gas volume = EP treated gas volume)

$As = \frac{\pi}{4}\ D_0^2$ (Convertor area)

$\triangle t = 1400 - 20$ (Temperature difference)

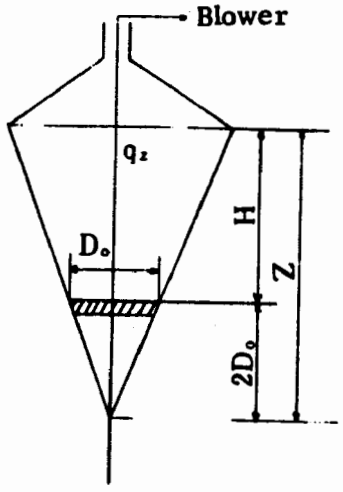

Fig. 3 shows the method to explain throretical amount of gas to be generated.

Fig. 3 Diagram of Theoretical volume of gas generated

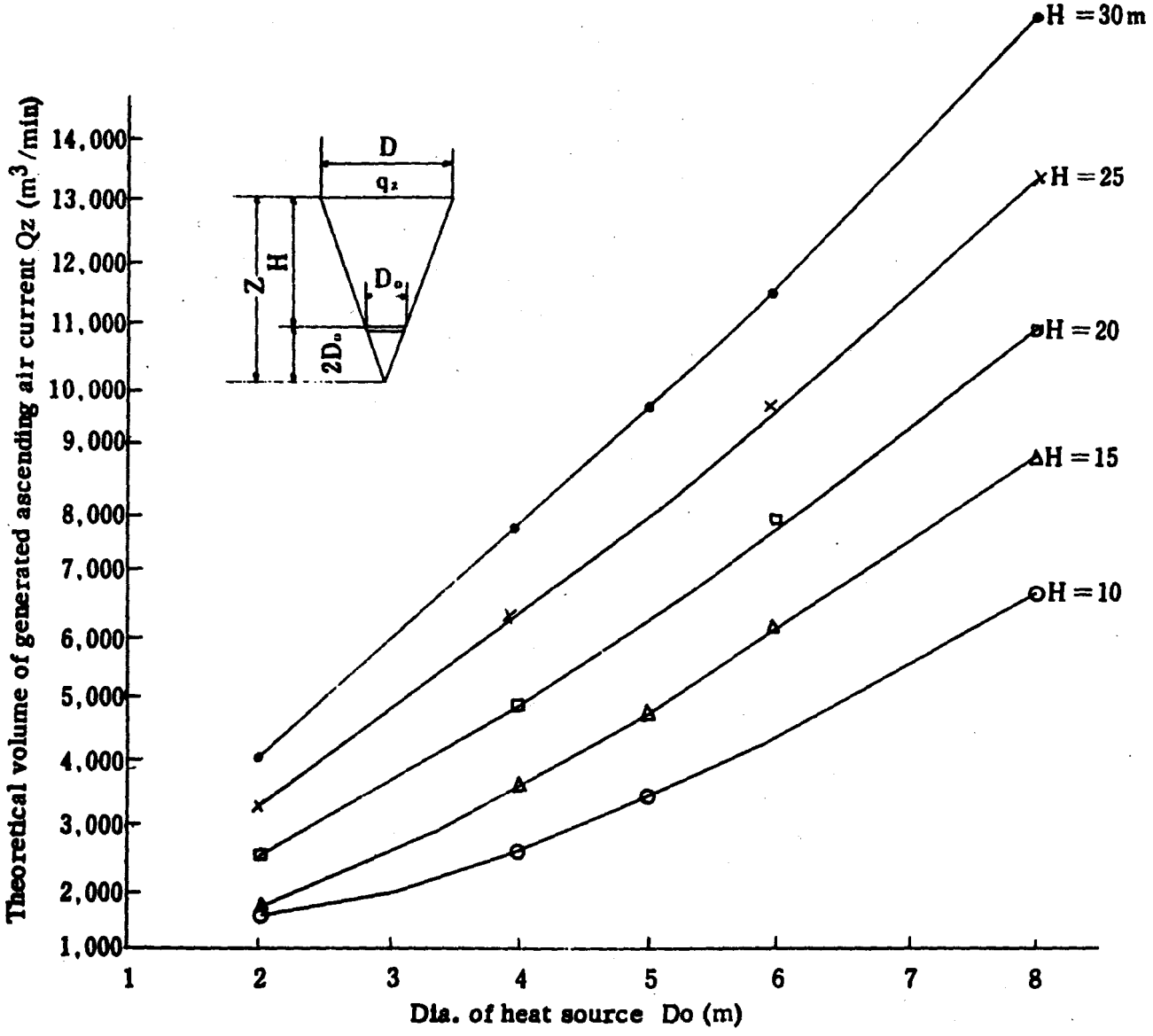

2) Generating dust

(a) Particle size distribution

The suspended particle diameter of the suspended dust within the workshop will differ according to the ascending speed and the workshop height.

If the generating dust is a minute particle, it is necessary to prevent the re-entrainment of collected dust upon taking into consideration the water spraying frequency of dust shaking.

(b) Dust generating volume

Since the dust generating volume is related to the dust generating source and the gas ascending speed, it is necessary to preliminarily perform measurement. In most cases, however, it seems that it does not matter to presume it as less than 1 g/Nm^3.

(c) Composition and electric resistance of dust

The gas temperature within the workshop is normally less than 60^oC and the moisture in the gas is approximately the same as the moisture in the atmosphere under that temperature. Thefore, the electric resistance of the dust is controlled by the composition and particle size of the dust.

It would be preferable to select a more economical size equipment by preliminarily measuring the composition and electric resistance of the dust.

Result of analysis of accumulated dust on a converter building monitor mesured at the planning of R-EP for converter delivered by our company are shown in Table No. 1

Quality Test Table of dust 1

1. Analysis Results of constituents

Name of Sample	T.Fe	SiO_2	Al_2O_3	T.S	MgO	Na_2O	K_2O	CaO	ZnO	PbO	T.C	NiO	MnO
A Co.	29.6	8.5	3.35	1.1	1.45	1.65	0.17	22.85	0.7	0.15	4.85		
B Co.	45.07	8.76	3.30	0.154	1.32	0.32	0.17	8.91	1.99	0.36	9.93	0.02	
C Co.	32.92	6.92	2.50	1.23	5.57	0.57	0.16	13.88	0.57	0.086	2.16		4.44

2. Grain size distribution Table 1 - B

	~10 μ	10~20 μ	20~50 μ	50 μ~	True specified gravity
A Co.	15.5	19.5	54	11	3.49
B Co.	4	11	53	32	4.27
C Co.	13.5	30.5	42.0	14.0	3.94

3. Electric resistivity & difficulty in dust collecting Table 1 - C

	30 ℃	60 ℃	90 ℃	Moisture	Difficulty in dust collecting
A Co.	6.78×10^{11}	6.83×10^{12}	1.04×10^{13}	Atmosphere	Normal
B Co.	5.3×10^{5}	9.6×10^{5}	5×10^{6}	〃	Good
C Co.	7.31×10^{12}	9.11×10^{12}	1.07×10^{13}	〃	Normal

3) Installation place of the electrostatic precipitator

It is not economical to mount an electrostatic precipitator to all monitors on top of the workshop. It is advisable to install it only at the part where the dust passes upon considering the diffusion distance of the smoke from the dust generating source and the variation width due to the direction of the wind.

Show the general arrangement of R-EP delivered by our company.

Fig. 2 General arrangement of buildings dust collecting system for A company

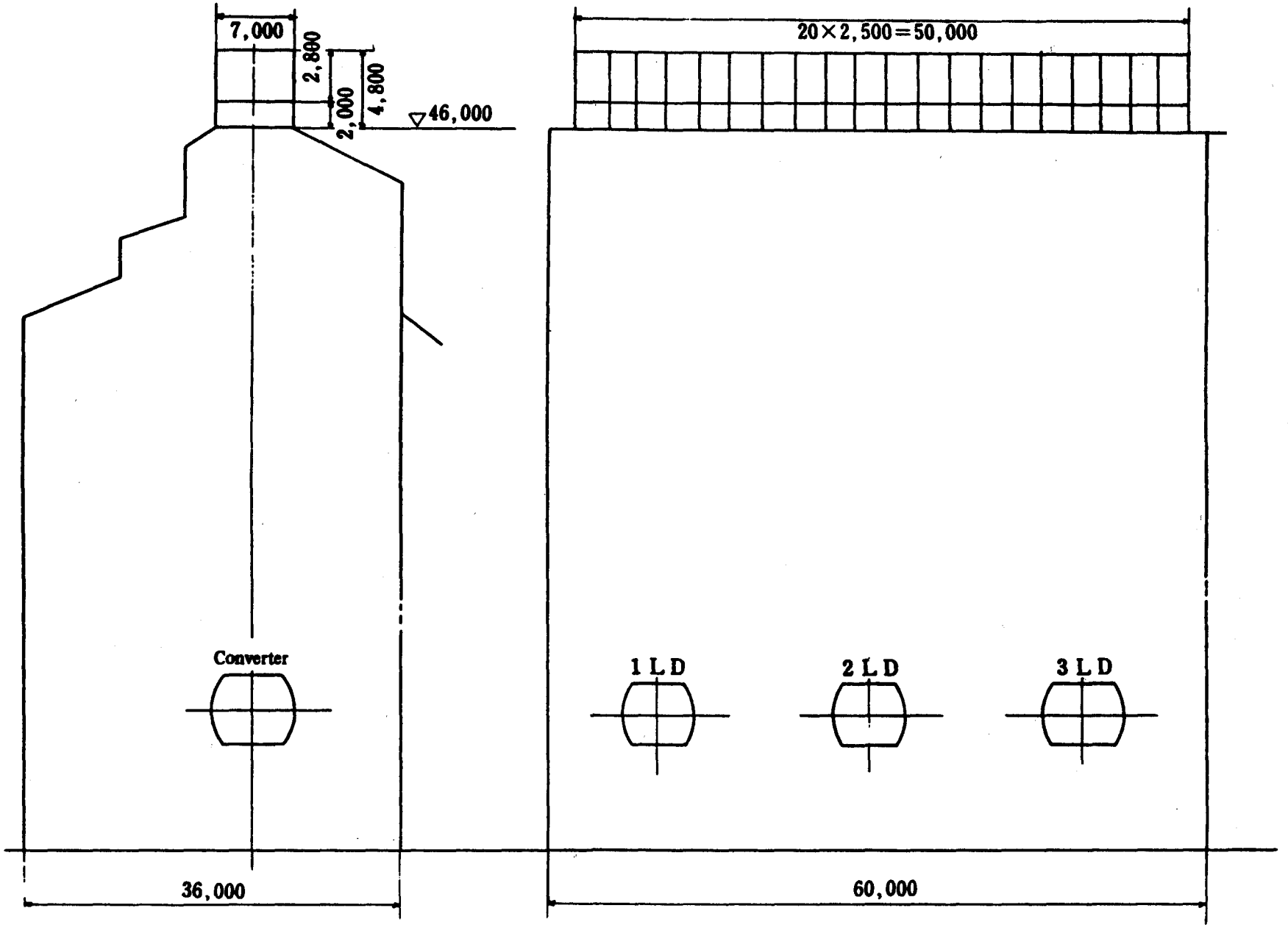

Fig. 3 General arrangement of buildings dust collecting system for B company

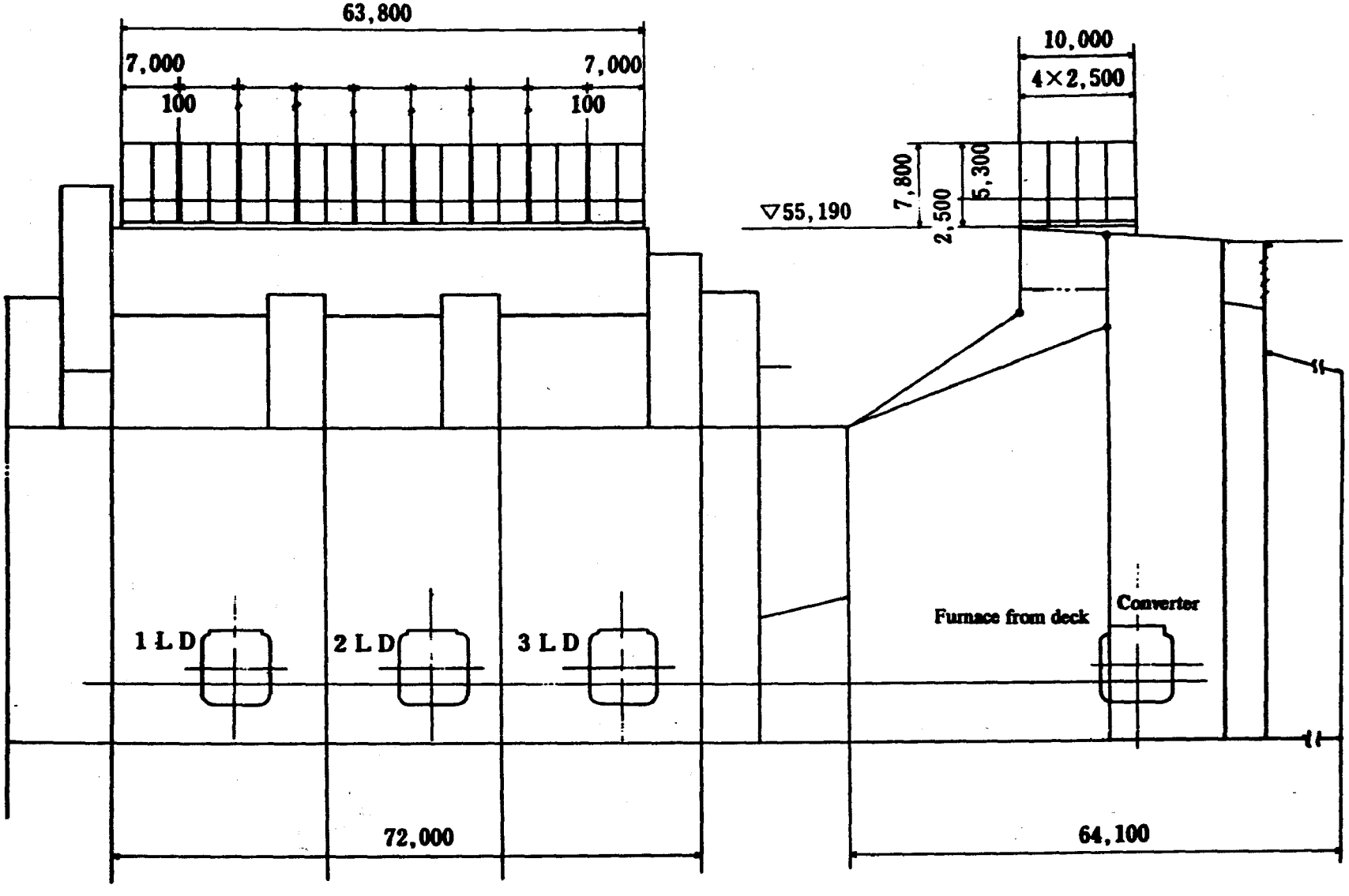

Fig. 4 General arrangement of buildings dust collecting system for C company

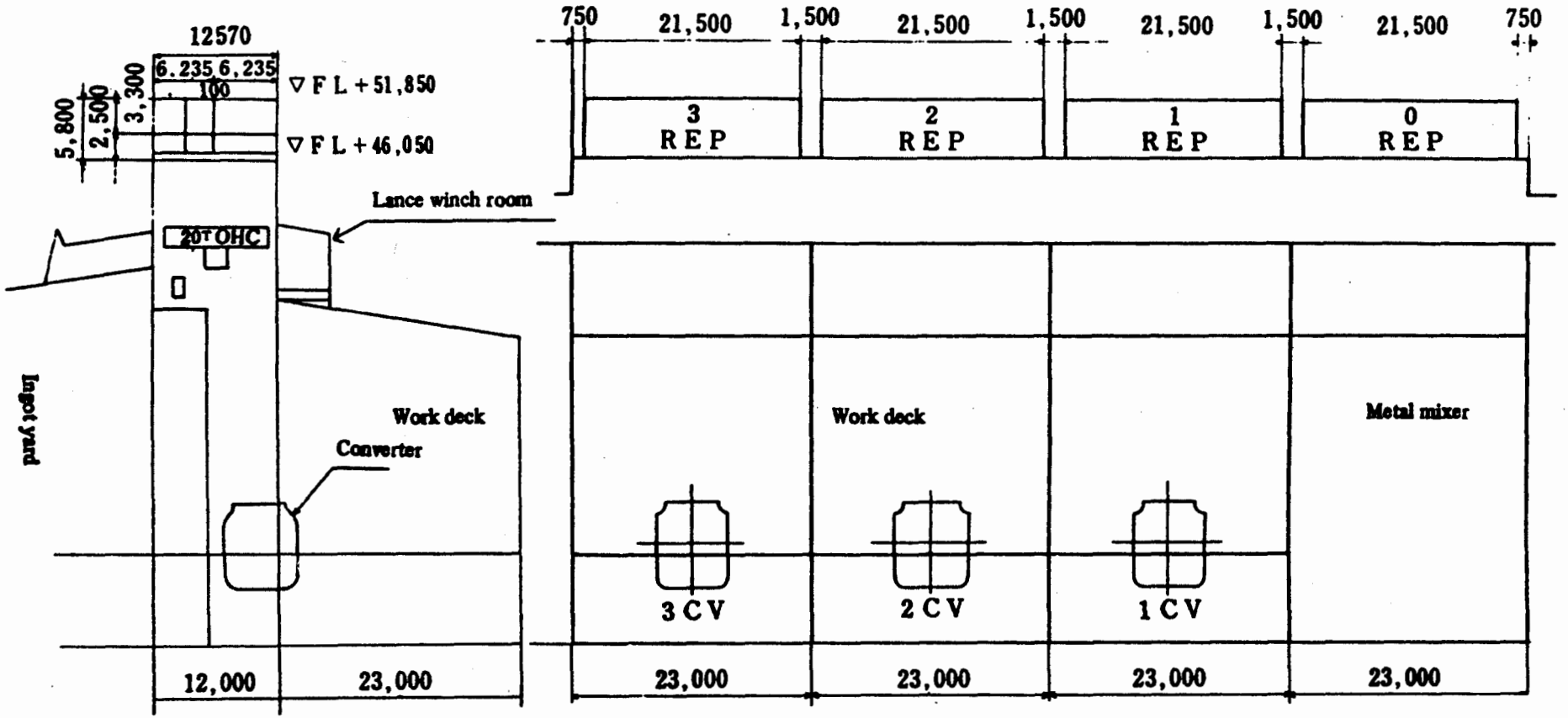

Fig. 5 General arrangement of buildings dust collecting system for D company

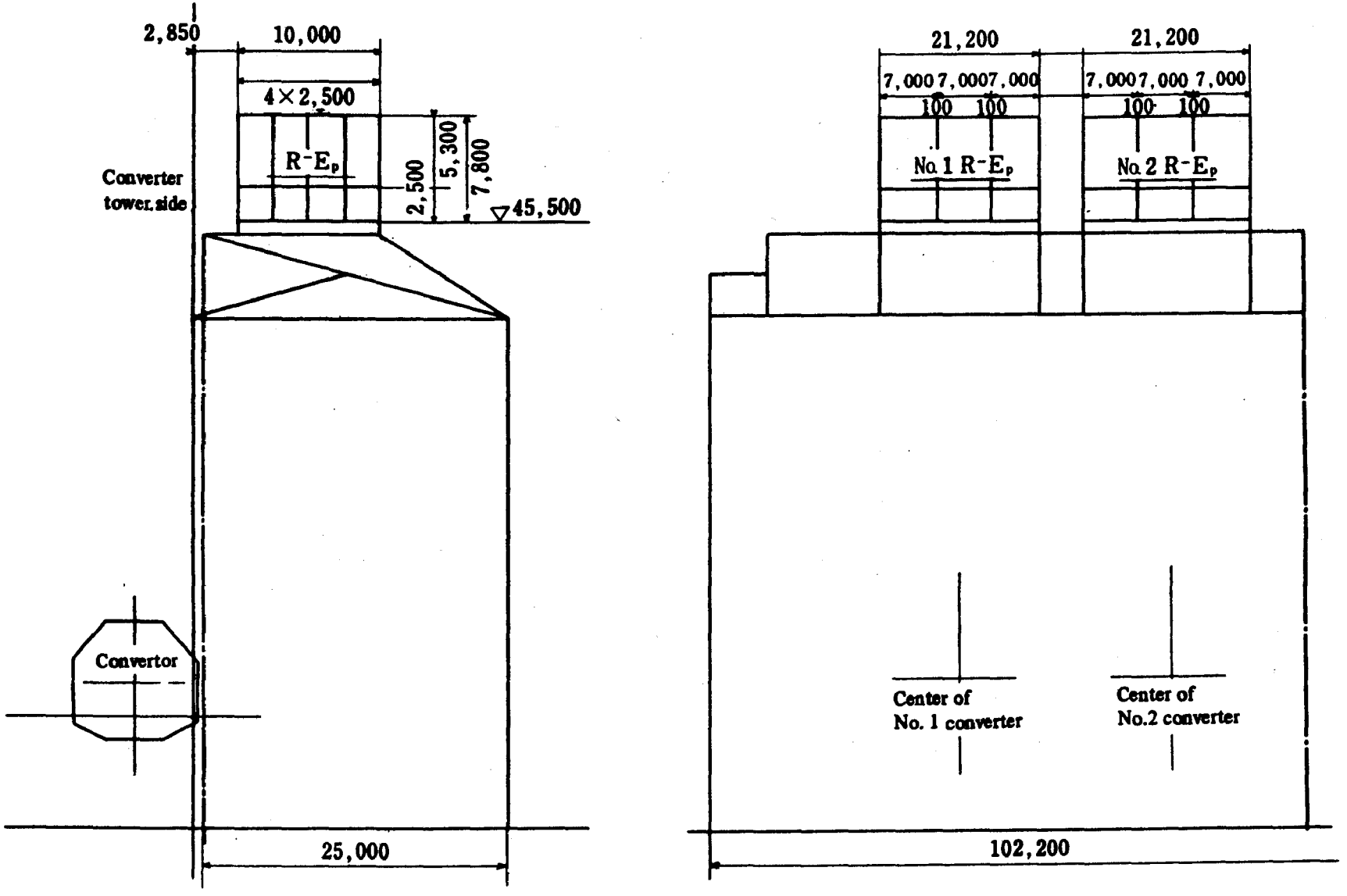

(4) Beam strength

It is necessary to investigate beforehand on the beam strength of the existing workshop when mounting on existing workshops.

(5) Installation term

In case of newly constructed workshops, it is merely a high place installation work, however, in case of existing workshops, caro should be provided since the installation work term will differ according to the conditions of location.

(6) Ventilation

As our building dust collector is of an electric dust collector of natural ventilation type, the pressure loss is very small as equal to or less than that of the monitor.

For ventilator, we take a) number of ventilation and b) the value of A/V.

In general, number of ventilation of less than 20 (A/V $1 - 4 \times 10^{-3}$) is considered as bad

a) Number of ventilation

Amount of gas treated m^2/H/building volume

b) A/V

A (Building upper opening area m^2)/B (Building volume m^3)

Ventilation data of our delivered R-EP are shown on the Table - 2.

Ventilation condition Table - 2

Delivered to	Title of converter	No. of revolution		A / V		Ventilation condition (visual inspect)
		in monitoring	after R-EP installed	in monitoring	After R-EP installed	
A Co.	80 T/CH x 3 L.D. Converter	1 1.1	1 4	1.1 2 $\times 10^{-3}$	2.2 $\times 10^{-3}$	Slightly bad
B Co.	250 T/CH x 3 L.D. Converter	1 5.6	1 5.6	1.7 3 $\times 10^{-3}$	2.4 2 $\times 10^{-3}$	Normal
C Co.	160 T/CH x 3 L.D. Converter	2 2.6	1 7.1	2.7 1 $\times 10^{-3}$	5.9 4 $\times 10^{-3}$	Normal
D Co	230 T/CH x 2 Q - BOP	—	2 0	—	3.3 5 $\times 10^{-3}$	Normal

(7) Comparison between designed value and result classified by delivered place

Design values and actual results of our derivered R-EP for converter are shown in the Table - 3

Comparison between designed value and actual result

Delivered to		Quantity of total gas m^3/min	Quantity of gas per converter m^3/min	R-EP flow rate m/S	Inlet dust contents g/Nm^3	Outlet dust contents g/Nm^3	Remarks
A 社	Design	24,000	8,000	1.77	0.1	0.02	Fitted with aux-dust collector LD
80T/Ch×3	Result	13,600~28,600	4,500~9,500	1.0~2.1	0.269(max)	0.047	
B Co.	Design	43,800	14,600	1.78	0.4	0.03	〃
250T/Ch×3	Result	51,000	17,000	1.9	0.33	0.02	
C Co.	Design	30,936	7,734	0.8	0.4	0.02	〃
160T/Ch×3	Result	31,902	10,634	1.1	0.35	0.02	
D Co.	Design	27,000	13,500	1.66	0.4	0.03	〃
230T/Ch×2	Result	27,000	13,500	1.66	0.3 – 0.8 Mainly 0.4 under	0.03 under	Q-BOP

6) Comparison in general between

R-EP and Bag Filter

Up to the present, forced suction type dust collectors have mainly been used, which collects dust by installaling a suction hood at the upper part of building and a suction on the ground which leads the gas to the bag filter.

Merits and demerits of this tipe and our R-EP are shown in the Table - 4 below;

Comparison in general between bag filter and R-EP

No.	Item	Bag filter	R - EP
1	Dust collecting system	Dust separation by collision, contacts diffusion, and filtering action	Separation of dust from gas by static current in electrifying grains with the corona discharge
2	Separable grain	Below 1 u	Below 1 u
3	Scope of Application (1) Gas temperature	in case of building dust collection, less than 60°C No problem	Same as left
	(2) Moisture contents of gas	No problem for building dust collection	Same as left
	(3) Dust properties	Not proper for hygroscopic gas	When electric resistance is between 10^6 - 10^{13} Ω -cm no problem

No.	Item	Bag filter	R - EP
4	Functions of dust collector		
	(1) Dust collecting capacity	Over 99% Exhaust gas density is less than 0.03 g/Nm^3	Exhaust gas density is 0.03 g/Nm^3 - 0.02 g/Nm^3
	(2) Pressure loss	Bag filter 150 - 200 mmAq piping etc. 150 - 250 mmAq Total 300 - 450 mmAq	Same level as monitor
	(3) Removal of grasped gas	Removal of dust grasped on cloth filter by filtrage 1 Reverse washing + mechanical vibration 2 Pulse pressure by high pressure air	Dust adhered to electrodes are washed away by water once a day
	(4) Water	Not required	Water required for the above 600 l/min x 10 min x 4 Unit No x 1 day
	(5) Draining Work	Not required	Drainings for the above is required.
	(6) Hood	Hood at the upper part of building ceiling and pipe duct from the hood to the bag filter are necessary	Not required but, piping for water is required
	(7) Ventilator	Air pressure 300 - 450 mmAq is required	Not necessary Ventilation fan for anti-polution for insulator is required (2.2KW - 3.7KW)
	(8) Pump	Not necessary	Pump 600 l/min is required

No.	Item	Bag filter	R - EP
4	(9) Area for installation	Instllation area for bag filter on the ground is required	R-EP is installed directly on the building
5	Utility	Electricity charge, exhaust for running cost are very large amount	No exhaust fan is required, as natural ventilation. Power for cottrel, ventilation fan, and water pump is about 1/10 - 1/20 of bag filter

7) Running cost

As explained previously, our R-EP is of natural ventilation system. Thus, no large type suction tan is required as bag-filter type, which reduces electric power consumption to a large extent or about 1/10 - 1/20 of the latter.

Washing water used for dust removal is also very small amount or 0.4 - 0.6 m^3/min in addition, the wasted water can be used again as circulating water after water treatment, therefor, the water really required to be supplied is only for replacement for dewatering cakes carried away and evaporated amount, and it is very small amount.

Comparison of electric power consumed between our delivered R-EP for converter and bag-filter in the Table - 5.

Comparison of consumed electric power between R-EP & bag-filter Table - 5

Delivered to	Treated gas volume m^3/min	Consumed electric KW	
		Bag-filter (assumption)	R — E p
A Co.	24,000	2,800 KW	R-EP source 32 KW Motor 9 KW 41 KW
B Co.	43,800	5,100 KW	R-EP source 110 KW Motor 40 KW 150 KW
C Co.	30,936	3,600 KW	R-EP source 89 KW Motor 80 KW 169 KW
D Co.	27,000	3,100 KW	R-EP source 61 KW Motor 27 KW 88 KW

Note: Power consumption of bag-filter is assumed as;
△ P = 450 mmAq.

8) Prior investigation methods

Since there are no suitable measures on the measuring method of exhaust gas from the workshop in JIS (Japanese Industrial Standard), the followings can be listed methods which tentatively conform to the present situation.

(1) Gas volume

A multi-point anemomaster (anemotherm) is installed at the monitor discharge port and continuous recording is made in the relation with operation and the gas volume is decided

from the timeelanse variation and the discharge volume.

Besides this, there are the windmill system and the Pitot tube system, however, the anemomaster is suited for the discharge speed (2 - 3 m/s) from the monitor.

(2) Dust concentration

Since it is not an uniformed dust generation and there are many cases where dust generation is made in a short period, it is considered suitable to measure a high volume air sampler which has the suction volume of about 1 - 2m^3/mm.

(3) Measuring method of electric resistance value

In this measuring method, there is the method of measuring the dust collected at the actual site upon taking it back to the laboratory and the method of performing direct measurement at the actual site flue. We will indicate below an example of the dust apparent resistivity measuring equipment which is used at the laboratory.

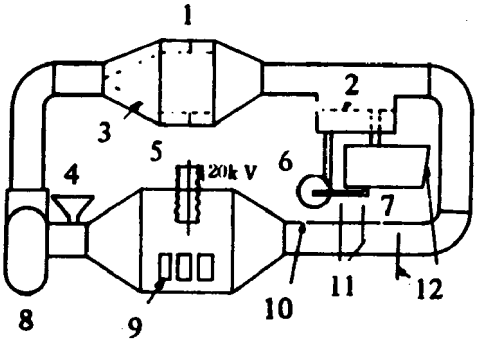

1 Electric heater
2 Heat retaining water bath
3 Baffle
4 Dust casting port
5 High voltage (-) teminal 20KV
6 Pump
7 Heater
8 Blower
9 (1) Needle-Plate dust collecting compartment housing
10 (2) Thermal refining port
11 Thermometer
12 Thermostat

Fig. 9 Dust resistivity measuring equipment (race track method)

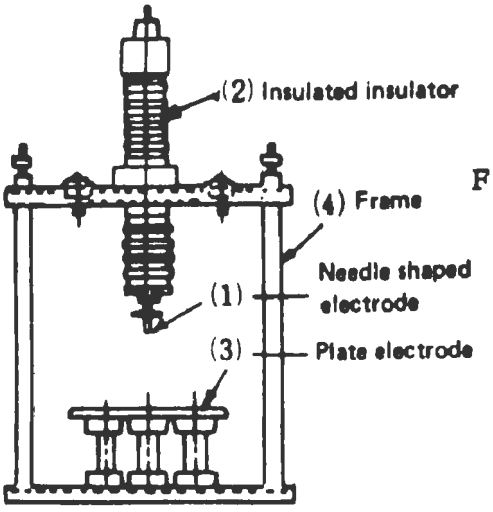

Fig. 10 Dust resistivity measure

Circulate the dusty gas in the dust collecting compartment housing (1) of Fig. 9 while maintaining the dusty gas at a desired temperature and humidity and collect and accumulate the dust on top of the plate electrode by corona discharge of the needle electrode and calculate the dust resistivity by measuring the current which flows within.

The gas temperature can be freely maintained from room temperature up to 300 - 400°C and the humidity can also be regulated up to the range of 0 - 40% by volume ratio.

Moreover, the dust collecting housing interior can also be maintained at an atmosphere which is close to the actual condition by imoregnating specific gas from port (2).

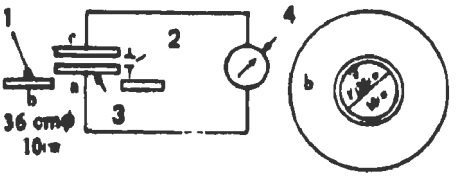

1 Guard electrode
2 Dust layer
3 Main electrode
4 Ohm Meter

Fig. 11 Dust layer resistivity measuring method (Parallel plate electrode method)

As shown in the drawing, when the resistance measuring opposed plate is lowered and closely contacted to the dust surface which has been collected and accumulated on top of the plate by the corona discharge between the needle-plate electrode, and voltage is applied between both electrodes and the current of the main electrode is measured, the apparent resistivity of the dust can be computed by the following formula.

$$v = i \cdot q \cdot \ell$$

$$q = \frac{v}{i \cdot \ell} \quad (\Omega - cm)$$

whereas,

V : Voltage placed on dust layer (V)

i : Current density (Reading of ampere meter − Area of main electrode) (A/cm^2)

ℓ : Thickness of dust layer

E.P. SUPPLY LIST

Sumitomo Heavy Industries, Ltd.

March, 1977

Company	Plant	Number	Size mm	Gas volume m³/min	Temp. °C	Inlet Dust load g/Nm³	Outlet Dust load g/Nm³	Date Installed
Kobe Steel, Ltd. Kobe Works	Steel converter	1 (Test Plant)	6,800W×5,000L (GL+43750)	2040	60	0.264	0.032	Mar. 1972
Kubota Tekko Co.,Ltd. Imamura-Works	Casting	2	3,400W×10,000L	1134	60	0.1	0.03	Jul. 1973
Pacific Metals Co., Ltd. Hachinohe-Works	Electric furnace	2	6,000W×10,500L (GL+28362)	2000×2	60	0.3	0.03	Aug. 1973
Kobe Steel, Ltd. Kobe Works	Steel converter	1	6,000W×30,000L (GL+43750)	24100	60	0.1	0.02	Nov. 1973
Pacific Metals Co., Ltd. Iyama-Works	Electric furnace	1	6,000W×16,500L (GL+26500)	4870	60	0.3	0.03	May 1974
Yamato Kogyo Co., Ltd. Hirohata Works	"	1	6,000W×10,000L (GL+21400)	2430	60	0.3	0.03	Sept. 1975
Kobe Steel, Ltd. Takasago Works	"	1	6,000W×30,000L (GL+37500)	8200	60	0.2	0.02	Jan. 1975
Kawasaki Steel Corporation Mizushima-Works	Steel converter	1	10,000W×25,000L (GL+33750)	43000	60	0.4	0.03	Mar. 1976
Sumitomo Metal,Ltd. Wakayama-Works	"	4	12,570W×21,000L × 4	10000×4	60	0.4	0.04	Mar. 1976
Kawasaki Steel Corporation Chiba-Works	Q-Bop	2	10,000W×21,000L (GL+43500)	13500×2	60	0.4	0.03	Dec. 1976
Ito Metal Abrasive Co.,Ltd.	Electric furnace	1	7,000W×8,000L (GL+15250)	2670	60	0.61	0.03	Sept. 1975
Komatsu, Ltd. Himi-Works	"	2	7,000W×11,000L × 2 (GL+27135)	2710×2	60	0.3	0.03	Dec. 1975
Washino Machine Co., Ltd. Imamura-Works	"	1	6,000W×7,500L (GL+16700)	3000	60	0.2	0.02	May 1976
Washino Machine Co., Ltd. Kumagai-Works	"	1	4,100W×15,000L (GL+15200)	2440	60	0.1	0.02	May 1976
Howa Machinery Ltd.	"	2	4,100W×15,000L (GL+15200)	4048	60	0.3	0.03	Apr. 1976
Tokyo Steel Manufacturing Co., Ltd. Hayama-Works	"	1	7,000W×22,200L (GL+35200)	9000	80	0.5	0.03	Dec. 1977
Kobe Steel, Ltd. Kakogawa-Works	Blast furnace	2	21,200W×20,000L 14,100W×20,000L (GL+37000)	15000 10000	40 ~ 90	0.6	0.03	Mar. 1978

APPENDIX E

NIPPON STEEL-KIMITSU WORKS

(no papers)

APPENDIX F

SHINWA TRADING AND ENGINEERING CO.

(no papers)

APPENDIX G

ISOGO POWER STATION

(no papers)

APPENDIX H

KYOTO UNIVERSITY

DYNAMICS OF NATURALLY COOLED HOT GAS DUCT

KAZUYUKI HOTTA, NOBORU YAMAMURO
AND KOICHI IINOYA
Department of Chemical Engineering, Kyoto University, Kyoto

(Reprinted with permission)
Reprinted from
JOURNAL OF
CHEMICAL ENGINEERING
OF
JAPAN
Vol. 7, No. 6 (1974)
Pages 455—461

DYNAMICS OF NATURALLY COOLED HOT GAS DUCT*

KAZUYUKI HOTTA, NOBORU YAMAMURO**
AND KOICHI IINOYA
Department of Chemical Engineering, Kyoto University, Kyoto

Damping characteristics of a pulse-wise temperature peak along a naturally cooled hot gas duct is studied experimentally with possible applications to bag filter systems in mind. In face of changes in gas properties, due to the temperature change, a linear model is found useful for approximate prediction of the transient. Charts for estimating the peak height of the outlet gas temperature are contrived to be readily used by design and operation engineers.

Introduction

In bag-filter operations for higher-temperature gases, the gases must be properly cooled prior to filtration. For this purpose, a spray tower or other positive means may be inserted in the duct system which leads the gas from the dust source to the filter. It is, however, possible to expect a considerable natural cooling along the duct if the source and the filter are separated by some distance. In this latter case, prediction of the temperature drop is not so simple as in the case of incompressible fluid, since the physical properties of the gas change with the temperature along the duct. Moreover, the gas temperature of the source often undergoes pulse-wise changes like those shown in Fig. 1.

The particular example shown is taken from an automatic record of the air temperature from a furnace plant in batch-wise operation.

Formulae for predicting the damping characteristics of the temperature peak are not yet found in

* Received on November 28, 1973
Presented at the 38th Annual Meeting of The Soc. of Chem. Engrs., Japan, April 4, 1973
** The Japanese Geon Co., Ltd.
〒060 札幌市北区北13条西8丁目
北海道大学工学部衛生工学科　堀田和之

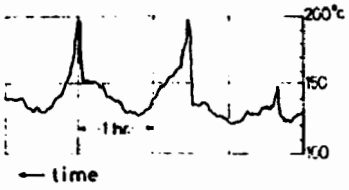

Fig. 1 Typical example of temperature change at dust sources

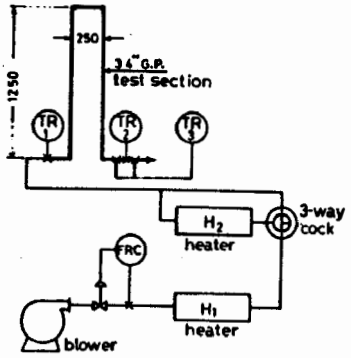

Fig. 2 Laboratory test model

standard handbooks. The system is naturally designed amply on the safe side, resulting in wasteful redundancy.

To supply the designers of such systems with some practical information, experimental as well as theoretical investigations were made and the results are presented in this paper. Even though the study was motivated by the problem in dust-collecting systems, we treated the problem as that of naturally cooled ducts in general without remarkable pressure drop along them. The effect of solid particles is not explicit, since it has an effect only on the inside film coefficient. Nor did we use dust-laden gas in the laboratory experiments. We assume here that the values of the heat transfer coefficients in the equations derived in this report are known from different sources.

1. Experiments

Experimental data were obtained through two different sources, one from a laboratory test model sketched in **Fig. 2**, the other from a full-scale industrial duct system for a bag filter system.

In the laboratory test model, the air flow rate was automatically controlled and the heater H_1 was used to set up a steady state. In dynamic test, this steady state was upset by adding another preheated heater H_2 to the pipe line and also boosting the power supply to the heater H_1. The gas temperature was measured by thermocouples with quick response at the inlet TR1 and the outlet TR2 of the test section. The outlet wall temperature was measured by pasting two identical sheet-thermocouples TR3 on the outer surface of the pipe at equal distance of about 5 cm up- and downstream from the outlet point. This

Table 1 Data used for estimation of statics

Mass flow rate [kg/m²·min]	Temperature [°K] ambient air	inlet	outlet	outlet wall
15.53	302.0	409.5	348.6	334.7
15.57	302.0	395.0	343.3	332.3
15.49	301.5	409.0	347.1	334.3
15.51	301.0	362.1	329.5	321.5
15.47	302.4	407.0	347.8	337.2
15.52	298.8	371.6	331.5	324.0

was done to avoid erroneous measurements due to the cooling effect of the nozzle tapped for gas temperature measurement. The mean value of the outputs of the two was adopted as the wall temperature at the outlet. Random breeze was generated by three fans to keep the average ambient condition constant.

The industrial system tested had a diameter of 582 mm with 3.2 mm wall thickness. The test section was 50.4 m long and the mass flow rate was around 8.8 kg/m²·sec. For this system, most of the data were obtained from the automatic records of the control systems.

2. Statics

To estimate the static characteristics of the laboratory test model, numerous sets of steady-state data, with varying inlet temperature and air flow rate, were obtained. However, we show in the following only the results obtained from several sets of data for which the air flow rate is around 15.5 kg/min·m², since the dynamic test was performed with this flow rate. The data used are shown in **Table 1**. As the static model of the system, the following simplified equations were used.

$$(\pi D_i^2 G/4)[d(c_p T)/dx]+\pi D_i h_i(T-T_w)=0 \qquad (1)$$

$$\pi D_i h_i(T-T_w)=\pi D_o h_o(T_w-T_a) \qquad (2)$$

As to the notations, the list at the end must be referred to. The underlying assumptions are obvious from the forms of the equations.

[case 1] As the first step, both the inside and outside film coefficient h_i and h_o were assumed to be constant and their values were sought by a computer search program so as to minimize the differences between the calculated and observed values of the outlet gas and wall temperature T_2 and T_w. The criterion function used in the search program was

$$\phi=\sum_{i=1}^{6}\{(\Delta T_{2i})^2+(\Delta T_{wi})^2\} \qquad (3)$$

where ΔT_{2i} and ΔT_{wi} are the differences mentioned above in the i-th run of the experiments.

The converged values for h_i and h_o are shown in the first row of **Table 2**, together with the value of ϕ.

In the model calculation for this case, the specific heat of the gas was estimated by Eq. (5) at the mean

Table 2 h_i and h_o in various models

	h_i [kcal/°C·m²·sec]	h_o [kcal/°C·m²·sec]	ϕ [°C²]
case 1	0.020253	0.0058569	20.311
case 2	$0.02054\ (T/T_{st})^{0.253}$	0.0058267	19.420
case 3	0.019930	$0.0046442+1.3196\times10^{-5}\ (T_w-T_s)^{1.1675}$	8.2348
case 4	$0.019930\ (T/T_{st})^{0.253}$	$0.0046541+1.3201\times10^{-5}\ (T_w-T_s)^{1.1673}$	7.6642

value of the inlet and outlet temperature.

[case 2] Next, the inside film coefficient h_i was assumed to change with gas temperature, while h_o was still kept constant. The following widely accepted formula was used to describe the change in value of the inside film.

$$Nu=k_i Re^{0.8} Pr^{0.4} \tag{4}$$

where k_i is a constant. Physical properties of the gas were assumed to change in accordance with the following simplified state equations. These are accepted[1] when the pressure change along the duct is not too excessive.

$$\left.\begin{aligned} \mu&=\mu_{st}(T/T_{st})^{0.67}\\ c_p&=c_{pst}(T/T_{st})^{0.066}\\ \kappa&=\kappa_{st}(T/T_{st})^{0.865}\\ \rho&=\rho_{st}(T/T_{st})^{-1} \end{aligned}\right\} \tag{5}$$

combination of Eq. (4) with Eqs. (5) yields

$$h_i=h_{ist}(T/T_{st})^{0.253} \tag{6}$$

In the second search, h_{ist}, instead of the constant h_i, was sought and the results are shown in Table 2.

[case 3] Thirdly, h_i was set back to constant and the constancy restriction on h_o was relaxed. To the value of h_o, natural convection, forced convection and radiation were supposed to contribute. But the attempt to fit a phenomenological equation for h_o was abandoned after some trials, because inconsistent results, such as the blackness of radiation beyond unity, were obtained by the computer search program. Prediction of the film coefficient being rather trivial for the purpose of this study, the following empirical equation was adopted.

$$h_o=h_{oo}+k_o(T_w-T_s)^n \tag{7}$$

The search program converged to the optimal values shown in the third row of Table 2. The drastic improvement of the value of the criterion function ϕ over the previous cases indicates the controlling influence of the nonlinearity of h_o on the system statics.

[case 4] Finally, both h_i and h_o were allowed to change in accordance with Eq. (6) and Eq. (7), respectively. The results obtained are listed in Table 2.

The results of the static experiments are summarized in Fig. 3. Here, the curve showing the relation between T and T_w is obtained by solving Eq. (2) for the case where T_s is equal to 300°K (as was approximately the case in experiments) and Eq. (6) and Eq. (7) are inserted for h_i and h_o.

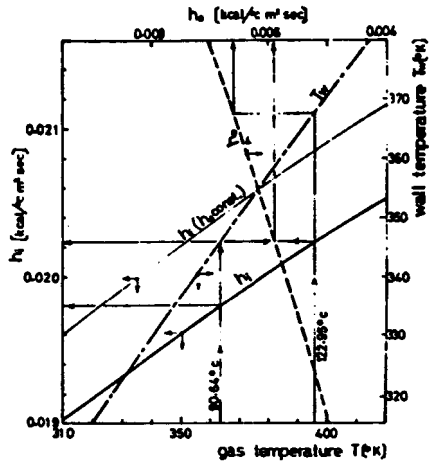

Fig. 3 Statics of laboratory test model

3. Dynamics

To investigate the dynamic dependency of the outlet temperature on the inlet temperature, pulse testing was used. The input pulses generated as depicted in section 1 of this paper were by no means similar in shape to those observed in practical systems, but were found good enough to stimulate the dynamics of the laboratory test model. A typical input and the response at the outlet of the test section are shown in Fig. 4 and Fig. 5.

In spite of the finding in the static study that the nonlinearity effect is significant, Fourier transforms of the input and output were tried to obtain approximate linear dynamics in the form of Bode diagrams, an example of which is shown in Fig. 6. The striking similarity of this diagram to those of heat exchangers for incompressible fluid, where nonlinearity plays but a minor role, suggested that the dynamics of the present system could be approximated by a linear model, at least for a small input change.

Thus a linear model was developed in a manner described in section 4 of this paper. First, the parameters of the model were estimated based on Case 1 of the static study and obtained the model frequency response shown in Fig. 6. The agreement with the observed response is only fairly good. But by more elaborate choice of parameters, which will be described later, the model behavior improves. Examples are shown in time domain in Fig. 5.

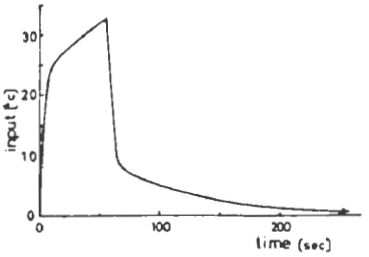

Fig. 4 Typical test input

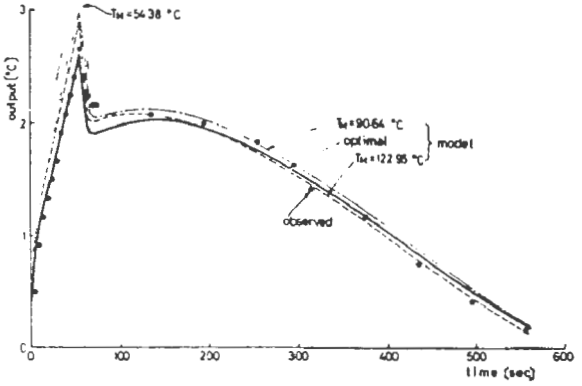

Fig. 5 Response of outlet temperature to the input of Fig. 4

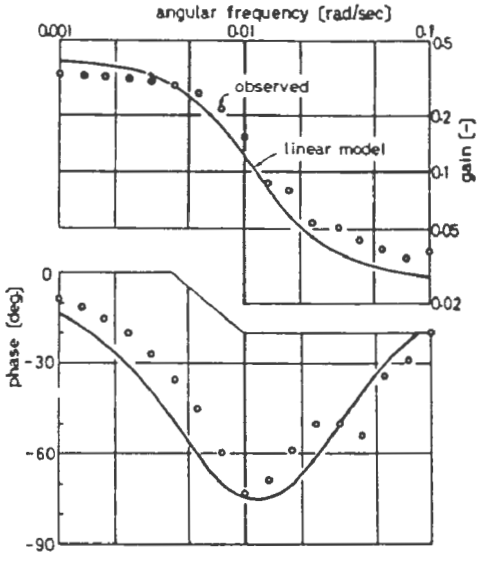

Fig. 6 Bode diagram of laboratory test model at $G \doteqdot 15.5$ kg/min·m²

Furthermore, the same type of linear model was formed for the industrial system and the response is compared in Fig. 7 with the observed response. Due to the rather complex geometry of the system and lack of exact static data, agreement is not as good as that of the test model, but seems good enough for most of design and operation planning purposes. This becomes more convincing when one considers the enormous time and memory space needed to solve a nonlinear partial differential equation model.

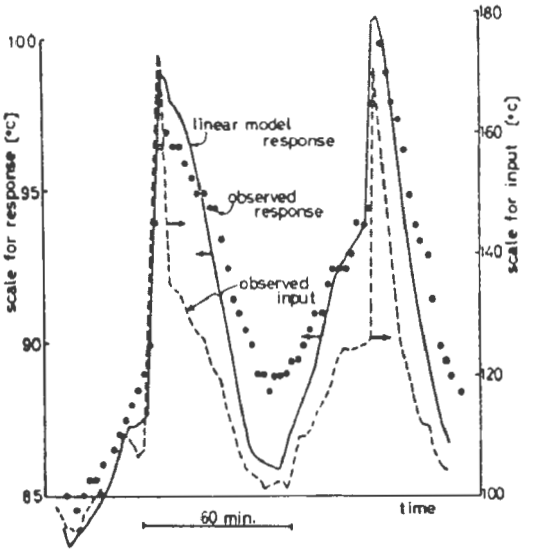

Fig. 7 Example of transient response of an industrial system and its linear model

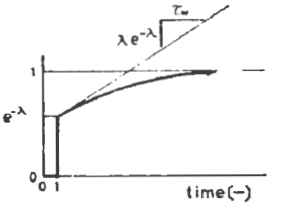

Fig. 8 A normalized step response of G (s)

4. Derivation of Linear Model

Here we treat the gas as if it were an incompressible fluid with constant physical properties. Then the discussion can be started with the following simplified equations.

$$\frac{\pi}{4}D_i^2\rho c\frac{\partial T}{\partial t}=-\frac{\pi}{4}D_i^2Gc\frac{\partial T}{\partial x}-\pi D_ih_i(T-T_w) \tag{8}$$

$$\frac{C_w}{L}\frac{\partial T_w}{\partial t}=\pi D_ih_i(T-T_w)-\pi D_oh_o(T_w-T_o) \tag{9}$$

A set of dimensionless variables and parameters are defined as follows:

$$\left.\begin{aligned}&\tau=t/(L\rho/G)\\&\xi=x/L\\&r_i=R_i/(R_i+R_o)=A_oh_o/(A_ih_i+A_oh_o)\\&r_o=1-r_i\\&\alpha=1/Wc(R_i+R_o)\\&\tau_w=(G/L\rho)C_w/(A_ih_i+A_oh_o)\end{aligned}\right\} \tag{10}$$

Then Eqs. (8) and (9) reduce to

$$\partial T/\partial\tau=-\partial T/\partial\xi-(\alpha/r_i)(T-T_w) \tag{11}$$

$$\tau_w(\partial T_w/\partial\tau)=r_o(T-T_w)-r_i(T_w-T_o)=r_oT+r_iT_o-T_w \tag{12}$$

The transfer function between inlet and outlet temperature is obtained[1] from these equations as

$$G(s)\equiv\Delta T_2(s)/\Delta T_1(s)=\exp\left[-\{s+\alpha+\lambda\tau_ws/(1+\tau_ws)\}\right] \tag{13}$$

where $\lambda=\alpha r_o/r_i$.

A normalized step response of $G(s)$ is schematically drawn in Fig. 8 and the mean delay time T_m for $G(s)$ is, as is easily found,

$$T_m=1+\lambda\tau_w=1+r_0^2C_w/C_g \tag{14}$$

The first term of T_m corresponds to a pure delay of one residence time of the gas. The second term accounts for the lag due to the heat capacity of the duct wall. When the inside fluid is a gas (liquid), the second (first) term usually dominates the other. In the industrial system investigated, the second term is approximately equal to 180 and in the laboratory test model it reaches as high as 1200, making it possible to neglect the first term without any loss of accuracy.

It then becomes important to know the characteristics of the transfer function

$$G_w(s)\triangleq\exp[-\lambda\tau_w s/(1+\tau_w s)] \tag{15}$$

which forms the essential part of the system dynamics. It is, however, not easy to calculate the response of this function to an arbitrary input. So an attempt was made to derive an approximate ordinary differential equation, which behaves similarly to Eq.(15), and enables us to use a computer routine such as the RKG method to calculate the response.

Instead of handling Eq. (15) directly, another related function $H_w(s)$ defined by

$$H_w(s)=G_w(s)-\exp(-\alpha r_o/r_i) \tag{16}$$

is introduced. Meaning of this separation of $G_w(s)$ into two parts is obvious from Fig. 8. Checked in terms of the frequency response, a first-order lag was not satisfactory in accuracy to simulate $H_w(s)$, so the following function was adopted.

$$H_w(s)\doteqdot H'_w(s)\equiv K(1+\tau_e s)/(1+vs+us^2) \tag{17}$$

The unknown parameters in $H'_w(s)$ were fixed so as that the following values coincide between $H_w(s)$ and $H'_w(s)$.

i) Initial slope of the step response.

ii) Up to second moments of the impulse response.

Introduction of the first condition is of advantage over the ordinary moment method in two respects. First it gives improved accuracy in the higher frequency range. Secondly, we can obtain explicit solutions for the unknown parameters as shown in Eq. (18), since the use of third moment, which inevitably introduces a cubic equation, is avoided.

The solutions thus obtained are:

$$\left.\begin{aligned} K&=1-\exp(-\lambda)\\ v&=(\lambda(\lambda+2)-2Ke^{\lambda})/(\lambda^2-K^2e^{\lambda})\cdot(\lambda\tau_w/2)\\ u&=(Kv-\lambda\tau_w)e^{\lambda}\tau_w/\lambda\\ \tau_e&=\lambda e^{-\lambda}u/(K\tau_w)\end{aligned}\right\} \tag{18}$$

Then

$$\left.\begin{aligned} &G_w(s)=H_w(s)+e^{-\lambda}\doteqdot(1+p_1s+p_2s^2)/(1+vs+us^2)\\ &\text{where}\\ &\quad p_1=ve^{-\lambda}+K\tau_e\\ &\quad p_2=ue^{-\lambda}\end{aligned}\right\} \tag{19}$$

Letting $\Delta T_{d1}(\tau)$ denote the input change $\Delta T_1(\tau)$ delayed in dimensionless time by unity or $\Delta T_{d1}(\tau)=\Delta T_1(\tau-1)$, Eq. (13) is approximately equivalent to

$$u\frac{d^2\Delta T_2}{d\tau}+v\frac{d\Delta T_2}{d\tau}+\Delta T_2 =e^{-\alpha}\left[\Delta T_{d1}+p_1\frac{d\Delta T_{d1}}{d\tau}+p_2\frac{d^2\Delta T_{d1}}{d\tau^2}\right] \tag{20}$$

This can be, in turn, rewritten into the following canonical form, amenable to computer treatment.

$$\left.\begin{aligned} \frac{dx_1}{d\tau}&=-\frac{v}{u}x_1+x_2-\left(\frac{v}{u}p_2-p_1\right)e^{-\alpha}\Delta T_{d1}\\ \frac{dx_2}{d\tau}&=-\frac{1}{u}x_1-\left(\frac{p_2}{u}-1\right)e^{-\alpha}\Delta T_{d1}\\ \Delta T_2&=(1/u)(x_1+e^{-\alpha}p_2\Delta T_{d1})\end{aligned}\right\} \tag{21}$$

where x_1 and x_2 are state variables of the system.

5. Discussion

Other than the geometry and the constant mass flow rate G, the values of h_i, h_o, c and ρ are needed to estimate the model parameters. We have Eq. (5) for c and ρ, and Fig. 8 for h_i and h_o. They are all dependent only on some representative gas temperature T_M during the transient. The input pulse of the experimental run, of which response is shown in Fig. 5, reaches 122.95°C at its peak starting from 90.64°C, while the output starts from 54.38°C staying within 3°C during the whole transient. Since both h_i and h_o are increasing functions of gas temperature, it is expected that the best representative gas temperature is located somewhere between these two extremes. The calculated responses with T_M set at the three different temperatures mentioned above do not meet this expectation. Not only does the curve for T_M=54.378°C considerably exceed the observed response, but the curve for T_M=122.95°C also does so in the early part of the response.

So, fixing the values of c and ρ at those of the mean inlet temperature (=106.8°C), we sought the best constant values for h_i and h_o on the least square error basis. The results are

h_i=0.02123 (205.7°C) [kcal/°C·m²·sec]

h_o=0.006488 (119.0°C) [kcal/°C·m²·sec]

and the corresponding response is shown in full line in Fig. 5.

The values put in parentheses above indicate the temperatures obtained from Fig. 3, the statics, corresponding to the best h_i and h_o. Even though h_o

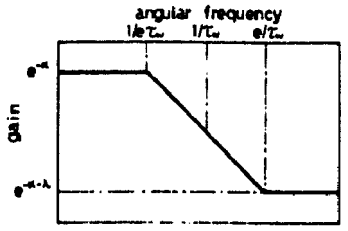

Fig. 9 Schematical gain diagram of linear model

value is fairly reasonable, the value of h_t is by no means in accordance with the results of the static experiments. For a mean temperature (=106.8°C) of the inlet, h_t should be around 0.02002, so the above value is some 6% higher. We suppose this was caused by the added turbulence due to valve operation to produce the temperature pulse in the dynamic test. Difficulty associated with the wall temperature measurements may be partly responsible for this discrepancy.

Furthermore, mathematical models generally tend to show quicker response than the real counterparts, since many minor factors causing delay, such as finite rate of heat conduction across the duct wall and mixing of the gas in axial direction, are neglected in model formulation.

In the present application of the linear model, however, a slight overestimation of the peak height is certainly tolerable. So we propose here using the peak temperature of the input pulse in the estimation of the parameters of the linear model.

A computer calculation based on Eq. (21) will yield the response to a input ΔT_{d1} of arbitrary pulse shape. However, in the situation where use of a computer is to be avoided, the peak height of the outlet temperature can be estimated based on the frequency response of the linear model. The gain diagram shown in Fig. 4 is essentially Z-shaped and can be schematized as Fig. 9. It is then expected that, if the angular frequencies of the major components of the input are less than $1/(e\tau_w)$, the ratio of the output peak height to that of the input is approximately $e^{-a}(\triangleq g_{max})$. As the frequency range of the input components extends beyond $\omega=1/(e\tau_w)$, or as the input pulse becomes sharper, the peak ratio will decrease, approaching the least value $e^{-a}e^{-\lambda}$ $(\triangleq g_{min})$. This reasoning is not rigorous, since phase shift is not taken into account. It is, however, found true for a triangular and a square input.

Let the peak height of the response of the linear model to an input shown in Fig. 10 (a) and (b) be p, and we define a sort of efficiency η as:

$$\eta=(p-g_{min})/(g_{max}-g_{min}) \qquad (22)$$

This index η is a function of λ and δ/τ_w. In the present application of the linear model, the range of the values that λ assumes is rather limited, and diagrams like those shown in Fig. 10 (a) and (b) are sufficient in practice to estimate the peak height of the output temperature, if the input can be approximated either by a triangle or a square. In Fig. 10 (a) the curve for $\lambda=4.0$ crosses that of $\lambda=3.0$. This is caused by the fact that as λ increses the response tends to show two peaks, one soon after the input peak and another considerably later. The height of the second one becomes higher than that of the first for the first time at $\lambda=4.0$ and at δ/τ_w is around unity. This however does not seem to happen in practical applications.

When a very high temperature peak is involved, the linear model should not be resorted to without more care. We do not have any experimental data to investigate this aspect of the problem. The example, taken from an industrial system and shown in Fig. 7, has higher temperature peaks. For this system we only knew an approximate value of the overall heat resistance R_1+R_2 from fairly steady operation data, and we set $r_i=0.3$ by guess. The model response thus obtained is seen to considerably overestimate the amplitude between peak and valley.

Conclusions

By a series of experimental studies, a linear dynamic model is found satisfactory to predict the damping characteristics of a temperature peak in a naturally cooled duct system. The theoretical linear model is transformed into a more convenient form for computer treatment. The method of estimating the constant values of the model parameters is studied and it is found that values based on steady-state operations result in overestimation of the temperature peak, a safer side prediction. For cases where the input is triangular or square, convenient charts are proposed to approximately estimate the peak height in design and operation planning problems.

Few studies have been made for the cases where temperature change is very large. We only show an example of applications to an industrial system with medium temperature change.

Acknowledgment

The authors would like to express their thanks to Shinto Dust Collector, Ltd., Showa Denko K. K. and Toyo Valve Co. for their great help in obtaining practical data needed for this research.

Nomenclature

A	= total area of heat transfer	[m²]
C_w	= total heat capacity of duct wall	[kcal/°C]
C_g	= total heat capacity of gas in duct	[kcal/°C]
c	= an equivalent uniform specific heat of gas	[kcal/°C·kg]

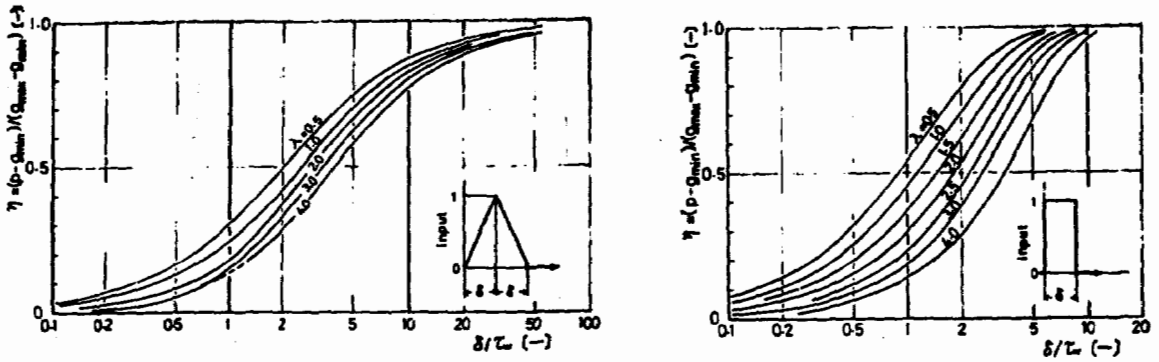

(a) triangular input (b) square input

Fig. 10 Diagrams for estimating approximate peak height for triangular and sqare input.

c_p	= specific heat at constant pressure	[kcal/°C·kg]	α	= defined in Eq. (10)	
D	= diameter of circular duct	[m]	δ	= duration of input pluse (refer to Fig. 10)	
G	= mass flow rate of gas	[kg/m²·sec]	η	= defined in Eq. (22)	
θ_{max}	= $e^{-\alpha}$	[—]	ε	= conductivity of heat for gas	[kcal/°C·m·sec]
θ_{min}	= $e^{-(\alpha+\lambda)}$	[—]	λ	= $\alpha r_o/r_i$	[—]
h	= film coefficient of heat transfer	[kcal/°C·m²·sec]	μ	= viscosity of gas	[kg/m·sec]
K	= a constant in Eq. (17)	[—]	ξ	= x/L	[—]
k_0	= a constant in Eq. (7)		ρ	= density of gas	[kg/m³]
L	= total length of duct	[m]	τ_o	= time constant in Eq. (17)	[sec]
n	= a constant in Eq. (7)		τ_w	= wall time constant defined in Eq. (10)	[sec]
p	= peak height	[°C]	ϕ	= criterion function	
p_1, p_2	= constants defined in Eq. (19)				
R	= heat resistance	[°C·sec/kcal]	⟨Prefix⟩		
r	= resistance ratio defined in Eq. (10)	[—]	Δ	= change from a steady state	
s	= Laplace transform parameter	[1/sec]	⟨Suffix⟩		
T	= gas temperature	[°K]	i	= inner surface of duct	
T_a	= ambient temperature	[°K]	o	= outer surface of duct	
T_M	= representative temperature of gas	[C°]	1	= inlet	
T_w	= wall temperature	[°K]	2	= outlet	
t	= time	[sec]	st	= standard condition	
u	= constant parameters in Eq. (17)	[sec⁻¹]			
v	= constant parameters in Eq. (17)	[sec]			
w	= flow rate of gas	[kg/sec]			
x	= distance from inlet of duct	[m]			

Literature Cited

1) Bankson C. A. and D. M. McEligot: *Int. J. Heat & Mass Trans.*, 13, 319 (1970)
2) Hotta, K. and M. Imaeda: *Kagaku Kōgaku*, 29, 980 (1965)

PARTICLE SIZE CLASSIFICATION BY DEPOSITION ANGLE IN A GAS CENTRIFUGE AT REDUCED PRESSURE

ZENNOSUKE TANAKA, HIROAKI TAKAI, NORISHIGE OKADA AND KOICHI IINOYA
Department of Chemical Engineering, Kyoto University, Kyoto, Japan

(Reprinted with permission)

Reprinted from
JOURNAL OF CHEMICAL ENGINEERING OF JAPAN
Vol. 4, No. 2 (1971)
Pages 167—171
THE SOCIETY OF CHEMICAL ENGINEERS, JAPAN

PARTICLE SIZE CLASSIFICATION BY DEPOSITION ANGLE IN A GAS CENTRIFUGE AT REDUCED PRESSURE*

ZENNOSUKE TANAKA, HIROAKI TAKAI**, NORISHIGE OKADA*** AND KOICHI IINOYA
Department of Chemical Engineering, Kyoto University, Kyoto, Japan

Centrifugal particle size classification by a gas centrifuge which produces a forced vortex was investigated at reduced pressures. In this method, different particle trajectories cause the formation of a continuous gradation of particle size on the rotor wall. Here, particles in the subsieve and submicron ranges were classified with good resolution because the 'Cunningham correction' increases as pressure decreases. Also, the computed solutions gave excellent agreement with the experimental results. The numerical solutions with and without the integral term for non-uniform motion have been compared, the approximate equation of best fit for the drag coefficient of spherical particles being used in both cases.

Introduction

The investigation of particle size classification based on the difference of deposition angle on the rotor wall of a gas centrifuge under forced vortex conditions at atmospheric pressure has been reported by Kriebel[1], and Burson et al.[2], but no study at reduced pressures has yet been reported.

In this method, the centrifuge produces centrifugal force fields within a forced vortex in the classification chamber. The particles travel from near the center to the rotor wall. In the classification chamber, the particle motion is delayed by Coriolis' force opposite to the direction of rotation, causing a gradation of particle size on the rotor wall. At reduced pressure, the mean free path of the gas molecules is of the same order of magnitude as, or greater than, the particle size. In that case, the effect of the slip factor in the 'Cunningham correction' is significant and the fine particles in the subsieve and submicron ranges can be classified with good resolution.

A comparison of experimental results with calculated results is presented for experiments at various pressures using glass beads, zinc powder and tungsten powder.

Experimental Apparatus and Procedure

A sketch of the centrifuge and associated equipment used to investigate particle size classification is shown in **Fig. 1.** As the centrifuge has an oil seal on the shaft to make it air-tight, it can be used at reduced pressures.

As shown in **Fig. 2**, the rotor is made of high-strength duralumin and the classification chamber is 19 cm inside diameter and 2 cm high. Two webs are installed in the rotor to ensure forced vortex conditions. The particle inlets to the classification chamber are mounted on the rotor, and rotate at the same angular velocity.

The powder is charged in an acrylic resin tube fitted with a screen of 325# or 1000# mesh on the bottom for dispersion. As shown in **Fig. 3**, this tube is placed inside a glass tube with a rubber plug to make it air-tight.

After the centrifuge attains the specified pressure and speed of rotation, a 60Hz vibration is applied to the feeding device to make the particles disperse, pass through the capillary and enter the classification chamber. Hence at the particle inlets, the particles attain the same angular velocity as the rotor.

In the classification chamber, the particles move from near the center ($r_0 = 1.19$ cm) to the rotor wall ($r = 9.5$ cm). On the way, the particles are classified and deposit on the rotor wall in accordance with particle size. As shown in Fig. 2, the motion of the particles relative to the rotor is opposite to the rotation of the rotor. The deposition angle, which is the difference between the angular displacement of the rotor and the particle on the rotor wall, that is $(\phi - \theta)|_{r=9.5}$, increases with increasing particle size.

12 mm transparent double-sided adhesive tapes are mounted on 15 mm transparent plastic strips and placed on the rotor wall. In the case of submicron particles, sheet meshes for the electron microscope are mounted on these strips.

After centrifuging, the particle sizes and the angular location are measured using an optical or elec-

* Received on November 17, 1970
Presented at the 36th Annual Meeting of the Soc. Chem. Engrs., Japan at Tokyo, April 3, 1971
** Yamanouchi Pharmaceutical Co., Ltd., Tokyo
*** Toray Industries Inc., Otsu

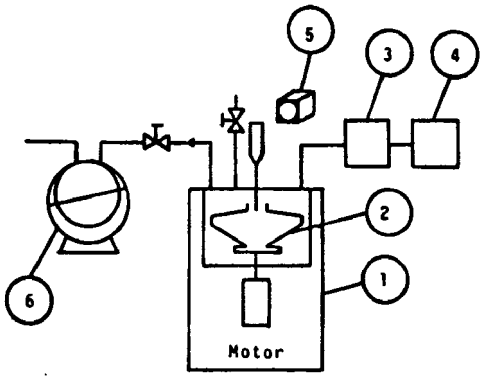

1 Centrifuge
2 Rotor
3 Vacuum gauge
4 Recorder for vacuum
5 Stroboscope
6 Vacuum pump

Fig. 1 Scheme of the experimental apparatus

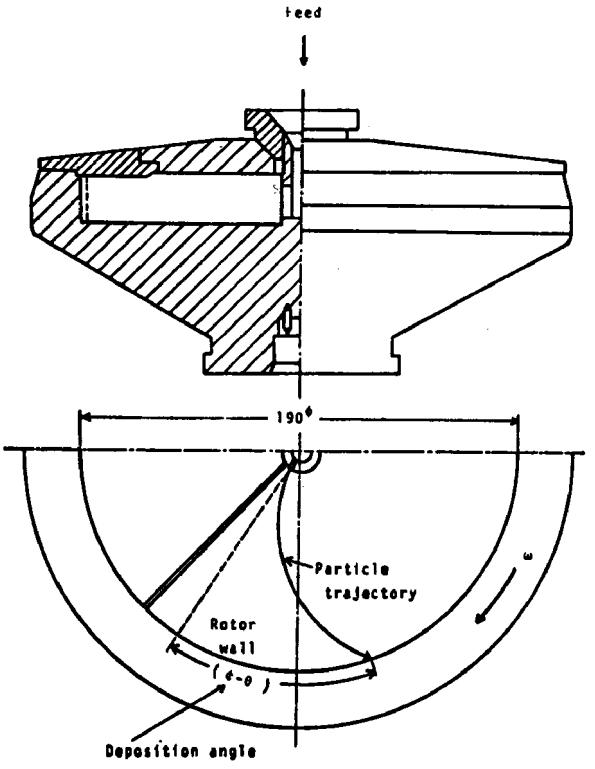

Fig. 2 Schematic design of the rotor

tron microscope.

Glass beads ($\rho_p = 2.5 g/cm^3$), zinc powder ($\rho_p = 7.0 g/cm^3$), and tungsten powder ($\rho_p = 19.2 g/cm^3$) were used as the test materials. Hollow particles in the glass beads were removed by flotation with a mixture of acetone and 1, 1, 2, 2-tetrabromoethane.

Theoretical Considerations

The particle motion in the centrifugal fields is always changing in both speed and direction, that is, the motion is non-uniform and curvilinear. The

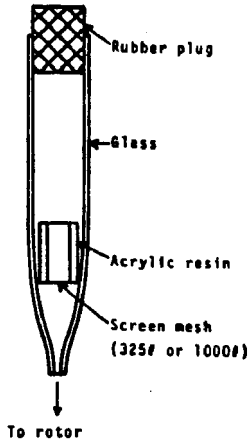

Fig. 3 Feeding device for powder

equations of motion for a spherical particle in polar coordinates are given by the following expression[1,3].

$$\frac{\pi}{6}D_p^3\left(\rho_p+\frac{1}{2}\rho_g\right)\frac{d^2r}{dt^2}+\frac{C_D}{C_c}\frac{\pi}{8}D_p^2\rho_g v\frac{dr}{dt}-\frac{\pi}{6}D_p^3\left(\rho_p+\frac{1}{2}\rho_g\right)r\left(\frac{d\theta}{dt}\right)^2+\frac{\pi}{4}D_p^3\rho_g r\left(\frac{d\phi}{dt}\right)^2+\frac{3}{2}\sqrt{\pi\mu\rho_g}D_p^2\int_0^t\left[\frac{d^2r}{dx^2}-r\left(\frac{d\theta}{dx}\right)^2+r\left(\frac{d\phi}{dx}\right)^2\right]\frac{dx}{\sqrt{t-x}}=0 \quad (1)$$

$$\frac{\pi}{6}D_p^3\left(\rho_p+\frac{1}{2}\rho_g\right)r\frac{d^2\theta}{dt^2}+\frac{C_D}{C_c}\frac{\pi}{8}D_p^2\rho_g v\,r\left(\frac{d\theta}{dt}-\frac{d\phi}{dt}\right)+\frac{\pi}{3}D_p^3\left(\rho_p+\frac{1}{2}\rho_g\right)\frac{dr}{dt}\frac{d\theta}{dt}+\frac{3}{2}\sqrt{\pi\mu\rho_g}D_p^2\int_0^t\left(r\frac{d^2\theta}{dx^2}+2\frac{dr}{dx}\frac{d\theta}{dx}\right)\frac{dx}{\sqrt{t-x}}=0 \quad (2)$$

in which

$$v=\sqrt{\left(\frac{dr}{dt}\right)^2+r^2\left(\frac{d\phi}{dt}-\frac{d\theta}{dt}\right)^2} \quad (3)$$

$$C_D=\frac{24}{Re}(1+0.15\,Re^{0.687}) \quad (4)$$

$$Re=\frac{D_p v\rho_g}{\mu} \quad (5)$$

$$C_c=1+\left[2.46+0.82\exp\left(-\frac{0.44D_p}{\lambda_m}\right)\right]\frac{\lambda_m}{D_p} \quad (6)$$

$$\lambda_m=0.653\times10^{-5}\times760/P \quad \text{[cm] for air} \quad (7)$$

These equations contain the slip factor 'Cunningham correction'[4,7] for the increase in mean free path of gas molecule and the approximate equation[9] for the drag coefficient of spherical particles.

The simultaneous integro-differential equations (1) and (2) are non-linear, so no analytical solution can be obtained. Thus numerical techniques using a digital computer were employed instead to obtain the solutions of Eqs.(1) and (2).

Let us now compare the following alternative solutions. One is a numerical solution of the simultaneous second-order ordinary differential equations without the last intergral terms of Eqs.(1) and (2) by the Runge-Kutta-Merson method[6].

The other is a numerical solution of the intergro-differential equations by the method given in the Appendix.

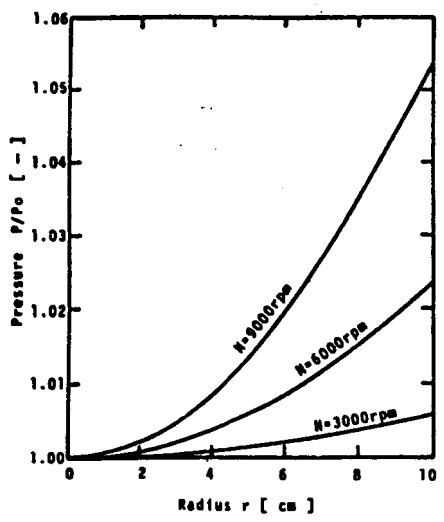

Fig. 4 Pressure distribution in a gas centrifuge

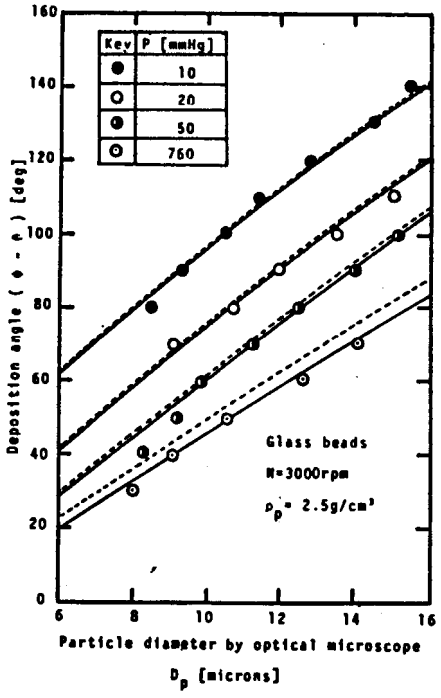

Fig. 5 Variation of deposition angle with pressure for glass beads (experimental and computed results)

Strictly speaking, the pressure distribution in the rotor should be considered, but this effect appears to be negligible. The pressure distribution of gas at a constant speed of rotation may be expressed by

$$\frac{dp}{dr} = \frac{\rho_g r \omega^2}{g_c} \tag{8}$$

For an ideal gas, the general relation between density and pressure is

$$\rho_g = p\rho_{go}/p_o \tag{9}$$

Substitution of Eq.(9) into Eq.(8) and integration of Eq.(8) with respect to r gives

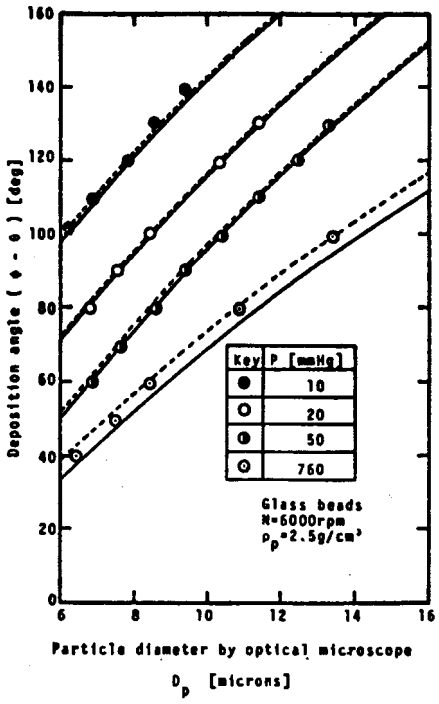

Fig 6 Variation of deposition angle with pressure for glass beads (experimental and computed results)

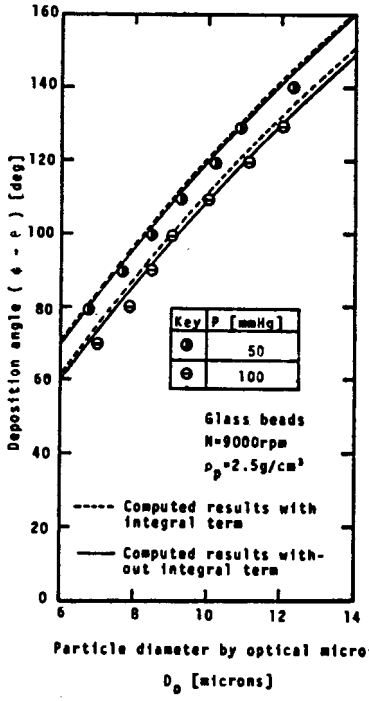

Fig. 7 Variation of deposition angle with pressure for glass beads (experimental and computed results)

$$\frac{p}{p_o} = \exp\left(\frac{1}{2}\frac{\rho_{go} r^2 \omega^2}{p_o g_c}\right) \tag{10}$$

using the boundary condition

B.C. at $r = 0$, $p = p_o$ (11)

The calculated pressure distributions are shown

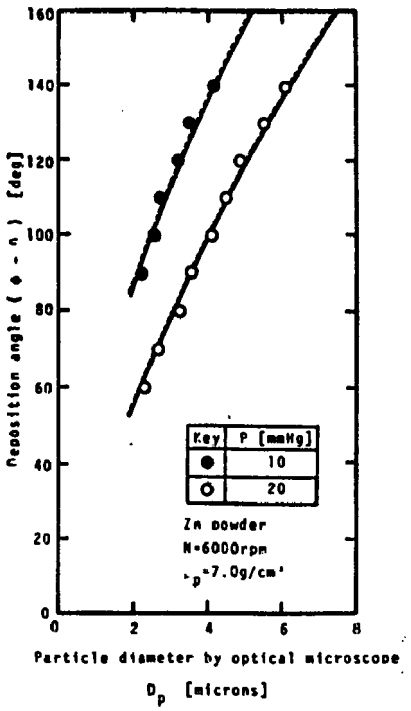

Fig. 8 Comparison of experimental and computed results for Zn powder

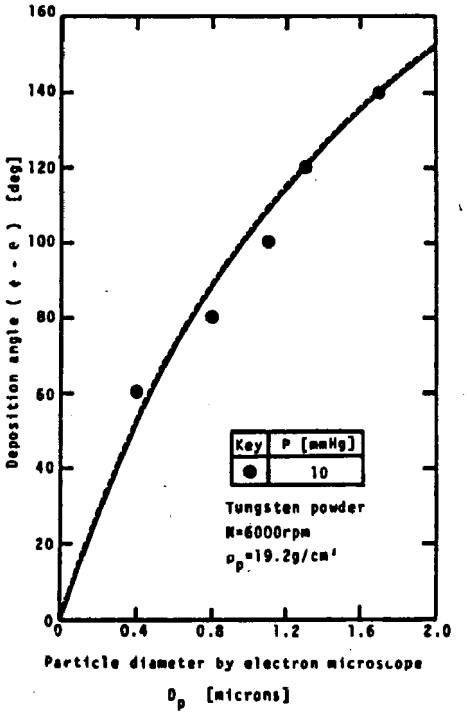

Fig. 9 Comparison of experimental and computed results for tungsten powder

in Fig. 4. The deviations of relative pressure p/p_0 between outer and inner parts of the rotor are less than a few percent.

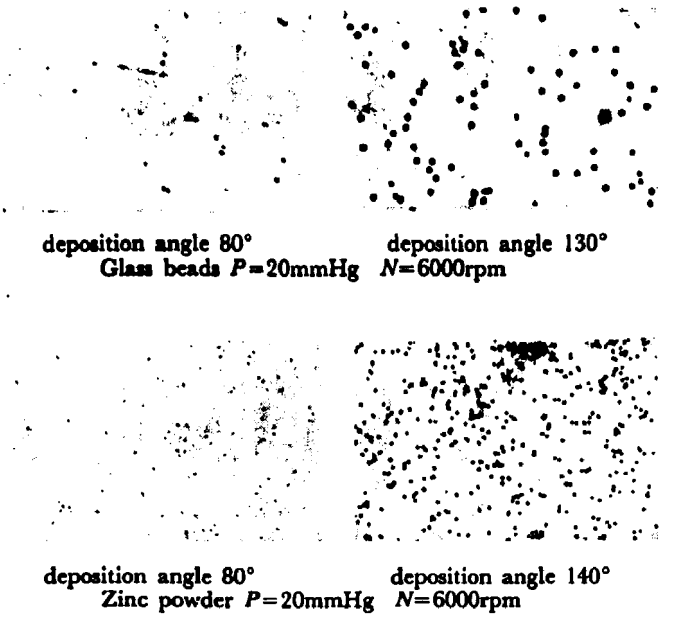

Fig. 10 Photomicrographs of experimental results

Experimental Results and Discussion

Figs. 5, 6 and 7 show the comparison of the experimental results and computed solutions for glass beads at various pressures and rotor speeds of 3000, 6000, and 9000 rpm. Figs. 8 and 9 present the results for zinc powder and submicron particles of tungsten powder, respectively.

The solid line represents the numerical solutions computed without the integral term in Eqs.(1) and (2), and the broken line represents the computed values of Eqs.(1) and (2). The solid and broken lines are computed at the following boundary conditions B.C. and initial conditions I.C., respectively.

B.C. $\frac{d\phi}{dt} = \omega$ (const.), that is, the gas rotates at the same angular velocity as the rotor. (12)

I.C. at $t = 0$, $r = r_0$ (13)

$\theta = 0$ (14)

$\frac{dr}{dt} = 0$ (15)

$\frac{d\theta}{dt} = \omega$ (16)

The experimental results agree well with the computed values. Fig. 10 shows photomicrographs for a couple of the experimental runs.

From the numerical calculation, the deposition angle calculated with the integral term included is slightly greater than the value obtained without the integral term. The effect of this term on the calculated value of the deposition angle is less than 10%. Furthermore, the effect decreases with decreasing pressure. Below 20mmHg the deviation is less than 1%, so the effect of the intergral term may be considered negligible.

If possible, the powder should be fed to the classifier in a well-dispersed aerosol, but the inital radial veloc-

ity of the aerosol at the inlet ports reduces the deposition angle. This has been confirmed by both the experimental and theoretical results. Also, it is difficult to ensure that the initial radial velocity of each particle is the same. Consequently, this non-uniform velocity results in poor classification. This problem may be solved in future, but deserves further attention.

Conclusion

Particle size classification in a gas centrifuge at reduced pressure has been investigated theoretically and experimentally, resulting in the following conclusions.

1) Particles down to the submicron range can be classified with good resolution, a gradation of particle size occurring on the rotor wall.
2) Agreement between experimental results and computed solutions is shown to be excellent.
3) The slip factor 'Cunningham correction' obtained by using Millikan's data for oil drops in air may be applied to various materials suspended in air and at various pressures.
4) Numerical solutions of the simultaneous integro-differential equations of a non-uniform curvilinear motion have been obtained.
5) The effect of the integral term for fine particles suspended in air is not very large.

As a consequence of these results, the development of a new particle size analyzer appears possible.

Appendix

The method of successive approximations is employed to solve the simultaneous integro-differential equations (1) and (2).

The calculation of the integral term is carried out using the relative velocity between the particle and the fluid, u, to simplify the notation.

The first stage of average acceleration is defined by

$$\left(\frac{du}{dt}\right)_{1m,1}=\frac{1}{2}\left\{\left(\frac{du}{dt}\right)_0+\left(\frac{du}{dt}\right)_{1,1}\right\} \tag{1a}$$

in which $(du/dt)_{i,j}$ denotes j-th approximation of i-th step and the subscript m denotes the mean value. The first approximation of the integral term after a small increment of time Δt is

$$\int_0^{\Delta t}\frac{\frac{du}{dx}}{\sqrt{\Delta t-x}}dx=2\left(\frac{du}{dt}\right)_{1m,1}\sqrt{\Delta t} \tag{2a}$$

Substituting Eq.(2a) in Eqs.(1) and (2), the second approximation $(du/dt)_{1,2}$ can be calculated. Then from Eq.(1a), $(du/dt)_{1m,2}$ may be evaluated. If the n-th approximation is nearly equal to the $(n-1)$-th approximation

$$(du/dt)_{1,n}-(du/dt)_{1,n-1}=\text{tolerance limit} \tag{3a}$$

Then defining the final approximation of the first step

$$(du/dt)_1=(du/dt)_{1,n} \tag{4a}$$

and the mean acceleration $(du/dt)_{1m}$ is calculated.

Thus from Eq.(2a), the value of the integral term at the end of the first increment of time can be evaluated. Similarly, $(du/dt)_{2m}$ and the integral term can be calculated. For the purpose of calculation, the time is divided into k steps (it is not necessary that each step be an equal interval) and the integral term is computed as follows

$$\int_0^t\frac{\frac{du}{dx}}{\sqrt{t-x}}dx=2\sum_{i=1}^{k}(du/dt)_{im}\{\sqrt{t-x_{i-1}}-\sqrt{t-x_i}\} \tag{5a}$$

Applying this method to the radial and angular directions, the numerical integration of Eqs.(1) and (2) by the RKM method gives the required results.

Odar[8] has proposed an equal-time interval method, but in that case, only the Runge-Kutta-Gill routine may be used for integration of the equations. For the method described here, the RKM routine is applicable.

Acknowledgement

We are very grateful to Professor C. Orr and Dr. J. H. Burson of the Georgia Institute of Technology for their assistance in the preparatory work for this study.

[Additional Note]

The numerical solutions presented in this paper were calculated with the FACOM-230-60 digital computer at the Data Processing Center, Kyoto University.

Nomenclature

C_c	= Cunningham correction factor	[—]
C_D	= drag coefficient	[—]
D_p	= particle diameter	[cm]
g_c	= gravitational conversion factor	$[(g/G)(\text{cm/sec}^2)]$
N	= revolutions per minute	[rpm]
P	= pressure	[mmHg]
p	= pressure	$[G/\text{cm}^2]$
r	= radius of gyration	[cm]
Re	= Reynolds number $= (D_p u \rho_g/\mu)$	[—]
t	= time	[sec]
u	= relative velocity between particle and fluid in general	[cm/sec]
v	= relative velocity between particle and fluid defined by Eq.(3)	[cm/sec]
x	= integral variable	[sec]
θ	= angular displacement of particle	[rad]
λ_m	= mean free path of gas molecule	[cm]
ρ_g	= density of gas	$[\text{g/cm}^3]$
ρ_p	= density of particle	$[\text{g/cm}^3]$
ϕ	= angular displacement of gas	[rad]
ω	= angular velocity of rotor	[rad/sec]

Literature cited

1) Basset, A. B.: *Phil. Trans. of the Royal Soc.*, **179**, 43 (1888)
2) Burson, J. H., E. Y. H. Keng and C. Orr: *Powder Technology*, **1**, 305 (1967/68)
3) Fuchs, N. A.: "The Mechanics of Aerosols", p. 75, Pergamon Press (1964)
4) Kennard, E. H.: "Kinetic Theory of Gas", p. 310, McGraw-Hill (1938)
5) Kriebel, A. R.: *Trans. of ASME, J. of Basic Engr.*, **83**, 333 (1961)
6) Lukehart, P. M.: *Communications of the ACM*, **6**, 737 (1963)
7) Millikan, R. A.: *Phys. Rev.*, **22**, 1 (1923)
8) Odar, F.: U.S. Army Cold Regions Research and Engineering Laboratory, Research Report 190 (1966)
9) Schiller, L. and A. Naumann: *Z. VDI.*, **77**, 318 (1933)

Journal of Electrostatics, 2 (1976/1977) 341—350
© Elsevier Scientific Publishing Company, Amsterdam — Printed in The Netherlands
(Reprinted with permission)

ELECTRIFICATION OF GAS—SOLID SUSPENSIONS FLOWING IN STEEL AND INSULATING-COATED PIPES

HIROAKI MASUDA, TAKAHIRO KOMATSU, NAOHIRO MITSUI, and KOICHI IINOYA
Department of Chemical Engineering, Kyoto University, Kyoto 606 (Japan)
(Received September 24, 1976; in revised form December 10, 1976)

Summary

Electrification of gas—solid suspensions flowing in steel and insulating-coated pipes are experimentally studied. It is found that the currents generated on insulating-coated pipes are higher than the currents generated on a steel pipe and the sign of the currents follows a kind of tribo-electric series. The currents are proportional to powder flow rate, proportional to mean air velocity to the power 1.4—1.9, and inversely proportional to the mean particle diameter. It seems that the currents are proportional to the pipe diameter. The effects of a bend and powder feeding inlet are also studied.

1. Introduction

In gas—solid pipe flow, particles are charged through their collisions with the pipe wall [1]. The wall is also charged, and the charge generated per unit time, which can be measured as a current to earth, is a function of several variables, such as the number of collisions, area of contact and duration of contact [2]. The current may also be affected by the wall material. In practical application of gas—solid flow, the pipe wall is sometimes made from insulators such as transparent glass, acryl and polyvinyl chloride.

In the present work, a steel pipe and pipes coated with various insulators are set in a pneumatic conveyor line, and the currents generated on those pipes are measured for several kinds of powder. The effects of a bend and a powder-feeding inlet on the generated current are also studied.

2. Experimental apparatus and procedures

Figure 1 shows the suction type pneumatic conveyor used in the experiment. Test pipes are listed in Table 1. Both ends of these test pipes are insulated with polyvinyl-chloride flanges (12 mm thick) and the pipes are set in the conveyor line at positions A, B and C in Fig. 1. The current generated is measured by a galvanometer. A 2000 μF condenser is, if necessary, connected in parallel in order to suppress fluctuations in the current. The conveyor line before and after the test section is grounded at one point.

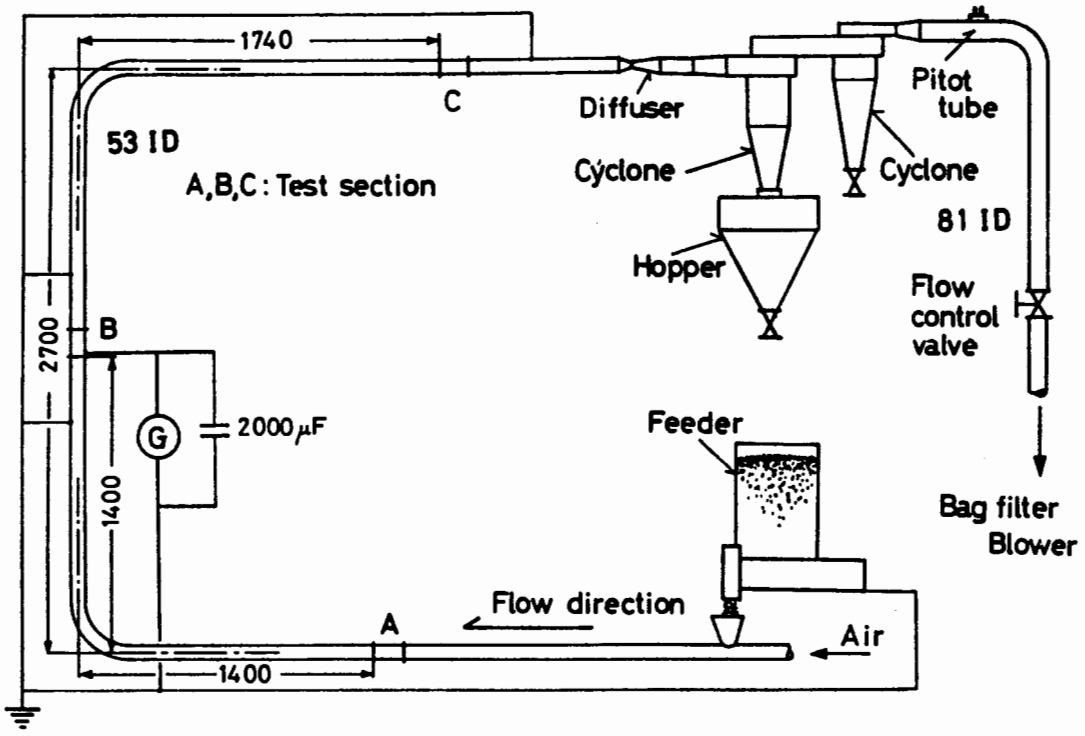

Fig. 1. Experimental setup (Lengths are shown in millimeters. A, C: horizontal, B: vertical).

As a preliminary experiment, test pipe A (steel, 15 cm long, 5.3 cm bore) is set at various positions and currents are recorded. Effects of the length of the test pipe (Δx) and pipe diameter (D) are also studied by use of steel pipes.

Powder-flow rates (W) are measured by a direct-measuring method. A calibrated diffuser [3] and a Pitot tube are used to measure the air-flow rate. Powders used in the experiments are listed in Table 2.

TABLE 1

Test pipes

Symbols	Materials	Insulator-thickness (mm)	Inside diameter (mm)	Length (cm)
A	steel	—	53	15
B	teflon	<0.1	53	30
C	polyvinyl chloride	1.5	50	15
D	glass	2.2	51	30
E	plastic*	0.1	53	15

*Mitsubishi Paper Mills Ltd., Hishirapit.

TABLE 2

Properties of powder materials

Powder	Mass median diameter D_{p50} (μm)	Mean particle diameter* $\bar{D}_p$ (μm)	Density ρ_p (g/cm^3)
Quartz sand			
ultra fine	16.8	14	2.65
No. 8	51	48	2.65
No. 5	440	329	2.65
Morundum			
(1)	58	50	3.97
(2)	73	63	3.97
(3)	93	93	3.97
(4)	126	126	3.97
(5)	180	180	3.97
(6)	340	340	3.97
(7)	515	515	3.97
(8)	760	760	3.97
Flour	57	37	1.44
PVC	115	111	1.41
Glass beads	55	53	2.42

* $\bar{D}_p = 1 \Big/ \int_0^\infty (f^{(3)}/D_p) \mathrm{d}D_p$.

3. Results and discussion

3.1 Current generated on steel pipes as a function of axial distance

The results are shown in Fig. 2. Higher currents are generated on the steel test pipe adjacent to the powder-feeding inlet and the bend. The effect of the inlet on the current extends downstream by $20D$, while that of the bend extends upstream by $10D$ and downstream by $20D$. Excess current generated between $x = 0$ and $x = 20D$ cquals that generated on the pipe line of length $10D$. The main cause of the higher current seems to lie in the higher number of collisions arising from the flow disturbance produced by the bend and the powder inlet.

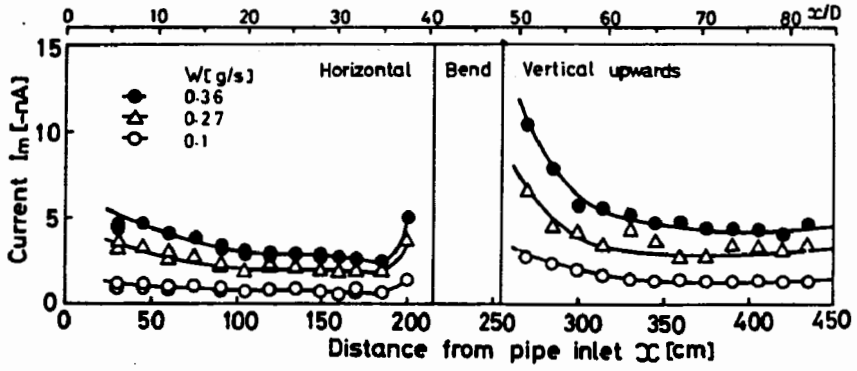

Fig. 2. Effect of a bend and a powder-feeding inlet on the generated current (test pipe A).

3.2 Effect of the length of test pipe

Figure 3 shows the effect of the length Δx on the current. The measurements are carried out between $x = 90$ and 195 cm where the currents shown in Fig. 2 are almost constant. However, the relation between the currents and the length Δx is not linear, but is expressed by the following empirical equation

$$I_m \cong KW \frac{\Delta x}{1 + k\Delta x}, \qquad k \cong 0.024 \text{ cm}^{-1} \tag{1}$$

or as a first-order approximation

$$I_m \cong KW(\Delta x + \Delta l), \qquad \Delta l \cong 27 \text{ cm} \tag{2}$$

Eqn. (2) suggests that the polyvinyl-chloride flanges at either end of the test pipe may have some effect. However, results obtained by use of 3 mm flanges are almost equal to those shown in Fig. 3. Further examination of the effect of the length of test pipe may be necessary.

3.3 Current generated on test pipes

When insulating-coated pipes are used, the sign of the current sometimes reverses in the initial period of powder flow. Figure 4 shows one such result. The negative current generated initially becomes positive after a short time. Test pipes and powders which showed such sign change are listed in Table 3.

For test pipe D (glass) and quartz sand the sign changed several times. For test pipe C (polyvinyl chloride) with quartz sand, the sign change in the initial period was seen in the first experiment, but did not occur on repeating the experiment after about one month. However, on repeating the experiment after seven months, the sign change was again observed.

Test pipe B (teflon) showed no sign change for any powder. Experiments in which no sign change was observed are:

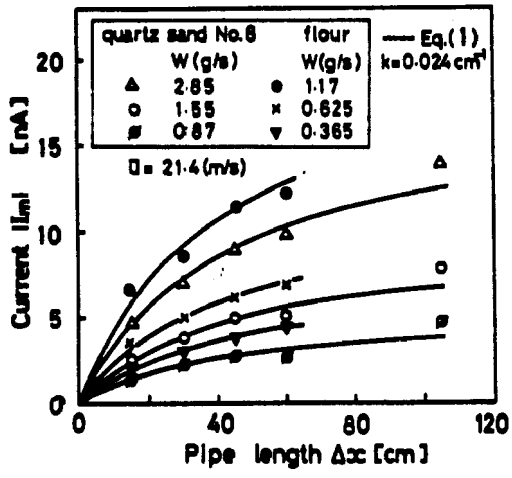

Fig. 3. Generated current as a function of length of test pipe.

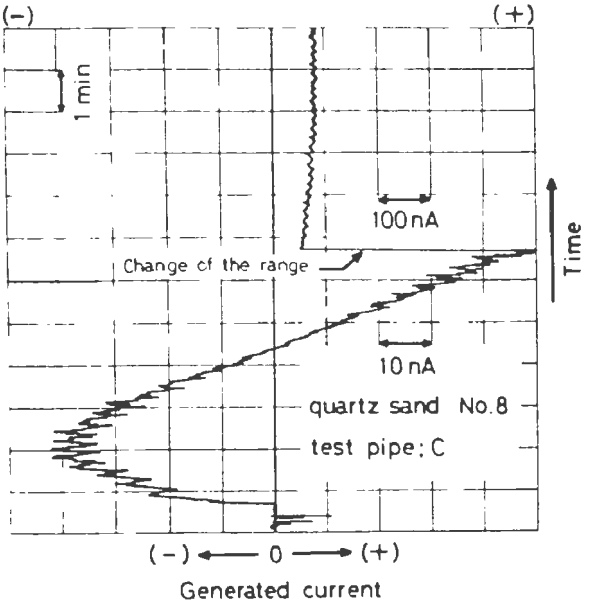

Fig. 4. Sign change of current in the initial period of experiment.

test pipe B (teflon) ... all powders,
test pipe C (polyvinyl chloride) ... glass beads, morundum, flour,
test pipe D (glass) ... PVC, flour.

Experiments were carried out in the following order:
test pipe B: quartz sand—PVC—flour—morundum,
test pipe C: quartz sand—PVC—glass beads—flour—morundum,
test pipe D: quartz sand—PVC—morundum—flour.

The above experimental facts are summarized as follows.

(1) Sign of the current generated may change when the charge of a particle leaving the preceding pipe line has the same sign as that generated in the test pipe.

(2) Sign of the generated current does not change when the particle charge generated in the preceding pipe line has opposite sign to that generated in the test pipe, nor when these particle charges have the same sign provided the current generated on the insulating-coated test pipe has the same sign as in the preceding experiments with a different powder.

TABLE 3

Sign change of current in the initial period of experiment

Pipe	Powder	Sign change
C	quartz sand	(−) → (+)
C	PVC	(+) → (−)
D	quartz sand	(+) → (−)
D	morundum	(+) → (−)
E	quartz sand	(−) → (+)

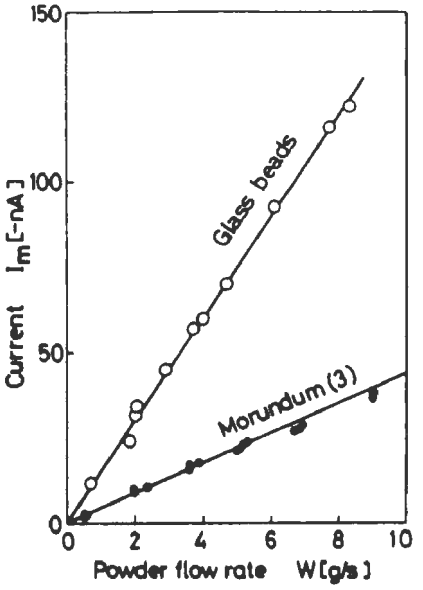

Fig. 5. Relationship between the generated currents and powder-flow rate (test pipe C, position B, $\bar{u}$ = 20 m/s).

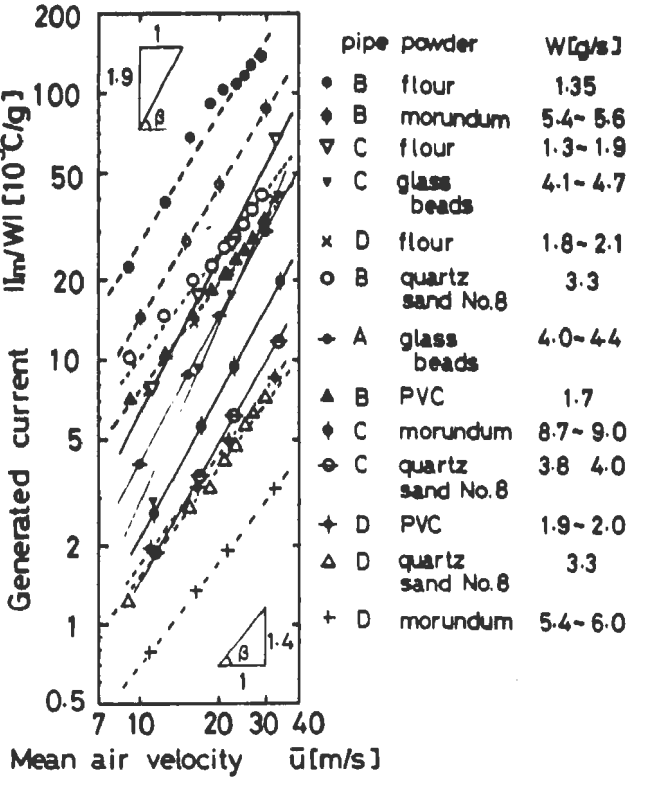

Fig. 6. Current generated per unit powder-flow rate as a function of the mean air velocity (position B).

From these results, it seems that the sign change depends on the polarization of the insulator (electret formation), or on the change of the physical property of wall material.

In the steady state, however, the current is reproducible and constant. The currents are proportional to powder-flow rate as shown in Fig. 5, provided the mass-flow ratio is less then about unity. Figure 6 shows the relation between the generated current per unit powder-flow rate and the mean air velocity. The results are represented by straight lines on log—log paper. These lines may be divided into two groups, one with a slope of about 1.4 and the other about 1.9. One possible explanation is that the contact area varies with the mode of wall deformation, elastic or plastic. The slope for elastic deformation may be about 1.4 and for plastic deformation about 1.9 [2]. In practice, collision will be partly elastic and partly plastic.

It is also confirmed that the currents are inversely proportional to the mean particle diameter. The results are shown in Fig. 7. It is found that the larger the pipe diameter, the higher the current generated. This fact is shown more clearly in Fig. 8.

It has been shown theoretically [2] that the current is expressed by

$$I_m = -\frac{We_0 V_c \Delta x \Delta t S}{m_p z_0 \tau} \frac{\Delta n}{\Delta x} \tag{3}$$

where the initial particle charge is neglected. Number of collisions per unit length of a particle $\Delta n/\Delta x$ is represented by [2]

$$\frac{\Delta n}{\Delta x} = m_p \pi D \xi \tag{4}$$

By substituting eqn. (4) into eqn. (3), the following equation is obtained:

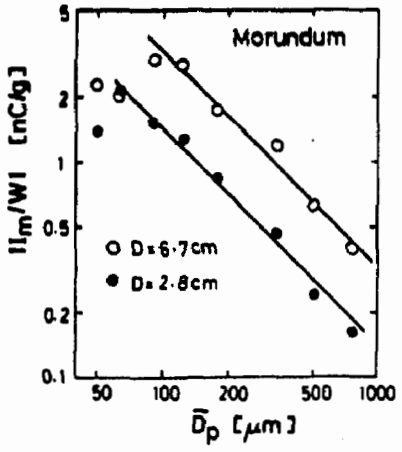

Fig. 7. Effects of particle diameter on the generated currents (steel pipe, position B, $\bar{u}$ = 20 m/s).

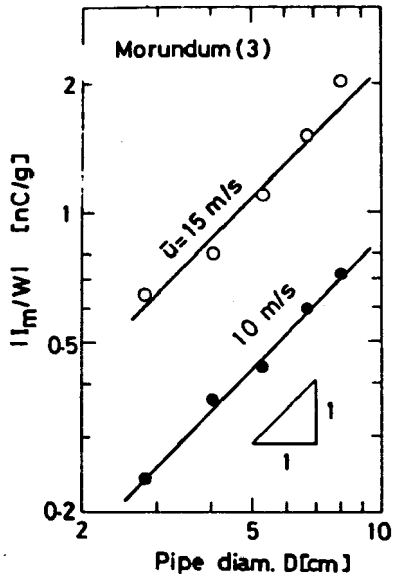

Fig. 8. Relationship between the generated currents per unit powder-flow rate and the pipe diameter (position B, steel pipe).

$$I_m = -\frac{W\epsilon_0 V_c S\Delta t \pi D x \xi}{z_0 \tau} \tag{5}$$

From the empirical eqn. (1) or (2), eqn. (5) may be modified as:

$$I_m = -\frac{\epsilon_0 V_c S\Delta t \xi}{z_0 \tau} W\Delta A\eta \tag{6}$$

where $\eta = \dfrac{1}{1+k\Delta x}$ or $1+\dfrac{\Delta l}{\Delta x}$ (7)

and $\Delta A = \pi D\Delta x$ (8)

Equation (6) means that the current is proportional to the pipe diameter provided ξ is constant. Experimental results are represented by the following semi-empirical equation:

$$I_m = \alpha\frac{\bar{u}^\beta}{\bar{D}_p} W\Delta A\eta \tag{9}$$

where

$$\alpha\frac{\bar{u}^\beta}{\bar{D}_p} = -\frac{\epsilon_0 V_c S\Delta t \xi}{z_0 \tau} \tag{10}$$

and [4]

$$\bar{D}_p = 1\Big/\int_0^\infty \frac{f^{(3)}}{D_p}\,dD_p \tag{11}$$

TABLE 4

Constants in eqn. 9*

Test pipes	Powder	$\alpha \times 10^{14}$	β (–)
A (steel)	quartz sand	1.6	1.9
	PVC	−4.9	1.9
	glass beads	−19	1.8
	morundum	−11	1.4
	flour	−14	1.9
B (teflon)	quartz sand	−86.5	1.3
	PVC	−157	1.3
	morundum	−138	1.6
	flour	−220	1.6
C (polyvinyl chloride)	quartz sand	9.1	1.7
	glass beads	−8.0	2.1
	morundum	−23.3	1.8
	flour	−18.6	1.9
D (glass)	quartz sand	4.6	1.3
	PVC	28.5	1.4
	morundum	−14.7	1.3
	flour	−27.1	1.5
E (plastic)	quartz sand	18.1	1.8

* $\bar{u}$ (m/s), $\bar{D}_p$ (cm), W (g/s), ΔA (cm^2), I_m (A).

Constants α and β are listed in Table 4. Absolute values of α for insulating-coated pipes are larger than that for the steel pipe by one or two orders. A teflon-coated test pipe generates the highest current. These high currents may be due to higher contact-potential differences and larger contact area. It is also noted in relation to the danger of dust explosion that flour is highly charged.

Table 5 shows a tribo-electric series obtained in this study.

TABLE 5

Tribo-electric series

(+) flour — morundum — glass — PVC — steel — quartz sand — teflon (–)

4. Conclusions

Electrification of gas—solid suspensions are experimentally studied and the following results are obtained.

(1) Electrification of powder depends on the wall material of the pipe.

Insulator pipes may cause greater electrification of powders than a steel pipe by one or two orders of magnitude.

(2) The sign of electrification follows a kind of tribo-electric series.

(3) The effects of powder-flow rate, air velocity and particle size on the current generated by insulating-coated pipes are similar to those in a steel pipe. They depend on the mode of collision.

(4) Sometimes the sign of current changes in the initial period of experiments with insulating-coated pipes.

(5) A bend and the powder inlet affect the electrification. Effect of the inlet extends downstream by $20D$, while that of the bend extends upstream by $10D$ and downstream by $20D$.

Nomenclature

ΔA $\pi D \Delta x$
D inside diameter of pipe
D_p particle diameter
$f^{(3)}$ particle-size distribution (weight basis)
Δl constant length introduced in approximate eqn. (2)
I_m current generated on an insulated pipe
K, k constants in eqn. (1)
m_p mass of a particle
n number of collisions of a particle
S area of contact
Δt duration of contact
u air velocity
V_c contact-potential difference
W powder-flow rate
x axial distance from inlet
z_0 gap between surface of particle in contact and pipe wall
α constant in eqn. (9)
β constant in eqn. (9)
ϵ_0 dielectric constant of air, 8.85×10^{-12} F/m
η defined by eqn. (7)
ξ number of collisions per unit area and unit mass of powder
τ relaxation time

References

1 B.N. Cole, M.R. Baum and F.R. Mobbs, Proc. Instn. Mech. Engrs., 184 (1969—70) 3C77.
2 H. Masuda, T. Komatsu and K. Iinoya, AIChE J., 22 (1976) 558.
3 H. Masuda, Y. Ito and K. Iinoya, J. Chem. Eng., Japan, 6 (1973) 278.
4 H. Masuda and K. Iinoya, Memoirs of the Faculty of Eng., Kyoto Univ., 34 (1972) 344.

JAPAN

K. Makino
K. Iinoya
M. Shibamoto
S. Toyama
M. Ikazaki

Experiments on the electrical dislodging of a dust layer

A new method for dislodging a dust layer from a flat surface by a non-uniform electrical field was studied experimentally. This was found to be effective for industrial dusts, such as sintering furnace dust and AVS resin powder, especially when a corona discharge was applied. Appropriate design factors were described.

Introduction

STATIC electricity causes various troubles in many processes for treating powders, so that the technology of coping with them has become significant as an engineering subject. On the other hand, electric charges have been utilized as in electrostatic precipitators. It has also been reported that the electric properties of powders are being applied to measuring the flow rate of powders [1, 2], the void fraction of the powder bed [3], and the particle-size distribution. Charged particles in a non-uniform alternating electrical field produced by electrodes are driven in the opposite direction, against the electrodes. Masuda et al. [5] analyzed theoretically the characteristics of electric screens of the standing and moving wave type, and verified it experimentally. However, this effect of the electrical screens falls sharply when either the particle size and the electrical charge are small or the velocities of the particles are high. This tendency makes direct application to dust collectors difficult. In this study, a new trial method for electrically dislodging a dust layer is examined in order to overcome the defects of this electrical curtain. This method enabled dust particles to be captured and deposited on the filter set-up, with electrodes in a suitable arrangement, and to be dislodged electrically. The typical characteristics of this method were examined at various points and found to be applicable to high-efficiency dust collectors.

This article was first published in *Kagaku Kōgaku Ronbunshu* (Proceedings of the Society of Chemical Engineers, Japan), Vol. 2, No. 1, pp. 31-37 (1976). Kazutaka Makino, Koichi Iinoya, and Masami Shibamoto are associated with the Department of Chemical Engineering, Kyoto University, Kyoto, and Shigeki Toyama and Fumikazu Ikazaki with the National Chemical Laboratory for Industry, Tokyo. Translated by one of the authors, Professor Kazutaka Makino.

1. Experimental apparatus and procedure

Lycopodium, ABS resin powder, and sintering-furnace dust, shown in Table 1, were used here as test dusts for the following reasons: Lycopodium has electrical charges of $1\text{–}4 \times 10^{-14}$ Coulomb/particle and it is convenient to examine the basic electrical phenomena on the powder. As for sintering furnace dust, it is difficult to capture it in electrical precipitators, due to the high electrical resistance of steel used; therefore, it can be captured and dislodged efficiently by our new method. This method is expected to be widely utilized for the same kind of dust. ABS resin powder was used in order to examine the effect of the number of electrical charges of the particles, by the corona-discharge method, on the dust-dislodging efficiency.

The experiments are performed in two ways. In experiment No. 1, the filter paper and the electrodes are lined up horizontally, as shown in Figure 1. Dust captured and accumulated on the filter from dust-laden air is electrically dislodged under some predetermined conditions by the application of a high AC voltage to these electrodes. In this experiment, the effects of the superficial air velocity, the quantity of electrical charges of the particles by the corona discharge method, etc., on the dust-dislodging efficiency were studied mainly from the practical point of view. In experiment No. 2, as shown in Figure 2, the acrylonitrile board and the electrodes are arranged horizontally. The sample

Table 1

Characteristics of test powders

Particle	D_{pm} [μ]	q [C/particle]	ρ [g cm⁻³]	k^* [—]
Lycopodium	28.0	$1\text{–}4 \times 10^{-14}$	1.30	4.83
Sintering furnace dust	7.2	Negligible	3.76	>10
ABS powder	6.0	Negligible	1.05	2–5

(Reprinted with permission) ©

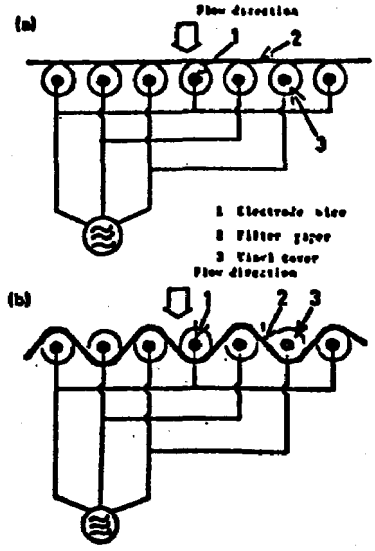

Fig. 1. Schematic diagram of arrangement of electrode and filter (Experiment No. 1).

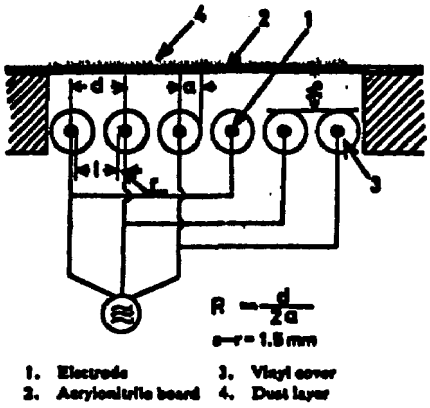

Fig. 2. Experimental apparatus No. 2 for electric dust dislodging.

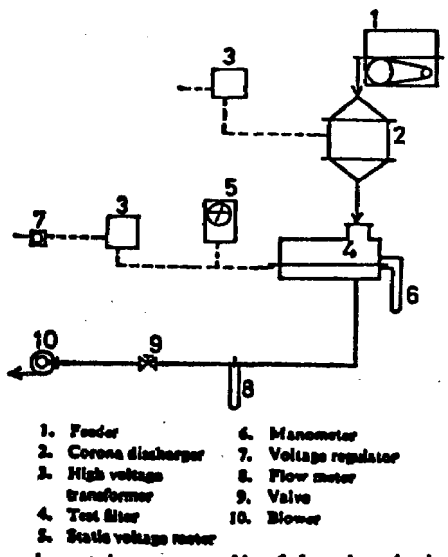

Fig. 3. Experimental apparatus No. 1 for electric dust dislodging.

dust deposited naturally on the sheet from the sieve is dislodged electrically in the same way as described above. Experiments on the effects of the diameter of the electrode wire 2r, the ratio of the electrode diameter to the distance between the centers of the electrodes R, the distance between the dust layer and the surface of the electrodes y_b, etc., on the dust-dislodging efficiency were performed in order to analyze the basic characteristics of this method.

In experiment No. 1, sample dust particles were filtered and accumulated on the test-filter paper under a constant suction of air using a blower and a constant feed of particles from a feeder, as shown in Figure 3. Then, a three-phase AC voltage (commercial frequency, maximum applied voltage 20 kV) was applied to the electrodes with the suction of pure air, when the pressure drop through the filter had reached a predetermined level. The dust particles were dislodged electrically in this way. The pressure drop through the test filter was measured after it had reached some predetermined level, and the residual dust load on the filter was estimated from a relationship experimentally obtained in advance, between the pressure drop of a dust-laden filter and the dust load, using the air velocity as a parameter. Therefore, the electrical dust-dislodging efficiency can be defined here as $(1 - m_2/m_1)$, where m_1 and m_2 are the dust loads on the filter, estimated from the relationship before and after the application of the AC voltage, respectively. A constant flow rate of air was attained by regulation of the valve (Figure 3). Insulated electrodes were used with a diameter of 3.8 mm, and the diameter of the electrode wire was 1.8 mm.

In experiment No. 2, copper pipes covered with vinyl-chloride tubing were used as electrodes, and the distance between the dust layer and the surface of the electrode y_b (in Figure 2) could be changed by varying the height of the leg attached to the acrylonitrile sheet. The definition of the electrical dust-dislodging efficiency was the same as in experiment No. 1, but this time m_1 and m_2 were weighed.

2. Calculation of strength of electric field

In this calculation, the electrical charges due to dielectric polarization must be considered, since thousands of volts are applied to electrodes lined up at intervals of a few millimeters. In the arrangement of the electrical charge and the dielectric material, the linear charge q is arranged parallel to a dielectric cylinder of diameter a with a dielectric constant k_2, in a medium with a dielectric constant k_1; the intensity of the electrical field is equal to a

situation in which the linear charges are arranged in the way shown in Figure 4, q at x = d, q' (= qx(k_2 −k_1)/(k_1 + k_2)) at x = a^2/d and −q' at x = 0 (see Appendix). It is reasonable to assume that the linear electrodes are infinitely aligned in a plane in our experiment, so the intensity of the electrical field is regarded as that formed by the linear electrical charges, by the dielectrical polarization mentioned above and the true charges.

In general, the potential function U is given by Equation (1)

$$U=-\frac{q}{2\pi k_2}\ln\sqrt{\cosh^2\left(\frac{\pi}{d}y\right)-\cos^2\left(\frac{\pi}{d}x\right)} \qquad (1)$$

for an infinite row of linear electrical charges at the regular interval d [6]. The intensity of the electrical field in the x and y directions can be given from the definition E = −grad U.

$$E_x=-\frac{q}{4dk_2}\times\frac{\sin\left(\frac{2\pi}{d}x\right)}{\cosh^2\left(\frac{\pi}{d}y\right)-\cos^2\left(\frac{\pi}{d}x\right)} \qquad (2)$$

$$E_y=-\frac{q}{4dk_2}\times\frac{\sinh\left(\frac{2\pi}{d}y\right)}{\cosh^2\left(\frac{\pi}{d}y\right)-\cos^2\left(\frac{\pi}{d}x\right)} \qquad (3)$$

For this arrangement of electrical lines, Equation (1) (or (2) or (3)) can be added to give the appropriate electrical charge. q in Equation (1) is calculated from the boundary condition that the potential U must be equal to the applied voltage V at any surface of the electrode wire.

From the above considerations, under the condition of a constant applied voltage, the variables are known to be y/d, x/d, a/d, d and r; these affect the intensity of the electrical field. Consequently, the dust-dislodging force increases with the increasing intensity of the electrical field; the dust-dislodging ability is discussed here as a function of the intensity of the electrical field or the initial dust-dislodging voltage.

3. Experimental results and discussion

Experiments were performed under the conditions of a temperature between 17 and 25°C and a relative humidity between 62 and 75% The experimental results of Figure 1 are described first. Figure 5 shows the initial dust-dislodging voltage with respect to a- and b-type filters shown in Figure 1. This figure shows that a b-type filter, in which the distance y_b between the dust layer and the surface of the electrode is less, is more efficient that the a-type. The calculated dimensionless intensity of the electrical field W = E/(V/1) is displayed in Figure 6 where W is known to be very heterogeneous near the electrodes, but depends on y only if it is rather far from the electrodes. W decreases linearly with increasing y. This tendency can explain the results in Figure 5.

Figure 7 shows a better dust-dislodging fraction with increasing dust load, due to the existence of a fixed undislodged zone in the dust layer, even in the electrical field. The initial dust-dislodging voltages in Figure 7 were observed to be almost the same. In Figure 8, the dust-dislodging fractions are shown for various distances between the centers of the electrodes d. The dust-dislodging fraction is higher

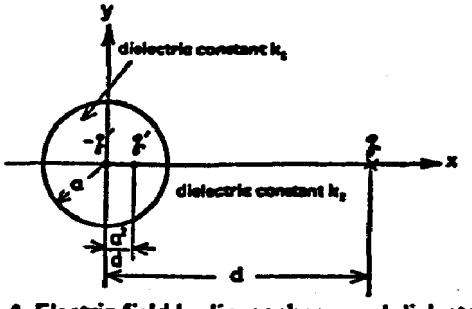

Fig. 4. Electric field by linear charge and dielectric.

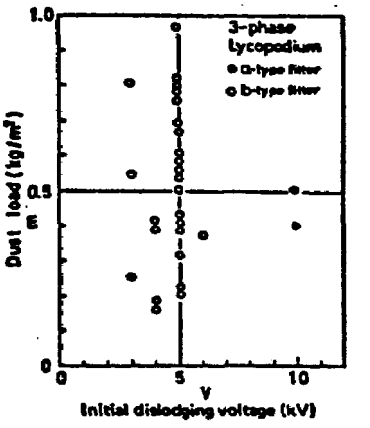

Fig. 5. Experimental initial dust dislodging voltage.

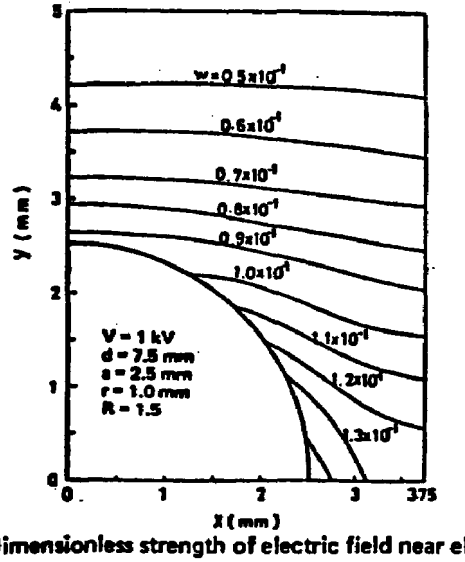

Fig. 6. Dimensionless strength of electric field near electrode.

and the initial dust-dislodging voltage is lower with smaller values of d. This shows that the term $q/4dk_2$ in Equations (2) and (3) is the principal factor in determining the intensity of the electrical field. Therefore, the capacity for dislodging the dust layer falls with increasing d. The effect of superficial air velocity on the capacity for dislodging the dust layer is shown in Figure 9. The result, showing a high efficiency, even under the severe conditions of a 30~ 50 cm/sec air velocity, is of technical interest, taking account of the usual superficial air velocity of a few cm/sec in bag filters. This suggests the possibility of dislodging the dust layer continuously, during the filtering of dust-laden air through the filter paper.

The effect of the magnitude of the electrical charge on a particle due to a corona discharge on the capacity for dislodging a dust layer was examined next. The capacity is almost doubled with a corona discharge, as can be seen in Figure 10. It has been confirmed that the particle charges have a great effect on the dislodging capacity; in other words, our new method would be also applicable to dust particles having only a few intrinsic electrical charges.

The results of experiment No. 2 are as follows. Figure 11 shows the limiting distance between the dust layer and the electrode surface to obtain a high dislodging efficiency. Then, it is shown that, with an applied voltage of 10 kV, a layer of sintering furnace dust can be electrically dislodged with an efficiency of 80% or more, in the case of y_b (see-

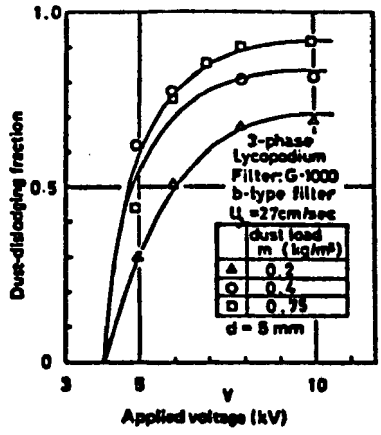

Fig. 7. Effect of dust load on dust dislodging fraction.

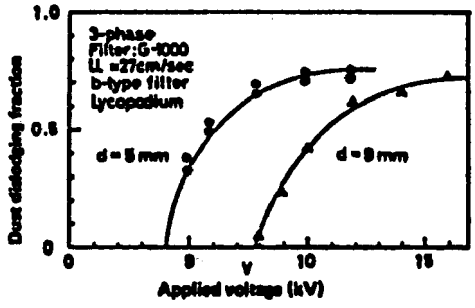

Fig. 8. Experimental dust dislodging fraction in case d = 5 and 9 mm.

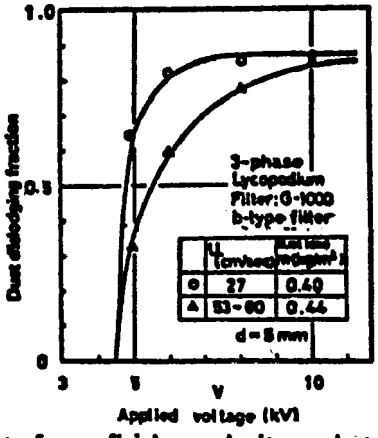

Fig. 9. Effect of superficial gas velocity on dust dislodging fraction.

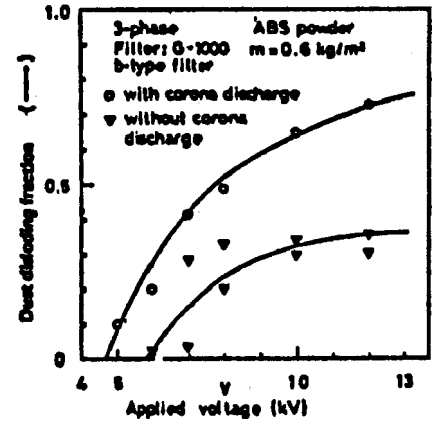

Fig. 10. Effect of electric charge of dust by corona discharge on dust dislodging fraction.

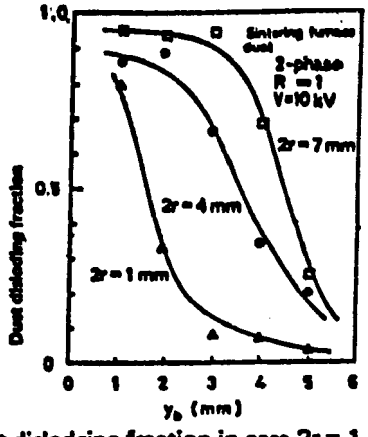

Fig. 11. Dust dislodging fraction in case 2r = 1, 4, 7 mm and y_b = 1, 2, 3, 4, 5 mm.

Figure 1) less than 1 mm with a diameter of the electrode wire 2r of 1 mm, y_b less than 2.5 at 2r of 4 mm, and y_b less than 7 mm at 2r of 7 mm. This result may be regarded as fairly good in comparison with those for an ordinary bag filter with a 30~40% dislodging fraction [7]. All the results on Figure 11 show a rapid drop at y_b, greater than some given value. The relationships between the dislodging efficiency and the frequency of the applied voltage are shown on Figure 12. The dust-dislodging fractions are almost the same at a frequency lower than the commercial one, while, at a higher one, they exhibit a considerable drop. This tendency was similar to that for other sample dusts. This is because the electrical force on a particle moving freely in an electrical field is proportional to $\{(2\pi f)^2 + (3\pi D_p\mu/M)^2\}^{-1}$ [8]. In a dislodging experiment with ABS powder at 500 Hz the powder covered the filter evenly and the pressure loss did not decrease. This is because the adhesion of dust particles is stimulated by the heat evolved in the dielectrical material by high frequency, as observed in our experiment. Figure 13 shows the dust dislodging-voltage for lycopodium as a sample dust with respect to y_b and R, and the ratio of the distance between the centers of the electrodes d to the electrode diameter 2a, in the case of a three-phase applied voltage. The optimum diameter of the electrode wire is determined for each y_b, and increases with an increase in y_b. The optimum diameters of electrode wire are almost the same for sintering furnace dust, since they are determined by the relative value of the intensity of the electrical field near the electrode, and are not affected by the characteristics of the dust itself, in our experimental range. On the other hand, the dust-dislodging voltage itself differs from that for lycopodium because of the different chargeability, i.e., furnace dust is apt to receive more charge by contact and friction than lycopodium.

The dust-dislodging efficiency turns out to be lower at R = 2 than at R = 1, according to Figure 1. Almost the same dislodging efficiency as for lycopodium was obtained for sintering-furnace dust and this new method is also applicable to such industrial dusts. Under the definite conditions of the relative humidity in our experiment, there was no appreciable effect on the efficiency. It was also confirmed that moving the filter paper, while the electrode was fixed, was much more effective; this new dislodging method using moving filter paper suggests the direction of future research and development.

Conclusions

The following results were obtained by experiments on the electrical dislodging of a dust layer.

1) The main factors in the arrangement of the electrodes and the filter paper which affect the dust-dislodging efficiency are the distance between the dust layer and the electrode surface, the diameter of the electrode wire, and the ratio of the pitch of the electrode to the electrode diameter.

2) The b-type filter turns out to be better than the a-type.

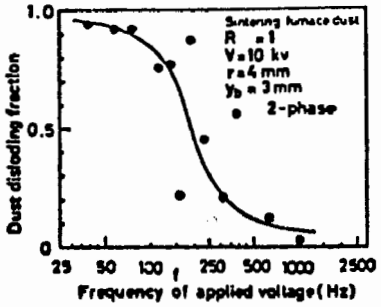

Fig. 12. Effect of frequency of applied voltage on dust dislodging fraction.

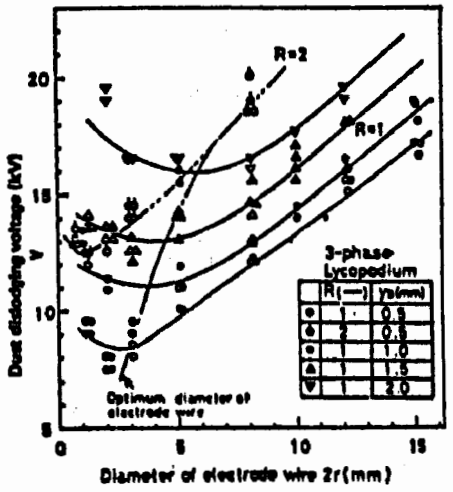

Fig. 13. Effect of diameter of electrode wire and distance from electrode surface on dust dislodging voltage in case of lycopodium.

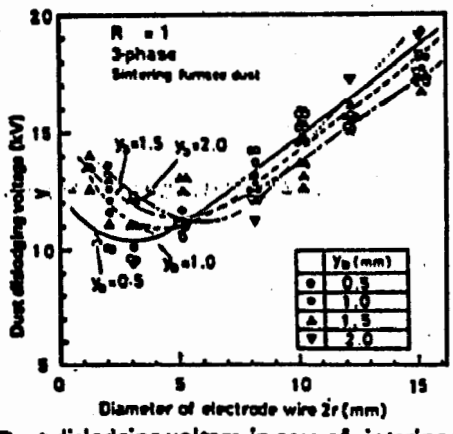

Fig. 14. Dust dislodging voltage in case of sintering furnace dust.

3) The dislodging efficiency increases linearly with the increasing initial dust load and with a decreasing ratio of the pitch of the electrode to the electrode diameter. It is not much reduced in the range of scores of cm/sec of superficial air velocity.

4) A higher dust-dislodging efficiency was obtained by increasing the electrical charge on a particle using a corona discharge.

5) A dust-dislodging efficiency of more than 80 pct for sintering furnace dust was obtained by the application of a 10 kV AC high voltage, in the case where the distance between the dust layer and the electrode surface was less than about 3.5 mm.

6) The applied frequency of the electrical power should be less than commercial frequency to avoid decreasing the performance.

7) The optimum diameters of electrode wire are most efficient in dislodging a dust layer electrically with a constant ratio R of the pitch of the electrode to the electrode diameter. They depend on the distance y_b between the dust layer and the electrode surface and increase linearly with an increase in the distance. An optimum diameter of electrode wire of 3~5 mm was obtained with a value of y_b of 1 mm and a value of R of 1 mm.

8) A higher performance was obtained with a relative movement between the electrode and the filter paper.

Finally, it is still necessary to study the adhesion and cohesion of dust in an AC electrical field and the time-dependent performance after a long run in order for the method to be widely applied.

Appendix

Under the condition that the linear electrical charge q is at the position $P_0(r_0, \theta_0)$ as shown in Figure 15, the potential U_p at the distance of R from P_0 is written in the form of Equation (i)

$$U_p = -\frac{q}{2\pi k_2} \ln R \qquad \text{(i)}$$

Equations (ii) and (iii) are derived with the application of the sine and cosine theorem to Equation (i).

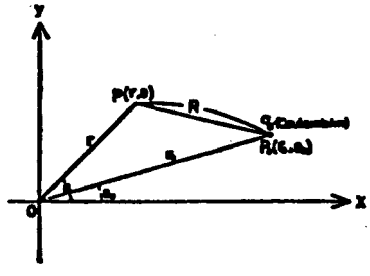

Fig. 15. Electric field by linear charge.

$$U_p = -\frac{q}{2\pi k_2}\left[\sum_{n=1}^{\infty}\frac{1}{n}\left(\frac{r_0}{r}\right)^n \times(\cos n\theta \cos n\theta_0 + \sin n\theta \sin n\theta_0) - \ln r\right] (r_0 < r) \qquad \text{(ii)}$$

$$U_p = -\frac{q}{2\pi k_2}\left[\sum_{n=1}^{\infty}\frac{1}{n}\left(\frac{r}{r_0}\right)^n \times(\cos n\theta \cos n\theta_0 + \sin n\theta \sin n\theta_0) - \ln r_0\right] (r_0 > r) \qquad \text{(iii)}$$

In the case of the existence of a linear charge q, $-q'$ and q' at $x = r_0$, 0 and a^2/r_0, respectively, on the x-axis, the potential U in the position $P(r, \theta)$ is obtained as follows, considering that $r < r_0$ and $r > a^2/r_0$ in our case.

$$U_{x=r_0} = -\frac{q}{2\pi k_2}\left[\sum_{n=1}^{\infty}\frac{1}{n}\left(\frac{r}{r_0}\right)^n \cos n\theta - \ln r_0\right] \qquad \text{(iv)}$$

$$U_{x=a^2/r_0} = -\frac{q'}{2\pi k_2}\left[\sum_{n=1}^{\infty}\frac{1}{n}\left(\frac{a^2}{r_0}\right)^n \frac{1}{r^n} \cos n\theta - \ln r\right] \qquad \text{(v)}$$

$$U_{x=0} = -\frac{q'}{2\pi k_2} \ln r \qquad \text{(vi)}$$

Summing Equations (iv), (v) and (vi) obtained above for $q' = qx(k_2 - k_1)/(k_1 + k_2)$,

$$U = -\frac{q}{2\pi k_2}\left[\sum_{n=1}^{\infty}\frac{1}{n}\left\{\left(\frac{r}{r_0}\right)^n + \frac{k_2 - k_1}{k_1 + k_2}\left(\frac{a^2}{r_0}\right)^n \frac{1}{r^n}\right\}\cos n\theta - \ln r_0\right] \qquad \text{(vii)}$$

On the other hand, Equation (viii) is obtained from the Laplace equation in cylindrical coordinate, by the method of separation of variables,

$$U = (\alpha\theta + \beta)(\gamma \ln r + \delta) + \sum_{n=1}^{\infty}(\alpha_n \cos n\theta + \beta_n \sin n\theta)(\gamma_n r^n + \delta_n r^{-n}) \qquad \text{(viii)}$$

where α, β, γ, δ, α_n, β_n, γ_n, and δ_n are integral constants. This equation exhibits the potential distribution of the linear electrical charges.

It can be seen that Equation (viii) is obtained by determining the integral constants.

Acknowledgment

The assistance of Izumi Sano is acknowledged.

Nomenclature

a	. . . radius of covered electrode, m
D_p	. . . particle diameter, m
d	. . . pitch of electrode, m
E	. . . intensity of electrical field, volt/m
f	. . . frequency of applied voltage, Hz
k	. . . dielectrical constant, F/m
k*	. . . specific dielectrical constant
l	. . . distance between adjacent electrode wire surfaces, m
M	. . . mass of particle, kg
m	. . . dust load, kg/m²

q . . . electrical charger per unit length of electrode, m
R . . . d/2a
r . . . radius of electrode wire, m
U . . . potential of electrical field, V
u . . . superficial gas velocity, cm/sec
V . . . applied voltage, V
w . . . E/(V/l)
x, y . . . coordinate from center of electrode, m
y_b . . . distance between bottom of dust layer and top of covered electrode surface, mm
μ . . . viscosity of air, kg/(m)(sec).

Literature cited

1. Nakajima, H., Goto, K., and Tanaka, T., *Kagaku Kōgaku* (Journal of the Society of Chemical Engineers, Japan) 31, p. 504 (1967).

2. Masuda, H., Ito, Y., Iinoya, K., and Sakai, K., *J. Res. Assoc. Powder Tech.* 10, p. 151 (1973).

3. Nakajima, H., Nakamura, A., and Tanaka, T., *J. Res. Assoc. Powder Tech.* 10, p. 3 (1973).

4. Nakajima, H., Mitsui, R., Kuramae, M., and Tanaka, *Kagaku Kōgaku* (Journal of the Society of Chemical Engineers, Japan) 36, p. 1243 (1972).

5. Masuda, S., Fujibayashi, K., and Ishida, K., *Staub-Reinhaltung der Luft* (Dust-Air Cleaning) 30, p. 449 (1970)

6. Oberhettinger, U., "Anwendung der elliptischen Funktion in Physik und Technik" (Application of Elliptic Functions to Physics and Engineering), p. 67 Berlin, Springer Verlag (1949).

7. Tanaka, N., Makino, K., and Iinoya, K., *Kagaku Kōgaku* (Journal of the Society of Chemical Engineers, Japan) 37 p. 718 (1973).

8. Masuda, S., "Textbook of 17th Powder Technology Course," p. 23, Res. Assoc. Powder Tech., Japan (1970)

COMPARISON OF DUST CLEANING PERFORMANCE OF COLLAPSE AND MECHANICAL SHAKING TYPES OF FABRIC FILTERS

K. Iinoya, K. Makino, Y. Mori,
J. Okutani and H. Kawabe
Kyoto University, Chemical Engineering Dept.

Introduction

The bag filter, one of the high performance dry type collectors, is currently increasing in importance. The main investigation of ordinary bag filter is characterized by the collection efficiency versus pressure drop during operation and there are not many investigations concerning dust cleaning characteristics.[1,2] However, in order to investigate the operation of a bag filter, the dust cleaning performance associated with this system is an important characteristic in determining its operating condition as well as an economically optimal design. Therefore this report, in recognizing this point, applies reverse collapse and mechanical shaking type dust cleaning operations which are widely used for filter cloths and presents the result of experimental comparison of them in terms of pressure drops.

1. Experimental Apparatus and Method

1.1 Sample Fly Ash and Filter

Two kinds of ashes (fine calcium carbonate I and II) are used as sample ashes and the measurement result of their particle size distribution is shown in Table 1. As filters, we used nylon (long fiber NR-9A) and teflon (long fiber TR-9A, short fiber TR-2020S) which are widely used in the industry. The bag is a cylinder type bag with inner diameter of 170 mm and length of 1,800 mm. Also the reverse collapse type bag filter was adjusted with spring to have a constant initial tensile force of 12.5 kg. For mechanical shaking type, the bag tension was adjusted so that the bag can move vertically about 20 mm while the middle of the bag is seized. Although it is generally believed that dust cleaning performance depends on type of ashes, the purpose of this report is to verify the qualitative characteristics of dust cleaning performance when the above mentioned sample ashes are used.

1.2 Experimental Apparatus

Figure 1 shows the experimental apparatus. Ashes travel from the feeder through the rotating impact type dispenser and diaphragm valve (V2) to bag filtering surface where they are collected. The cleaning air which passed through the bag travels

through the valve (V1) and the flow measuring orifice and is exhausted. On the other hand, for reverse collapse type dust cleaning operations, four valves (V1 ∿ V4) are operated reversely and air for reverse dust cleaning goes through valve 3 (V3) and bag surface in a reverse direction to the collected ash accumulated at the inside wall of the bag, and passes through valve (V4) and orifice before exhausted. For mechanical shaking type dust cleaning operations, only one valve (V1) is closed, as compared to the collecting operation, to terminate the air flow after passing through the bag. The shaking equipment (450 rpm) on top of the system is started to clean the accumulated ashes. The cleaned ashes fall into the dust chamber.

1.3 Experimental Method

1) Supply sample ashes quantitatively (at a constant rate) and start collection, 2) stop collection when the bag pressure drop reaches at pre-determined value, 3) start dust cleaning and stop after pre-determined time τ, 4) weigh ashes which fell into dust chamber, 5) restart collection with only cleaning air passing through bag and measure pressure drops, 6) repeat above operations 3), 4), and 5) and continue measurements until there will be no ashes. Assume the final dust cleaning pressure drop as Δp_∞.

2. Experimental Results

2.1 Final Dust Cleaning Pressure Drop Δp_∞

Table 2 shows a relationship between the final dust cleaning pressure drop Δp_∞ and the initial dust cleaning pressure drop Δp_{max} for reverse collapse type and mechanical shaking type systems. According to this, the final dust cleaning pressure drop for reverse collapse type system is considerably higher than that of mechanical shaking type system. On the other hand, when the dust accumulating condition of the filter cloth surface is observed at the final dust cleaning operation, the former one has a considerable amount of secondary accumulation layer and ashes on the surface are in a mottled pattern while the latter one is observed with only a primary accumulation layer. Also the value of Δp_∞ is independent with Δp_{max} and is almost constant.

2.2 Effect of Local Dust Cleaning Duration Time τ

Figure 2 shows a representative relationship between the cumulative cleaning duration time $t_0 (= n\tau)$ and residual fraction of pressure drop after cleaning, Λ_p, for the reverse collapse type system and Figure 3 shows that of mechanical shaking type system. Based on this, the former one will have the minimum value for residual fraction after cleaning Λ_p at a certain value of τ (10 ∿ 30 sec) while the latter one has a smaller Λ_p with a shorter τ.

2.3 Effect of Initial Dust Cleaning Pressure Drop Δp_{max}

Figure 4 and 5 show a relationship between Δp and t_0 as a parameter of the dust cleaning initial pressure drop Δp_{max} for both systems and it is seen that, when t_0 is constant, the value of Δp is smaller with higher Δp_{max}. This can also be predicted from above 2.1.

2.4 Dust Cleaning Curve

The dust cleaning curve is defined as the relationship between pressure drop and dust load when collection is continued until the pressure drop becomes the same value as that of initial dust cleaning after ashes were uniformly accumulated on filter cloth. The dust cleaning operation was continued until no more ash was removed. Figure 6 and Figure 7 show typical dust cleaning curves. For the reverse collapse type system, the larger the dust load at initial cleaning is, the larger the residual dust load is. Also when the bag pressure drop at reversing decreases to less than a certain value, there will be no dust cleaning function. It is also noticed that the increase rate of pressure drop, when the system was switched to collection after achieving pressure drop Δp_∞, is much bigger than that of cleaning filter cloth. For the mechnical shaking type system, the residual dust load is a constant value which is independent with initial condition of dust cleaning and most of the secondary dust layer is cleaned out. This is explained by the fact that the increase rate of pressure drop after the system is switched to collection from final achieving pressure drop is consistent with that of collection. Namely, the latter one is different from the former one and is perfect in cleaning out secondary layer. These characteristics also apply to short fiber materials and its example is shown in Figure 8.

3. Consideration

3.1 Estimation of Dust Cleaning Process

When the sample ashes are uniformly accumulated on filter cloth, the initial cleaning pressure drop Δp_{max} and the final cleaning pressure drop Δp_∞ are expressed in the following equations,*

$$\Delta p_{max} = U(A + B\mu_{max}\ \delta) \qquad (1)$$

$$\Delta p_\infty = UA \qquad (2)$$

* Pressure drop characteristic coefficients A,B and δ in equations (1) and (2): In this experiment, A is measured at the condition with very little residual dust load after complete cleanings. Therefore, A has a close value as a (the pressure drop characteristic coefficient only for clean filter). B and δ have close values as b and δ respectively. Please refer Reference 3) and 5) for definition of a, b, and δ.

If dust cleaning is started from equation (1)'s condition, the bag pressure drop gradually decreases from Δp_{max} and reaches at Δp_{∞}. When the dust accumulation condition at a certain point of dust cleaning process was observed, it was determined that the dust layer consisted of the part where dust had not fallen, the part only with initial dust layer after others fell off and the part which is in between of above two parts and has a part of secondary layer. It was also determined that the mechanical shaking type has mostly the former two cases and has mottled falling.**

Considering above results of observation, introduce the model like Figure 9 in which θ is defined as the ratio of intermediate part with residual secondary layer to all filtering area. Using this model, the pressure drop Δp at a certain point during cleaning process is obtained by the following equation (refer Appendix).

$$\Delta p = \frac{\Delta p_{\infty}}{(1-\theta)-(1-\alpha)(\Lambda-\frac{1}{2}\theta) + \int_0^{\theta} \frac{\alpha\theta^{\delta}}{\alpha\theta^{\delta} + (1-\alpha)\, x^{\delta}}\, dx} \qquad (3)$$

Δp_{∞}, Δp and Λ in Equation (3) can be measured experimentally. Also if δ is experimentally determined with same dust and filter material, θ at a certain t_0 can be calculated by Equation (3).

Figure 10 shows a typical result of reverse collapse type. According to this, θ has a tendency to increase from 0 to a certain value when t_0 increases. This means that the cleaning process initially has only the mottled fallings and has less mottled fallings later, but even at a final stage the mottled fallings still exist. Also when t_0 is constant θ has a minimum value and especially under Figure 11's condition θ has a minimum value at Δp_{max} = 120mm H_2O. Causes of this phenomenon will need to be investigated fundamentally in the future. On the other hand the result of observation shows $\theta = 0$ for the mechanical shaking type and this can be seen that the calculated cleaning curve with $\theta = 0$ in Equation (3) is consistent with experimental value as shown in Figure 8. Also similar results were obtained for calcium carbonate and metallic silicon which have different particle size distributions. As shown in Figures 2-5, mechanical shaking type can complete dust cleaning in a much shorter time (10-30 sec(practical region)) than reverse collapse type.

**"Mottled falling" in this report means that the dust residual condition at cleaning process consists of one part where no dust had fallen off like (1-θ) section of Figure 9 and the other part where only initial dust layer is left.

Namely mechanical shaking type precedes dust cleaning by mottled fallings and eventually most of the secondary layer will be cleaned off. Therefore, the drastic increase in pressure drop due to mottled falling during re-collection does not exist.

3.2 Estimation of Optimal Single Cleaning Duration Time τ_{opt}

The cleaning mechanism characteristics of accumulated dust are known to be approximated by one step later (4). Thus, if it is cleaned for time τ and the time τ cleaning is repeated for n times after a stop, the drag coefficient (drag resistance) due to dust falling at ith process can be obtained by following equation.

$$R_{fi} - R_{ai} = (R\infty_i - R_{ai})\{1-\exp(-\tau/T_i)\} \tag{4}$$

Here, R_{ai}, R_{fi} and $R_{\infty i}$ are the initial drag coefficient at ith cleaning process, the final drag coefficient after cleaning and the hypothetical drag coefficient after infinite cleaning processes. Since R_{fi} is equal to R_{ai+1}, in Equation (4) is varied to obtain Equation (5).

$$R_{fn} - R_{al} = \sum_{i=1}^{n} [(R_{\infty i} - R_{ai})\{1-\exp(-\tau/T_i)\}] \tag{5}$$

Since the result of experiments show that T_i is constant and is independent with i, $T_i = T$ leads to the following Equation.

$$R_{fn} - R_{al} = \{1-\exp(-\tau/T)\} \sum_{i=1}^{n} (R_{\infty i} - R_{ai}) \tag{6}$$

The left side of Equation (6) indicates a decrease in drag resistance after nth cleaning process. Also if Equation (6) is expressed by residue fraction of pressure loss after cleaning Λ_p,

$$\Lambda_p = 1 - \{1-\exp(-\tau/T)\} \cdot G \tag{7}$$

where $G = \sum_{i=1}^{n} (\Lambda_{pai} - \Lambda_{p\infty i})$. Namely G is a total sum of the difference between the residue fraction at cleaning duration τ of each cleaning process and the hypothetical residue fraction after an infinite cleaning duration ∞. Equation (7) indicates that the residue fraction Λ_p after nth cleaning can be determined by T, τ, and G. If T is measured separately, since Λ_{pai} and Λ_{pfi} are experimentally determined, the value indicated in the following equation is possible to determine.

$$\Lambda_{pai} - \Lambda_{p\infty i} = \frac{\Lambda_{pai} - \Lambda_{pfi}}{1 - \exp(-\tau/T)} \tag{8}$$

Therefore, G can be experimentally obtained by using Equation (8) and our review for the combination of the dust and the filter material used in this experiment shows that it can be determined by the following equation.

$$G = k_i \log n + k_2 \quad (k_i, k_2; \text{ experimental constant} > 0) \qquad (9)$$

Thus, G is proportional to a logarithm of number of cleanings n. The comparison of experimental results and the calculational values of Λ_p which was obtained by substituting Equation (9) into Equation (7) is shown in Figure 12. It is seen that both match fairly closely. Also this result suggests that, if k_i and k_2 are determined by certain experimental values with a constant τ, it is possible to estimate the optimal single cleaning duration time τ_{opt}.

Conclusion

After comparing the cleaning phenomena of reverse collapse type and mechanical shaking type bag filters, the following results were obtained.

1) When the cumulative cleaning duration time t_0 is constant, the reverse collapse type has the most optimal value for a single cleaning duration time τ but the mechanical shaking type has a better cleaning performance with smaller τ.

2) The final cleaning pressure drop Δp_∞ is generally higher for the reverse collapse type than for the mechanical shaking type. For both cases, the final cleaning pressure drop Δp_∞ has a constant value independently with initial cleaning pressure drop Δp_{max}. The higher initial cleaning pressure drop Δp_{max} is the more residue fraction of pressure drop after cleaning decreases.

3) The reverse collapse type initially has only mottled falling and its ratio will decrease with time to have more intermediate cleaning layer. However, fairly large amounts of mottled falling (θ = 20-50%) will also be left. The mechanical shaking type rapidly proceeds cleaning by mottled falling and most of the secondary dust layer is cleaned off eventually. Namely there is almost no rapid pressure drop increase at collection during mottled falling.

4) One method to determine experimentally the most optimal value of single cleaning duration time τ for reverse collapse type was obtained.

The cleaning performance should also be reviewed in conjunction with collection performance and this will be one of the important topics in a future.

Appendix

Suppose the accumulating condition at certain point of cleaning process is expressed by the model shown in Figure 9,

θ part; $\Delta p = u(x)(A+BM(x)^{\delta})$ (i)

where $M(x) = M_{max} \cdot F(x)$

$(1-\theta)(1-\lambda)$ part; $\Delta p = Au_i$ (ii)

$(1-\theta)\lambda$ part; $\Delta p = u_2(A+BM_{max}^{\delta})$ (iii)

Since air flow rate Q is considered to be almost a constant,

$$Q/S = \int_0^{\theta} u(x)\, dx + [u_1(1-\lambda) + u_2\lambda](1-\theta) = u_{\infty} = u_{max} \quad \text{(iv)}$$

Following Equation is obtained from Equations (1), (2), and (iv),

$$M_{max}\delta = (\Delta p_{max} - \Delta p_{\infty} \frac{u_{max}}{u_{\infty}}) / (Bu_{max})$$

$$= (\Delta p_{max} - \Delta p_{\infty}) / (Bu_{max}). \quad \text{(v)}$$

Substitute Equation (v) into Equations (i) and (iii),

$$\Delta p = u(x)[A + \frac{1}{u_{max}} (\Delta p_{max} - \Delta p_{\infty})\, F(x)^{\delta}] \quad \text{(vi)}$$

$$\Delta p = u_2[A + \frac{1}{u_{max}} (\Delta p_{max} - \Delta p_{\infty})]. \quad \text{(vii)}$$

Also obtain u_1, $u(x)$, and U_2 from Equations (ii) and (vi) and (viii) and substitute them into Equation (iv),

$$\int_0^{\theta} \frac{\Delta p}{A + (\Delta p_{max} - \Delta p_{\infty})(u_{max} F(x)^{\delta}} \, dx$$

$$+ [\frac{\Delta p}{A} (1-x) + \frac{\Delta p}{A + (\Delta p_{max} - \Delta p_{\infty})/u_{max}} \lambda] \times (1-\theta)$$

$$= u_{\infty} = \frac{\Delta p_{\infty}}{A} \quad \text{(viii)}$$

Substitute $u_{max} = u_\infty/A$ into Equation (viii) and introduce a dimensionless parameter $\alpha = \Delta p_\infty / p_{max}$ to obtain following equation.

$$\int_0^\theta \frac{\alpha dx}{\alpha + (1-\alpha)F(x)^\delta} + (1-\alpha)[1 - (1-\alpha)\lambda] = \frac{\Delta p_\infty}{\Delta p} \qquad \text{(ix)}$$

The residue fraction after cleaning Λ which is possible to measure experimentally is expressed by following equation.

$$\Lambda = \lambda(1-\theta) + \Phi \cdot \theta \qquad \text{(x)}$$

where

$$\Phi = \int_0^\theta M_{max} F(x)dx/(M_{max}\cdot\theta) = \theta^{-1} \int_0^\theta F(x)dx$$

Obtain λ from Equation (x),

$$\lambda = (1-\theta)^{-1}(\Lambda - \int_0^\theta F(x)dx). \qquad \text{(xi)}$$

Substitute Equation (xi) into (ix) to obtain Δp,

$$\Delta p = \Delta p_\infty / [\int_0^\theta \frac{\alpha dx}{\alpha + (1-\alpha)\ F(x)^\delta}$$

$$+ (1-\theta) - (1-\alpha)(\Delta - \int_0^\theta F(x)dx)] \qquad \text{(xii)}$$

Now, when $\theta=0$ whatever the function $F(x)$ is Δp can be determined by α, Λ, and Δp_∞. But when $\theta \neq 0$, Δp depends on the form of $F(x)$, but if we assume $F(x) = (x/\theta)^n$ $0.5 \leq n \leq 2.0$, Δp did not vary significantly with the value of n. Therefore if we assume the dust layer thickness distribution as $F(x) = x/\theta$, Equation (3) in this report will be obtained.

ON THE ECONOMICALLY OPTIMAL DESIGN OF BAG FILTER

K. Iinoya, K. Makino and N. Tanaka
Kyoto University
Dept. of Chemical Engineering

Introduction

We have already done a theoretical review of the operation of multi-compartment bag filter and verified how the pressure drop and the cleaning cycle of bag filters are affected by cleaning residual fraction, number of bag compartments and pressure drop characteristics. Based on these, this report gives a theoretical review concerning economically optimal design of bag filter.

There are already some reports which deal with economical design of bag filter as a large system including cooling system or which deal with economical design by assuming that the life of filter cloth is a function of filtering velocity. Our economical design report of air-filter is essentially the same as these.

Based on a relationship between operating pressure drop and cleaning cycle obtained in previous reports, this report provides optimal operating pressure drop, optimal filtering velocity and optimal cleaning cycle as variables for the optimal problem by expressing a strict relation of process amount and by assuming that the life of filter cloth can be determined by number of cleaning or operational time. The pressure drop of the bag filter is expressed as a sum of the pressure drop of filter itself and the pressure drop due to dust load. An analytical solution can be obtained when the former one can be neglected against the latter one. The parameters used in this analysis were determined after contacting several users and manufacturers in order to get more practical calculations. Also by obtaining relative sensitivity of each parameter to optimal solution, it was shown that the calculations in this report can be easily applied to actual cases and is the important factor in economical design.

1. Derivation of Equation for Economical Calculation

Generally the fixed and operating costs of instrument are necessary to know for resolving the economically optimal problem of systems. The design of bag filter requires information for the fixed and installed costs of bag filters, the fixed installation costs of the fan and the cost of replacing filter cloth due to damage. The operating cost of bag filter is mainly the cost of power for cleaning and this can be neglected as compared with other costs. Although it is also necessary to consider the manpower cost for changing filter cloth, it is difficult to formulate this and it can be included in the cost of filter cloth.

Here, the fixed cost of the device is expressed as a product of the cost of instrument (including installation cost) and the certain annual rate, including tax, interest, repair cost and depreciation cost. However, the fixed cost of bag filter is considered not to include changing cost of filter material.

1.1 Fixed Cost of Fan

As a result of cost analysis of fan (mainly turbo-fan) in the ranges of 200~500 mm H_2O air pressure and 200~5,000 m^3/min air flow, there is a linear relation between motor power cost (including costs of motor and installation) as shown in Equation (1). Also as shown in Equation (2) there is a linear relation between motor power and the product of air pressure and air flow.

$$Y_1 = h_1 P = 2.7P \tag{1}$$

$$P = h_2 \Delta p \cdot Q = 0.019 \Delta p \cdot Q \tag{2}$$

If the annual rate of tax and depreciation is set as k_1, the fixed cost of fan is as follows:

$$C_1 = k_1 h_1 P \equiv K_1 \Delta p \cdot Q \tag{3}$$

Now as a standard value, $k_1 = 0.2$ is considered. Substitute Equations (1) and (2) into Equation (3).

$$K_1 = h_1 h_2 k_1 = 0.010$$

Here, the coefficient of Equation (2) is consistent with the report by Iinoya.

1.2 Power Cost of Fan

The power cost of fan can be expressed by the following equation

$$C_2 = e \cdot \varepsilon \cdot P \tag{4}$$

where e is a unit power cost and ε is an annual operating time. Substitute Equation (2) into this and you will get the following equation.

$$C_2 = e \cdot \varepsilon \cdot h_2 \Delta p \cdot Q \equiv K_2 \Delta pQ \tag{5}$$

When $h_2 = 0.019$, $\varepsilon = 8{,}000$ hr/yr, e = 5 yen/Kw·hr as standard values, $K_2 = 0.076$.

1.3 Fixed Cost of Bag Filter

As a result of cost survey (including installation cost) of bag filter, it was found that the cost is about the same for mechanical shaking cleaning type and reverse air-flow cleaning type and that the cost is in exponential relation with filtering area as shown in Figure 1. The pulse air type is slightly higher in cost than these. Assuming the annual rate is k_3, the fixed cost can be expressed by the following equation using the cost of bag filter in Figure 3:

$$C_3 = k_3(h_3 S^{q_3}) \equiv K_3 S^{q_3} \tag{6}$$

As a standard value, assume $k_3 = 0.2$. Also from Figure 1, when $S>300$ m^2 it is seen that $h_3 = 2.5$ and $q_3 = 0.89$ and when $S<300$ m^2, $h_3 = 12.3$ and $q_3 = 0.61$. Thus, $K_3 = 0.50$ ($S>300$) and $K_3 = 2.46$ ($S<300$).

1.4 Filter Cloth Replacing Cost

Although filter damage depends on complicated factors and there is not a complete definition of the lifetime (θ) of filter cloth, filter damage can be considered due to following two cases; damage caused in a certain time θ_0 due to long-time exposure to high temperature gases, and damage caused by a certain number of cleanings R due to numerous dust cleaning operations. These two cases can be expressed respectively as follows:

$$\theta = \theta_0 \quad (\theta_0 = \text{constant}) \tag{7}$$

$$\theta = RT \quad (R = \text{constant})$$

where T is the total period of the cleaning cycle required to have cleaning operation through all compartments. Also, the allowable repeated number of cleaning operations is about 10~20 thousand although it may depend on filter material and cleaning type. The lifetime is 1~2 years for ordinary glass fiber and 2~3 years for mixed fiber.

Now the filter cloth replacing cost can be expressed by the following equation.

$$C_4 = fS\varepsilon/\theta \tag{9}$$

where f is a cost of filter cloth and is about 1,000 yen/m^2 except for certain more expensive ones.

1.5 Cleaning Cycle and Operational Pressure Drop

The pressure drop through the bag filter can be expressed as a sum of pressure drops of filter cloth itself and of dust load.

$$\Delta p = u(a + bm^q) \tag{10}$$

where a, b and q are constants determined by experiments. The values of constants are different if they are determined by above equation using new filter cloth or old filter cloth which was used for some cleaning operations and the constants used in this report are those of latter case. Generally the pressure drop due to filter cloth itself is considered to be minimal and we assume $a \fallingdotseq 0$ by considering that the big advantage of this is the optimal solution can be analytically obtained. The case when the value of a cannot be neglected is reviewed in Section 2.3. Now Equation 10 can be expressed as follows:

$$\Delta p \fallingdotseq bum^q \tag{11}$$

When the filter is constantly operated in a certain cleaning cycle (it is generally called as a timer type), a relation between cleaning cycle T and operational pressure drop Δp_s can be expressed by the following equation.

$$\Delta p_s \fallingdotseq \tilde{p}_s bu(c\eta uT)^q \tag{12}$$

On the other hand, when it is constantly operated with a certain maximum operational pressure drop Δp_s (it is called as a differential pressure type), the cleaning cycle T is expressed as follows.

$$T \fallingdotseq \frac{1}{c\eta u}\left(\frac{\Delta p_s}{bu}\right)^{1/q}(N\tilde{\tau}_s) \tag{13}$$

where $\Delta\tilde{p}_s$ and $N\tilde{\tau}_s$ are functions of the constant q which can be determined by cleaning residual rate ξ, number of bag compartment N and characteristics of filter cloth and dust.

$$(\Delta\tilde{p}_s)^{1/q} = (N\tilde{\tau}_s)^{-1} = \frac{1}{1-\xi}\left[\sum_{i=1}\frac{1}{N}\left\{\xi^{q+1} + \frac{i}{N}(1-\xi^{q+1})\right\}^{-q/1+q}\right]^{-1/q} \tag{14}$$

Since the relation between p_s and T in Equations (12)-(14) is the same for both timer type and differential type; the following solution can be applied for both operations. Also, the dust load in the bag compartment immediately before the cleaning operation (x_{N_3}) can be obtained by the following equation.

$$(1-\xi)x_{N_3} + c\eta uT \tag{15}$$

1.6 Annual Total Cost

Based on above, the annual total cost can be obtained.

$$C_T = (K_1+K_2)\Delta p_s \cdot Q+K_3 S^{q_3}+f\varepsilon S/\theta \qquad (16)$$

It was assumed here that the pressure drop through the duct does not affect the optimal solution and that the air pressure of fan is equal to operational pressure drop of bag filter. Although the above equation has three variables (filtering air velocity, operational pressure drop and cleaning cycle), it is actually a two variables function since there is a relationship as equations (12) and (13) for these variables. Also, when the lifetime of the filter cloth can be determined by its operational time as described later, it will be a one variable function since the cleaning cycle can be determined easily.

1.7 Calculation of Optimal Solution

Now we have a simple consideration concerning annual cost.

First, when operational pressure drop Δp_s is assumed as a constant and the filtering air velocity u is changed, the fixed cost of bag filter is cheaper with large u but the replacing cost of filter increases with frequent cleaning cycles. Thus, the optimal filtering air velocity exists. Similarly when the filtering air velocity is assumed as a constant, the optimal operational pressure drop exists.

When a = o, the optimal condition can be analytically obtained from Equations (12) and (16). However, there are two analytical solutions (2·1 and 2·2) for two filter cloth lifetime equations (Equations (7) and (8). Also, even if there are upper and lower limits in variables Δp_s, u and x_{N_3}, solutions can be easily obtained (2·1·1~2·1·3). However, when the lifetime is determined by operational time θ_0 (one variable optimal problem), the solutions are naturally the same as limiting values when variables Δp_s. u and x_{N_3} exceed upper and lower limits. Thus, it is not included here.

2.1 Optimal Solution When Lifetime of Filter Cloth is Determined by Number of Cleanings (a ≒ o)

Place $\partial C_T/\partial u = \partial C_T/\partial \Delta p_s = o$ in Equation (16) and substitute Equations (8) and (12) into this to obtain solution. However, there are two solutions because the fixed cost equation of bag filter has different coefficients at S = 300 m^2.

i) S ≠ 300 m^2.

$$p_{s,opt} = \left(\frac{f\varepsilon}{Rq}\right)^{qq_3/\alpha} (K_1 + K_2)^{-(1+qq_3)/\alpha} \{b\Delta\tilde{p}_s(c\eta)^q\}^{q_3/\alpha} (q_3K_3)^{1/\alpha} Q^{(q_3-1)/\alpha} \quad (17)$$

$$u_{opt} = \left(\frac{f\varepsilon}{Rq}\right)^{-q/\alpha} \{(K_1 + K_2)b\Delta\tilde{p}_s(c\eta)q\}^{-1/\alpha} (q_3K_3)^{(1+q)/\alpha} Q^{(q_3-1)(1+q)/\alpha} \quad (18)$$

$$T_{opt} = \left(\frac{f\varepsilon}{Rq}\right)^{(1+q+q_3)/\alpha} \{(K_1 + K_2)b\Delta\tilde{p}_s(c\eta)^q\}^{(1-q_3)/\alpha} (q_3K_3)^{-(2+q)/\alpha} Q^{(q_3-1)(1+q)/\alpha} \quad (19)$$

$$C_{T,min} = \left(1+\frac{1}{q_3}+q\right)\left(\frac{f\varepsilon}{Rq}\right)^{qq_3/\alpha} \{(K_1 + K_2)b\Delta\tilde{p}_s(c\eta)^q\}^{q_3/\alpha} (q_3K_3)^{1/\alpha} Q^{q_3(2+q)/\alpha} \quad (20)$$

where $\partial \equiv 1 + q_3 + qq_3$ (21)

The parameters in the first parenthesis on the right side of Equation (20) indicates that the ratio among the fixed cost and power cost of fan, the fixed cost of bag filter and the filter cloth replacing cost is $1:(1/q_3):q$.

ii) $S = 300\ m^2\ (\equiv S_b)$

$$\Delta p_{s,opt} = \left(\frac{f\varepsilon}{Rq}\right)^{q/(q+1)} (K_1 + K_2)^{-q/(q+1)} \{b\Delta\tilde{p}_s(c\eta)^q\}^{1/(q+1)} \left(\frac{Q}{S_b}\right)^{1/(q+1)} \quad (22)$$

$$u_{opt} = Q/S_b \tag{23}$$

$$T_{opt} = \left(\frac{f\varepsilon}{Rq}\right)^{1/(q+1)} \{(K_1 + K_2)b\Delta\tilde{p}_s(c\eta)^q\}^{-1/(q+1)} \left(\frac{Q}{S_b}\right)^{-(q+2)/(q+1)} \tag{24}$$

$$C_{T,min} = K_2 S_b^{q3} + (1+a)\left(\frac{f\varepsilon}{Rq}\right)^{q/(q+1)} \{(K_1 + K_2)b\Delta\tilde{p}_s(c\eta)^q\}^{1/(q+1)} \left(\frac{Q}{S_b}\right)^{(q+2)/(q+1)} \tag{25}$$

The result of numerical calculation for various Q and $c\eta$ is shown in Figure 2. The values of used constants are those standard values described earlier and parameters $f\varepsilon/R = 300$ and $b\Delta\tilde{p}_s = 10^5$ are for cost of filter cloth f = 0.2 ten thousand yen/m^2, annual operational time ε = 8,000 hr/year, allowable repeated times of cleaning operation $R = 2 \times 10^4$ and for these constants in Equation (12) such as operational pressure drop Δp_s = 200 mm H_2O, collecting dust amount $c\eta uT = 0.1$ Kg/m^2 and filtering air velocity u = 0.02 m/sec, and these are standard values. According to the Figure, the effect of Q to the optimal solution is minimal except for a small Q but the optimal condition of operational pressure drop and filtering air velocity needs to be changed for dust concentration of carrying gas.

2.1.1 When Filtering Air Velocity is Limited

When the filtering air velocity has upper limit $\bar{u}$ or lower limit $\underline{u}$ from restrictions of filter collection performance and system design and when the solution u_{opt} obtained with assuming no restrictions (limits) exceeds these upper and lower limits, the optimal solution is when u_{opt} is consistent with $\bar{u}$ or $\underline{u}$. Therefore $\bar{u}$ or $\underline{u}$ needs to be sutstituted for Q/S_b in Equations (22)~(25)

2.1.2 When Operational Pressure Drop if Limited

When the operational pressure drop Δp_s has an upper limit $\Delta\bar{p}_s$ from filter cloth strength and when the solution obtained with assuming no limits exceeds $\Delta\bar{p}_s$, the optimal solution is when Δp_{opt} is consistent with $\Delta\bar{p}_s$. Other solutions can be obtained by differentiating Equation (16).

$$u_{opt} = \left(\frac{f\varepsilon}{Rqq_s K_s}\right)^{-q/(1+qq_s)} \times \left\{\frac{b\Delta\tilde{p}_s (c\eta)^q}{\Delta\bar{p}_s}\right\}^{-1/(1+qq_s)} Q^{q(q_s-1)/(1+qq_s)} \quad (26)$$

$$T_{opt} = \left(\frac{f\varepsilon}{Rqq_s K_s}\right)^{(q+1)/(1+qq_s)} \times \left\{\frac{b\Delta\tilde{p}_s (c\eta)^q}{\Delta\bar{p}_s}\right\}^{(1-q_s)/(1+qq_s)} Q^{(q+1)(1-q_s)/(1+qq_s)} \quad (27)$$

$$C_{T,min} = (K_1+K_2)Q\Delta\bar{p}_s + K_s(qq_s+1) \times \left(\frac{f\varepsilon}{Rqq_s K_s}\right)^{qq_s/(1+qq_s)} \left\{\frac{b\Delta\tilde{p}_s (c\eta)^q}{\Delta\bar{p}_s}\right\}^{q_s/(1+qq_s)} \times Q^{q_s(1+q)/(1+qq_s)} \quad (28)$$

Figure 8 shows the result of this calculation. This figure indicates no significant changes due to limits in operational pressure drop. Especially T_{opt} is not affected by this.

2.1.3 When Dust Load is Limited

There may be some limits in dust load on filter cloth in order to have an effective cleaning operation. Therefore, we review the case when there is generally an upper limit M or lower limit $\underline{M}$ and the dust load obtained with no limits exceeds these values.

The following optimal solution can be obtained from Equation (16) under a condition of Equation (15).

$$\Delta p_{s,opt} = \left(\frac{K_1+K_2}{q_3 K_3}\right)^{-1/(1+q_3)}$$

$$\times \{b\Delta\tilde{p}_s(1-\xi)^q \chi_{Ns}{}^q\}^{q_3/(1+q_3)} Q^{(q_3-1)(1+q_3)} \tag{29}$$

$$u_{opt} = \left\{\frac{(K_1+K_2)}{q_3 K_3} b\Delta\tilde{p}_s(1-\xi)^q \chi_{Ns}{}^q\right\}^{-1/(1+q_3)} Q^{(q_3-1)/(1+q_3)} \tag{30}$$

$$T_{opt} = \frac{(1-\xi)\chi_{Ns}}{c\eta}$$

$$\times \left\{\frac{(K_1+K_2) b\Delta\tilde{p}_s(1-\xi)^q \chi_{Ns}{}^q}{q_3 K_3}\right\}^{1/(1+q_3)} Q^{(1-q_3)/(1+q_3)} \tag{31}$$

$$\chi_{Ns} = \overline{M}, \text{ or } \underline{M} \tag{32}$$

$$C_{T,min} = \left(1+\frac{1}{q_3}\right)\{(K_1+K_2) b\Delta\tilde{p}_s$$

$$\times (1-\xi)^q \chi_{Ns}{}^q\}^{q_3/(1+q_3)} (q_3 K_3)^{1/(1+q_3)} Q^{2q_3/(1+q_3)}$$

$$+ \frac{f\varepsilon Q c\eta}{R(1-\xi)\chi_{Ns}} \tag{33}$$

The result of this equation is shown in Figure 9. As seen from the above equations, under a conditon of constant dust load, $\Delta p_{s,opt}$ and u_{opt} are constant and are independent with $c\eta$ and T_{opt} is inversely proportional to $c\eta$.

2.2 Optimal Solution When Lifetime of Filter Cloth is Determined by Operational Time ($a \fallingdotseq o$)

In this case, the minimum cleaning cycle T_{min} possible to have for the system will naturally be the optimal solution. Therefore it is a one variable optimal problem. The following equation can be obtained by substituting Equation (12) into Equation (16) and setting $\partial C_T/\partial u = o$.

$$(1+q)(K_1+K_2)b\Delta\tilde{p}_s(c\eta T_{min})^q U_{opt}^{q+2} = q_3K_3Q^{q_3-1}u_{opt}^{1-q_3}+f\varepsilon/\theta_0 \tag{34}$$

By substituting the optimal solutions U_{opt} obtained from above equation into Equations (12) and (16), $\Delta p_{s,opt}$ and $C_{T,min}$ can be determined respectively. And the following approximate solution can be obtained by

$$f\varepsilon/\theta_0 \ll q_3K_3Q^{q_3-1}u_{opt}^{1-q_3}$$

$$u_{opt} \fallingdotseq \left\{\frac{q^3K^3Q^{q_3-1}}{(1+q)(K_1+K_2)b\Delta\tilde{p}_s(c\eta T_{min})^q}\right\}^{1/(1+q+q_3)} \tag{35}$$

$$\Delta p_{s,opt} \fallingdotseq \{b\Delta\tilde{p}_s(c\eta T_{min})^q\}^{q_3/(1+q+q_3)}$$

$$x\left\{\frac{q_3K_3Q^{q_3-1}}{(1+q)(K_1+K_2)}\right\}^{(q+1)/(1+q+q_3)} \tag{36}$$

$$C_{T,min} \fallingdotseq \left[1 + \frac{1+q}{q_3} + \frac{f\varepsilon}{\theta_0}\right.$$

$$x\{(K_1+K_2)b\Delta\tilde{p}_s(c\eta T_{min})^q Q^{2+q}\}^{(1-q_3)/(1+q+q_3)}$$

$$\left.x\left(\frac{q_3K_3}{1+q}\right)^{-(2+q)/(1+q+q_3)}\right]$$

$$x\{(K_1+K_2)b\Delta\tilde{p}_s(c\eta T_{min})^q Q^{2+q}\}^{q_3/(1+q+q_3)}$$

$$x\left(\frac{q_3K_3}{1+q}\right)^{(1+q)/(1+q+q_3)} \tag{37}$$

Figure 3 shows an example of numerical result for various Q and $c\eta$ by using Equation (34). Also it shows approximate solutions by Equations (35)~(37). It is seen from the Figure that the approximate solution is a good approximation for Equation (34). The parameter $f\varepsilon/\theta_0 = 0.05$ in this Figure is for $f = 0.1$ ten thousand yen/m^2, $\varepsilon = 8{,}000$ hr/yr and $\theta_0 = 16{,}000$ hr.

2.3 Optimal Solution When Pressure Drop of Filter Cloth Cannot Be Neglected.

As discussed in Section 1.5, when the pressure drop Equation (10) is experimentally determined, the value of a may not be neglected. In this case those solutions obtained in Sections 2.1 and 2.2 cannot be obtained and you have to obtain solutions by an iterative method. Now the pressure drop Δp_s through multi-compartment bag filter can be expressed by following equation.

$$\Delta p_s = \Delta \tilde{p}_s u\{a+b(c\eta uT)^q\} \tag{38}$$

Also $\Delta \tilde{p}_s$ cannot be obtained by Equation (14) and has to be determined numerically by the model in another report.

The calculational result of the case when the lifetime of filter cloth is determined by cleaning numbers is shown in Figure 4 with variation of the value of a. $a = 1{,}000$ is an according value for $\Delta \tilde{p}_s au = 40$ mm H_2O when $u = 0.02$ m/sec and $\Delta \tilde{p}_s = 2$. The figure indicates some effect of neglecting a when dust concentration is small but the tendency of solution does not change. On the other hand, T_{opt} seems to be affected considerably.

3. Effect of Parameters to Optimal Solution

Since the solutions in Equations (17)~(20) are most important among those solutions obtained in Section 2, we will calculate a sensitivity of each parameter to optimal solution by using these analytical solutions.

3.1 Effect of Coefficient Parameters K_1, K_2, K_3 and $f\varepsilon/R$.

Table 1 shows the relative sensitivity of parameters (K_1+K_2) K_3 and $f\varepsilon/R$ to the optimal solution using Equations (17)~(20). Figure 5 represents the calculational results for $q_3 = 0.89$ and 0.61 by varying q. Based on the figure, the relative sensitivity to annual cost is about 0.3 from (K_1+K_2) and $f\varepsilon/R$ and is about 0.4 from K_3, and it is indicated that the annual cost is changed in a same degree with changes in each cost such as the fixed cost and power cost of fan, filter material replacing cost and the fixed cost of bag filter. T_{opt} is considerably affected by $f\varepsilon/R$ and K_3, but not affected by (K_1+K_2).

In order to show how the optimal solution is affected by improving filter material specific cost and endurance limit, the calculational results for several $f\varepsilon/R$ is shown in Figure 6. Namely, by reducing $f\varepsilon/R$, u_{opt} will be larger and $\Delta p_{s,opt}$ be small and thus it will be possible to reduce the size of system.

3.2 Effect of Operating Conditions Q and $c\eta$

The relative sensitivity of Q and $c\eta$ to optimal solution, from Equations (17)~(20), is in Table 1. Figure 7 shows the calculational results for $q_3 = 0.89$ and 0.61 by varying q. The annual cost is, according to the Figure, proportional to the 0.8 power of process gas amount for a small system and to the power of 0.9 for the big system. Also T_{opt} cannot be affected by Q and $c\eta$ except for the case of small gas flow amount ($q_3 = 0.61$). $\Delta p_{s,opt}$ is roughly proportional to $(c\eta)^{0.3}$ and u_{opt} is inversely proportional to $(c\eta)^{0.4}$. This was also shown in Figure 2.

3.3 Effect of a, b and q of Pressure Drop Characteristics Equation

The relative sensitivity of b to optimal solution obtained from Equations (17)~(20) is shown in Table 1 and Figure 7. T is not affected by b while $\Delta p_{s,opt}$ and $C_{T,min}$ are roughly proportional to $6^{0.3}$ and u_{opt} is inversely proportional to $6^{0.4}$. This is shown in Figure 8.

The effect of a to optimal solution, as already discussed in 2.3, cannot be neglected when $c\eta$ is small.

Figure 9 shows the example the effect of q. It is seen from the Figure that q has a significant effect. Thus, it is important to accurately obtain pressure drop characteristics, including a and b for determining optimal operating condition.

3.4 Effect of Cleaning Residual Rate ξ and Bag Compartment Numbers N

Since the parameter $\Delta\tilde{p}_s$ is a function of bag compartment numbers and cleaning residual rate, the effect of N and ξ to optimal solution was obtained as a parameter of $\Delta\tilde{p}_s$ and the result is shown in Tables 2 and 3.

According to Table 2 which shows changes in optimal solution when only N changes, it is noted that N does not have any effect. Especially, the annual cost can only be reduced by multi-compartment with at most 20% for $\xi = 0$ and by several percent for $\xi = 0.8$.

According to Table 3 which shows changes in optimal solution when only ξ changes, it is noted that ξ has a considerable effect. Especially, when ξ is large, it will require the annual

cost of twice as much as that of $\xi = 0$. However, T_{opt} is not affected by ξ when Q is large ($q_3 = 0.89$).

Conclusion

We have derived the equation showing that the annual cost of the bag filter consists of the fixed cost cost and power cost for the fan, the fixed cost of bag filter and filter cloth replacing cost. We assumed that the lifetime of filter cloth can be determined by cleaning times (numbers) and operating times. Since analytical solutions can be obtained when the pressure drop of filter cloth itself is neglected, the analytical solutions were obtained for various cases including the case when there are limits in operational pressure drop, filtering air velocity and dust load.

Then numerical solutions were obtained for a practical case using constant values obtained from users and manufacturers. Also relative sensitivity was calculated in order to estimate the effects of each parameter on the optimal solution.

The following are major conclusions obtained by this research:

1) The optimal operating condition is not affected by gas flow amount except for the case of small flow amount a about 1 m^3/sec. Also the annual cost is roughly proportional to gas flow amount with a power of 0.8 for a small system and with 0.9 for a large system.

2) The optimal operating condition is affected by dust concentration in process gas except for the optimal cleaning cycle. Namely the optimal operating pressure drop and the annual cost per unit flow amount increase with an increase in dust concentration, while the optimal filtering air velocity decreases in an increase in dust concentration.

3) The ratio among the fixed cost and power cost of fan, the fixed cost of bag filter and the filter cloth replacing cost in the annual cost is $1:(1/q_3):q_3$.

4) The relative sensitivity of proportional constants K_1, K_2, K_3 and $f\varepsilon/R$ of each cost to the optimal solution is about 0.3~0.4. However, the relative sensitivity of (K_1+K_2) to optimal operating pressure drop, the relative sensitivity of K_3 to the optimal filtering air velocity and the relative sensitivity of K_3 and $f\varepsilon/R$ to the optimal cleaning cycle are big and are about 0.8~1.2 in absolute value.

5) Since the pressure drop characteristic equation (Equation (10)) has a significant effect in optimal operating condition, a determination of pressure drop equation is important.

6) An increase in number of bag compartment does not change optimal operating condition. Especially the annual cost can only be reduced by multi-compartment with at most 20% for $\xi = 0$ and with a several percent for $\xi = 0.8$.

7) The effect of residual rate to the optimal operating condition is considerable and the improvement in residual rate has a significant effect in reducing annual cost.

Example Problem

Assume that the cost f of the selected filter cloth is 0.4 ten thousand yen/m^2 including manpower cost for replacement and that the allowable repeated times of cleaning operation is 20,000. Also the pressure drop equation can neglect the pressure drop at no dust load and assume $\Delta p = 50{,}000$ um ($a = 0$, $q = 1$, $b = 50{,}000$). Number of bag compartment N is 4, collection efficiency η is 100% and cleaning residual rate ξ is 0.6. When the operating condition is at the process gas amount $Q = 10$ m^3/sec and the dust concentration $c = 2$ q/m^3, determine the economically optimal filtering air velocity and operating pressure drop.

Solution

Assuming the annual operating time ε is 8,000 hr (2.88×10^7 sec), $f\varepsilon/R$ is $f\varepsilon/R = 0.4 \times (2.88 \times 10^7)/(2 \times 10^4) \fallingdotseq 600$. Using the given condition ($N = 4$, $a = 0$, $q = 1$ and $\xi = 0.6$), $\Delta\tilde{p}_s \fallingdotseq 2$ from Equation (14). Therefore $b\Delta\tilde{p}_s \fallingdotseq 10^5$. The following optimal conditions are obtained using Figure 6 or Equations (17)~(21). Also, the constants discussed early in this report were used in this calculation except those constants given in above problem.

$$\begin{cases} \Delta p_{s,opt} = 153 \text{ mm } H_2O \text{ (Maximum Operating Pressure Drop)} \\ u_{opt} = 1.0 \text{ m/min (Average Filtering Air Velocity)} \\ T_{opt} = 45 \text{ min (one cleaning cycle)} \\ \chi_{Ns,opt} = 0.23 \text{ Kg/m}^2 \text{ (Maximum Dust Load Before Cleaning)} \\ C_{T,min} = 411 \text{ ten thousand yen/yr (Annual Total Cost)} \end{cases}$$

Based on these values, the lifetime of filter cloth θ/ε is $\theta/\varepsilon = RT_{opt}/\varepsilon \fallingdotseq 1.9$ year and the filtering area S is

$$S = Q/u_{opt} = 600 \text{ m}^2.$$

NOMENCLATURE

a,b,q = constants used in Eq. (10)

C_1 = fixed cost of fan, including maintenance cost [10^4 YEN/year]

C_2 = electrical cost of fan per a year [10^4 YEN/year]

C_3 = fixed cost of bag filter, including maintenance cost except C_4) [10^4 YEN/year]

C_4 = renewal cost of filter cloth per a year [10^4 YEN/year]

C_T = total cost per year [10^4 YEN/year]

c = dust concentration at inlet [kg/m^3]

e = electric power rate [10^4 YEN/kW·hr]

f = price of cloth [10^4 YEN/m^2]

h_1,k_1,K_1 = constants used in Eqs. (1) and (3)

h_2,K_2 = constants used in Eqs. (2) and (5)

h_3,K_3,k_3, q_3 = constants used in Eq. (6)

m = dust load on bag filter [kg/m^2]

N = number of compartments [—]

P = power of fan [kW]

Δp = pressure drop [mmAq]

Δp_s = pressure drop across bag filter [mmAq]

$\Delta \tilde{p}_s$ = dimensionless pressure drop defined in our previous paper [—]

Q = gas flow rate [m^3/sec]

R = allowable repeated times of cleaning operation [—]

S = filtering area of bag filter [m^2]

T = total period of cleaning cycle [sec]

u = average filtering velocity (=Q/s) [m/sec]

χ_{Ns} = maximum dust load on bag through all compartments [kg/m^2]

Y	= cost of equipment	[10^4 YEN]
α	= parameter defined by Eq. (21)	[—]
ε	= operating time for a year	[sec/year]
η	= collection efficiency	[—]
θ	= lifetime of filter cloth	[sec]
θ_0	= allowable duration time of filter cloth	[sec]
τ	= dimensionless partial period of cleaning operation defined in our previous paper	[—]
ξ	= residue fraction of dust load after cleaning	[—]

<Scripts>

min	= minimum
opt	= optimal condition
$\bar{}$, $\_$	= upper or lower value

PERFORMANCE OF A MICRO-CYCLONE*

Koichi Iinoya**, Aishi Nakai***

1. Introduction

The cyclone, having a simple configuration and low installation cost, has been widely used in various fields but has a disadvantage of low efficiency. It is also not known how much the collection efficiency can be improved by significantly reducing the size of cyclone. Although it is believed that greatly reducing its size is unrealistic, the measurement of the micro-cyclone performance, which we have designed, has given interesting results.

2. Experimental Apparatus and Method

Figure 1 shows the size and the concept of the cyclone and Figure 2 shows a flow sheet of the experimental apparatus. The sample aerosol is produced by generating stearic acid particles through the Sinclair-Lamer type monodisperse particle generator and by mixing them well with clean air (about 10 l/min) in a mixing chamber. The aerosol is sent to the cyclone entrance through the high concentration side of dust concentration meter, and passes through the low concentration side of dust concentration meter, filter paper and glass orifice by the action of the vacuum pump. The dust concentration meter (indicator) used in this experiment is the relative concentration indicator (Shibata Chemical Instrument Industry Co.) using light scattering. The glass orifice was monitored by the wet test gas meter. The milipore-filter was used to protect the orifice and vacuum pump. The pressure drop across the cyclone was measured by a water or mercury manometer.

3. Experimental Result and Consideration

3.1 Pressure Drop

The pressure drop across the cyclone can usually be expressed as a function of cyclone inlet velocity.

---

* Report received on 1/21/69.

** Regular member, Department of Engineering, Kyoto University, Yoshida Honmachi, Sakyoku, Kyotoshi.

*** Research Institute for Production Department, Morimotocho, Shimogamo, Sakyoku, Kyoto.

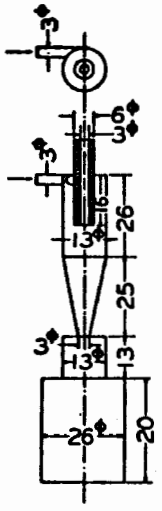

Fig. 1. A micro-cyclone.

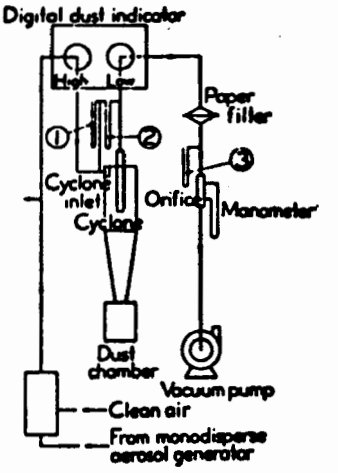

① Manometer for absolute pressure
② Manometer for pressure drop
③ Manometer for absolute pressure

Fig. 2. Flow sheet of experimental apparatus.

$$\Delta p = F \times \frac{1}{2g}\gamma U_i^2 \qquad (1)$$

In this case, the cyclone is used on the suction side of vacuum pump (namely, with negative pressure) and the inside of the cyclone is under a considerable low pressure as compared to ambient pressure. Therefore, the measured pressure drop Δpm is actually the apparent pressure drop and it is desirable to correct the specific weight of gas at inlet (γ) to a standard condition. This correction can be done by the following equation.

$$\Delta p_s = \Delta p_m \frac{\gamma s}{\gamma} = \Delta p_m \frac{P_s T}{P T_s} \qquad (2)$$

As shown in Figure 3, the relationship between the measured Δp_m and U_i is that Δp_m is not proportional to the square of U_i as indicated in equation (4). But Δp_s which is corrected by equation (2) is proportional to the square of U_i. If this correction is made for the case when the cyclone is used in a considerable range of pressure, it will be seen that the pressure drop is proportional to the square of inlet velocity. On the other hand, there have been many simple equations reported to estimate the pressure drop coefficient F from the configuration of cyclone, and when F is calculated by using the typical Iinoya and First's Equation, the value of pressure drop coefficient $F_s = 20.5$. Also the Reynolds number Re_i at cyclone inlet is about 10^3~10^4 which is the range of turbulent flow.

3.2 Collection Efficiency

Figure 4 shows the relationship between inlet velocity U_i and collection efficiency η as a parameter of particle size using the experimental results. Based on this, it is indicated that the ordinary cyclone inlet velocity (about 20 m/sec) with a smaller cyclone will lead to about 90% of collection efficiency for about 1 μ dust particles ($P_p = 1.0$ g/cm^3) and that the high velocity (50 m/sec) will even lead to 90% of collection efficiency for 0.25 μ dust particles without having an efficiency reduction for the high velocity. Therefore, if many small cyclones can be designed to operate in parallel, it is possible to have a high efficiency multi-clone.

On the other hand, only the inertia force has been considered to be the controlling factor in the collection mechanism of the cyclone. But when the collection efficiency η of this experiment was plotted as a function of inertia parameter

$$\Psi = \frac{P_p U_i D_p^2 C_m}{18 \mu D},$$

it will give a different curve for a different particle size. When η is plotted as a function of $\Psi/(D_p/D)$ or Ψ/N_{sc}, it gives a

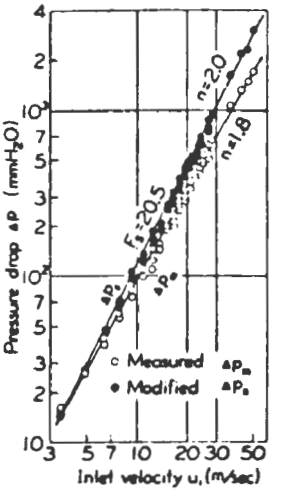

Fig. 3. Relation between inlet velocity u_i and pressure drop Δp.

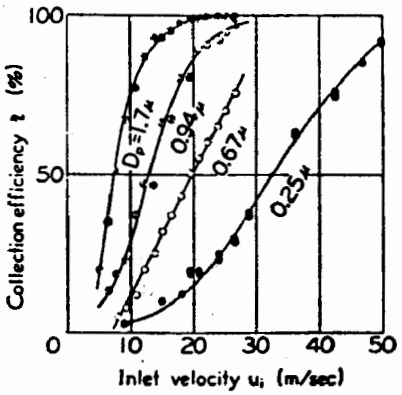

Fig. 4. Relation between inlet velocity and collection efficiency.

single curve. When it is plotted on a log-log paper, one linear graph is obtained as shown in Figure 5. In this case the effect of particle concentration may be considered as another factor and it may be necessary to consider the particle diffusion phenomena as one of the collection mechanisms. This is considered to be a question in the collection mechanism of cyclone.

4. Conclusion

As a result of measuring the performance of sample micro-cyclone, the following conclusions were obtained.

1) It was confirmed that the pressure drop is accurately proportional to the square of inlet velocity, by an appropriate correction, even when the cyclone is used over a considerable large pressure range.

2) Even submicron particles can be collected with a considerably high efficiency for an extremely small cyclone and a high velocity.

3) Although it was believed that the inertia force was the only controlling factor in the collection mechanism of cyclone, it was recognized that the effect of particle size also needs to be considered.

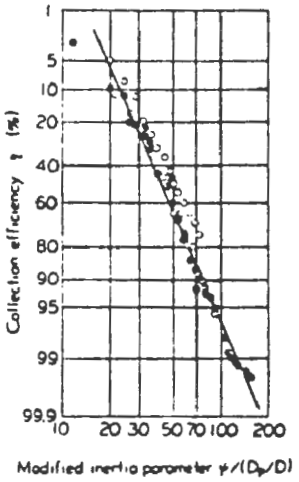

Fig. 5. η and $\Psi/(D_p/D)$ (log-normal distribution).

International Seminar on
Dust Collection

I Date and Time

May 24 (Tuesday) 1977, 1.00p.m. - 7.00p.m.

II Place

Kyoto International Conference Hall
Takaragaike, Sakyo-ku, Kyoto, Japan 606
Phone: 075-791-3111

III Lectures 13.00 - 15.30

1. Introduction K. Iinoya, Professor, Kyoto University
2. Concept of Research in Particle Gas Separation
   F. Löffler, Professor Institut für Mechanische Verfahrenstechnik der Universität Karlsruhe, Richard-Willstätter-Allee, 7500 Kerlsruhe, 1, Germany 434
3. New Ideas in Electrostatic Precipitation Technology
   E.C.Potter, Leader
   Process Chemistry Section, Division of Process Technology Minerals Research Laboratories, Commonwealth Scientific and Industrial Research Organization, Australia, P.O.Box 136, Delhi Road North Ryde, N.S.W. Australia, 2113,
4. Current Research on Particle Removal at the Harvard Air Cleaning Laboratory
   M. First, Professor, Department of Environmental Health Sciences, School of Public Health, Harvard University, 665 Huntington Avenue, Boston Massachusetts 02115, U. S. A. 452
5. Size-Selective Aerosol Collection with Centrifuges,
   W. Stöber, Professor, Institut für Aero Biologie, 5948 Schmallenberg-Grafshaft, Germany

IV Coffee Break 15.30 - 16.00

V Discussion 16.00 - 17.00

Chairman, S. Masuda, Professor Tokyo University

Co-chairman, T. Yoshida, Professor Osaka Prefectural University

VI Party with International Communications
17.30 - 19.00

Organizer, K. Iinoya, Department of Chemical Engineering
Kyoto University, Sakyo-ku, Kyoto, 606 Japan
Phone: 075-751-2111 ext. 5566 (5586, 5576)

Concept of Research in Particle-Gas-Separation

Prof.Dr.-Ing.F.Löffler

Institut für Mechanische Verfahrenstechnik der Universität Karlsruhe

Particle-Gas-Separation is considered as one of the important unit operations of "Mechanische Verfahrenstechnik" (Process technology). Apart from its technical significance it plays an important role in general and political interest.

We are working since many years on the problems of separation of particles (solid particles or liquid drops) from gases at the Institute founded in the year 1957 by Prof. Dr.-Ing. Hans Rumpf who unfortunately passed away a few months ago.

A section for dust collection and cleaning of air has been in existence since 1965.

Research and development works are not pursued having only environmental pollution control in view, but also in view of material recovery within the processes of production.

We are at present working on the following separating principles: Centrifugal separator (cyclone), wet scrubber and fibre filter. Besides this, some general topics from other fields other than dust collection are also considered; for instance, dust feeding and desagglomeration of fine dust particles in gases, or agglomeration and deposition on the walls under the consideration of the effect of electrostatic charges. The works done in the measuring technique group will also be counted along with these themes.

On the one hand, basic studies are being done in these fields with an object of explaining the processes by a detailed study of single phenomena and also to see if they can lead to reliable methods for design, or to imporved or new techniques. On the other hand, problems in practice in direct collaboration with the industry are also treated. A brief illustration regarding a few problems are given below and as far as possible with representation of typical results.

Centrifugal separators - also called as cyclones - are simple in construction, cheap and sturdy. They have become more popular as they are reliable and safe to operate. But still the quota of cyclones in the total turnover (1974) for dust collectors was 15 % that corresponds to a higher part of flow rate because of the low investing costs of cyclones.

Problems lie in the proper design and in recognizing the possible range of application. The particles are separated by the centrifugal force acting in a rotating flow. In the apparatus looking simple outwardly a very complicated, three dimensional, turbulent rotational flow predominates which evades an exact calculation. This holds even more when one considers the effect of material on the flow.

Pressure drop, the collection efficiency and preferably the grade efficiency curve are to be determined as characteristic parameters for each of the separators. The grade efficiency curve gives the collection efficiency in terms of particle size.

Simplified models of flow field have to be used provided one does not forego a calculation from the beginning and counts only on the pragmatic value, and also realizes the importance of calculation possibilities for the design especially, the optimization of the set up.

This was done by Rumpf and his co-workers |1| for flow without dust. The object of the investigation that is running at present is to verify such models experimentally. In particular the applicability on dust loaded flows is verified. This is possible by measuring the loss in the moment of momentum at different parts of the surface of the cyclone to obtain the wall coefficient of friction in terms of operating parameters, the particle size distribution, dust load and rate of air flow.

Measurements of velocity in cyclone and the determination of the grade efficiency curve will also be added to this. The works on the very complicated experimental set up are in operation and results will be reported in the near future.

Studies on a high efficient cyclone for the separation of fine graphite particles from a gas flow is mentioned as an example for a problem in practice. The object was to obtain a separating curve as fine as possible.

In figure (1) the degree of separation T(x) is plotted against particle size. $\dot{V}$, the volume flow rate is the parameter. The curves show the typical behaviour for cyclones. As usual the cut size is defined as those particle sizes from which 50 % are separated. The figure shows that a cut size of about 2 µm was obtained. However, it was hardly possible to remain still under this value, although the theoretically predicted values were below 1 µm. This experience, on one hand, points out the necessity of demarcation of experiments from the theoretical models and on the other hand shows an important effect of turbulence on the separation. Turbulence acts against separation particularly

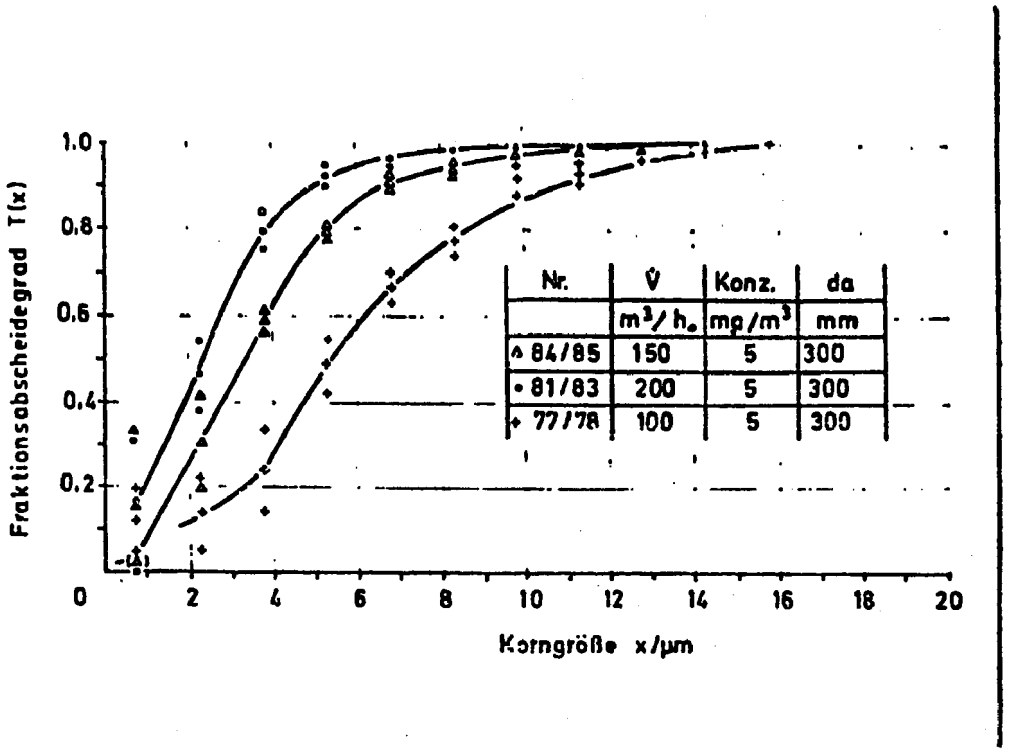

Fig. (1): Grade efficiency curve of a cyclone for graphite dust

in the range below 5 µm. The object of the basic investigation is to explain this effect in more detail.

Wet scrubbers count today 30 % to the sales of dust collectors. In these equipments the particles are separated by means of mixing a washing fluid with the gas flow. In doing so the dust particles are caught by the fluid, get bound there and are separated together with the fluid. In addition to the separation of particles, an absorption of gases by this washing fluid at the same time can possibly take place in these scrubbers. But in the following section only the particle separation has been discussed

The physical underlying principles of the resulting processes are still not explained extensively. In particular, not much is known about the capture process and thereby occuring interaction between particles and liquid. Therefore, till now the predetermination of scrubbers is often regarded as uncertain and impossible.

This condition is not only unsatisfactory scientifically, but is also disadvantageous with respect to the design of collectors in practice; moreover, the calculation of optimization cannot be made. Our object, therefore, is to explain the physical fundamental phenomena so that we could arrive at the equations of design.

The investigations take place in three stages: Single drop processes, behaviour of drop swarms, effect of collectors.

Till now we were dealing with the experimental work particularly about the production of drops with the specified size and velocity, and intensively with the measurement of drop size distribution by different methods as well. The chosen range of drop size ranges from some hundreds of μm till about 0.5 μm.

Theoretical collection efficiency calculations for single drops were verified experimentally by suspending the drop on a 5 μm diameter wire and photographing the paths of the dust particles with the help of a high speed camera (till 32000 pictures/sec.). It could be observed directly that all the impinged dust particles on the drop could not be retained there, some of them were rebounding.

Experimental results of the studies made on a scrubber, designed together with Prof. Leschonski, Institut für Mechanische Verfahrenstechnik, Technische Universität Clausthal, agreed with the theoretically predicted high collection efficiencies.

Fibre filters are employed in the technology in two basic forms. In the case of deep bed filters the separation takes place within the fibre layer that has passed through the flow. After a particular dust embedment, that is, when a predetermined pressure drop has reached the filters are extended and are thrown away frequently. Some types can be cleaned by washing or by blowing out. This filter, therefore, can be used mainly in the case of low dust contents up to a few mg/cm^3, so in the ventilation system for laboratories, production plants, (clean rooms) or operation rooms.

The second type of filters are the surface or cleanable filters. Here the separation takes place mainly on the surface of the filter cloth. A dust layer (filter cake) will be build up which separates effectively. Because of the raise in the flow resistance this dust layer which occurs periodically during the operation by different methods has to be removed frequently. This filter can be employed in the case of high dust content (up to a few hundreds of g/cm^3) and also in the branch of industrial dust collection or in production recovery. There, it has been proved as the most efficient fine dust collector.

Deep bed filters are highly porous filters in which the part of fibre volume amounts to less than 1 % and seldom more than 5 %. The spacing of fibres are big compared with that of particle size. Therefore the particles are not separated by sieving, but they will have to be brought to the fibre surface by different transportation methods and then must be retained there. The collection efficiency is, therefore, a product of degree of impingement and probability of adhesion.

We are trying to explain the transport and adhesion phenomena by our studies and investigations using single fibre, fibre grids as model filters and also on technical filters. At present we are concentrating on the particle size range say above 0.5 - 1 µm and flow velocities from say 10 cm/sec. onwards, and in this range the Brownian movement of the particle can be neglected. Forces of gravity, inertia and electrostatic forces are at the disposal of transport phenomena.

Muhr |2,3| in his theoretical and experimental studies, was able to point out the important significance of electrostatic charging, in particular for the separation of particles below say 3 µm and he could describe this quantitatively.

Fig. (2) shows some curves of an exar ple where single fibre collection efficiencies φ , that were calculated back from the measured values for the total model filter are plotted against the so called inertia parameter ψ. In this representation the

Reynolds Number calculated using fibre diameter and free flow velocity is the parameter. For comparison two theoretical curves are drawn where electrostatic forces are not taken into account. We can see that in the range $\psi < 1$ the measured collection efficiencies are much higher than the predicted theoretical ones for the particles and fibres that are free of charge. These high values can be accounted for with an explanation that the particles as well as the fibres are charged and therefore the Coulomb-forces had an effect.

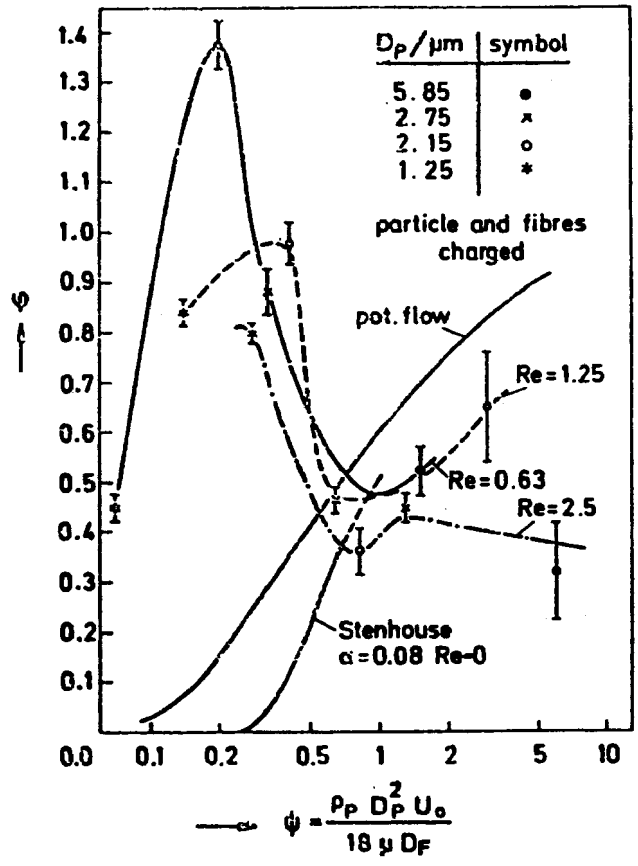

Fig. (2): Collection of NaCl-particles in model filters

This was proved by the measurements of charge as well as by the experiments with discharged particles and fibres, and was also established by the theoretical model calculations.

In addition to this it can be seen in fig. (2) that at the increasing particle size and/or increasing velocity the collection efficiencies were lower than the predicted theoretical ones -

this in particular can be clearly seen on the curve for Re = 2.5. This, as we already know from our experience in practice and from other investigations, would lead to the ovservation that the particles bigger than 3 µm do not positively adhere to the fibre surface so that the probability of adhesion is less than 100 %.

If the particle has to remain adhere, firstly it should not rebound and secondly it should not be detacted subsequently.

In order to explain the second stipulation we made a detailed study on adhesive force some time ago and found out that when once the separated particle adheres it can be hardly detached |4|.

In one of the works that has been completed recently, resistance and buoyancy forces exerted by a flow on the sphere-shaped particle deposited at a surface have been determined |5|. The results of this investigation are not just restricted to the filter problem, but is can be, for instance, applied to the wall depositon in pipes and machines.

Measurements on filter and adhesive forces showed clearly that the rebound action is very decisive. We, therefore, developed an equipment with which we could study the impact process on a single fibre photographically. The films could be evaluated quantitatively. An example of such a result is shown in fig. (3).

In this figure flow velocity v is plotted against probability of adhesion h, where h is defined as the ratio of the number of adhering particles at the first impingement to the total number of impinging particles. Experimental parameters were particle type, its size and fibre type.

Particles begin to rebound obviously at velocities between 5 and 15 cm/sec. Probability of adhesion decreases quickly with the increasing velocity and reaches below 10 % at 1 m/sec for 10 µm-particles. 5 µm-particles rebound more than 10 µm-particles.

Round glass spheres rebound more vigorously than the irregularly shaped quartz particles which is obviously an effect of geometry. Quartz particles can have multi-point contact or surface contact whereas glass spheres can have only single-point contact.

Studies on solid wax particles and oil drops of sizes from 5 to 10 µm showed surprisingly that partly these particles also show elastic behaviour and rebound likewise in the velocity range shown here. These investigations will be continued.

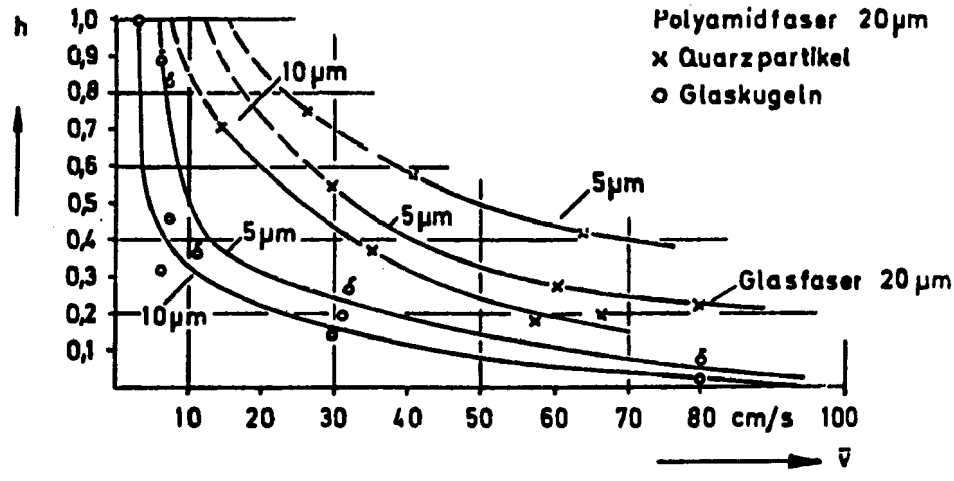

Fig. (3): Probability of adhesion of rigid particles on a polyamide-fibre

In addition to the studies on single fibres and fibre grids, we are making some studies on the separating behaviour of commercial filter media for different types of particles in a filter testing apparatus. At present the separation of clouds (oil clouds, fat droplets) carries and special weight.

In the branch of cleanable filter, an experimental set up is being arranged with an object of studying the cleaning behaviour of filter bags. As already mentioned, the pressure drop raises with increasing dust deposition and at the same time the collection efficiency becomes better. Now when it is cleaned the collection effciency also falls down |6|. Hence, in this work which is very close to the conditions in practice optimum cleaning conditions are investigated for filter bags in technical dimensions.

Dosage and dispersion of solids are not only important for sciencitfic studies, but also from the technology point of view they have a significance. Here the difficulties arise especially when the particle size is less than 10 µm, as the adhesive forces for these particles are bigger than their own weight by a few orders in magnitude. Therefore, these particles have a characteristic tendency for agglomeration and adherence.

Since the dust feeders available in the market or the ones displayed in the publications do not function satisfactorily in the range below 10 µm, we developed a device for dust feeder whose schematic representation is shown in fig. (4).

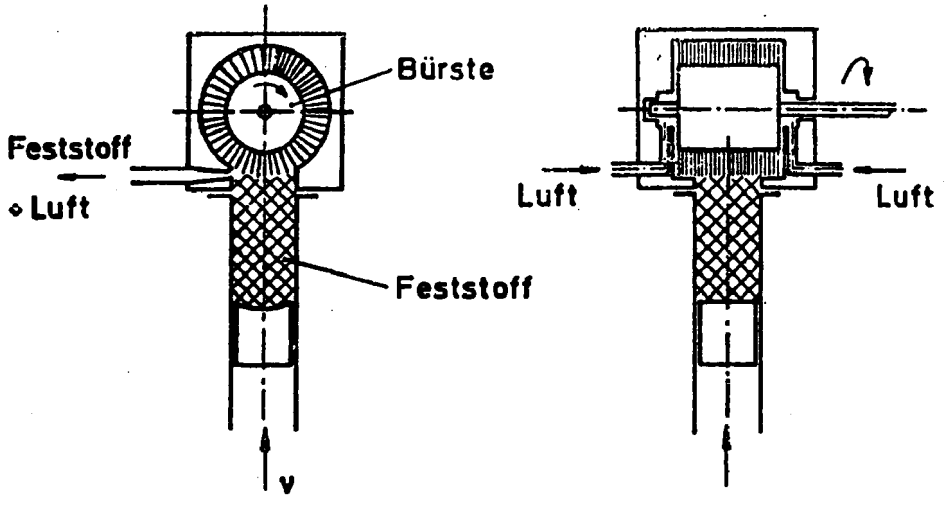

Fig. (4): Schematical diagram of the dust feeder

Solid is carried away by a rotating brush and a jet of air by the surface of the packing. A piston takes care of the dust supply. Using this principle mass flows in different quantities between 0.01 and 6000 g/h with higher stability can be produced |7|.

Investigations on the conditions for desagglomeration using forces of flow or wall impact |8| on a baffle plate showed that the agglomerates could be effectively desagglomerated from the primary particles of 2 µm on a baffle plate at velocities of 200 m/sec, whereas this was possible without a baffle plate only up to the primary particles of 5 µm. The required jet velocity decreases with the increasing particle size.

In the measuring technique branch of our studies we emphasize on the optical methods that are suitable for the determination of the distributions of particle concentration, particle size and velocity, and also on the visuadization of the movement of flow and particles. Partly it is also to investigate the applicability and the limit of error of the known methods and if the necessity arises to adapt them to our problems. Partly some methods and instruments are also developed up to commercial specification. This often contains the clarification of basic mechanisms.

Studies were made and are still being made on the following methods individually:

- Photometric determination of concentration in particle deposits and in flowing gases |9|;
- Particle size determination using scattered light techniques |10|;
- Measurement of flow velocities according to spark-tracing method |11|;
- Particle velocity measurement according to Laser-Doppler method;
- Determination of the paths and velocities of the particles using high speed photography ;
- Determination of particle concentration, size and velocity using impulse holography.

Some hints with regard to only two of these methods are given.

The method of photometric determination of concentration is employed technically, say for dust deposition in a standard filter test technique and for the emission control of slacks. The well known Lambert-Beer law is the basis for this method. Difficulties always arise when the concentration and particle size distribution change simultaneously, and if these changes are uncontrollable which, for example is often the case in brown coal-power plants. With this the basis of calibration also changes. A highly uncertain inference on the dust content is bound to be drawn in case of not carrying out additional experimental runs. This was verified by our experiments.

Some special advancement has been made with regard to the development and application of scattering light method for the determination of particle size distribution. This method can be used directly in the flow to make a very quick measurement of the local size distribution of particles larger than 0.3 µm and concentrations up to 10^6 particles/cm^3, and this is possible without the particles are being separated. The particle size distribution is obtained by measuring and analysing the impulse of the scattering light which are produced by single particles while passing through a small and pure optically circumscribed measuring volume in flow field. The theory of Mie is the basis for this which is about the scattering of light on spherical homogeneous particles. The special feature of this method (apart from the fact that the distribution state of the particle is not disturbed) is that the particle distribution can be seen at high measuring velocity. Depending upon the concentration and velocity nearly 100 000 particles per minute can be counted and measured. Very often it is sufficient to count small quantities of particles for the analysis of the processes so that the measuring times could lie in the range of 10 sec. The evaluation and graphical representation of the measurement can be done very quickly as the processing of the impulse can be done with the help of a calculator and also electronically.

Typical examples of application are the investigation of dispersion and desagglomeration processes, of dust injectors, the determination of drop size distributions of atomizer nozzles.

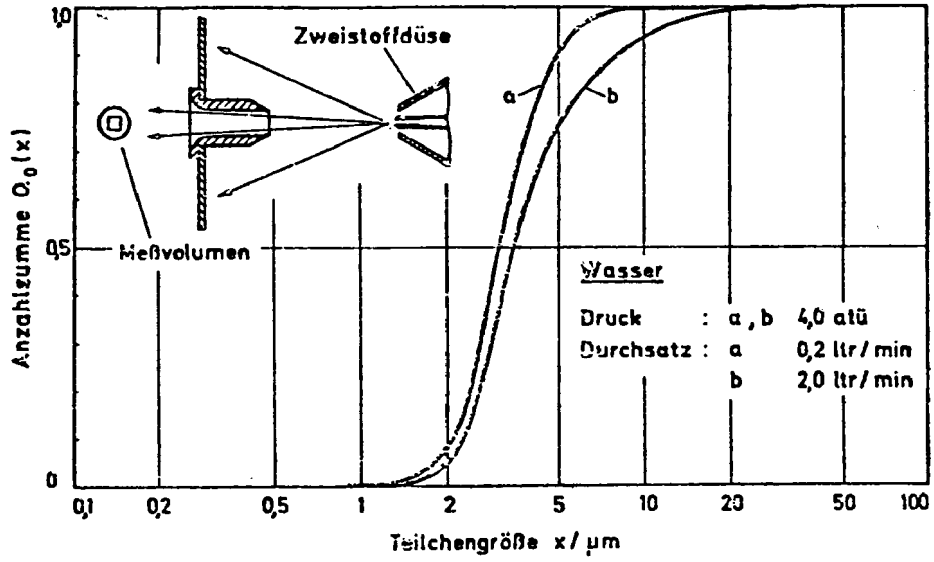

Fig. (5): Drop size distribution of an atomizer nozzle

The cumulative number distributions of water drops that are produced in an atomizer nozzle is shown as an example in fig. (5). The rate of flow of water was varied in this experiment. In the above figure the measuring arrangement is sketched on the left.

If the number distributions represented here will be calculated in terms of volume distribution a more clear difference can be seen than that of shown in fig. (5). Quick evaporation of the drops is a problem in the measurement of distribution of drops. Hence an immediate measurement is absolutely necessary and this is possible with scattering light equipment.

Only a few examples are mentioned here from the numerous application possibilities of this method. On the other hand, it should be mentioned that more investigation is to be done for answering some basic questions like for example, the effect of particle shape. Some efforts regarding the further technical developments are performed.

Nevertheless, with the already available equipment at the moment, grade efficiency curves of the dust collectors down to 0.3 µm can be obtained quickly and reliably. This was not the case till now since in the previous methods and above all in the range below 5 µm, uncontrollable changes because of agglomeration and other processes had to be accepted.

Studies in this particle size range are necessary considering today's high demand for fine dust separation.

References

|1| Rumpf, H., K.Borho, H.Reichert:
Optimale Dimensionierung von Zyklonen mit Hilfe vereinfachender Modellrechnungen.
Chemie-Ing.-Technik 40 (1968) 1072-1082

|2| Muhr, W.:
Theoretische und experimentelle Untersuchung der Partikelabscheidung in Faserfiltern durch Feld- und Trägheitskräfte.
Dissertation Universität Karlsruhe, 1976

|3| Muhr, W., F.Löffler:
Abscheideverhalten von Faserfiltern bei elektrostatischer Aufladung.
Maschinenmarkt 82 (;976) 669-672

|4| Löffler, F.:
Über die Haftung von Staubteilchen an Faser- und Teilchenoberflächen.
Staub - Reinhaltung der Luft 28 (1968) 456-462

|5| Rubin, G., F.Löffler:
Widerstands- und Auftriebsbeiwerte von kugelförmigen Partikeln in laminaren Grenzschichten
Chemie-Ing.-Technik 48 (1976) 563

|6| Löffler, F.:
Abscheidegrad und Druckverlust von Filterstoffen verschiedener Struktur bei unterschiedlichen Bedingungen.
Staub - Reinhaltung der Luft 30 (1970) 518-522

|7| Zahradnicek, A., F.Löffler:
Eine neue Dosiervorrichtung zur Erzeugung von Aerosolen aus vorgegebenen feinkörnigen Feststoffen.
Staub - Reinhaltung der Luft 36 (1976) H. 11

|8| Zahradnicek, A.:
Untersuchung zur Dispergierung von Quarz- und Kalksteinfraktionen im Korngrößenbereich 0.5 - 10 µm in strömenden Gasen.
Dissertation Universität Karlsruhe, 1976

|9| Umhauer, H., F.Löffler:
Einfluß der Partikelgrößenverteilung bei der fotometrischen Bestimmung der Konzentration industrieller Stäube in Gas-Feststoff-Strömungen
1. Europäisches Symposium "Partikelmeßtechnik", Nürnberg, 17. - 19. September 1975, hrsg. von Prof.Dr.-Ing.H.Rumpf, Karlsruhe und Prof.Dr.-Ing.K.Leschonski, Clausthal, in Zusammenarbeit mit der DECHEMA

|10| Umhauer, H.:
Ermittlung von Partikelgrößenverteilung in Aerosolströmungen hoher Konzentration mit Hilfe einer Streulichtmeßeinrichtung
CIT 47 (1975) 7, 297

|11| Bernotat, S., H.Umhauer:
Applications of spark tracing-method tc flow measurements in an air classivier
Opto-electronics 5 (1973), 107/118

|12| Löffler, F., H.Umhauer:
Eine optische Methode zur Bestimmung der Teilchenabscheidung in Filterfasern
Staub - Reinhaltung der Luft 31 (1971) 2, 51/55

In the previous report the works done at the "Institut für Mechanische Verfahrenstechnik" in the field of dust collection and its measuring techniques were described.

The great interest of the public in the field of environmental protection led to a plenty of research projects in industry and research Institutes. A review about these projects given in "Umweltforschungskatalog 1976" which contains about 1300 poges may not be complete, but it is impressiv and informativ. Publisher: Umweltbundesamt, Berlin. Many projects have been dealt with special processes of production.

A list of the names of some research workers and Institutes which is certainly not complete is given below.

It is emphasized that the names given in the list are purely incidental and are in no way in order of importance of the works.

Prof.F.Mayinger, Institut für Verfahrenstechnik, Universität Hannover,
(Ventury scrubbers-studying, atomization and energy-dissipation in the venturi-throat)

Lit.: F.Mayinger, W.Neumann, DECHEMA-Monographien Nr. 1639-1669, Band 80, Teil 2, Seite 637

Prof.E.Weber, Institut für Mechanische Verfahrenstechnik, Universität Essen
(Wet scrubbing with emphasis to absorption of gases, distribution of dust concentration in elektrostatic precipitators etc.)

Prof.R.Quack, Institut für Verfahrenstechnik, Universität Stuttgart
(Electrostatic precipitation)

Staubforschungsinstitut Bonn, Direktor Dr.A.Schütz
(Testing of HEPA-Filters, development of dust measuring equipment etc.)

Dr.Schikarski, Kernforschungszentrum Karlsruhe
(Deep bed filtration in sand filters)

Prof.Stöber, Institut für Aerobiologie der Fraunhofer-Gesellschaft, Grafschaft
(Different projects on air pollution control and measurement)

Techn.Hochschule Leuna-Merseburg (DDR), Sektion Verfahrenstechnik, Prof.Jugel
(Fibre Filtration with emphasis on bag filters)

Dr.Stenhouse, Dep. of Chemical Engineering, University of Loughborough
(Deep bed fibre filters, adhesion probability, i.e. similar work as we are doing)

Prof.Papai, Institut für Strömungsmaschinen, Technische Universität Budapest, Ungarn
(Big technical bag filters)

Dr.Benarie, IRCHA, Frankreich
(Different works on different subjects)

Prof.Dr.K.Leschonski, Institut für Mechanische Verfahrenstechnik, Techn.Universität Clausthal-Zellerfeld
(On-line measurement of particle size distribution)

Dr.J.Gebhart, Gesellschaft für Strahlen- und Umweltforschung, Paul-Ehrlich-Str. 20, 6 Frankfurt/Main
(measurement of particle concentration and size distribution)

CURRENT RESEARCH ON PARTICLE REMOVAL AT THE HARVARD AIR CLEANING LABORATORY,

Melvin W. First

1. Fabric Filters

Our current fabric filter research program has three major objectives: (1) Basic mechanisms of cake formation for a full range of filtration velocity, pressure drop across the cake, and dust characteristics that are typical of industrial fabric filter applications. Filter cakes have been fixed in place by infusions of a liquid plastic monomer and, after polymerization, the rigid cakes may be sectioned, polished, and examined under the scanning electron microscope to quantify the internal geometry of the cake and relate this to the principal filtration parameters. (2) Retention and penetration characteristics of full-scale pulse jet cleaned felted filter bags. Dust penetration has been found to occur by straight through passage, by seepage, and by pinhole plug losses from the formed cake. These several penetration mechanisms have been quantified in relation to filtration velocity, particle size, and the period in the cycle since the last cleaning pulse and it has been found that different dust penetration mechanisms predominate at different periods during the cycle. (3) Decreasing filter size by increasing filtration velocity through the fabric. Higher filtration velocities reduce equipment cost but result in increased filter resistance and dust penetration in conventionally constructed units. Substantially higher velocities with low dust penetration depend upon the development of inproved cake removal methods that are gentler and more efficient.

2. Incinerator Off-Gas Cleaning

Interest in hot gas filtration by moving granular beds is being studied in our laboratory because it has several applications to nuclear waste treatment. For conventional incineration of combustible materials contaminated with low levels of radioactivity, particle size will be relatively large and removal will be principally by inertia; favoring high filtration velocities. The temperature resistance and cleanability of mineral or ceramic granules make them attractive for this service. Efficiency may be regulated by selection of granule sizes, thickness of the bed, and filtration velocity. Application of moving granular beds for vitrification of high level wastes in preparation for storage is a more complex application because of the very high temperatures generated (825°C) and the very small size of particles formed by vaporization and subsequent condensation. Investigations are underway to employ a moving granular bed as a cooler as well as a filter and, in the process, utilize the strong thermophoretic particle separating forces that can be generated inside a bed of cool granules when a hot gas passes through it.

Research Activities on

Dust Collection

Study on the moving behaviour of dust particles in a precipitator by laser Doppler velocimeter

Research Institute of Applied Electricity, Hokkaido University
Sapporo, Hokkaido

Professor	Toshimitsu Asakura
Assistant professor	Hiromichi Mishina
Research Associate	Yasushi Kawase
Research Associate	Yoshio Shindo

(1) Construction of laser Doppler velocimeter for measurements of the moving velocity of dust particles in a precipitator

A laser Doppler velocimeter with high spatial resolution and high accuracy has been constructed to measure the moving velocity of dust particles in a precipitator. To achieve the high sampling rate, the period-measuring system is used for obtaining the velocity data from the laser Doppler velocimeter which are directly transferred to a minicomputer and are analyzed. A new analyzing system is being developed for measuring the particle size of dust particles together with their moving velocity.

(2) Velocity measurement of dust particles moving in an electric precipitator

The moving velocity of dusts in an electric precipitator is measured in detail by using the laser Doppler velocimeter. The experimental results show that the thickness of the boundary layer near the collection electrodes in the precipitator decreases with the decrease of a supplying voltage between the electrodes. Accurate measurements of the moving direction of dusts have been performed in the whole space of the precipitator. The present experimental study may give the useful information for the collection efficiency of the precipitator.

1) Department of Electrical Engineering University of Tokyo

2) Senichi Masuda, Professor

Kensuke Akutsu, Assistant

4) Electrostatic Precipitation of Aerosol Particles inside an Electron Beam Irradiated Field

5) SO_x and NO_x pollutants are rapidly converted into aerosol particles by the irradiation of high energy electron beam. These particles can be effectively removed by an electric field formed inside the irradiation space. The distributions of positive and negative ion concentrations, field intensity, particle charge and particle migration velocity were calculated. As a result, the theoretical possibility of particle collection was advanced. Experiments, using $CaCO_3$ powder and the aerosol particles produced from SO_2 pollutant by electron beam irradiation, confirmed the high collection performance of this method. Also the desulfuration or denitration rate seemed to be enhanced by simultaneous field application.

DEPARTMENT OF CHEMICAL ENGINEERING
THE FACULTY OF ENGINEERING
UNIVERSITY OF TOKYO
BUNKYO-KU, TOKYO, JAPAN

1. Department of Chemical Engineering, University of Tokyo
2. Akira Suganuma (Associate Professor)
3. Research and Development of Dust Cloud Generator
   - 3-1: measurement of aerodynamic particle size distribution of agglomerated airborne dust
   - 3-2: dispersion of agglomerated fine powder by high speed air stream
   - 3-3: development of dust cloud generator for testing dust collectors

[1] Nagoya University, Department of Chemical Engineering,
(Furocho, Chikusa-ku, Nagoya, 464)

[2] GENJI JIMBO, Professor.
RYOHEI YAMAZAKI Assistant
JUN-ICHIRO TSUBAKI Assistant

[3] * Measurement of adhesion force of powder particles.

The adhesion force of powder particles is measured by several methods including centrifugal separation method, vibration separation method, split cell method and fluidized bed method. These results are compared, and the cause of very big difference between these measured values is investigated.

* Measurement of deagglomeration phenomenon of agglomerated powders in air stream.

The size reduction phenomenon of agglomerated powder particles is measured by pulverizing these particles in negative acceleration field of air stream. The results obtained are investigated with the data of adhesion force of powders.

* Dislodging mechanism of particle layer collected on fabric filter.

The structure of particle layer on a fabric filter is investigated, and the size distribution of agglomerated powders dislodged from a fabric filter is also measured.

1. Daido Institute of Technology

2. Yasunori MIYOSHI (Professor)

3. Researches on corona discharge characteristics in various types of gap geometries and approach to improvement of Electrostatic-Precipitator Design

   i Discharge characteristics and discharge regions of negative point-to-plane gap in air.

   ii Onset of coronas.

   iii Transition from negative corona to spark.

   iv Sparkover characteristics of negative point-to-plane gap with a minor auxiliary discharge on the plane.

SUZUKA COLLEGE OF TECHNOLOGY
SHIROKO-CHO, SUZUKA-SHI, MIE-KEN, JAPAN

(1) Norio KIMURA, Professor

(2) Suzuka College of Technology,
Department of Industrial Chemistry

(3) Research subject:

High temperature gas filtration by granular moved bed:
This subject is studying on the thermophoretic deposition of aerosol particles by a granular moved bed.

Collection efficiency of fibrous filter with dust loading:
The collection efficiency of an air filter increases with the filtration time by the interference effect of collected particles. In this study, the collection efficiency is obtained by experiment and a simple theory.

Dust collection performance of Louver type dust collector:
The particle separation mechanism of the louver dust separator is mainly inertia and particle rebound on the blades. We produced many blades of two dimensional type and tested its efficiency, the theoretical collection efficiency is given by a simulation method.

Kanazawa University, Department of Chemical Engineering
Faculty of Engineering, Kodatsuno, Kanazawa, Japan

Hitoshi Emi (Professor, Dr.)
Chikao Kanaoka (Assistant Professor, Dr.)

Subject of Research

1. Air Filtration
   - @ Filtration of Aerosols by Fibrous Filter
   - @ Collection Efficiency of Aerosols by Microscreen
   - @ Inertial Deposition of Aerosols on the Surface of Micro-perforated Plate or Nuclepore Filter
   - @ The Effect of Mist or Dust Loading on the Performance of Fibrous Filter
2. Particle Deposition on the Wall from Moving Aerosols
   - @ Deposition of Aerosols in Fully Developed Turbulent Pipe Flow
   - @ Deposition of Aerosols near the Entrance of Pipe
   - @ Deposition of Aerosols in a Bifurcation Tube
3. Measurement of Adhesion Forces
   - @ Measurement of Adhesion Forces between Two Particles by Centrifugal Method
   - @ Detachment of Particles from a Cylinder by Aerodynamic Drag

Staff Members and Research Project in Iinoya Laboratory

Department of Chemical Engineering, Kyoto University,
Sakyo-ku, Kyoto 606, Phone (075) 751-2111 Ext. 5566-9

as of spring in 1977

Staff Members

Professor	Koichi Iinoya	Dr. of Eng.
Assistant Professor	Kazutaka Makino	Dr. of Eng.
Research Assistant	Hiroaki Masuda	Dr. of Eng.
Research Assistant	Kenichi Ushiki	
Ph. D. Candidates	Hideto Yoshida, Yasushige Mori, Michitaka Suzuki	

Research Projects

(1) Dust Collection Performance of Bag Filter

(2) Dislodging Characteristics of Powder Cake on Filter Fabric and on Collecting Electrode of Electrostatic Precipitator

(3) In Stream Measurement of Flow Rate in Powder Pneumatic Conveyor

(4) Dust Sampling Techniques in Stack and Environment

(5) Electrification of Particles

(6) Measurement of Dust Concentration by Electrification

(7) Virtual Impactor for Particle Size Measurement

(8) Mist or Inertia Separator

(9) Mist Size Measurement

(10) Powder Layer Mechanics and Stability

AEROSOL RESEARCH BY PROFESSOR YOSHIDA'S GROUP

(Department of the Chemical Engineering, University of Osaka Prefecture, Sakai 591, Japan)

STAFF
Professor Tetsuo Yoshida
Assist. Professor Yasuo Kousaka
Research Assist. Kikuo Okuyama

Our researches are about "Particle growth of aerosol particles of sub-micron diameter by condensation and coagulation, and its application to industrial dust collection".

In these studies, the particle size distribution and the particle number concentration were determined by the measurement method using an ultramicroscope developed by us.

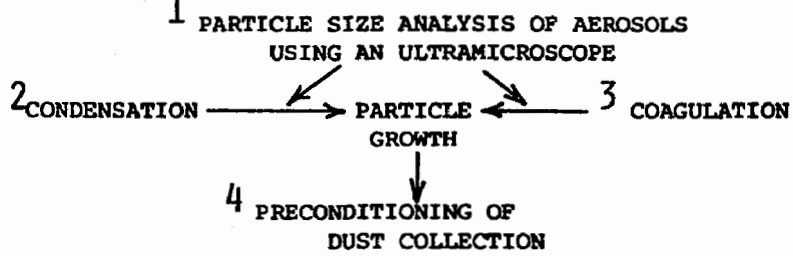

1. A New Technique of Particle Size Analysis of Aerosols and Fine Powders Using an Ultramicroscope. (Ind. Eng. Chem. Fundam., 14, 47(1975))

2. Condensation of Water Vapor on Aerosol Particles
   - i) Condensation Growth of Aerosols by Mixing Hot Saturated Air with Cold Air. (Ind. Eng. Chem. Fundam., 15, 37(1976))
   - ii) Condensation Growth of Aerosols by Injection of Steam into Air. (unpublished work)
   - iii) Dependence of the Evaporation Rate of Micron Order Droplet on Particle Number Concentration. (unpublished work)
   - iv) Experimental Study of Thermophoresis of Aerosols (J. Chem. Eng. Japan, 9, 147(1976))

3. Coagulation of Aerosol Particles
   - i) Change in Particle Size Distribution of Polydisperse Aerosols Undergoing Brownian Coagulation. (J. Chem. Eng. Japan, 8, 317(1975))
   - ii) Turbulent Coagulation of Aerosols in a Stirred Tank. (J. Chem. Eng. Japan, 10, 142(1977))
   - iii) Turbulent Coagulation of Aerosols in a Pipe. (unpublished work)
   - iv) Behavior of Aerosols Undergoing Brownian Coagulation, Brownian Diffusion and Gravitational Settling Between Two Horizontal Walls. (J. Chem. Eng. Japan, 8, 137(1975))
   - v) Behavior of Aerosols Undergoing Brownain Coagulation, Brownian Diffusion and Gravitational Settling in a Closed Chamber. (J. Chem. Eng. Japan, 9, 140(1976))
   - vi) Effects of Brownian Coagulation and Brownian Diffusion on Fine Particle Size Analysis by Sedimentation Method. (J. Chem. Eng. Japan, 10, 46(1977))

4. Application of Particle Growth to Industrial Dust Collection
   - i) Application of Aerosol Growth by Condensation to Industrial Dust Collection. (to be presented at The Second Pacific Chemical Engineering Congress (Pachec'77))
   - ii) Effectiveness of Particle Growth in Dust Collection by Wet Scrubber. -Venturi Scrubber, Sieve Plate Type Scrubber and so on-

5.
   - i) Dispersion of Powders into Air. (unpublished work)
   - ii) Aerodynamic Diameter of Non-spherical (Needle-like and Aggregate) Particles Using an Ultramicroscope. (unpublished work)

1. Okayama University

Department of Industrial Chemistry

Faculty of Engineering

3-1-1, Tsushima-naka, Okayama, Japan, 700

2. Zennosuke TANAKA (Assistant Professor, Dr.)

3. Performance of Centrifugal Dust Separator

Developing the new equipment of hybrid dust separator (centrifugal dust separator with rotating fibrous filter i.e. centrifugal bag filter).
The device is designed to remove particulate matter by filtration and centrifugation, Centrifugal forces play the roles in precleaning a heavy loading of large particles and dislodging the collected material on filter.

1. Department of Electronic Engineering , Tokushima University

2. Prof. Y. GOSHO

3. Increase in Breakdown Voltage of Non-Uniform Field Gap by Adding Electronegative Gases

In a non-uniform field gap such as Electrostatic Precipitator, when the potential across the gap is raised, corona occurs at a corona onset potential and the corona current increases with increasing the potential. At a certain potential breakdown occurs across the gap. In these conditions, by adding a small amount of electronegative gases, the breakdown voltage was found to be greatly increased. With a point-plane geometry with a 15 mm gap in air, the increments of the breakdown voltage and the corona current prior to breakdown were 20 percent and 70 percent respectively with the addition of 3 percent of SF_6. It will be expected that the efficiency of precipitation of E P is improved by applying this means.

1. Faculty of Engineering, Yamaguchi University.

2. Takayoshi Adachi, Associate Professor.

3. Ionic Wind and Behavior of Particles dragged by Ionic Wind in an Electrostatic Precipitator.

(1). Velocity distribution of ionic wind in the corona discharge space consisting of point to plate electrodes has been observed by means of laser-doppler flowmeter and schlieren photograph method, and also theoretically studied by treating Poisson's equation, equations of electric current continuity, Navier-Stokes equations, and the main equation by use of computer.

(2). The drastic influence of ionic wind on submicron particles was experimentally confirmed in its collection process.

(3). The effect of the force acting on particles was discussed in terms of two components of the ionic wind force and the Coulomb force which were analyzed from the observation in the EPsystem with a sham ionic wind.

1. Kyushu Institute of Technology

2. Shinichi Yuu (Assistant Professor)

3. Particle turbulent Diffusion in Dust Laden Flows

Attention has been focused on the diffusion of small particles in various flow fields. Such a phenomenon is of interest in numerous cleaning devices (electrostatic precipitator etc.) and atomized fuel injection systems. The principal purpose of this study is to reveal the mechanism of the particle turbulent diffusion in dust laden flows by predicting particle turbulent diffusivities theoretically and measuring them experimentally. Turbulent particle Lagrangian trajectories and velocities in a round and a plane air jets were calculated by using fluid integral scales, intensities and average velocities. From the calculated results the turbulent diffusivity and the local time-averaged velocity of particles are obtained. Measurements of local mean aerosol concentration were made with a photo-electronic dust counter and a dust tube. From the measurements the experimental particle diffusivity is obtained and compared with the theoretical calculation. The results indicate that the particle diffusivity decreases with the increase of the particle inertia. In general the turbulent diffusivity of particles is smaller than that of fluid scalar quantities. The particle inertia and the fluid large eddies, which are expressed by the Stokes number and the integral scale, respectively, play an important role in the transport mechanism of particles in the dust laden flow.

1. Department of Applied Science, Faculty of Engineering,
Kyushu University

2. Terutoshi Murakami (Professor of Applied Physics)

3. Scavenging of Aerosol Particles by Liquid Droplets

4. As a basic research of scavenging of aerosol particles by liquid droplets, the interaction between the particles and the droplets are investigated in two cases.

(i) Aerosol particles of 5μ m in diameters of Rhodamine B aqueous solution are generated by ultrasonic method, and the amount of the particles collected by falling water droplet is measured by spectrophotometer. To obtain correct collection efficiency, the distribution of the small particles and the aerodynamic flow patterns around the falling droplet are observed by pulse laser holography.

(ii) A small cylinder of 1 mm in diameter are set up in the high speed aerosol flow produced in a shock tube, then the flow patterns around the cylinder are investigated by means of the laser holography or shadow photographs. We intend to scavenge the aerosol particles by water droplets dispersed in the shock tube.

1. Prof. M. AKAZAKI

2. Kyushu University, Faculty of Engineering,
   Department of Electrical Engineering

3. Discharge Phenomena in the Electrostatic Precipitator

   (a): Characteristics of DC Corona Discharge in the Particle Collection Space (High Temperature, High Humidity and Flying Particles)

   (a-1) The effect of Experimental Condition* for Corona Discharge (*Voltage Waveform, Electrode Shape and Gas Condition)

   (2-2) Characteristics of Corona Pulses from the Polluted Electrode Surface

   (b): Charging Mechanism of Dust Particle by Corona Streamer

   (b-1) Mechanism of Streamer Propagation in the Air Containing Dust Particles

   (b-2) Mechanism of Electric Breakdown in the Dust Layer on the Electrode

   (c): Mechanism of Particle Reentrainment

   (d): Mechanism of Back Discharge

AUSTRALIAN COAL INDUSTRY RESEARCH LABORATORIES LTD.

P. O. Box 83. NORTH RYDE. N.S.W. 2113. AUSTRALIA

Telephone: 88-0276: 888-5341

Australian Coal Industry Research Laboratories Limited comprises five laboratories, each registered by the National Association of Testing Authorities, and located in the Australian States of Queensland and New South Wales.

The laboratories are staffed by over 100 employees and provide facilities for analytical investigations and pilot plant studies which support the specialised consulting capabilities that have been developed in the fields of coal preparation.

A.C.I.R.L. through its testing and consulting activities has been particularly active in the area of pollution control. These activities have caused research to be undertaken into various areas, which has resulted in the development of new techniques.

Included in these new techniques in the unique facility that was developed, which enables small samples of coal, usually derived from bore cores, to be processed into a laboratory fly ash by controlled firing through a micro furnace. The laboratory fly ash which is similar to a Power Station fired fly ash, is then electrically, chemically, physically and microscopically examined in order to assess its potential capability to be electrostatically precipitated. The electrical assessment includes determinations of both Resistivity and Voltage Current Corona characteristics over the range of potential operating temperatures and under varying moisture contents in a simulated flue gas environment.

This whole technique enables an investigation to be carried out of a coal area which is intended for use in a proposed power station, without having to first mine the area. It is the only means known whereby an estimated assessment of the combustion and electrostatic precipitation characteristics of such a coal area may be made at the pre-development stage of a proposed Power Station project.

J.W. Baker, B.Sc., B.E. -Mechanical Engineer, ACIRL Ltd.

K.M. Sullivan, B.E., FIEAust., FInstF., -Principal Fuel Engineer, ACIRL Ltd.

Directory of Foreign Attendants

May, 1977

1	F. Löffler	Professor, Institut für Mechanische Verfahrenstechnik der Universität Karlsruhe Richard-Willstätter-Allee, 7500 Karlsruhe 1, Germany
2	E.C. Potter	Leader, Process Chemistry Section, Division of Process Technology Minerals Research Laboratories, Commonwealth Scientific and Industrial Research Organization, Australia P.O.Box 136 Delhi Road North Ryde, N.S.W. Australia, 2113
3	M. First	Professor, Department of Environmental Health Sciences, School of Public Health, Harvard University 665 Huntington Avenue, Boston, Massachusetts 02115, U. S. A.
4	W. Stöber	Professor, Institut für Aero-Biologie, 5948 Schmallenberg-Grafshaft, Germany
5	R.W. McIlvaine	President, The McIlvaine Company 2970 Maria Avenue Northbrook, Illinois 60062, U. S. A.
6	K.M. Sullivan	Principal Fuel Engineer, ACIRL Ltd. P.O.Box 83, North Ryde,N.S.W. Australia, 2113

7 J.W. Baker — Mechanical Engineer, ACIRL Ltd.
P.O.Box 83, North Ryde N.S.W.
Australia, 2113

8 R.H. Horning — Vice President, Combustion Power Co.,
Menlo Park, California, U. S. A.

International Seminar on Dust Collection

- Attendants (University) - 24, May 1977

Univ. or College	Name	Adrress
1. Hokkaido Univ. Res.Inst.of Applied Electricity	Hirotatsu Mishina	Nishi 6-chome, Kita 12 Jyo, Kita-ku, Sapporo (060)
2. Tokyo Univ. Dept. of Elec.Eng.	Senichi Masuda	Hongo, Bunkyo-ku, Tokyo (113)
3. "	Akio Akutsu	"
4. Tokyo Univ. Dept. of Chem.Eng.	Akira Suganuma	"
5. Nagoya Univ. Dept. of Chem.Eng.	Genji Jinbo	Furo-cho, Chikusa-ku, Nagoya (464)
6. "	Junichiro Tsubaki	"
7. Daido Inst. of Tech. Dept. of Elec. Eng.	Yasunori Miyoshi	2-21, Daido-cho, Minami-ku, Nagoya (457)
8. Suzuka Technical College	Norio Kimura	Shirako-cho, Suzuka, Mie (510-02)
9. Kanazawa Univ. Dept. of Chem. Eng.	Hitoshi Emi	2-40-20, Kotachino, Kanazawa (920)
10. "	Chikao Kanaoka	"
11. Doshisha Univ. Dept.of Chem.Eng.	Satoshi Okuda	Karasuma Imadegawa, Kamigyo-ku, Kyoto (602)
12. "	Hiroshi Takano	"
13. Kyoto Univ. Dept.of Chem. Eng.	Kōichi Iinoya	Yoshida Honmachi, Sakyo-ku, Kyoto (606)
14. "	Kazutaka Makino	"
15. "	Hiroaki Masuda	"
16. "	Kenichi Ushiki	"
17. "	Hideto Yoshida	"
18. "	Yasushige Mori	"
19. "	Michitaka Suzuki	"

20.	Osaka Pref.Univ. Dept.of Chem. Eng.	Tetsuo Yoshida	4-804, Mozuume-cho, Sakai, Osaka (591)
21.	"	Kikuo Okuyama	"
22.	Okayama Univ. Dept.of Ind.Chem.	Zennosuke Tanaka	3-1-1, Tsushimanaka, Okayama (700)
23.	Tokushima Univ. Dept.of Elec.Eng.	Koshichi Gosho	2-1, Minami Tsunemishima-cho, Tokushima (770)
24.	Kyushu Inst. of Tech. Research Inst.of Powder Tech.	Shinichi Yuu	1, Sensui-cho, Tobata-ku, Kitakyushu (804)
25.	Kyushu Univ. Dept.of Applied Physics	Terutoshi Murakami	Hakozaki, Higashi-ku, Fukuoka (812)
26.	Kyushu Univ. Dept.of Elec. Eng.	Masanori Akazaki	"
27.	Kansai Univ. Dept,of Chem.Eng.	Takuzo Matsuyama	Senriyama, Suita, Osaka (564)

International Seminar on Dust Collection

- Attendants (Company) - 24, May 1977

	Company	Name	Adrress
1.	Hosokawa Iron Works Ltd.	Teruaki Suzuki	9, 1-chome, Shodai Tajika, Hirakata, Osaka (573)
2.	"	Takashi Kitamura	"
3.	Nitta Gelatin Co., Ltd.	Yoshihiro Nonaka	Futamata, Yao, Osaka (581)
4.	Matsushita Seiko Co., Ltd.	Toshio Shibahara	4811, Marunouchi, Takagicho, Kasugai, Aichi (486)
5.	Sankyo Dengyo Co., Ltd.	Kazuo Saito	1-8-11, chuo-cho, Meguro-ku, Tokyo (152)
6.	Nippon Donaldson, Co., Ltd.	Tsutomu Shibuya	100, Imadera, Ōme, Tokyo (198)
7.	Mitsui Miike Co., Ltd.	Hideo Noziri	1-1, Kokubu-cho, Tochigi (328-03)
8.	Denka Consultant & Engineering Co., Ltd.	Ryusuke Araki	1-4-1, Yūraku-cho, Chiyoda-ku, Tokyo (100)
9.	Izumi Kakoki Co., Ltd.	Chiaki Shiota	3-7, Nakanoshima, Kita-ku, Osaka (530)
10.	Nippon Felt Co., Ltd.	Ikuo Yasui	2-2, 2-chome, Marunouchi, Chiyoda-ku, Tokyo (100)
11.	Sinto Dust Collector Ltd.	Takeshi Yoneda	1, Nishinagane, Kodacho, Sakazaki, Nukata-gun, Aichi(441-01)
12.	Sanko Engineering & Construction Co., Ltd.	Akio Furukawa	4-6-29, Namamugi, Tsurumi-ku, Yokohama (230)
13.	"	Toshio Seki	"
14.	Hitachi Plant Engineering & Construction Co.,Ltd.	Hiroshi Yamada	1-13-3, Kitaotsuka, Tokyo(170)
15.	Sumitomo Kinzoku Kozan Co., Ltd.	Ken Takimoto	5-11-3, Shinbashi, Minato-ku, Tokyo (105)
16.	Yamamoto Industries Co., Ltd.	Rinkan Kawamura	1-2-2, Kawashiro, Tobata-ku, Kitakyushu (804)
17	NGK Insulators Co., Ltd.	Shigeharu Kito	1, Maegata-cho, Handa (475)
18.	Kobe Steel Ltd.	Hiroyuki Kohama	1-3-18, Wakihama-cho, Fukiai-ku, Kobe (651)

19.	Kobe Steel Ltd.	Akira Wakabayashi	1-3-18, Wakihama-cho, Fukiai-ku, Kobe (651)
20.	Sinto Dust Collector Ltd.	Takeo Hisatsune	1, Nishinagane, Sakazaki, Kodacho, Nukata-gun, Aichi (441-01)
21.	Kurimoto Tekkosho Co., Ltd.	Ryota Ito	1-56, Oike-dori, Kitahorie, Nishi-ku, Osaka (550)
22.	"	Akira Hama	"
23.	Hosokawa Research Inst. of Powder Tech.	Tōhei Yokoyama	9, 1-chome, Shodai Tajika, Hirakata, Osaka (573)
24.	Kawasaki Heavy Industries, Ltd.	Kimihiro Funahashi	16-1, 2-chome, Nakamachi-dori, Ikuta-ku, Kobe (650-91)

ERROR IN MEASUREMENT OF GAS FLOW RATE IN GAS-SOLIDS TWO-PHASE FLOW BY USE OF A HORIZONTAL DIFFUSER*

HIROAKI MASUDA, YOSHIFUMI ITO
AND KOICHI IINOYA
Department of Chemical Engineering, Kyoto University, Kyoto, Japan

(Reprinted with permission)

© Reprinted from
JOURNAL OF CHEMICAL ENGINEERING OF JAPAN
Vol. 6, No. 3 (1973)
Pages 278—282

ERROR IN MEASUREMENT OF GAS FLOW RATE IN GAS-SOLIDS TWO-PHASE FLOW BY USE OF A HORIZONTAL DIFFUSER*

HIROAKI MASUDA, YOSHIFUMI ITO
AND KOICHI IINOYA
Department of Chemical Engineering, Kyoto University, Kyoto, Japan

Measurement of gas flow rate in gas-solids two-phase flow is studied both theoretically and experimentally by use of a horizontal diffuser. Since the pressure recovery in the diffuser varies with both the solid flow rate and diffuser length, the gas flow rate measured by the diffuser generally has some error. The relative error for the measurements is a monotone-increasing function of the measuring length, but never exceeds the value of the mass flow ratio. It is also shown that there is a length at which the error vanishes. This length can be estimated using an analytical equation. The effects of powder properties on the magnitude of the error are also discussed in detail.

1. Introduction

The measurement of the mass flow rate of solids, or of the flow rate ratio for solids to gas in a two-phase system is complicated by the fact that the measured value, such as pressure drop along the pipeline, is also a function of gas flow rate. Therefore the gas flow rate must be measured simultaneously by an independent method. Farbar[1], Barth *et al.*[2], Goto *et al.*[3], and Sakata[4], examined the possibility of using a diffuser to make such measurement on a two-phase system. They concluded that pressure recovery in the diffuser decreased with increasing solids rate. However, the manner in which the error of the measured gas flow rate varies with the distance along the diffuser has not yet been determined, as was mentioned by Sakata.

This study will examine the nature and extent of error, and, where the error offers a problem, methods for estimating the error theoretically and design methods for minimizing the error. In particular, it is shown that there is a design method for reducing the error to zero. Following the suggestion of Goto *et al.*, the investigation is carried out for the horizontal part of a pneumatic conveyor, and is mainly concerned with particles smaller than 100 microns.

* Received on May 6, 1972
Presented at the 37th Annual Meeting of the Soc. of Chem. Engrs., Japan, April 5, 1972
〒606 京都市左京区吉田本町
京都大学工学部化学工学教室　井伊谷研　増田弘昭
** see also Eq.(18)

2. Theoretical Approach

If it is assumed that the particles are uniformly suspended and in rather low concentration, the wall-friction of particles may be regarded as negligible in a diffuser[2,3]. Therefore, the following momentum balance equation is obtained[5].

$$-dP_m=\rho_a u du+m\rho_a u dv \tag{1}$$

The relative error on the basis of the pressure difference is defined by the following equation**.

$$E=m\frac{\int_{v_0}^{v} u dv}{\int_{u_0}^{u} u du}=m\frac{\int_0^x uv'dx}{\int_0^x uu'dx} \tag{2}$$

where u_0 and v_0 denote the gas velocity and the particle velocity at the inlet of the diffuser, respectively. The prime represents the derivative with respect to the coordinate x. In this equation, the denominator shows the pressure recovery for gas flow alone, and the numerator shows the additional recovery by the solids momentum.

Assuming the incompressibility of gas flowing in the diffuser section, the velocity u can be expressed by the equation

$$u=\frac{u_0}{(1+\alpha x)^2},\quad \alpha=\frac{\tan\theta}{r} \tag{3}$$

On the assumption that the wall friction of particles may be neglected in the diffuser, the particle velocity u is given by the following equation of motion[5]:

$$v'=\frac{C_1(u-v)+C_2(u-v)^{3/2}}{v} \tag{4}$$

where C_1 and C_2 are constants which are given by

$$C_1\equiv 18\frac{\mu_a}{D_p^2\rho_p} \tag{5}$$

and

$$C_2\equiv 3\frac{\mu_a}{D_p^2\rho_p}\left(\frac{D_p\rho_a}{\mu_a}\right)^{1/2} \tag{6}$$

Fig. 1 shows the velocities u, v and the trend of the relative error calculated by numerical integration using Schiller and Naumann's[6] drag coefficient. Particle velocity v_0 at the inlet is smaller than the corresponding gas velocity u_0, because the particles have been affected by wall friction in the straight pipe section just before the diffuser. The relative error monotonously increases with the coordinate x. This trend of the error is analytically explained by Eqs.(2), (3) and (4).

From Eq.(2), it can be seen that the error is zero at $x=x_0$ or $v=v_0$;

$$E_{x_0}=m\frac{\int_{v_0}^{v_0} udv}{\int_{u_0}^{u} udu}=0 \tag{7}$$

Applying l'Hospital's theorem to Eq.(2), the limiting value of the error as $x\to\infty$ is given by the equation

$$\lim_{x\to\infty}E=m\lim_{x\to\infty}\frac{uv'}{uu'}=m \tag{8}$$

If the position x_0 can be estimated in some way, the gas flow rate in suspensions may be measured very accurately. Now, assuming that x_0 is determined, the residual error arising from the difference between the measuring point x and x_0 may be estimated from the gradient of the error curve at the position x_0. Taking the equation $E_{x_0}=0$ into consideration, the following equation holds in the neighborhood of x_0;

$$E=m\frac{\int_0^x uv'dx}{\int_0^x uu'dx}\simeq 2m\frac{u_{x_0}}{u_0^2-u_{x_0}^2}(v_0-v) \tag{9}$$

If the relation $v_0-v\simeq|v'_{x_0}|(x-x_0)$ is substituted in the above equation, Eq.(9) reads

$$E\simeq 2m\frac{u_{x_0}}{u_0^2-u_{x_0}^2}|v'_{x_0}|(x-x_0) \tag{10}$$

Note that $E_{x_0}=0$, and hence the differential form of this equation is

$$\left.\frac{dE}{dx}\right|_{x_0}\simeq 2m\frac{u_{x_0}}{u_0^2-u_{x_0}^2}|v'_{x_0}| \tag{11}$$

Eliminating v'_{x_0} by use of the equation of motion (4), a more explicit form of Eq.(11) is obtained as

$$\left.\frac{dE}{dx}\right|_{x_0}\simeq 36m\frac{\mu_a}{D_p^2\rho_p}\left[1+\frac{1}{6}\left\{\frac{D_p\rho_a}{\mu_a}(v_0-u_{x_0})\right\}^{2/3}\right]\times\frac{u_{x_0}(v_0-u_{x_0})}{v_0(u_0^2-u_{x_0}^2)} \tag{12}$$

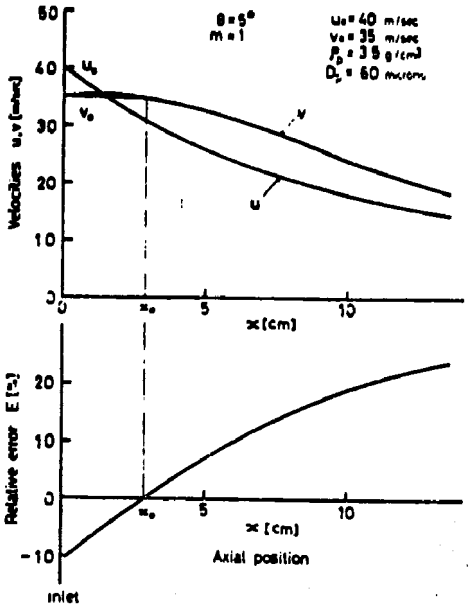

Fig. 1 Velocities u, v and the trend of the relative error (numerical integration)

In practical applications, the second term in the brackets may be regarded as negligible. From this fact and the relation $u_0>v_0>u_{x_0}$, Eq.(12) may be simplified as follows;

$$\left.\frac{dE}{dx}\right|_{x_0}\lesssim 18m\frac{\mu_a}{D_p^2\rho_p v_0} \tag{13}$$

This equation shows that the error presents a problem when the inertial force of a particle is smaller than the viscous force of the fluid.

The next problem is to estimate the position at which the error vanishes. From the above results concerning the gradient of the error, the second term of Eq.(4) is seen to be negligible. Then Eq.(4) may be rewritten as

$$v'=C_1(u/v-1) \tag{14}$$

A first approximation by Picard's method[7] gives

$$v=v_0+C_1\left[\frac{1}{v_0}\left\{\frac{u_0}{\alpha}-\frac{u_0}{\alpha(1+\alpha x)}\right\}-x\right] \tag{15}$$

Now, the equation for x_0 is obtained from Eq.(15) where $v=v_0$:

$$\alpha x_0=\frac{1-\phi_0}{\phi_0},\quad\text{where}\quad \phi_0\equiv\frac{v_0}{u_0} \tag{16}$$

This equation shows that the first approximation of x_0 is determined by the dimensions of the diffuser and the velocity ratio ϕ_0. The characteristics of the powder are not included explicitly in this equation.

3. Apparatus and Experimental Procedure

In this experiment, a pneumatic conveyor line operated under negative pressure is used. The experimental setup is shown in **Fig. 2**. The diffusers used are shown in **Fig. 3**. The selected diffuser is placed in the hori-

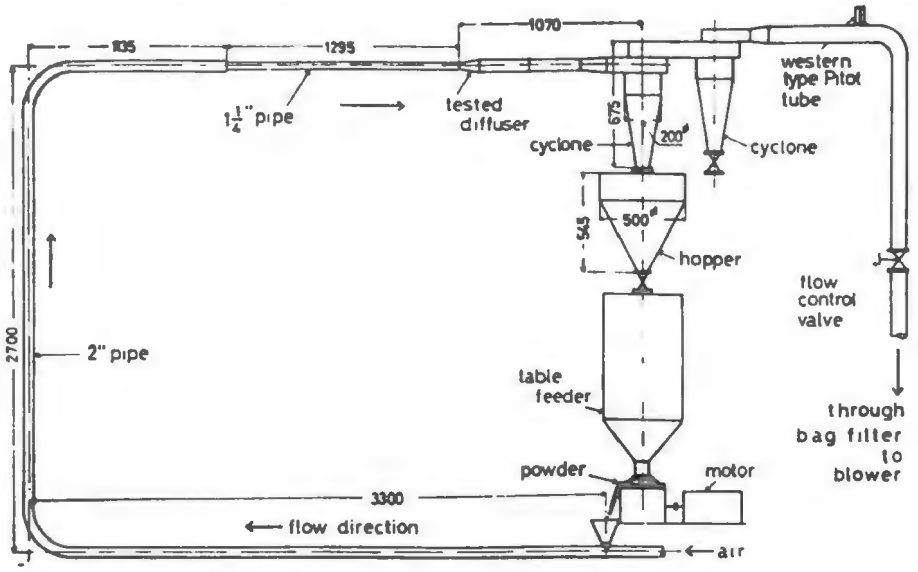

Fig. 2 Schematic diagram of the experimental setup

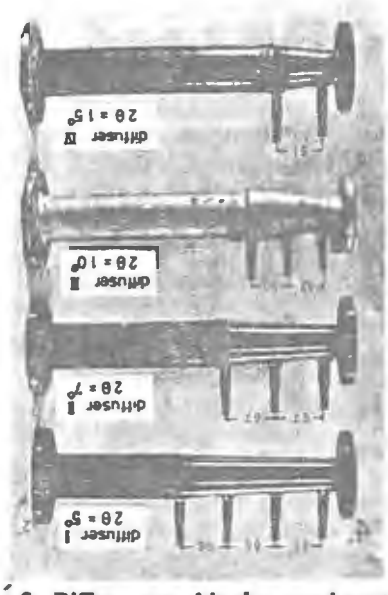

Fig. 3 Diffusers used in the experiments

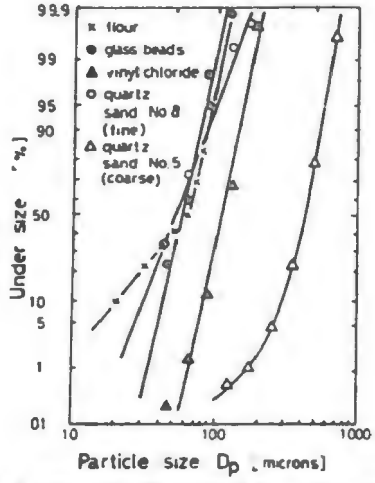

Fig. 4 Size distribution of the solid materials (Log-normal) (determined by sieving; for flour, the sedimentation method is used.)

Table 1 Properties of the powder materials

Materials	Mass median dia. D_{p50} [microns]	Mean particle dia. $\bar{D}_p$ [microns]	Density of a particle ρ_p [g/cm³]
Quartz sand No. 8	51	45	2.65
Glass beads	55	52	2.42
Vinyl chloride	115	108	1.41
Flour	57	28	1.44
Quartz sand No. 5	380	295	2.65

zontal section of the piping, allowing for the appropriate approach length. To charge the solid particles into the conveyor, a table feeder is used. Materials used are quartz sand No. 8 (fine), glass beads, vinyl chloride powder, flour, and quartz sand No. 5 (coarse). The properties of these powders are shown in **Table 1**, and their size distributions are presented in **Fig. 4**.

Air flow is monitored by a Pitot tube, and strain-gauges, transducers, and an on-line hybrid computer (CLAOP 2000) are used to measure pressure difference. The system used for these on-line studies is shown schematically in **Fig. 5**.

4. Results and Discussion

The analytical values calculated by Eq.(13) are compared with the results of numerical integration obtained by a digital computer (FACOM 230-60). **Fig. 6** shows a set of the results on the gradient of the error. **Fig. 7** shows a comparison between x_0 calculated by Eq.(16) and x_0 obtained by numerical integration. When particle size is large, the coincidence of the analytical and numerical results is not good. The disagreement is not serious, however, because the gradient of the error itself is very small in this case.

The relative error E has been defined in relation to the pressure difference measurements. Now, the corresponding relative error for measuring the gas flow rate

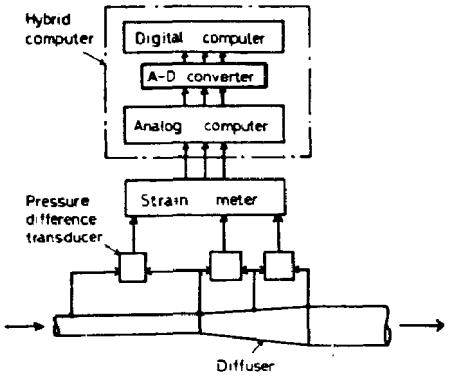

Fig. 5 Schematic diagram of the on-line system

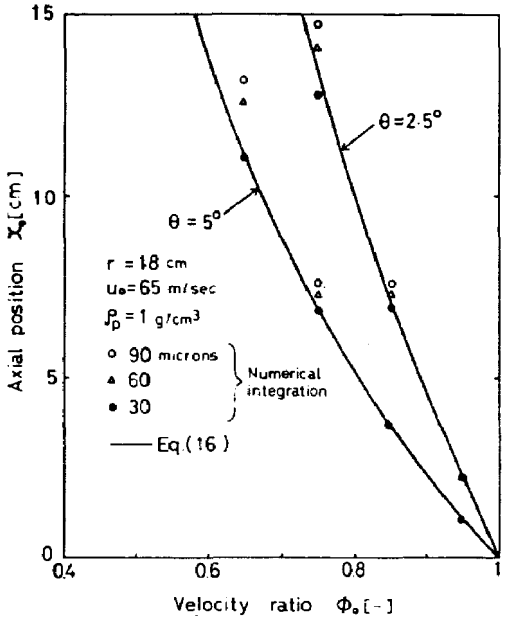

Fig. 7 Comparison between x_0 calculated by Eq.(16) and that obtained by numerical integration

is introduced as follows;

$$e \equiv (Q_m - Q)/Q \qquad (17)$$

As the pressure difference is in proportion to the square of the gas flow rate, Eq.(17) may be rewritten as

$$e = \sqrt{\Delta P_m/\Delta P_a} - 1 = \sqrt{1+E} - 1 \simeq \frac{1}{2}E \qquad (18)$$

The results presented in **Fig. 8** indicate the magnitude of the error. Calculated values are shown by lines. The mean particle diameters defined by the following

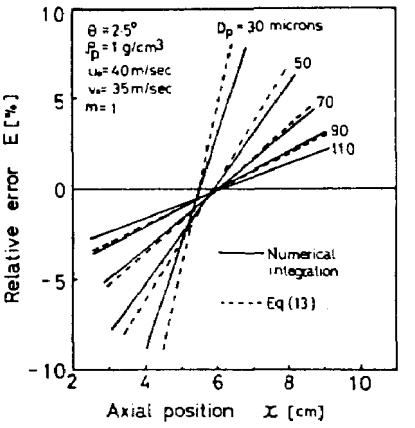

Fig. 6 Comparison between the gradient of the error obtained by numerical integration and that calculated by Eq.(13)

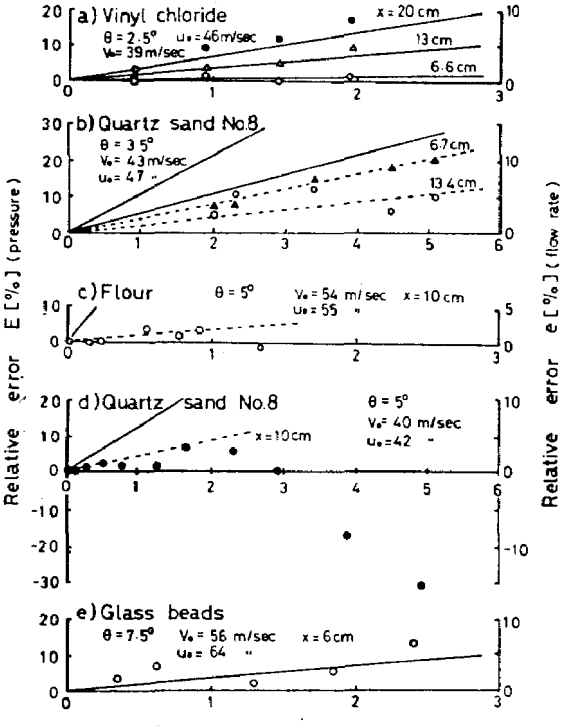

——— calculated by Eq.(13)
..... calculated as $\bar{D}_p = 70\mu$ for the quartz sand No. 8, and $\bar{D}_p = 90\mu$ for the flour.
The symbols indicate experimental values.

Fig. 8 Relative error as a function of mass flow ratio

equation[8] are used in the calculations.

$$\bar{D}_p = \sqrt{1/\sum(f_i/D_{pi}^2)} \qquad (19)^*$$

The particle velocity v_0 and the velocity-ratio ϕ_0 are calculated from the pressure difference measured at the straight pipe section just before the diffuser[10].

The calculated values for the quartz sand No. 8 and the flour are fairly large**, as shown in b) and c) of Fig. 8. In the case of the vinyl chloride powder and the glass beads, the calculated errors agree with the experimental data, as shown in a) and e) of Fig. 8.

* When the particle size distribution is log-normal, Eq.(19) is equivalent to[9] $\bar{D}_p = \exp(\ln D_{p50} - \sigma^2)$, where $\sigma = \ln D_{p84} - \ln D_{p50}$. The mean particle diameters of the quartz sand No. 8, the glass beads, and the vinyl chloride powder are calculated using this equation.

** These differences between the experimental and the theoretical result may be attributable to the agglomeration of the finer particles[11]. For reference, the mean particle diameter determined by the reverse calculation are, approximately, 70 and 90 microns for quartz sand No. 8 and flour, respectively.

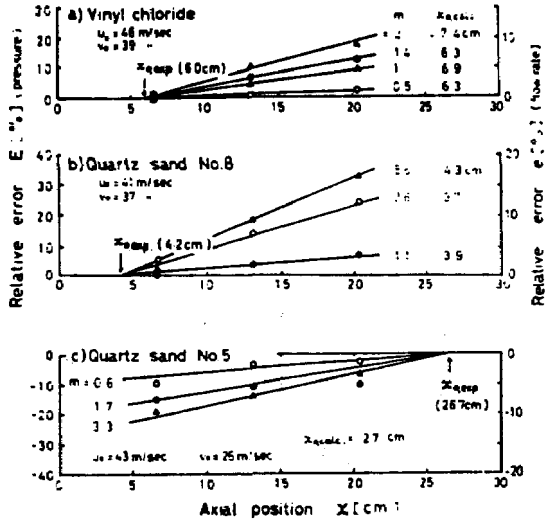

Note: x_0 indicates the position at which the error vanishes. The values of $x_{0,calc.}$ are determined by use of Eq.(16).

Fig. 9 Relative error as a function of axial position

Fig. 8 d) shows some of the results obtained using diffuser III (θ=5°). In this case, the error becomes negative with increasing particle velocity v_0 and mass flow ratio m. This phenomenon may arise from the separation of the fluid from the wall*. As the flow disturbance is aggravated by the particles, the separation occurs more readily. When the diverging angle is fixed, this phenomenon occurs more easily at smaller mass flow ratios as the particle velocity becomes higher. As shown in Fig. 8 e), however, this phenomenon cannot be seen in the experiments with smaller mass flow ratio and lower particle velocity, even when θ=7.5°. Further, this phenomenon depends on the shape of the particle, and occurs more readily for quartz sand No. 8 than for glass beads.

Fig. 9 shows the experimental results proving the existence of a position x_0 at which the relative error is zero. Calculated values, $x_{0,calc.}$, are also indicated in this figure. From these results, it is found that the coincidence between the experimental and the calculated x_0 is very satisfactory. Fig. 9 c) shows the experimental results obtained when the measuring position x is shorter than the x_0 estimated by Eq.(16). In this case, the error is negative, as is estimated by the theory. These data are similar to those of Farbar, Barth *et al.*, Goto *et al.*, and Sakata.

The following discussion is concerned with the effects of powder properties on the magnitude of the error. The difference in the magnitude of error obtained by several authors using coarse particles may arise from differing values of $(x-x_0)$. The equivalent difference $(x-x_0)$, which gives rise to an error of equal magnitude for the systems 1 and 2, is given by Eq.(20), which is developed from Eq.(13).

$$\frac{(x-x_0)_2}{(x-x_0)_1}=\left(\frac{D_{p2}}{D_{p1}}\right)^2\left(\frac{\rho_{p2}}{\rho_{p1}}\right)\left(\frac{v_{02}}{v_{01}}\right) \tag{20}$$

Summarizing the above discussion, the published data for large particles and the results of this study for small particles have been explained consistently, taking into account the nature of the variation in magnitude of the error and the fact that there is a position at which the error vanishes. Eq.(8), showing that the error does not exceed the mass flow ratio, will prove useful when a low mass flow ratio system such as a dust collector is involved. In a system using large particles, the velocity ratio ϕ_0 is constant[12-14] without recourse to the mass flow ratio m and the gas velocity u. The position x_0 can, therefore, be estimated knowing the properties of the particles and the dimensions of the diffuser.

* If we assume that this phenomenon arises from failure of the original assumption, that the wall friction of the particles is negligible in the diffuser, we cannot explain the fact that the phenomenon is not observed when a diffuser with small diverging angle is used.

Nomenclature

C_1, C_2 = constants, Eqs.(5) and (6)
D_p = particle diameter
$\bar{D}_p$ = mean particle diameter, Eq.(19)
E = relative error defined by Eq.(2)
ε = relative error defined by Eq.(17)
f_i = particle size distribution
ΔP_m = pressure recovery of gas-solids suspensions flowing in the diffuser
ΔP_a = pressure recovery of gas flow alone
Q_m = gas flow rate calculated by ΔP_m
Q = actual gas flow rate
r = inside radius of the diffuser inlet pipe
u = gas velocity
v = particle velocity
x = coordinate in axial direction
x_0 = position at which the error E or ε vanishes

<Greek letters>

α = constant determined with θ and r, defined by Eq.(3)
θ = half of the diverging angle of the diffuser
μ_a = viscosity of the gas
ρ_a = density of the gas
ρ_p = density of the particle
ϕ_0 = velocity ratio defined by Eq.(16)

Literature Cited

1) Farbar, L.: *Trans. of the ASME*, **75**, 943 (1953)
2) Barth, W., R. Nagel and K. van Waveren: *Chemie-Ing.-Techn.*, **29**, 599 (1957)
3) Iinoya, K. and K. Goto: *Kagaku Kōgaku* (*Chem. Eng.*, Japan), **27**, 80 (1963)
4) Sakata, M.: *Trans. of the Japan Soc. of Mech. Engrs.*, **37**, 1560 (1971)
5) Пащацкий Н. В. и Н. И. Сыромятников: *инженерно-физический журнал*, **17**, 26 (1969)
6) Schiller, L. and A. Naumann: *Z. V. D. I.*, **22**, 318 (1933)
7) Lapwood, E. R.: "The International Encyclopedia of Physical Chemistry and Chemical Physics", Topic 1, Vol. 1, p. 179, Pergamon Press London (1968)
8) Masuda, H. and K. Iinoya: Memoirs of the Faculty of Eng., Kyoto Univ., **34**, 344 (1972)
9) Masuda, H. and K. Iinoya: *J. Chem. Eng. Japan*, **4**, 60 (1971)
10) Weidner G.: *Forschung*, **21**, 145 (1955)
11) Boothroyd, R. G.: *Trans. of the ASME*, ser. B, **91**, 303 (1969)
12) Iinoya, K., T. Kamimura and Y. Tsukada: *Kagaku Kōgaku* (*Chem. Eng.*, Japan), **23**, 400 (1959)
13) Barth, W.: *Chemie-Ing.-Techn.*, **30**, 171 (1958)
14) Konno, H., S. Saito and S. Maeda: *Kagaku Kōgaku*, **31**, 243 (1967)

DUST CLEANING DYNAMICS IN REVERSE COLLAPSE TYPE BAG FILTER

Kazutaka Makino, Yasushig Mori
Naomi Takado, Koichi Iinoya

The bag filter which is one of the typical high efficiency collectors requires a dust cleaning operation. However, research on bag filters so far are mainly about collection efficiency and pressure drop characteristics,[3,4] While there are not many studies concerning dust cleaning characteristics which is an important factor in design of filter operations. Furthermore, there are very few reports concerning the dust cleaning dynamics which is especially necessary in the determination of dust collection charateristics.

Therefore, this report related to the reverse flow type collector, a typical dust cleaning method, reviews and investigates its dynamics experimentally and presents the results. Here, the dust cleaning dynamics mean the variance of a combined flow resistance of dust and filter material in time due to reverse flow after starting dust cleaning operations.

Estimation of Transfer Function for Each Component in Measurement System

Figure 1 shows the block diagram of dust cleaning Dynamics Measurement System in this experiment. In order to estimate the transfer function of recorder and transmitter, five kinds of pressures were applied for each case as an input and the step responses were measured. The result of this measurement shows that there is a linear relationship between the above mentioned inputs and the outputs (response value indicated at recorder) and that it can be approximated by one step later (one order later). The transfer function for reverse air flow value was obtained by experimentally approximating the general transfer function which is the product of transfer function of recorder and transmitter and above transfer function, after doing step response experiment for certain air flow with 5 different positions of flow control value and after assuming the transfer function of reverse air flow value to be dead time 1 order later. Each transfer function estimated this way is shown in Figure 1.

Estimation Result of Dust Cleaning Dynamics

For dust cleaning operation due to reverse flow, if the combined flow resistance of dust and filter material of the bag due to reverse air flow is assumed to be R(t). R(t) will probably

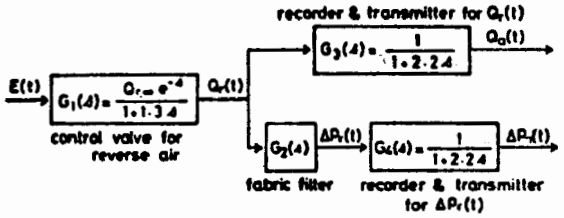

Fig. 1 Block diagram of fabric filter system including measuring instruments

decrease as dust cleaning proceeds. However, it is difficult at the present time to directly measure this process quantitatively. Thus in this report a model is set and dust cleaning dynamics are estimated. Also, it should be noticed that the transfer function $G_2(s)$ of bag filter itself is not a Laplace transformation of R(t).

Here the bag pressure drop $\Delta p_r(t)$ during reverse air flow can naturally be expressed by the following equation.

$$\Delta p_r(t) = L^{-1}\left[\frac{1}{s} G_1(s)G_2(s)\right] = Q_r(t)R(t)/S \qquad (1)$$

Now the reverse air flow rate $Q_r(t)$ is obtained as the following equation from Figure 1.

$$Q_r(t) = L^{-1}\left[\frac{1}{s} G_1(s)\right] = Q_{r,\infty}E(t-1)\left\{1-\exp\left(-\frac{t-1}{1.3}\right)\right\} \qquad (2)$$

Also the apparent pressure drop $\Delta p_a(t)$ across the bag filter shown in recorder during reverse air flow is expressed as follows using tranfer function $G_4(s)$.

$$\Delta p_a(t) = L^{-1}\left[\frac{1}{s} G_1(s)G_2(s)G_4(s)\right]$$

$$= L^{-1}\left[L[\Delta p_r(t)]\ G_4(s)\right] \qquad (3)$$

Now for the combined flow resistance R(t) of dust and filter material during above mentioned cleaning process, consider a model to approximate by dead time and 1 order later.

$$\frac{R(t) - R_{max}}{R_\infty - R_{max}} = D(t-\theta)\left\{1-\exp\left(-\frac{t-\theta}{T}\right)\right\} \qquad (4)$$

This is the case when the dimensionless resistance coefficient $[=(R(t)-R_{max})/(R_\infty-R_{max})]$ can be approximated as 1 order late. The reason why a dead time θ was considered was because there is a case when a start of reverse air is not consistent with a start of cleaning. In this case $\Delta p_a(t)$ is expressed by the following equation from Equations (1)-(4).

$$\Delta p_a(t) = \frac{Q_{r,\infty}R_{max}}{S}\left\{1-\frac{22}{9}\exp\left(-\frac{t-1}{2.2}\right) + \frac{13}{9}\exp\left(-\frac{t-1}{1.3}\right)\right\} E(t-1)$$

$$+ \frac{Q_{r,\infty}(R_\infty-R_{max})}{S}E(t-\theta)\left[1 + \left\{\frac{2.2}{T-2.2} - \frac{13}{9}\exp\left(-\frac{\theta-1}{1.3}\right)\right.\right.$$

$$\left.\left. - \frac{\exp(-(\theta-17/1.3)}{1-2.2(1/1.3+1/T)}\right\}\exp\left(-\frac{t-\theta}{2.2} + \frac{13}{9}\exp\left(-\frac{t-1}{1.3}\right)\right.\right.$$

$$\left.\left. - \frac{T}{T-2.2}\exp\left(-\frac{t-\theta}{T}\right) + \frac{\exp(-(\theta-1)/1.3)}{(-2.2(1/1.3 + 1/T)}\right.\right.$$

$$\left.\left. x\ \exp\left\{-(t-\theta)\left(\frac{1}{1.3} + \frac{1}{T}\right)\right\}\right] \qquad (5)$$

Now if you set T→0, T(t) can be approximated only by a dead time. Thus it is assumed as one order late model with dead time θ when T ≠ 0 and as dead time model (dead time θ = λ) when T→0. If you plot the results of actual measurement on the $\Delta p_a(t)$ vs t line figures which were drawn by assuming various cleaning time constant T, cleaning dead time θ or λ, T,θ,λ during actual dust cleaning process can be estimated. The fine calcium carbonate (D_{p50} = 5.4 μm) was used as sample dust and we have changed the most typical filter materials (tetron and nylon fibers) as well as number of so-called rings which are installed to prevent the bag insides from contacting during reverse collapse operations. The installation of bag is similar to that of previous report (bag with 1,800 mm long and 170 mm Φ inner diameter). Figures 2 and 3 show typical examples of this experiment results. Based on these, it is seen that the approximation by the dead time 1 order late system in Equation (5) is appropriate. Table 1 shows the ranges of T, θ and λ obtained in this experiment. According to this, each case is within several seconds and it is indicated that several ten seconds will be enough as a single cleaning duration time for reverse bag filters.

For tefron long fabric filter cloth, when one ring is installed, the time constant is minimum and it is suggested that there is the most optimal number of rings, namely the most optimal ring installation distance, in light of cleaning dynamics. Also when it is switched to collection process after reverse cleaning and to have only clean air, the pressure drop, as shown in Table 1 will be smaller as the number of rings increases. This will probably require future investigations. It was also confirmed that the dust load changes at the start of dust cleaning does not considerably affect the above mentioned T, θ and λ.

Conclusion

After investigating the cleaning dynamics of reverse collapse type bag filter, the following conclusions were obtained.

1) After the combined flow resistance variation of dust and filter material due to reverse air flow was investigated with 1 order late and dead time models at reverse air flow, it is relatively well approximated with a time constant less than several seconds for this experimental region ($1.0 \leq u_r \leq 1.42$ m/min, $45 \leq \Delta p_{max} \leq 150$ mm H_2O).

2) The effect of ring numbers is not significant to the time constant but is fairly important to the cleaning final pressure drop.

Although this report experimentally investigated the qualitative characteristics of reverse bag filter cleaning dynamics, a quantitative consideration as well as a scale factor consideration will be necessary in a future.

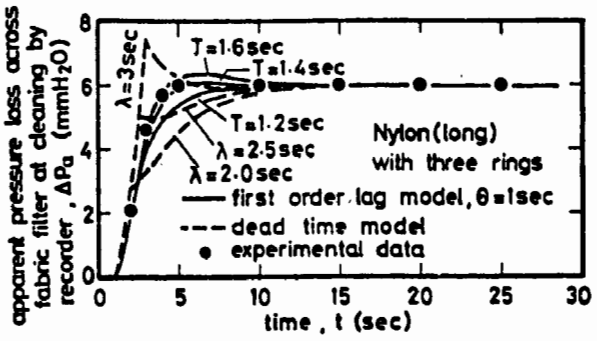

Fig. 3 A fitting example of two models (First order lag model & Dead time model) to experimental data (Nylon fabric, fine calcium carbonate dust, u_f=1 m/min, Δp_{max}=95 mmH_2O)

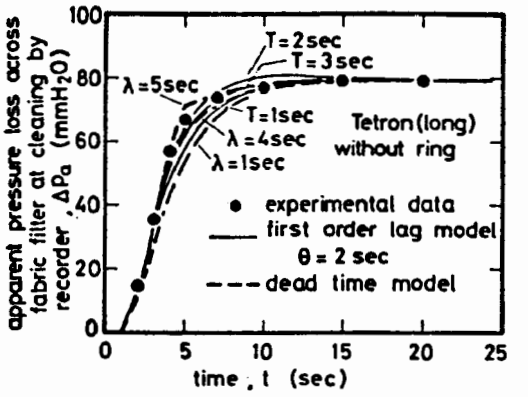

Fig. 2 A fitting example of two models (First order lag model & Dead time model) to experimental data (Tetron fabric, fine calcium carbonate dust, $u_r = 1$ m/min, $\Delta p_{max} = 95$ mmH$_2$O)

Table 1 Estimated values of time constant T and dead time θ, λ

Filter media	Number of rings	First order lag model: time constant T [sec] θ=1 sec	First order lag model: time constant T [sec] θ=2 sec	Dead time model: dead time λ [sec]	Pressure loss given by filtering air flow after infinite cleaning [mmH_2O]
Tetron (long)	0	4	2	4	70.0
	1	1	1	2	67.5
	3	3	2	3	40.5
Nylon (long)	1	1	1	2	44.0
	3	1.5	0.7	3	25.5

A METHOD OF MEASURING PRESSURE DROP PARAMETERS FOR MULTI-COMPARTMENT BAG FILTER
—MECHANICAL SHAKING TYPE AND REVERSE COLLAPSE TYPE—

K. Iinoya, K. Makino, K. Ueshima,
M. Lin and Y. Mori
Kyoto University, Dept. of Chemical Engr.

Introduction

Generally bag filters will have a long continuous operation of one or two years after a clean filter cloth is installed. Therefore, it is necessary to investigate the collection efficiency and variation of pressure drop characteristics with time in order to estimate bag filter performance and to determine a method for design. Especially the variation of pressure drop characteristics with time is important for economically optimal design and operation of bag filter. However this pressure drop characteristic is difficult to measure in the laboratory because of the following two reasons:

1) The pressure drop characteristics necessary for bag filter design and operation are usually for one or two years of operation when pressure drop parameters are stable after installation. It is very difficult to have such a long investigation in the laboratory. However, the initial characteristics are naturally important in the fundamental base and this report will also investigate this case,

2) Even if the same composition of some dusts and filter materials as actual field is obtained, it is technically and economically difficult to reproduce the actual (field) dust distributions, dust supply condition, gas composition, temperature and humidity in the laboratory.

Therefore the pressure drop characteristics have to be obtained directly from the actual pressure drop data of multi-compartment bag filters which is operating in the field. This method has never been utilized.

We have established the method to qualitatively estimate pressure drop parameters, which are necessary for economically optimal design and operations, using the field measurement data of pressure drop variations of mechanical shaking type and reverse collapse type bag filters. This report presents this method as well as the results of actual applications.

1. Fundamental Theory

Many experimental equations are reported for bag filter pressure drop characteristics and this report applies the following equations

$$\Delta p = u(A+BM^{\delta}) \tag{1}$$

Here, A, B and δ are the pressure drop parameters determined by the characteristics of dust and filter material and by dust cleaning method. Especially A is the value which, in addition to filter material and primary accumulation dust layer, includes residual secondary dust layer after dust cleaning.

Generally the collection characteristic for the multi-compartment bag filter is the repeat of (N-1) compartment collection with one compartment being cleaned while the N-1 compartments are collecting. Now we call the former the cleaning time and the latter the collection time. There is a following relationship between the dimensionless dust load $\tilde{x}_i$ and the dimensionless filtering velocity $\tilde{u}_i$ in the ith compartment at the dimensionless time $\tilde{t}$ in this cycle.

$$d\tilde{x}_i = \tilde{u}_i d\tilde{t} \tag{2}$$

Also the dimensionless pressure drop $\Delta\tilde{p}(\tilde{t})$ is given by the following equation,

$$\Delta\tilde{p}(\tilde{t}) = \{\alpha+(1-\alpha)\tilde{x}_i^{\delta}\}\tilde{u}_i \tag{3}$$

where
$$\alpha = A/\{A+B(C\eta\bar{u}_n'T)^{\delta}\}. \tag{4}$$

Figure 1 shows one example of the typical pressure drop variation pattern for collection and cleaning cycles for the mechanical shaking type and reverse collapse type multi-compartment bag filters. Generally the process gas quantities during cleaning collection time are approximately equal. Thus, there is a following relationship between the average filtering velocity at cleaning time and collection time.

$$\tilde{\bar{u}}_{n-1} = \{N/(N-1)\}\tilde{\bar{u}}_n' \tag{5}$$

Thus the following equations are obtained.

$$\sum_{i=1}^{n-1} \tilde{u}_i = N \tag{6}$$

$$\sum_{i-1}^{n} \tilde{u}_i = N \tag{7}$$

Integrating equation (2) from $\tilde{t}=0$ to $\tilde{t}=\tilde{\tau}_o$ (cleaning time) and from $\tilde{t}=\tilde{\tau}_o$ to $\tilde{t}=\tilde{\tau}$ (collection time) and add the former one from i=1 to i=(n-1) and the latter one from i=1 to i-N to obtain the following equation:

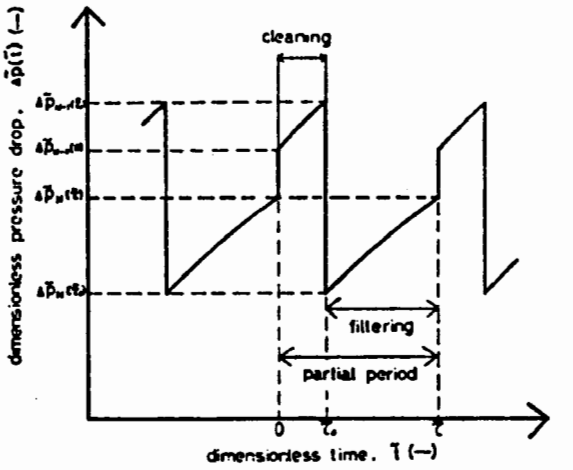

Fig. 1 Conceptional diagram of pressure drop of a multi-compartment bag filter

$$(\tilde{x}_1,\tilde{\tau}_0-x_{1,0})+(\tilde{x}_2,\tilde{\tau}_0-\tilde{x}_{2,0})+\cdots$$
$$+(\tilde{x}_{(n-1),\tilde{\tau}_0}-\tilde{x}_{(n-1),0})=\int_0^{\tilde{\tau}}\sum_{i=1}^{n-1}\tilde{u}_i d\tilde{t}=N_{\tilde{\tau}0} \tag{8}$$

$$(\tilde{x}_1,\tilde{\tau}-x_2,\tilde{\tau}_0)+(\tilde{x}_2,\tilde{\tau}-\tilde{x}'_2,\tilde{\tau}_0)+\cdots$$
$$+(\tilde{x}_{n,\tilde{\tau}}-x_{n,\tilde{\tau}_0})=\int_{\tilde{\tau}_0}^{\tilde{\tau}}\sum_{i=1}^{N}\tilde{u}_i' d\tilde{t}=N(\tilde{\tau}-\tilde{\tau}_0) \tag{9}$$

There is generally the following relation between the dust loads at each specific point of collection and cleaning cycle.

(cleaning finish time) (collection starting time)

$$\tilde{x}_{i,\tilde{\tau}_0} = \tilde{x}_{i+1,\tilde{\tau}_0} \tag{10}$$

(cleaning start time) (collection finish time)

$$\tilde{x}_{i,o} = \tilde{x}_{i,\tilde{\tau}} \tag{11}$$

where i = 1,2,...,N-1

Consider equations (10) and (11) and add each side of equations (8) and (9).

$$\tilde{x}_{n,\tilde{\tau}}-\tilde{x}'_{1,\tilde{\tau}_0}=N\tilde{\tau} \tag{12}$$

Consider $\tilde{x}'_{1,\tilde{\tau}_0}=o$ and $T=N_\tau$ here to obtain the following equation:

$$\tilde{x}'_{n,\tilde{\tau}} = 1 \tag{13}$$

Also the following equation can be obtained from equations (2) and (3)

$$\{\alpha+(1-\alpha)\tilde{x}_i^{\delta}\}d\tilde{x}_i = \Delta\tilde{p}(\tilde{t})d\tilde{t} \tag{14}$$

Integrate equation (14) as described above over cleaning time and collection time, and add the former one from i=1 to i=(n-1) and the latter one from i=1 to i=n.

$$\{y(\tilde{x}_{i,\tilde{\tau}_0})-y(\tilde{x}_{1,0})\}+\{y(\tilde{x}_2,\tilde{\tau}_0)-y(x_{2,0})\}+\cdots$$
$$+\{y(\tilde{x}_{(n-1)\tilde{\tau}_0})-y(\tilde{x}_{(n-1),0})\}=(n-1)\int_0^{\tilde{\tau}}\Delta\tilde{p}(\tilde{t})d\tilde{t} \tag{15}$$

$$\{y(\tilde{x}'_{i,\tilde{\tau}})-y(\tilde{x}'_{i,\tilde{\tau}_0})\}+\{y(\tilde{x}'_{2,\tilde{\tau}})-y(\tilde{x}'_{2,\tilde{\tau}_0})\}+\cdots$$

$$+\{y(\tilde{x}'_{n,\tilde{\tau}})-y(\tilde{x}'_{n,\tilde{\tau}_0})\}=N\int_{\tilde{\tau}_0}^{\tilde{\tau}}\Delta\tilde{p}(\tilde{t})\,d\tilde{t} \tag{16}$$

$$\text{where } y(\tilde{x})=\alpha\tilde{x}+\{(1-\alpha)/(1+\alpha)\}\tilde{x}^{1+\delta} \tag{17}$$

Consider equations (10), (11) and (13) and add each side of equations (15) and (16).

$$\begin{aligned}\dot{y}(\tilde{x}'_{n\tilde{\tau}}) = y(1) &= \alpha+\frac{1-\alpha}{1+\delta}\\ &= (n-1)\int_0^{\tilde{\tau}_0}\Delta\tilde{p}(\tilde{t})\,d\tilde{t}+N\int_{\tau_0}^{\tilde{\tau}}\Delta\tilde{p}(\tilde{t})\,d\tilde{t}\\ &= (n-1)\int_0^{\tilde{\tau}}\Delta\tilde{p}(\tilde{t})\,d\tilde{t}+\int_{\tilde{\tau}_0}^{\tilde{\tau}}\Delta\tilde{p}(\tilde{t})\,d\tilde{t}\end{aligned} \tag{18}$$

Next, we will describe the determination method of each pressure drop parameter.

1.1 Determination of $\Delta\tilde{p}_n(\tilde{t})$ and α

$$\Delta\tilde{p}_n(\tilde{t}) = \frac{N}{\sum_{i=1}^{N}\{\alpha+(1-\alpha)\tilde{x}'^{\delta}_{i,\tilde{\tau}}\}^{-1}} \tag{19}$$

$$\Delta\tilde{p}_{n-1}(0) = \frac{N}{\sum_{i=1}^{n-1}\{\alpha+(1-\alpha)\tilde{x}^{\delta}_{i,0}\}^{-1}-1} \tag{20}$$

Equation (20) can generally be changed to the following in considering equation (13).

$$\begin{aligned}\Delta\tilde{p}_{n-1}(0) &= \frac{N}{\sum_{i=1}^{N}\{\alpha+1-\alpha)\tilde{x}'^{\delta}_{i,\tilde{\tau}}\}^{-1}}\\ &= \frac{N\Delta\tilde{p}_n(\tilde{\tau})}{N-\Delta\tilde{p}_n(\tilde{\tau})}\end{aligned} \tag{21}$$

Obtain $\Delta\tilde{p}_n(\tilde{\tau})$ from this.

$$\Delta\tilde{p}_n(\tilde{\tau}) = N\frac{\Delta p_{n-1}(0)-\Delta p_n(\tilde{\tau})}{\Delta p_{n-1}(0)} = N\beta \tag{22}$$

Now make same consideration for $\Delta\tilde{p}_n(\tilde{\tau}_0)$ and $\Delta\tilde{p}_{n-1}(\tilde{\tau}_0)$.

$$\Delta\tilde{p}_n(\tilde{\tau}_0) = \frac{N}{1/\alpha+N/\Delta\tilde{p}_{n-1}(\tilde{\tau}_0)} \tag{23}$$

Obtain α from this

$$\alpha=\beta\frac{\Delta p_{n-1(\tilde{\tau}_0)}}{\Delta p_{n-1(\tilde{\tau}_0)}-\Delta p_{n(\tilde{\tau}_0)}}\cdot\frac{\Delta p_{n(\tilde{\tau}_0)}}{\Delta p_{n(\tilde{\tau})}} \tag{24}$$

Here, since the right sides of equations (22) and (24) can be easily measured, these can be used as the equations to determine $\Delta p_{n(\tilde{\tau})}$ and α.

1.2 Determination of A, B and δ

Based on the definition, the pressure drop characteristics parameters A and B have the following relationships with α.

$$A = \frac{A\bar{u}_n'}{\Delta p_f}\cdot\frac{\Delta P_f}{\bar{u}_n'} = \alpha\frac{\Delta p_f}{\bar{u}_n'} = \alpha\frac{\Delta p_{n(\tilde{\tau})}}{\bar{u}_n'\Delta p_{n(\tilde{\tau})}} \tag{25}$$

$$B = \frac{\bar{u}_n'\{A+B(c\eta\bar{u}_n'T)^{\delta}\}-\bar{u}_n'A}{\bar{u}_n'\{A+B(c\eta\bar{u}_n'T)^{\delta}}\times\frac{\bar{u}_n'A+B(c\,u_n\,T)}{\bar{u}_n'(c\eta\bar{u}_n'T)^{\delta}}$$

$$= \frac{\Delta p_f-u_n'A}{\Delta p_f}\cdot\frac{\Delta p_f}{\bar{u}_n'(c\eta\bar{u}_n'T)^{\delta}} = \frac{(1-\alpha)\Delta p_f}{\bar{u}_n'(c\eta\bar{u}_n'T)^{\delta}} \tag{26}$$

As mentioned above α and $\Delta\tilde{p}_n(\tilde{\tau})$ can be obtained from equations (22) and (24), thus equations (25) and (26) are the fundamental equations to estimate A and B. Also, using above results, δ can also be determined by equation (18). But the equation (18) requires the time integration of pressure drops and is actually very difficult. Therefore, the actual region of pressure drop was considered and numerically reviewed, and it was determined that δ can be considered physically as 1. (See Appendix.) This determination will make this measurement method very easy and practical.

2. Application to Actual System

2.1 Mechanical Shaking Type System

This measurement method was applied to the mechanical shaking type bag filter for an electric boiler collection and its pressure drop was measured. Table 1 shows its operating and installation conditions while Figure 2 presents its pressure drop measurement results. The time regions 1, 3, 5, 7 and 9 in Figure 2 are so-called cleaning times and all process gas amounts are those when collection is occurring in the compartments other than cleaning compartments are collecting. Our method theoretically requires the variation in pressure drop of one partial cleaning cycle, which means the data from five measurements. The pressure drop parameters estimated by applying our approximation method to these data are shown in Table 2 along with other various values. The pressure drop characteristics in this case can be expressed by the following equation.

$$\Delta p = u(7.63\times10^{3} + 1.27\times10^{5}\ M) \qquad (27)$$

Also when the same data were analyzed by the numerical integration method, this will be expressed by the following equation which gives almost the same result as equation (27).

$$\Delta p = u(7.53\times10^{3} + 1.42\times10^{5}\ M^{1.08}) \qquad (28)$$

2.2 Reverse Collapse Type System

This method was applied, similarly to the previous section, to reverse collapse type bag filter for electric boiler particulate collection and its pressure drop was measured. Table 1 shows its operating and installation conditions and Figure 3 shows the results of pressure drop measurements. (a) in Figure 3 is the pressure drop change of other compartments when one compartment is during cleaning and (b) in Figure 3 is the pressure drop change of the compartment which is being cleaned at the same time as (a). Although for (a) and (b) in Figure 3, we have programed the period 6 in which very small amount of air is introduced at the initial stage of collection, its existence does not essentially affect our method. However, the collection amount can be neglected in period 6, it is necessary to consider the total period of the cleaning cycle after subtracting period 6. By applying our method to Figure 3, the pressure drop parameters are obtained as shown in Table 2. The pressure drop characteristics in this case can be expressed by the following equation

$$\Delta p = u(1.40\times10^{4} + 6.40\times10^{4}\ M) \qquad (29)$$

Also the results of equations (27) and (29) can be estimated as reasonable based on the operating condition of Table 1. Now we have to review the accuracy of these measurement results statistically. According to this, if the measurements can be done, in considering actual experience and five measurement results of pressure drop

Table 1 Operating conditions of an industrial multi-compartment bag filter

Type of dust cleaning	Mechanical Shaking	Reverse air
Filter medium	Tetron 2020S	Tetron 5203
Number of compartments N [—]	10	6
Filter area [m²]	5150	5489
Gas flow rate [m³/min]	3840	5880
Total period of cleaning cycle T [min]	45	120
Average filtering velocity $\bar{u}_{fv}$ [m/min]	0.74	1.07
Dust concentration c [g/m³]	1.7	0.30
Dust	withdrawn by suction directly from ferrochrome electric furnace	withdrawn by suction from the roof of a factory housing of a steelmaking electric furnace
Total hours operated after installation [hrs]	408	1600

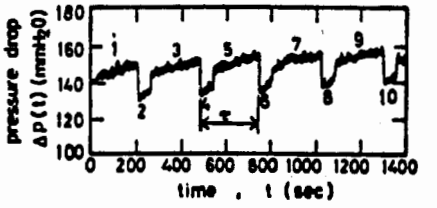

Fig. 2 Example of pressure drop cycle of an industrial multi-compartment bag filter (Mechanical Shaking Type)

Table 2 Examples of Estimation of Pressure Drop Parameters in Multi-Compartment Bag Filters

Type of dust cleaning	Mechanical Shaking						Reverse Air							
Items / Run	1	2	3	4	5	Average	1	2	3	4	5	6	7	Average
Δp_f [mmH_2O]	182	180	192	189	175	184	286	267	286	286	286	225	230	267
$\Delta p_{N-1}(0)$ [mmH_2O]	143	146	149	150	153	148	242	232	242	242	242	235	243	238
$\Delta p_{N-1}(r_e)$ [mmH_2O]	151	153	155	157	158	155	247	247	247	247	247	247	247	247
$\Delta p_N(r_e)$ [mmH_2O]	129	131	133	135	137	133	207	202	207	207	207	196	195	203
$\Delta p_N(z)$ [mmH_2O]	133	135	138	139	141	137	212	207	212	212	212	200	200	208
$\Delta \bar{p}_N(r)$ [—]	0.73	0.75	0.72	0.73	0.80	0.75	0.74	0.78	0.74	0.74	0.74	0.89	0.87	0.78
a [—]	0.48	0.53	0.47	0.52	0.58	0.52	0.87	0.89	0.87	0.87	0.87	0.78	0.78	0.84
$A \times 10^{-8}$ [$mmH_2O \cdot sec/m$]	7.05	7.69	7.27	7.93	8.23	7.63	14.0	13.5	14.0	14.0	14.0	10.0	10.0	12.8
$B \times 10^{-4}$ [$mmH_2O \cdot (m^2/kg)$]	13.4	12.0	14.4	12.8	10.5	12.7	6.40	5.05	6.40	6.40	6.40	8.40	9.50	6.94
Bg [mmH_2O/m]	228	204	245	218	179	215	19.2	15.2	19.2	19.2	19.2	25.2	28.5	20.8

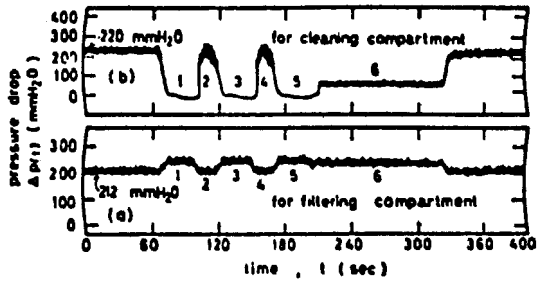

Fig. 3 Example of pressure drop cycle of an industrial multi-compartment bag filter (Reverse Air Type)

cycle in Figure 2, by certain accuracy (each pressure drop with ±1%, average filtering velocity with ±10% and one cycle cleaning frequency ±1%), it was concluded that the estimated accuracy of pressure drop parameter A and B are ±10% and ±40%, respectively. This means that the estimation of B is more difficult than that of A. However, increasing the number of measurements will increase its accuracy and will not require too long a time. Thus this method is very well applicable to industrial usage. However, since the estimation of B by this method definitely requires an accurate measurement of dust concentration in the bag, it will be expected in the future to have a pressure drop characteristic measurement and the instantaneous measurement of concentration. Also since A is the value directly related to the cleaning performance and takes a more important part than B in determination of bag filter operating condition, this method has the practical significance in giving a more accurate value of A. Here the dust concentration of the bag part was assumed to be equal to that concentration at the entrance of bag filter itself, but when the dust concentration of the bag part cannot be measured, equation (26) is the fundamental equation to estimate the product of B and c (where $\delta = 1.0$). Table 2 shows the value of Bc as a reference.

Conclusion

The estimation methods of pressure drop characteristics A, B and δ of mechanical shaking type and reverse collapse type bag filters from field data were reviewed and the following conclusions were obtained.

1) The pressure drop parameters A, B and δ can be estimated by time variation in partial cleaning cycles of mechanical shaking type and reverse collapse type multi-compartment bag filters pressure drops.

2) It was shown that assuming $\delta \fallingdotseq 1$ is industrially permissible for the practical range of pressure drop parameters.

3) We have shown the actual measurement results of the application of this method to mechanical shaking type and reverse collapse type bag filters.

Appendix

When the pressure drop characteristic coefficient α of clean filter material is used, the pressure drop is expressed by the following equation.

$$\Delta p = \bar{u}(a+bm^q) \qquad (i)$$

Where, m is the total dust amount on the surface of filter cloth [= Mo (cleaning residual dust amount) + M (cleaning dust amount]. The relationship between each amount in equations (i) and (1) are given by the following equations based on definitions.

$$A = a + b\ Mo^{q} \qquad \text{(ii)}$$

$$BM^{\delta} = b(Mo+M)^{q} - b\ Mo^{q} \qquad \text{(iii)}$$

The general pressure drop characteristics will have the regions given by following equations.

$$\begin{aligned} 30 &< a < 1400 \\ 4000 &< b < 17000 \\ 0.5 &< q < 1.5 \end{aligned} \qquad \text{(iv)}$$

For the regions of equation (iv), A, B and δ were estimated as a parameter of M by using the least squares method. As a result, it was determined by B, if b and q are constants, will have approximately a constant value independent of Mo and δ will have a certain relationship with q, as a parameter of Mo, independent of a and b as shown in Figure 4. The especially interesting point is that even if q changes significantly, δ is always about 1.0. Thus, for the region of equation (iv), the pressure drop estimation by assuming δ=1.0 and applying the approximate pressure drop coefficient B will only have errors within $\pm$ several %. Therefore the approximation of δ=1.0 is industrially sufficient.

Acknowledgment

We express our sincere appreciation to Shinto Dust Collector Company and Clean Filter Company concerning important field pressure drop data for multi-compartment bag filters for this research.

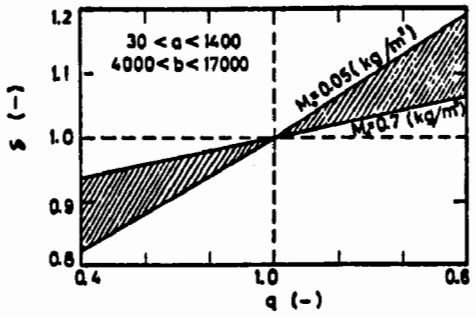

Fig. 4 Relationship between q and s

PERFORMANCE OF FIBROUS POWDER BED FILTER

Koichi Iinoya, Kazutaka Makino,
Tsutomu Imamura, and Hiroshi Okura
Kyoto University, Chemical Engineering Dept.

The filter collector is relatively efficient and practically important for eliminating micron and submicron particles. Here, fibrous bed and filter paper are mainly used for air purifications, and the estimate of their performance is reasonably accurate due to the relatively wide fundamental studies of their behavior.

Although the fabric filter was considered mainly for industrial applications, the method of accumulating fibrous powder on the filter cloth is being recognized for air purifications. This is due to the following reasons: 1) It is relatively easy to evenly accumulate fibrous powder on the filter cloth; 2) as a consequence of this, the fibrous bed is formed on the filter cloth surface and the initial collection performance is improved; 3) utilization of fibrous powder has a less pressure drop than ordinary powder; 4) since particles are mainly collected by fibrous powder which will be swept off after certain amount of particle collection, it is easy to sweep off the collected tiny particles and easy for the prevention of filter cloth clogging. Whereas, there has been hardly any fundamental research for fibrous powder bed filters, thus this report presents the experimentally investigated results.

Experimental Apparatus and Method

The experimental apparatus is exactly the same as shown in the previous reports. The fibrous powder bed filter was formed by accumulating fibrous powder in a stratiform on the filter paper or cloth. The experimental procedure was to first measure the collection rate of filter paper or cloth and the overall collection rate of the entire fibrous powder bed filter under predetermined conditions. Next, the penetration rate of the fibrous powder bed was obtained as a ratio of the latter one to the former one. The stearic-acid-single-diffusion-particles by Lamer type generator were used as the sample aerosol and the aerosol concentration was measured by the digital dust counter (manufactured by Shibata Kagaku Co.) simultaneously at filter entrance and exit. Table 1 shows the characteristics of the fibrous powder used in this experiment.

Experimental Results

The penetration rate and the pressure drop across fibrous powder bed filter:

Table 1 Characteristics of test fibrous powder

	Fiber length l [μ]	Fiber diameter D_f [μ]	Specific surface area S_v [m²/m³]
Precoat (●)	220	22	1.98×10^5
Cellulose powder A (▲)	180	18	2.03×10^5
Cellulose powder B (■)	110	17	2.20×10^5
Cellulose powder C (▼)	80	15	2.43×10^5

* <Performance of Fibrous Powder Bed Filter>
Received on February 22, 1973
化学工学協会第5回秋季大会（大阪, 1971年10月）にて研究発表
** Keiichi Iinoya (正会員), Kazutaka Makino (正会員), Tsutomu Imamura (学生会員) and Hiroshi Okura (学生会員) Dept. of Chem. Eng., Kyoto Univ., Kyoto, Japan

Figure 1 shows a relationship between penetration rate and amount of fibrous powder for the fibrous powder bed filter. According to this, the cellulose powder has a lower penetration rate than the precoat. This is probably due to the fact that the true density of the filter material for the former one (ρ_f = 1.7 g/cm^3) is smaller than the latter one (ρ_f = 2.2 g/cm^3) and that the former one has a larger filling volume and collection surface area for the same fibrous powder amount. The relationship between the volume fraction and the thickness of fibrous powder bed is shown in Figure 2 as a reference. Based on this the precoat has a larger volume fraction and a smaller thickness than the cellulose powder. On the other hand, both have about the same penetration rate for the apparent velocity through filter of 1~10 cm/sec. Also in this region of apparent velocity, the pressure drop ΔP_d across the fibrous powder bed is given by the following equation based on the Kozeny-Carman's law.

$$\Delta P_d = 60 \frac{\mu S_v^2 (1-\varepsilon_f) u_s m_o}{g_c \quad \varepsilon_f^3 \quad \rho_f} \quad (\pm 10\%) \qquad (1)$$

Here, the void fraction ε_f can be easily estimated in Figure 2. For example, when m_o = 1 Kg/m^2 and u_s = 1 cm/sec. ΔP_d will be $\fallingdotseq$ 6 mm-water. This value is somewhat smaller than that of ordinary powder.

Single Fiber Collection Efficiency of Fibrous Powder Bed Filter:

The experimental results were converted to single fiber collection efficency (η_ε) by the following logarithmic permeable equation and the relationship between η_ε and $(1-\varepsilon_f)\cdot L$ was investigated.

$$\frac{1-\eta_d}{1-\eta_o} = \exp\left\{-\frac{4(1-\varepsilon_f)L}{\pi D_f}\eta_\varepsilon\right\} \qquad (2)$$

As a result, in the region of $(1-\varepsilon_f)\cdot L \leq 0.15$. η_ε is constant and is independent with changes of $(1-\varepsilon_f)\cdot L$. Namely, since $(1-\varepsilon_f)\cdot L = m_o/\rho_f$ in this region and the permeability $(1-\eta_d)$ will decrease as an exponential function of m_o. Also all the data of this experiment is shown in Figure 3 as a correlation between η_ε and $1-\varepsilon_f)$. This result can be used as a simple estimation method of collection efficiency of fibrous powder bed filter. The solid line in Figure 3 is given by the following equation,

$$\ln\eta_\varepsilon = -1.3(1-\varepsilon_f) - 2.9 \qquad (3)$$

However, the applicable region of this equation is for the apparent velocity across filter of 1~10 cm/sec and particle size of 0.3~0.8μ for fibrous powder with diameter of 10~20μ and with length of 100~200μ.

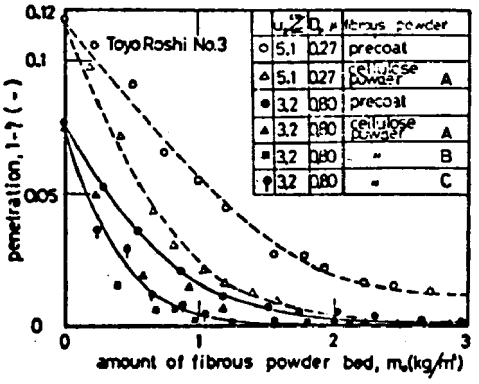

Fig. 1 Relations between penetration (1−η) and amount of fibrous powder bed m_0

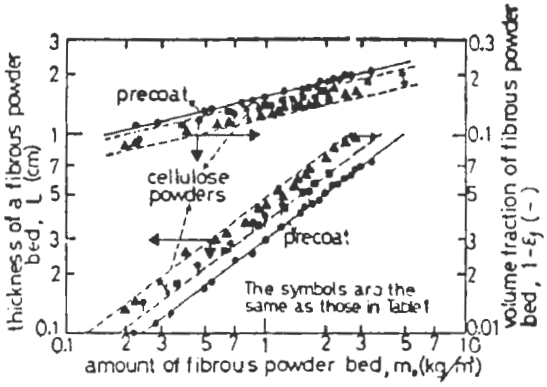

Fig. 2 Relations between m_s and L or $(1-\varepsilon_f)$

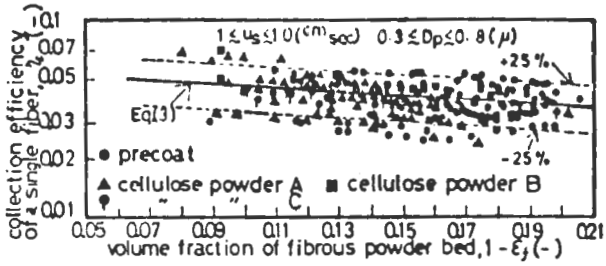

Fig. 3 Relation between collection efficiency of single fiber η_s and volume fraction $(1-\varepsilon_f)$ of fibrous powder in bed

Also, in order to estimate overall collection efficiency of fibrous powder bed filter, an information concerning collection efficiency of filter paper or filter cloth itself other than equation (3) is required. Please refer to Reference (2) and (5), respectively, for this information. Also, the theoretical correlation between single fiber collection efficiency obtained this report and ordinary fibrous filter will require future evaluation.

This experiment used the powder bed filter with short fiber (about 20μ diameter and 100μ long) previously untested and measured its performance experimentally. As a result, a simple estimation equation for collection performance and pressure loss was obtained.

APPENDIX I

UNIVERSITY OF OSAKA

REPRINTED FROM I&EC

FUNDAMENTALS

Growth of Aerosol Particles by Condensation

Tetsuo Yoshida, Yasuo Kousaka, and Kikuo Okuyama

(Reprinted with permission)

Reprinted from I&EC Fundamentals ©
VOL. 15 NO. 1 FEBRUARY 1976

Growth of Aerosol Particles by Condensation

Tetsuo Yoshida, Yasuo Kousaka,* and Kikuo Okuyama

Department of Chemical Engineering, University of Osaka Prefecture, Sakai, 591, Japan

The rate and the extent of growth of submicron aerosol particles introduced into a supersaturated atmosphere of water vapor were studied from both theoretical and experimental points of view. It was found that the rate of growth of aerosol particles undergoing condensation was very rapid, and that the volume-mean diameter of grown particles was determined by the number concentration of aerosol particles and the initial state of supersaturation in the surrounding gas. The supersaturation which was necessary to cause condensation of water vapor around particles was produced by mixing hot saturated air with cold air. The size distribution of grown particles or grown water droplets was determined by the ultramicroscopic size analysis previously developed by the authors. The results suggest that particle growth by condensation is one of the most promising preconditioning techniques for industrial dust collection.

Introduction

The cost of removal of submicron dust particles from exhaust gas has been considered to be very expensive. If the growth of such particles into larger ones (to a few microns or more in diameter) can be easily attained, such preconditioning techniques of dust collection will facilitate air pollution control. Condensation of water vapor on particle surfaces has been proposed as one of the most promising techniques to promote particle growth (Fahnoe et al., 1951; Schauer, 1951; Lapple et al., 1955; Lancaster et al., 1971). Because of the difficulty in measuring the size distribution of water droplets smaller than several microns in diameter, the overall effect of condensation on the rate and extent of particle growth still remains unknown. In this study the rate and extent of particle growth by condensation were studied from both theoretical and experimental points of view. In order to effect condensation on particle surfaces, a supersaturated atmosphere of water vapor was produced by mixing hot saturated air with cold air into which several kinds of submicron particles, not consisting of soluble substances, were introduced. The size distribution of grown water droplets was measured by a new technique previously developed by the authors (1975).

Rate of Growth of Polydisperse Aerosol Particles

When a water droplet with radius r is put into a supersaturated atmosphere, the rate of growth of the droplet has been given as follows (Fuchs, 1959):

$$\frac{dr}{dt} = \frac{DM}{rR\rho_s T}\{Sp_s(T_\infty) - p_0(T_0, r)\}\left\{1 + \frac{p_0(T_0, r) + p_s(T_\infty)}{2p_t}\right\} \quad (1)$$

This equation is based on Maxwell's equation for the sta-

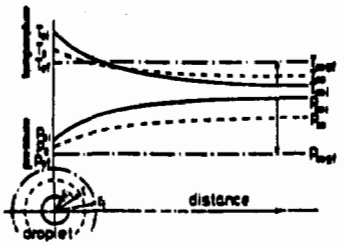

Figure 1. Illustration of temperature and pressure fields around a growing droplet.

tionary evaporation of a spherical droplet motionless relative to an infinite uniform medium and, in addition to the Maxwell equation, the correction for the effect of Stefan flow is made. S in the equation represents supersaturation, which is larger than unity in this study, but when S is less than unity, the equation represents the diminishing rate of a droplet by evaporation. p_0 represents the vapor pressure at the surface of a droplet which is assumed to be equal to its equilibrium pressure known as the Kelvin equation

$$p_0(T_0, r) = p_s(T_0) \exp \frac{2M\sigma}{\rho_w R T r} \tag{2}$$

The rise in temperature of a condensing droplet is given by the following equation taking account of Stefan flow:

$$T_0 = \frac{LDM}{KRT}\{Sp_s(T_\infty) - p_0(T_0, r)\} \times \left\{1 + \frac{p_0(T_0, r) + p_\infty(T_\infty)}{2p_t}\right\} + T_\infty \tag{3}$$

This equation is derived under the assumptions that heat transfer by convection and radiation is negligible and that the quantity of heat transferred to the media from the droplet equals the amount generated in condensation. Figure 1 illustrates the changes of temperature and pressure fields around a growing droplet which is put into a closed and insulated cell initially having a certain degree of supersaturation. The rate of growth of a single water droplet with radius r will then be determined by above equations. In order to apply these equations to aerosol particles instead of water droplets, one must assume that the surface of each particle is covered by a thin water film at the start of condensation. This assumption is based upon the instability of a supersaturated atmosphere, where water vapor immediately condenses upon any particles as the condensation nuclei. This will be discussed later. When aerosol particles are polydisperse, the change in size distribution of the growing particles is then derived from the conservation of mass

$$\frac{\partial n(r, t)}{\partial t} = -\frac{\partial}{\partial r}\left[n(r, t)\frac{dr(t)}{dt}\right] \tag{4}$$

Before computing the above equations, it is necessary to determine the degree of supersaturation, S. Consider a system where aerosol particles are steadily introduced into the supersaturated atmosphere which is produced by continuously mixing hot saturated air with cold air in an insulated chamber. Such a system may be thought of more simply as a system where a certain number of aerosol particles are put uniformly into a closed and insulated chamber containing air initially having a certain degree of supersaturation. In the system the degree of supersaturation will decrease as condensation increases, and after a sufficient time it approaches unity. The relation between the degree of supersaturation and the amount of condensed vapor may be easily understood with the aid of the humidity chart shown in

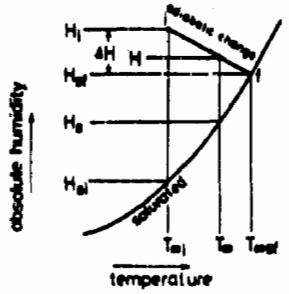

Figure 2. Change in humidity and temperature due to condensation.

Figure 2, where i indicates the initial state just before aerosol particles are introduced. When particles are suddenly dispersed uniformly into the chamber, condensation upon the particles occurs, and as a consequence there is a decrease in humidity and a simultaneous rise in the temperature of the air as the condensation progresses. Thus the change is indicated by the slope of the adiabatic change shown in Figure 2. Temperature, humidity, and supersaturation during the successive condensation are then given by the following expressions.

$$T_\infty = \frac{(H_i - H)L}{0.24 + 0.45H_i} + T_{\infty i} \tag{5}$$

$$H = H_i - \frac{4}{3}\pi\rho_w\left\{\int_0^\infty r^3 n(r, t)\,dr - \int_0^\infty r^3 n(r, 0)\,dr\right\} \tag{6}$$

$$S = \frac{p_\infty(T_\infty)}{p_s(T_\infty)} = \frac{H(0.622 + H_s)}{H_s(0.622 + H)} \tag{7}$$

ΔH in Figure 2, which will be important in a later discussion, indicates the quantity of condensable water vapor per unit mass of dry air or the quantity of water adhering to the total surface of the particles in unit mass of dry air. The value of ΔH is obtained from the following enthalpy and material balances in the case of mixing of hot saturated air with cold air.

$$R_h i_{sh} + (1 - R_h) i_{si} = i_{sf} + \Delta H i_{wf} \tag{8}$$

$$R_h H_s(T_h) + (1 - R_h) H_s(T_1) = H_s(T_f) + \Delta H \tag{9}$$

While the change of the system is unsteady, unsteady fields of temperature and pressure are established around each growing particle. It is difficult, however, to calculate the change in size distribution of particles strictly taking account of the unsteady fields. Then a quasi-stationary analysis, where temperature and pressure fields were considered to be constant during each short step of time, was made. It was assumed in the calculation that the initial size distribution of aerosol particles was of log-normal form. The size between 0.1 and 10 μ in diameter was divided into about 60 subdivisions on a log scale, and the time step was taken to be from 10^{-6} to 10^{-3} sec according to the rate of growth. The size distribution of newly formed particles after each time step was calculated numerically by the method of Kovetz and Olund (1969); the calculation was repeated until the degree of supersaturation became nearly equal to unity. The temperature dependence of the physical properties appearing in the above equations was taken into consideration in the computation. Some of the results of the calculation are shown in Figure 3. The figure indicates that the rates of growth are very rapid and the size distributions become narrower as particles grow. When the vapor pressure of the surface of droplets, $p_0(T_0, r)$, is close

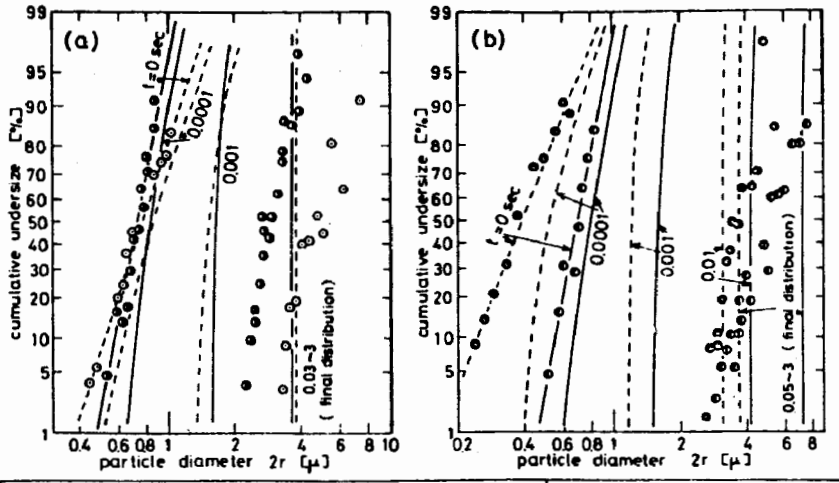

experimental conditions									change of D_v and σ_g					
particle					saturated air			ΔH	after 0.001 sec		at final time(0.05 ~ 3sec)			
key	material	n_0	D_{vi}, μ	σ_{gi}	T_h, °C	T_l, °C	R_h		D_{vm}	σ_{gm}	D_{vf}		σ_{gf}	
									cal.		exp.	cal.	exp.	cal.
○	tobacco	2.66×10^8	0.85	1.34	78	21	0.26	0.0070	1.63	1.11	5.06	3.81	1.26	1.021
⊙	stearic acid	3.31×10^8	0.75	1.20	80	20	0.27	0.0078	1.61	1.05	3.10	3.63	1.17	1.006
●	DOP	3.83×10^7	0.75	1.26	81	19	0.26	0.0075	1.65	1.05	6.20	7.30	1.35	1.002
●	carbon black	2.54×10^8	0.47	1.42	81	28	0.27	0.0067	1.26	1.05	3.95	3.71	1.23	1.006

Figure 3. Change in particle size distribution with time.

to the saturated vapor pressure, $p_s(T_\infty)$, in the present case, the growth rate of small droplet is generally greater than that of a large one as shown in eq 1. Thus the difference of growth rates will make the size distributions narrower in the figures. The final distributions in Figure 3 were taken as those when the growth rates of each droplet became nearly zero in the numerical calculation. Such distributions will be, strictly speaking, unstable, since the evaporation of smaller droplets among polydisperse droplets will occur with a decrease in supersaturation. This effect of evaporation, however, was so small in the calculation that the size distributions did not change significantly within a few seconds.

Estimation of the Extent of Particle Growth to Be Expected

The analysis described above was on the rate process. In this section a discussion will originate from another point of view. While ΔH represents the quantity of condensable water vapor per unit mass of dry air as described before, the following relation must be satisfied when all of the vapor corresponding to ΔH is assumed to condense upon particle surfaces.

$$\Delta H = \frac{4}{3}\pi\rho_s \left\{ \int_0^\infty r^3 n(r, \infty)\, dr - \int_0^\infty r^3 n(r, 0)\, dr \right\} = \frac{\pi}{6}(D_{vf}^3 - D_{vi}^3) n_0 \rho_s \quad (10)$$

This equation indicates that the volume mean diameter of grown particles, D_{vf}, can be evaluated when the value of ΔH and the volume mean diameter of particles before growth, D_{vi}, are known. When D_{vf}^3 is large enough compared with D_{vi}^3 and ρ_s is nearly unity as it may be in most cases, the volume mean diameter of grown particles, D_{vf}, can be written in a simpler form as

$$D_{vf} \simeq (6\Delta H/\pi n_0)^{1/3} \qquad (D_{vf}^3 \gg D_{vi}^3;\ \rho_s \simeq 1) \quad (11)$$

The straight line in Figure 4 shows this relation.

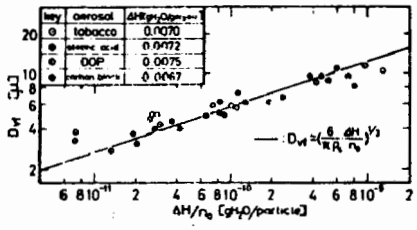

Figure 4. Volume mean diameter of grown particle.

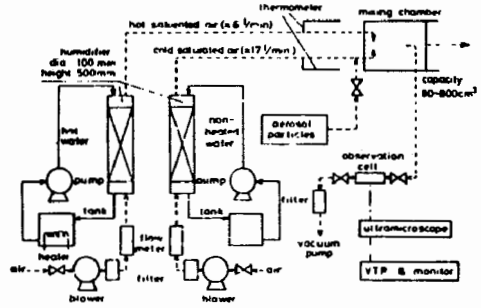

Figure 5. Schematic diagram of experimental apparatus.

Experimental Apparatus

Figure 5 indicates the schematic diagram of the experimental apparatus. Two kinds of saturated air, one of which was humidified by contact with hot water and the other with nonheated water, were continuously mixed in a mixing chamber to produce a supersaturated atmosphere. The degree of supersaturation or the quantity of condensable water vapor ΔH was controlled by changing their mixing ratio and the combination of their temperatures. Aerosols were continuously introduced into the supersaturated atmosphere at a constant rate. The size distributions of the aerosol particles used in the experiment were obtained by an ultramicroscopic size analysis (Yoshida et al., 1975) and

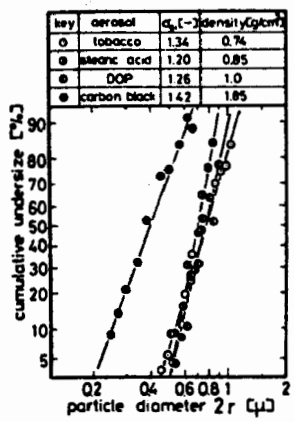

Figure 6. Size distributions of aerosol particles used.

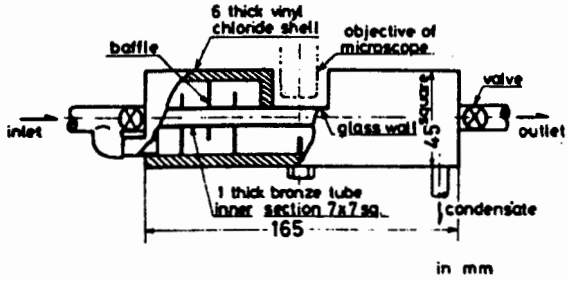

Figure 7. Observation cell of ultramicroscope.

are shown in Figure 6. The size distributions of grown particles were also determined by the same method. In order to prevent any change in the size of the water droplets due to evaporation or condensation, the temperature and pressure in the observation cell for the size analysis were kept the same as those in the mixing chamber. The double-tube cell shown in Figure 7 was used for this purpose.

Experimental Results and Discussion

As discussed before, the rate of growth was so fast compared with the time scale of measurement that the size distribution of a growing particle at each stage of the elapsed time could not be observed. However, observations obtained by varying the residence time of particles in the mixing chamber suggested that the particle growth was completed within 1 sec. Some of the experimental results of the size distribution of grown particles were plotted in Figure 3. The width of the size distribution of grown particles did not become narrower as compared to theory. The wider distribution obtained from the experiments was thought to be caused by a lack of spatial uniformity in the degree of supersaturation. The widths of size distributions of grown particles undergoing condensation were observed, in all cases including those in Figure 3, to be neither wider nor narrower.

The estimation of the volume mean diameter of the grown particles, which would be important for industrial purposes, was determined by experiments. Figure 4 shows the comparison of an estimated line with the experimental results. The abscissa of the figure corresponds to the mean quantity of condensable vapor per single particle. The figure indicates that even the hydrophobic particles, such as carbon black and D.O.P., grow well. The growth of such particles may be caused by the instability of a supersaturated atmosphere as described previously. This fact will be especially important when the present technique is developed into industrial applications.

For instance, one may consider exhaust gas which contains dust particles 1 μ in volume mean diameter, 2.5 g/cm^3 in density, and 500 mg/m^3 in concentration. In this case, the dust particles will grow to 3 μ in volume mean diameter when ΔH of 0.005 g of condensable vapor per gram of dry air is established.

Conclusion

The rate and the extent of growth of polydisperse aerosol particles introduced into a supersaturated atmosphere were studied, and the following results were obtained. (1) The rate of growth of aerosol particles was very rapid. The width of size distributions of grown particles obtained experimentally was not narrow, while a narrower distribution was expected from the theoretical analysis. (2) The extent of particle growth was evaluated in volume mean diameter and was confirmed by experiments. (3) Even the hydrophobic particles grew well.

These results suggested the particle growth by condensation will be one of the most promising preconditioning techniques for dust collection. The technique of establishing a supersaturated atmosphere will be important for the industrial application of these results.

Acknowledgment

F. Nomura, T. Yasumune, and T. Miyazaki were very helpful in the experimental work.

Nomenclature

D = diffusion coefficient of vapor, cm^2/sec
D_{vi}, D_{vm}, D_{vf} = volume mean diameter before, in the middle of, and after growth, respectively, μ or cm
H = absolute humidity, g of H_2O/g of dry air
ΔH = condensable water vapor, g of H_2O/g of dry air
i = enthalpy, cal/g of dry air
K = heat conductivity, cal/cm sec °C
L = latent heat of condensation, cal/g
M = molecular weight of condensing substance, g/mol
n = particle number concentration, 1/g of dry air
n_0 = total particle number concentration, 1/g of dry air
p = vapor pressure, mmHg
R = gas constant, cm^3 mmHg/mol °C
r = radius of particle, μ or cm
R_h = mixing ratio, g of dry air of hot saturated air/g of dry air
S = degree of supersaturation defined by eq 7
T = temperature, °C
$\bar{T}$ = mean temperature between T_0 and T_∞, °C
t = time, sec

Greek Letters

ρ_s = density of condensed liquid, g/cm^3
σ = surface tension, dyn/cm
σ_{gi}, σ_{gm}, σ_{gf} = geometric standard deviation before, in the middle of and after growth, respectively

Subscripts

f = final state shown in Figure 2
h = hot saturated air
i = initial state
l = cold saturated air
s = saturated
t = total
w = water
0 = particle surface
∞ = far away from particle

Literature Cited

Fahnoe, F., Lindroos, A., Abelson, R. J., *Ind. Eng. Chem.*, **43**, 1336 (1951).
Fuchs, N. A., "Evaporation and Droplet Growth in Gaseous Media", Pergamon Press, London, 1959.
Kovetz, A., Olund, B., *J. Atmos. Sci.*, **26**, 1060 (1969).
Lancaster, B. W., Strauss, W., *Ind. Eng. Chem., Fundam.*, **10**, 362 (1971).
Lapple, C. E., Kamack, H. J., *Chem. Eng. Prog.*, **51** (3), 110 (1955).
Schauer, P. J., *Ind. Eng. Chem.*, **43**, 1532 (1951).
Yoshida, T., Kousaka, Y., Okuyama, K., *Ind. Eng. Chem., Fundam.*, **14**, 47 (1975).

Received for review December 16, 1974
Accepted September 5, 1975

Presented at the Chemical Engineering Meeting in Japan, April 1974.

STABILITY OF FINE WATER DROPLET CLOUDS

YASUO KOUSAKA, KIKUO OKUYAMA,
KENJI SUMI AND TETSUO YOSHIDA

Department of Chemical Engineering, University of Osaka Prefecture, Sakai, Japan

STABILITY OF FINE WATER DROPLET CLOUDS

Abstract

The stability of fine water droplet clouds was studied for two standpoints. In the first, the rate of evaporation of monodisperse water droplets was evaluated by numerically solving the modified Maxwell's equation assuming the cellular model for a droplet cloud. In the second, the equilibrated system, where a water droplet cloud is steadily mixed with unsaturated air, was analysed on the basis of enthalpy and material balance of the system to evaluate the total volume change of the droplets. Some of these analyses were verified by the experiment using the ultramicroscopic technique which is useful for droplet size analysis.

1. INTRODUCTION

It is well known that under a certain supersaturation of water vapor excess water vapor condenses upon aerosol particles as the condensation nuclei to generate small water droplets. Such water droplet clouds are usually found when a combustion gas is cooled, a highly humid gas in high temperature is mixed with that in low temperature, or steam is injected into a gas. These droplets often have diameters less than ten microns and they are thought to be unstable because of their high vapor pressure at the surface. When these droplets being contained in an industrial exhaust gas are required to be collected from the gas, it will be necessary to evaluate the effect of unstability of droplets or the decrease in droplet sizes and number concentrations in a collector system under various operating conditions. The stability of droplet clouds is also important in measuring droplte size distribution and in evaluating the behavior of atmospheric aerosols.

In discussing about the stability of water droplet clouds, two kinds of approach to the subject were made in this paper. In the first, the rate of evaporation of monodisperse pure water droplets, which are led uniformly into a closed vessel initially containing air having certain humidity and temperature, is discussed using cellular model(Fuchs (1959) Zung (1967)). It is the main purpose in this discussion to evaluate the lifetime or the time required to be equilibrated of water droplets in terms of various initial sizes and number concentrations of droplets as well as various

initial air conditions. In the second, the equilibrium state of droplets in the system where a droplet cloud is steadily mixed with unsaturated fresh air will be discussed from enthalpy and material balance of the system for various conditions.

As the experimental technique, the ultramicroscopic size analysis previously developed by the authors (1975) was applied. Because of the difficulty in measuring the unsteady size change during rapid evaporation, most of the experiment were limited to verify the analysis of the equilibrium state of droplet clouds.

2. RATE OF EVAPORATION OF A WATER DROPLET CLOULD

In this section, the rate of evaporation of a water droplet cloud is discussed using the cellular model(Fuchs (1959) Zung (1967)). In the cellular model, a droplet cloud, where the droplets are distributed equidistantly each other, is assumed, and the cloud is divided into a number of identical cubic cells each of which is supposed to contain a single droplet in the center. The length of the edge of such a cube is then given as:

$$b = \sqrt[3]{1/n_0'} \qquad (1)$$

In this model the evaporation of a droplet cloud may be reduced to the single droplet evaporation. In the conditions where n_0' is less than about 10^6 particles/cm^3 and the droplet radius is less than several microns, the rate of change in droplet

radius r′ in one cell almost agrees with that of an isolated droplet according to Fuchs (1959) and Davies (1973), which can given as :

$$\frac{dr'}{dt'} = -\frac{DM}{r'\rho_s R}\left\{\frac{p_0(T_0,r')}{T_0} - \frac{Sp_s(T_\infty)}{T_\infty}\right\}\left\{1 + \frac{p_0(T_0,r')+Sp_s(T_\infty)}{2p_t}\right\} \times\left\{\frac{Kn+1}{1.333Kn^2+1.71Kn+1}\right\} \quad (2)$$

S in the equation represents the degree of saturation, and $p_0(T_0,r')$ represents the vapor pressure at the surface of a droplet which is assumed to be equal to its equilibrium pressure known as the Kelvin's equation.

$$p_0(T_0,r') = p_s(T_0)\exp\left(\frac{2M\sigma}{\rho_s RT_0 r'}\right) \quad (3)$$

The fall in temperature of a evaporating droplet is given by the following equation taking account of Stefan flow.

$$T_0 = T_\infty - \frac{LDM}{KR}\left\{\frac{p_0(T_0,r')}{T_0} - \frac{Sp_s(T_\infty)}{T_\infty}\right\}\left\{1+\frac{p_0(T_0,r')+p_\infty(T_\infty)}{2p_t}\right\} \quad (4)$$

The rate of evaporation of a single droplet in a cell will be determined by the above equations, if the changes in temperature T_∞ and vapor pressure $p_\infty(T_\infty)$ at the periphery of the cell are evaluated as follows.

When the radius of a spherical droplet, r_1', decreases to r_2' according to Eq.(2), the quantity of evaporated water vapor, or water vapor diffusing to the medium, per unit mass of dry air can be given as follows,

$$\Delta H_e = 4\pi(r_1'^3 - r_2'^3) n_w \rho_s / 3 \tag{5}$$

where, $n_w = n_0'/v_H$ (6)

In consequence of evaporation of a droplet, there are an increase in humidity and a simultaneous fall in temperature of air. These changes are indicated by the slope of the adiabatic change in the humidity chart as shown in Fig. 1. The temperature, the humidity and the degree of saturation during the successive evaporation are given by the following expressions.

$$T_{\infty 2} = T_{\infty 1} - \Delta H_e L/(0.24 + 0.45H_2) \tag{7}$$

$$H_2 = H_1 - \Delta H_e \tag{8}$$

$$S = p_\infty(T_\infty)/p_s(T_\infty) = H(0.622+H_s)/\{H_s(0.622+H)\} \tag{9}$$

While the change of the system is unsteady, the unsteady fields of temperature and pressure are established around each evaporating droplet. It is difficult, however, to calculate the change in particle radius strictly taking account of the unsteady fields. Then a quasi-stationary analysis, where temperature and pressure fields were considered to be constant during each step of time, was made. In calculation, the change in droplet radius was first evaluated by numerically solving Eq.(2) with Runge-Kutta-Merson method, and then the consequent change in the state of surrounding air was calculated by Eq.(5)~Eq.(9), and this step was repeated until the driving force for evaporation became zero. The temperature dependence of the physical properties appearing in the above equations was taken into consideration in the computation.

Some of the results thus calculated are shown in Figs. 2 and 3. Fig. 2 shows the time dependent change in radius of evaporating droplets under various particle number concentrations n_0' in intially saturated air(S=1). It can be seen that the fine droplets of micron order and having low number concentration tend to evaporate even in saturated air because of the Kelvin's effect. The broken lines in the figure show the analytical solutions by Davies (1973) for the evaporation rate of an isolated droplet(refer to Appendix). With the increase of number concentration n_0', the decreasing rate in droplet radius becomes slow, and at n_0' larger than about 10^5 particles/cm^3 the droplets of 0.5 μ in radius seems to be almost stable. Fig. 3 shows the dependence of evaporation rate of droplets on the degree of saturation under various conditions. As seen from Figs. 2 and 3, the stability of water droplet clouds depends greatly upon the initial degree of saturation S_0 and number concentration n_0'. Under the low values of S_0 and n_0', the quantity of water vapor produced by evaporation of droplets is not enough to saturate surrounding air and therefore droplets disappear completely. On the other hand, under the high values of S_0 and n_0', droplets continue to evaporate until the equilibrium vapor pressure as given by Eq.(3) is attained and because of the sufficient amount of water vapor to be evaporated in this case, the droplets are stable after a slight change in size.

3. EVALUATION OF THE CHANGE IN DROPLET SIZE UNDER EQUILIBRIUM

Since the change in radius of a droplet by evaporation proceeds in a short time, as calculated in the former section, the droplet cloud which we can actually observe will be in the equilibrium state. Therefore there is an importance to analyse the equilibrium state of a droplet cloud for various situations.

Figure 4 shows a schematic diagram to be analysed in this section. Such a system, for instance, may be interpreted by that where an exhaust gas containing a certain amount of small water droplets encounters unsaturated air resulted from some leakage in a dust collector system.

As shown in Fig. 4, when air containing droplets is mixed with unsaturated fresh air at a certain mass ratio, the amount of water droplet containing in the resultant air is expected to be decreased. In such a system the following enthalpy and material balance equations are derived under the assumption of the existence of droplets in the equilibrium state after mixing of air, that is, $\Delta H_f \geq 0$:

(material balance of water)

$$R_m H_m + (1-R_m)H_{si} + (1-R_m)\Delta H_i = H_{sf} + \Delta H_f \qquad (10)$$

(enthalpy balance of the system)

$$R_m i_m + (1-R_m)i_{si} + (1-R_m)H_i i'_{wi} = i_{sf} + \Delta H_f i'_{wf} \qquad (11)$$

Another expression of Eq.(11) may also be written as follows:

$$R_m\{0.24T_m+(597.1+0.45T_m)H_m\}+(1-R_m)\{0.24T_{si}+(597.1+$$

$$+0.45T_{si})H_{si}\} + (1-R_m)\Delta H_i T_{si} = 0.24T_{sf} + (597.1+0.45T_{sf})H_{sf} + \Delta H_f T_{sf} \quad (11')$$

where, $H_{sf} = f(T_{sf})$ (12)

ΔH in the equations represent the mass of water droplets suspending in air per unit mass of dry air, and R_m the mixing ratio of unsaturated air to resultant air in mass basis of dry air. Since the Kelvin's effect is small enough in the case of droplets larger than 0.1 μ in diameter, it was neglected in the following analysis.

In the case of $\Delta H_f = 0$ The quantity of water droplets after mixing of unsaturated air, ΔH_f, in Eqs.(10) and (11) decreases with the increase of the mixing ratio of unsaturated air, R_m, and finally ΔH_f becomes zero, that is, all droplets disappear by evaporation. The relation among each variables appears in the above equations at such a critical condition can be calculated by putting $\Delta H_f=0$ in the equations. If the conditions before mixing are known, the values of R_m, H_{sf} and T_{sf} are obtainable from Eqs.(10), (11) and (12). Some of the calculated results are shown in Figs. 5 and 6.

In the case of $\Delta H_f > 0$ The containable quantity of water droplets after mixing of air, ΔH_f kg water per kg dry air, can be essentially evaluated by Eqs.(10), (11) and (12). The relation among the variables in the equations, however, is more complicated in this case. Some of the calculated results are shown in Figs. 7 and 8.

Evaluation of ΔH_f and D_{vf}. If the initial conditions of a droplet cloud and the state of unsaturated mixing air are given, the quantity of water droplets after mixing of air, ΔH_f, can be evaluated as described above. The volume mean diameter of the droplets after mixing of unsaturated air is then evaluated knowing the number concentration of the droplets, n_w, as follow.

$$D_{vf} = \left\{ \frac{\Delta H_f}{(\pi/6) n_w \rho_s} \right\}^{1/3} \tag{13}$$

4. EXPERIMENTAL APPARATUS AND METHOD

Figure 9 shows the schematic diagram of the experimental apparatus to examine the analysis in section 2. The water droplet cloud was steadily generated by mixing hot saturated air with cold saturated air by the authors (1976). The hot saturated gas contains small dust particles having diameters around 0.05 μ which are generated in burning fuel gas and the gas is mixed with cold saturated air to produce supersaturation which causes droplet formation on the dust particles as condensation nuclei. Thus obtained saturated air containing a certain amount of small water droplets was continuously led into a vinyl chloride pipe with diameter of 26 mm to make a turbulent flow. The length of the pipe was 10 m, at inlet and outlet of the pipe the aerosols were sampled with isokinetic condition. The second experiment to observe the analysis in section 3 was made by introducing the saturated air containing droplets into a mixing chamber instead of the pipe, where unsaturated

air was mixed. Then a part of the mixture was drawn out for observation. Size analysis and determination of concentration of droplets were made by the same method using an ultramicroscope as those previously developed by the authors. In order to prevent any change in size of droplets due to evaporation or condensation during observation, the temperature and the pressure in the observation cell must be kept same as those in the mixing chamber. A heat exchanger type cell as shown in Fig. 10 was used for this purpose.

5. EXPERIMENTAL RESULTS AND DISCUSSIONS

Fig. 11 indicates the comparison of the particle size distribution between at inlet and outlet of the pipe. The residence time of droplets in the pipe is about 4 second in this case. If the evaporation theory of an isolated droplet is applied to this case the droplets smaller than about 1.6 μ disappear by evaporation. As seen from the graph, however, no appreciable change in the droplet size distribution occurs. This fact will be reasonable because a droplet cloud having high number concentration, 10^6 particles/cm^3 in this experiment, is expected to be stable from the analysis shown in Fig. 2.

Fig. 12 shows some examples of droplet size distributions obtained by the second experiment where the droplet cloud is mixed with unsaturated air in a mixing chamber. Fig. 12(a) is the size distribution of droplets before mixing of unsaturated air, and Figs. 12(b) and (c) are those after mixing of

unsaturated air. Slight difference is found among these three distributions, whereas fair difference among them in particle number concentration is found. All of the other experimental results showed the same tendency as those illustrated in these figures. Loss of water droplets due to mixing of unsaturated air shown in Figs. 12 (b) and (c) will be caused by evaporation of some of the droplets.

Since the vapor pressure of small droplets is higher than that of larger ones as expected by the Kelvin's equation, the droplets once decreased their sizes for a certain reason, for instance local lack of uniformity of humidity, can easily evaporate. The smaller the droplets becomes, the quicker progresses their evaporation, and in consequence smaller droplets may not exist. It is an interesting phenomena that droplet sizes do not decrease uniformly but number concentration only decreases by mixing of unsaturated air, preserving the initial droplet size distribution itself. This phenomena will not be undesirable for dust collection, because some of the droplets produced by condensation upon small dust particles decrease their sizes to those of the former small dust particles which are difficult to collect.

Fig. 13 shows the comparison of the mixing ratios, R_m, calculated from Eqs.(10), (11) and (12) with those observed, when droplets just disappear by evaporation, that is, $\Delta H_f = 0$. Good correlation is found between them.

Some examples of the experimental results for $\Delta H_f > 0$ are shown in Figs. 14 and 15. Fig. 14 shows the effect of the

mixing ratio R_m and the temperature of mixing air T_m on the quantity of droplets remaining in air, ΔH_f, which was determined by Eq.(13). This figure suggests that loss of droplets is significant, when leakage of fresh air having high temperature into a droplet cloud exists. The deviation of the experimental results from the calculated curves may be caused by the experimental error of D_{vf} which effects on ΔH_f at third power as seen in Eq.(13). Fig. 15 shows the relation between the temperature after mixing of unsaturated air, T_{sf}, and the mixing ratio R_m. It is obvious that T_{sf} decreases with R_m because the droplet evaporation requires latent heat.

6. CONCLUSION

The stability of pure water droplet clouds was studied for two standpoints. In the first, the rate of evaporation of monodisperse water droplets was evaluated by numerically solving the modified Maxwell's equation assuming the cellualr model for a droplet cloud. The lifetime of a droplet cloud or the time required for a cloud to be equilibrated was illustrated for some typical conditions for the better understanding of the phenomena. The experimental verification for the analysis, especially for the unsteady droplet size change, could not be made because of the difficulty in measuring the droplet size undergoing rapid evaporation. However, for the equilibrated state, which is easily attained in a droplet cloud with high number concentrations, reasonable experimental results were

obtained using the ultramicroscopic technique.

In the second, the equilibrated system, where a water droplet cloud is steadily mixed with unsaturated air, was analysed on the basis of enthalpy and material balance of the system to evaluate the quantitative change of the total volume of the droplets. The analysis was verified by experiemtns. As to the manner of the decrease in total volume of droplets, the unexpected decrease in droplet number concentration was observed instead of droplet size change.

ACKNLWLEGMENT

Y. Sakata was very helpful in the experimental work.

APPENDIX

Davies (1973) derived the following equations expressing the decrease in size of an isolated liquid particle due to evaporation for two situations:

(i) Evaporation of liquid particle into a vapor-saturated air(S=1).

$$\frac{dy}{dt'} = - D_f K' \frac{y+1}{y(y^2+1.71y+1.333)} \qquad \text{(A-1)}$$

(ii) Evaporation of liquid particle into a vapor-free air (S=0)

$$\frac{dy}{dt'} = - D_f (1+K'/y) \frac{y+1}{y^2+1.71y+1.333} \qquad \text{(A-2)}$$

where, $D_f = DM\rho_s/RT\rho_s\lambda^2$, $K' = 2M\sigma/RT\rho_s\lambda$, $y = r'/\lambda$

REFERENCES

Davies, C. N. (1973) Faraday Simp. of Chem. Soc., No.7, 34.

Fuchs, N. A. (1959) Evaporation and droplet growth in gaseous media, Pergamon Press.

Yoshida, T., Kousaka, Y. and Okuyama, K. (1975) Ind. Eng. Chem. Fundam. 14, 47.

Yoshida, T., Kousaka, Y. and Okuyama, K. (1976) Ind. Eng. Chem. Fundam. 15, 37.

Zung, J. T. (1967) J. Chem. Phys. 46, 2064.

Nomenclarure

b	: length of the edge of a cubic cell	[cm]
D	: diffusion coefficient of vapor	[cm^2/sec]
D_v	: volume mean diameter of the droplets	[μ] [cm]
D_f	: diffusion factor used in appendix	[1/sec]
H	: absolute humidity	[kg H_2O/kg dry air]
ΔH_e	: quantity of evaporated water vapor	[kg H_2O/kg dry air]
ΔH	: quantity of water droplets	[kg H_2O/kg dry air]
i	: enthalpy	[kcal/kg dry air]
Kn	: Knudsen number ($=\lambda/r'$)	[-]
K	: heat conductivity	[kcal/m sec °C]
K'	: Kelvin factor used in appendix	[-]
L	: latent heat of vaporuzation	[kcal/kg]
M	: molecular weight of evaporating substance	[kg/kmole]
n_0'	: droplet number concentration	[particles/cm^3]
n_w	: droplet number concentration on mass basis	[particles/kg dry air]
p	: vapor pressure	[mmHg]
p_t	: total pressure	[mmHg]
R	: gas constant	[m^3 mmHg/kgmole °C]
R_m	: mixing ratio	[kg unsaturated air in dry air basis/kg total dry air]
r'	: droplet radius	[μ] [cm]
r_g'	: geometric mean radius	[μ] [cm]
S	: degree of saturation	[-]
T	: temperature	[°C] [°K]

t'	: time	[sec]
v_H	: humid volume	[m^3/kg dry air]
y	: ($=Kn^{-1}$)	[-]

Greek letters

λ	: mean free path	[cm]
ρ_s	: density of droplet	[kg/m^3]
σ	: surface tension	[dyne/cm]
σ_g	: geometric standard deviation	[-]
ϕ	: percentage humidity	[%]

Subscripts

f	: final state of air after mixing
i	: initial state of air before mixing which contains water droptets
m	: unsaturated mixing air
s	: saturated
w	: water
0	: droplet surface
∞	: far away from droplet

Superscript

'	: for water

Capations of figures

Fig. 1 Change in humidity and temperature due to evaporation

Fig. 2 Evaporation of fine water droplet clouds into vapour-saturated air

Fig. 3 Evaporation of fine water droplet clouds into air with various degrees of saturation

Fig. 4 Schematic diagram of the system to be analysed

Fig. 5 Correlation among mixing ratio R_m, mixing air temperature T_m and percentage humidity ϕ_m in the case of $\Delta H_f = 0$

Fig. 6 Correlation among mixing ratio R_m, mixing air temperature T_m, droplet quantity contained in air before mixing ΔH_i and temperature of the same air T_{si} in the case of $\Delta H_f = 0$

Fig. 7 Effects of the quantity of initial droplets on those after mixing of unsaturated air

Fig. 8 Effects of every variable on containable droplet quantity, ΔH_f, after mixing of unsaturated air

Fig. 9 Schematic diagram of the experimental apparatus

Fig.10 Observation cell

Fig.11 Comaprison of the particle size distribution between at inlet and outlet of the pipe

Fig.12 Change in size and number concentration of droplets before and after mixing of unsaturated air

Fig.13 Comparison of mixing ratios, R_m, calculated and observed in the case of $\Delta H_f = 0$

Fig.14 Effect of mixing ratio R_m and temperature of mixing air T_m on remaining droplet quantity ΔH_f

Fig.15 Effect of mixing ratio R_m and temperature of mixing air T_m on air temperature after mixing of unsaturated air, T_{sf}

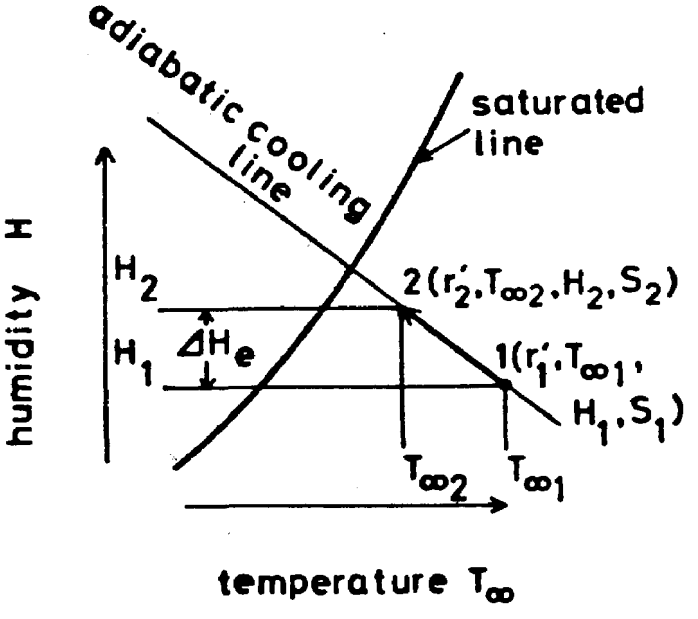

Fig. 1 Change in humidity and temperature due to evaporation

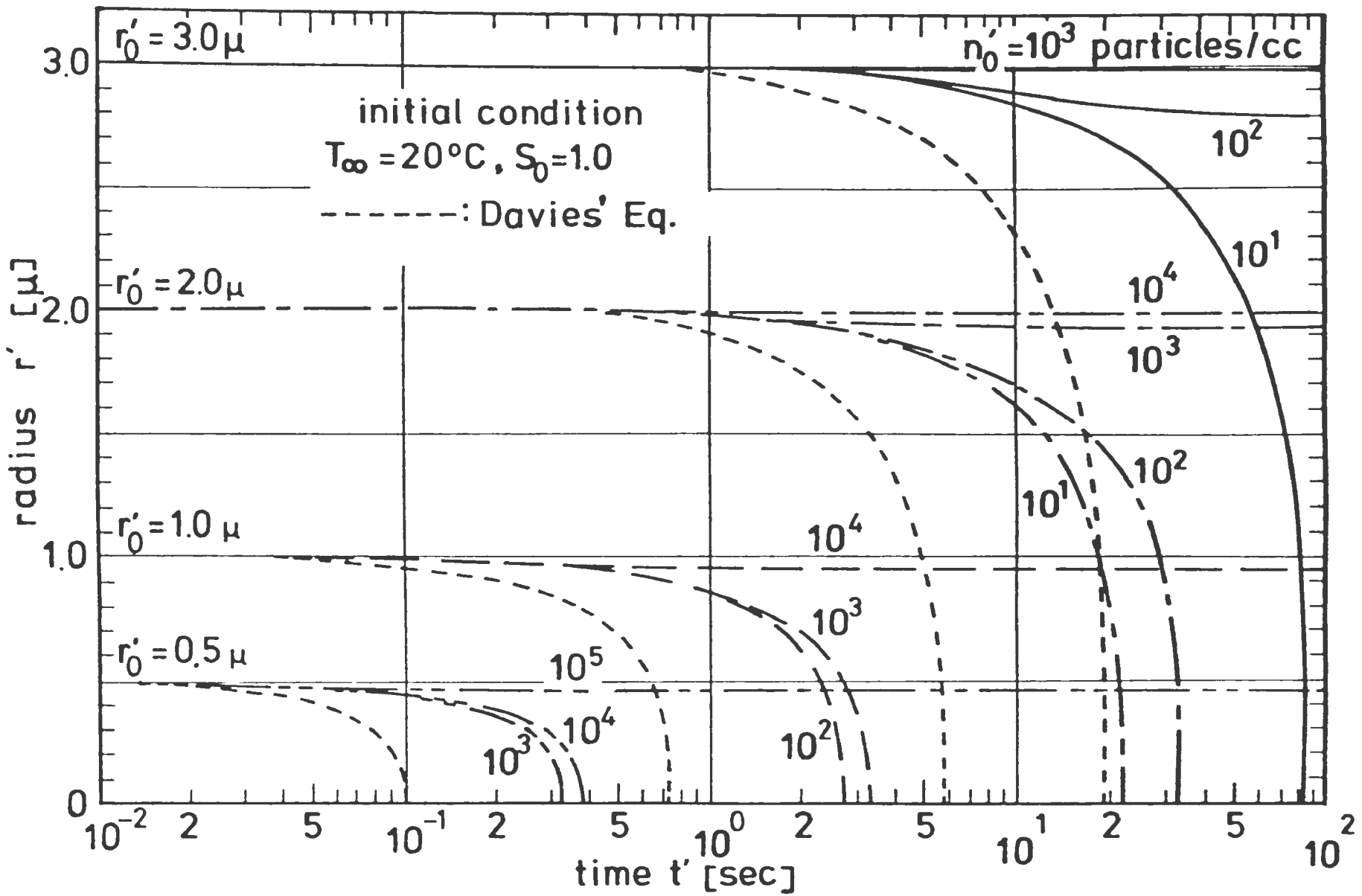

Fig. 2 Evaporation of fine water droplet clouds into vapour-saturated air

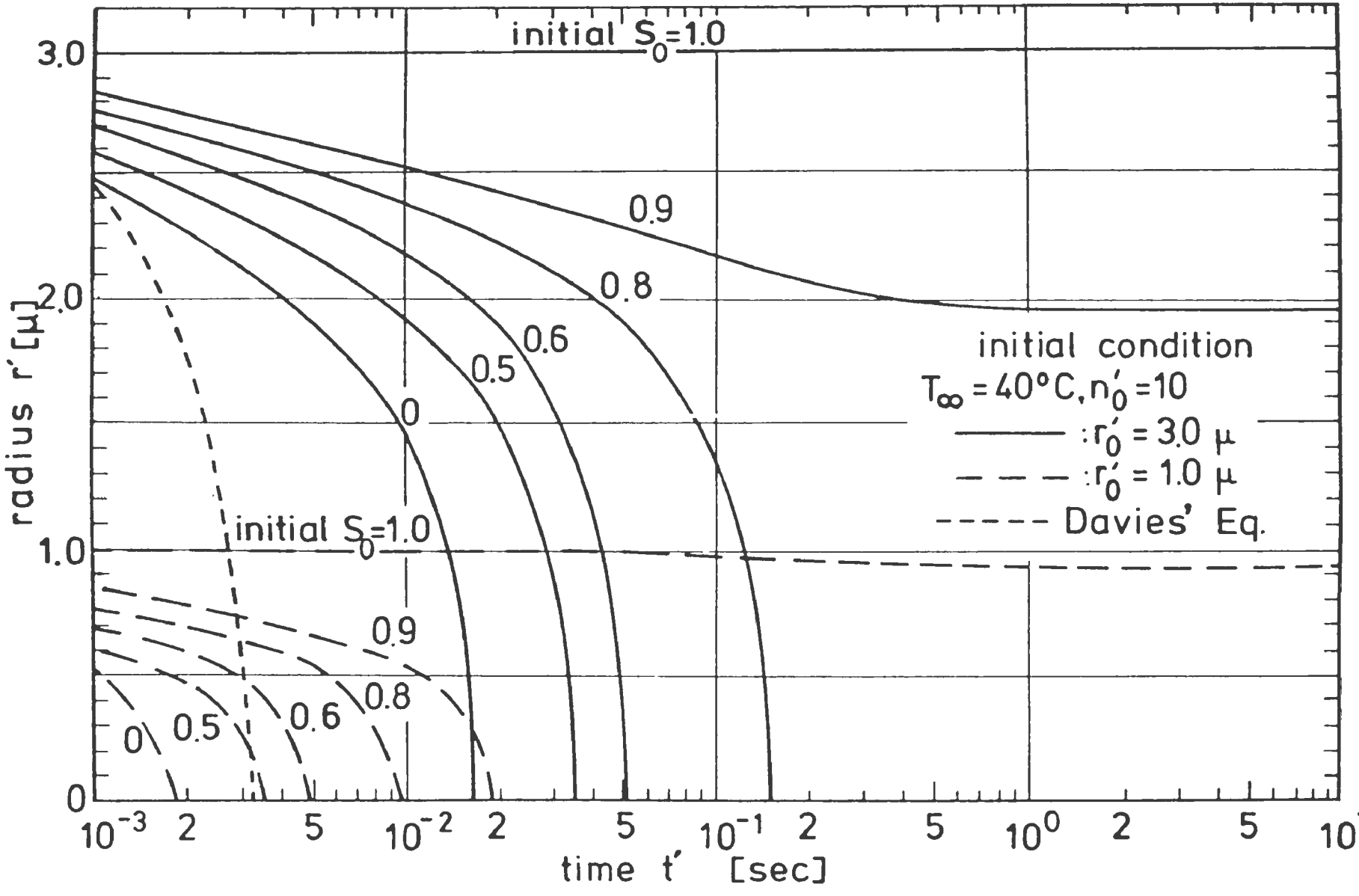

Fig. 3 Evaporation of fine water droplet clouds into air with various degrees of saturation

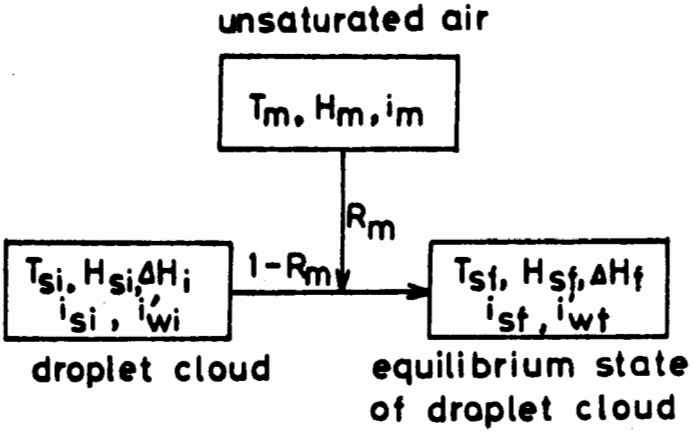

Fig. 4 Schematic diagram of the system to be analysed

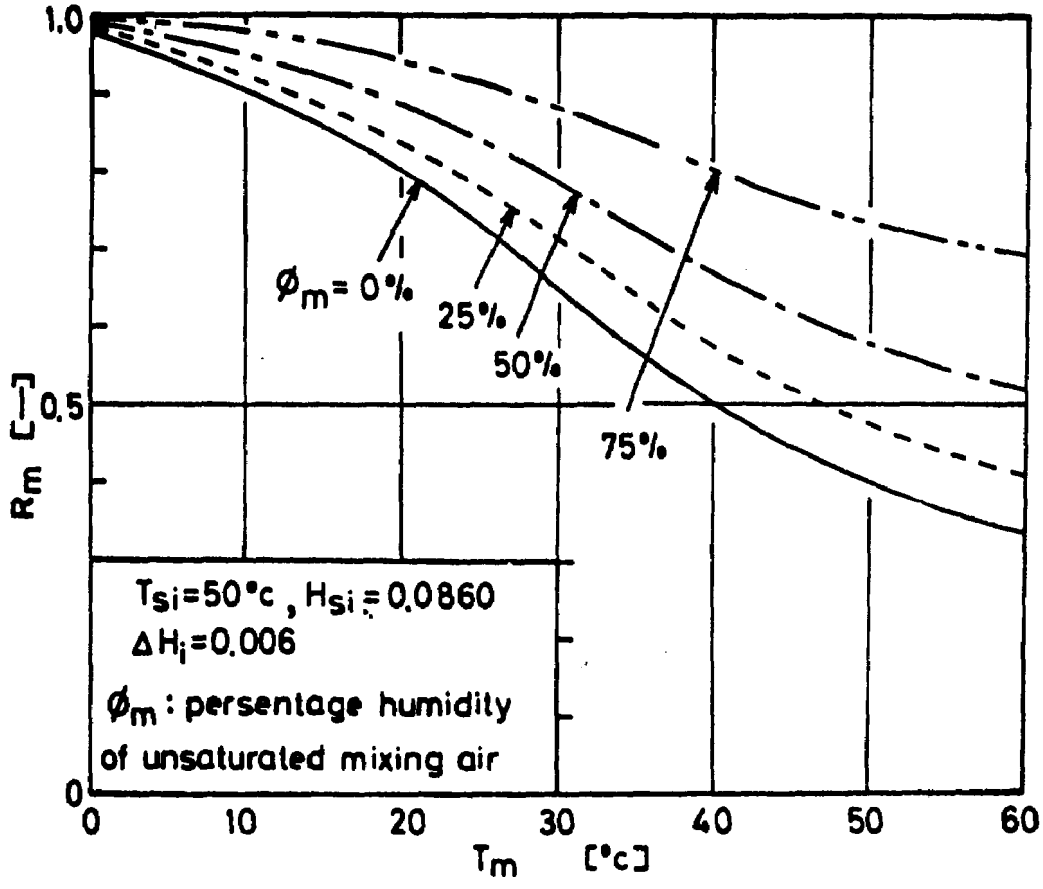

Fig. 5 Correlation among mixing ratio R_m, mixing air temperature T_m and percentage humidity ϕ_m in the case of $\Delta H_f = 0$

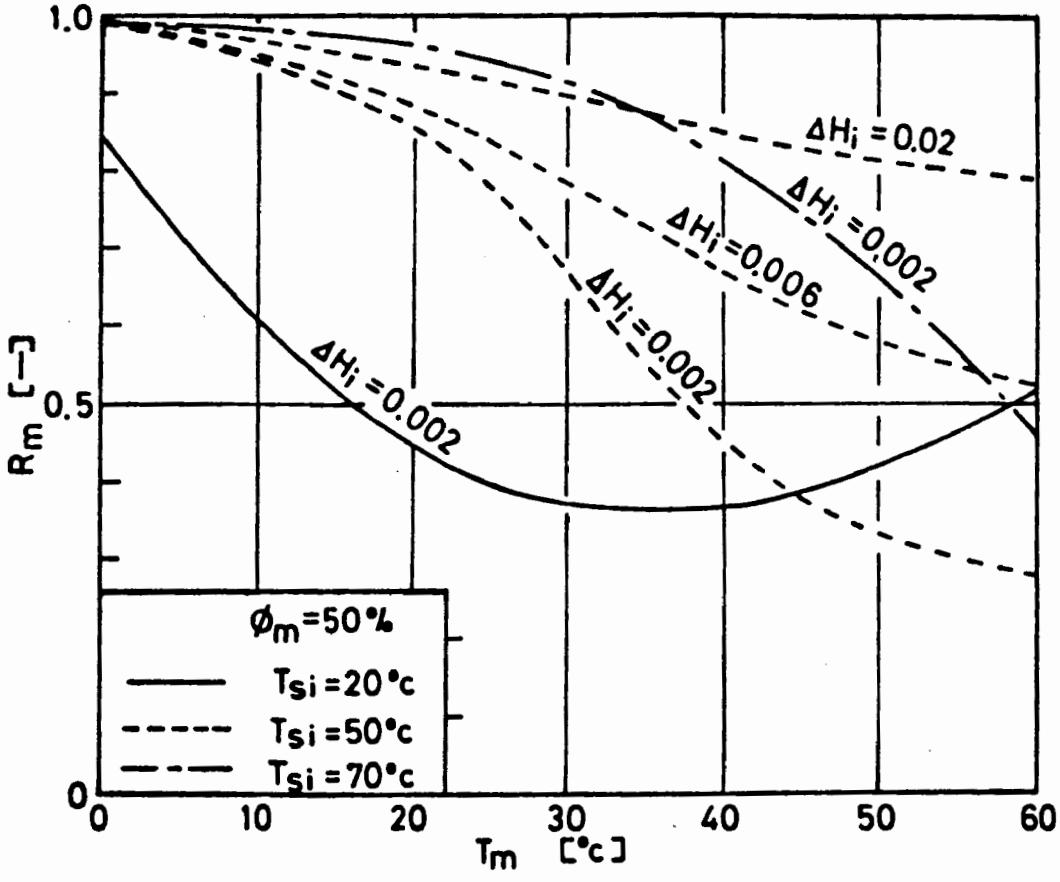

Fig. 6 Correlation among mixing ratio R_m, mixing air temperature T_m, droplet quantity contained in air before mixing ΔH_i and temperature of the same air T_{si} in the case of $\Delta H_f = 0$

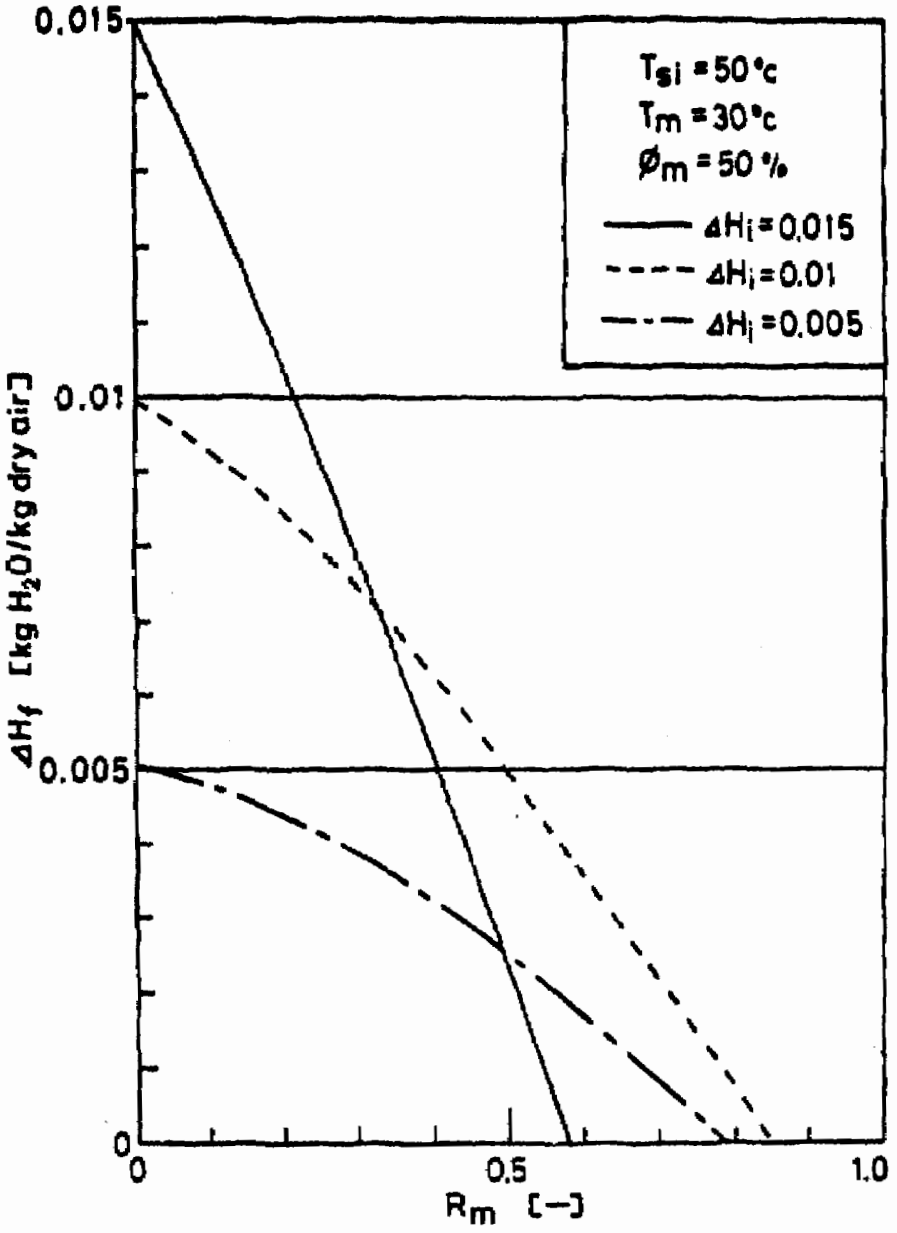

Fig. 7 Effects of the quantity of initial droplets on those after mixing of unsaturated air

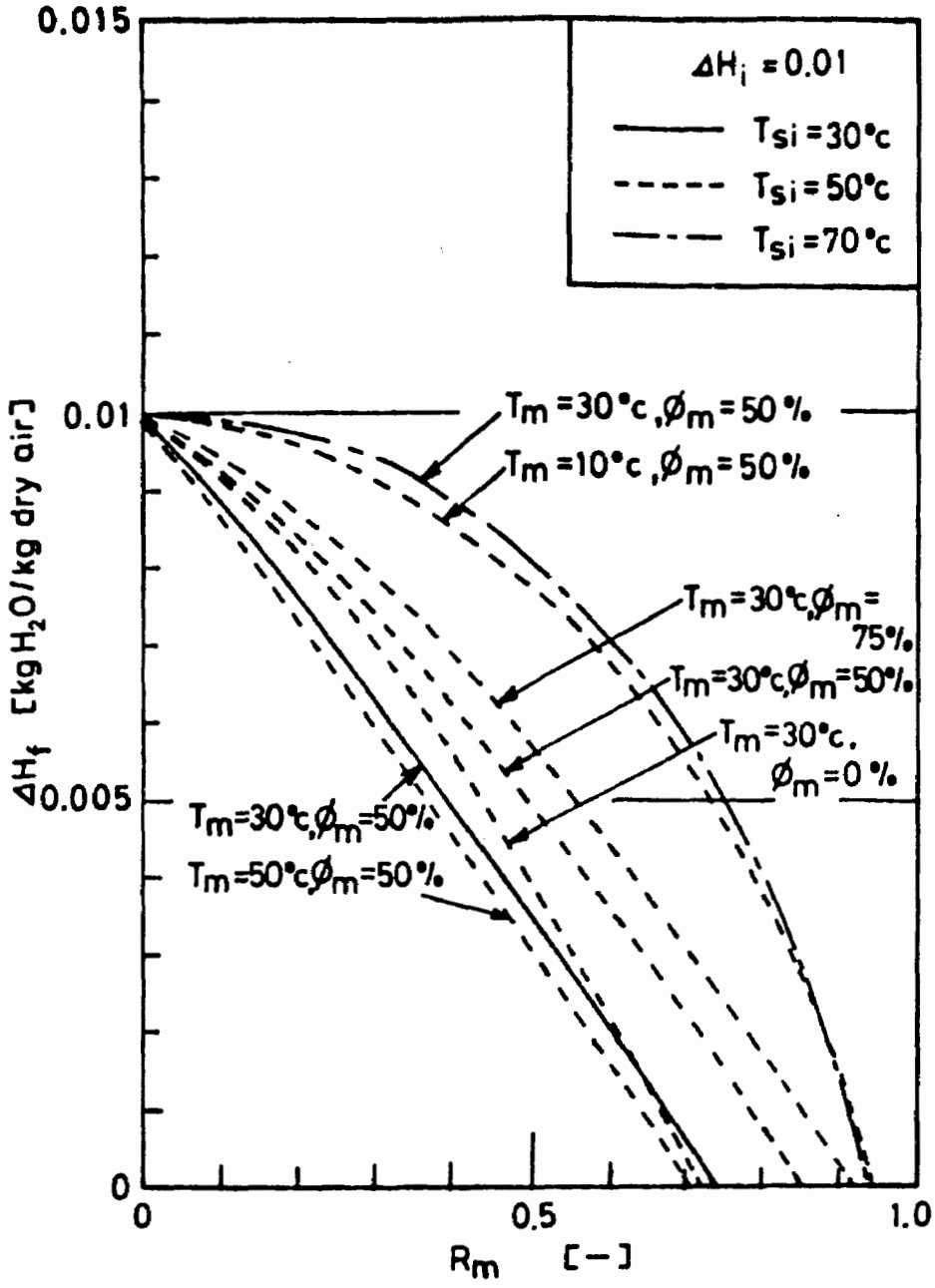

Fig. 8 Effects of every variable on containable droplet quantity, ΔH_f, after mixing of unsaturated air

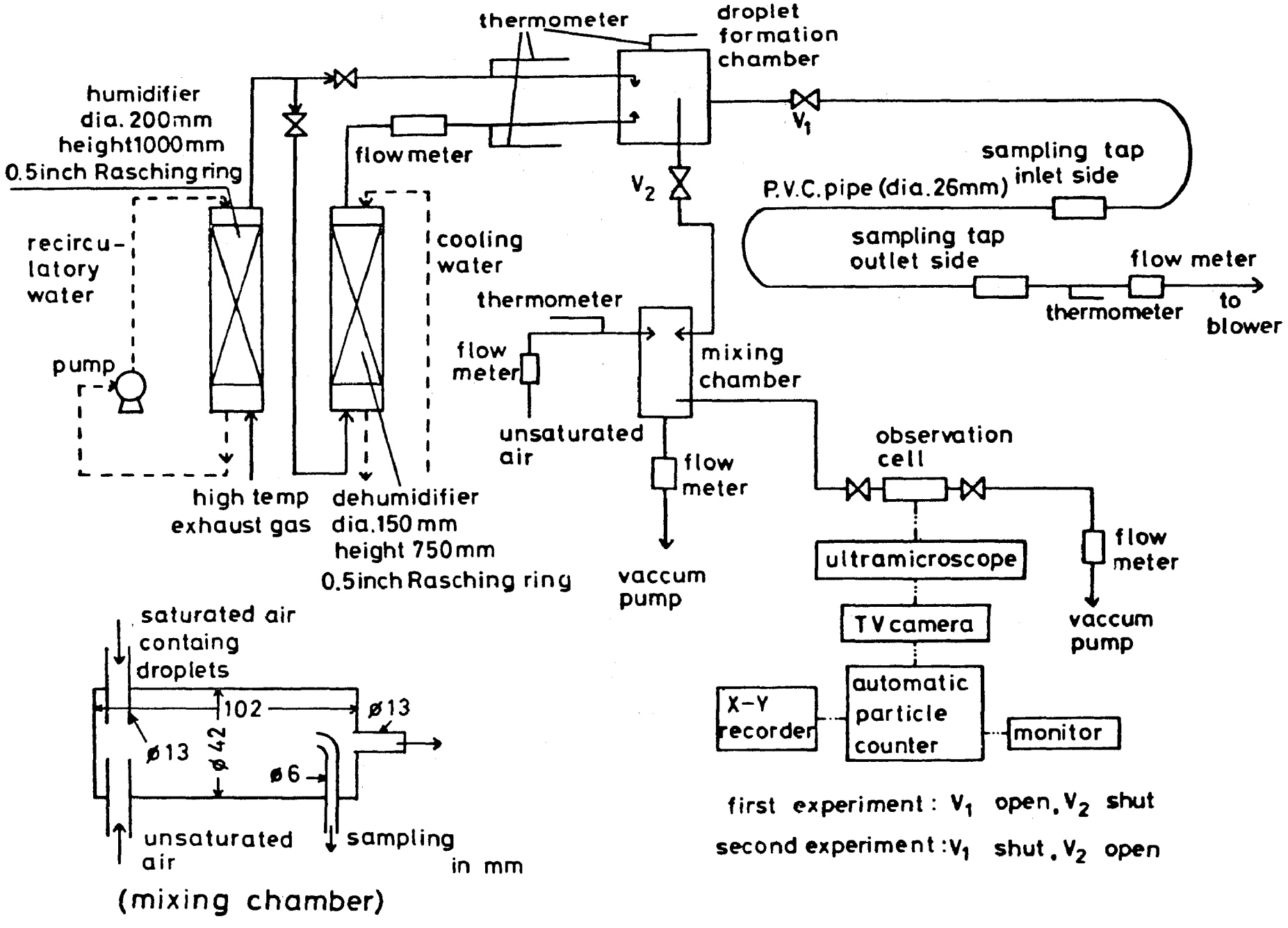

Fig. 9 Schematic diagram of the experimental apparatus

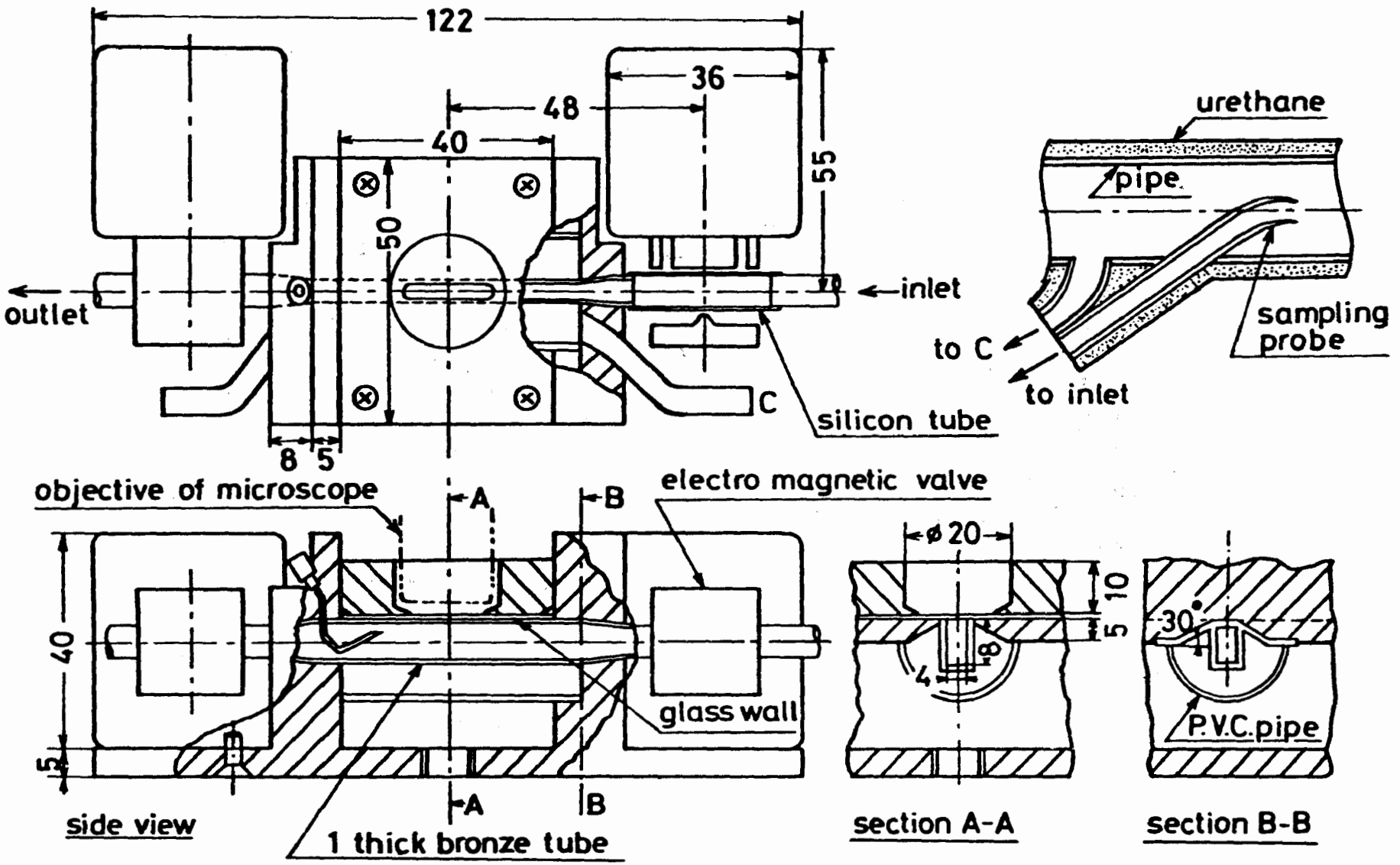

Fig.10 Observation cell

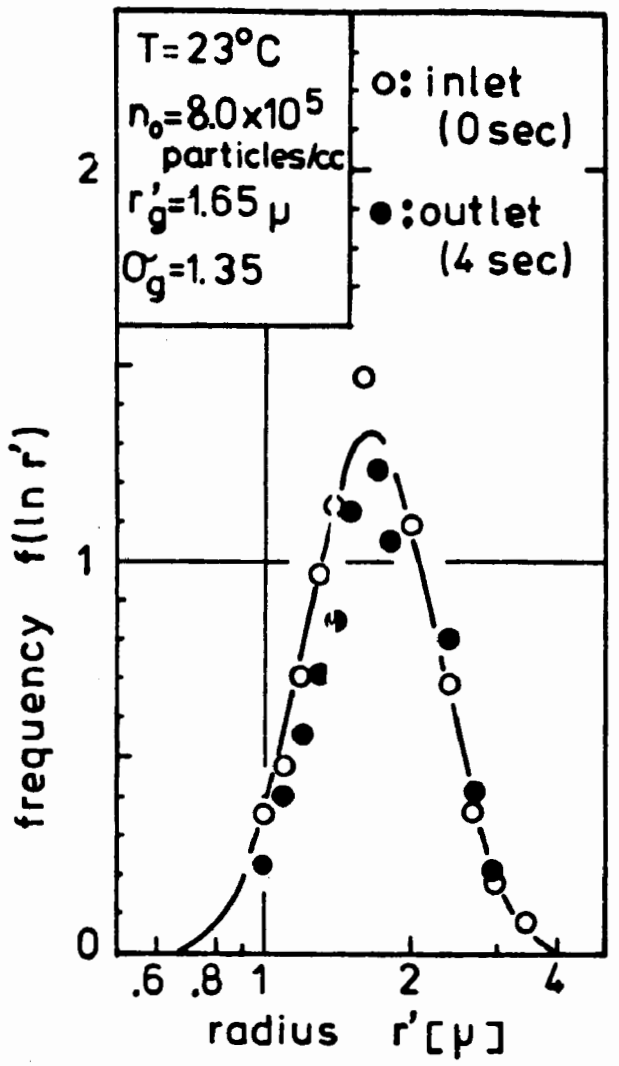

Fig.11 Comaprison of the particle size distribution between at inlet and outlet of the pipe

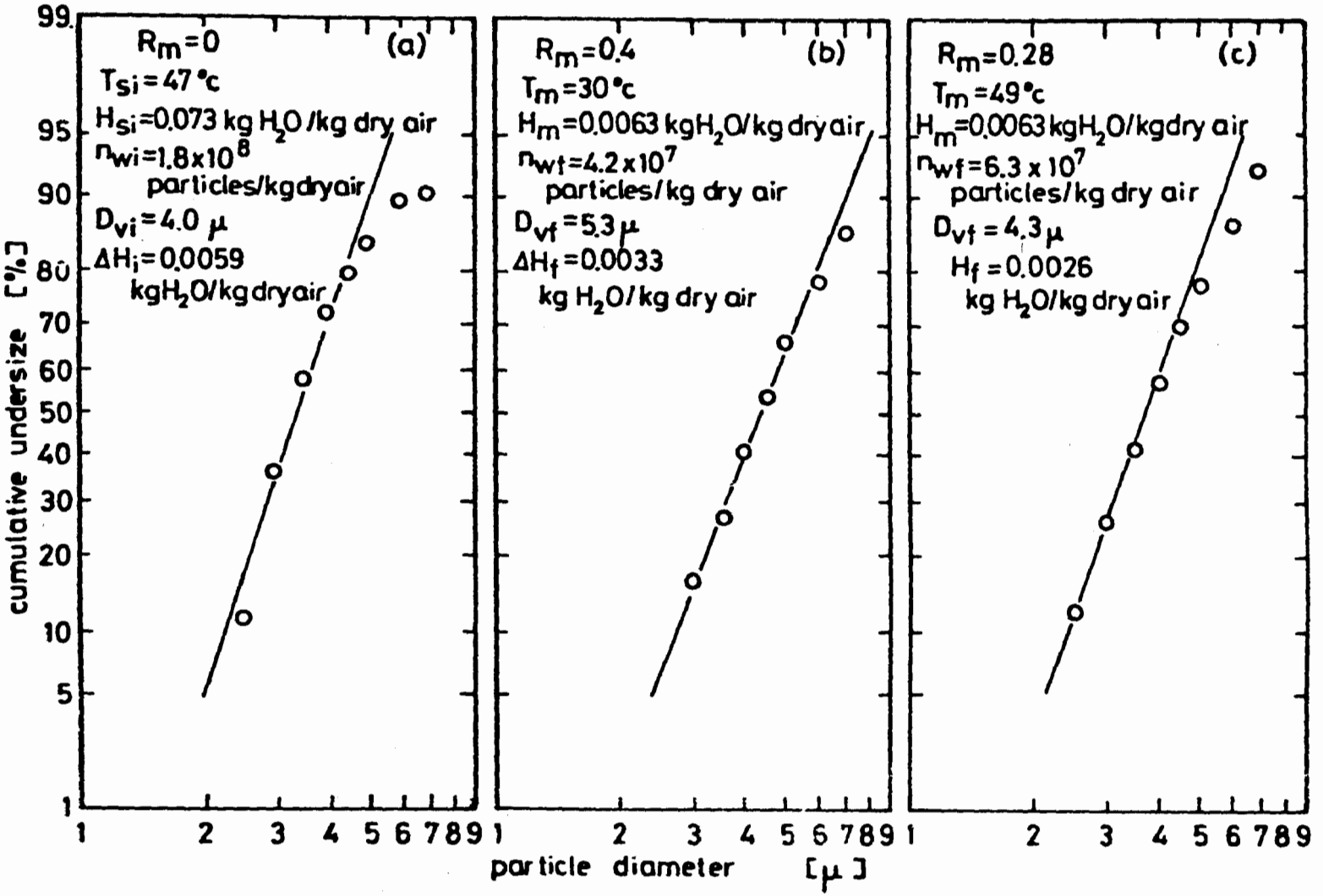

Fig.12 Change in size and number concentration of droplets before and after mixing of unsaturated air

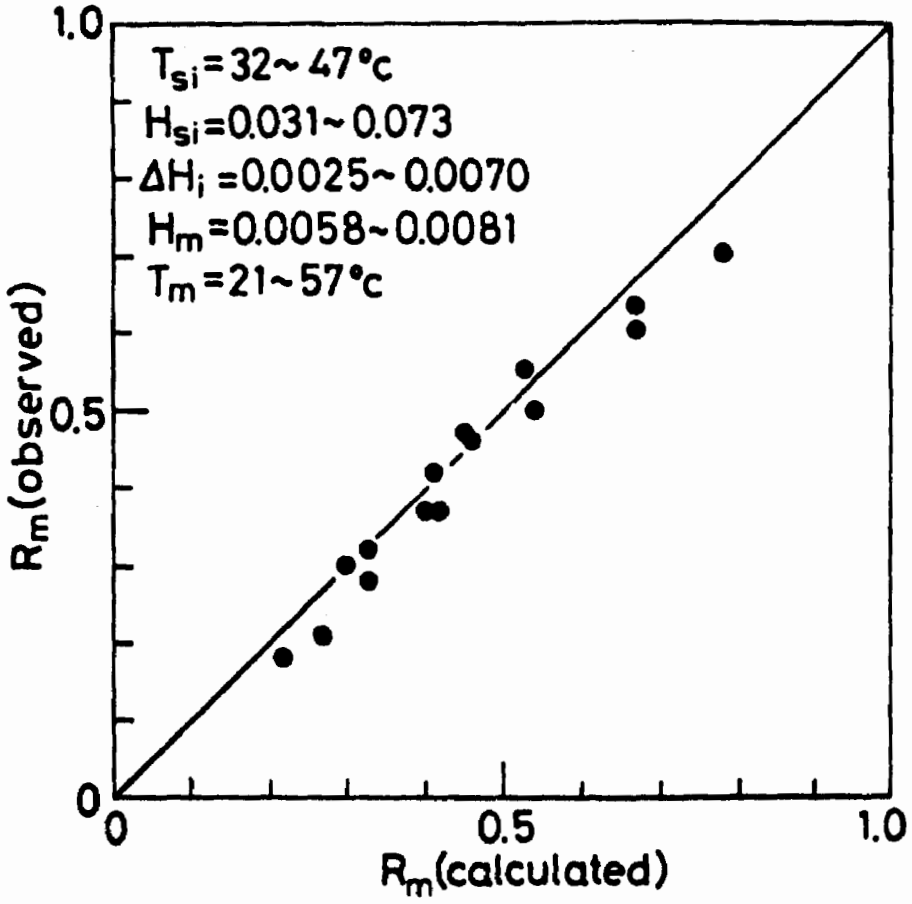

Fig.13 Comparison of mixing ratios, R_m, calculated and observed in the case of $\Delta H_f = 0$

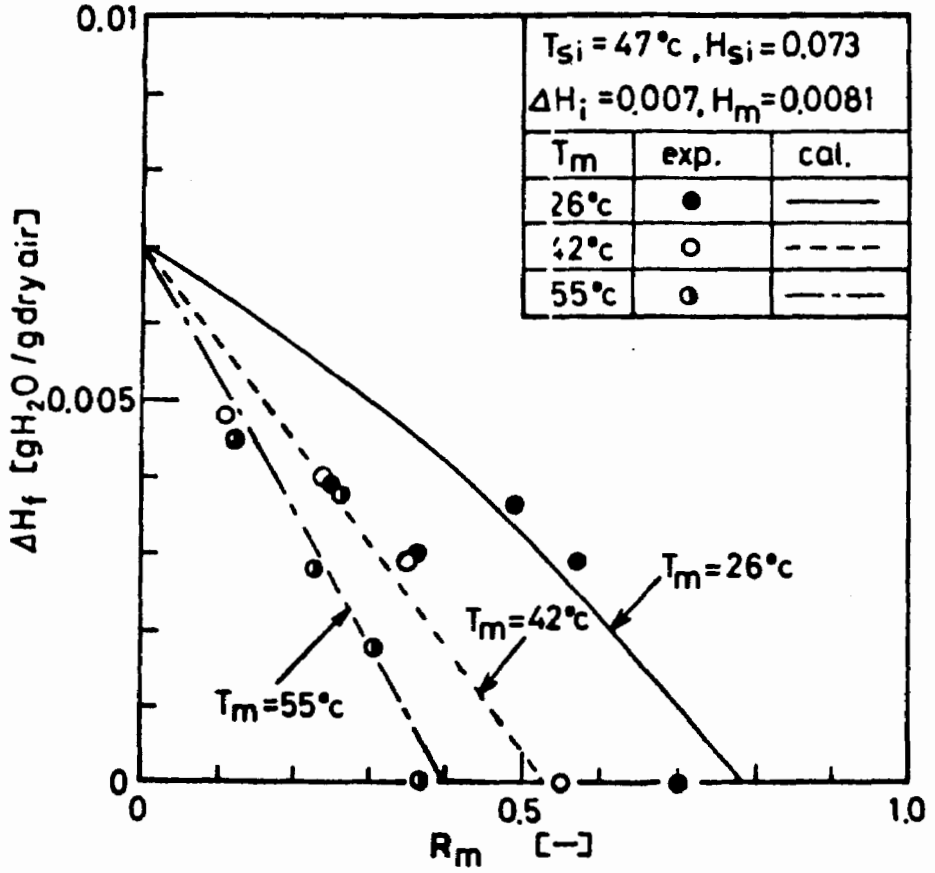

Fig.14 Effect of mixing ratio R_m and temperature of mixing air T_m on remaining droplet quantity ΔH_f

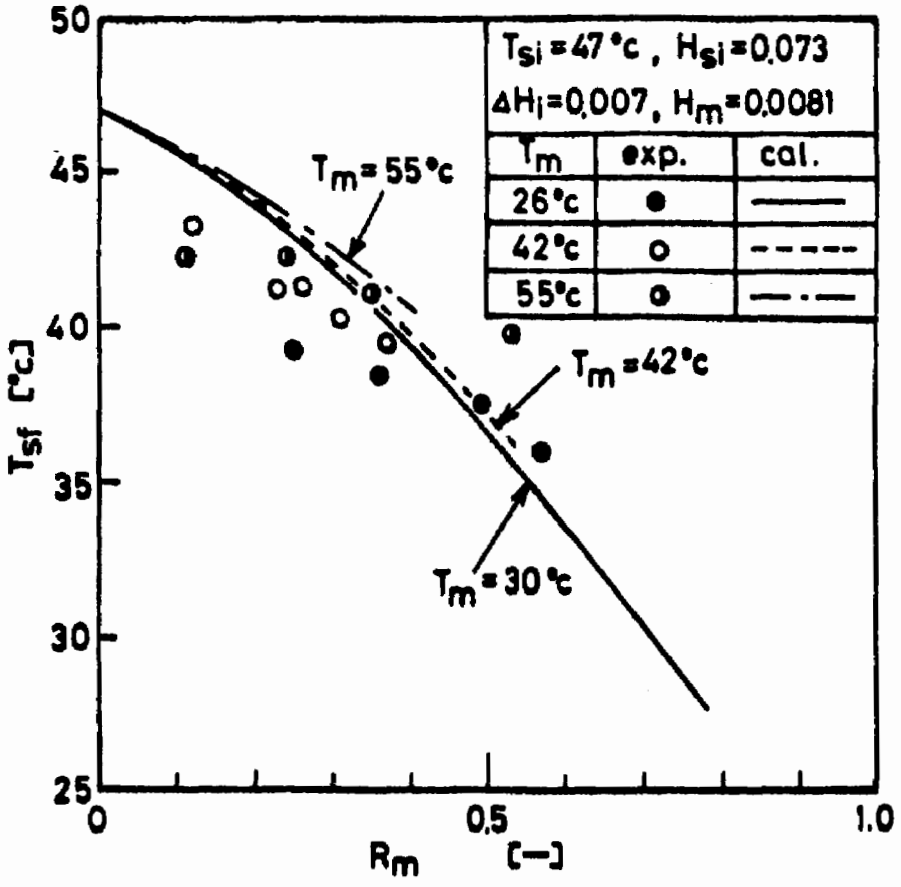

Fig.15 Effect of mixing ratio R_m and temperature of mixing air T_m on air temperature after mixing of unsaturated air, T_{sf}

BEHAVIOR OF AEROSOLS UNDERGOING BROWNIAN COAGULATION, BROWNIAN DIFFUSION AND GRAVITATIONAL SETTLING IN A CLOSED CHAMBER

KIKUO OKUYAMA, YASUO KOUSAKA
AND TETSUO YOSHIDA
Department of Chemical Engineering, University of Osaka Prefecture, Sakai, 591

(Reprinted with permission)

Reprinted from
JOURNAL OF
CHEMICAL ENGINEERING
OF
JAPAN
Vol. 9, No. 2 (1976)
Pages 140 146

BEHAVIOR OF AEROSOLS UNDERGOING BROWNIAN COAGULATION, BROWNIAN DIFFUSION AND GRAVITATIONAL SETTLING IN A CLOSED CHAMBER

KIKUO OKUYAMA*, YASUO KOUSAKA
AND TETSUO YOSHIDA
Department of Chemical Engineering, University of Osaka Prefecture, Sakai, 591

The behavior of aerosols undergoing Brownian coagulation, Brownian diffusion and gravitational settling in a closed chamber was studied by solving the basic equation, the so-called population balance equation, numerically for a polydisperse aerosol system and analytically for a monodisperse system, and then the results were examined by experiment. In solving the basic equation, two dimensionless parameters, which are determined by the initial properties of an aerosol and the chamber dimension and also characterize the relative effects of Brownian coagulation and Brownian diffusion to gravitational settling, were introduced in order to generalize the behavior under arbitrary conditions. The calculated results, the time-dependent changes in particle number concentration and particle size distribution for a polydisperse system, were presented graphically by using the above two parameters. And further using these parameters, the domains of the three controlling factors were mapped to show the extent of each effect of these factors under various conditions for a monodisperse system. Some of the calculated results were compared with the experimental results obtained by the ultramicroscopic size analysis previously developed by the authors.

Introduction

The behavior of aerosols in a closed chamber is generally characterized by coagulation, diffusion, sedimentation, thermophoresis, existence of generation sources of aerosol and so on. Brownian coagulation increases the size of aerosol particles, resulting in decrease of number concentration. Brownian diffusion decreases the concentration of aerosol particles as the result of the deposition of small particles at the walls, while gravitational settling decreases the concentration as the result of the deposition of larger particles at the bottom wall. The effects of these three factors on aerosol behavior, change in size and number concentration of aerosol particles in a closed chamber are discussed in this paper.

Several theoretical[1,4,5,7,10] and experimental[2-4,9,11] studies of this behavior have been reported in the field of nuclear power reactors, where the behavior of radioactive aerosol generated by an accident in the reactors is considered to be important from a safety viewpoint. In theoretical studies, basic equations considering Brownian coagulation and sedimentation[1,5,10], sedimentation and diffusion[8], or three effects[4,5,7,11] have been solved numerically on the assumption that the concentration is uniform except very close to the walls. Experimental studies, on the other hand, have been carried out by observing the change in mass concentration and particle size distribution of aerosol in the observation chamber. The agreement between their calculations and experiments has been found to be fairly good[4,11]. These results, however, are obtained under particular conditions and so they seem insufficient to predict the general behavior under various conditions such as various particle size distributions, number concentrations and chamber sizes.

In this paper, the basic equation in dimensionless form taking account of these three effects was solved numerically under various conditions for polydisperse aerosols and analytically for monodisperse aerosols. In calculations two dimensionless parameters which characterize the relative effect of gravitational settling to Brownian coagulation and Brownian diffusion were introduced. By using these parameters, the calculated results of the change in particle number concentration and size distribution with time were graphed so that the behavior of aerosols under various conditions is ready for prediction. Some of the

Received August 29, 1975.
Presented at the 40th Annual Meeting of The Soc. of Chem. Engrs., Japan at Nagoya, April 3, 1975 (entilted "Behavior of Aerosols in a Closed Chamber").

calculated results were confirmed by experiment, using the ultramicroscopic size analysis previously developed by the authors[12].

Theoretical Consideration

Polydisperse aerosol

Suppose an aerosol is dispersed throughout a chamber, within which aerosol convective currents, though small, arise due to small temperature variations. As a result, aerosol concentration in the chamber is kept uniform except very close to the walls[4,6,8]. In this case the basic equation expressing the time dependence of the size distribution of aerosol particles undergoing Brownian coagulation, Brownian diffusion and gravitational settling is given as[1,4,5,10,16], when the particle size distribution is a discrete spectrum.

$$\frac{\partial n'(r_i',t')}{\partial t'} = \sum_{\rho_i'=r_{imin}'}^{r_i'/\sqrt[3]{2}} K(\sqrt[3]{r_i'^3-\rho_i'^3},\rho_i')n'(\sqrt[3]{r_i'^3-\rho_i'^3},t') \times n'(\rho_i',t')\left(\frac{r_i'}{\sqrt[3]{r_i'^3-\rho_i'^3}}\right)^3 - \sum_{\rho_i'=r_{imin}'}^{r_{imax}'} K(r_i',\rho_i')n'(r_i',t') \times n'(\rho_i',t') - \frac{u_i(r_i')}{H}n'(r_i',t') - \frac{D(r_i')S}{\delta V}n'(r_i',t') \qquad i=imin\ldots imax \tag{1}$$

Eq. (1) is described as a differential equation, but it can be rewritten as a partial integro-differential equation in the case of a continuous spectrum. The left side of Eq. (1) represents the change in particle number concentration of size r_i' with time. The first term on the right side represents the rate of formation of particles of size r_i' and the second term the rate of loss of particles of size r_i' due to coagulation. $K(r_i',\rho_i')$ is the coagulation function and in the case of Brownian coagulation it is given by[12]

$$K(r_i',\rho_i') = K_0(r_i'+\rho_i')\{C_m(r_i')/r_i' + C_m(\rho_i')/\rho_i'\},$$
$$K_0 = 2\kappa T/3\mu \tag{2}$$

The third term represents the loss of particles due to sedimentation with the terminal settling velocity, and the last term expresses Brownian diffusion onto chamber walls, which is evaluated on the basis of film theory characterized by the thickness of concentration boundary layer δ[4].

Eq. (1) was derived on the following assumptions.

(1) There exist no external forces except gravity.

(2) Particles are spherical and electrically neutral.

(3) Particles collide with each other to form a single new spherical particle whose mass may be the same as the combined mass of the two smaller particles.

(4) The aerosol concentration is spatially uniform except within the boundary layer of thickness δ, and it changes with linearity within the layer[4].

(5) The chamber has a vertical cylindrical shape.

The initial particle size spectrum in the chamber was assumed to be established instantaneously with the following log-normal form:

$$n'(r_i',0) = \frac{n_0'}{\sqrt{2\pi}\ln\sigma_{g0}}\exp\left(-\frac{\ln^2(r_i'/r_{g0}')}{2\ln^2\sigma_{g0}}\right)d\ln r' \tag{3}$$

To generalize the solution the following dimensionless variables, which have been used in the case of Brownian coagulation alone[15], were chosen:

$$\left.\begin{aligned} n(r_i,t) &= n'(r_i',t')/n_0', \quad t_C = K_0 n_0' C_m(r_{g0}')t' \\ r_i &= r_i'/r_{g0}', \quad k(r_i,\rho_i) = K(r_i',\rho_i')/K_0 C_m(r_{g0}') \end{aligned}\right\} \tag{4}$$

Substitution into Eq. (1) gives the following equation:

$$\frac{\partial n(r_i,t_C)}{\partial t_C} = \sum_{\rho_i=r_{imin}}^{r_i/\sqrt[3]{2}} k(\sqrt[3]{r_i^3-\rho_i^3},\rho_i)n(\sqrt[3]{r_i^3-\rho_i^3},t_C)n(\rho_i,t_C) \times\left(\frac{r_i}{\sqrt[3]{r_i^3-\rho_i^3}}\right)^3 - \sum_{\rho_i=r_{imin}}^{r_{imax}} k(r_i,\rho_i)n(r_i,t_C)n(\rho_i,t_C) - \frac{C_m(r_i')r_i^3}{CGC_m(r_{g0}')}n(r_i,t_C) - \frac{DGC_m(r_i')}{CGC_m(r_{g0}')r_i}n(r_i,t_C) \qquad i=imin\ldots imax \tag{5}$$

where

$$\left.\begin{aligned} CG &= \frac{9\mu H K_0 n_0'}{2(\rho_p-\rho)g r_{g0}'^2} = \frac{1}{2}\left\{\frac{2K_0 n_0'^2 C_m(r_{g0}')}{u_i(r_{g0}')n_0'/H}\right\} \\ DG &= \frac{3\kappa HST}{4\pi\delta(\rho_p-\rho)g r_{g0}'^3 V} = \frac{D(r_{g0}')Sn_0'/\delta V}{u_i(r_{g0}')n_0'/H} \end{aligned}\right\} \tag{6}$$

CG and DG are dimensionless parameters which can be evaluated from initial aerosol properties and chamber dimensions. The parameter CG indicates the relative importance of coagulation to sedimentation and the other parameter DG expresses that of diffusion to gravitational settling[14]. From the defintion of CG and DG, the relative importance of coagulation to diffusion can be estimated by the parameter $CD=CG/DG$. These dimensionless parameters CG and DG are convenient to predict the behavior of aerosols having various initial properties in closed chambers. Since Eq. (5) cannot be solved analytically, the Runge-Kutta-Merson method was employed to solve it[15]. To make clear each effect of the parameters CG, DG and σ_{g0} on the behavior of aerosols, calculations were made in the range of $r_{g0}'=0.1\sim1.0\,\mu$, $\sigma_{g0}=1.3\sim2.0$, $CG=0.001\sim200.0$ and $DG=0.001\sim200.0$.

Monodisperse aerosol

When an aerosol is monodisperse, Eq. (1) becomes

$$\frac{dn'}{dt'} = -2K_0C_m(r_0')n'^2 - \frac{u_i(r_0')}{H}n' - \frac{D(r_0')S}{\delta V}n' \tag{7}$$

The dimensionless time t_C was taken as that of coagulation basis in Eq. (4), but the following two kinds of dimensionless time are now further introduced:

$$\left.\begin{aligned} t_G &= u_i(r_0')t'/H \quad \text{gravitational settling basis} \\ t_D &= D(r_0')St'/\delta V \quad \text{Brownian diffusion basis} \end{aligned}\right\} \tag{8}$$

Three kinds of non-dimensional equation corre-

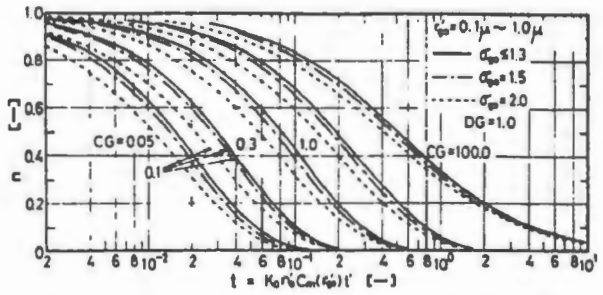

Fig. 1 Decrease in particle number concentration with time

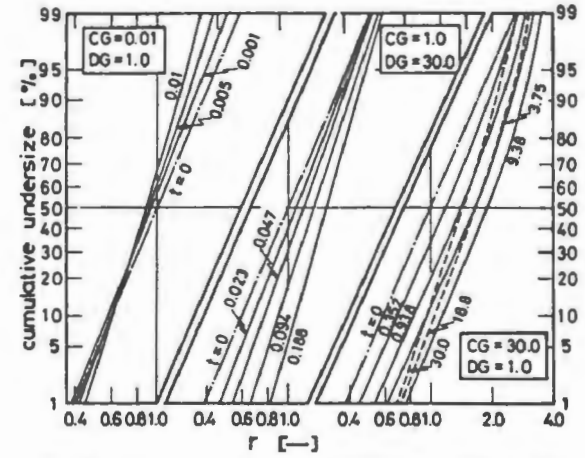

Fig. 2 Change in particle size distribution with time for aerosols with $r'_{g0}=0.35\ \mu$ and $\sigma_{g0}=1.3$

sponding to these three dimensionless times and their analytical solutions for monodisperse system are shown in Table 1 as a function of *CG* and *DG*, together with the time $t_{n=0.5}$ when particle number concentration reduces to half of the initial one.

Calculation Results and Discussion

Particle number concentration

Fig. 1 shows the normalized number concentration, which is defined as the ratio of the concentration at any time to the initial one, as a function of the dimensionless time based on Brownian coagulation. The graph also shows the effect of *CG*, σ_{g0} and r'_{g0} on the change in concentration under a constant *DG*. With increase in *CG* the curves move toward the right and tend to converge to that of $CG=100$, which coincides with that of Brownian coagulation alone[18]. Though the time-dependent change in particle number concentration does not depend on r'_{g0} in the range of $r'_{g0}=0.1\sim1\ \mu$, it seems to depend on σ_{g0}. In the region of $\sigma_{g0}\leq1.3$, however, the effect of polydispersion was negligible and the curves agreed quite well with the analytical solutions for the monodisperse system. This agreement suggests that the procedure of the numerical calculation is correct and that the analytical

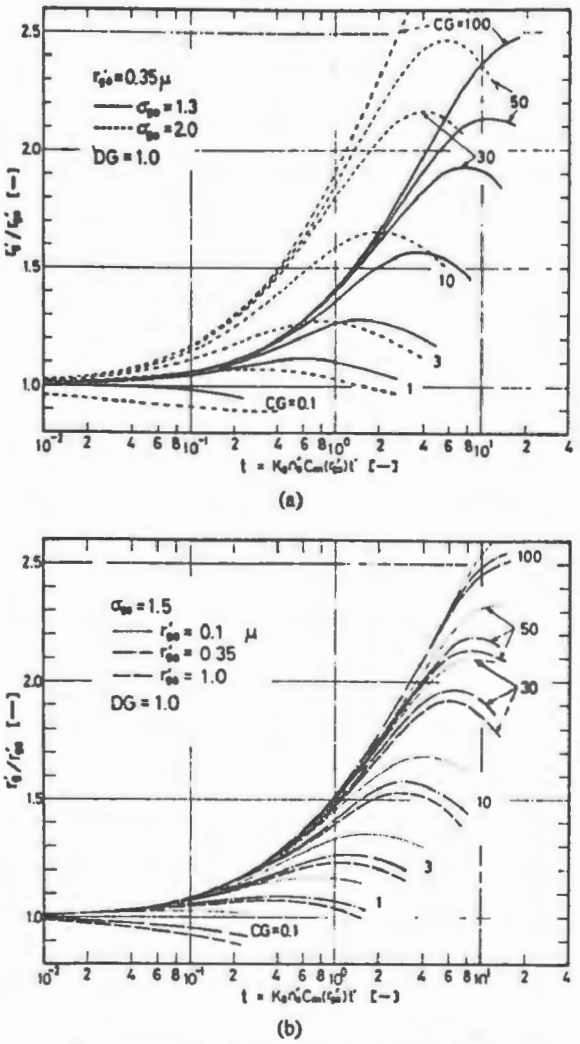

Fig. 3 Variation of nominal geometric mean radius with time

solutions for the monodisperse system will be practically useful for the polydisperse system.

Particle size distribution

Fig. 2 indicates the calculated results for the change of particle size distribution with time for different *CG* and *DG*. The manner of the change seems to depend on the values of *CG* and *DG*. When *CG* and *DG* are small, as shown on the left side of the figure, where sedimentation is controlling, the particle size distributions swing to smaller radius due to gravitational settling of larger particles. When *DG* is large and *CG* is small in the middle of the figure, where diffusion is controlling, they swing to larger radius becuase of the deposition of small particles on the walls by diffusion. When *CG* is large and *DG* is small on the right side of the figure, where coagulation is controlling, they shift toward larger radius due to particle coagulation. It is complicated, however, to discuss time-dependent changes under arbitrary con-

Table 1 Time-dependent change in particle number concentration for monodisperse aerosol

Controlling factor and dimensionless time	Basic dimensionless equation	Time-dependent change in particle number concentration	$t_{n=0.5}$
Coagulation $t_C=K_0 n_0' C_m(r_0')t'$	$dn/dt_C=-2n^2-A_0 n$	$\frac{A_0\exp(-A_0 t_C)}{2[1-\exp(-A_0 t_C)]+A_0}$	$\frac{1}{A_0}\ln\left(1+\frac{A_0}{2+A_0}\right)$
Sedimentation $t_G=u_t(r_0')t'/H$	$dn/dt_G=CG(-2n^2-A_0 n)$	$\frac{A_0\exp(-CGA_0 t_G)}{2[1-\exp(-CGA_0 t_G)]+A_0}$	$\frac{1}{A_0 CG}\ln\left(1+\frac{A_0}{2+A_0}\right)$
Diffusion $t_D=D(r_0')St'/\delta V$	$dn/dt_D=CD(-2n^2-A_0 n)$	$\frac{A_0\exp(-CDA_0 t_D)}{2[1-\exp(-CDA_0 t_D)]+A_0}$	$\frac{1}{A_0 CD}\ln\left(1+\frac{A_0}{2+A_0}\right)$

where $n=n'/n_0'$, $A_0=(1+DG)/CG$, $CD=CG/DG$

ditions by means of curves of cumulative percentage against particle size like Fig. 2. Generally two parameters, a geometric mean radius and a geometric standard deviation, are used to characterize the particle size and the width of distribution when the particle size distribution follows log-normal form. Though there existed some deviation from log-normal form in this case, a nominal geometric mean radius and a nominal geometric standard deviation are now introduced as follows:

$$\left.\begin{aligned}\ln r_g'&=\left[\sum_{r_i'=r_{i\min}'}^{r_{i\max}'}\{n'(r_i',t')\ln r_i'\}\right]\Big/n'\\ \ln\sigma_g&=\left[\left\{\sum_{r_i'=r_{i\min}'}^{r_{i\max}'}n'(r_i',t')\ln^3(r_i'/r_g')\right\}\Big/n'\right]^{1/3}\end{aligned}\right\}\qquad(9)$$

where $$n'=\sum_{r_i'=r_{i\min}'}^{r_{i\max}'}n'(r_i',t')$$

The change of size distribution with time will be discussed by the aid of r_g' and σ_g. The change in the ratio of r_g' to the initial one is shown in Fig. 3(a) using various values of CG. Distinct maxima at CG larger than 1.0 appear in the figure. The increasing regions of r_g'/r_{g0}' will be controlled by the particle growth due to coagulation. The decreasing regions, on the other hand, are controlled by gravitational settling, where the enhanced settling velocities of large particles being grown by coagulation will contribute to the decrease. In both regions, however, r_g' of the larger standard deviation changes faster than that of the smaller one. As seen from Fig. 3(b), which shows the effect of r_{g0}', particles with small r_{g0}' grow much more than those with larger r_{g0}'. This dependence on r_{g0}' seems to be caused by coagulation function $K(r_i',\rho_i')$, which increases with decreasing r_{g0}'. Fig. 4 shows the change in σ_g with time. In spite of the variation of σ_{g0}, the curves seems to converge to certain values which will be determined by CG and DG. The effect of r_{g0}' on the change of σ_g with time is not so large in the range of $r_{g0}'=0.1\sim1.0\,\mu$. The curves of $CG=100$ in both Fig. 3 and Fig. 4 agree well with those of Brownian coagulation alone[10].

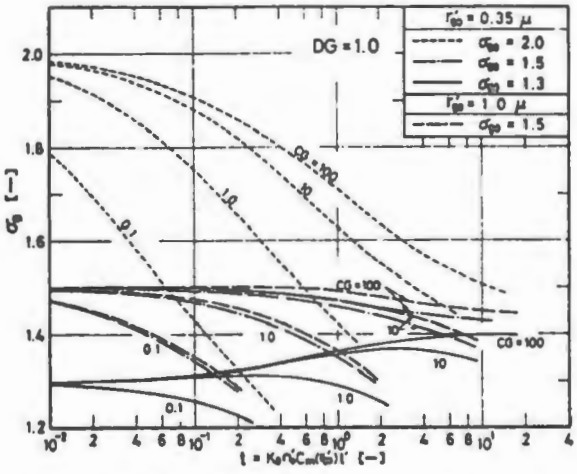

Fig. 4 Variation of nominal geometric standard deviation with time

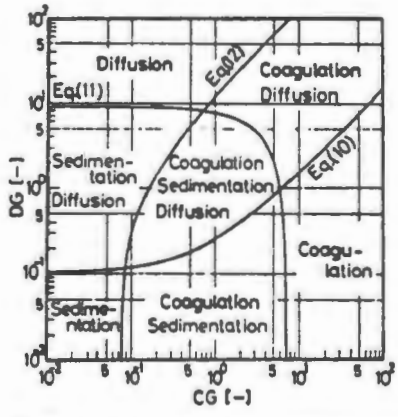

Fig. 5 The domains of the three controlling factors

Controlling factor under arbitrary conditions

Fig. 5 shows the domains of the three controlling factors on CG-DG coordinates. Each domain was determined essentially from the dependence of $t_{n=0.5}$ for monodisperse aerosol shown in Table 1 on CG and DG. In the case where one of the three factors, coagulation, diffusion and sedimentation, is ignored, $t_{n=0.5}$ can be determined by a parameter (CG, DG or CD) consisting of two remaining factors as shown in

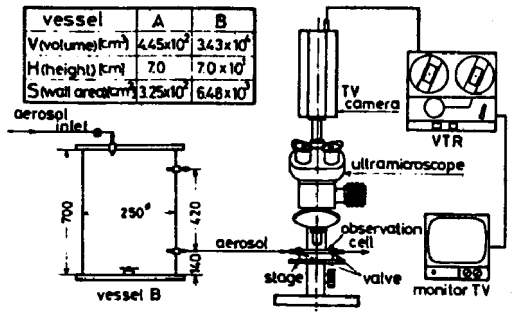

Fig. 6 Schematic diagram of experimental appratus

Table 2 Determination of the domains of the three controlling factors

Negligible factor	$t_{n=0.5}$ by two remaining factors	Equation expressing the domain where the factor is ignored
Diffusion $DG\to 0$ or $CD\to\infty$	$\lim_{\substack{DG\to 0 \text{ or} \\ CD\to\infty}} (t_C)_{n=0.5} = CG\ln\left(1+\frac{1}{1+2CG}\right)$	$\frac{1}{1+DG}\ln\left(1+\frac{A_0}{2+A_0}\right) \geq 0.9\ln\left(1+\frac{1}{1+2CG}\right)$ (10)
	$\lim_{\substack{DG\to 0 \text{ or} \\ CD\to\infty}} (t_D)_{n=0.5} = \ln\left(1+\frac{1}{1+2CG}\right)$	
Sedimentation $CG\to\infty$ or $DG\to\infty$	$\lim_{\substack{DG\to\infty \text{ or} \\ CG\to\infty}} (t_C)_{n=0.5} = CD\ln\left(1+\frac{1}{1+2CD}\right)$	$\frac{DG}{1+DG}\ln\left(1+\frac{A_0}{2+A_0}\right) \geq 0.9\ln\left(1+\frac{1}{1+2CD}\right)$ (11)
	$\lim_{\substack{DG\to\infty \text{ or} \\ CG\to\infty}} (t_D)_{n=0.5} = \ln\left(1+\frac{1}{1+2CD}\right)$	
Coagulation $CG\to 0$ or $CD\to 0$	$\lim_{\substack{CG\to 0 \text{ or} \\ DG\to 0}} (t_n)_{n=0.5} = \frac{1}{1+DG}\ln 2$	$\ln\left(1+\frac{A_0}{1+A_0}\right) \geq 0.9\ln 2$ (12)
	$\lim_{\substack{CG\to 0 \text{ or} \\ DG\to 0}} (t_D)_{n=0.5} = \frac{DG}{1+DG}\ln 2$	

Table 2, and then, thus calculated $t_{n=0.5}$ agrees with $t_{n=0.5}$ in Table 1 which includes the three factors. The boundary relations, which express whether one factor is ignored or not, were obtained as Eqs. (10) (11) and (12) in Table 2 by regarding one factor as negligible if the difference between two kinds of $t_{n=0.5}$ in Table 1 and Table 2 is less than 10% of $t_{n=0.5}$ in Table 2.

Experimental Apparatus and Method

A schematic diagram of the experimental apparatus is shown in **Fig. 6**. Aerosols used in this study were tobacco smoke, stearic acid and DOP. Aerosols of both stearic acid and DOP were generated by a La Mer-Sinclair type generator, and tobacco smake was generated by a simple apparatus[18] by which number concentration of particles was controlled from 10^6 to 10^8 particles/cc. Aerosols thus generated were introduced promptly throughout the chamber. To maintain gentle mixing of the aerosol in the chamber, the aerosol was mechanically stirred with a small fan set at the bottom of the chamber. Aerosol sampled at every given residence time was introduced into the observation cell installed on the stage of an ultramicroscope to measure its particle size distribution and particle number concentration. This measurement method using an ultramicroscope was developed previously by the authors[13]. Experiments were carried out by changing the intitial particle number concentration and changing the chamber dimension to obtain the experimental data for a wide range of CG and DG.

Experimental Results and Discussion

In a comparison of experimental data with theory, the boundary layer thickness δ in DG must be determined. Several investigators have experimentally obtained the values of δ, as shown in **Table 3**, by combining the deposition rate on the wall per unit area with the suspended mass concentration. The values of δ are scattered in the range of $\delta=0.01\sim 1.9\,\mu$. **Figs. 7, 8** and **9** show comparisons of the change in particle number concentration between experimental data and theoretical curves taking as $\delta=0.2\,\mu$ and $1.6\,\mu$. As shown in Fig. 7, there is no difference caused by stirrer speed or sampling position, and these facts suggest that neither turbulent coagulation nor turbulent diffusion occurs and that particle number concentration is uniform throughout the chamber. In every case in the figures experimental data agree with the curves of $\delta=1.6\,\mu$ rather than those of $\delta=0.2\,\mu$. Estimating the controlling factors from Fig. 5, it is found that coagulation in Fig. 7, coagulation and diffusion in Fig. 8 and coagulation, sedimentation and diffusion in Fig. 9 are controlling. **Fig. 10** shows a comparison of the change in nominal geometric mean radius with time between experimental data and calculation curves. The agreement is fairly good and it is seen that aerosol having the larger CG grows much greater than the smaller one, as expected from theoretical calculations. **Fig. 11** is an example of a series of photographs, taken by a camera directly attached to the ultramicroscope, which correspond to the data plotted in Fig. 7. It is seen that particle number concentration decreases gradually, accompanying particle growth due to Brownian coagulation.

Conclusion

The behavior of aerosols undergoing Brownian coagulation, Brownian diffusion and gravitational

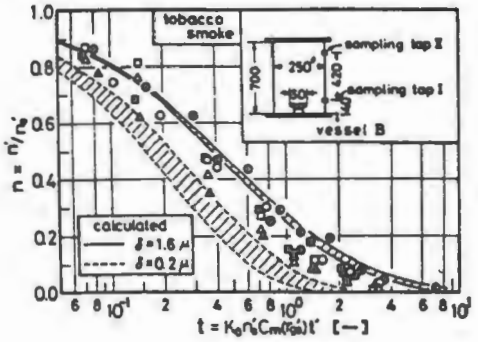

key	CG	DG δ=1.6μ	DG δ=0.2μ	r'go(μ)	σg
○	28.5	5.96	47.7	0.60	1.35
●	29.6	5.96	47.7	0.60	1.35
●	38.2	14.1	113	0.46	1.32
△	26.9	5.96	47.7	0.60	1.35
▲	37.9	9.75	78.0	0.51	1.32
□	37.5	9.75	78.0	0.51	1.32
■	35.3	9.75	78.0	0.51	1.32

n'o = 5.64×10⁴ ~ 7.46×10⁴

key	stirrer speed (rpm)	sampling tap
○ ● ◐	1950	I
△ ▲	3060	I
□ ■	1950	II

Fig. 7 Experimental and calculated time-dependent change in particle number concentration

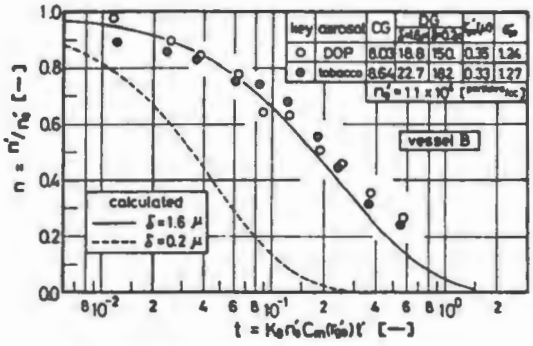

Fig. 8 Experimental and calculated time-dependent change in particle number concentration

Table 3 Boundary layer thickness

Investigator	Aerosol	Particle radius [μ]	δ [μ]
Kitani *et al.*[8]	Na_2O	0.32~1.0	0.01~1.9 (*av.* 0.34)
Greenfield *et al.*[4]	Na_2O	0.29~0.5	1.75
Nelson *et al.*[8,11]	Na_2O	1.0~1.5	0.7~1.6

settling in a closed chamber was studied theoretically and experimentally. To generalize the analysis, two dimensionless parameters *CG* and *DG*, which express the relative effect of coagulation and of diffusion to gravitational settling, were introduced in solving the basic equation. By using these two parameters, the results of numerical calculation for polydisperse aerosol having various initial size distributions with log-normal form were presented graphically, and in the case of monodisperse aerosol analytical solutions were obtained. So far as the change in total number concentration with time was concerned, the calculation results of polydisperse aerosol agreed closely with those of monodisperse aerosol. The manner of change in particle size distribution with time was found to depend on the values of *CG* and *DG* as shown in Figs. 2, 3 and 4. As the results of analytical solution for a monodisperse system, the domains where each of the three factors becomes controlling were mapped on *CG-DG* coordinates, which permitted a general understanding of the behavior of aerosols

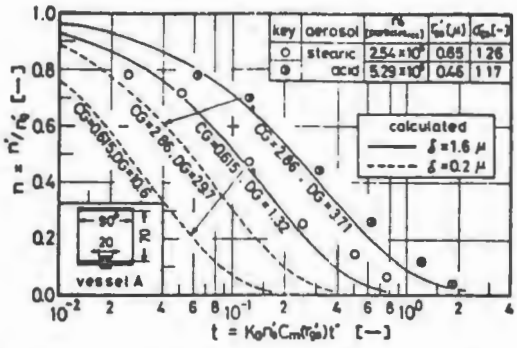

Fig. 9 Experimental and calculated time-dependent change in particle number concentration

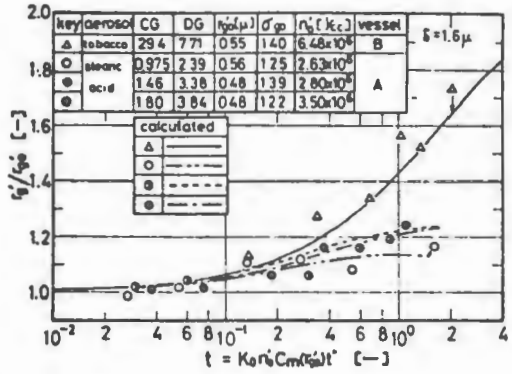

Fig. 10 Experimental and calculated variation of nominal geometric mean radius with time

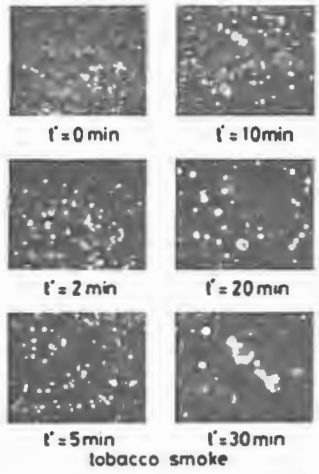

Fig. 11 Change of particle number with time

under various conditions. Some of the calculated results were examined experimentally and were found to be in good agreement when the boundary layer thickness δ was taken as 1.6 μ.

The results obtained in this paper and in the previous one[14], which showed the effect of Brownian coagulation and diffusion on gravitational settling considering the variation of particle number concentration in the direction of sedimentation, provide a basic and representative concept for predicting the actual behavior of aerosols in a closed system.

Nomenclature

A_0	= constant shown in Table 1 ($=(1+DG)/CG$)	[—]
CD	= dimensionless parameter ($=CG/DG$)	[—]
CG	= dimensionless parameter defined in Eq. (6) ($=9\mu HK_0n_0'/2(\rho_p-\rho)gr_{g0}'^3$)	[—]
$C_m(r_i')$	= Cunningham's correction factor of r_i'	[—]
DG	= dimensionless parameter defined in Eq. (6) ($=3\kappa HST/4\pi\delta(\rho_p-\rho)gr_{g0}'^3V$)	[—]
$D(r_i')$	= diffusion coefficient ($=C_m(r_i')\kappa T/6\pi\mu r_i'$)	[cm²/sec]
g	= acceleration of gravity	[cm/sec²]
H	= chamber height	[cm]
K_0	= coefficient in Eq. (2)	[cm³/sec]
$K(r_i', \rho_i')$	= coagulation function for two particles of size r_i' and ρ_i'	[cm³/sec]
$k(r_i, \rho_i)$	= dimensionless coagulation function ($=K(r_i', \rho_i')/K_0C_m(r_{g0}')$)	[—]
$\Delta \ln r'$	= size width between r_i' and r_{i+1}'	[—]
$n'(r_i', t'), n(r_i, t)$	= number and dimensionless number concentration of aerosol particles ($=n'(r_i', t')/n_0'$)	[particles/cc] [—]
n', n	= total and dimensionless total particle number concentration ($=n'/n_0'$)	[particles/cc] [—]
n_0'	= total particle number concentration at time zero	[particles/cc]
r_i', r	= particle radius and dimensionless particle radius ($=r_i'/r_{g0}'$)	[cm], [μ], [—]
r_g'	= geometric mean radius	[cm], [μ]
r_0'	= particle radius of monodisperse aerosol	[cm], [μ]
S	= wall area of chamber	[cm²]
T	= absolute temperature	[°K]
t'	= time	[sec]
t_c	= dimensionless time based on coagulation ($=n_0'K_0C_m(r_{g0}')t', n_0'K_0C_m(r_i')t'$)	[—]
t_D	= dimensionless time based on diffusion ($=D(r_i')St'/\delta V$)	[—]
t_G	= dimensionless time based on gravitational settling ($=u_i(r_0')t'/H$)	[—]
$t_{n=0.5}$	= dimensionless time when n reduces to half	[—]
$u_i(r_i')$	= terminal settling velocity ($=2C_m(r_i')(\rho_p-\rho)gr_i'^2/9\mu$)	[cm/sec]
V	= chamber volume	[cm³]
δ	= boundary layer thickness	[μ] [cm]
σ_g	= geometric standard deviation	[—]
κ	= Boltzman's constant ($=1.38\times10^{-16}$)	[erg/°K]
μ	= viscosity of fluid	[g/cm·sec]
ρ, ρ_p	= fluid and particle density	[g/cm³]
ρ_i', ρ_i	= particle radius and dimensionless particle radius in Eqs. (1) (2) and (5)	[cm] [—]

〈Subscripts〉

i	= the number particle size
min	= minimum
max	= maximum
0	= at time zero

Literature Cited

1) Ahn, C. H. and J. W. Gentry: *Ind. Eng. Chem. Fundam.*, **11**, 483 (1972).
2) Devier, S. E.: *J. Colloid Sci.*, **18**, 744 (1963).
3) Devier, S. E.: *J. Colloid Interface Sci.*, **21**, 9 (1966).
4) Greenfield, M. A., R. L. Koontz and D. F. Hausknecht: *ibid.*, **35**, 102 (1971).
5) Huang, G. M., M. Kerker and E. Matijevic: *ibid.*, **33**, 529 (1970).
6) Takahashi, K.: *Kuki Seijo*, **10**, 27 (1972).
7) Takahashi, K. and M. Kasahara: *Atmos. Environ.*, **2**, 441 (1968).
8) Kitani, S., H. Matsui, S. Uno, M. Murata and J. Takada: *J. Nucl. Sci. Technol.*, **10**, 566 (1973).
9) Langstroth, G. and T. Gillespie: *Cand. J. Research*, **25B**, 455 (1947).
10) Lindauer, G. C. and A. W. Castleman, Jr.: *J. Aerosol Sci.*, **2**, 85 (1971).
11) Nelson, C. T., L. Baurmash and R. L. Koontz: Proc. 9th AEC Air Cleaning Conf. (ACE Report CONF-660904), 454 (1966).
12) Smoluchowski, M.: *Phys. Chem.* (*Leipzig*), **92**, 127 (1917).
13) Yoshida, T., Y. Kousaka and K. Okuyama: *Ind. Eng. Chem. Fundam.*, **14**, 47 (1975).
14) Yoshida, T., Y. Kousaka, K. Okuyama and S. Nishio: *J. Chem. Eng. Japan*, **8**, 137 (1975).
15) Yoshida, T., K. Okuyama, Y. Kousaka and Y. Kida: *ibid.*, **8**, 317 (1975).
16) Zebel, G.: *Kolloid-Z.*, **156**, 102 (1958).

A New Technique of Particle Size Analysis of Aerosols and Fine Powders Using an Ultramicroscope

Tetsuo Yoshida, Yasuo Kousaka,* and Kikuo Okuyama

Faculty of Engineering, University of Osaka Prefecture, Osaka, Japan

A new technique to determine the particle size distribution of fine powders and aerosols including those of fine liquid droplets was developed. The technique is in principle somewhat similar to the Andreasen pipet method, but has some distinctive features as follows: (1) sedimentation is made in air as well as in water according to the particle size; (2) sedimentation depth is extremely shallow; (3) particle concentration at a given depth in a sedimentation cell is detected by an ultramicroscope on the number basis. The lower limit of the measurable particle size is several tenths of a micron in diameter and the upper more than several tens of microns. By sedimentation mostly in air at depths less than a few millimeters, very quick measurement was possible even for submicron particles. It is desirable for the particle number concentration to be high.

Introduction

In recent years an increasing interest in the size analysis of aerosols has arisen in connection with air pollution control. In existing ultramicroscopic techniques of particle size analysis (Richardson, *et al.*, 1956; Mukaibo *et al.*, 1962), the settling velocities of hundreds of individual particles must be observed by an ultramicroscope to determine the size distribution, and thus the techniques require much time. The technique developed in this study is quite different from the existing ones and, above all, has the distinctive feature of quick analysis of size distribution for particles, including water droplets, of more than several tenths of a micron in diameter. The technique is also applied to the determination of the particle number concentration of aerosols and, by some additional devices, the density of particles. Although the technique described below is limited to aerosols of small particles dispersed in air, for the powders of larger particles the technique can be applied when they are dispersed in water.

Principle

The principle of the method is almost same as that of the Andreasen pipet method, but the concentrations of particles at a given depth as sedimentation progresses are detected by an ultramicroscope on the number basis. Sedimentation in air or in water with shallow sedimentation lengths makes it possible to analyze smaller particles in a short time, whereas in the Andreasen pipet method sedimentation is usually made in water with a deep sedimentation length. The sedimentation length is from about 0.5 to a few millimeters, so that, for example, a water droplet 1 μ in diameter is measured within several tens of seconds. The detection of particle number concentrations by ultramicroscope and then the analysis of particle size distribution is made by the following procedure: aerosol is introduced into a small cell having valves at both inlet and outlet sides, the flow of the aerosol is instantaneously stopped by closing the valves, and then sedimentation is started. When the focus of the ultramicroscope is preliminarily set at depth h shown in Figure 1, the aerosol particles existing in the volume v_m are recognized because of their shining at the depth of the focus but they are as yet unknown in sizes. The particles appearing in the microscope are photographed or recorded by a video recorder as sedimentation continues until the particles disappear from sight.

The terminal settling velocity of a particle is represented by the equation

$$U_t = \frac{g(\rho_p - \rho_f)D_p^2 C_m}{18\mu} \tag{1}$$

U_t in this equation is replaced by h/t, where h is the depth of sedimentation preliminarily set; then the particle diameter D_p is determined in accordance with the sedimentation time t, that is

$$D_p = F(h/t) \tag{2}$$

The particle with the diameter D_p calculated by eq 2 at time t is the maximum one which can be recognized at the depth h; that is, the particles larger than it have already passed below the depth h. Thus the particle number in sight at time t after the start of sedimentation is given by the equation

$$N(t) = N(0)\int_0^{D_p} f(D_p)\, dD_p \tag{3}$$

The integral term of this equation indicates cumulative fraction undersize, then

$$F = \int_0^{D_p} f(D_p)\, dD_p = N(t)/N(0) \tag{4}$$

$N(0)$, the particle number in the volume v_m in Figure 1 at the beginning of sedimentation, and $N(t)$, the numbers at various elapsed times, are counted by slow video. Then the size distribution is determined by eq 4. Table I shows the analysis procedure.

In the procedure, to prevent photophoresis, thermophoresis, and thermal convection, the lighting of the microscope must be extinguished during the intervals between successive observations.

Another method may also be true in principle. If the sedimentation depth h is varied instantaneously at constant elapsed time, the particle size distribution can be determined by almost the same procedure described above. The particle number concentration, n_0, is given as follows, when the volumes v_m or v_h shown in Figure 1 are predetermined

© Ind. Eng. Chem., Fundam., Vol. 14, No. 1, 1975
(Reprinted with permission)

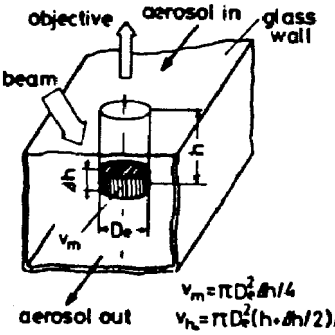

Figure 1. Illustration of observation cell.

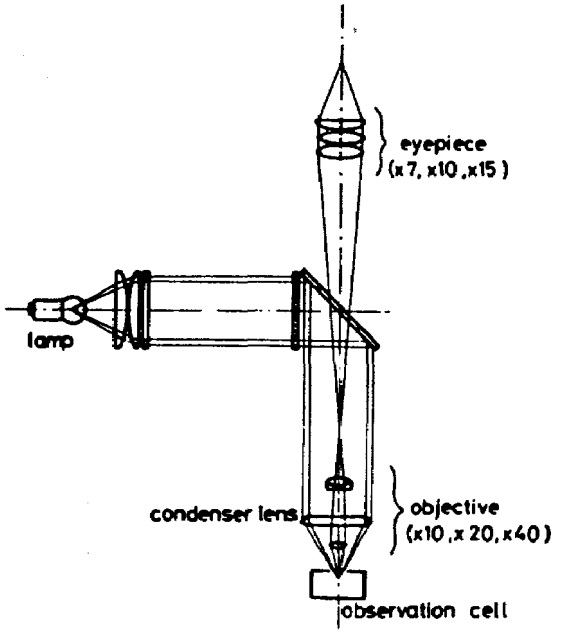

Figure 2. Arrangement of ultramicroscope.

Table I. Procedure of Analysis

t, time elapsed	$N(t)$, number of particle in v_m	D_p, particle diameter	F, cumulative undersize
0	$N(0)$		1
t_1	$N(t_1)$	$F(h/t_1)$	$N(t_1)/N(0)$
t_2	$N(t_2)$	$F(h/t_2)$	$N(t_2)/N(0)$
:	:	:	:
:	:	:	:
t_n	$N(t_n)$	$F(h/t_n)$	$N(t_n)/N(0)$

$$n_0 = N(0)/v_m \quad (5)$$

$$n_0 = N_{total}/v_h \quad (5')$$

where N_{total} is the particle number in the volume v_h which is obtained by counting all the particles passing through the volume v_m during sedimentation. Equation 5′ is especially useful when the particle number concentration is small. In this procedure, however, since the microscope must be kept lighted during the measurement, it is not suitable to measure the size distribution of particles smaller than about 1 μ in diameter, where thermophoresis and thermal convection affect sedimentation.

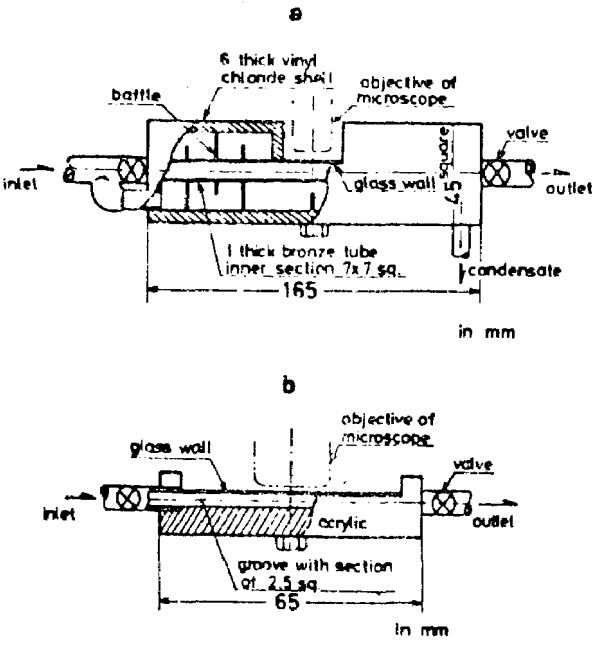

Figure 3. (a) Observation cell for fog particle. (b) Observation cell for small particle.

The estimation of Δh in Figure 1, the depth in focus, is made as follows. Small numbers of particles to be analysed are first deposited on a glass in some way. The glass is mounted on the stage of the ultramicroscope and the deposited particles are observed while shifting the stage up and down. Then Δh is given as the total displacement of the stage over which the images of the particles are in sight with a certain clearness.

When the particle number concentration is thus obtained, and when the particle weight concentration is separately determined by another appropriate way such as filtering, the particle density is, in principle, obtainable by means of the above technique of size analysis.

In the principle described here Brownian coagulation and diffusion are neglected. When the particle number concentration exceeds 10^7 particles per cubic centimeter, the effect of the Brownian coagulation will not be negligible (Fuchs, 1964), and when there are particles less than about 0.4 μ in diameter, diffusion influences the gravitational settling (Davies, 1949). The development of some devices to remove these effects by forced sedimentation, such as by thermophoretic or centrifugal forces, or theoretical methods to compute the effects will be desirable in order to extend the application of this technique.

Apparatus

The ultramicroscope used in this study is shown in Figure 2. It has a 150-W halogen lamp and an observation cell on its stage. The magnification of the objective and the eyepiece were selected according to the particle size and the particle number concentration. Two typical types of the observation cell are shown in Figure 3. The cell shown in Figure 3a consists of a double cell. The outer cell is provided for temperature control of the aerosol to be observed in the inner one. This type is useful for the analysis of fog particles or other volatile particles which can vary their size by evaporation or condensation with change of temperature. The cell shown in Figure 3b has a small sectional area so that the effect of convection is removed.

The aerosol particles tested in this study were generated

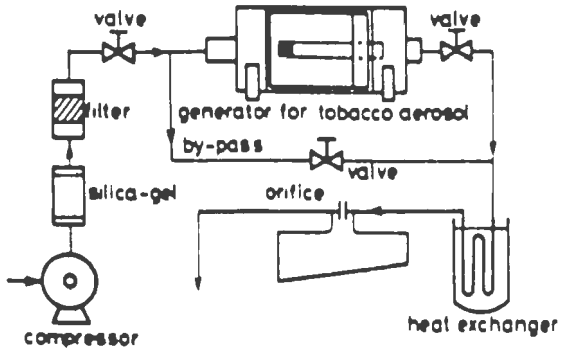

Figure 4. Arrangement of tobacco aerosol generator.

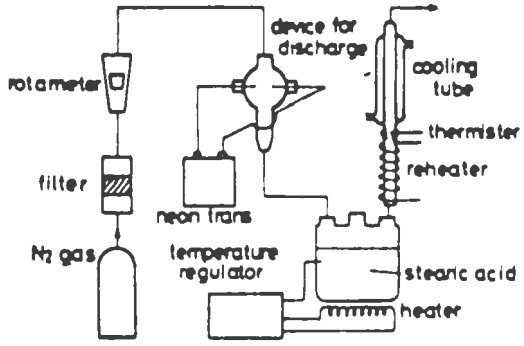

Figure 5. Stearic acid aerosol generator

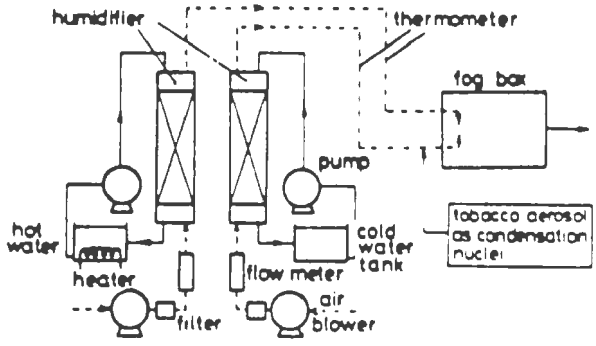

Figure 6. Fog particle generator.

as shown in Figures 4, 5, and 6. Figure 4 shows a tobacco aerosol generator. The particle number concentration of tobacco aerosol was controlled from 10^6 to 10^8 particles per cubic centimeter by air flow rate through tobacco and the rate of the by-pass. The particle size was controlled by residence time in the aging chamber from 0.7 to 2 μ in geometrical mean diameter. The stearic acid particles were generated by a La Mer generator shown in Figure 5, but because of the rough control of temperature they were not monodisperse. Figure 6 shows a fog generator. The fog particles were formed around the tobacco particles as condensation nuclei, and the particle number concentration and the particle size as well were controlled by changing the number of the condensation nuclei. The controlled size was from 1 to 10 μ and the concentration was from 10^3 to 10^6 particles/cm^3.

Experimental Section

Some characteristics regarding the ultramicroscope used were predetermined before experiments. Table II shows the results. The last column gives a criterion of the particle number concentration to be required for analysis. When the concentration is less than the criterion, observation must be repeated until a sufficiently large number is obtained. Otherwise the whole number in the volume v_m must be counted for the analysis, which is accomplished by slow video. For aerosols with lower concentrations, the visual field of the microscope or the volume v_m may be enlarged by giving a horizontal sweep to the observation cell. In any case the more dense the particle number concentration is, the easier is the analysis in this method.

Figure 7. Change of particle number with the lapse of time (stearic acid aerosol). (a) t = 0 sec after the start of sedimentation; (b) t = 40 sec; (c) t = 50 sec; (d) t = 60 sec; (e) t = 70 sec

Table II. Characteristics of the Ultramicroscope Used

Eyepiece × objective	Δh, μ	v_m, cm^3	Visible particle diam, μ	n, [particles/cm^3] equiv to over 50 particles in volume, v_m
10 × 10	125	1.9×10^{-4}	$\gtrsim 2$	$\gtrsim 3 \times 10^5$
10 × 20	40	1.4×10^{-5}	$\gtrsim 0.2$	$\gtrsim 4 \times 10^6$
10 × 40	15	1.2×10^{-6}	$\gtrsim 0.05$	$\gtrsim 4 \times 10^7$

A series of the photos which illustrate the change of the particle number as time elapses is shown in photos (a) to (e) in Figure 7. These pictures are only for illustration and the most of the size analysis were made by the slow video system because of the more rapid analysis than the photographic one.

Figure 8 shows the result of the analysis. No differences in the size distribution are found for various depths of sedimentation. This agreement indicates that the aerosol introduced into the cell is homogeneously dispersed and also indicates almost no effect of diffusion or thermophoresis, which probably appears at the vicinities of the upper or the lower wall of a cell because of the larger gradients

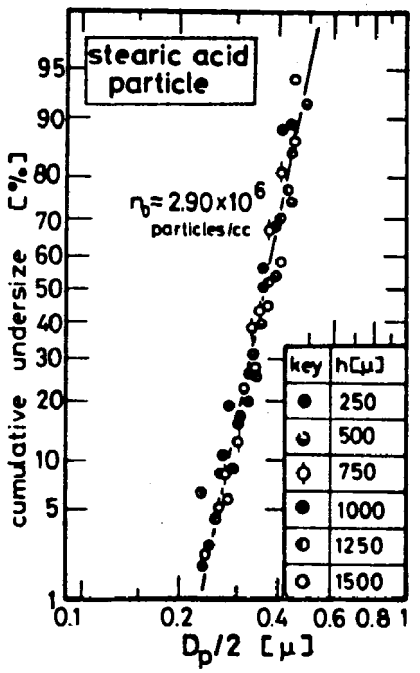

Figure 8. Particle size distribution of stearic acid aerosol for various sedimentation depths.

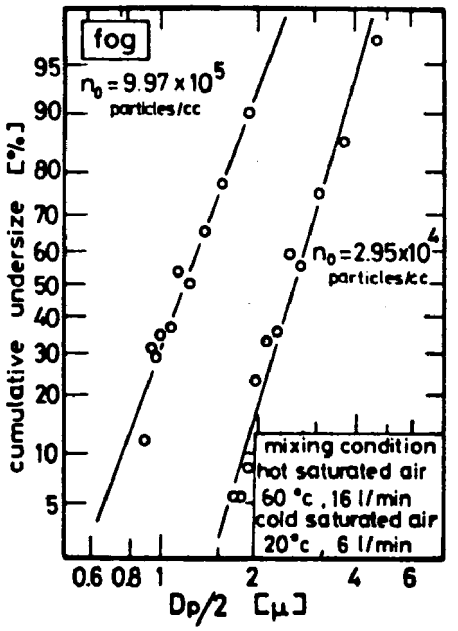

Figure 9. Particle size distribution of fog.

of concentration and temperature, respectively. The agreement, moreover, indicates that Brownian coagulation, which must progress with the lapse of time or with the depth of sedimentation, has no effect on the size analysis below 10^7 particles/cm^3.

Figure 9 shows the result of the analysis of fog particles or water droplets, which have been thought difficult to analyze without any disturbance as they are in suspension in air. In these cases the particle number concentrations were so small that the size analyses were made by counting the whole number in the volume v_h.

Figure 10 shows the two kinds of size distributions of tobacco aerosols ("Cherry" made by the Japan Monopoly Corp.). One is that obtained for low concentration and the other is that for particles grown by Brownian coagulation after sufficient aging time. The wide size distribution of the latter indicates a typical feature when coagulation oc-

Table III. Representative Experimental Data

Time elapsed, t, sec	No. of particles in sight, $N(t)$	Particle diam by eq 2, D_p, μ	Cumulative undersize, $F = N(t)/N(0)$	Remarks
(Run 1; stearic acid, h = 1000 μ in Figure 8)				
0	47			
20	46	1.31	0.98	× eyepiece
40	42	0.90	0.89	× objective
50	32	0.80	0.68	× 10 × 20
60	24	0.73	0.51	ρ_p = 0.84 g/cm^3
70	12	0.67	0.26	
80	7	0.62	0.15	
90	8	0.58	0.17	
100	4	0.55	0.085	
110	1	0.51	0.021	
120	1	0.48	0.021	
(Run 2; tobacco, left side in Figure 10)				
0	145			
15	144	1.64	0.99	× 10 × 20
30	124	1.12	0.86	ρ_p = 0.75 g/cm^3
45	110	0.92	0.76	
55	89	0.82	0.61	h = 1000 μ
70	68	0.72	0.47	
80	52	0.66	0.36	
90	37	0.63	0.26	
100	29	0.59	0.20	
120	13	0.53	0.083	
140	8	0.49	0.055	
160	6	0.45	0.041	
180	2	0.42	0.014	
(Run 3; iron oxide pigment in Figure 11)				
0	31			
2	31	1.74	1.00	× 10 × 20
6	30	0.98	0.97	ρ_p = 0.52 g/cm^3
8	27	0.84	0.87	
10	21	0.74	0.68	h = 1000 μ
16	11	0.56	0.36	
20	11	0.50	0.36	
30	9	0.40	0.29	
40	4	0.34	0.13	
50	4	0.28	0.13	

(Run 4; fog, right side in Figure 8)

t	$N_{tot}(t)$	D_p	$N_{tot}(t)/N_{tot}(0)$	Remarks
0–0.5	111			
0.5–1.0	107	9.5	0.97	× 10 × 10
1.0–1.5	95	7.4	0.86	ρ_p = 1.0 g/cm^3
1.5–2.0	84	6.2	0.76	
2.0–2.5	61	5.5	0.55	h = 2000 μ
2.5–3.0	65	5.0	0.59	$N_{tot}(t)$ is the sum of 7 observations
3.0–3.5	39	4.6	0.35	
3.5–4.0	37	4.3	0.33	
4.0–4.5	25	4.0	0.23	
4.5–5.0	9	3.8	0.081	
5.0–5.5	6	3.6	0.054	
5.5–6.0	6	3.4	0.054	

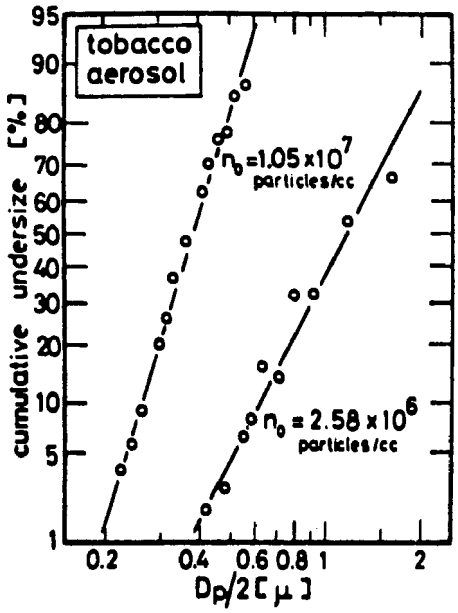

Figure 10. Particle size distribution of tobacco aerosol.

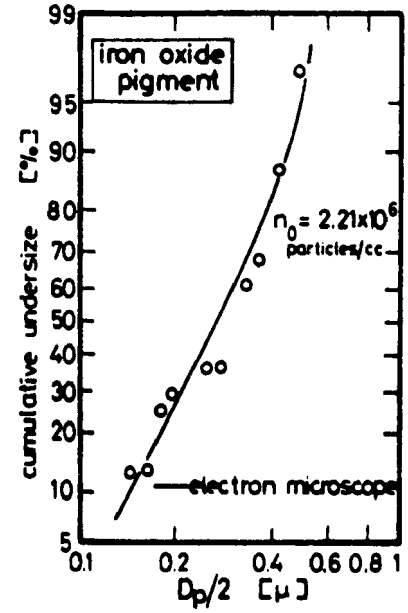

Figure 11. Particle size distribution of powder of iron oxide pigment.

curs. Although the sizes of tobacco particles reported by other investigators (Sano, *et al.*, 1954; Keith and Derrick, 1960; Porstendorfer and Schraub, 1972) are smaller than those in Figure 10, such difference is thought to be caused by the existence of water, which is expected to adhere to the particle surface.

Figure 11 shows one of the results of analysis of fine powders. In this analysis iron oxide pigment powder was dispersed into air by a mixer-type disperser. It probably takes a few days to measure by the Andreasen pipet method while only a few minutes was required by this method. The result of size analysis by an electron microscope for the same powder is also plotted in the figure. They agree fairly well. Some of the representative data are shown in Table III.

Conclusion

The technique developed in this study was found to be useful for the particle size analysis of fine powders and aerosols, including those of fine water droplets. The technique has the advantage of sedimentation methods in which particles are observed while they are suspended. Moreover, the usual disadvantage of sedimentation procedures, that much time is needed for the fall of small particles, was overcome by air sedimentation with an extremely shallow sedimentation depth. As a result, the size analysis of particles, including water droplets, which are larger than several tenths micron in diameter, was possible in a short time. The ultramicroscopic detection of the particle concentration on a number basis and its recording by a video system served for quick analysis without disturbing the aerosols during observation. The particle number concentration, however, must be rather high, a fact which is both an advantage and a disadvantage of the method.

Acknowledgment

T. Miyazaki was very helpful in the experimental work.

Nomenclature

C_m = Cunningham's correction factor
F = cumulative fraction undersize
D_e = effective diameter of microscopic sight shown in Figure 1, cm
D_p = particle diameter, μ or cm
$f(D_p)$ = particle size distribution function
h, Δh = values shown in Figure 1, cm
$N(t)$ = particle number observed by microscope at t sec after the start of sedimentation
$N_{int}(t)$ = particle number observed by microscope during a certain period of observation at t sec after the start of sedimentation
N_{total} = total particle number in volume v_h
n_0 = particle number concentration, particles/cm^3
t = time elapsed, sec
U_t = terminal settling velocity, cm/sec
v_h, v_m = volumes shown in Figure 1, cm^3

Greek Letters

μ = viscosity, g/(cm sec)
ρ_p = density of particle, g/cm^3
ρ_f = density of fluid, g/cm^3

Literature Cited

Davies, C. N., *Proc. Roy. Soc., Ser. A*, 200, 100 (1949).
Fuchs, N. A., "The Mechanics of Aerosols," Pergamon Press, 1964.
Keith, C. H., Derrick, J. C., *J. Colloid Sci.*, 15, 340 (1960).
Mukaibo, T., *et al.*, *Sogo Shikensho Nempo*, 20, No. 2 (1962).
Porstendorfer, J., Schraub, A., *Staub*, 32 (10), 33 (1972).
Richardson, J. F., Wooding, E. R., *J. Photogr. Sci.*, 4, 75 (1956).
Sano, K., Fujiya, Y., Sakata, S., *J. Chem. Soc. Jap.*, 74, 664 (1954).

Received for review April 1, 1974
Accepted September 6, 1974

Presented at the Chemical Engineering Meeting in Japan.

TURBULENT COAGULATION OF AEROSOLS IN A PIPE FLOW

KIKUO OKUYAMA, YASUO KOUSAKA AND TETSUO YOSHIDA

Department of Chemical Engineering, University
of Osaka Prefecture, Sakai 591, Japan

TURBULENT COAGULATION OF AEROSOLS IN A PIPE FLOW

KIKUO OKUYAMA, YASUO KOUSAKA AND TETSUO YOSHIDA

Department of Chemical Engineering, University of Osaka Prefecture, Sakai 591, Japan

Abstract

Turbulent coagulation of aerosol particles was studied experimentally by observing the time-dependent changes in particle number concentration of aerosol suspended in various turbulent pipe flows, using the ultramicroscopic size analysis. And these experimental results were confirmed with the calculation results obtained by numerically solving the population balance equation, which contained the simultaneous effect of Brownian coagulation or turbulent deposition in addition to turbulent coagulation. The effects of Brownian coagulation and turbulent deposition on turbulent coagulation were estimated using the values of two dimensionless parameters K_D and T_D, and negligible regions of these effects were indicated.

Introduction

For high concentration aerosol particles suspended in a turbulent flow, turbulent coagulation is essential for characterizing the behavior of aerosols, but most of previous studies on turbulent coagulation have been restricted to theoretical ones where the coagulation rate is discussed.[1,4,6] Though the changes in properties of aerosol undergoing turbulent coagulation in a stirred tank were observed and experimental data were compared with theoretical calculation results in the previous paper,[5] experimental study is insufficient to check the property of the theories. The largest cause of the lack in experimental data is the difficulty in accurate measurement of the change in properties of high concentrated aerosol.

In this paper, the changes in particle number concentration of polydisperse aerosols undergoing turbulent coagulation in a turbulent pipe flow were observed for various conditions using the ultramicroscopic size analysis previously develpoed by the authors.[9] And the observed changes of particle number concentrations with time were compared with those obtained by numerically solving the basic equation for polydisperse aerosol. In this case, these calculations were made for some representative turbulent coagulation rate constants. Moreover two dimensionless parameters were introduced to estimate the amount of the effects of Brownian coagulation and deposition by turbulent diffusion on turbulent coagulation.

1. Theoretical Consideration

The population balance equation describing the time-dependent change in particle size distribution of polydisperse aerosol undergoing turbulent coagulation alone can be written as[11]

$$\frac{\partial n'(r',t')}{\partial t'} = \int_{\rho'=0}^{\rho'=r'/\sqrt[3]{2}} K_T(\sqrt[3]{r'^3-\rho'^3},\rho')\, n'(\sqrt[3]{r'^3-\rho'^3},t')\, n'(\rho',t') \left(\frac{r'}{\sqrt[3]{r'^3-\rho'^3}}\right)^2 d\rho'$$

$$- \int_{\rho'=0}^{\rho'=\infty} K_T(r',\rho')\, n'(r',t')\, n'(\rho',t')\, d\rho' \qquad (1)$$

In the case of turbulent pipe flow, the time t' corresponds to the residence time which is approximately the ratio of pipe length to average flow velocity

$$t' = L / u \qquad (2)$$

$K_T(r',\rho')$ is the turbulent coagulation function for particles of radii r' and ρ', and the representative theoretical equations denoting the collision rate by the turbulent flow have been proposed by Saffman et al.[6] and Levich[4]. Generally collisions between particles in a turbulent fluid are considered to be caused by two independent and essentially different mechanisms. In the first coagulation mechanism particles may collide with each other as the result of different velocities between particles because of the spatial non-homogenities characteristic of turbulent flow. For this mechanism, Saffman et al. has proposed next equation denoting the turbulent coagulation rate,

$$K_T(r',\rho') = 1.30(r'+\rho')^3\sqrt{\varepsilon_0/\nu} \qquad (3)$$

The second coagulation mechanism may be caused by a relative motion of each particle differing from that of turbulent air because of its inertia will not be the same as equivalent mass of air. Saffman et al. also obtained the following equation for the simultaneous collision rate by first and second coagulation mechanisms including the collision brought by gravity

$$K_T(r',\rho') = \sqrt{8\pi}(r'+\rho')^2\left[(1-\rho_f/\rho_p)^2\{\tau(\rho')-\tau(r')\}^2(1.3\nu^{-0.5}\varepsilon_0^{1.5} + \frac{1}{3}g^2) + \frac{1}{9}(r'+\rho')^2\varepsilon_0/\nu\right]^{1/2} \quad (4)$$

where $\tau(r')$ is the particle relaxation time, equal to $2r'^2\rho_p/9\mu$. This equation reduces to next equation assuming that particles move with air.

$$K_T(r',\rho') = 1.67(r'+\rho')^3\sqrt{\varepsilon_0/\nu} \quad (5)$$

which is a form similar to Eq.(3). A detailed comparison of Eqs.(3) and (4) with experimental results, which is one of the most important purposes of this paper, has not been made at all. Levich's equation, however, was omitted because it was found that this equation overestimated the coagulation rate as shown in the previous paper[5]

In either mechanism, the coagulation rate depends mainly on particle size and velocity gradient evaluated from the energy dissipation rate per unit mass of fluid, because Eqs.(3) and (4) were derived assuming the theory of isotropic turbulence. In the case of turbulent pipe flow, the average value of the energy dissipation rate ε_0 has been suggested by Laufer[8] as next equation

$$\varepsilon_0 = fu^3/D \quad (6)$$

As the distribution of energy dissipation rate through a pipe results in coagulation rate distribution, a difference exists between the coagulation rate based on the average energy dissipation rate ε_0 and that based on the local energy dissipation rate and its distribution through a pipe. In this study, however, the distribution of energy dissipation rate was neglected and the average value ε_0 was used to evaluate the coagulation rate for a first approximation.

Integrating Eq.(1) with respect to r' from 0 to ∞, the total particle number concentration n' of polydisperse aerosol can be given as

$$\frac{dn'}{dt'} = -\frac{1}{2}\int_0^\infty\int_0^\infty K_T(r',\rho')n'(r',t')n'(\rho',t')dr'd\rho' \qquad (7)$$

where

$$n' = \int_0^\infty n'(r',t')dr' \qquad (8)$$

On the other hand, when an aerosol is monodisperse having particle radius r'_0, Eq.(1) becomes

$$\frac{dn'}{dt'} = -\frac{1}{2}K_T(r_0',r_0')n'^2 \qquad (9)$$

Consequenlty the following ratio of the value of Eq.(7) to that of Eq.(9) means the effect of polydispersity of aerosol on coagulation rate

$$\zeta = \frac{1}{2}\int_0^\infty\int_0^\infty K_T(r',\rho')n'(r',t')n'(\rho',t')dr'd\rho' \Big/ \frac{1}{2}K_T(r_0',r_0')n'^2 \qquad (10)$$

which is called "polydispersion factor".

Since Eqs.(1) and (10) cannot be solved analytically, the Runge-Kutta- Merson method for differentiation and Simpson method for integral were employed to solve them. In this case, the initial particle size distribution at the entrance of pipe was assumed to be established instantaneously with the following log-normal form

$$n'(r',0)dr' = \frac{n_0'}{\sqrt{2\pi}\ln\sigma_{g0}}\exp\left(-\frac{\ln^2(r'/r_{g0}')}{2\ln^2\sigma_{g0}}\right)d\ln r' \qquad (11)$$

In the calculation of Eq.(1), as a numerical check the total mass of aerosol was calculated every few time steps and compared with the initial value.

1.1 Polydispersion factor

Figure 1 shows the polydispersion factor ζ against the geometric standard deviation σ_{g0} of Eq.(11). In this case the particle

radius r_0' and the partical number concentration of monodisperse aerosol were assumed to be r_{g0}' and n_0'. As seen from the graph, ζ tends to increase with σ_{g0}, but the increasement of ζ calculated by using Eq.(4) as $K_T(r',\rho')$ is much greater than that by using Eq.(3) for even the small value of ε_0. From the value of ζ at Brownian coagulation, which is calculated by introducing the following Brownian coagulation function[7] $K_B(r',\rho')$ in replace of $K_T(r',\rho')$ in Eq.(10),

$$K_B(r',\rho') = K_0(r'+\rho')\{C_m(r')/r' + C_m(\rho')/\rho'\} \qquad (12)$$

where $K_0 = 2kT/3\mu$

the effect of polydispersity is found to be small in comparison with those of turbulent coagulation.

1.2 Particle size distribution

Figure 2 shows the time-dependent changes in particle size distributions for three different initial log-normal forms. The frequency f(ln r') was calculated by the next equation

$$f(\ln r') = n'(r',t')r'/n_0 \qquad (13)$$

The dimensionless time t was expressed in terms of the coagulation time, which is the ratio of the actual elapsed to the half-life time $t_{n=0.5}$, which is given by the next equation from Eq.(9)

$$t_{n=0.5} = 1/5.2\, r_{g0}'^3 \sqrt{\varepsilon_0/\nu}\, n_0' \qquad (14)$$

In the particle size distribution of σ_{g0}=1.1 at t=2.39 the second mode, which corresponds to the coalescence of two particles having the initial geometric mean radius, has begun to appear. In other cases the particle size distributions broaden rapidly with the dimensionless time t, and its tendency in calculation results by Eq.(4) is especially large.

1.3 Particle number concentration

Figure 3 shows the normalized number concentration, which is defined as the ratio of the concentration at any time to the initial time, versus the dimensionless time based on turbulent coagulation. There exist very large differences between the calculation results by Eq.(3) and that by Eq.(4) due to the loss by second turbulent coagulation mechanism. Even a calculation results of σ_{g0}=1.1 by Eq.(3), which is nearly monodisperse, particle number concentration comes to decrease faster than that of monodisperse aerosol with the elapse of time, because particle size distributions expand with time as shown in Fig.2.

1.4 Effect of Brownian coagulation

The basic equation expressing the time-dependence of the size distribution of polydisperse aerosol undergoing simultaneous Brownian and turbulent coagulations can be written as, assuming that both coagulation mechanisms are independent each other.

$$\frac{\partial n'(r',t')}{\partial t'} = \int_{\rho'=0}^{\rho'=r'/\sqrt[3]{2}} \left\{ K_B\left(\sqrt[3]{r'^3-\rho'^3}, \rho'\right) + K_T\left(\sqrt[3]{r'^3-\rho'^3}, \rho'\right) \right\} n'\left(\sqrt[3]{r'^3-\rho'^3}, t'\right) n'(\rho', t') \times \left(\frac{r'}{\sqrt[3]{r'^3-\rho'^3}}\right)^2 d\rho' - \int_{\rho'=0}^{\rho'=\infty} \left\{ K_B(r',\rho') + K_T(r',\rho') \right\} n'(r',t') n'(\rho',t') d\rho' \qquad (15)$$

When an aerosol is monodisperse having particle radius r_{g0}'

$$\frac{dn'}{dt'} = -\left\{ \frac{1}{2} K_T(r_{g0}', r_{g0}') + \frac{1}{2} K_B(r_{g0}', r_{g0}') \right\} n'^2 \qquad (16)$$

Substituting Eqs.(3) and (12), Eq. (16) becomes

$$\frac{dn'}{dt'} = -\left\{ 5.2\, r_{g0}'^3 \sqrt{\varepsilon_0/\nu} + 2K_0 C_m(r_{g0}') \right\} n'^2 \qquad (17)$$

As described in the previous paper,[5] the importance of turbulent coagulation relative to Brownian coagulaiton can be estimated by the following dimensionless parameter K_D

$$K_D = \{K_T(r_{g0}', r_{g0}') + K_B(r_{g0}', r_{g0}')\} / K_B(r_{g0}', r_{g0}')$$

$$= 1 + 5.2\, r_{g0}'^3 \sqrt{\varepsilon_0/\nu} \,/\, 2K_0 C_m(r_{g0}') \qquad (18)$$

Normalizing Eq.(17) by the following dimensionless variables,

$$t = 5.2\, r_{g0}'^3 \sqrt{\varepsilon_0/\nu}\, n_0' t', \quad n = n'/n_0' \qquad (19)$$

the basic equation comes to next equation.

$$dn/dt = -\{K_D/(K_D-1)\} n^2 \qquad (20)$$

Solving Eq.(20) under the initial condition that n=1 at t=0,

$$n = 1/(1 + \frac{K_D}{K_D-1} t) \qquad (21)$$

Figure 4 shows the effect of K_D on the change in the normalized number concentration as a function of dimensionless time based on turbulent coagulation. As the value of K_D increases the curves move toward the right and tend to converge to that of K_D=100~∞ which coincides with that of turbulent coagulation alone. The graph also shows that the effect of Brownian coagulation can be almost ignored at the value of K_D greater than 10.0. Though the time-dependent changes for polydisperse aerosol were obtained by solving Eq.(15) numerically assuming the initial particle size distribution to be log-normal form, their tendencies by K_D are found to almost agree with those of monodisperse aerosol.

1.5 Effect of particle deposition

In a turbulent pipe flow of aerosol, particles tend to deposite by turbulent diffusion and gravitational settling. The basic equation expressing the time-dependent changes in particle number concentration of aerosol undergoing turbulent deposition alone can be given as follows.

$$\frac{\partial n'(r',t')}{\partial t'} = -\frac{4St^*_{av}(r')u^*}{D} n'(r',t') \qquad (22)$$

$$St^*_{av} = \frac{1}{\pi}\int_0^{\pi} St^*(r')\,d\theta \qquad (23)$$

where $St^*(r')$ denotes the local dimensionless deposition velocity and is given

$$St^*(r') = V/u^* \qquad (24)$$

As this $St^*(r')$ is different by the effect of gravitational settling in the case of horizontal pipe flow, $St^*_{av}(r')$ is the average one around the periphery of the pipe. There exist many theoretical and experimental researches on evaluating the values of $St^*(r')$.

Combining the Eqs.(1) and (22), the basic equation for coagulation and deposition can be given as follows.

$$\frac{\partial n'(r',t')}{\partial t'} = \int_{\rho'=0}^{\rho'=r'/\sqrt[3]{2}} K_T(\sqrt[3]{r'^3-\rho'^3},\rho')\,n'(\sqrt[3]{r'^3-\rho'^3},t')\,n'(\rho',t')\left(\frac{r'}{\sqrt[3]{r'^3-\rho'^3}}\right)^2 d\rho'$$
$$-\int_{\rho'=0}^{\rho'=\infty} K_T(r',\rho')\,n'(r',t')\,n'(\rho',t')\,d\rho' - 4St^*_{av}(r')u^*n'(r',t')/D \qquad (25)$$

When an aerosol is monodisperse, Eq.(25) reduces to

$$\frac{dn'}{dt'} = -5.2\,r'^3_{g0}\sqrt{\varepsilon_0/\nu}\,n'^2 - 4St^*_{av}(r'_{g0})u^*n'/D \qquad (26)$$

Substitution of Eq.(19) into this equation gives the following equation

$$dn/dt = -n^2 - T_D n \qquad (27)$$

where

$$T_D = 4St^*_{av}(r'_{g0})u^*/5.2\,r'^3_{g0}D\sqrt{\varepsilon_0/\nu}\,n_0' \qquad (28)$$

T_D is a dimensionless parameter which can be evaluated from initial aerosol properties and intensity of turbulence. As seen from the definition, this parameter T_D means the ratio of deposition rate to turbulent coagulation rate, and therefore T_D denotes the relative importance of deposition to turbulent coagulation. Integrating Eq.(27) under the initial condition

n=1 at t=0, the time-dependent change in particle number concentration can be given as

$$n = T_D \exp(-T_D t) / \{ T_D + 1 - \exp(-T_D t) \} \qquad (29)$$

Figure 5 shows the dependence of particle number concentration change on T_D. With the increase of T_D the particle number decreases faster due to the larger effect of deposition, but the effect of deposition can be almost ignored at the value of T_D less than 0.1 as seen from this graph. Though the discussion described above is for monodisperse aerosol, it will be essentially valid for polydisperse one.

2. Experimental Apparatus and Method

The apparatus used in this work consists of the following parts- blower, aerosol generator, aerosol chamber, P.V.C. pipe and devices for ultramicroscopic particle size analysis as shown in Fig.7. Aerosol used was fog of aqueous ammonium chloride solution. Clean air coming from a blower through a glass fibrous filter and being regulated the orifice flow meter was first bubbled into the hydrochloric acid solution and subsequently bubbled into the aqueous ammonia solution, when ammonia chloride smoke was produced. During the bubbling of the ammonia chloride smoke at the final vessel containing water, aerosols were changed into the fog droplets of aqueous amminium chloride to absorb water vapor. At the same time, the excess gas, chiefly ammonia gas, is absorbed through the water. The aerosol generation by this method was examined by Fujitani[2] in detail. Aerosols thus generated were continuously led into vinyl chloride pipe with diameter of 13 or 26 mm to make turbulent flow. The length of

pipe was changed to be 20, 52 and 100 m, before and after of which the aerosol was sampled by sampling tap with isokinetic sampling condition. Aerosol sampled was introduced into the observation cell installed on the stage of an ultramicroscope to measure its particle size distribution and particle number concentration. The measurement method using as ultramicroscope was developed previously by the authors.[9]

Experiments were carried out by changing the initial partical number concentrations and by increasing the particle radius using particle growth in a ageing chamber. Representative experimental conditions and properties of aerosols are shown in Table 1.

3. Experimental Results and Discussion

In a comparison of experimental data with theoretical calculation results, the residence time of aerosol in a pipe can be calculated by Eq.(2), and ε_0 by Eq.(5). Figure 8 shows a comparison of the change in particle number concentration between experimental and theoretical curves. Particle number concentrations obtained experimentally tend to decrease with the dimensionless time t indicating some scattering. Theoretical curves denoted by solid lines, broken lines and one point broken line show the particle number concentration change of aerosols undergoing turbulent coagulation alone, which were calculated by solving Eq.(1) for polydisperse aerosol and Eq.(8) for monodisperse one. Experimental data decrease faster than the calculated results of monodisperse aerosol because of the polydispersity, and their tendencies almost agree with those calcu-

lated using Eq.(3) as the turbulent coagulation function, but they do not agree with those calculated using Eq.(4) at all. Some of experimental data are found to be affected by Brownian coagulation or turbulent deposition as seen from the values of K_D and T_D, but the deposition by Brownian diffusion can be ignored in these experimental conditions according to Gromely et al.[3] . In the calculation of T_D, Yoshioka at al's[10] equation was used as the value of $St^*(r')$, which is a relatively simple form and showed the better fitting with many experimental data in comparison with other equations. Fig.8(a) shows a comparison of experimental data(the values of K_D are less than 10.0) with the calculation results of Eq.(15) to examine the effect of Brownian coagulation, and Fig.8(b) a comparison of experimental data(the values of T_D are larger than 0.1) with the calculation results of Eq.(25) to examine the effect of deposition. Most of experimental data almost agree with the tendency of the calculated curves, and the effect of Brownian coagulation or turbulent deposition is found to increase as K_D decreases or T_D increases.

Fig.9 shows a comparison of experimental data, where the particle radius is large to be about 0.7 μ in comparison with Fig.8, with the calculation results obtained by solving Eq.(25). Most of experimental particle number concentrations tend to decrease faster than those of calculation results, that is, it is found that these differences can be explained by neither Brownian coagulation and turbulent deposition. These are considered to be due to the loss of particles by second turbulent coagulation mechanism which comes to appear with increasing of the turbulent intensity and particle size, but they can not be explained by Saffman at al's Eq.(4).

From experimental conditions of Figs. (7) and (9), the second coagulation mechanism by turbulent flow may be essential when the values of $r'^{3}_{g0}\sqrt{\varepsilon_0}$ is larger than 2.5×10^{-10}. These kinds of experimental data as shown in Figs. (7) and (9) have not been reported because of the difficulty in accurate measurement of changing number concentration of particles with time.

Conclusion

Turbulent coagulation of aerosol particles was studied experimentally and theoretically, and the following results were obtained.

1) At $r'^{3}_{g0}\sqrt{\varepsilon_0}$ less than 2.5×10^{-10} the time-dependent change in particle number concentration by turbulent coagulation can be evaluated by the solution of population balance equation using Eq.(3) as coagulation function, that is, particles coagulate by first coagulation mechanism alone in this case. But at larger than this value the second coagulation mechanism was found experimentally to be appeared.

2) The effect of Brownian coagulation relative to turbulent coagulation can be ignored when the dimensionless parameter K_D is larger than 10.0.

3) The effect of deposition on turbulent coagulation can be predicted by the value of the dimensionless parameter T_D. The deposition can be almost ignored when the value of T_D is less than 0.1.

Literature Cited

1) Beal, S. K.: J. Aerosol Sci., 3, 113(1972)

2) Fujitani, Y.: Bull. Chem. Soc. Japan, 30, 683(1957)

3) Gormley, P. G. and M. Kennedy: Proc. Roy. Irish. Acad., 52-A, 163(1949)

4) Levich, V. G.:"Physicochemical Hydrodynamics", Prentice-Hall(1962)

5) Okuyama, K., Y. Kousaka, Y. Kida and T. Yoshida: J. Chem. Eng. Japan, 10, 142(1977)

6) Saffman, P. G. and J. S. Turner: J. Fluid Mech., 1, 16(1956)

7) Smoluchowski, M. von Z: Phys. Chem., 92, 129(1917)

8) Uhl, V. W. and J. B. Gray:"Mixing-theory and practice", Academic Press, 75(1966)

9) Yoshida, T., Y. Kousaka and K. Okuyama:Ind. Eng. Chem. Fundam., 14, 47(1975)

10) Yoshioka, N., C. Kanaoka and H. Emi: Kagaku Kogaku, 36, 1010(1972)

11) Zebel, G.:Kolloid-Z., 156, 102(1958)

Table 1 Experimental Conditions and Properties of Aerosols

key	Re [-]	ε_0 [cm^2/sec^3]	n'_0 [particles/cm^3]	r'_{g0} [μ]	σ_{g0} [-]	K_D [-]	$St^*_{av}(r'_{g0})$ [-]	T_D [-]	$r'^3_{g0}\sqrt{\varepsilon_0}$ [$cm^4/sec^{3/2}$]
Pipe diameter D = 13 mm									
◑	5000	1.35×10^6	$3.66\sim6.06 \times 10^7$	0.27~0.32	1.20~1.31	2.11	8.80×10^{-6}	0.0502	$2.29\sim3.81 \times 10^{-11}$
◐	"	"	$2.61\sim3.07 \times 10^6$	0.34~0.43	1.24~1.60	3.56	1.49×10^{-5}	0.667	$4.57\sim9.24 \times 10^{-11}$
◈	"	"	$3.98\sim4.64 \times 10^7$	0.35~0.43	1.21~1.30	"	"	0.0450	$4.98\sim9.24 \times 10^{-11}$
⊙	8000	4.93×10^6	$5.69\sim6.63 \times 10^7$	0.25~0.27	1.22~1.31	2.33	4.42×10^{-6}	0.0249	$3.47\sim4.37 \times 10^{-11}$
○	"	"	6.71×10^6	0.36~0.38	1.25~1.32	5.14	8.93×10^{-6}	0.160	$1.04\sim1.22 \times 10^{-10}$
◉	"	"	$2.54\sim3.98 \times 10^7$	0.32~0.41	1.30~1.40	"	"	0.0329	$0.73\sim1.53 \times 10^{-10}$
●	7400	3.98×10^6	$1.01\sim2.37 \times 10^7$	0.37~0.41	1.21~1.38	5.39	1.06×10^{-5}	0.0669	$1.01\sim1.37 \times 10^{-10}$
◍	10000	9.11×10^6	$1.10\sim3.17 \times 10^7$	0.30~0.48	1.23~1.27	7.64	8.23×10^{-6}	0.0459	$0.82\sim3.34 \times 10^{-10}$
⊖	13000	1.98×10^7	$1.85\sim2.09 \times 10^6$	0.31~0.34	1.32~1.48	6.60	5.30×10^{-6}	0.352	$1.29\sim1.70 \times 10^{-10}$
⊜	22400	8.38×10^7	3.62×10^7	0.30	1.18	9.74	1.35×10^{-5}	0.0502	2.47×10^{-10}
Pipe diameter D = 26 mm									
⊟	5000	8.47×10^4	$1.22\sim4.45 \times 10^7$	0.46~0.48	1.25~1.38	2.16	4.33×10^{-5}	0.113	$2.83\sim3.22 \times 10^{-11}$
▭	"	"	$0.46\sim4.71 \times 10^6$	0.30~0.44	1.25~1.38	1.54	2.68×10^{-5}	1.565	$0.79\sim2.48 \times 10^{-11}$
■	10000	5.69×10^5	$1.49\sim5.18 \times 10^7$	0.32~0.45	1.25~1.38	2.66	1.62×10^{-5}	0.045	$2.47\sim6.87 \times 10^{-11}$
▪	"	"	$0.77\sim3.74 \times 10^6$	0.35~0.40	1.25~1.38	2.54	1.54×10^{-5}	0.665	$3.23\sim4.83 \times 10^{-11}$
△	"	"	$1.18\sim4.16 \times 10^6$	0.55~0.80	1.36~1.58	10.6	4.94×10^{-5}	0.321	$1.26\sim3.86 \times 10^{-10}$
◆	15000	1.74×10^6	$4.60\sim9.94 \times 10^5$	0.63~0.83	1.37~1.67	21.8	4.03×10^{-5}	0.630	$3.30\sim7.54 \times 10^{-10}$
▲	"	"	$1.31\sim2.19 \times 10^6$	0.55~0.90	1.35~1.51	21.8	"	0.263	$2.19\sim9.62 \times 10^{-10}$

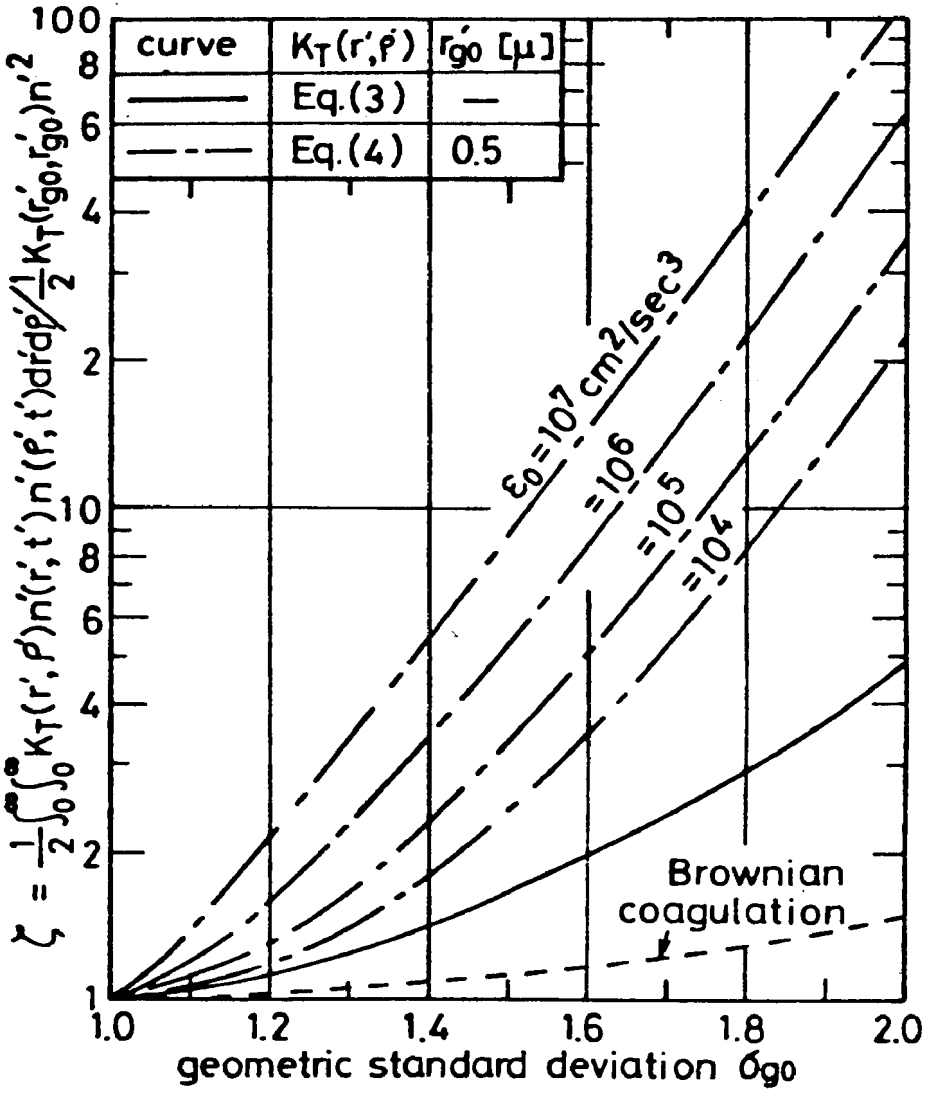

Fig. 1 Polydispersion factor

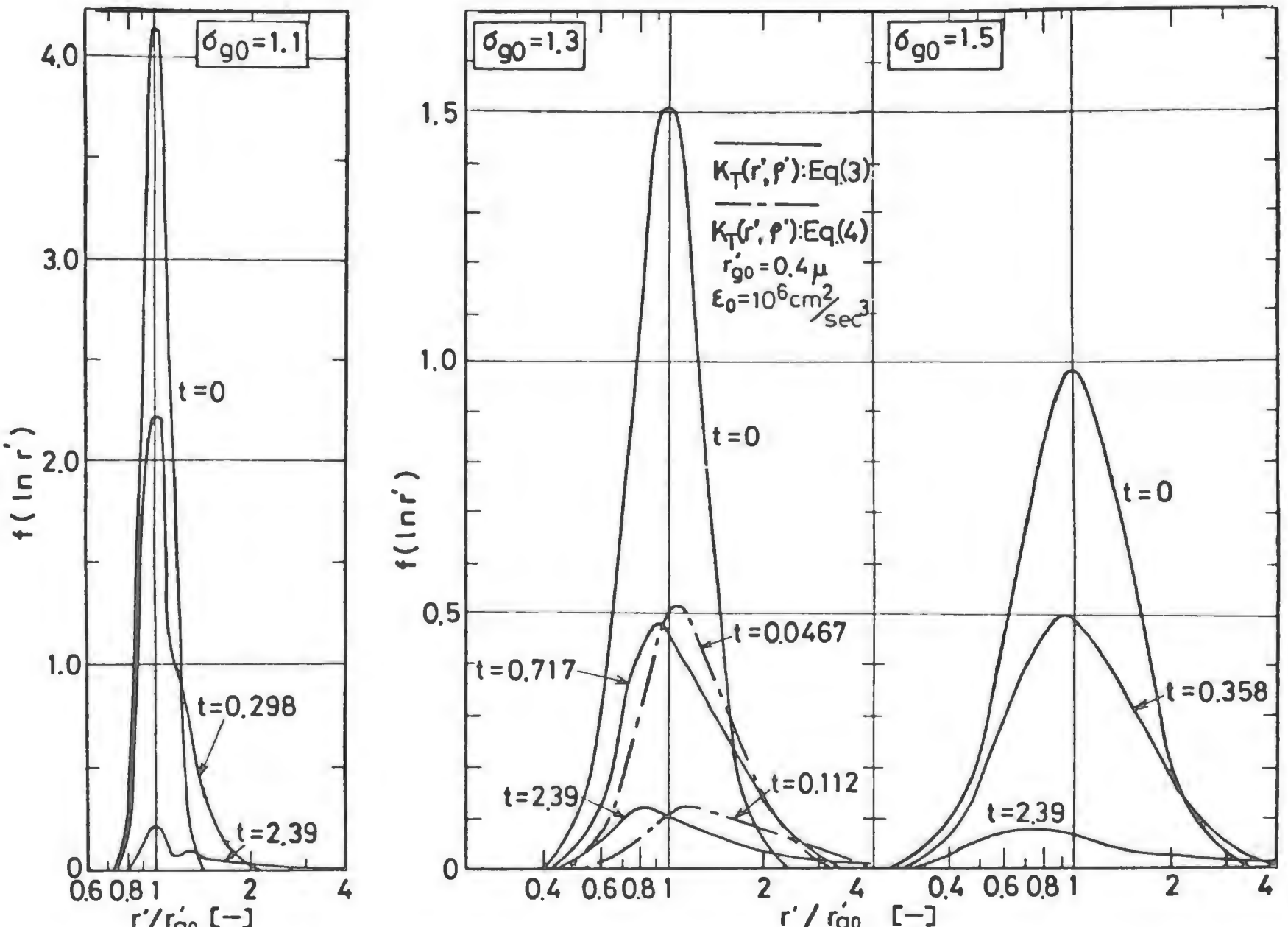

Fig. 2 Time-dependent changes in size distribution of particles undergoing turbulent coagulation

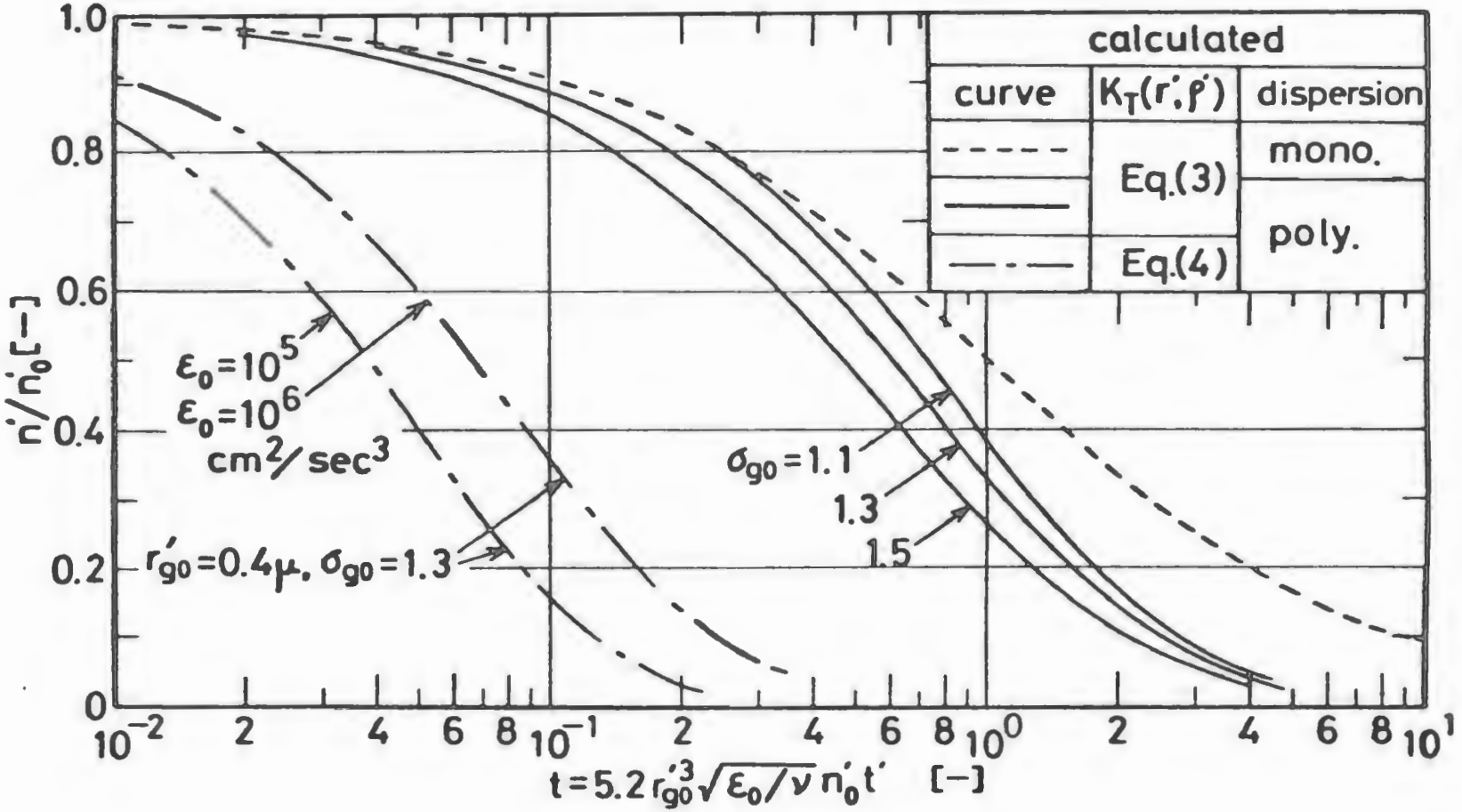

Fig. 3 Time-dependent changes in number concentration of particles undergoing turbulent coagulation

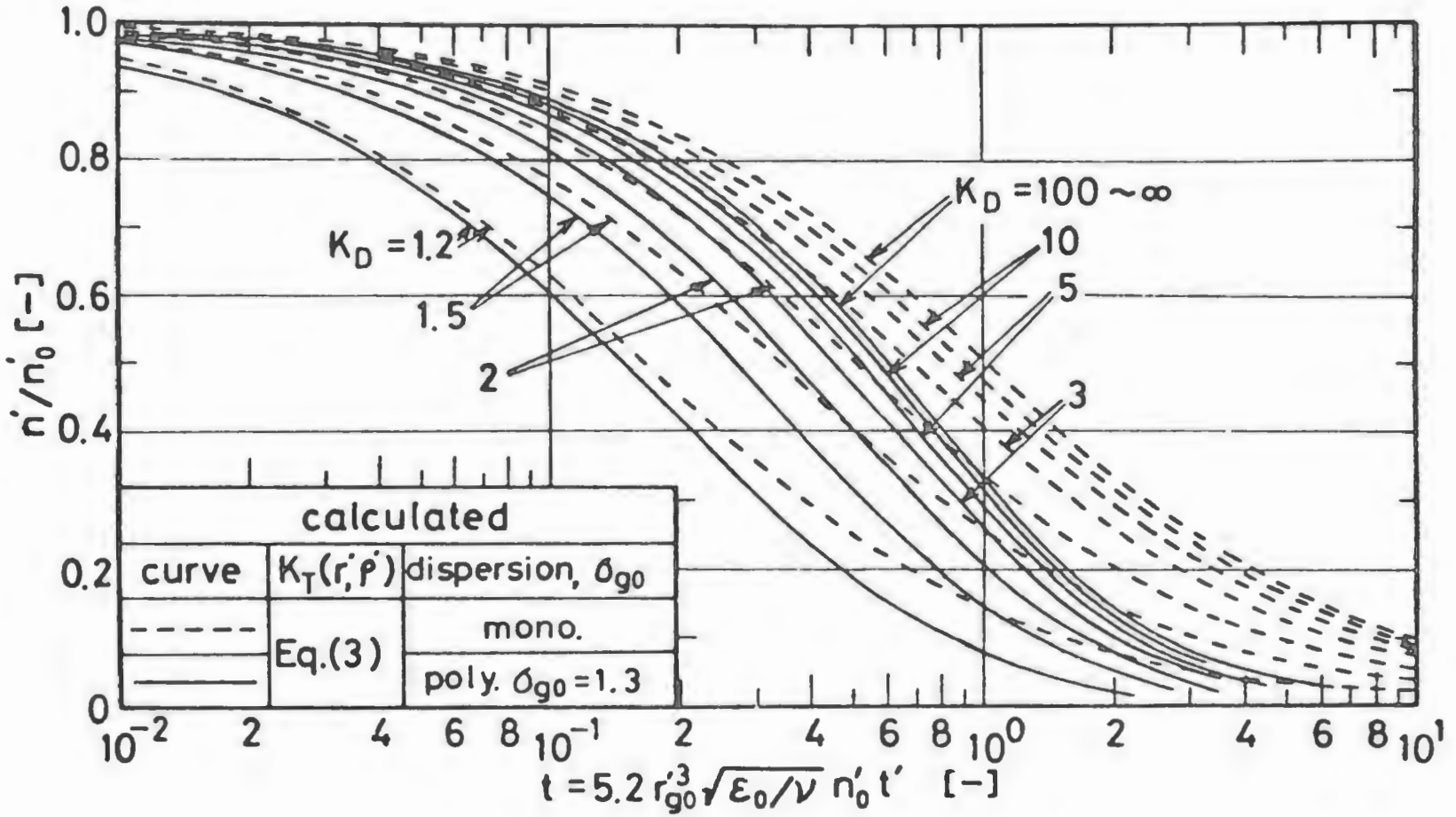

Fig. 4 Time-dependent changes in number concentration of particles undergoing turbulent and Brownian coagulations

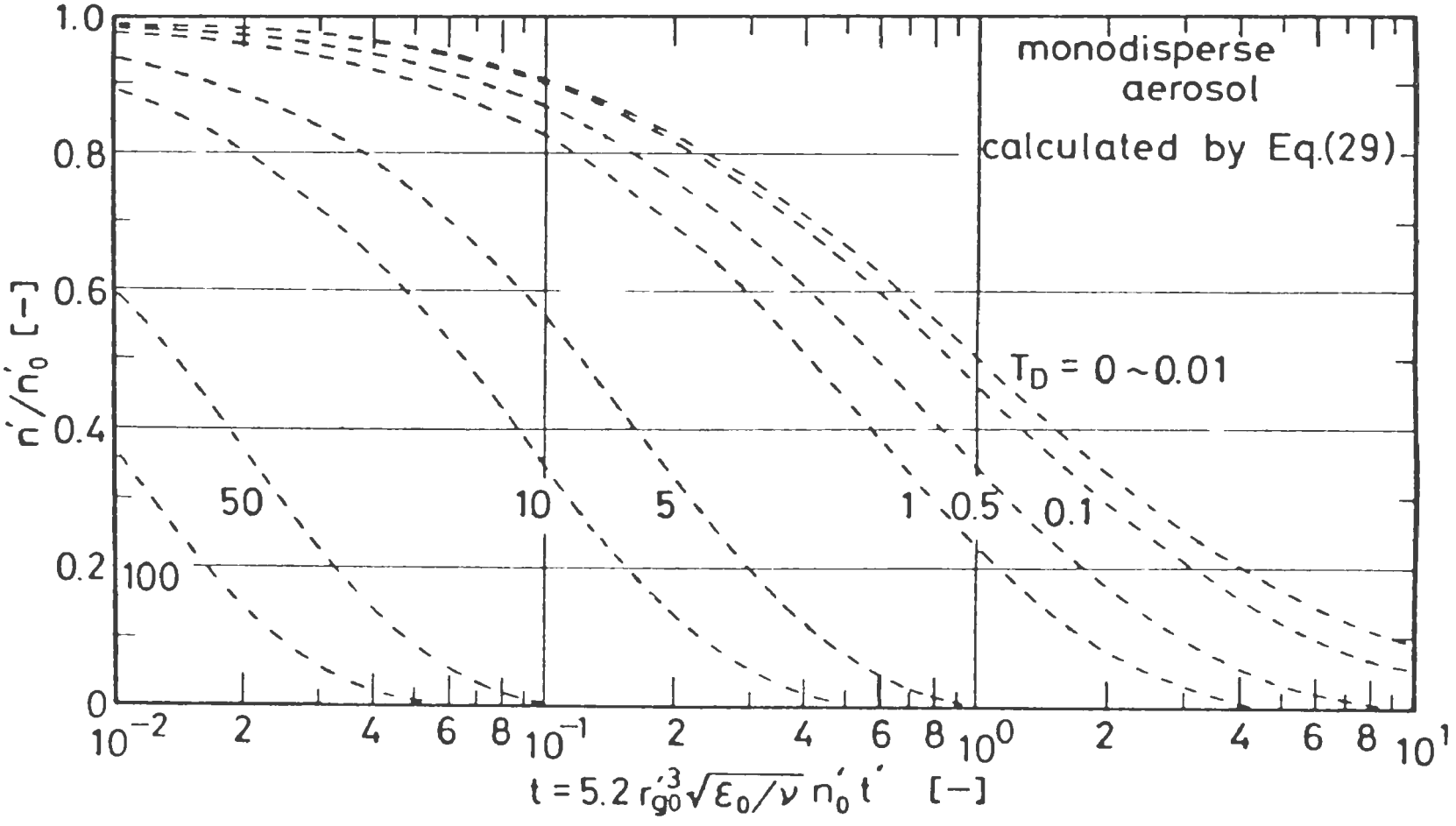

Fig. 5 Time-dependent changes in number concentration of particles undergoing turbulent coagulation and deposition

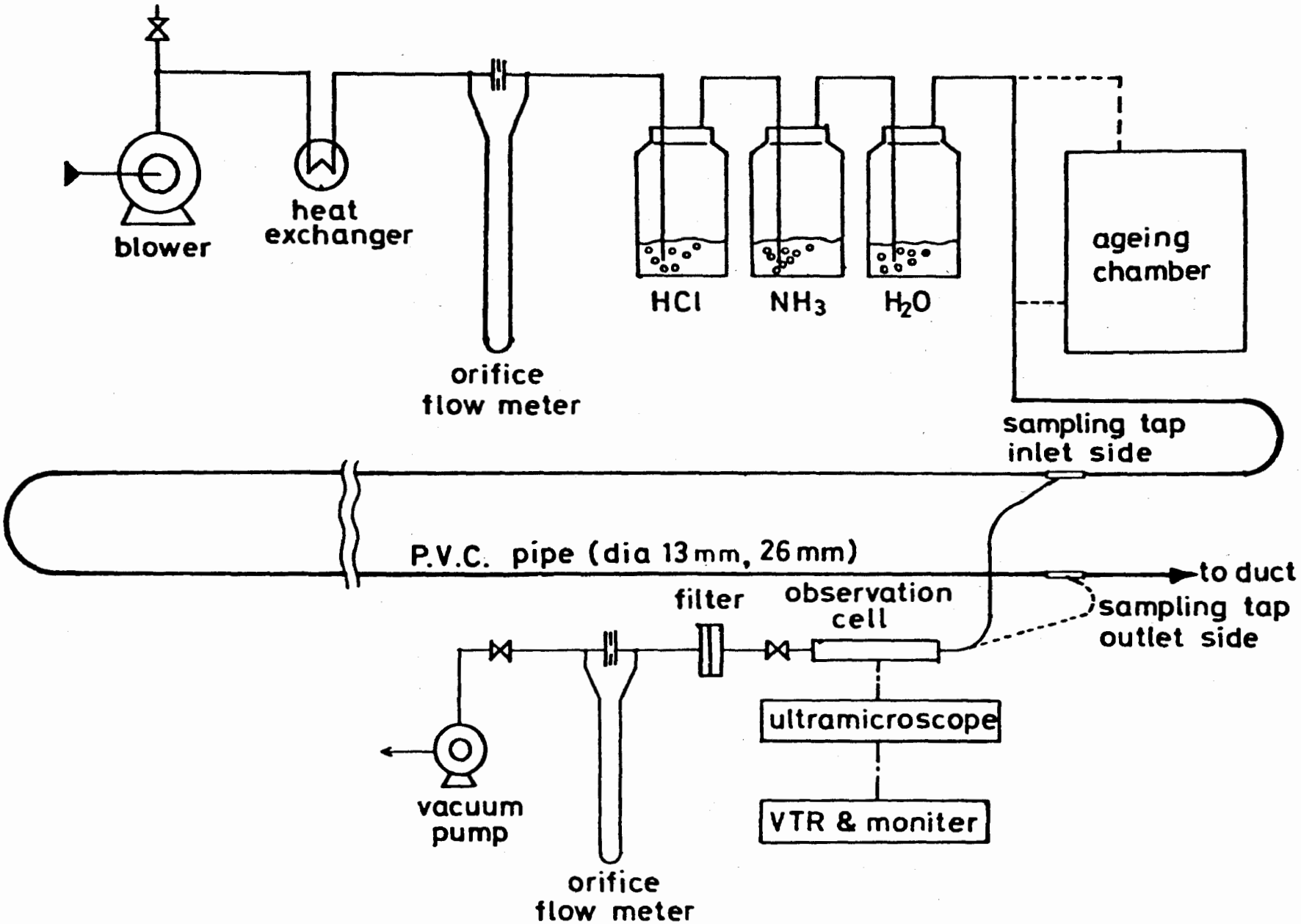

Fig. 6 Experimental apparatus

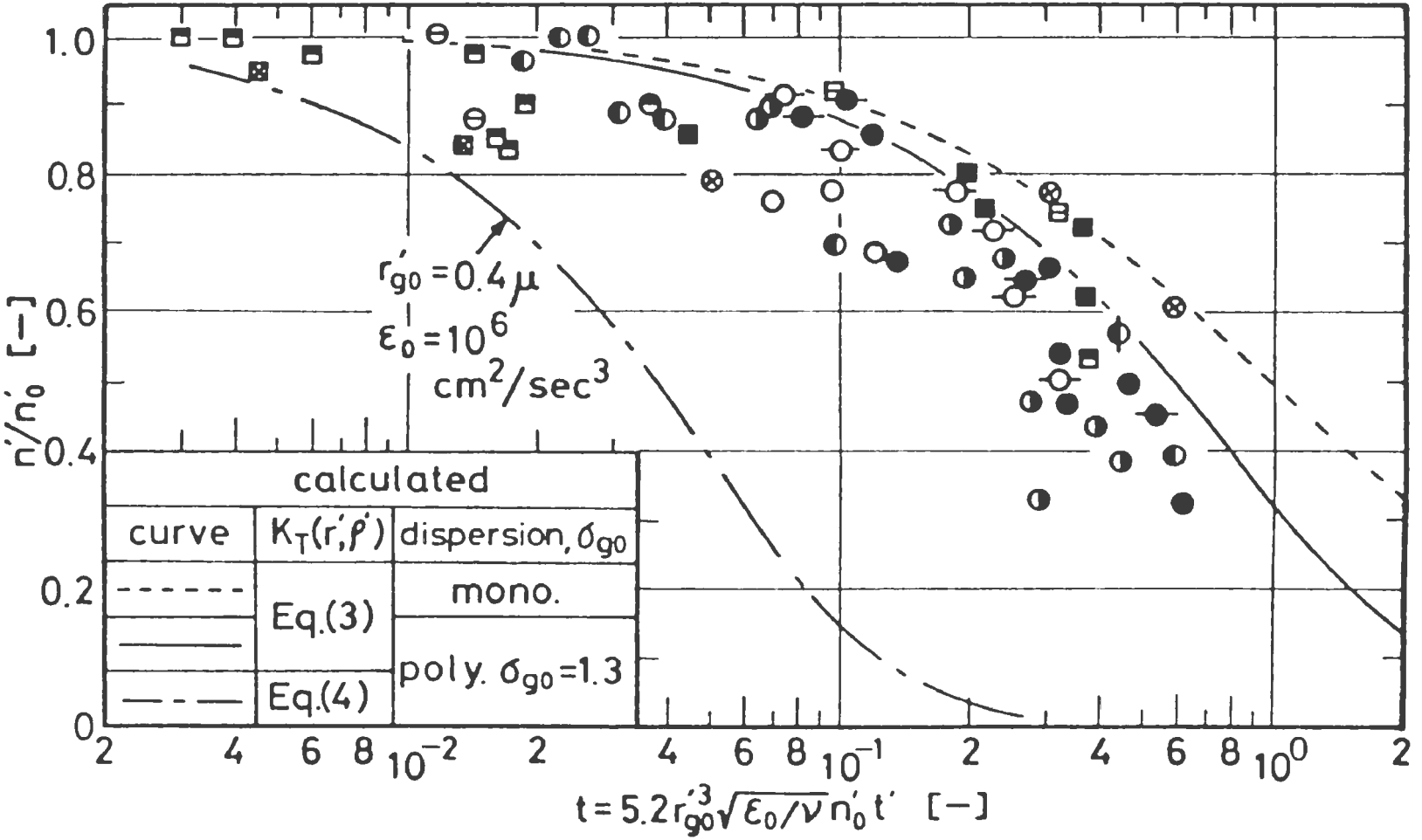

Fig. 7 Comparison of experimental particle number concentration changes with calculated ones

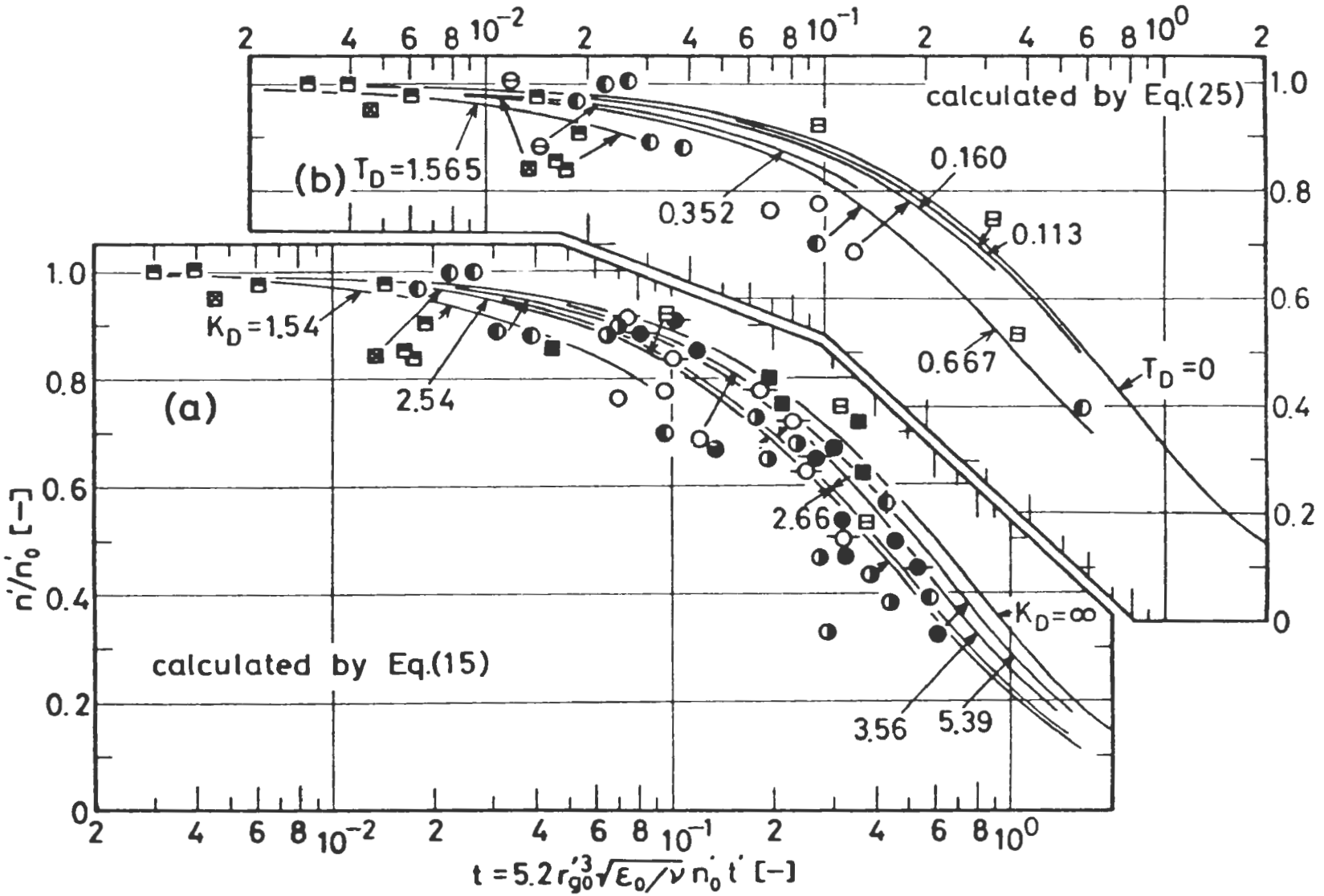

Fig. 8 Effect of Brownian coagulation or turbulent deposition on decrease in particle number concentration

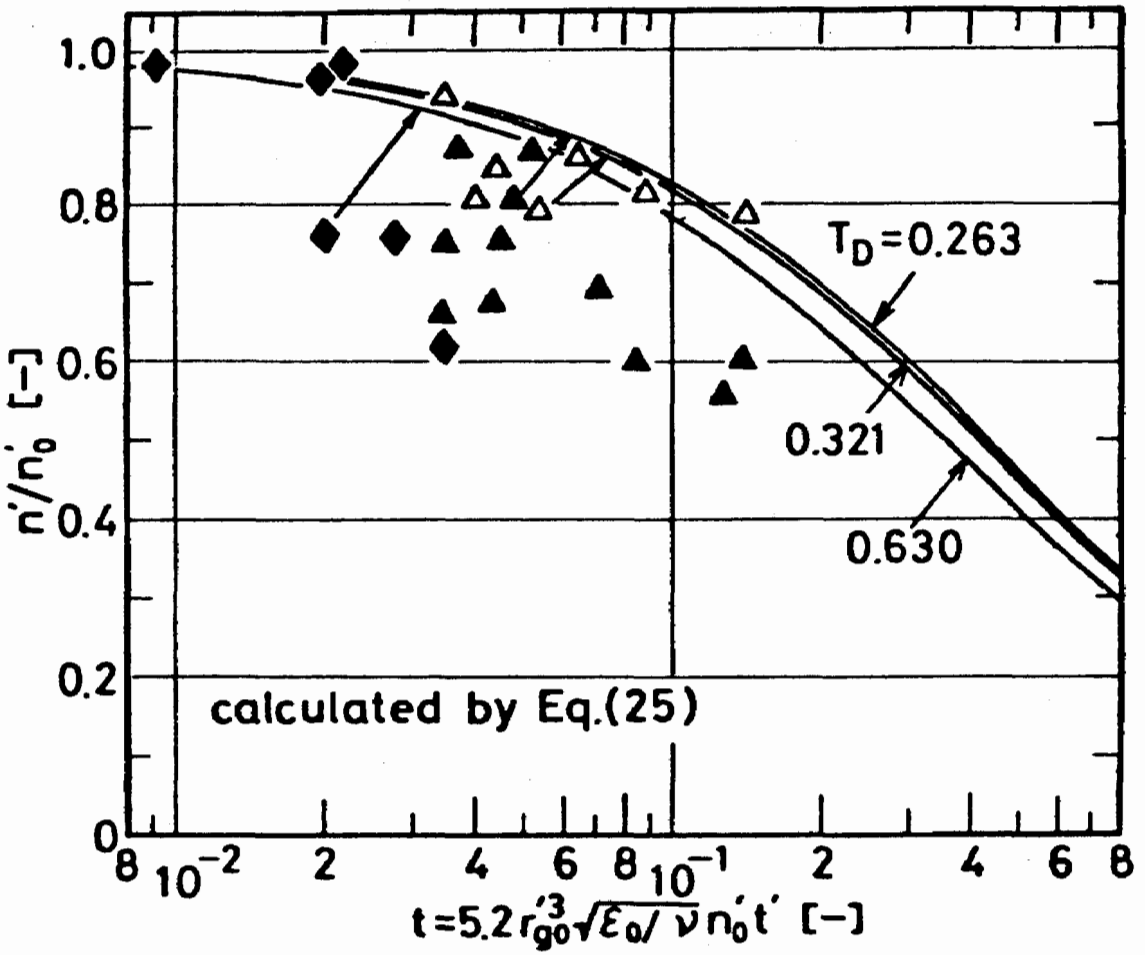

Fig. 9 Comparison of experimental particle number concentration changes with calculated ones

EFFECTS OF BROWNIAN COAGULATION AND BROWNIAN DIFFUSION ON FINE PARTICLE SIZE ANALYSIS BY SEDIMENTATION METHOD

KIKUO OKUYAMA, YASUO KOUSAKA,
TOSHIHIRO MIYAZAKI AND TETSUO YOSHIDA
Department of Chemical Engineering, University of Osaka Prefecture, Sakai 591

Conventional particle size analysis by sedimentation method does not give true size distributions but only apparent ones, when Brownian coagulation and Brownian diffusion exist. The difference of true and apparent size distributions was theoretically evaluated by numerically solving the population balance equation under various conditions. Then some of the theoretical results were verified experimentally for particles having various sizes and number concentrations which were obtained under sedimentation in air, in water and in centrifugal field by means of ultramicroscopic size analysis. In addition to these analyses, two parameters consisting of given measuring conditions, which were proposed herein, were found to be useful to predict whether or not coagulation and diffusion effects exist in actually observed size distributions.

Introduction

Sedimentation method for determining particle size distribution has been widely used because of its convenience and its accuracy in size analysis. In this method, the relation of Stokes-Cunningham equation is usually applied. However, when the particles once sufficiently dispersed coagulate each other during sedimentation, the Stokes-Cunningham equation will not be satisfactory for size analysis by this method. Such coagulation will occur in water by using inappropriate dispersion agents and also will be unavoidable in air having particles in high concentration. When the particles are small, such as in submicron ranges, on the other hand, diffusion of particles to walls and a free surface of a sedimentation cell by Brownian motion occurs and the Stokes-Cunningham equation becomes also meaningless. Some studies on the later cases and none on the former cases have been made, but they are still insufficient to evaluate the quantitative effects of those on sedimentation method[3,4,5].

The effects of diffusion and coagulation on sedimentation method were theoretically evaluated under various sizes, concentrations and other various measuring conditions. The limit of the conditions where no influences of these effects exist was discussed and the conditions to avoid these influences by means of centrifugal force were also discussed. Some of the theoretical analyses were then compared with experimental results which were obtained by the ultramicroscopic technique of particle size analysis[6].

Received March 12, 1976. Correspondence concerning this article should be addressed to K. Okuyama. T. Miyazaki is with Matsushita Denko, Co. Ltd., Kadoma 571.

1. Theoretical Consideration

In the sedimentation method for particle size analysis, cumulative undersize F of particle radius r_i' is usually obtained as follows, when the concentration of particles decreases only by sedimentation.

$$F=\int_0^{r_i'} f(r')dr' = N_S/N_0 \qquad (1)$$

where N_S is the concentration at the point y' below the surface of suspension at every lapse of time, N_0 the initial particle concentration, and r_i' is given by Stokes-Cunningham equation as

$$r_i' = \sqrt{9\mu y'/2(\rho_p-\rho)C_m(r_i')gt'} \quad \text{for gravitational settling} \qquad (2)$$

When the settling depth is sufficiently small compared with the radius of rotation, r_i' will be given as follows

$$r_i' = \sqrt{9\mu y'/2(\rho_p-\rho)C_m(r_i')gt'z} \quad \text{for centrifugal settling} \qquad (3)$$

When the concentration N_S decreases to N by particle deposition due to diffusion to the wall of the sedimentation cell or by particle coagulation as shown in **Fig. 1**, such a system can not be solely described by Stokes-Cunningham relation. Accordingly, the value N/N_0 observed does not give the true cumulative undersize F, but only the apparent one. Though particles diffuse

© JOURNAL OF CHEMICAL ENGINEERING OF JAPAN
(Reprinted with permission)

to both vertical and horizontal walls of the sedimentation cell, horizontal particle diffusion was ignored in order to simplify the analysis. The change in particle concentration in the system where Brownian diffusion, coagulation and gravitational settling are simultaneously taken into account should be evaluated by solving the following equation of population balance in number concentration basis[7].

$$\frac{\partial n(r_i,t)}{\partial t}=DG\frac{C_m(r_i')}{C_m(r_{g0}')}\frac{\partial^2 n(r_i,t)}{r_i\partial y^2}-\frac{C_m(r_i')}{C_m(r_{g0}')}r_i^3\frac{\partial n(r_i,t)}{\partial y}$$
$$+CG\sum_{\rho_i=r_{i\min}}^{r_i\sqrt[3]{2}}k(\sqrt[3]{r_i^3-\rho_i^3},\rho_i)n(\sqrt[3]{r_i^3-\rho_i^3},t)n(\rho_i,t)$$
$$\times\left(\frac{r_i}{\sqrt[3]{r_i^3-\rho_i^3}}\right)^3-CG\sum_{\rho_i=r_{i\min}}^{r_{i\max}}k(r_i,\rho_i)n(r_i,t)n(\rho_i,t)$$
$$i=i\min\ldots i\max \qquad (4)$$

All the quantities are normalized as follows

$$\left.\begin{aligned}&t=u_t(r_{g0}')t'z/H,\quad y=y'/H,\quad r_i=r_i'/r_{g0}'\\&n(r_i,t)=n'(r_i',t')/n_0',\quad n_0'=\sum_{r_i'=r_{i\min}'}^{r_{i\max}'}n'(r_i',0)\\&k(r_i,\rho_i)=K(r_i',\rho_i')/K_0C_m(r_{g0}')\\&K(r_i',\rho_i')=K_0(r_i'+\rho_i')\{C_m(r_i')/r_i'+C_m(\rho_i')/\rho_i'\}\\&K_0=2\kappa T/3\mu\end{aligned}\right\}\quad(5)$$

$$CG=K_0n_0'C_m(r_{g0}')H/u_t(r_{g0}')z,\ DG=D(r_{g0}')/Hu_t(r_{g0}')z \quad (6)$$

The centrifugal effect z disappears in the case of gravitational sedimentation only in Eqs. (5) and (6). The dimensionless parameters CG and DG, which are determined from initial particle properties and physical conditions, are convenient for predicting the overall influences of coagulation and diffusion. Eq. (4) was solved numerically in the previous paper[7] for various values of CG and DG assuming initial particle size distribution to be log-normal form. Vertical particle diffusion was considered in Eq. (4) and so the calculation results can be applied directly to evaluate the effects of coagulation and diffusion on sedimentation method, when the vertical boundaries are small in area compared with the horizontal walls in sedimentation cell. The effect of horizontal particle diffusion will be discussed in the later section.

Normalizing Eq. (2) or (3) by Eq. (5), the dimensionless equivalent spherical radius is given by

$$r_i\sqrt{C_m(r_i')/C_m(r_{g0}')}=\sqrt{y/t} \qquad (7)$$

As Cunningham's correction is not significant in most liquid sedimentation, then Eq. (7) reduces to

$$r_i=\sqrt{y/t} \qquad (8)$$

The following dimensionless particle number concentration n, which is obtained by solving Eq. (4) under a certain sedimentation length y and a certain time t, is now defined

$$n=\sum_{r_i=r_{i\min}}^{r_{i\max}}n(r_i,t) \qquad (9)$$

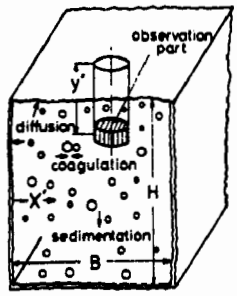

Fig. 1 Sedimentation cell

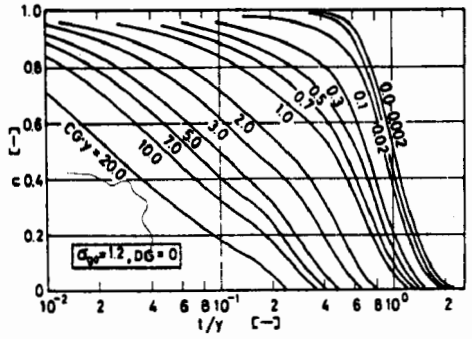

Fig. 2 Time-dependent change in number concentration of particles undergoing sedimentation and coagulation

Thus defined, n corresponds to N/N_0 which is actually observed at y' and t' in sedimentation method under the influence of coagulation or diffusion, and n never provides true cumulative undersize defined by Eq. (1) in this case. The dimensionless equivalent spherical radius r_i determined by Eq. (7) or (8) has a reasonable physical meaning in gravitational settling only, it is, however, applied conventionally to the case where the influence of diffusion or coagulation exists in this study. Then the relation of r_i and N/N_0 or n, both determined by observation and by Eq. (4), gives a true particle size distribution if no influence of diffusion or coagulation exists ($CG=DG=0$). However, it does not give a true distribution, or it gives only the apparent distribution, if one of the above influences exists ($CG>0$ or $DG>0$). The difference of the thus obtained apparent distributions from a true distribution will be discussed in the following sections.

1. 1 Effect of Brownian coagulation

Particle size distribution actually changes as coagulation proceeds in sedimentation cell, and so it is necessary to set up a certain distribution to be standard. In this respect the size distribution at $t=0$, that is, initial size distribution, was regarded as the standard and true distribution. Figure 2, quoted from previous paper[7], indicates the time-dependent change in particle number concentration at every depth y when the influence of coagulation exists. Two parameters in the figure were introduced to describe the local effect

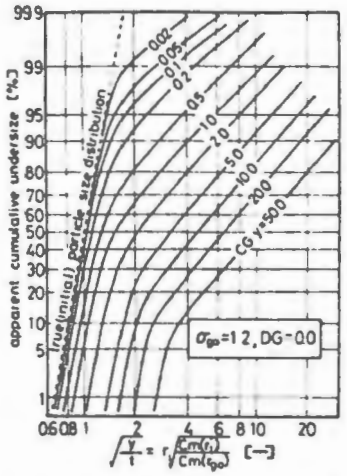

Fig. 3 Apparent particle size distributions due to the effect of coagulation

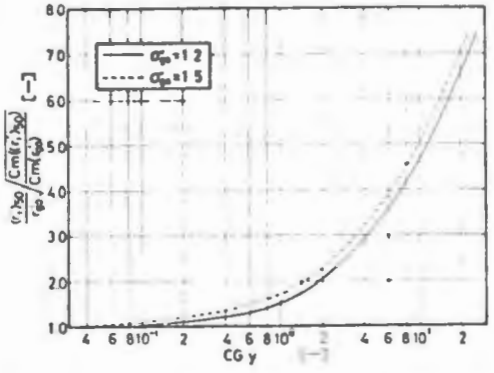

Fig. 4 Variation of 50%-radius in apparent particle size distributions by $CG\ y$

of coagulation

$$CG\cdot y=K_0 n_0' C_m(r_{g0}')y'/u_t(r_{g0}')z$$
$$t/y=u_t(r_{g0}')t'z/y \qquad (10)$$

Replotting the values of $\sqrt{y/t}$ and n from Fig. 2 to Fig. 3, apparent particle size distributions defined in the former section are obtainable. It can be shown that apparent particle size distributions tend to shift towards larger radii with the values of $CG\cdot y$. At the same time the distributions depart from the log-normal form. The difference between the apparent distribution and initial (true) one is caused by the decrease in particle number by coagulation and at the same time by the increase in settling velocities of grown particles. Figure 4 shows the variation in 50%-radius of apparent size distributions by the dimensionless parameter $CG\cdot y$. It can be seen that the curve of $\sigma_{g0}=1.5$ is slightly larger than that of $\sigma_{g0}=1.2$ because of the effect of polydispersity, and also that, at the values of $CG\cdot y$ less than 0.04, the effect of coagulation can be ignored.

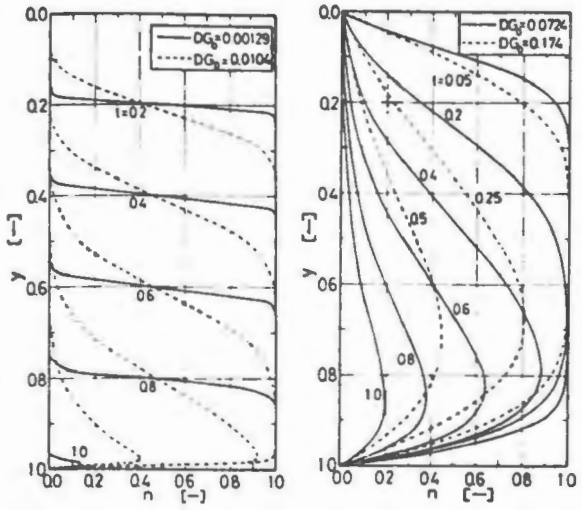

(a) (b)

Fig. 5 Time-dependent change in number concentration of particles undergoing sedimentation and diffusion

1.2 Effect of Brownian diffusion

True particle size distribution in this case was defined as that where the influence of diffusion would be perfectly removed in some way. The effect of diffusion is very complicated in comparison with that of coagulation, because of its larger dependence on particle radius and its irregular dependence on sedimentation depth y. To examine this effect in simple form, particles are now considered to be monodisperse. The basic equation in this case, expressing the timedependent change in concentration of particles undergoing diffusion and sedimentation, becomes

$$\frac{dn}{dt}=DG_0\frac{d^2n}{dy^2}-\frac{dn}{dy} \qquad (11)$$

where

$$DG_0=D(r_0')/Hu_t(r_0')z$$

Equation (11) was solved analytically by C. N. Davies[11] under two kinds of boundary conditions: one is that both top and bottom walls are absorbing ones, and another is that the top wall is a free surface where no particles cross this wall. As the convergence in solution is very slow for small values of DG_0 which are characteristic of larger particles, Eq. (11) was solved numerically by the same method as the previous paper[7] assuming both walls to be absorbing. Figure 5 shows the calculation results of the time-dependent change in particle number concentration. Particle number concentration must change with remaining sharp boundaries, which can be found for such a small value of DG_0 as 0.00129 in the figure. The effect of diffusion, however, is found to become larger with the values of DG_0 and the particle number concentration is found to tend to change with the smooth boundary

in the figures. The decrease in particle number near the bottom wall appears at DG_0 larger than about 0.07. Some of these calculation results agreed with Davies' solutions. It is interesting to find that the solutions solved under the boundary conditions of free surface of the upper did not differ significantly from those solved under absorbing upper wall in the case of $DG_0<0.01$. **Figure 6** shows the apparent particle size distribution obtained from Fig. 5, which is shown by the same explanation as those in Fig. 3. It is found that in the case of $DG_0=0.00129$, the results by calculation, assuming two absorbing walls almost coincide with the true monodisperse distribution irrespective of y. The deviations from the true monodisperse distribution become larger with increase of DG_0, which means that the plot of actually observed results by means of conventional sedimentation analysis under the effect of diffusion considerably differs from that of the true distribution. The apparent size distributions in this case give those as if they were polydisperse in spite of the actually monodisperse particles. **Figure 7** shows the region which is determined by putting $\sigma_g<1.1$ in Fig. 6 where the effect of diffusion may be almost ignored. The region thus defined is given as

$$y\geq 0.384 \ln DG_0+2.304,\ 0.05\leq y\leq 0.95 \qquad (12)$$

When the sedimentation cell is not a shallow one, the effect of particle diffusion to vertical boundaries must be taken into account. This effect of vertical walls, however, can be avoided when the following relation is satisfied (refer to **Appendix**).

$$B>\sqrt{50}\, DG_0 H \qquad (13)$$

The discussion above is for monodisperse particles, but it will be essentially valid for polydisperse particles.

1.3 Dependence of particle radius on the above two effects

As is found by the definition of CG and DG, the effects of coagulation and diffusion depend upon particle properties, fluid properties and dimensions of a sedimentation cell. Among these the remaining values except particle radius are usually known or can be suitably chosen in measurement. In this section, the methods to predict the effects of coagulation and diffusion will be discussed by two parameters M_C and M_D which do not consist of unknown value of particle radius.

The parameter $CG\cdot y$, which appeared in a previous section, can be rewritten as follows, separating particle radius:

$$CG\cdot y=10^{-8}\, M_C/r_{g0}'^3 \qquad (14)$$

where

$$M_C=9\,\mu y' K_0 n_0'/2\times 10^{-8}(\rho_p-\rho)gz$$

The parameter M_C consists of known valuables. **Figure 8** shows the dependence of 50%-radius $(r_i')_{50}$ of

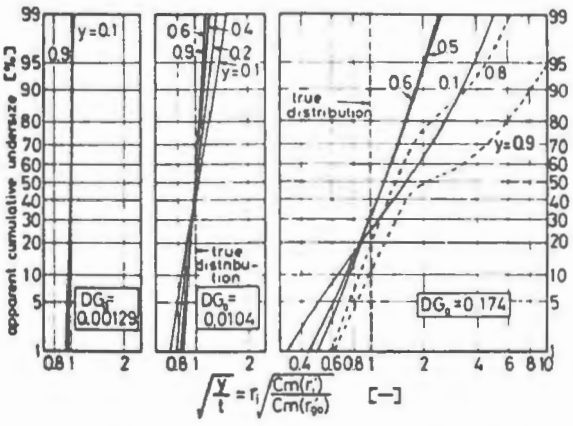

Fig. 6 Apparent particle size distributions due to the effect of diffusion

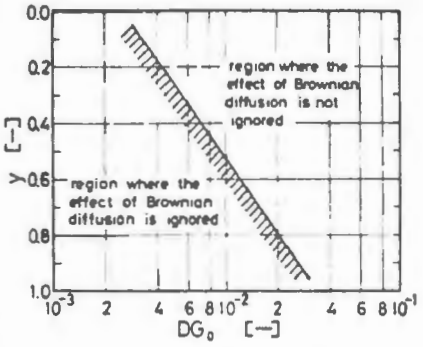

Fig. 7 Region where the effect of diffusion is ignored

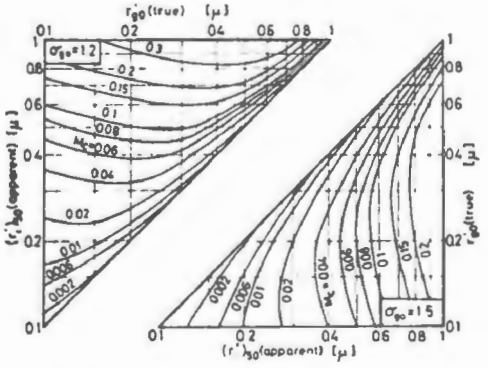

Fig. 8 Dependence of $(r_i')_{50}$ on M_C and r_{g0}'

apparent particle size distributions on M_C and initial or true r_{g0}', which was obtained from Fig. 4 by determining the values of r_{g0}' and M_C. It can be found that 50%-radius $(r_i')_{50}$ agrees with r_{g0} when M_C is less than 0.001 in the case of $r_{g0}'>0.1$ and $\sigma_{g0}<1.5$. The true geometric mean radius r_{g0}' can be roughly estimated by using Fig. 8 knowing the observed apparent 50%-radius $(r_i')_{50}$ under the effect of coagulation.

In a similar way, a parameter M_D for diffusion is defined as follows

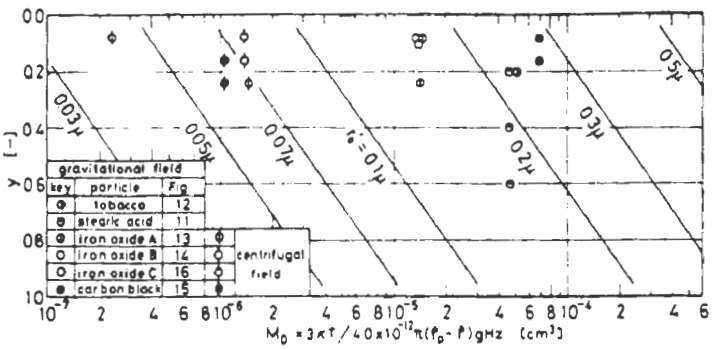

Fig. 9 Dependence of r_0' on M_D and y

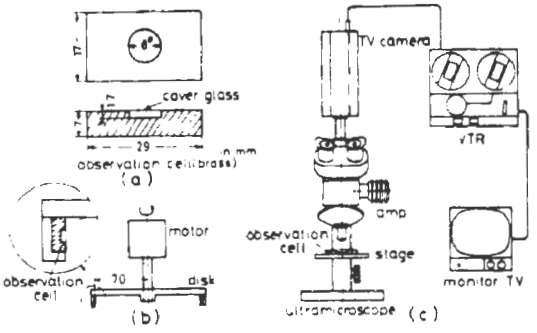

Fig. 10 Experimental apparatus

$$DG_0 = 10^{-12} M_D / r_0'^3 \qquad (15)$$

where

$$M_D = 3\kappa T/4 \times 10^{-12}\pi(\mu_p - \mu)gHz$$

Substituting M_D into Eq. (12), the minimum particle radius r_0' where the effect of diffusion can be ignored becomes as follows

$$\ln r_0' \geq 0.333 \ln M_D - 0.868\, y - 7.209 \qquad (16)$$

Figure 9 shows the dependence of r_0' in Eq. (16) on the $M_D - y$ coordinate which are both determined by measuring conditions. The left-lower regions of each equi-radius line in the figure indicate that the effect of diffusion of particles having radius r_0' denoted can be ignored. For example, the minimum particle radius r_0' where the effect of diffusion can be negligible is about 0.05 μ, when $M_D = 10^{-8}$ and $y = 0.5$. If the observation depth y is shallowed to 0.1, r_0' moves to 0.07 μ. Since true particle radius r_0' or r_{g0}' is usually unknown in actual sedimentation tests, it is unavoidable to use the observed value $(r_t')_{50}$ instead of r_0' or r_{g0}' for the check whether or not influence of diffusion exists in observed data. If the radius obtained by Fig. 9 using the known values of M_D and y is smaller than observed value $(r_t')_{50}$, the effect of diffusion may be negligible, that is, the observed radius $(r_t')_{50}$ is true under the condition of no effect of coagulation or under enough small value of M_C. If the radius obtained by Fig. 9 is the same order of $(r_t')_{50}$ or larger

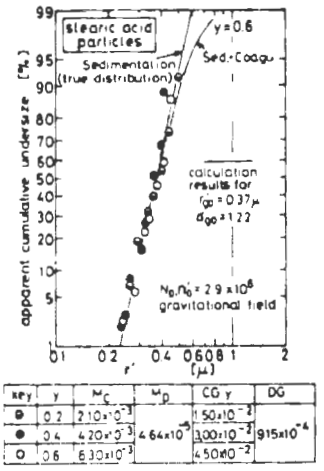

key	y	M_C	M_D	CO y	DG
⊕	0.2	2.10×10^{-3}		1.50×10^{-2}	
●	0.4	4.20×10^{-3}	4.64×10^{-8}	3.00×10^{-2}	9.15×10^{-4}
○	0.6	6.30×10^{-3}		4.50×10^{-2}	

Fig. 11 Particle size distributions for stearic acid particles

than $(r_t')_{50}$, it is necessary to observe again varying the measuring conditions to decrease the value of M_D.

The effects of coagulation and diffusion may be minimized under centrifugal sedimentation because the values of M_C and M_D become smaller by the centrifugal effect z.

2. Experimental Apparatus and Method

The ultramicroscopic technique for size analysis was used to examine the above analyses experimentally, which can give accurate particle number concentration at any given depths. The sedimentation cell for air sedimentation was the same as those which appeared in the previous paper[7]. The cell for sedimentation in water is shown in **Fig. 10 (a)**. The cell has a shallow sedimentation length compared with the distance between vertical surrounded walls so that Eq. (13) is satisfied in most cases. The particles used in this study were two kinds of aerosols and four kinds of fine powders. The aerosol particles were stearic acid particles generated by a La Mer-Sinclair type generator and tobacco smoke generated by a simple smoking apparatus by which the number concentration of particles was controlled from 10^6 to 10^8 particles/cc. The carbon black and three kinds of iron oxide particles were provided for the sedimentation test in water. The carbon black particles were quite spherical, the iron oxide particles A and B were cubic with rounded corners, and the iron oxide particles *C* were needlelike having a length-to-diameter ratio of six. A detailed description of the measuring procedure by gravitational sedimentation for aerosol particles appeared in the previous paper[8]. The measurement procedure for fine powders in water sedimentation is as follows. A given amount of powder was first dispersed uniformly into pure water

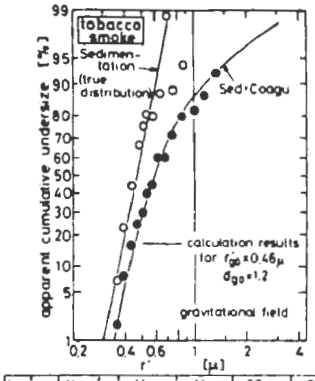

key	y	N_0, n_0'	M_C	M_D	CG·y	DG
○	0.2	3.50×10^6	2.78×10^{-3}	5.05×10^{-5}	1.49×10^{-2}	5.19×10^{-4}
●		8.10×10^7	6.43×10^{-2}		3.39×10^{-1}	

Fig. 12 Particle size distributions for tobacco smoke

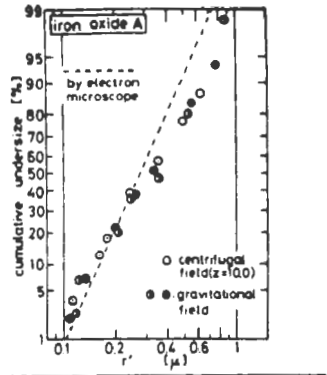

key	y	N_0, n_0'	M_C	M_D	CG·y	DG
●	0.08	6.09×10^6	2.39×10^{-4}	1.40×10^{-5}	2.19×10^{-3}	3.90×10^{-4}
●	0.24		7.16×10^{-4}		6.57×10^{-3}	
○	0.24	7.97×10^6	9.37×10^{-5}	1.40×10^{-5}	8.60×10^{-4}	3.90×10^{-5}

Fig. 13 Particle size distributions for iron oxide A

without any dispersing agents, but with mechanical stirring to obtain suspension. Then the suspension was poured gently into the sedimentation cell shown in Fig. 10 (a) with a syringe, and it was covered with a thin glass. Putting the sedimentation cell on the stage of an ultramicroscope as shown in Fig. 10 (c), particle number at a certain depth in the cell was observed at every lapse of time by using VTR. The initial particle number concentration, $N_0(=n_0')$, was determined by knowing the initial particle number of images and the observation volume which corresponds to the focussed volume of the ultramicroscope preliminarily determined[8]. For centrifugal sedimentation, on the other hand, the cell was set to a centrifuge to obtain a given value of centrifugal effect z as shown in Fig. 10 (b). Experimental conditions and properties of particles are shown in **Table 1**.

3. Experimental Results and Discussion

Figures 11 and **12** show the comparisons of apparent particle size distribution data in air sedimentation under the effect of coagulation obtained experimentally with theoretical results. No difference between them is found irrespective of sedimentation depth y in Fig. 11. The size distribution of highly concentrated aerosol shown in Fig. 12, on the other hand, seems to shift to a larger radius. The minimum particle radius r_0' where the effect of diffusion can be ignored is obtained to be about 0.2 μ from Fig. 9 in those case of Figs. 11 ($M_D=4.64\times10^{-8}$) and 12 ($M_D=5.05\times10^{-8}$). This value is sufficiently smaller than those experimentally obtained $(r_i')_{50}$, which suggests no effect of diffusion. The value of M_C of highly concentrated aerosol in Fig. 12 is found from Fig. 8 to be large enough to be effected by coagulation. The tendency of the shift in Fig. 12 is well described by calculation results of Eq. (4) taking into account the coagulation effect.

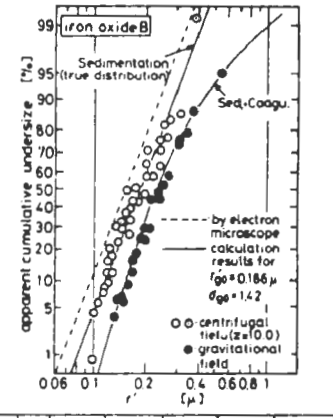

key	y	N_0, n_0'	M_C	M_D	CG·y	DG
○	0.08	1.78×10^7	6.86×10^{-5}	1.36×10^{-6}	1.98×10^{-3}	2.11×10^{-4}
⊙	0.16		1.37×10^{-4}		3.96×10^{-3}	
●	0.08	2.25×10^8	8.70×10^{-3}	1.36×10^{-5}	0.26	2.11×10^{-3}

Fig. 14 Particle size distributions for iron oxide B

Table 1 Experimental conditions

Gravitational sedimentation in air
- Aerosols; stearic acid particles, tobacco smoke
- $r_{g0}'=0.3\ \mu$–$0.5\ \mu$, $\sigma_{g0}=1.2$–1.4
- Density of particles; $\rho_p=0.85$ g/cm³ (stearic acid particles)
  $=0.78$ g/cm³ (tobacco smoke)
- Concentration of particles; $n_0'=10^6$–10^8 particles/cc

Gravitational and centrifugal sedimentation in water
- Powders; iron oxide A, B and C
  carbon black
- $r_{g0}'=0.09\ \mu$–$0.4\ \mu$
- $\sigma_{g0}=1.3$–1.6
- Density of powders; $\rho_p=5.2$ g/cm³ (iron oxide A and B)
  $=4.9$ g/cm³ (iron oxide C)
  $=1.85$ g/cm³ (carbon black)
- Concentration of powders; $n_0'=10^6$–10^8 particles/cc
- Centrifugal effect; $z=10$–67

- $y'=100\ \mu$–$1500\ \mu$ $(y=0.08$–$0.6)$
- $CG=0.07$–2.2, $DG=10^{-5}$–10^{-1}

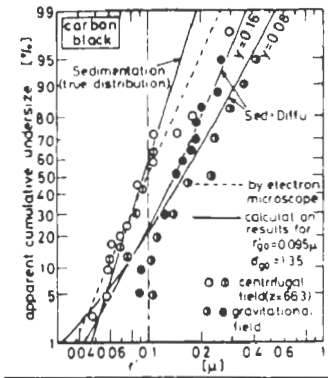

key	γ	N_0, n_0'	M_C	M_D	CG γ	DG
⊕	0.08	2.75×10^6	5.33×10^{-4}	6.93×10^5	5.91×10^{-2}	8.06×10^{-2}
●	0.16		1.07×10^{-3}		1.19×10^{-1}	
⊕	0.16	9.80×10^6	5.73×10^{-5}	1.05×10^6	6.35×10^{-3}	1.22×10^{-3}
○	0.24		8.59×10^{-5}		9.52×10^{-3}	

Fig. 15 Particle size distributions for carbon black

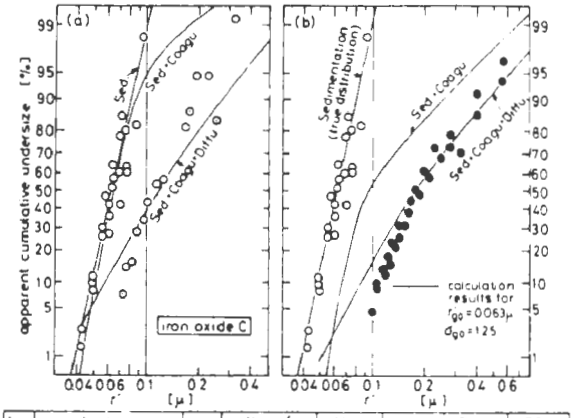

key	field	γ	N_0, n_0'	M_C	M_D	CG γ	DG
○	centrifugal field(z=663)	0.08	8.40×10^6	5.60×10^{-6}	2.35×10^{-4}	1.45×10^{-3}	9.40×10^{-4}
○	gravitational field	0.08	4.67×10^6	1.94×10^{-4}	1.46×10^{-5}	5.00×10^{-2}	5.84×10^{-2}
●			9.60×10^7	3.99×10^{-3}		1.03	

Fig. 16 Particle size distributions for iron oxide C

Figures 13 to **16** show the comparisons of apparent size distribution data in gravitational and centrifugal field in water sedimentation obtained experimentally with calculated results. The effects of coagulation and diffusion are found to be negligible in the case of Fig. 13. This fact is also readily expected by the values of M_C, M_D, γ and $(r_i')_{50}$. The experimental results obtained in gravitational field in Figs. 14 and 15 are found to shift towards a larger radius in comparison with those in centrifugal field. This shift in Fig. 14 is mainly due to the effect of coagulation because of the larger value of M_C. The shift in Fig. 15, on the other hand, is caused by larger values of M_D and small value of $(r_i')_{50}$. The minimum radius r_0' in those cases is predicted to be above 0.28 μ from Fig. 9, while the apparent radius $(r_i')_{50}$ observed is about 0.15 μ. Then it is obvious that the effect of diffusion is thought to be significant in gravitational sedimentation in Fig. 15. The calculation results from Eq. (4) taking account of diffusion effect are found to describe the experimental results fairly well in the figure.

Some examples of apparent size distributions where both effects of coagulation and diffusion are significant under gravitational sedimentation are shown in Fig. 16. The effects of coagulation and diffusion seem to be negligible by applying centrifugal sedimentation in those cases, which can be easily understood by checking M_C, M_D, γ and $(r_i')_{50}$. As to the experimental results obtained by gravitational sedimentation in Fig. 16 (a), the effect of diffusion obviously exists because the value of r_0' determined by Fig. 9 is 0.17 μ, while $(r_i')_{50}=0.12$ μ. The effect of coagulation in this case is not significant, the amount of which is shown by (Sed.+Coagu.)-curve in the figure. Apparent particle size distribution in Fig. 16 (b) is influenced not only by diffusion but by coagulation, because the particle number concentration is higher than that of Fig. 16 (a). However, it is difficult to predict the effect of diffusion under the existence of significant coagulation such as that of Fig. 16 (b). It is necessary in such cases to eliminate first the effect of coagulation and then the effect of diffusion must be checked. Both experimental results obtained by gravitational sedimentation in Figs. 16 (a) and (b) are found to agree well with those obtained by directly solving Eq. (4) under the same condition of the experiment.

The theoretical consideration on coagulation in this paper is not strictly applicable to solid and nonspherical particles, because the calculations are based on the assumption that particles are spherical and particles collide with each other to form a new spherical particle whose mass may be the same as the combined mass of the two smaller particles. It is suggested, however, that the assumption seems to be fairly effective even for solid and nonspherical particles, judging from the fair agreement of theory with experiment so far as the experimental conditions of this study were concerned.

Conclusion

The effects of Brownian coagulation and diffusion on particle size analysis by sedimentation method, which are of major problem for determining the size of sub-micron particles, were studied, and the following results were obtained. 1) The change in number concentration of particles was numerically solved, when particles exist between two horizontal walls and are undergoing gravitational sedimentation accompanying Brownian coagulation and diffusion. The calculated results were figured to show the difference of true size distribution from apparent size distributions which were numerically obtained by conventional sedimentation analysis under the effects of coagulation

and diffusion. 2) Two parameters, M_C for estimating coagulation effect and M_D for diffusion effect, were proposed to predict whether the influence of coagulation or diffusion exists or not in actually observed size distribution, that is, whether the size distribution obtained is true one or apparent one. These parameters are useful as a criterion to determine the measuring conditions to avoid the influences of coagulation and diffusion. 3) The above theoretical results were experimentally examined under various conditions, such as air sedimentation, water sedimentation, centrifugal sedimentation and various particles, by means of ultramicroscopic size analysis, and the theoretical consideration presented in this paper was found to be valid for prediction and prevention of the effects of Brownian coagulation and diffusion in a sedimentation size analysis.

Appendix

The time-dependent change in number concentration of particles existing in the space surrounded by two vertical walls and also undergoing Brownian diffusion was solved by N. A. Fuchs[2] as follows

$$n'(x', t') = \frac{4n_0'}{\pi} \sum_{\nu=1}^{\infty} \frac{1}{2\nu-1} \sin\left[(2\nu-1)\frac{\pi x'}{B}\right] \times \exp\left[-\frac{(2\nu-1)^2\pi^2 D(r_0')t'}{B^2}\right] \quad \text{(A-1)}$$

The change at the middle of B is given as follows

$$n'\left(\frac{B}{2}, t'\right) = \frac{4n_0'}{\pi} \sum_{\nu=1}^{\infty} \frac{1}{2\nu-1} \sin\left[(2\nu-1)\frac{\pi}{2}\right] \times \exp\left[-\frac{(2\nu-1)^2\pi^2 D(r_0')t'}{B^2}\right] \quad \text{(A-2)}$$

The maximum time when the decrease in particle number by diffusion is almost negligible is given by Eq. (A-2) as $B^2/50D(r_0')$. Normalized value of this time by Eq. (5) comes to $B^2/50H^2DG_0$. Most particles have been already settling down below H at $t \approx 1.0$ in the horizontal walls, consequently the effect of particle diffusion to vertical walls can be relatively ignored when $B^2/50H^2DG_0 > 1$.

Nomenclature

B	= width of the sedimentation cell	[cm]
CG	= dimensionless parameter defined in Eq. (6) $(=9\,\mu HK_0n_0'/2(\rho_p-\rho)gr_{g0}'^3z)$	[—]
$C_m(r_i')$	= Cunningham's correction factor of r_i'	[—]
DG	= dimensionless parameter defined in Eq. (6) $(=3\kappa T/4\pi(\rho_p-\rho)gHr_{g0}'^3z)$	[—]
DG_0	= dimensionless parameter defined in Eq. (11) $(=3\kappa T/4\pi(\rho_p-\rho)gHr_0'^3z)$	[—]
$D(r_i')$	= diffusion coefficient of r_i' $(=C_m(r_i')\kappa T/6\pi\mu r_i')$	[cm²/sec]
F	= cumulative undersize	[—]
$f(r')$	= particle size distribution function	[—]
g	= acceleration of gravity	[cm/sec²]
H	= height of the sedimentation cell	[cm]
K_0	= coefficient in Eq. (5) $(=2\kappa T/3\,\mu)$	[cm³/sec]
$K(r_i', \rho_i')$	= coagulation function for two particles of sizes r_i' and ρ_i'	[cm³/sec]
$k(r_i, \rho_i)$	= dimensionless coagulation function $(=K(r_i', \rho_i')/K_0C_m(r_{g0}'))$	[—]
M_C	= parameter for coagulation defined in Eq. (14) $(=9\,\mu K_0n_0'y'/2\times10^{-8}(\rho_p-\rho)gz)$	[cm²]
M_D	= parameter for diffusion defined in Eq. (15) $(=3\kappa T/4\times10^{-12}\pi(\rho_p-\rho)gHz)$	[cm²]
N, N_0, N_S	= measured particle concentration	[particles/cc]
$n'(r_i', t'), n(r_i, t)$	= number concentration and dimensionless number concentration of particles $(=n'(r_i', t')/n_0)$	[particles/cc] [—]
n	= dimensionless total number concentration of particles $(=\sum n(r_i, t))$	[—]
n_0'	= total number concentration of particles at time zero	[particles/cc]
r'	= particle radius for continuous spectrum	[cm]
r_i', r_i	= particle radius and dimensionless particle radius $(=r_i'/r_{g0}')$	[μ] [cm] [—]
r_0'	= particle radius of monodisperse particles	[μ] [cm]
$(r_i')_{50}$	= 50%-radius in apparent particle size distribution	[μ]
r_{g0}'	= geometric mean radius at time zero	[μ] [cm]
T	= absolute temperature	[°K]
t', t	= time and dimensionless time $(=u_i(r_{g0}')t'z/H)$	[sec] [—]
$u_i(r_i')$	= terminal settling velocity of r_i' $(=2C_m(r_i')(\rho_p-\rho)r_{g0}'^2g/9\mu)$	[cm/sec]
x'	= horizontal distance from one wall of the sedimentation cell	[cm]
y', y	= vertical and dimensionless vertical distance from top of the sedimentation cell $(=y'/H)$	[cm] [—]
z	= centrifugal effect	[—]
σ_g	= geometric standard deviation of apparent particle size distribution	[—]
σ_{g0}	= geometric standard deviation at time zero	[—]
κ	= Boltzman's constant $(=1.38\times10^{-16})$	[erg/°K]
μ	= viscosity of fluid	[g/cm·sec]
ρ_i', ρ_i	= particle radius and dimensionless particle radius $(=\rho_i'/r_{g0}')$	[cm] [—]
ρ, ρ_p	= fluid and particle density	[g/cm³]

〈Subscripts〉

i	= refers to the number of particle size
max	= maximum
min	= minimum

Literature Cited

1) Davies, C. N.: *Proc. Roy. Soc.*, **A200**, 100 (1949).
2) Fuchs, N. A.: "The Mechanics of Aerosols", Pergamon Press (1964).
3) Irani, R. R. and C. F. Callis: "Particle Size; Measurement, Interpretation and Application", Willey (1963).
4) Jelinek, Z.: "Particle Size Analysis", Willey (1974).
5) Moore, D. W. and C. Orr, Jr.: *Powder Technol.*, **8**, 13 (1973).
6) Yoshida, T., Y. Kousaka and K. Okuyama: *Ind. Eng. Chem., Fundam.*, **14**, 47 (1975).
7) Yoshida, T., Y. Kousaka, K. Okuyama and S. Nishio: *J. Chem. Eng. Japan*, **8**, 137 (1975).

(Presented at Hokkaido Meeting of The Soc. of Chem. Engrs., Japan at Muroran, July 24, 1975 and 9th Autumn Meeting of The Soc. of Chem. Engrs., Japan at Fukuoka, Oct. 17, 1975.)

CONSTANT PRESSURE FILTRATION OF POWER-LAW NON-NEWTONIAN FLUIDS

MOMPEI SHIRATO, TSUTOMU ARAGAKI, EIJI IRITANI, MASAAKI WAKIMOTO, SATOSHI FUJIYOSHI, AND SHŌJI NANDA
Department of Chemical Engineering, Nagoya University, Nagoya 464

A filtration theory for the power-law non-Newtonian fluids is developed on the basis of the extended Rabinowitsch-Mooney equation, and several definitions of non-Newtonian filtration characteristics are defined. The equations presented in this paper may be considered as equations applicable both for non-Newtonian filtration and for conventional Newtonian filtration. Methods for evaluating the overall characteristics of non-Newtonian filtration are suggested by using the compression permeability data. In order to confirm the validity of the theory, constant pressure filtration experiments are carried out under various conditions of the flow behavior index N ranging from 0.404 to 0.504 and the filtration pressure p from 1000 to 3000 G/cm², and it is shown that the methods presented in this paper are valid. It is also shown that the average specific filtration resistance varies considerably with change in the N-value of the power-law, and the cakes formed from non-Newtonian filtration of pseudo-plastic fluid are denser than those from usual Newtonian filtration.

Introduction

In spite of the basic importance of non-Newtonian filtration in broad fields of petrochemical and food processing industries etc., very little has been studied in theories and experiments, while W. Kozicki *et al.*[7,8] have made valuable contributions to the filtration theory of power-law non-Newtonian fluids.

In this paper, the conventional filtration theory of Newtonian fluids at constant pressure is reexamined in view of the power-law for flow of non-Newtonian fluids. In order to provide a useful mathematical tool of simplified form to industrial filtration, a generalized theory which is applicable to both non-Newtonian and conventional Newtonian filtration is presented in this paper. It will also be demonstrated that the non-Newtonian filtration behaviors can be calculated on the basis of compression-permeability cell measurements and the estimated results are compared with constant pressure filtration experiments of pseudo-plastic non-Newtonian fluids.

1. Experimental Equipment and Procedures

The experimental filter, shown in **Fig. 1**, essentially consists of a plexiglass cylinder of 130 mm inside diameter, a brass upper plate with a connection for applying air pressure and a stainless-steel bottom plate which supports a perforated plexiglass plate with a filter paper on it.

In order to conduct non-Newtonian filtration experiments, the selection of solid materials is important and it is essential that addition of non-Newtonian liquid to suspensions may not substantially affect particle flocculation, and that the viscous characteristics of the filtrate do not vary during filtration process[17]. Several kinds of slurry materials (i.e., Gairome clay, Korean kaolin, calcium carbonate, fine silica sand, Filter-Cel, Standard-Supercel, Hyflo-Supercel and Radiolite) have been examined. The last two materials have proven to be appropriate in the above mentioned views and Radiolite (# 1100)* is used for the experiments attempted in this study.

The non-Newtonian fluids used in this study are

(rest of paper is missing)

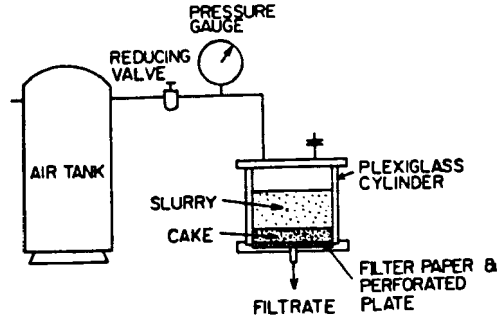

Fig. 1 Schematic diagram of experimental apparatus

* Diatomaceous filter aid, Showa Kagaku Kogyo Co., Ltd.

Received August 12, 1976. Correspondence concerning this article should be addressed to M. Shirato. M. Wakimoto is with Noritake Co., Ltd., Nagoya 451, S. Fujiyoshi is with Shin-Nippon Iron & Steel Co., Ltd., Tokai 476 and S. Nanda is with Japan Catalytic Chem. Ind. Co., Ltd., Himeji 671-12.

EXPERIMENTAL STUDY OF THERMOPHORESIS OF AEROSOL PARTICLES

YASUO KOUSAKA, KIKUO OKUYAMA,
SHIGERU NISHIO AND TETSUO YOSHIDA
Department of Chemical Engineering, University of Osaka Prefecture, Sakai, 591

(Reprinted with permission)

Reprinted from
JOURNAL OF
CHEMICAL ENGINEERING
OF
JAPAN
Vol. 9, No. 2 (1976)
Pages 147 - 150

EXPERIMENTAL STUDY OF THERMOPHORESIS OF AEROSOL PARTICLES

YASUO KOUSAKA*, KIKUO OKUYAMA,
SHIGERU NISHIO AND TETSUO YOSHIDA
Department of Chemical Engineering, University of Osaka Prefecture, Sakai, 591

The velocity of thermophoresis of aerosol particles in the slip flow region, about which no conclusion has yet been drawn from the many results of experimental and theoretical work, was studied from the experimental point of view. A new experimental method using an ultramicroscope was developed to meet most of the necessary conditions to obtain reliable data on thermophoresis, such as accurate observation of velocity under an accurately known temperature gradient and prevention of the action of any forces except thermal force. The experimental results were compared with some of the most representative theories, and were found in good agreement with Derjaguin's theory.

Introduction

Because of the practical interest in particle deposition on heat exchanger tubes and in particle collection by scrubbers and thermal precipitators, as well as the theoretical interest in evaluating the phenomenon, extensive experimental investigations of thermophoresis have been made[5].

In the large-Knudsen number region $Kn \gg 1$, theory and experiment are found to be in satisfactory agreement. In the smaller region or the slip flow region, $Kn \leq 1$, though various theories have been proposed, sufficient reliable experimental data to verify them have not been obtained because of the difficulty in accurate measurement of the velocity of thermophoresis.

This paper presents experimental data on the velocity of thermophoresis in the slip flow region obtained by a new technique developed to determine the accurate velocity of thermophoresis. The data are then compared with some representative theories of thermophoresis[1-3,6,8-10].

Experimental Method

Several experimental methods to determine the velocity of thermophoresis have been developed. Derjaguin examined the available experimental methods which had been reported and classified them into four types[5]. Each of them, however, seems to have some unavoidable faults. In accurate determination of the velocity of thermophoresis, the following conditions should be essentially satisfied: 1) to know the accurate temperature gradient where the velocity of particles is just observed; 2) to prevent the action of any non-thermal forces, such as fluid drag due to fluid flow, photophoretic and electric forces; 3) to avoid convective flow of aerosol induced by the temperature difference[7]; 4) to know accurately the diameter of spherical particles; and 5) to observe the velocity itself directly under the above conditions. Considerable spread in experimental data obtained by different authors is thought to be caused by lack of some of the above conditions. The experimental method presented in this paper was developed so that the above conditions were satisfied as much as possible.

The experimental technique applied in this study is in principle much the same as that previously developed by the authors for size analysis of aerosol particles[11]. The only difference between them lies in the observation cells.

Fig. 1 shows the experimental apparatus. The observation cell fixed on the stage of an ultramicroscope has a water jacket into which cooling water controlled in temperature ranging 0°C to room temperature is circulated to cool the bottom wall of the cell. The bottom wall was made from brass plate which has a large heat capacity. The upper wall of the observation cell consists of a glass plate through which the particles suspended in the cell were observed by the ultramicroscope. The side walls of the cell were made from polyvinyl chloride for thermal insulation. A temperature gradient was formed between the upper glass wall and the bottom one, and its extent was controlled by changing the temperature of the

Received September 19, 1975.
Presented at the Tokushima Meeting (at Tokushima, July 1975) of The Soc. of Chem. Engrs., Japan.

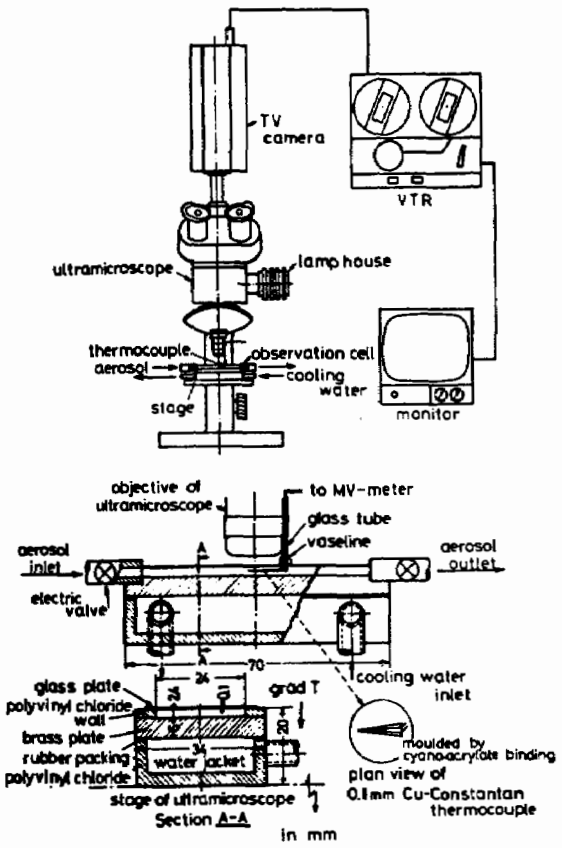

Fig. 1 Experimental apparatus

bottom wall, the upper wall being left at room temperature. The ratio of cell width to height was selected as ten so that convective flow induced by temperature gradient in the cell could be avoided[7].

The aerosol to be observed is cooled by a heat exchanger to the mean temperature in the cell and is introduced into the cell. After several seconds of admitting the aerosol, the flow is instantaneously stopped by closing the electric valves shown in Fig. 1. Then a linear temperature field is formed within a short time throughout the cell except in the vicinity of the side walls. The value of the time interval, τ, needed for the aerosol in the cell to warm up is given by[8]

$$\tau = h_d^2 \rho_f C_p / K_a \qquad (1)$$

where C_p is the specific heat of the aerosol, ρ_f density, K_a thermal conductivity of the aerosol and h_d half of the cell depth. In the present case τ comes to 0.05 seconds, which is negligibly small compared with the observation period $t_{1/2}$ described later. Exact solution of this problem can be obtained by an analogical method in solving the establishment of Couette flow, and it gives a still smaller value. Thus the field may be regarded as at steady state.

The focus of the ultramicroscope was set at a given depth h from the inner surface of the upper glass wall by adjusting the height of the stage, on which the cell was fixed, up and down. Thus the particle numbers at various depths was observed. The temperature gradient in the cell, on the other hand, was also preliminarily measured by a small thermocouple in the cell shown in Fig. 1, the depth of which was also adjusted by displacement of the stage. The stage displacement in these measurements was determined by the height gauge installed in the microscope.

Aerosol particles in the cell start to settle just after closing the valves of the cell under the influence of gravity and thermophoresis. The particles appearing in sight of the microscope, which is focused at a certain depth of the cell, h, are recorded by a video recorder as sedimentation progresses until the particle disappears from sight. Knowing the depth h and the time $t_{1/2}$ at which half of the initial particles disappear from sight of the microscope, the settling velocity of a particle having median diameter D_{p50}, though it is resultant velocity shown below, is determined:

$$U_G(D_{p50}) + U_T(D_{p50}) = h/t_{1/2} \qquad (2)$$

$U_G(D_{p50})$ represents the gravitational settling velocity and is easily obtainable by measurement where no temperature gradient is formed in the cell. Furthermore, $U_G(D_{p50})$ can be converted into the median diameter of the particles, D_{p50}, by using the Stokes-Cunningham equation. Thus the values of both $U_G(D_{p50})$ and D_{p50} are accurately evaluated. In consequence the velocity of thermophoresis of a particle of D_{p50} in diameter, $U_T(D_{p50})$, can be determined by observing $t_{1/2}$ under existence of temperature gradient. Eq. (2) is valid when resultant velocity of U_G and U_T increases monotonously with particle diameter. As it is well known that the dependence of particle size on the velocity of thermophoresis is small this condition will be satisfied in most cases unless there exists an extremely large temperature gradient.

Aerosol particles used in this study were tobacco smoke, stearic acid and DOP. Aerosols of both stearic acid and DOP were generated by a La Mer-Sinclair type generator and tobacco smoke was generated by a simple smoking apparatus[11]. Aerosols thus generated were cooled by a heat exchanger and were then observed.

The size distributions of aerosol particles are shown in Fig. 2. They were obtained by the ultramicroscopic method[11] using the same cell as shown in Fig. 1 but having no temperature gradient in it.

Experimental Results and Discussion

Figs. 3 and 4 show the experimental results. The temperature gradients measured in the cell are shown at the right side of the figures. They seem to be

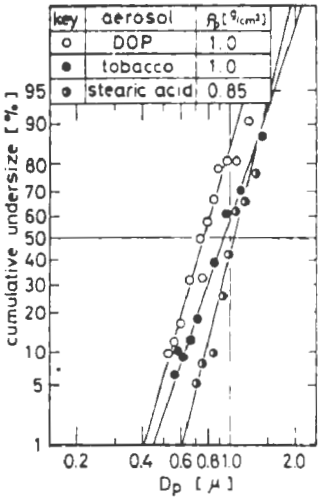

Fig. 2 Size distribution of aerosol particles

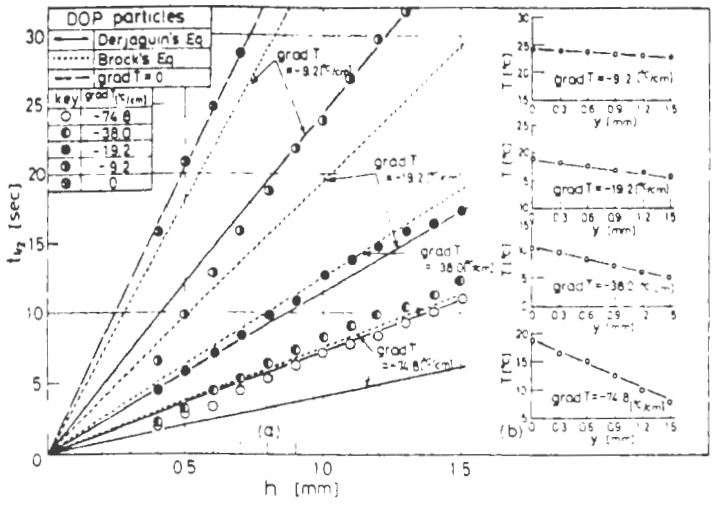

Fig. 3 (a) Relation between $t_{1/2}$ and h (b) Temperature gradient

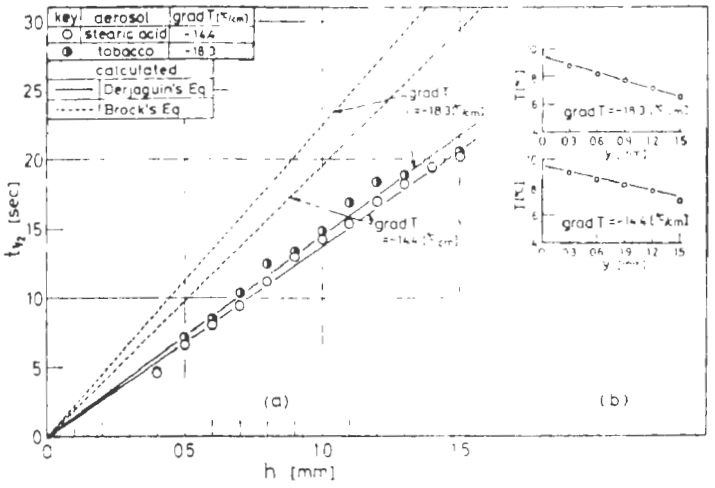

Fig. 4 (a) Relation between $t_{1/2}$ and h (b) Temperature gradient

linear. The abscissa of the figures, y, indicates the depth from an arbitrary position which roughly corresponds to 0.15 mm in actual depth h from the upper wall. In the left-side figure, the relation between $t_{1/2}$ in Eq. (2), at which half of the initial particles disappear from sight of the microscope, and h, the depth from the inner surface of the upper wall of the cell, were plotted. To compare these experimental values with theoretical ones, the following two representative theoretical equations proposed by Derjaguin[3] and Brock[1] were adopted.

$$U_T^p(D_p) = -3\frac{\mu}{\rho T}\left\{\frac{K_e + C_t K_t(2\lambda/D_p)}{2K_e + K_t + 2C_t K_t(2\lambda/D_p)}\right\} \times \left\{\frac{\text{grad } T}{1 + 2C_m(2\lambda/D_p)}\right\} \quad (3)$$

$$U_T^p(D_p) = \frac{1}{2} \times U_T^p(D_p) \quad (4)$$

Since the gravitational settling velocity, $U_G(D_{p50})$, and accordingly the median diameter of the particles, D_{p50}, have been already determined by experiment, substitution of $U_G(D_{p50})$ and $U_T(D_{p50})$ which can be calculated by the above equations knowing D_{p50} and other experimental constants into Eq. (2) gives the theoretical relation between $t_{1/2}$ and h. The solid and dotted lines in Figs. 3 and 4 are those thus predicted by Derjaguin and Brock, respectively. It can be found that good agreement exists between the solid lines calculated on the basis of Derjaguin's theory and the experimental values, except only the case of large temperature gradient, grad T = -74.8°C/cm. The experimental data of grad T = -74.8 C/cm were obtained under an undesirable condition where hot air was blown onto the surface of the upper wall of the cell to obtain a large temperature gradient. The deviation from Derjaguin's theory in this case is

Table 1 Comparison of experimental results with theories

Aerosol	grad T [°C/cm]	$U_T(D_{p50})$ [cm/sec] Exp.	Eq. (3)	Eq. (4)	notice
DOP	−9.2	2.72×10^{-3}	2.64×10^{-3}	1.33×10^{-3}	$K_s=5.9\times10^{-5}$ [cal/cm·sec·°K][3]
	−19.2	5.83×10^{-3}	5.51×10^{-3}	2.75×10^{-3}	$K_i=3.0\times10^{-4}$ [cal/cm·sec·°K][4]
	−38.0	9.90×10^{-3}	1.09×10^{-2}	5.45×10^{-3}	$D_{p50}=0.6\sim0.8$ [μ]
	−74.8	1.16×10^{-2}	2.14×10^{-2}	1.07×10^{-2}	convective flow occurs
Stearic acid	−13.5	3.39×10^{-3}	3.83×10^{-3}	1.91×10^{-3}	$K_i=3.0\times10^{-4}$ [6]
	−14.4	3.86×10^{-3}	4.08×10^{-3}	2.04×10^{-3}	$D_{p50}=1.04$
Tobacco smoke	−18.3	4.93×10^{-3}	4.82×10^{-3}	2.41×10^{-3}	$K_i=5.0\times10^{-4}$ [5], $D_{p50}=0.94$

caused by poor temperature control of the upper wall of the cell and also by convective flow of aerosol in the cell owing to the large temperature gradient.

The velocities of thermophoresis in various experimental conditions were determined by the slope of Figs. 3 and 4, subtracting those at zero temperature gradient. The results are shown in **Table 1**. Good agreement is also found between the experimental results and the values calculated by Eq. (3).

In ultramicroscopic observation of particle numbers at a certain depth of the cell, h, it was noteworthy that the particles disappeared suddenly from sight of the microscope at the time $t_{1/2}$ while they disappeared gradually under zero temperature gradient. This sudden disappearance shows the small dependence of particle diameter on the velocity of thermophoresis, as expected from Eqs. (3) and (4).

The particle number concentration of aerosols in experiment was about $4\times10^6\sim8\times10^6$, which corresponds to about 50∼100 particles in sight of the microscope. At these concentrations almost no effect of Brownian coagulation on the change in particle number concentration occurs[12]. The effect of photophoresis by illumination of the ultramicroscope on settling velocity was completely avoided by intermittent lighting.

Conclusion

The velocity of thermophoresis in the slip flow region was studied experimentally. The experimental method presented herein was developed to meet most of the necessary conditions for accurate measurement of thermophoresis, and it gives very reliable data on thermophoresis compared with those so far reported. The results were compared with the theories proposed by Derjaguin and by Brock, and were found in good agreement with Derjaguin's theory rather than Brock's.

Acknowledgment

I. Nishioka was very helpful in the experimental work.

Nomenclature

C_m	=	tangential momentum first-order slip coefficient[1] ≈1.23	[—]
C_t	=	temperature jump first-order slip coefficient[1] ≈2.16	[—]
D_p	=	diameter of particle	[cm], [μ]
h	=	depth from inner surface of the upper wall of a cell	[cm], [mm]
K_s, K_i	=	thermal conductivity of gas and particle, respectively	[cal/cm·sec·°K]
T	=	temperature of gas	[°C], [°K]
$t_{1/2}$	=	the time when half of the initial number disappear	[sec]
$U_G(D_p)$	=	velocity of gravitational settling	[cm/sec]
$U_T(D_p)$	=	velocity of thermophoresis	[cm/sec]
y	=	depth from an arbitrary position in a cell	[mm]
λ	=	mean free path of gas molecules	[cm]
μ	=	viscosity of fluid	[g/cm·sec]
ρ	=	density of fluid	[g/cm^3]
ρ_p	=	density of particle	[g/cm^3]

〈Subscript〉

$_{50}$ = for median diameter

〈Superscripts〉

D = for Derjaguin

B = for Brock

Literature Cited

1) Brock, J. R.: *J. Colloid Sci.*, **17**, 768 (1962).
2) Derjaguin, B. V. and Y. Yalamov: *J. Colloid Sci.*, **20**, 555 (1965).
3) Derjaguin, B. V. and Y. Yalamov: *J. Colloid and Interface Sci.*, **22**, 195 (1966).
4) Gudzinowicz, B. J.: *J. Chem. Eng. Data*, **9**, 79 (1964).
5) Hidy, G. M. and J. R. Brock: "Topics in Current Aerosol Research (Part 2)", Chapter 5, Pergamon Press Inc. (1972).
6) Jacobsen, S. and J. R. Brock: *J. Colloid Sci.*, **20**, 544 (1965).
7) Paranjpe, M. K.: *Proc. Indian Acad. Sci.*, **4a**, 423 (1936).
8) Phillips, W. F.: *Physics of Fluids*, **18**, No. 2, 144 (1975).
9) Sone, Y., K. Aoki and Y. Onishi: *J. Japan Soc. Aero. Space Sci.*, **23**, 568 (1975).
10) Sone, Y. and K. Aoki: *ibid.*, **23**, 575 (1975).
11) Yoshida, T., Y. Kousaka and K. Okuyama: *Ind. Eng. Chem., Fundam.*, **14**, 47 (1975).
12) Yoshida, T., Y. Kousaka, K. Okuyama and S. Nishio: *J. Chem. Eng. Japan*, **8**, 137 (1975).

TURBULENT COAGULATION OF AEROSOLS IN A STIRRED TANK

KIKUO OKUYAMA, YASUO KOUSAKA,
YOSHINORI KIDA AND TETSUO YOSHIDA
Department of Chemical Engineering, University of Osaka Prefecture, Sakai 591

(Reprinted with permission)

Reprinted from
JOURNAL OF
CHEMICAL ENGINEERING
OF
JAPAN
Vol. 10, No. 2 (1977)
Pages 142—147

TURBULENT COAGULATION OF AEROSOLS IN A STIRRED TANK

KIKUO OKUYAMA, YASUO KOUSAKA,
YOSHINORI KIDA AND TETSUO YOSHIDA
Department of Chemical Engineering, University of Osaka Prefecture, Sakai 591

Turbulent coagulation of aerosol particles was studied experimentally by observing the time-dependent changes in particle number concentration and size distribution of aerosol for various intensities of stirring in a stirred tank, using the ultramicroscopic size analysis. From the observed data on the decrease in particle number concentration of aerosol, the rate constants of turbulent coagulation were evaluated and compared with some of the most representative theories, and were found in good agreement with Saffman and Turner's theory. Further, the changes in particle size distribution observed were confirmed by those obtained by numerically solving the equation of coagulation for polydisperse aerosol, the so-called population balance equation.

Introduction

The rate of coagulation of aerosol particles depends on Brownian motion of particles and turbulent motion of the fluid in which particles are entrained, when particles are not electrically charged. Brownian coagulation controls the rate of coagulation under small particle sizes and small turbulence, while the effect of turbulent coagulation begins to exceed Brownain coagulation with the increase of particle radius and turbulent intensity. The behavior of polydisperse aerosols undergoing Brownian coagulation has been studied by many researchers[1,6,10,12] and a general understanding of the behavior under various conditions has been almost obtained. Previous studies[1,7,9] on turbulent coagulation, on the other hand, have been limited to theoretical ones where coagulation rate is discussed, but few experimental data are available to verify the theories because of the difficulty in accurate measurement of the change in properties of highly concentrated aerosol[3].

In this paper, the changes in particle number and size of aerosols undergoing turbulent coagulation in a stirred tank were observed for various intensities of stirring, using the ultramicroscopic size analysis previously developed by the authors[13]. Then the rate constants of turbulent coagulation were evaluated from the observed data on the decrease in particle number of aerosols, and they were compared with some representative theories on turbulent coagulation. Furthermore, the changes in particle size distribution observed were compared with those obtained by numerically solving the equation of coagulation for polydisperse aerosols.

Received September 1, 1976. Correspondence concerning this article should be addressed to K. Okuyama. Y. Kida is with Kuraho Co., Ltd., Hirakata 573.

1. Experimental Apparatus and Method

A schematic diagram of the experimental apparatus is shown in **Fig. 1**. The vessel used was made of acrylic resin, and equipped with four vertical baffles each of which has a width of one tenth of the tank diameter. The stirrer was six flat-bladed turbine. The vessel and stirrer dimensions are standard ones as shown in Fig. 1. Aerosol used in this study was tobacco smoke generated by a simple smoking apparatus[12], by which number concentration of particles was controlled from 10^6 to 10^8 particles/cc. Aerosols thus generated were introduced promptly throughout the chamber and was mechanically stirred for a short period with extremely low revolution to make the aerosol uniform. Then the revolution of the stirrer was raised to the desired speed. The stirrer speed was checked by a photo tran-

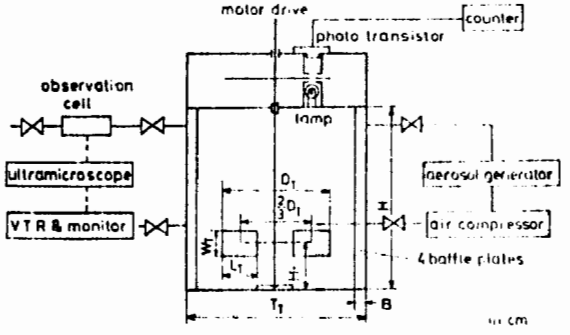

	H	T_T	D_T	H_T	W_T	L_T	B
stirred tank I	10.0	10.0	5.2	$T_T/3$	1.0	2.9	$T_T/10$
stirred tank II	20.5	19.0	8.9	$0.17T_T$	1.8	2.2	$T_T/10$

Fig. 1 Experimental apparatus

Table 1 Experimental conditions and properties of aerosols

N	Re	n_0'	r_{p0}'	σ_{p0}	ε_0	K	β	K_D	$\beta n_0'/Kn_0'^2$
Stirred tank I									
600	1.81×10^3	2.00×10^7	0.47	1.34	3.00×10^4	1.02×10^{-9}	2.32×10^{-3}	2.9	1.14×10^{-1}
1800	5.44×10^3	2.00×10^7	0.42	1.31	8.10×10^5	1.28×10^{-9}	1.09×10^{-3}	3.6	4.26×10^{-1}
3780	1.14×10^4	2.00×10^7	0.45	1.38	7.45×10^6	6.44×10^{-9}	6.37×10^{-3}	18.2	5.23×10^{-2}
5000	1.51×10^4	1.75×10^7	0.45	1.40	1.74×10^7	1.25×10^{-8}	6.91×10^{-3}	35.2	3.16×10^{-2}
9000	2.72×10^4	1.50×10^7	0.45	1.40	1.01×10^8	3.76×10^{-8}	1.78×10^{-2}	106	3.16×10^{-2}
Stirred tank II									
1440	1.28×10^4	1.30×10^7	0.47	1.34	8.10×10^6	2.11×10^{-9}	1.14×10^{-3}	6.0	4.16×10^{-2}
3000	2.66×10^4	1.80×10^6	0.40	1.33	7.45×10^5	3.66×10^{-9}	1.89×10^{-3}	10.1	2.86×10^{-1}
〃	〃	1.00×10^7	0.46	1.28	〃	5.65×10^{-9}	7.33×10^{-3}	16.0	1.30×10^{-1}
〃	〃	6.25×10^6	0.64	1.48	〃	1.13×10^{-8}	1.68×10^{-3}	33.5	2.38×10^{-2}
5400	4.78×10^4	1.00×10^7	0.47	1.46	4.35×10^7	1.30×10^{-8}	3.68×10^{-3}	37.0	2.38×10^{-2}

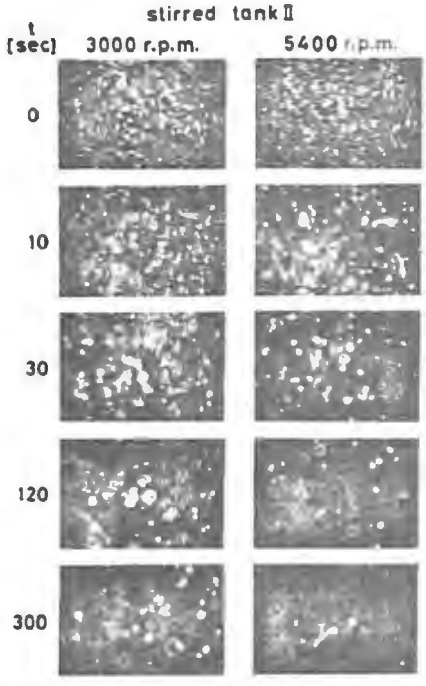

Fig. 2 Photographs on time-dependent changes in aerosol

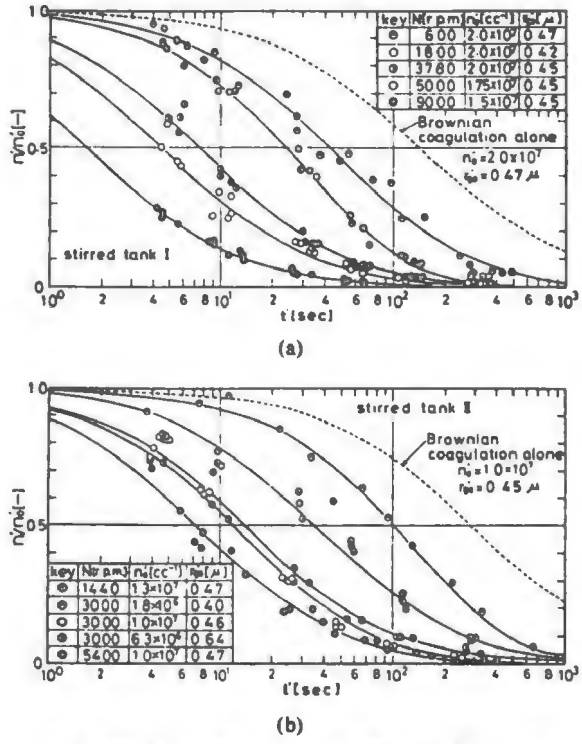

Fig. 3 Effect of stirrer speed on decrease in particle number concentration of aerosol

sistor and was varied from 300 to 9000 rpm. Aerosol sampled at any given residence time was introduced into the observation cell installed on the stage of an ultramicroscope to measure its particle size distribution and particle number concentration[13]. Experiments were carried out by changing initial particle number concentrations, particle sizes, stirrer speeds and sampling positions. Representative experimental conditions and properties of aerosols are shown in **Table 1**.

2. Experimental Results and Discussion

No difference in experimental results was found in changing sampling positions, which indicates that the aerosol is uniform throughout the tank. **Figure 2** is an example of a series of photographs, taken by a camera directly attached to the ultramicroscope. It is seen that particle number decreases rapidly with time, and the decrease is more rapid at higher revolution of the stirrer. The particle growth due to turbulent coagulation is also found in the photographs.

2. 1 Particle number concentration

Figure 3 shows experimental relations between the ratio of particle number concentrations at any time with those at initial time and stirring time in a tank. It can be seen that particle number concentrations in all cases decrease faster than the estimated ones from the equation of Smoluchowski[10] for monodisperse aerosols undergoing Brownian coagulation, which is given by

$$1/n'-1/n_0'=2K_0C_m(r_{p0}')t',\ K_0=2\kappa T/3\mu \qquad (1)$$

These differences increase with the intensity of stirring when initial aerosol properties are of the same order.

In the case of same stirrer speed, the decrease in particle number depends on the initial particle number concentrations and initial particle sizes. As these experimental results depend not only on coagulation but on deposition loss of particles to the walls, it is impossible to compare directly these results with the theory of coagulation alone. According to Gillespie and Langstroth[5], the effects of coagulation and deposition on the decrease in particle number concentration can be seperated quantitatively by introducing the following equation

$$dn'/dt' = -Kn'^2 - \beta n' \qquad (2)$$

where K denotes the coagulation rate constant and β the deposition rate constant.

As both K and β may be considered to depend to some extent on particle size distributions which are subject to change during the ageing of an aerosol, they will be a function of time. Since it is very complicate to introduce the change of particle size into Eq. (2), time-dependences of K and β were disregarded here. Integration of Eq. (2) gives

$$1/n' + K/\beta = (1/n_0' + K/\beta)\exp(\beta t') \qquad (3)$$

The coagulation rate constant K and deposition rate constant β were determined by fitting the experimental data to Eq. (3) using the nonlinear squares method. The curves in Fig. 3 are the fitting curves thus obtained. The values of K and β are shown in Table 1 for various conditions. As seen from the table, values of K ranged from 10^{-9} to 4×10^{-8} cm³/sec, while β from 10^{-3} to 2×10^{-2} 1/sec. The values of K and β seem to increase with the stirrer speed and initial particle size.

2.2 Coagulation rate

The values of K evaluated from experimental results include both effects of Brownian and turbulent coagulation, and turbulent coagulation is first discussed in this section.

Turbulence can affect coagulation by two different mechanisms. In the first mechanism, since the turbulent flow brings spatial non-homogeneities, different velocities in neighbouring particles appear and, as a result, particles collide with each other by a mechanism analogous to the mechanism of laminar shearing flow. A second coagulation mechanism is caused by the relative motion of each particle differing from that of the turbulent air, because its inertia will not be the same as an equivalent mass of air[6]. This second mechanism may be neglected[8] when

(1) the sum of colliding particle radii is small compared to the smallest eddies in the fluid, and

(2) the particles follow the fluid motion completely. In either mechanism, the coagulation rate depends mainly on particle size and velocity gradient evaluated from the energy dissipation rate per unit mass of fluid. In the case of stirred tank, the average value of the energy dissipation rate ε_0 is taken to be equal to the power consumption rate per unit mass of mixing fluid. Some investigators including Schwartzberg and Treyball[9] give ε_0 for the standard stirred tank used in this experiment as, from the data for water

$$\varepsilon_0 = 7.9 N_s^3 D_T^2 / T_T^2 H \quad \text{at } Re > 5000 \qquad (4)$$

The distribution of energy dissipation rate through a tank results in coagulation rate distribution. That is, a difference exists between the coagulation rate based on the average energy dissipation rate ε_0 and that based on the local energy dissipation rate and its distribution through a tank. Kuboi, Komasawa and Otake, however, suggested that the effect of energy dissipation rate distribution through a tank on the mass transfer coefficient is relatively small. For a first approximation, the coagulation rate experimentally obtained was connected with average value of ε_0 neglecting the effect of local values of energy dissipation rate in this study. The values of ε_0 are shown in Table 1. According to the theory of isotropic turbulence proposed by Kolmogoroff, the micro-scale of the turbulence λ_0 is given by the next following equation from ε_0[7]

$$\lambda_0 = (\nu^3/\varepsilon_0)^{1/4} \qquad (5)$$

Under the present experimental conditions, the minimum value of λ_0 is about 25 μ, which is sufficiently large compared with the particle radius. As the relaxation time is sufficiently small for sub-micron particles, the particles will follow fluid motion completely.

From these discussions it can be concluded that, in the present case, the above second mechanism of turbulent coagulation due to the inertia of the particles may be ignored and the first mechanism is important. The representative theoretical equations denoting the collision rate by the first coagulation mechanism have been proposed by

Saffman and Turner[8];

$$K_T(r_i', r_j') = 1.30(r_i' + r_j')^3(\varepsilon_0/\nu)^{1/2} \qquad (6)$$

Levich[7];

$$K_T(r_i', r_j') = \frac{12\pi\delta(\varepsilon_0/\nu)^{1/2}(r_i' + r_j')^3}{1 + 2/7\{(r_i' + r_j')/\lambda_0\}^3} \qquad (7)$$

The value δ which appears in the equation is given as about 0.25 by Fuchs[1]. Equation (7) reduces to next equation when $r_i' + r_j'$ is less than λ_0

$$K_T(r_i', r_j') = 12.6(r_i' + r_j')^3(\varepsilon_0/\nu)^{1/2} \qquad (8)$$

The comparison of these equations with experimental results has not been made so far. When an aerosol is monodisperse, coagulation rate K_T is given as

$$K_T(r_0') = K_T(r_0', r_0')/2 \qquad (9)$$

The values of K evaluated from experimental results including the effects of both Brownian and turbulent coagulation as described before, the following value

K_D was next introduced to obtain the importance of turbulent coagulation relative to Brownian coagulation

$$K_D = K/K_B(r'_{g0}) = \{K_T(r'_{g0}) + K_B(r'_{g0})\}/K_B(r'_{g0}) \qquad (10)$$

where $K_B(r'_{g0}) = 2K_0 C_m(r'_{g0})$, which can be easily determined. The values of K_D are shown in Table 1. **Figure 4** shows the variation of K_D against the values of $r'^3_{g0}\sqrt{\varepsilon_0}$, together with the theoretical curves of K_D from Eq. (6) by Saffman and Turner and Eq. (8) by Levich. It will be seen that the experimental data agree with the curve of Saffman and Turner's equation rather than that of Levich. Turbulent coagulation can be ignored at $r'^3_{g0}\sqrt{\varepsilon_0}$ less than 2×10^{-12}, while Brownian coagulation can be ignored at $r'^3_{g0}\sqrt{\varepsilon_0}$ larger than 2×10^{-10}. When particle size increases significantly by turbulent coagulation, comparison of experimentally obtained K_D with the theoretical one by using the initial geometric mean radius will be erroneous.

2. 3 Deposition rate

Figure 5 shows the dependence of the deposition rate β obtained experimentally on the energy dissipation rate ε_0, together with the theoretical values calculated by next equation

$$\beta = \frac{8}{\pi T_T}\{K_\varepsilon D(r'_0)\}^{1/2} + \frac{u_t(r'_0)}{H}\coth\left\{\frac{\pi u_t(r'_0)}{4\sqrt{K_\varepsilon D(r'_0)}}\right\} \qquad (11)$$

Equation (11) was derived by Takahashi and Kasahara[11] for a cylindrical vessel in the same way as Corner and Pendlebury[3] for a cubic vessel, which gives the deposition rate due to Brownian and turbulent diffusion accompanying the gravitational settling. In Eq. (11), K_ε is equal to $\kappa' du/dx$, where κ' is the Karman's constant (≈0.4) and du/dx is given by Saffman and Turner[8] as follows

$$du/dx = (2\varepsilon_0/15\nu)^{1/2} \qquad (12)$$

Figure 5 suggests that experimental values agree approximately with the theoretical ones and that the values of stirred tank I are larger than those of stirred tank II, because the tank I has a larger ratio of wall surface to the volume.

When the values of $\beta n'_0/Kn'^2_0$ in Table 1, the ratio of deposition rate to coagulation rate at the initial ageing stage, are less than about 0.1, it is found that the effect of deposition on the decrease of particle number is relatively small. **Figure 6** shows the comparison of actual time-dependent change in particle number concentration with calculated curves obtained by ignoring the one of the values of K and β in Eq. (3). It is seen that experimental results agree with the curve of coagulation alone. **Figure 7** shows the effect of initial particle number concentration n'_0 on decrease in particle number concentration. Particle number of highly concentrated aerosol decreases faster than that of lower

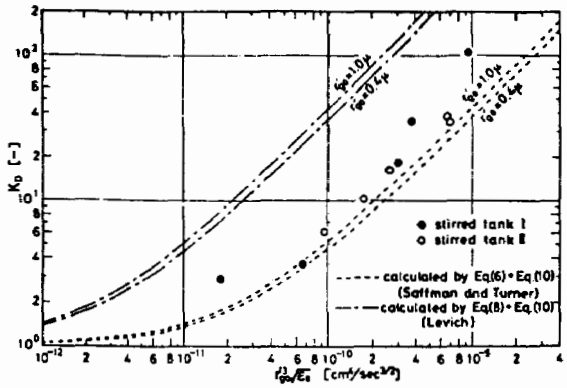

Fig. 4 Comparison of the values K_D obtained in the present experiments with calculated ones

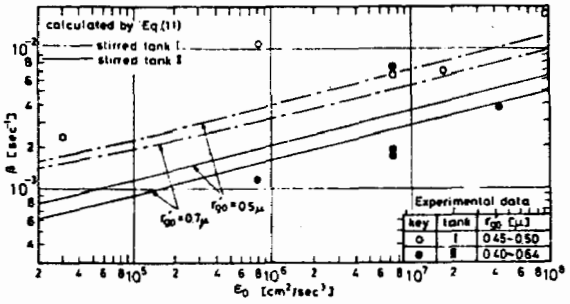

Fig. 5 Comparison of the deposition rates with theoretical ones

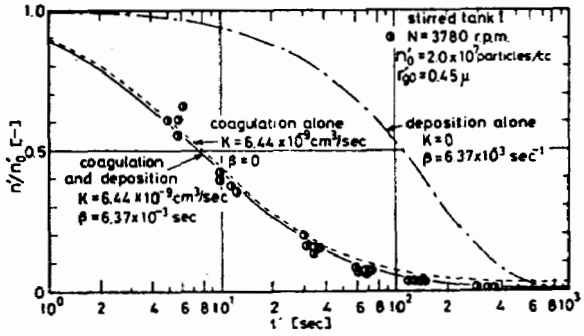

Fig. 6 Effects of deposition and coagulation on decrease in particle number concentration

one, which indicates that the effect of deposition is not significant since the effect of deposition must be independent of n'_0. These results suggest that the behavior of aerosol for one micron order in a stirred tank is dominated by coagulation when particle number concentration is larger than 5×10^8 particles/cc.

2. 4 Particle size distribution

The basic equation for the time-dependent change in particle size distribution of polydisperse aerosols undergoing Brownian and turbulent coagulation can be written as[16]

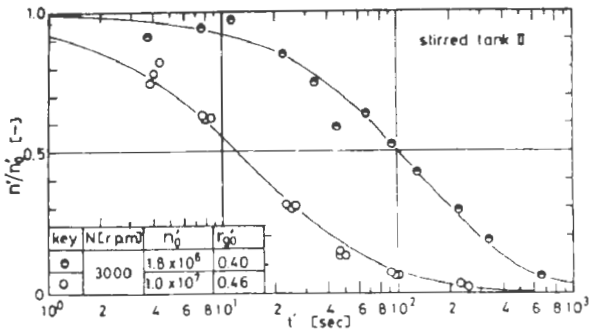

Fig. 7 Effect of initial particle number concentration on decrease of particle number concentration

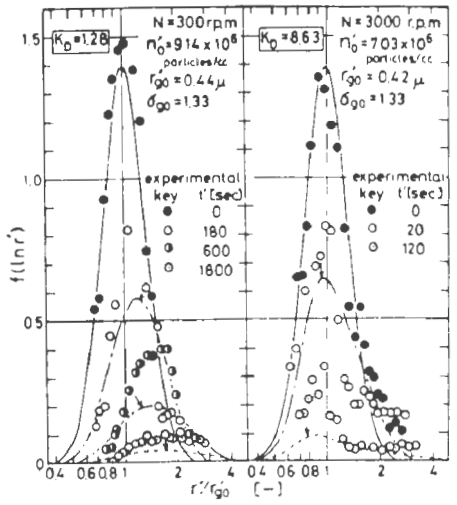

Fig. 8 Change in particle size distribution with time

$$\partial n'(r',t')/\partial t' = \int_{\rho'=0}^{\rho'=r'/\sqrt[3]{2}} \{K_B(\sqrt[3]{r'^3-\rho'^3}, \rho') + K_T(\sqrt[3]{r'^3-\rho'^3}, \rho')\} \times n'(\sqrt[3]{r'^3-\rho'^3}, t')n'(\rho', t')\left(\frac{r'}{\sqrt[3]{r'^3-\rho'^3}}\right)^2 d\rho' - \int_{\rho'=0}^{\rho'=\infty} \{K_B(r',\rho') + K_T(r',\rho')\}n'(r',t')n'(\rho',t')d\rho' \quad (13)$$

$K_B(r',\rho')$ is the Brownian coagulation function and is given[10] by

$$K_B(r',\rho') = K_0(r'+\rho')\{C_m(r')/r' + C_m(\rho')/\rho'\} \quad (14)$$

Saffman and Turner's Eq. (6) was used here as $K_T(r', \rho')$, the turbulent coagulation function, which showed better fitting with experimental results.

The left side of Eq. (13) is the change in particle number concentration of size r' with time. The first term on the right side represents the rate of formation of particles of size r' due to coagulation of two particles smaller than size r' and the second term the rate of loss of particles of size r' due to their coagulation with particles of other sizes including r'.

The initial particle size distribution was assumed to be established instantaneously with the following log-normal form

$$n'(r',0)dr' = \frac{n'_0}{\sqrt{2\pi}\ln\sigma_{g0}} \exp\left(-\frac{\ln^2(r'/r'_{g0})}{2\ln^2\sigma_{g0}}\right)d\ln r' \quad (15)$$

Since Eq. (13) cannot be solved analytically, the Runge-Kutta-Merson method was employed to solve it[14]. As a numerical check the total mass of aerosol was calculated every few time steps and compared with the initial value. **Figure 8** shows the comparison of time-dependent change in particle size distribution between calculated and experimental ones. The frequency $f(\ln r')$ was calculated by the next equation

$$f(\ln r') \quad n'(r', t')r'_i n_0 \quad (16)$$

The manner of the change by calculation seems to depend on the value of K_D which expresses the relative importance between Brownian and turbulent coagulation. When the value of K_D is 1.28, as shown on the left side of the figure where Brownian coagulation is controlling, the particle size distributions shift towards the larger radius with time. When the value of K_D is large, as shown on the right side of the figure, where turbulent coagulation is controlling, the mode radius in the particle size distribution does not tend to move to the larger radius. These tendencies will be caused by the difference in the dependences of the coagulation functions on particle sizes, that is, the dependence of Brownian coagulation function on particle radius is not very large for $r'_0 > 0.1\ \mu$, while turbulent coagulation function is propotional to the cube of particle size. The decreasing rate of total particle number concentration by turbulent coagulation is found to be very large in comparison with that by Brownian coagulation in Fig. 8. The figure indicates that the calculation results agree approximately with experimental results including the small effect of deposition.

Conclusion

Turbulent coagulation of aerosols was studied experimentally by observing the time-dependent change in particle number concentration and size distribution of aerosols in a stirred tank, and the coagulation rate and the deposition rate were determined. The turbulent coagulation rate experimentally obtained was compared with the theories proposed by Saffman and Turner, and by Levich, and were found to be in good agreement with that proposed by Saffman and Turner rather than that by Levich. The deposition rate agreed approximately with the theory proposed by Takahashi and Kasahara. The time-dependent changes in particle size distributions were evaluated by numerically solving the coagulation equation for polydisperse aerosols using the turbulent coagulation function proposed by Saffman and Turner, and then they

were compared with experimental ones. The change in size distribution by turbulent coagulation obtained by both calculation and experiment give a distinctive feature which is different from those by Brownian coagulation. It was found that at $r_{g0}'^3\sqrt{\varepsilon_0}$ less than 2×10^{-13} turbulent coagulation is not effective and at $r_{g0}'^3\sqrt{\varepsilon_0}$ larger than 2×10^{-10} Brownain coagulation can be ignored.

Acknowledgment

N. Hishio was very helpful in the experimental work.

Nomenclature

$C_m(r_i')$	= Cunningham's correction factor of radius r_i'	[—]
$D(r_i')$	= Diffusion coefficienct ($=C_m(r_i')\kappa T/6\pi\mu r_i'$)	[cm²/sec]
D_T	= stirrer diameter	[cm]
g	= acceleration of gravity	[cm/sec²]
H	= height of a stirred tank	[cm]
K	= overall coagulation rate constant	[cm³/sec]
K_0	= coefficient in Eq. (1)	[cm³/sec]
$K_B(r_0')$	= Brownian coagulation rate constant for monodisperse aerosol	[cm³/sec]
$K_B(r_i', r_j')$	= Brownian coagulation function for two particles of size r_i' and r_j'	[cm³/sec]
K_D	= defined by Eq. (10)	[—]
K_s	= $\varepsilon' du/dx$	[1/sec]
$K_T(r_0')$	= turbulent coagulation rate constant for monodisperse aerosol	[cm³/sec]
$K_T(r_i', r_j')$	= turbulent coagulation function for two particles of size r_i' and r_j'	[cm³/sec]
N, N_s	= stirrer speed	[1/min][1/sec]
n'	= total particle number concentration at any time	[particles/cm³]
$n'(r', t')$	= particle size distribution	[particles/cm³·cm]
n_0'	= total particle number concentration at time zero	[particles/cm³]
Re	= Reynolds number based on stirrer tip velocity ($=\rho_f N_s D_T^2/\mu$)	[—]
r'	= particle radius	[cm]
r_{g0}'	= geometric mean radius	[cm][μ]
r_0'	= particle radius for monodisperse aerosol	[cm][μ]
T	= absolute temperature	[°K]
T_T	= diameter of a stirred tank	[cm]
t'	= time	[sec]
u	= average velocity in a stirred tank	[cm/sec]
$u_t(r')$	= terminal settling velocity ($=2C_m(r')(\rho_p-\rho_f)gr'^2/9\mu$)	[cm/sec]
x	= arbitrary direction in a stirred tank	[cm]
β	= deposition rate constant	[1/sec]
ε_0	= average energy dissipation rate	[cm²/sec³]
κ	= Boltzman's constant ($=1.38\times10^{-16}$)	[erg/°K]
κ'	= Karman's constant (≈0.4)	[—]
λ_0	= turbulent micro-scale	[cm][μ]
μ	= dynamic viscosity	[g/cm·sec]
ν	= kinematic viscosity	[cm²/sec]
ρ'	= particle radius in Eq. (13)	[cm]
ρ_f, ρ_p	= fluid and particle density	[g/cm³]
σ_{g0}	= geometric standard deviation at time zero	[—]

Literature Cited

1) Beal, S. K.: *J. Aerosol Sci.*, **3**, 113 (1972).
2) Corner, J. and E. D. Pendlebury: *Proc. Phys. Soc.*, **B64**, 645 (1951).
3) Gillespie, T. and C. O. Langstroth: *Canad. J. Chem.*, **30**, 1003 (1952).
4) Huang, C. M., M. Kerker and E. Matijevic: *J. Colloid Interface Sci.*, **33**, 529 (1970).
5) Kuboi, R., I. Komasawa and T. Otake: *Chem. Eng. Sci.*, **29**, 65 (1974).
6) Lai, F. S., S. K. Friedlander, J. Pich and G. M. Hidy: *J. Colloid Interface Sci.*, **39**, 395 (1972).
7) Levich, V. G.: "Physicochemical Hydrodynamics", Prentice-Hall, London (1962).
8) Saffman, P. G. and J. S. Turner: *J. Fluid Mech.*, **1**, 16 (1956).
9) Schwartzberg, H. G. and R. E. Treybal: *Ind. Eng. Chem., Fundam.*, **7**, 1 (1968).
10) Smoluchowski, M. von Z.: *Phys. Chem.*, **92**, 129 (1917).
11) Takahashi, K. and M. Kasahara: *Atmos Environ.*, **2**, 441 (1968).
12) Yoshida, T., Y. Kousaka and K. Okuyama: *Ind. Eng. Chem., Fundam.*, **14**, 47 (1975).
13) Yoshida, T., K. Okuyama, Y. Kousaka and Y. Kida: *J. Chem. Eng. Japan*, **8**, 317 (1975).
14) Zebel, G.: *Kolloid-Z.*, **156**, 102 (1958).

THE EFFECT OF NEIGHBOURING FIBERS ON THE SINGLE FIBER INERTIA-INTERCEPTION EFFICIENCY OF AEROSOLS

HITOSHI EMI, KIKUO OKUYAMA
AND MOTOAKI ADACHI
Department of Chemical Engineering, Kanazawa University, Kanazawa 920

The effect of the volume fraction of the fibers in fibrous air filters on the collection efficiency of a single fiber has been examined both theoretically and experimentally in the inertia predominant region.

Numerical solutions have been obtained for the flow around a circular cylinder in a cell determined by the volume fraction of the fibers for a Reynolds number of 10 and the potential flow. Particle trajectories have been calculated in the cell by introducing the above numerical values into the equations of particle motion. As a result, the inertia-interception efficiency was evaluated through four parameters; inertia parameter, interception parameter, Reynolds number and volume fraction.

Experimental data on model filters, which are made of a uniform parallel arrangement of wires orientated at right angles to the flow direction have shown good agreement with the calculation results in the intermediate Reynolds numbers region.

Introduction

In the filtration of aerosols by a high-porosity fibrous filter ($\varepsilon > 0.98$), the collection efficiency due to inertial impaction, Brownian diffusion, gravitational settling and direct interception can be predicted using an isolated fiber model. In the previous paper[4], some appropriate expressions on collection efficiency of an isolated fiber were shown and a method was proposed to predict the efficiency readily under arbitrary operating conditions. When the porosity becomes lower, however, the efficiency will deviate from that of an isolated fiber. This deviation from an isolated fiber is known as the interference effect between neighbouring fibers, and in classical filtration, the empirical correction had been made by Chen[1] and others[2,8,12], without any certain theoretical background. A modern filtration theory on the interference effect was developed by Kirsch, Stechkina and Fuchs[9,13] on the basis of Kuwabara's flow field[10] transverse to a random assembly of parallel cylinders. After the Kuwabara's flow had been confirmed valid experimentally at low Reynolds number, they showed a method to estimate the combined diffusion and interception efficiency which correlated very well with experimental results by model filters and by real ones. In the inertia predominant region they also calculated the collection efficiency for $St \ll 1$ by an analytical procedure[14] using Kuwabara's stream function. Stenhouse calculated the particle trajectory by a stepwise method[16] using Happel's flow field and gave the inertia-interception efficiency as the function of the volume fraction of the filter. These theoretical treatments have not taken into account the effect of Reynolds number, which is not negligible especially in the inertia predominant region.

In the present work, the collection efficiencies due to inertia and interception have been calculated numerically from the flow pattern around a circular cylinder on the basis of a cell model. Calculation results are compared with the experimental ones obtained by model filters.

1. Flow Pattern in Fibrous Filter

Most fibrous filters are built up from fiber layers, in which individual fibers are arranged nearly perpendicular to the flow and keep a proper distance from each other corresponding to the volume fraction of the fibers. The flow pattern around a circular cylinder, therefore, is influenced by its neighbours, and a filter may be considered to consist of a number of cells, each of which comprises a single fiber surrounded by a concentric envelope of air. Though Kuwabara[10] and Happel[6] solved the viscous flow equation in one cell for a small Reynolds number as a function of only the volume fraction of the fibers, the flow in the cell should be determined by both volume fraction and

Received June 1, 1976. Correspondence concerning this article should be addressed to H. Emi. K. Okuyama is at Dept. of Chemical Engineering, University of Osaka Prefecture, Sakai 591. M. Adachi is at Radiation Center of Osaka Prefecture, Sakai 593.

REPRINTED FROM I&EC

PROCESS DESIGN AND DEVELOPMENT

Pressure Drop and Collection Efficiency of an Irrigated Bag Filter

Tetsuo Yoshida, Yasuo Kousaka, Shigeo Inake, and Shigeyuki Nakai

Reprinted from I&EC Process Design and Development
Volume 14, April 1975, Page 101 ©
Copyright 1975 by the American Chemical Society and reprinted by permission of the copyright owner

Pressure Drop and Collection Efficiency of an Irrigated Bag Filter

Tetsuo Yoshida, Yasuo Kousaka,* Shigeo Inake, and Shigeyuki Nakai

Faculty of Engineering, University of Osaka Prefecture, Osaka, Japan

An irrigated bag filter has been developed to improve performances of existing dry bag filters. Irrigation to filter surface by spraying or overflowing water prevents filter media from firing in handling hot gas and makes it possible to wash away the precipitated dusts from filter surfaces. Some characteristics regarding pressure drop and dust collection of an irrigated filter which were quite different from dry ones were studied, and then basic mechanisms of them were discussed. A series of studies suggested that this kind of collector will be useful in certain industrial fields.

Introduction

An irrigated bag filter described here is quite different from existing dry bag filters, because the surface of filter media is covered by water. It has been reported that an irrigated bag filter can treat high-temperature and highly humid gas, and that sweepage procedures of dust cake necessary for a dry filter are not needed because of water falling along the filter surface (Minami, *et al.*, 1969). It has been also reported that the relation between pressure drop and gas flow rate is peculiar compared with that of dry filters (Muhlrad, 1970) and that collection efficiency is fairly high (Minami, *et al.*, 1969).

In this paper, pressure drop and collection efficiency of irrigated bag filters were tested and their basic mechanisms were studied by using nets of standard wire meshes instead of bag cloths.

Experimental Section

One of the experimental apparatuses used in this study is shown in Figure 1. Water is supplied along the inside of a ring dam to the top of the bag cloth. Gas flows out from the inside of the bag cloth just contacting with falling water in the manner of crossflow. Superficial filtering gas velocities were varied within 20 cm/sec and water rates were from 2 to 20 l./min. The dust particle used was $CaCO_3$ having a median diameter of 3.6 μ (in weight base) and concentrations at the inlet were from 2 to 8 g/m^3. Some physical properties of bag cloths are shown in Table I.

Pressure Drop. Figure 2 shows the comparison of the pressure drop of irrigated bag filters and that of dry ones when they are clean. As is shown in Figure 2 the characteristics of pressure drop considerably differ from each other. Figure 3 indicates the same comparison but with dust loads. Because of washing action against deposited dusts by the down stream of water, almost no pressure rise occurred in irrigated bag filters. For certain dusts, however, which contain some tar substances, the pressure drop increased with operation period.

Collection Efficiency. Figure 4 indicates the collection efficiency of irrigated bag filters. The collection efficiencies seem to be correlated to the pressure drops as shown in Figure 3. Although other experimental conditions of various water rates ranged from 2 to 10 l./min and those of superficial gas velocities from 1.5 to 8 cm/sec were also examined, almost no differences among them were found.

Discussion

In this section, some basic mechanisms of pressure drop and dust collection of an irrigated filter are studied by using nets of standard wire meshes instead of bag cloths.

Pressure Drop. Figure 5a indicates a model of the mesh over which a water film covers. The equilibrium of force is given as follows when pressure difference exists between the two sides of the film.

$$\Delta P D_A D_B g_c = 2(D_A + D_B)(\tau_1 \cos \varphi_1 + n\tau_2 \cos \varphi_2) \tag{1}$$

or

$$\Delta P = 4\sigma_s \xi / D_H g_c \tag{2}$$

The pressure difference ΔP gives the critical one at which the film is just broken. In existing wire meshes, because of a three-dimensional structure shown in Figure 5b, the direction of the force of surface tension varies with positions of a mesh. Then this factor was included in ξ in eq 2. The coefficient, ξ, however, must be constant when the material of the meshes, the manner of weaving, and liquid, respectively, are the same. Equation 2 indicates that the pressure drop to break a film is inversely proportional to the opening size of a mesh.

An irrigated net of wire meshes whose openings have a size distribution is next discussed. When the pressure difference between both sides of the net is gradually raised, the film covering over a mesh with the maximum opening size, in this case, will be broken first because of the minimum pressure to break it as shown in eq 2. Subsequently, with a slight pressure rise, the film over a mesh with the next larger opening size is then broken. Thus films are broken in order of their opening sizes as pressure rises. When the film over the mesh having a hydraulic diameter of D_{Hi} of the ith size is just broken at the pressure of

$$\Delta P_i = 4\sigma_s \xi / D_{Hi} g_c > \Delta P_1 \tag{3}$$

gas must flow out through the opening with the velocity of v_i to keep pressure drop in ΔP_i. The pressure required to break the ith film against the force of surface tension is caused by the resistance of gas flow through the openings over which films are already broken. Then

$$\Delta P_i = \left(4f \frac{\dot{d}}{D_{Hi}} + K_c + K_e\right) \frac{\rho}{2g_c} v_i^2 \tag{4}$$

This equation indicates the flow resistance on the ith opening, and on other openings there must be the following relations

Table I. Properties of Filters Used

Filter cloth	Fabric	Resistance coefficient, 1/m	Hydraulic mean radius, cm	Porosity
A Teviron	Filament, plain	0.432×10^7	76.9×10^{-4}	6.07×10^{-2}
B Tetoron	Spun, plain	2.10×10^7	48.5×10^{-4}	4.46×10^{-2}
C Tetoron	Spun, plain	1.48×10^7	65.8×10^{-4}	7.67×10^{-2}
D Kanekalon	Spun, plain	2.66×10^7	64.1×10^{-4}	4.47×10^{-2}
E Saran	Filament, satin	---	---	---

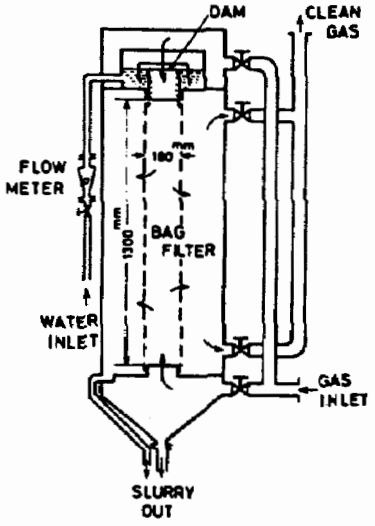

Figure 1. Experimental apparatus.

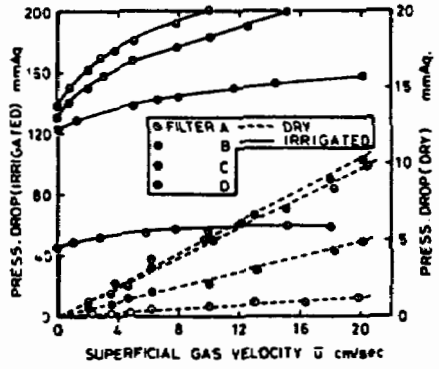

Figure 2. Comparison of pressure drop of irrigated and dry bag filters with no dust load.

$$\Delta P_1 = \left(4f\frac{d}{D_{H1}} + K_c + K_o\right)\frac{\rho}{2g_c}v_1^2$$

$$\Delta P_1 = \left(4f\frac{d}{D_{H2}} + K_c + K_o\right)\frac{\rho}{2g_c}v_2^2$$

$$\vdots \qquad\qquad \vdots$$

$$\Delta P_1 = \left(4f\frac{d}{D_{H1-1}} + K_c + K_o\right)\frac{\rho}{2g_c}v_{1-1}^2 \qquad (5)$$

When meshes with a narrow size distribution, such as standard wire meshes, are concerned, each gas velocity through openings is expressed as

$$v_1 \doteqdot v_2 \doteqdot \cdots \doteqdot v_1 \qquad (6)$$

Then superficial gas velocity will be written by

$$\bar{U}_1 \doteqdot A_1 v_1/A \qquad (7)$$

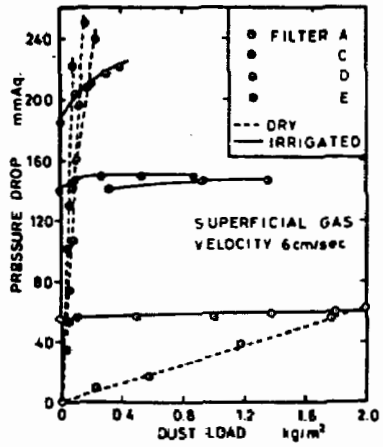

Figure 3. Comparison of pressure drop of irrigated and dry bag filters with dust load.

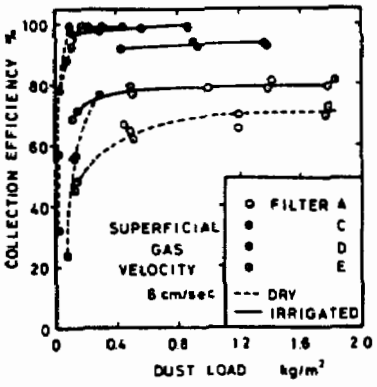

Figure 4. Comparison of collection efficiency of irrigated and dry bag filters.

When all of openings may be regarded as almost square, A_1 is represented as

$$A_1 \doteqdot \sum_{i=1}^{i} D_{Hi}^2 = N\int_{D_{H1}}^{D_{H1}} f(D_H, \sigma^2)D_H^2 dD_H \qquad (8)$$

The above equations give the relation between superficial gas velocity and pressure drop, when the size distribution of meshes, two-dimensional porosity of a mesh, surface tension of liquid, and its correction factor ξ are known. When A_1 is first assumed, then D_{H1}, ΔP_1, v_1, and $\bar{U}_1$ are given respectively by using eq 8, 3, 4, and 7. Repeating the same procedure for various A_1, the correlation of ΔP and $\bar{U}$ is obtainable.

The experimental apparatus to test the above analysis was essentially similar to that of Figure 1, but a net of standard wire meshes was installed instead of a bag cloth and the size of the apparatus was about half of that of Figure 1. Table II shows some physical properties of wire meshes used in the experiment. The dust particle used in

Table II. Properties of Standard Wire Meshes

Wire mesh	Fabric	Hydraulic mean diameter, $\bar{D}_H$, mm	Porosity, ϵ_c	Size distribution
JIS 500	Plain	0.499	0.426	$f = \exp\left\{-\frac{(D_H - \bar{D}_H)^2}{2 \times 7.13^2}\right\}/7.13\sqrt{2\pi}$
M 60	Plain	0.172	0.401	$\exp\left\{-\frac{(D_H - \bar{D}_H)^2}{2 \times 4.78^2}\right\}/4.78\sqrt{2\pi}$
JIS 149	Plain	0.149	0.338	$\exp\left\{-\frac{(D_H - \bar{D}_H)^2}{2 \times 2.68^2}\right\}/2.68\sqrt{2\pi}$
JIS 74	Plain	0.073	0.318	$\exp\left\{-\frac{(D_H - \bar{D}_H)^2}{2 \times 1.81^2}\right\}/1.81\sqrt{2\pi}$

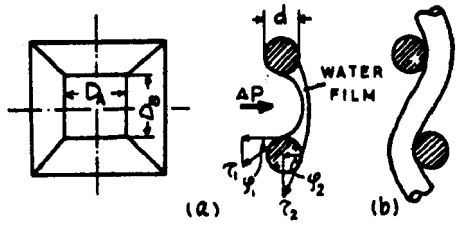

Figure 5. Model of wire mesh.

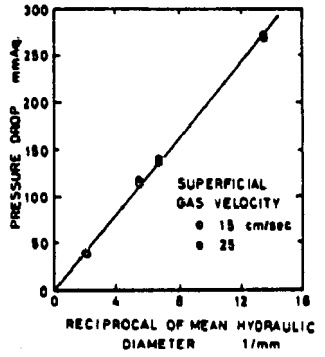

Figure 6. Relation between pressure drop and mean hydraulic diameter of wire mesh.

the experiment was clay having a median diameter of 7.5 μ in weight basis.

Figure 6 shows the relation between the mean hydraulic diameter of meshes and the pressure drop under a constant superficial gas velocity. The figure suggests that eq 2 is valid. Figure 7 shows the comparison of the experimental result with the calculated one on ΔP *vs.* $\bar{U}$ for standard wire meshes. In the calculation, the value of ξ was put as 0.72 for each mesh in Table II. The broken lines in Figure 7 indicate the relation between ΔP_l and $\bar{U}_l$ which is calculated by eq 4 and 7. The values of N_l/N in the figure indicate the ratio of the number of openings having broken film to that of the total openings of meshes. It is one of the interesting characteristics that the number of openings having broken film is extremely small. This phenomenon was also observed on photographs.

Dust Collection. The observation of the surface of an irrigated net of wire meshes by high-speed camera suggested that two marked mechanisms of dust collection existed. As discussed in the former section, the number of openings having broken film is extremely small, so one of the two mechanisms may be modeled after that of the collection by an orifice in an infinite plane. It was also found with precise observation that each opening having broken film was not stable but after an instant, after 1/1000 sec or less, it was recovered by a water film. The period of films being kept broken, which was observed by high-

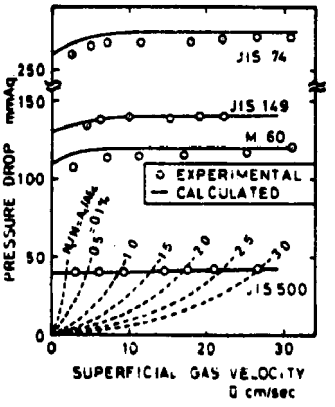

Figure 7. Comparison of experimental and calculated results of pressure drop.

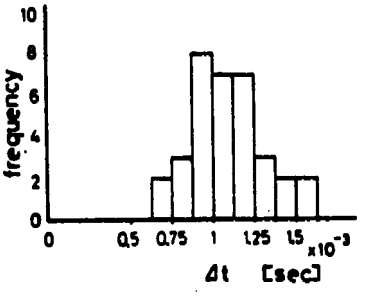

Figure 8. Interval of water film being kept broken (JIS 500).

speed camera, is shown in Figure 8. This sudden opening and closing action of an orifice, that is shutter action of an orifice, may be considered as another mechanism of collection.

Collection by an Orifice in an Infinite Plane. The collection efficiency by an orifice in an infinite plane can be obtained when the stream line around the orifice and then the trajectory of a particle in the stream are calculated. In order to estimate the collection efficiency, potential flow for stream line and Stoke's law for drag of a particle are here assumed. The stream function of ideal gas around an orifice in an infinite plane is given by (Lamb, 1932)

$$\psi = \frac{-r}{2\pi a} \int_0^\infty e^{-kz} J_1(kr) \frac{\sin(ka)}{k} dk \qquad (9)$$

The gas velocities are also given as

$$v_r = \frac{1}{2\pi a} \int_0^\infty e^{-kz} J_1(kr) \sin(ka) dk \qquad (10)$$

$$v_z = \frac{1}{2\pi a} \int_0^\infty e^{-kz} J_0(kr) \sin(ka) dk \qquad (10')$$

When the stream is thus given, trajectories of a particle in

the stream are computed as follows by assuming Stokes' law and no disturbance in the stream by the particle. The dimensionless equations of motion of a particle are expressed as follows when any external forces including gravity may be ignored

$$2\Psi \frac{d^2R}{dT^2} + \frac{dR}{dT} - V_r = 0 \tag{11}$$

$$2\Psi \frac{d^2X}{dT^2} + \frac{dX}{dT} - V_x = 0 \tag{12}$$

where

$$R = \frac{r}{a}\ ;\ X = \frac{x}{a}\ ;\ T = \frac{v_0 t}{a}\ ;\ V_x = \frac{v_x}{v_0};\ V_r = \frac{v_r}{v_0};$$

$$\Psi = \frac{\rho_p d_p^2 v_0}{36\mu a}$$

At a point far away from the orifice, the velocity of a particle is assumed to be equal to that of fluid, so the initial conditions are

$$T = 0;\ \frac{dX}{dT} = -V_x(X_0, R_0) \tag{13}$$

$$\frac{dR}{dT} = -V_r(X_0, R_0) \tag{13'}$$

The trajectories of a particle for various values of Ψ are obtained by performing numerical calculation of above equations. Figure 9 illustrates the relation of a stream line and a trajectory of a particle. The collection efficiency of a particle of d_p in diameter is consequently given as the ratio of the volumetric gas flow rate Q_p to the total flow rate Q as shown in Figure 9. Figure 10 indicates the result of calculation of the efficiency defined above. The figure suggests that the interceptional collection is important in this case, and so collection efficiency cannot be expected to be too great unless the interceptional parameter is sufficiently large.

Collection by Shutter Action of an Orifice. One may suppose a case where a shutter which covers an orifice is suddenly opened and then gas flows out through the orifice. In this case, if dust particles are contained in gas, dust-free gas only may flow out at first while it takes some instants to accelerate the dust particles. When the orifice is recovered by a shutter in the next instant, the particles go straight ahead to be caught to the shutter. If the interval of the shutter being kept open is short enough, a fair contribution to dust collection is expected.

The analysis of this mechanism of collection may be accomplished by calculating the unsteady particle motion in an unsteady velocity field of fluid around the orifice. It will be difficult, however, to estimate the unsteady velocity profile of gas around the orifice which is confronted with the sudden opening and closing action. It is assumed here that a steady velocity profile of gas may be instantaneously built up at opening and that the flow may also be instantaneously stopped at closing. This assumption may be valid only for rough estimation of the extent of the collection efficiency described above. Under the assumption, the collection efficiency of sudden closing of the orifice may be defined as follows (see Appendix)

$$\eta_s = \frac{q_{stop}}{\pi a^2 \bar{v}_0 \Delta t + q_{stop}} \tag{14}$$

In the equation q_{stop} represents the volume surrounded by a stopping distance shown in Figure 11. The stopping distance of a particle with d_p in diameter and ρ_p in density is given by

$$x_{stop} = \frac{d_p^2 \rho_p u_0}{18\mu} \tag{15}$$

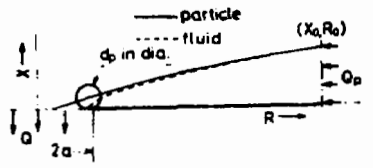

Figure 9. Illustration of collection efficiency of an orifice in an infinite plane.

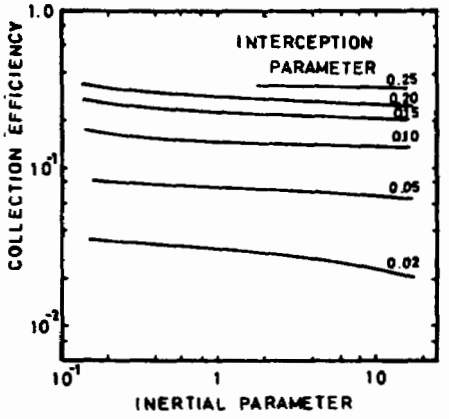

Figure 10. Collection efficiency by an orifice.

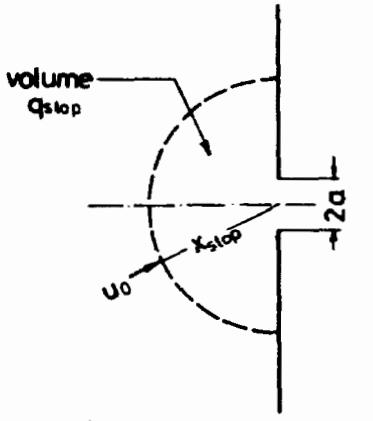

Figure 11. Illustration of collection mechanism by sudden closing of an orifice.

u_0 is the initial velocity of the particle which is regarded as same as the surrounding gas velocity just before the flow stops. Figure 12 shows the result of numerical calculation of η_s. From the figure the shutter action seems to be very effective for collection, especially when the opening period is very short. If the collection by a shutter being just opened is considered in addition, the efficiency will be about twice as much as that in Figure 12.

Figure 13 indicates the experimental result of collection efficiency for an irrigated net of standard wire meshes, the conditions of which are almost same as those of Figure 12. It was pointed out previously that dust collection by an orifice in an infinite plane could not be expected unless the interceptional parameter was large. In the case of Figure 13, the interceptional parameter is small and thus the efficiency in the figure may be roughly compared with that by shutter action of an orifice. Although good agreement is not expected because of the simplified analysis of the phenomena, some resemblances may be found between Figures 12 and 13.

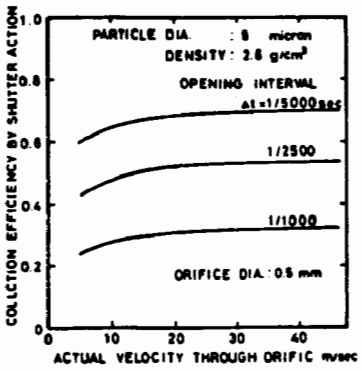

Figure 12. Collection efficiency when shutter being just closed.

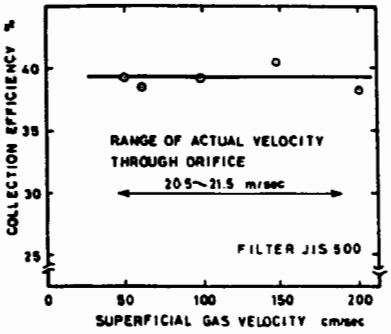

Figure 13. Collection efficiency obtained by standard wire mesh experiment.

Conclusion

The manner of change in pressure drop with gas velocities of irrigated bag filters was first tested and was found to be very peculiar compared with the dry ones. The mechanism of pressure drop was then analyzed from the equilibrium of forces such as surface tension and static pressure of gas, and the result of the analysis was found to agree well with that of experiments using a net of standard wire meshes. The slight change in pressure drop over the wide range of gas velocities seemed to be one of the interesting characteristics of this type of filter. It was also found that almost no pressure rise occurred after a long operation for dusts not containing tar substances.

The collection efficiency of an irrigated bag filter was found to be fairly high. It was impossible to give a full explanation of the experimental results because of the complexity of collection mechanisms. However, two mechanisms of collection, one by an orifice in an infinite plane and another by shutter action of an orifice, were pointed out by a simplified analysis in the case of standard wire meshes being irrigated.

Acknowledgment

S. Magono, K. Yamadaki, T. Yasumune, and Y. Adachi were very helpful in the experimental work.

Appendix

The material balance before and behind the collector with orifices having shutter action is expressed as

$$c_i Q - c_m Q_{stop} = c_0 Q$$

where c_i, c_0, and c_m represent respectively the dust concentration at inlet, outlet, and at collection chamber shown in Figure 14. Q represents the volumetric gas flow rate, and Q_{stop} the total volume of q_{stop} formed in collection chamber in unit time and is given by

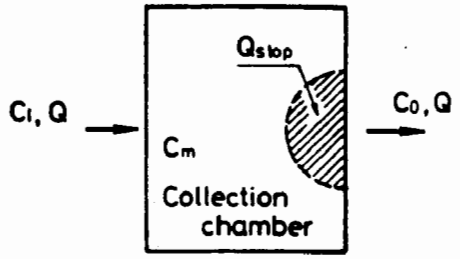

Figure 14. Illustration of collection efficiency by sudden closing of orifice.

$$Q_{stop} = q_{stop} \frac{n}{\Delta t}$$

where n is the number of orifices whose shutters are open. Q is also expressed as $Q = \pi a^2 n \bar{v}_0$. When the collection by an orifice in an infinite plane without shutter action is negligible, the dust concentration before and behind the orifice is equal, then $c_0 = c_m$. By using these correlations, collection efficiency is given as

$$\eta_s = 1 - \frac{c_0}{c_i} = \frac{Q_{stop}}{Q_{stop} + Q} = \frac{q_{stop}}{q_{stop} + a^2 \bar{v}_0 t}$$

Nomenclature

a = orifice radius, m
A = total area of a net of wire meshes, m²
A_i = area defined by eq 8, m²
d_p = particle diameter, m
d, D_A, D_B = values illustrated in Figure 5, m
D_H, $\bar{D}_H$ = hydraulic and hydraulic mean diameters, m
f = friction factor
I = interception parameter = $d_p/2a$
K_c, K_e = friction loss factor of contraction and expansion
m = correction factor of wetted length
N, N_i = number of total openings and of openings with broken film
ΔP = pressure drop, mm Aq
q_{stop} = volume surrounded by stopping distance shown in Figure 11, m³
Q = volumetric gas flow rate, m³/sec
Q_p = gas flow rate shown in Figure 9, m³/sec
r = radial distance, m
Δt = interval of shutter being open, sec
$\bar{U}$ = superficial gas velocity, m/sec
v, v_r, v_x = gas velocity, m/sec
v_0 = $1/\pi a^2$, m/sec
$\bar{v}_0$ = mean actual velocity through orifice, m/sec
x = axial distance, m

Greek Letters

ϵ_c = two-dimensional porosity
μ = viscosity of fluid, kg/sec m
ξ = coefficient defined by eq 2
ρ = density of gas, kg/m³
ρ_p = density of particle, kg/m³
σ_s = surface tension, kg/sec²
τ_1, τ_2 = force by surface tension shown in Figure 5, kg/sec²
φ_1, φ_2 = angle shown in Figure 5
Ψ = inertial parameter

Subscripts

1,2,3, . . . , i = order of opening size

Literature Cited

Lamb, H., "Hydrodynamics," 6th ed, p 138, McGraw-Hill, New York, N. Y., 1932.
Minami, T., Suzuki, T., *Funsai*, No. 14.74, Hosokawa Micromeritics Laboratory, 1969.
Muhlrad, W., *Staub*, 30, 74 (1970).

Received for review September 23, 1973
Accepted November 21, 1974

(Reprinted with permission)

© JOURNAL OF CHEMICAL ENGINEERING OF JAPAN Vol. , No.

[illegible] (○で囲む) [illegible]文 (Short Communication) · Letter to the Editor [illegible] No. E- (19)
(i)[illegible] (ii)その他

英文題名 (大文字) [illegible]

GROWTH OF AEROSOL PARTICLES BY STEAM INJECTION

[illegible]	
1 19	2

和文題名

蒸気の吹込みによるエアロゾルの粒子成長

著者名 (英文, 大文字)

TETSUO YOSHIDA, YASUO KOUSAKA, KIKUO OKUYAMA
AND FUMINORI NOMURA

[illegible] (英文で[illegible])

Department of Chemical Engineering, University of Osaka Prefecture, Sakai 591

脚注 ([illegible]) → [illegible]
Received

Correspondence concerning this article should be addressed to Y. Kousaka.

F. Nomura is now with Kanebo Co., Ltd., Osaka

連絡先 (和文) 〒591 大阪府堺市百舌鳥梅町
大阪府立大学工学部化学工学科

連絡者氏名 向阪保雄 TEL.(0722 - 52 - 1161) 内線 (2322)

[illegible]		本文	Tables 枚	[illegible]	Figs 枚	Figs 枚	計 枚	[illegible]	刷上りページ数	備考
1		7	- (0)	1	1 - 7 (7)	(0)	(7)	1	(2.8) ページ	
			- ( )		- ( )	( )	( )		( ) ページ	
			- ( )		- ( )	( )	( )		( ) ページ	
			- ( )		- ( )	( )	( )		( ) ページ	
			- ( )		- ( )	( )	( )		( ) ページ	

Introduction

It has been reported that steam injection into scrubber systems improves dust collection performance[1~5]. Two mechanisms have been suggested for this improvement : (1) condensation of water vapor upon dust particles, which increases particle size to improve inertial dust collection at scrubbers, (2) deposition of particles on condensing surface by the Stefan flow. The first mechanism, which remains unevaluated by theory so far, was first studied theoretically in this paper. The analysis was then examined by the experiment where the ultramicroscopic technique for droplet size analysis previously developed by the authors[6] was applied.

1. Estimation of Particle Growth

When steam is injected into dust free air, a certain degree of supersaturation will be produced according to the condition and the quantity of both steam and air. Figure 1 illustrates the change of air initially in the stage of "g" to a supersaturated state "i" by steam injection on a humidity chart. If some particles as condensation nuclei were introduced into the supersaturated air, condensation of water vapor upon the particles occurs to decrease supersaturation. This change was illustrated in "i-f" line in the figure. In actual case where some condensation nuclei

or aerosol particles exist in air before steam injection, the change like "i-f" will not take place because condensation occurs before the point "i" in Fig. 1 is attained. Thus the point "i" is imaginary, but even in such a case the amount of the condensable water vapor per unit mass of dry air will be coincide with the value, ΔH, shown in the figure if the process is adiabatic. The value of ΔH and the equilibrium temperature T_{sf} of the system after steam injection will be determined by the following enthalpy and material balances on dry air basis:

$$i_g + H_{st}\left\{x\, i''_{st} + (1 - x)\, i'_{st}\right\} = i_{sf} + H_{st}(1 - x)\, i'_{wf} + \Delta H\, i'_{wf} \quad (1)$$

$$H_g + H_{st}\, x = H_{sf}(T_{sf}) + \Delta H \quad (2)$$

The fianl state of air was regarded saturated in the above equations because the vapor pressure at the surface of grown particles having diameter over 0.1 micron, as is predicted by the Kelvin's equation, is nearly equal to that of saturation.

The calculated value of ΔH against the quantity of steam injection per unit mass of dry air was shown in Fig. 2. It will be noteworthy that ΔH considerably decreases with the increase of air temperature. The temperature at the equilibrium state after steam injection, T_{sf}, was also shown in Fig. 3. The steam condition in these calculations was taken as that of 100°C in temperature, 1 atm. abs. in pressure and 1.0 in dryness fraction. When the dryness fraction x is less than unity, the value of ΔH decreases

with the decrease of x shown in Fig. 4. When supersaturated steam is injected into air, ΔH will decrease with the degree of superheat of the steam.

Whlie ΔH represents the quantity of condensable water vapor per unit mass of dry air as described before, the following relation must be satisfied when all of the vapor corresponding to the amount of ΔH are assumed to condense upon particles contained in air[7]

$$H = \frac{\pi}{6}\left(D_{vf}^3 - D_{vfi}^3 \right) n_0 \rho_s \fallingdotseq \frac{\pi}{6} D_{vf}^3 n_0 \qquad \text{for } D_{vf}^3 \gg D_{vi}^3 \text{ and } \rho_s \fallingdotseq 1 \qquad (3)$$

where n_0 represents the particle number concentration of aerosol on dry air basis. D_{vi} and D_{vf} represent the volume mean diameters of the particles before and after steam injection respectively, or before and after growth of particles. The increase in size of aerosol particles by steam injection can then be evaluated in volume mean diameter D_{vf} knowing the value ΔH from Eqs. (1) and (2), and the value n_0. The line in Fig. 5 shows the relation of Eq. (3).

2. Experimental Method

Figure 6 shows the schematic diagram of the experiemntal method. Air having T_g in temerature and H_g in humidity was introduced into an 1 inch insulated pipe and then the aerosol particles, tobacco smoke in this study, were dispersed into the air stream. Steam having 100°C in temperature, 1 atm abs. in

pressure and dryness fraction of nearly unity was injected at the point of 2 meter down stream from that of the particle dispersion point. The air flow rate was about 180 l/min and the quantity of steam injection was ranged from 0.05 to 0.5 gram steam/gram dry air. The particle number concentration and size distribution of the aerosol particles at the point of 1.5 meter down stream from the steam injection point were observed by the ultramicroscopic technique[6]. The observation cell used in this study was the same as that used in the previous paper[6], which was composed of a double tube to prevent the change in size of grown particles or water droplets due to the temperature change. When the temperature of the aerosol to be observed was high, the cell was further surrounded by a cover into which air with controlled temperature was blown.

3. Experimental Results and Discussions

Figure 7 shows one of the experimental results of particle size distribution of the grown particles together with the initial size distribution of tobacco aerosol particles. It will be found that the considerable increase in size occurs by steam injection. The width of size distribution seems to become neither narrower nor wider. The similar results were also found in the previous work where the particle growth was promoted by mixing hot saturated air with cold saturated air[7]. Furthermore, as found in the

previous work, the rapid growth rate was also suggested in this case judging from the fact that the residence time of aerosols in the pipe was very short.

The volume mean diameters of grown particles obtained by experiment were plotted in Fig. 5. In spite of the difficulty in measuring the size of grown particles or water droplets in high temperature, the experimental results agree with the estimation line.

Conclusion

The effect of steam injection into dust-laden air on the increase in the size of dust particles was studied. The procedure of the estimation of ΔH, the amount of condensable water vapor per unit mass of dry air by steam injection, which is effective for particle growth, was made clear for various conditions of air and steam injected. By using the value of ΔH, the increase in size of aerosol particles having number concentration of n_0 was then evaluated in volume mean diameter. These analysis was verified by directly measuring the size of grown particles using the ultramicroscopic technique previously developed by the authors.

The results suggested that the particle growth by steam injection will be one of the most promising pre-conditioning technique to improve scrubber performance, especially for an exhaust gas having low temperature.

Acknowledgment

K. Yamadaki was very helpful in the experimental work.

Nomenclature

D_p	= particle diameter	[μ]
D_{vi}, D_{vf}	= volume mean diameter before and after growth	[cm] [μ]
H	= absolute humidity	[g H_2O/g dry air]
H_{st}	= quantity of steam injection	[g steam/g dry air]
ΔH	= condensable water vapor	[g H_2O/g dry air]
i_g	= enthalpy	[cal/g dry air]
i_{st}	= enthalpy	[cal/g steam]
i'_{wf}	= enthalpy	[cal/g water]
n_0	= particle number concentration	[1/g dry air]
T	= temperature	[°C]
x	= dryness fraction of steam	[-]
ρ_s	= density of condensed liquid	[g/cm^3]

Subscripts

f	= final state
g	= initial state of air
i	= initial state
s	= saturated
sf	= saturated air in final state
st	= steam

wf = water in final state

Superscripts

" = dry

' = wet

Literature Cited

1) Calvert, S. and N. C. Jhaveri : J. Air Pollu. Control Assoc., 24, 946(1974)

2) Fahnoe, F., A. Lindroos and R. J. Abelson : Ind. Eng. Chem., 43, 1336(1951)

3) Lancaster, S. W. and W. Strauss : Ind. Eng. Chem. Fundam., 10, 362(1971)

4) Lapple, C. E. and H. J. Kamack : Chem. Eng. Progr., 51, No. 3, 110(1953)

5) Schauer, P. J. : Ind. Eng. Chem., 43, 1532(1951)

6) Yoshida, T., Y. Kousaka and K. Okuyama : Ind. Eng. Chem. Fundam., 14, 47(1975)

7) Yoshida, T., Y. Kousaka and K. Okuyama : Ind. Eng. Chem. Fundam., 15, 37(1976)

Captions of Figures

Figure 1. Change in humidity and temperature by steam injection

Figure 2. Condensable water vapor ΔH against quantity of steam injection H_{st}

Figure 3. Temperature T_{sf} at the equilibrium state after steam injection

Figure 4. Effect of dryness fraction x of steam on condensable water vapor ΔH

Figure 5. Relation between volume mean diameter of grown particle D_{vf} and parameter $\Delta H/n_0$, condensable water vapor per single particle

Figure 6. Experimental method

Figure 7. Change in size distribution by steam injection

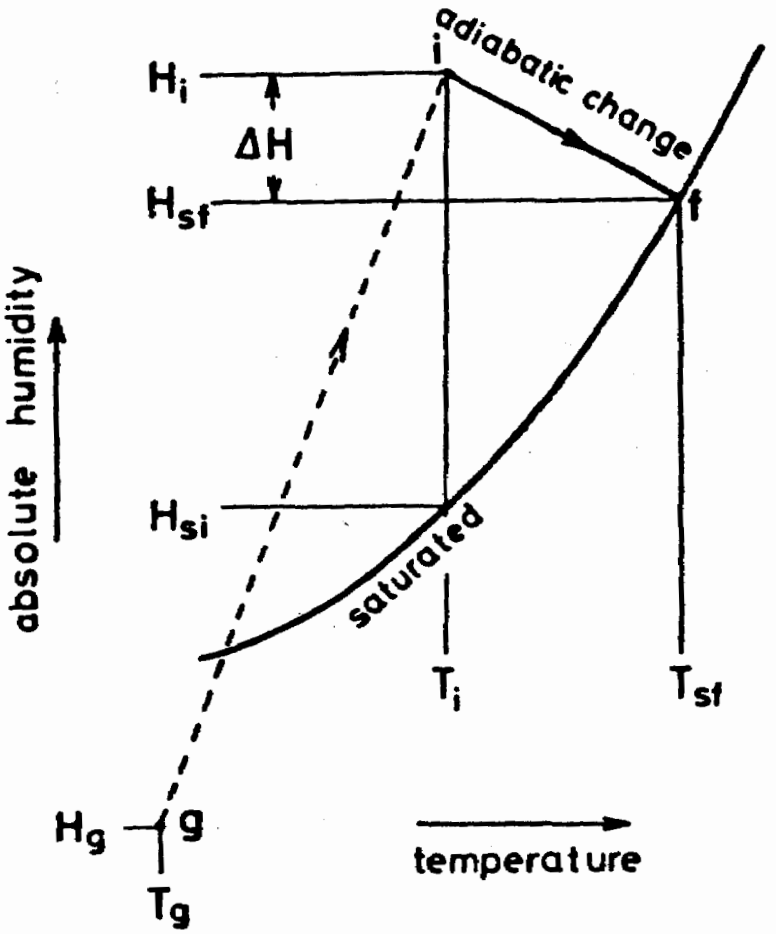

Figure 1. Change in humidity and temperature by steam injection

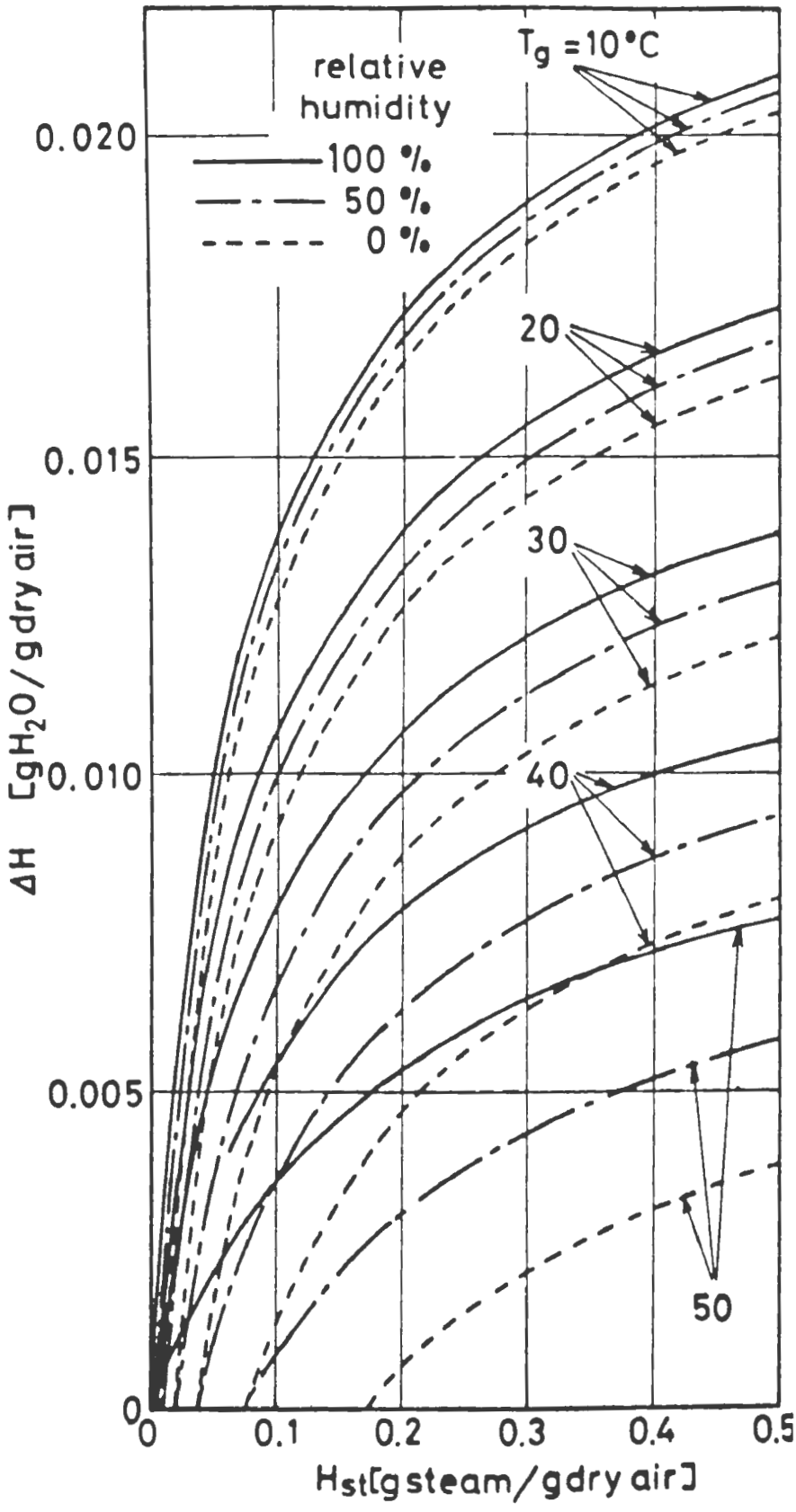

Figure 2. Condensable water vapor ΔH against quantity of steam injection H_{st}

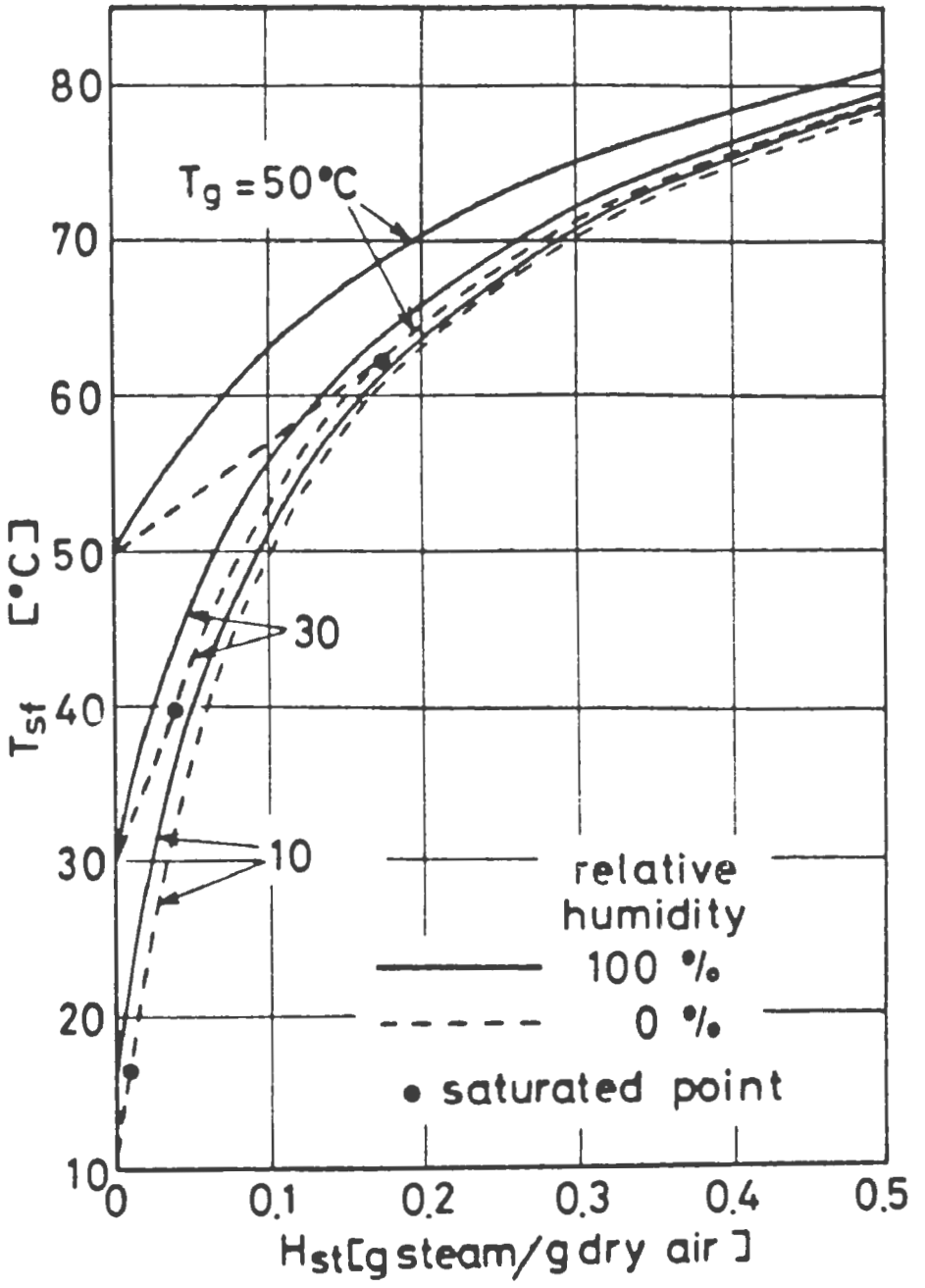

Figure 3. Temperature T_{sf} at the equilibrium state after steam injection

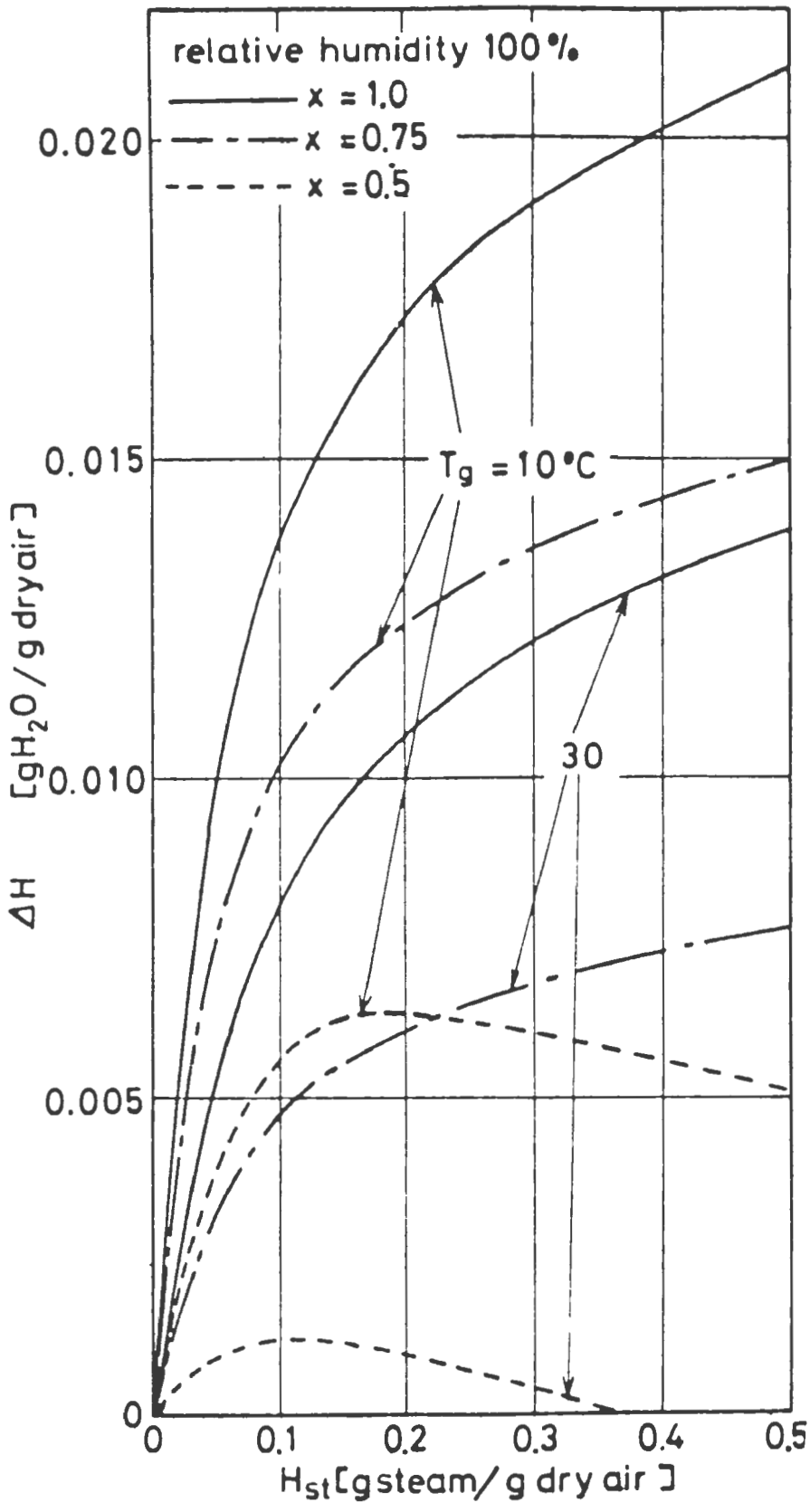

Figure 4. Effect of dryness fraction x of steam on condensable water vapor ΔH

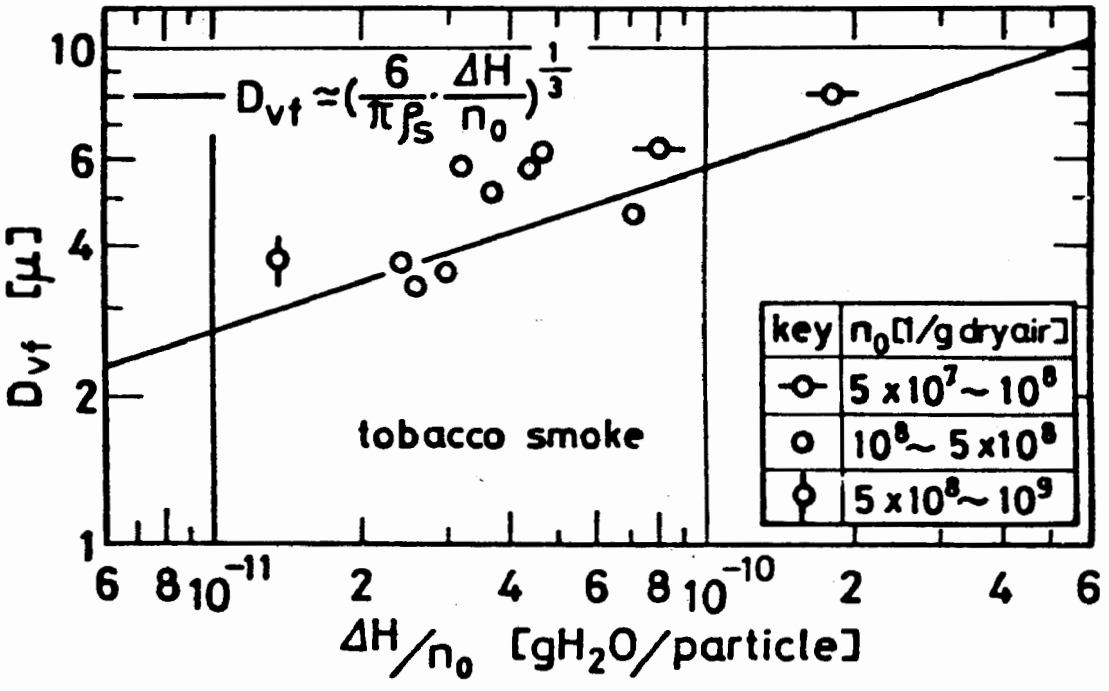

Figure 5. Relation between volume mean diameter of grown particle D_{vf} and parameter $\Delta H/n_0$, condensable water vapor per single particle

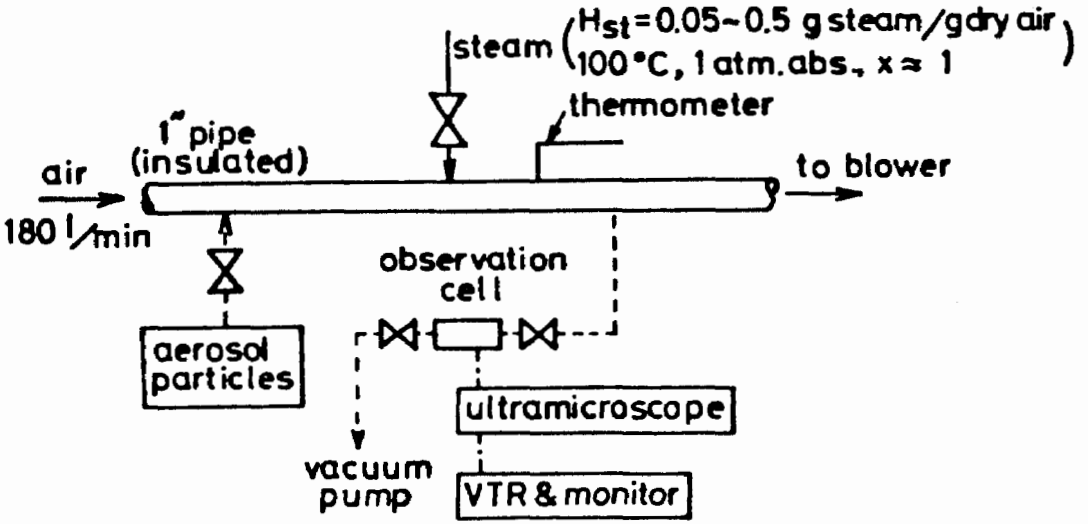

Figure 6. Experimental method

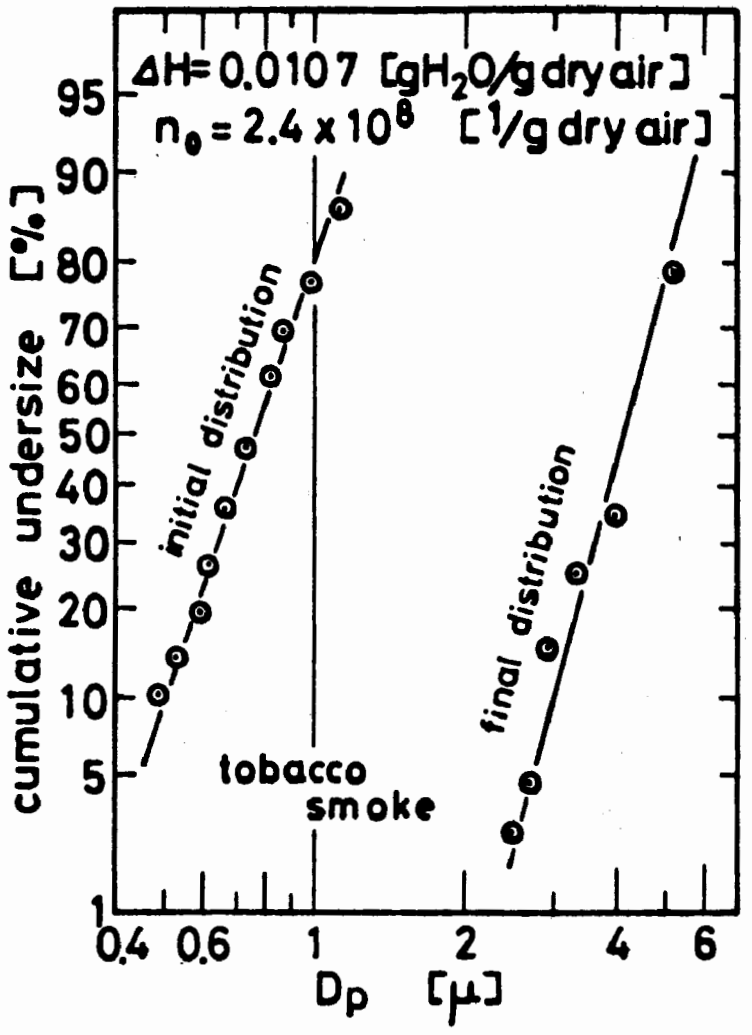

Figure 7. Change in size distribution by steam injection

EFFECT OF BROWNIAN COAGULATION AND BROWNIAN DIFFUSION ON GRAVITATIONAL SETTLING OF POLYDISPERSE AEROSOLS

TETSUO YOSHIDA, YASUO KOUSAKA, KIKUO OKUYAMA AND SHIGERU NISHIO
Department of Chemical Engineering, University of Osaka Prefecture, Sakai, 591

(Reprinted with permission)

Reprinted from
JOURNAL OF
CHEMICAL ENGINEERING
OF
JAPAN
Vol. 8, No. 2 (1975)
Pages 137—142

EFFECT OF BROWNIAN COAGULATION AND BROWNIAN DIFFUSION ON GRAVITATIONAL SETTLING OF POLYDISPERSE AEROSOLS

TETSUO YOSHIDA, YASUO KOUSAKA, KIKUO OKUYAMA* AND SHIGERU NISHIO
Department of Chemical Engineering, University of Osaka Prefecture, Sakai, 591

The behavior of aerosol particles of sub-micron diameter undergoing Brownian coagulation, Brownian diffusion and gravitational settling was studied by numerically solving the equation of population balance and by experimentally observing the change of aerosol properties with time. In calculation, two dimensionless parameters, which are determined by the initial properties of aerosols and vessel dimension in which aerosols are suspended, were introduced to evaluate the magnitude of influence of Brownian coagulation and Brownian diffusion on gravitational settling. The results of numerical calculation were indicated by graphical representation, which is usable for quantitative estimation of the magnitude of these two effects. These computational results were found to be in good agreement with the experimental results obtained by an ultramicroscopic technique of particle size analysis.

Introduction

The behavior of aerosols is influenced by coagulation, diffusion, sedimentation, the rate of generation of particles, particle characteristics and the dynamics of the fluid in which particles are suspended. For aerosol particles of sub-micron diameter, coagulation by Brownian motion and deposition by Brownian diffusion as well as gravitational settling are essential for characterizing the behavior of aerosols[4].

As basic research in the size distribution which changes with time undergoing Brownian coagulation and gravitational settling, a few analytical solutions[3,7] and numerical solutions[1,5,6,8] have been obtained under some simplified or particular conditions. As one of the representative studies G. C. Lindauer *et al.*[8] and C. H. Ahn *et al.*[1] showed the effect of Brownian coagulation on gravitational settling by a numerical method, but they included the unrealistic assumption that particle concentrations are always uniform in the direction of settling.

The purpose of this paper is to discuss the effect of Brownian coagulation and Brownian diffusion on gravitational settling considering the variation of particle concentrations in the direction of sedimentation. The equation including these three effects has been solved numerically on the assumption that the initial particle size spectrum is of log-normal form. In calculation, two dimensionless parameters were introduced to estimate the amount of the effect of Brownian coagulation and of Brownian diffusion on gravitational settling. The calculated results were arranged in graphs to predict these two effects quantitatively, and some of them were compared with experimental results obtained by an ultramicroscopic technique[11].

Received July 6, 1974.
Presented at the 39th Annual Meeting of The Soc. of Chem. Engrs., Japan, at Kobe, April 4 1974 (entitled "Effect of Brownian Coagulation on Gravitational Settling of Polydisperse Aerosols".)

Theoretical Calculation

Basic equation

Consider an aerosol located between parallel horizontal walls as shown in **Fig. 1** on which aerosol particles are deposited by Brownian diffusion and by gravitational settling accompanying Brownian coagulation. The basic equation expressing the time-dependent variation in particle number concentration of aerosols can be given by the population balance of the element $\Delta y'$ (refer to **Appendix**)[9,12]. The basic

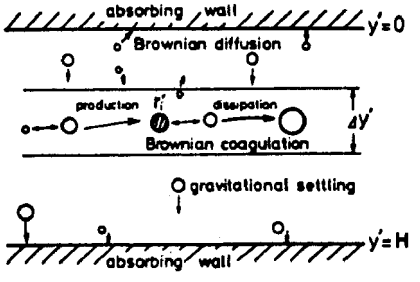

Fig. 1 Behavior of aerosols between two horizontal walls

equation written in dimensionless form becomes

$$\frac{\partial n(r_i,t)}{\partial t}=DG\frac{C_m(r_i')}{C_m(r_{g0})}\frac{\partial^2 n(r_i,t)}{r_i\partial y^2}-\frac{C_m(r_i')}{C_m(r_{g0})}\frac{r_i^2\partial n(r_i,t)}{\partial y}$$
$$+CG\sum_{\rho_i=r_{i\min}}^{r_i/\sqrt[3]{2}}k(\sqrt[3]{r_i^3-\rho_i^3},\rho_i)n(\sqrt[3]{r_i^3-\rho_i^3},t)$$
$$\times n(\rho_i,t)\left(\frac{r_i}{\sqrt[3]{r_i^3-\rho_i^3}}\right)^2$$
$$-CG\sum_{\rho_i=r_{i\min}}^{r_{i\max}}k(r_i,\rho_i)n(r_i,t)n(\rho_i,t)$$
$$i=i\min\cdots\cdots i\max \qquad (1)$$

where

$$n(r_i,t)=n'(r_i',t')/n_0,\ t=u_t(r_{g0})t'/H,\ y=y'/H,$$
$$r_i=r_i'/r_{g0},\ k(r_i,\rho_i)=K(r_i',\rho_i')/K_0C_m(r_{g0}) \qquad (2)$$

$$CG=\frac{9\mu HK_0n_0}{2(\rho_p-\rho)gr_{g0}^2}=\frac{1}{2}\{2K_0n_0^2C_m(r_{g0})\}\left(\frac{u_t(r_{g0})n_0}{H}\right)$$
$$DG=\frac{3\kappa T}{4(\rho_p-\rho)gr_{g0}^3\pi H}=\frac{1}{2}\left(\frac{2D(r_{g0})n_0}{H^2}\right)\left(\frac{u_t(r_{g0})n_0}{H}\right) \qquad (3)$$

$K(r_i',\rho_i')$ is the coagulation function of particles, and in the case of Brownian coagulation $K(r_i',\rho_i')$ is given by[10]

$$K(r_i',\rho_i')=K_0(r_i'+\rho_i')\{C_m(r_i')/r_i'+C_m(\rho_i')/\rho_i'\},$$
$$K_0=2\kappa T/3\mu \qquad (4)$$

In Eq. (1), the first term accounts for Brownian diffusion, the second for gravitational settling, and the third represents the number of newly formed particles with radius r_i by collision of two particles, while the last term represents the decrease in number of particles with radius r_i by collision with other particles.

CG and DG are dimensionless parameters which can be evaluated from initial aerosol properties and physical conditions. As seen from the definition, the parameter CG means the ratio of Brownian coagulation rate to deposition rate by gravitational settling.

Another parameter DG, which was proposed by C. N. Davies[2] to evaluate the concentration change of monodisperse aerosols undergoing diffusion and gravitational settling in the non-coagulation field, describes the deposition rate ratio of Brownian diffusion to gravitational settling. Though the parameters CG and DG are based on an initial geometric mean radius, they are convenient parameters to predict the influence of Brownian coagulation or Brownian diffusion relative to gravitational settling.

In the derivation of Eq. (1), the following assumptions were made:

(1) There exist no external forces except gravity and the medium is in stationary state with no convection.

(2) Particles are spherical and electrically neutral.

(3) Particles collide with each other to form single new spherical particle whose mass may be the same as the combined mass of two smaller particles.

(4) All particles colliding with two horizontal walls are caught by them.

The initial particle size spectrum is assumed to be of log-normal distribution and to be generated instantaneously with spatial uniformity; then

$$n(r_i,0)=\frac{1}{\sqrt{2\pi}\ln\sigma_{g0}}\exp\left(-\frac{\ln^2 r_i}{2\ln^2\sigma_{g0}}\right)\Delta\ln r_i,$$
$$\text{for } 0<y<1$$
$$n(r_i,0)=0,\ \text{at } y=0 \text{ and } 1 \qquad (5)$$

The boundary conditions are given as

$$n(r_i,t)=0,\ \text{at } y=0 \text{ and } 1,\ \text{when } t>0 \qquad (6)$$

If the coefficient $C_m(r_i')/C_m(r_{g0})$ on the right-hand side of Eq. (1) is normalized about r_{g0}, solutions depend on σ_{g0} and two dimensionless parameters CG and DG.

Finite difference approximation and calculation method

Since Eq. (1) is a nonlinear differential equation, it cannot be solved analytically. It is approximated by using central difference formulae accurate to second order, and then the finite difference equation is given as follows:

$$n(r_i,y,t+\Delta t)=n(r_i,y,t)-\{C_m(r_i')r_i^2/C_m(r_{g0})\}$$
$$\times\left\{\frac{n(r_i,y,t)-n(r_i,y-\Delta y,t)}{\Delta y}\right\}\Delta t+DG\frac{C_m(r_i')}{C_m(r_{g0})r_i}$$
$$\times\left\{\frac{n(r_i,y+\Delta y,t)+n(r_i,y-\Delta y,t)-2n(r_i,y,t)}{\Delta y^2}\right\}\Delta t$$
$$+CG\Delta t\left\{\sum_{\rho_i=r_{i\min}}^{r_i/\sqrt[3]{2}}k(\sqrt[3]{r_i^3-\rho_i^3},\rho_i)n(\sqrt[3]{r_i^3-\rho_i^3},y,t)\right.$$
$$\times n(\rho_i,y,t)\left(\frac{r_i}{\sqrt[3]{r_i^3-\rho_i^3}}\right)^2-\sum_{\rho_i=r_{i\min}}^{r_{i\max}}k(r_i,\rho_i)$$
$$\left.\times n(r_i,y,t)n(\rho_i,y,t)\right\},\qquad i=i\min\cdots\cdots i\max \qquad (7)$$

Calculation was started by assigning initial values of particle number concentration by Eq. (5) at every interior point between two walls. Being stepped by Δt, new values of particle number concentration were calculated by Eq. (7), and this step was repeated until particle number came to zero.

Calculation Results and Discussion

It can be considered that the main factors which influence the time dependence of particle size distribution are initial properties of particles such as geometric mean radius, number concentration and geometric standard deviation. Therefore solutions were obtained for various values of them. The results are shown in **Table 1**, together with the values of CG, DG and computational parameters.

The effect of Brownian diffusion

According to the definition the parameter DG increases as particle radius decreases, and consequently the effect of Brownian diffusion becomes large. **Fig. 2** shows the time dependence on dimensionless number

Table 1 Conditions for calculation

r_{g0} [μ]	σ_{g0} [—]	n_0 [particles/cc]	CG [—]	DG [—]
0.1	1.2	10^8	3.10×10^{-1}	3.94×10^{-8}
0.2	1.2	4.0×10^8	3.10×10^{-1}	4.92×10^{-8}
		10^9	3.44×10^{-8}	
		9.0×10^8	3.10×10^{-1}	
		10^7	3.44×10^{-1}	
0.3	1.2	10^8	3.44×10^{0}	1.46×10^{-8}
		10^9	3.44×10^{1}	
		10^{10}	3.44×10^{2}	
		10^8	1.24×10^{-8}	
	1.2	10^7	1.24×10^{-1}	
0.5		10^8	1.24×10^{0}	3.15×10^{-4}
	1.5	10^9	1.24×10^{1}	
		10^{10}	1.24×10^{2}	
		10^8	3.10×10^{-8}	
		10^7	3.10×10^{-8}	
1.0	1.2	10^8	3.10×10^{-1}	3.94×10^{-8}
		10^9	3.10×10^{0}	
		10^{10}	3.10×10^{1}	

$\Delta\ln r=0.077$, $\Delta y=0.01, 0.02$, $\Delta t=0.01, 0.002, 0.0004$
$\rho_p=1.0$ g/cm^3, $H=0.25$ cm

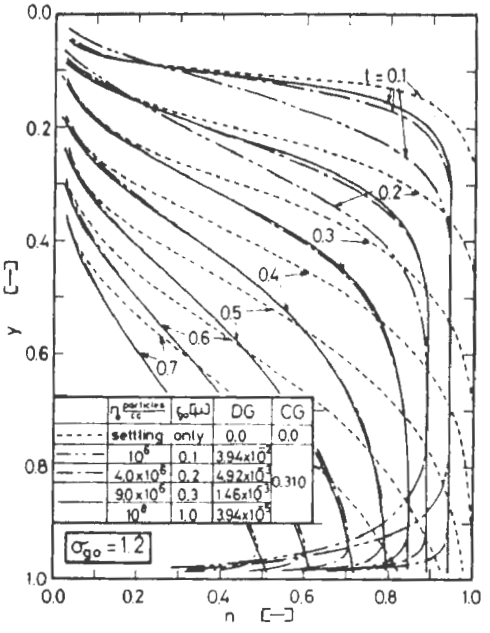

Fig. 2 Distribution of aerosol concentration undergoing Brownian coagulation, Brownian diffusion and gravitational settling

concentration of paricles n at each height under constant CG. When coagulation and diffusion occur, that is $CG>0$ and $DG>0$, more rapid decrease of particle concentrations is seen in the figure in comparison with those of gravitational settling ($CG=0$ and $DG=0$). When the values of DG are small enough, the difference from gravitational settling depends mainly on Brownian coagulation, and then particle concentrations are determined by the values of CG and σ_{g0}. It may be seen from Fig. 2 that in the case of $DG<0.004$ the effect of Brownian diffusion

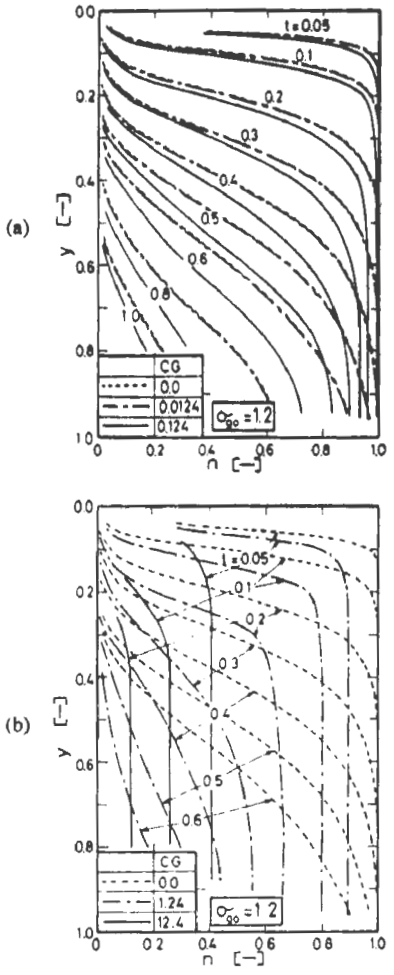

Fig. 3 Effect of Brownian coagulation on gravitational settling

seems to be negligible, which almost agrees with Davies' analytical solution[3] obtained for monodisperse aerosols undergoing Brownian diffusion and gravitational settling. So far as aerosol particles of more than several tenths micron in diameter are concerned, the effect of Brownian diffusion may be negligible. In the following section, the effect of Brownian coagulation on settling aerosols in the absence of Brownian diffusion will be discussed.

The effect of Brownian coagulation

The curves of concentration change with time for various values of CG are shown in **Figs. 3 (a)** and **(b)**. As the values of CG increase the decrease of particle concentration proceeds more rapidly because of the loss of particles by coagulation and because of enhanced settling velocity due to the growth of particles by coagulation. Moreover, for a constant value of CG, the discrepancy in concentration change from that of gravitational settling ($CG=0$) increases with time and settling depth. This is also due to the loss and the growth of particles by coagulation which

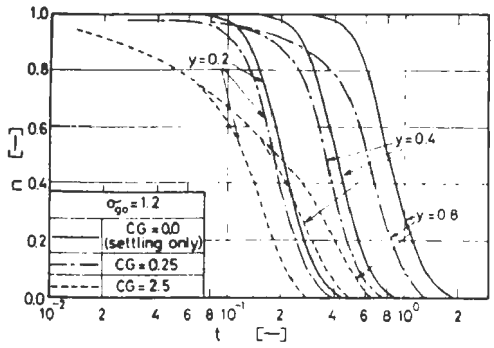

Fig. 4 Dependence of aerosol concentration on settling depth

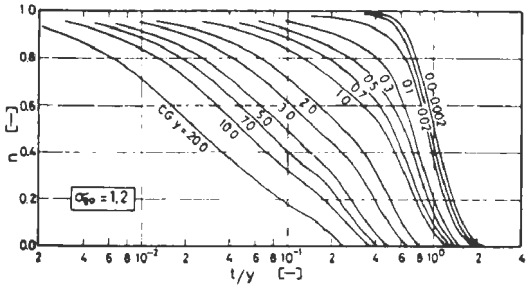

(a) $\sigma_{g0}=1.2$

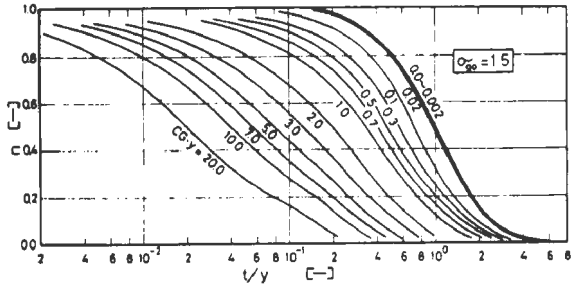

(b) $\sigma_{g0}=1.5$

Fig. 5 Decrease in aerosol concentration with time

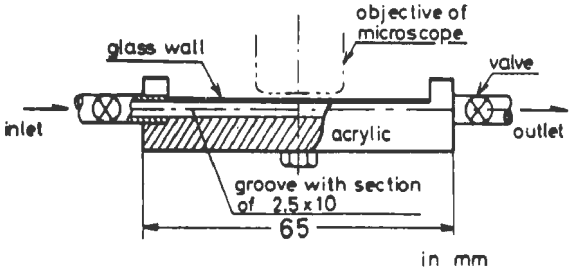

Fig. 6 Observation cell

proceed as aging time grows longer. This tendency may be obvious in Fig. 4, which shows the dependence of particle concentration on height. It is impossible to predict the local effect of Brownian coagulation at any height by using the parameter CG. However, CG shows the overall effect of coagulation between

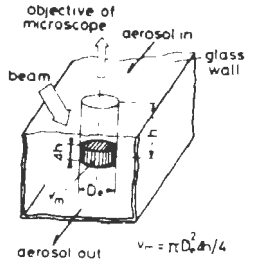

Fig. 7 Illustration of observation cell

two walls, and at values of CG below 0.02 the effect of coagulation seems to be negligible. To estimate the variation of particle concentration with time at any height, CG and t are transformed into the following forms.

$$CG\cdot y=\left(\frac{9\mu HK_0n_0}{2(\rho_p-\rho)gr_{g0}^2}\right)\cdot\left(\frac{y'}{H}\right)=\frac{y'K_0n_0C_m(r_{g0})}{u_t(r_{g0})}$$

$$t/y=\left(\frac{2(\rho_p-\rho)gr_{g0}^2C_m(r_{g0})t'}{9\mu H}\right)\left(\frac{y'}{H}\right)=\frac{u_t(r_{g0})t'}{y'} \quad (8)$$

Thus the concentration change of aerosols is arranged as shown in Figs. 5 (a) and (b). It may be seen from these graphs that at values of $CG\cdot y$ below 0.02 the effect of coagulation may be ignored and the change in concentration of particles depends mainly on gravitational settling. With the values of $CG\cdot y$, the curves have more gentle slopes than that of gravitational settling only. At values of $CG\cdot y$ above 20.0 the concentration change is dominated only by coagulation, almost regardless of the initial standard deviation. Figs. 5 (a) and (b) for two initial geometric standard deviations enabled one to predict the concentration change of aerosols having various initial size distributions.

Experimental Apparatus and Method

In this study it is necessary to measure accurately the variation in number concentration of aerosols over short periods of time. For this purpose, an ultramicroscopic technique[11] was used. The observation cell installed on the stage of an ultramicroscope, as shown in Fig. 6, has a small sectional area to prevent the effect of thermal convection. Aerosols used in this study were stearic acid particles and tobacco smoke. Stearic acid aerosols were generated by a La Mer-Sinclair type generator. Tobacco smoke was generated by a simple apparatus[11] by which number concentration was controlled from 10^6 to 10^8 particles/cc. The experimental procedure is as follows. After the focus of the ultramicroscope is preliminarily set at the depth h shown in Fig. 7, aerosol is introduced into the observation cell and the flow of aerosol is instantaneously stopped by closing the valves. From that moment aerosol particles existing in the volume v_m, which are recognized because of their

Table 2 Experimental conditions

Kinds of aerosols: stearic acid particles, tobacco smoke
Initial geometric mean radius: $r_{g0}=0.3\,\mu\sim0.5\,\mu$
Initial geometric standard deviation: $\sigma_{g0}=1.2\sim1.4$
Density of particles: $\rho_p=0.85$ g/cm³ (stearic acid particles)
$=0.78$ g/cm³ (tobacco smoke)
Concentration of aerosols: $n_0=10^4\sim10^6$ particles/cc
h : $200\,\mu\sim1500\,\mu$
v_m : 1.4×10^{-4} cm³ (eyepiece × objective, 10×20)
1.2×10^{-6} cm³ (" , 10×40)
CG : $0.03\sim1.7$
DG : $4.7\times10^{-4}\sim1.7\times10^{-6}$

shining, are recorded by a video recorder, until all particles disappear in the sight. The number of particles at any given time are counted by reproducing the recorder.

Initial number concentration of particles, n_0, is given as follows by the initial particle number of images $N(0)$ and the observation volume v_m:

$$n_0=N(0)/v_m \tag{9}$$

The particle size spectrum was also determined by the ultramicroscopic technique developed previously by the authors[11], whose principle is almost the same as that of the Andreasen-Pipette method. Experimental conditions and physical properties of aerosols are shown in **Table 2**.

Experimental Results and Discussion

Fig. 8 shows a comparison of the relative concentration change with time between experimental data and theoretical curves. In this comparison the decreases of the experimental values seem to be slightly slower than those of the predicted ones. However, overall agreement is good within experimental error. As seen from the values of CG and DG, the effect of Brownian coagulation and diffusion on particle concentration can be almost ignored. This agreement indicates that convection, photophoresis and thermophoresis do not occur in the observation cell.

Fig. 9 shows the experimental data of the relative concentration change on tobacco smoke and stearic acid particles, together with corresponding theoretical curves. Experimental data are in good agreement with the tendency of the calculated curves, and the effect of Brownian coagulation increases as the values of $CG\cdot y$ increase. This kind of experimental data has not been reported because of the difficulty in accurate measurement of changing number concentration of particles with time. In this experiment the values of $CG\cdot y$ were rather small, but the effect of Brownian coagulation on gravitational settling was clearly found to be characterized. These experimental results might indicate, in a certain sense, that the conception used in deriving the basic equation, above all the assumption that particles stick together upon impact and will not repel, are basically correct.

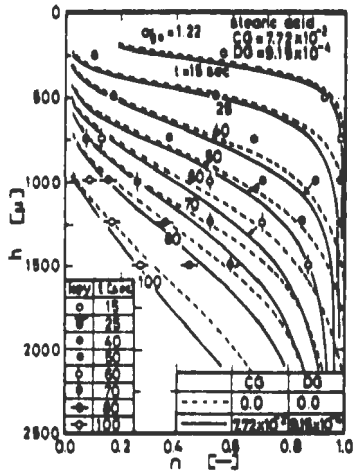

Fig. 8 Comparison of experimental aerosol concentration with calculated ones

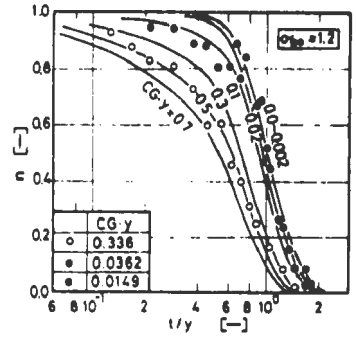

Fig. 9 Comparison of experimental aerosol concentration with calculated ones

One more sensitive test of the coagulation theory could be made by the change of concentration of each species of particle size distribution.

Conclusion

The behavior of aerosols undergoing Brownian coagulation, diffusion and gravitational settling between two horizontal walls was studied theoretically and experimentally.

The basic equation considering the above three effects and the variation of particle concentration in the direction of sedimentation was solved numerically for various initial particle size spectrums. The overall effect of diffusion or coagulation on particle concentration of settling aerosol particles was estimated using the values of two dimensionless parameters DG and CG respectively. At values of CG less than 0.02, the effect of coagulation was then found to be negligible, and in the regions of $DG\leq$ 0.004 the effect of diffusion could be ignored. In the absence of Brownian diffusion the change of particle concentration with time at every height could

be estimated by introducing a new dimensionless parameter $CG \cdot y$. Some of these theoretical results were examined by a technique of ultramicroscopic size analysis and were found to be in good agreement with experimental ones.

The calculation results presented in this paper are an elementary step in providing a theoretical approach to predict the behavior of aerosols in a closed vessel and also will be useful to estimate the influence of Brownian coagulation or diffusion on particle size analysis of aerosols by sedimentation methods.

Appendix

The basic equation expressing the time dependence of the size distribution of aerosols undergoing Brownian coagulation, Brownian diffusion and gravitational settling is given[4,9,12] by:

$$\frac{\partial n'(r', t')}{\partial t'} = D(r')\frac{\partial^2 n'(r', t')}{\partial y'^2} - u_t(r')\frac{\partial n'(r', t')}{\partial y'} + \int_{\rho'=0}^{r'/\sqrt[3]{2}} K(\sqrt[3]{r'^3-\rho'^3}, \rho')\, n'(\sqrt[3]{r'^3-\rho'^3}, t') \times n'(\rho', t')\left(\frac{r'}{\sqrt[3]{r'^3-\rho'^3}}\right)^2 d\rho' - \int_{\rho'=0}^{\infty} K(r', \rho')\, n'(r', t')\, n(\rho', t')\, d\rho'$$

where $D(r')$ is the diffusion coefficient and $u_t(r')$ is the terminal settling velocity.

Acknowledgment

T. Miyazaki and Y. Kida were very helpful in the experimental work.

Nomenclature

CG	=	dimensionless parameter defined in Eq. (3) $(=9\mu HK_0 n_0/2(\rho_p-\rho)gr_{g0}^3)$	[—]
$C_m(r_i')$	=	Cunningham's correction factor of r_i'	[—]
D_e	=	effective diameter of microscopic sight shown in Fig. 7	[cm]
DG	=	dimensionless parameter defined in Eq. (3) $(=3\kappa T/4(\rho_p-\rho)gr_{g0}^3\pi H)$	[—]
$D(r_i')$	=	diffusion coefficient $(=C_m(r_i')\kappa T/6\pi\mu r_i')$	[cm²/sec]
g	=	acceleration of gravity	[cm/sec²]
H	=	height between two horizontal walls	[cm]
h	=	values shown in Fig. 7	[μ][cm]
K_0	=	coefficient in Eq. (4)	[cm³/sec]
$K(r_i', \rho_i')$	=	coagulation function for two particles of sizes r_i' and ρ_i'	[cm³/sec]
$k(r_i, \rho_i)$	=	dimensionless coagulation function $(=K(r_i', \rho_i')/K_0 C_m(r_{g0}))$	[—]
$\Delta \ln r$	=	dimensionless size width between r_i and r_{i+1}	[—]
$n'(r_i', t'), n(r_i, t)$	=	number and dimensionless number of aerosol particles $(=n'(r_i', t')/n_0)$	[particles/cc][—]
n	=	dimensionless total number of particles $(=\sum n'(r_i', t')/n_0)$	[—]
n_0	=	total number of particles at time zero	[particles/cc]
$N(0)$	=	number of aerosol particles in v_m at time zero	[particles]
r', r	=	particle radius and dimensionless particle radius	[μ][—]
r_{g0}	=	geometric mean radius at time zero	[μ]
T	=	absolute temperature	[°K]
t', t	=	time and dimensionless time	[sec][—]
Δt	=	dimensionless time step	[—]
$u_t(r_i')$	=	terminal settling velocity $(=2C_m(r_i')(\rho_p-\rho)r_i'^2 g/9\mu)$	[cm/sec]
v_m	=	volume shown in Fig. 7	[cm³]
y', y	=	vertical and dimensionless vertical distance from top of the cell	[cm][—]
$\Delta y', \Delta y$	=	mesh width and dimensionless mesh width along the vertical direction	[cm][—]
σ_{g0}	=	geometric standard deviation at time zero	[—]
κ	=	Boltzman's constant $(=1.38\times10^{-16})$	[erg/°K]
μ	=	viscosity of fluid	[g/cm·sec]
ρ, ρ_p	=	fluid and particle density	[g/cm³]
ρ_i	=	dimensionless particle radius	[—]

⟨Subscripts⟩

i	=	refers to the number particle size
min	=	minimum
max	=	maximum

Literature Cited

1) Ahn, C. H. and J. W. Gentry: *Ind. Eng. Chem., Fundam.*, **11**, 483 (1972).
2) Davies, C. N.: *Proc. Roy. Soc.*, **A200**, 100 (1949).
3) Friedlander, S. K. and C. S. Wang.: *J. Coll. Int. Sci.*, **22**, 126 (1966).
4) Fuchs, N. A.: "The Mechanics of Aerosols," Pergamon Press, Oxford, (1964).
5) Greenfield, M. A., R. L. Koontz and D. F. Hausknecht: *J. Coll. Int. Sci.*, **35**, 102 (1971).
6) Hauck, H.: *Staub-Reinhalt. Luft.*, **33**, 1233 (1973).
7) Langstroth, G. and T. Gillespie: *Cand. J. Research*, **25B**, 455 (1947).
8) Lindauer, G. C. and A. W. Castleman, Jr.: *Aerosol Science*, **2**, 85 (1971).
9) Mori, Y. and A. Yoshizawa: *Kagaku Kōgaku*, **32**, 1233 (1968).
10) Smoluchwoski, M.: *Phys. Chem.* (Leipzig), **92**, 129 (1917).
11) Yoshida, T., Y. Kousaka and K. Okuyama: *Ind. Eng. Chem. Fundam.*, **14**, 47 (1975).
12) Zebel, G.: *Kolloid-Z*, **156**, 102 (1958).

CHANGE IN PARTICLE SIZE DISTRIBUTIONS OF POLYDISPERSE AEROSOLS UNDERGOING BROWNIAN COAGULATION

TETSUO YOSHIDA, KIKUO OKUYAMA, YASUO KOUSAKA AND YOSHINORI KIDA
Department of Chemical Engineering, University of Osaka Prefecture, Sakai, 591

(Reprinted with permission)

Reprinted from
JOURNAL OF CHEMICAL ENGINEERING OF JAPAN
Vol. 8, No. 4 (1975)
Pages 317—322

CHANGE IN PARTICLE SIZE DISTRIBUTIONS OF POLYDISPERSE AEROSOLS UNDERGOING BROWNIAN COAGULATION

TETSUO YOSHIDA, KIKUO OKUYAMA*, YASUO KOUSAKA AND YOSHINORI KIDA
Department of Chemical Engineering, University of Osaka Prefecture, Sakai, 591

The time-dependent change in particle size distributions of highly concentrated polydisperse aerosols undergoing Brownian coagulation was studied by numerically solving the basic equation of coagulation for various size distributions initially having log-normal form. The results were plotted in the forms of the change with time in cumulative size distributions and the changes in nominal geometric mean radius, as well as standard deviation for various initial distributions of aerosols. These figures showed that size distributions approached certain asymptotic ones, which might correspond to SPDF (self-preserving distribution function), almost independently of initial distributions as coagulation proceeded. The process of the approach to asymptotic distributions was also made clear by the graphs. Some of these results were verified by experimental results obtained by the ultramicroscopic size analysis previously developed by the authors.

Introduction

In the previous paper[15], the change in particle number concentration of polydisperse aerosols undergoing gravitational settling, Brownian diffusion and Brownian coagulation was discussed, and Brownian coagulation was found to be important when high concentration aerosols were concerned. Analytical solutions[3,11], asymptotic solutions[5,6,8,13] and numerical solutions[6,12] have been reported for the change in paricle size distribution of polydisperse aerosols with time undergoing Brownian coagulation. These solutions, however, have been obtained under some simplified or specialized conditions, and seem unsatisfactory for understanding the general aspects of time-dependent change in particle size distributions of polydisperse aerosols. In experimental studies, because of the difficulty in accurate measurement of particle size distribution of highly concentrated aerosol, sufficient amounts of available data have not been reported[7,10].

In this paper, the change in particle size distribution of highly concentrated polydisperse aerosols was studied by numerically solving the basic equation for Brownian coagulation with various initial log-normal size distributions. The results of the calculation were graphically presented to show the effect of polydispersion on the change in size distribution of aerosols, and then were confirmed by experimental results obtained by the technique of ultramicroscopic size analysis previously developed by the authors[14]. The study presented here gives one of the basic properties of polydisperse aerosols, and is useful, for instance, for estimation of the extent of the contribution of particle growth to industrial precipitators.

Received November 6, 1974.
Presented at the 8th Autumn Meeting of The Soc. of Chem. Engrs., Japan at Tokyo, Oct. 8, 1974. ("Particle Growth of Polydisperse Aerosols by Brownian Coagulation")

Theoretical Calculation

The basic equation for the time-dependent size distribution change of aerosols undergoing Brownian coagulation has been reported by Müller[9,10] and its dimensionless form can be written as

$$\frac{\partial n(r_i,t)}{\partial t} = \sum_{\rho_i=r_{i\min}}^{r_i/\sqrt[3]{2}} k(\sqrt[3]{r_i^3-\rho_i^3},\rho_i)n(\sqrt[3]{r_i^3-\rho_i^3},t)n(\rho_i,t) \times \frac{r_i^2}{(\sqrt[3]{r_i^3-\rho_i^3})^2} - \sum_{\rho_i=r_{i\min}}^{r_{i\max}} k(r_i,\rho_i)n(r_i,t)n(\rho_i,t) \qquad i=imin....imax \qquad (1)$$

where,

$$\left.\begin{aligned} n(r_i,t)&=n'(r_i',t')/n_0,\ t=K_0n_0C_m(r_{g0})t',\ r_i=r_i'/r_{g0},\\ k(r_i,\rho_i)&=K(r_i',\rho_i')/K_0C_m(r_{g0}),\ K_0=2\kappa T/3\mu \end{aligned}\right\} \qquad (2)$$

$K(r_i',\rho_i')$ is the coagulation function of particles and in the case of Brownian coagulation it is given by[11]

$$K(r_i',\rho_i')=K_0(r_i'+\rho_i')\{C_m(r_i')/r_i'+C_m(\rho_i')/\rho_i'\} \qquad (3)$$

The left side of Eq. (1) is the change in particle concentration of size r_i with time. The first term on the

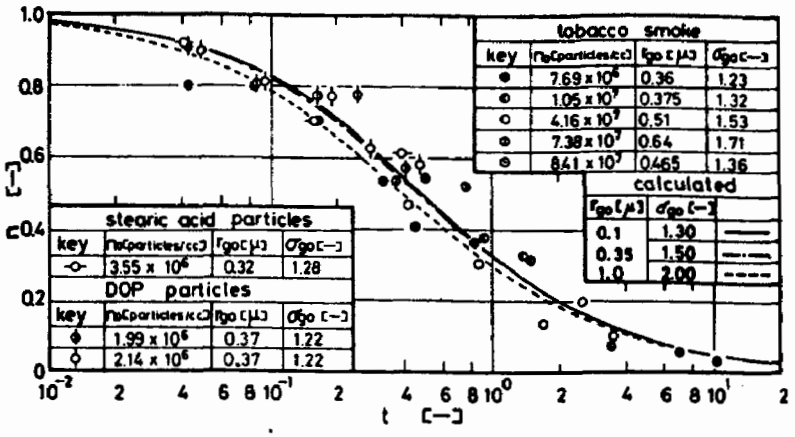

Fig. 1 Experimental and calculated time-dependent change in particle number concentration

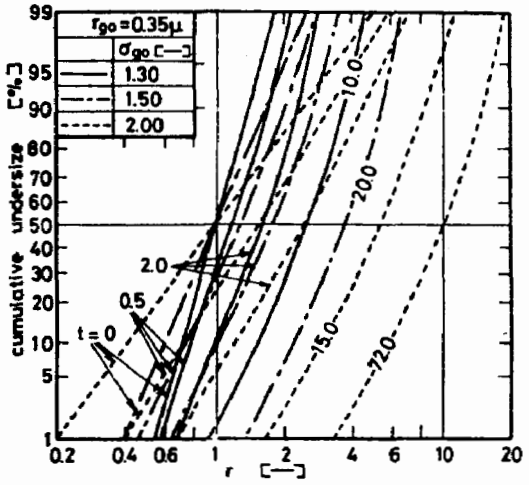

Fig. 2 Change in particle size distribution with time

right side represents the rate of formation of particles of size r_i due to coagulation of two particles smaller than size r_i, and the second term the rate of loss of particles of size r_i due to their coagulation with particles of any other sizes including r_i.

In the derivation of Eq. (1), the following assumptions are made:

(1) There exist no external forces and the medium is in stationary state with no convection.

(2) Particles are spherical and electrically neutral.

(3) Particles collide with each other to form a new spherical particle whose mass may be the same as the combined mass of the two smaller particles.

Initial particle size spectra are assumed to be of log-normal distributions and to be generated instantaneously with spatial homogeneity. Then the discrete expression for the spectrum is written as

$$n(r_i,0)=\frac{1}{\sqrt{2\pi}\ln\sigma_{g0}}\exp\left(-\frac{\ln^2 r_i}{2\ln^2\sigma_{g0}}\right)\Delta\ln r \qquad (4)$$

where

$$\Delta\ln r=\{\ln(r'_{i\max}/r_{g0})-\ln(r'_{i\min}/r_{g0})\}/M$$

M represents the number of divisions of radius.

Equation (1) is approximately normalized on r_{g0} (refer to Appendix). Since Eq. (1) cannot be solved analytically, the Runge-Kutta-Merson method was employed to solve it. To compare the effect of various initial sizes and their distributions on their changes with time, calculations were made for values of r_{g0} from 0.1 μ to 1.0 μ and σ_{g0} from 1.3 to 2.0. In most computations $r'_{i\min}$ was chosen for 0.01 μ and $r'_{i\max}$ for 10 μ. The number of divisions of radius M was chosen as one hundred, the validity of which was checked by recomputing over finer subdivisions. As a numerical check the total mass of aerosols was calculated every few time steps and the error was found to be within 5% during the progress of coagulation until the fall in number concentration to 10% of the initial value.

Calculation Results and Discussion

Particle number concentration

The curves in Fig. 1 show the calculated relation between the ratio of particle number concentration at any time to the initial value and the dimensionless time. The effect of the degree of polydispersion on particle number concentration seems not to exceed the order of 10%. The curve for σ_{g0}=1.3 agrees with the estimated one from the well-known coagulation equation of Smoluchowski for monodisperse aerosols[11], which is given by

$$\frac{dn}{dt}=-2n^2 \qquad (5)$$

In the case of $r_{g0}\geq 0.1$ μ the effect of r_{g0} on the concentration change seems to be negligible in the figure.

Particle size distribution

Figure 2 indicates the calculated results for the change of particle size distribution with time for three different initial size distributions. Size distributions of aerosols tend not to remain log-normal but asymptotically approach equilibrium states as time proceeds. The shapes of asymptotic distributions

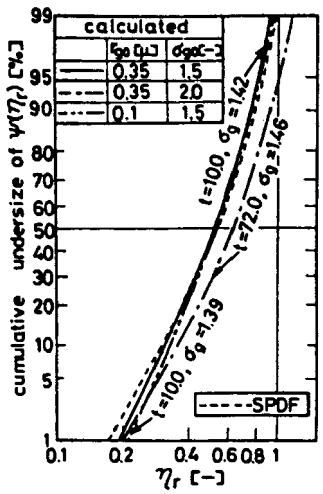

Fig. 3 Comparison of self-preserving size distributions

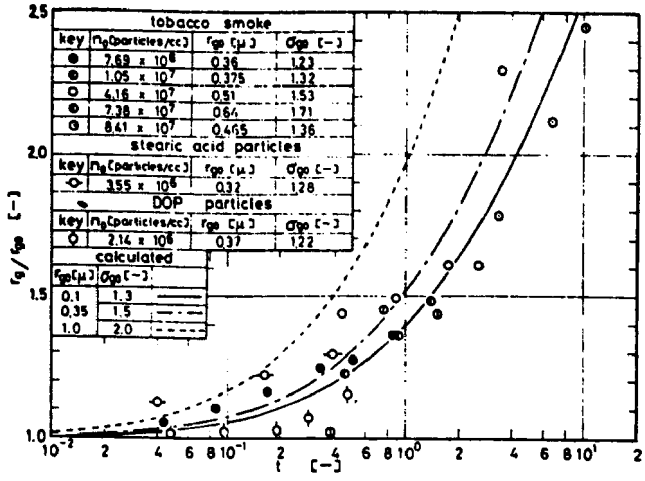

Fig. 4 Experimental and calculated variation of nominal geometric mean radius with time

after long periods of time resemble each other irrespective of initial geometric standard deviations. These asymptotic distributions at equilibrium state correspond to self-preserving distribution function (SPDF) which was derived by Friedlander[13] using the similarity theory. To compare asymptotic size distributions numerically obtained in this study with SPDF given by Friedlander the following common variables used among most investigators are introduced[1,13]

$$\eta_r = r_i'(n'/\phi)^{1/3}$$
$$\psi(\eta_r) = n'(r_i', t')\phi^{1/3}/\Delta r' n'^{4/3} \qquad (6)$$

where

$$n' = \sum_{r_i'=r_{i\min}'}^{r_{i\max}'} n'(r_i', t'), \quad \phi = \frac{4}{3}\pi \sum_{r_i'=r_{i\min}'}^{r_{i\max}'} r_i'^3 n'(r_i', t')$$

The correlation of $\psi(\eta_r)$ and η_r after sufficiently long periods of coagulation is shown in Fig. 3 together with SPDF given by Wang and Friedlander[12] for Brownian coagulation without the Stokes-Cunningham correction. Though the agreement among them is fairly good, $\psi(\eta_r)$ numerically obtained in this study seems to depend slightly on initial r_{g0} and σ_{g0}. This dependence on initial r_{g0} and σ_{g0} seems to be caused by Cunningham's correction $C_m(r_i')/C_m(r_{g0})$, which increases with decreasing r_{g0} and increasing σ_{g0}.

The change of size distribution with time will be next discussed by the aid of two parameters described below. Representative particle size and width of distribution will be characterized by two well known parameters, geometric mean radius and geometric standard deviation, when the particle size distribution follows log-normal form. However, when size distribution does not follow any laws of size distribution, it cannot be characterized by any simple parameters, but only by the curve of frequency against particle size or cumulative percentage against particle size. It is complicated, however, to discuss this by the curves themselves, and here two parameters, a nominal geometric mean radius r_g and a nominal geometric standard deviation σ_g, are introduced as follows, even if some deviation from log-normal form in size distribution exists

$$\left.\begin{aligned} \ln r_g &= \left[\sum_{r_i'=r_{i\min}'}^{r_{i\max}'} \{n'(r_i', t') \ln r_i'\}\right]/n' \\ \ln \sigma_g &= \left[\left\{\sum_{r_i'=r_{i\min}'}^{r_{i\max}'} n'(r_i', t') \ln^2 (r_i'/r_g)\right\}/n'\right]^{1/2} \end{aligned}\right\} \qquad (7)$$

In Fig. 4 the ratio of the nominal geometric mean radius to the initial one is presented as a function of dimensionless time. It may be understood that r_g of the larger standard deviation grows faster than that of the smaller one. Figure 5 shows the variation of the nominal geometric standard deviation with time. It is found that nominal geometric standard deviations decrease with time when σ_{g0} equals 1.5 and 2.0, while they increase when σ_{g0} equals 1.3. They seem to converge to certain equilibrium values which will be expected to lie between 1.3 and 1.5.

Experimental Apparatus and Method

A schematic diagram of experiment is shown in Fig. 6. Aerosols used in this study were tobacco smoke, stearic acid and DOP. Aerosols of both stearic acid and DOP were generated by a La Mer-Sinclair type generator and tobacco smoke was generated by a simple apparatus[14] by which number concentration of particles was controlled from 10^6 to 10^8 particles/cc. Aerosols thus generated were cooled to room temperature by a heat exchanger to prevent thermal convection, and continuously led into an acrylic pipe with diameter of 4.2 cm to make vertical upward flow. Most experiments were carried out

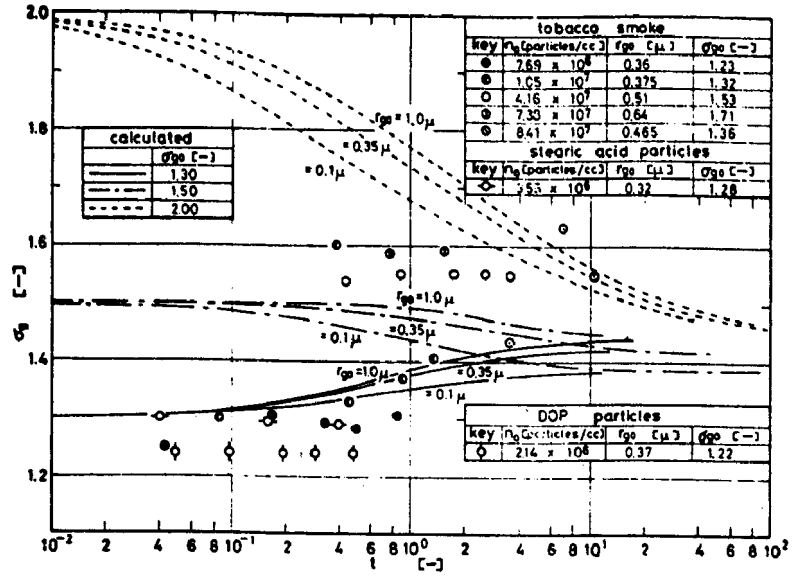

Fig. 5 Experimental and calculated variation of nominal geometric standard deviation with time

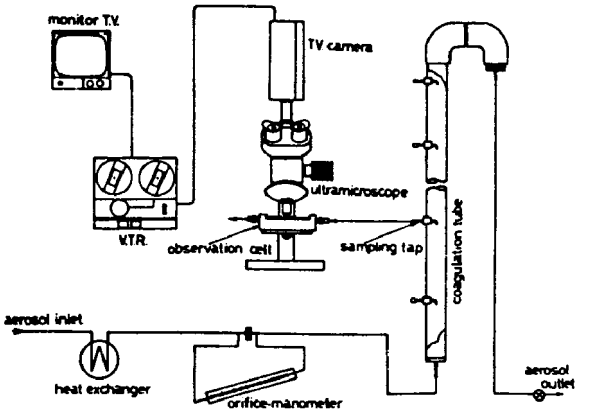

Fig. 6 Schematic diagram of experimental apparatus

with flow rates ranging from 0.25 to 0.5 *l*/min, and at these flow rates the flow in the pipe was observed to be plug flow rather than laminar flow. The loss effect by Brownian diffusion was evaluated to be negligible[4]. Aerosols sampled at every given residence time were introduced into the observation cell installed on the stage of an ultramicroscope to measure their particle size distributions and particle number concentration. The measurement method using an ultramicroscope was developed previously by the authors[14], and the procedure is as follows: After the focus of the ultramicroscope is preliminarily set at a given depth of the observation cell, the flow of introduced aerosol is instantaneously stopped by closing valves. From that moment particles existing in the field of vision are recorded until all particles disappear from sight, and the number of particles at any given time are counted by reproducing the recorder. From these data, size distributions are obtained by a method almost same as the Andreasen Pipette method, and initial number concentration, n_0, is given by the initial particle number of images $N(0)$ and the observation volume v_m:

$$n_0 = N(0)/v_m \tag{8}$$

Experimental Results and Discussion

Figure 1 shows a comparison of the relative concentration change with time between experimental data and theoretical curves. Agreement between them for $r_{g0} \geq 0.3\ \mu$ and $\sigma_{g0} \leq 1.7$ is fairly good. The effect of r_{g0} and σ_{g0} on the concentration change is found to be negligible, as discussed in theory. This fact shows, in a sence, that probability of contact may be regarded as unity, or that no repulsion may occur when they collide. A detailed comparison of the theoretical calculations with experiments shown in Fig. 1 will be made by turning the point to the change in particle size distribution with time.

In Fig. 7, changes of size distribution of tobacco smoke are shown together with corresponding theoretical curves for comparison. The agreement is fairly good. A comparison of the change of nominal geometric mean radius with time between experimental data and calculation curves is shown in Fig. 4. Figure 5 shows a comparison of the change of experimental nominal geometric standard deviations with theoretical ones. Although some scatter is found in experimental results, the effect of polydispersion on the change of particle size distribution with time is approximately confirmed for σ_{g0} less than 1.6. Theoretical curves for larger σ_{g0}, however, cannot be confirmed by experiment. This is due to the difficulty of constantly generating aerosols having larger geometric standard deviation. Keith and Derrick[7] performed experiments to obtain data on the change of size distribution. In their experiments tobacco smoke produced by a burning cigarette was used,

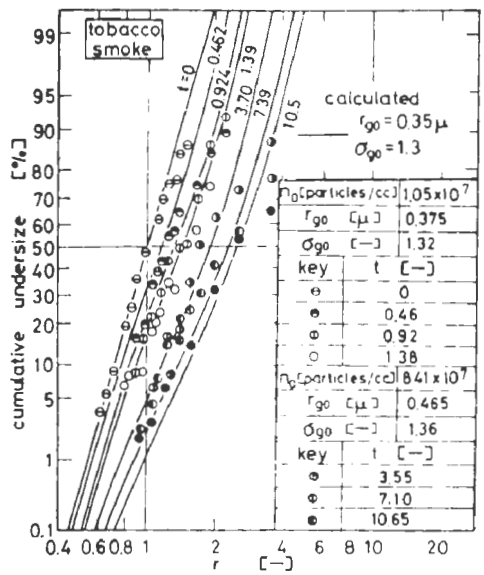

Fig. 7 Comparison of experimental particle size distribution changes with calculated ones

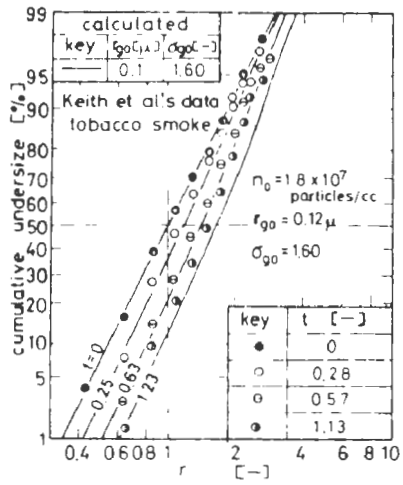

Fig. 8 Comparison of calculated particle size distribution changes with Keith *et al.*'s experimental data

and size distribution as well as concentration was measured by a conifuge. **Figure 8** shows a comparison of Keith and Derrick's data with calculation results in this study. Good agreement is found again. It is interesting that particle size distribution is found to grow wider with lapse of time in Fig. 7, while they grow narrower in Fig. 8. These facts suggest that an equilibrium size distribution may exist.

In these experiments no difference between solid particles such as stearic acid particles and liquid particles such as DOP particles and tobacco smoke (semi-liquid) is found.

Figure 9 shows the half-life of particle number concentration and also shows the time required to grow to a geometric mean radius twice the initial one for various initial number concentrations and for various initial geometric standard deviations. It can be understood that at n_0 above 10^7 particles/cc particles grow in a short time.

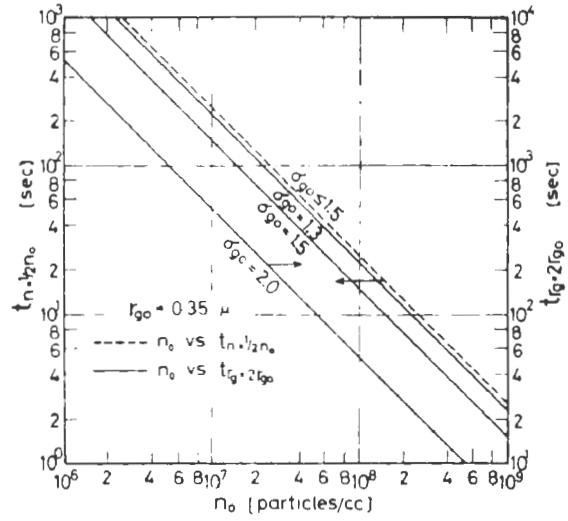

Fig. 9 Dependence of values of $t_{n=(1/2)n_0}$ and $t_{r_g=2r_{g0}}$ on initial particle number concentration

Conclusion

The change in size distribution of highly concentrated polydisperse aerosols undergoing Brownian coagulation was studied. The results of numerical calculation for aerosols having various initial size distributions which followed log-normal form were presented graphically. So far as the change in total number concentration of polydisperse aerosols with time was concerned, the results of calculation almost coincided with that of monodisperse aerosols, which was simply predicted from Smoluchowski's theory. This was also confirmed experimentally. The manner of change in size distribution with time, on the other hand, was found to be different among initial size distributions, which can not be evaluated from Smoluchowski's theory. Geometric standard deviation decreased with lapse of time when initial deviations were larger than about 1.5, and increased when initial deviations were smaller than about 1.3. Some of these results were also ascertained by experiment within experimental error, and the existence of SPDF was suggested.

The graphs presented in this paper are useful for industrial purpose where the extent or the rate of particle growth of highly concentrated polydisperse aerosols is important.

Appendix

From Eqs. (2) and (3), it follows that

$$k(r_i, \rho_i) = (r_i + \rho_i)\left(\frac{C_m(r_i')}{C_m(r_{g0})r_i} + \frac{C_m(\rho_i')}{C_m(r_{g0})\rho_i}\right) \qquad \text{(A-1)}$$

If in Eq. (A-1) values of $C_m(r_i')/C_m(r_{g0})$ do not depend on r_{g0},

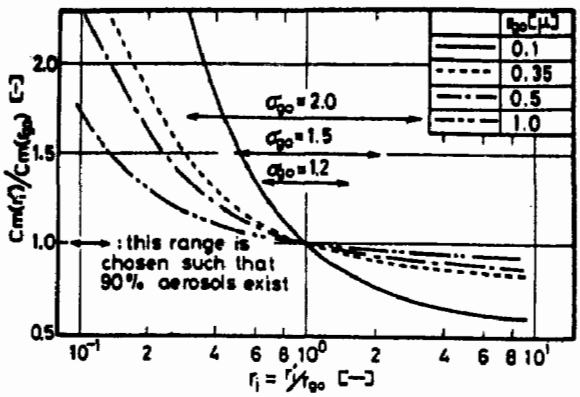

Fig. A Dependence of values of $C_m(r_i')/C_m(r_{gi})$ on initial particle size distribution

Eq. (1) can be normalized on r_{g0}. Fig. A shows the dependence of $C_m(r_i')/C_m(r_{g0})$ for various r_{g0} against dimensionless particle radius. So far as small σ_{g0} or large r_{g0} is concerned, values of $C_m(r_i')/C_m(r_{g0})$ are approximately the same, Eq. (1) thus can be considered to be almost normalized on r_{g0}.

Acknowledgment

S. Nishio was very helpful in the experimental work.

Nomenclature

$C_m(r_i')$	= Cunningham's correction factor of radius r_i'	[—]
K_0	= coefficient in Eq. (2) $(=2\kappa T/3\mu)$	[cm³/sec]
$k(r_i, \rho_i)$	= dimensionless coagulation function $(=K(r_i', \rho_i')/K_0C_m(r_{g0}))$	[—]
$K(r_i', \rho_i')$	= coagulation function for two particles of sizes r_i' and ρ_i'	[cm³/sec]
$d\ln r$	= dimensionless size width between r_i and r_{i+1}	[—]
M	= number of divisions in radius	[—]
$n'(r_i', t')$, $n(r_i, t)$	= number and dimensionless number concentration of aerosol particles $(=n'(r_i', t')/n_0)$	[particles/cc] [—]
n', n	= total and dimensionless total number concentration $(=\sum n'(r_i', t')/n_0)$	[particles/cc] [—]
n_0	= total particle number concentration at time zero	[particles/cc]
$N(0)$	= number of aerosol particles in v_m at time zero	[particles]
r', r	= particle radius and dimensionless particle radius $(=r'/r_{g0})$	[cm] [μ] [—]
dr'	= particle size width between r_i' and r_{i+1}'	[cm]
r_g	= geometric mean radius	[μ]
T	= absolute temperature	[°K]
t', t	= time and dimensionless time $(=n_0K_0C_m(r_{g0})t')$	[sec] [—]
v_m	= observation volume of ultramicroscope	[cm³]
η_r	= size scaling function for self-preserving function	[—]
κ	= Boltzman's constant $(=1.38\times10^{-16})$	[erg/°K]
μ	= viscosity of fluid	[g/cm·sec]
ρ_i	= another dimensionless particle radius in Eq. (1)	[—]
σ_g	= geometric standard deviation	[—]
ϕ	= total volume of particles per unit volume	[cm³/cc]
$\psi(\eta_r)$	= self-preserving number density for aerosol size distribution	[—]

⟨Subscripts⟩

i	= refers to the number of particle size
min	= minimum
max	= maximum
0	= at time zero

Literature Cited

1) Clark, W. and K. Whitby: *J. Atmos. Sci.*, **24**, 677 (1967).
2) Cohen, E. C. and E. V. Vaughan: *J. Colloid Int. Sci.*, **35**, 612 (1971).
3) Friedlander, S. K. and C. S. Wang: *J. Colloid Sci.*, **22**, 126 (1966).
4) Gormley, P. G. and M. Kennedy: *Proc. Roy. Irish. Acad.*, **52-A**, 163 (1949).
5) Hidy, G. M.: *J. Colloid Sci.*, **20**, 123 (1965).
6) Huang, C. M., M. Kerker and E. Matijevic: *J. Colloid Int. Sci.*, **33**, 529 (1970).
7) Keith, C. H. and J. C. Derrick: *J. Collold Sci.*, **15**, 340 (1960).
8) Lai, F. S., S. K. Friedlander, J. Pich and G. M. Hidy: *J. Colloid Int. Sci.*, **39**, 395 (1972).
9) Müller, H.: *Kolloidbeihefte*, **27**, 233 (1928).
10) Nicolaon, G., M. Kerker, D. D. Cooke and E. Matijevic: *J. Collold Int. Sci.*, **38**, 460 (1972).
11) Smoluchowski, M von Z: *Phys. Chem.*, **92**, 129 (1917).
12) Takahashi, K. and M. Kasahara: *Atmos. Environ.*, **2**, 441 (1968).
13) Wang, C. S. and S. K. Friedlander.: *J. Colloid Int. Sci.*, **24**, 170 (1967).
14) Yoshida, T., Y. Kousaka and K. Okuyama: *Ind. Eng. Chem. Fundam.*, **14**, 47 (1975).
15) Yoshida, T., Y. Kousaka, K. Okuyama and S. Nishio: *J. Chem. Eng. Japan*, **8**, 137 (1975).
16) Zebel, G.: *Kolloid-Z*, **156**, 102 (1958).

Application of Particle Enlargement by Condensation to Industrial Dust Collection

Tetsuo Yoshida, Yasuo Kousaka,
Kikuo Okuyama, and Fuminori Nomura
Chemical Engineering Department,
University of Osaka Prefecture,
Sakai, 591, Japan

Application of Particle Enlargement by Condensation to Industrial Dust Collection

Tetsuo Yoshida, Yasuo Kousaka,
Kikuo Okuyama, and Fuminori Nomura
Chemical Engineering Department,
University of Osaka Prefecture,
Sakai, 591, Japan

(Abstract)

Application of the phenomena of particle growth by condensation to industrial dust collection was studied. The analysis to evaluate the extent of size enlargement was first introduced for the two essential and industrially useful methods, one of which is that by mixing hot saturated air with cold one and the other by injection of steam into air. Four typical processes were proposed in their effective application to industrial exhaust gas and the procedure of utilization of these processes was illustrated according to the various conditions of exhaust gas. The technique for size enlargement of aerosol particles by condensation was found to be essentially applicable to any industrial exhaust gas which contains submicron dust particles in low number concentration, when the appropriate process shown herein was selected.

Introduction

Fundamental analysis and experiment for growth of aerosol particles by condensation were made in our previous papers (1976; 1977), where it was suggested that the particle growth by condensation would be one of the most promising preconditioning techniques for the collection of submicron dust particles. Industrial application of the fundamental results was developed in this paper.

Condensation of water vapor on aerosol particles, not consisting of soluble substances, will essentially occur wherever a certain degree of supersaturation is produced around the particles. The fundamental analysis of two essential methods to produce supersaturation, one of which is that by mixing hot saturated air with cold air (Yoshida et al.,1976) and the other by injection of steam into air (Yoshida et al.,1977), was first briefly introduced. The establishment of economic processes to produce supersaturation using these methods will be important from the industrial point of view. Processes for this purpose were discussed and developed under consideration of various conditions, such as temperature and humidity, of industrial exhaust gas. Some processes were proposed according to various conditions of exhaust gas and they were arranged into several charts for the facility of the design of a preconditioner of industrial dust collection.

Basic Consideration

In this section the fundamental aspects for particle growth by condensation, which were made clear in the previous papers (1976; 1977), will be briefly introduced.

The point "i" on the humidity chart of Figure 1 indicates a state of supersaturation of air. When this point is attained in an insulated chamber by some methods and a certain amount of

aerosol particles is introduced into the chamber as condensation nuclei, condensation upon the particles will occur. And as the result the state of air changes along the adiabatic line to the point "f" which almost coincides with the saturated state. Then the value of ΔH shown in the figure which represents the quantity of condensed water vapor per unit mass of dry air will be produced. In order to attain point "i" or a supersaturated state, two methods were suggested to be effective: one of which is that by mixing high temperature saturated air with low temperature saturated air and the other by steam injection into air. Existence of aerosol particles, the value of ΔH in both methods is given by the following enthalpy and material balances on dry air mass basis:

(mixing method)

$$R_h i_{sh} + (1 - R_h) i_{sl} = i_{sf} + \Delta H i'_{wf} \tag{1}$$

$$R_h H_{sh} + (1 - R_h) H_{sl} = H_{sf} + \Delta H \tag{2}$$

(steam injection method)

$$i_g + Q_{st}\left\{x i''_{st} + (1 - x) i'_{st}\right\} = i_{sf} + Q_{st}(1 - x) i'_{wf} + \Delta H i'_{wf} \tag{3}$$

$$H_g + Q_{st} x = H_{sf} + \Delta H \tag{4}$$

Some of the calculated results are shown in Figures 2 and 3.

When all of the vapor corresponding to the amount of ΔH are assumed to condense upon particles which are introduced into supersaturated air, the following relations must be satisfied:

$$\Delta H = \frac{4}{3}\pi\rho_s\left\{\int_o^\infty r^3 n(r,\infty)\,dr - \int_o^\infty r^3 n(r,0)\,dr\right\} = \frac{\pi}{6}(D_{vf}^3 - D_{vi}^3) n_0 \rho_s \tag{5}$$

$$D_{vf} \doteqdot (6\Delta H/\pi n_0)^{1/3} \qquad \text{when } D_{vf}^3 \gg D_{vi}^3 \text{ and } \rho_s \doteqdot 1 \tag{6}$$

n_0 represents the particle number concentration of aerosol on dry air mass basis. D_{vi} and D_{vf} represent the volume mean diameters of the particles before and after growth respectively. The increase in size of aerosol particles undergoing condensation can then be

evaluated in volume mean diameter D_{vf} knowing the values ΔH and n_0 in most cases.

The growing rate of particles undergoing condensation was found to be very rapid in the previous paper (1976), so the above analysis in equilibrium state only will be essential in developing this technique to industrial application.

Typical Operations to Obtain High Temperature and Low Temperature Saturated Air

(High temperature saturated air)

(a) adiabatic humidification

When exhaust gas has high temperature or moderate temperature with high humidity, direct contact of the gas with recirculating water in a humidifier will be effective. This operation is simple and any heat source is unnecessary. The operation is illustrated as line (a) on the humidity chart of Figure 4.

(b) humidification by contacting with heated water

When the exhaust gas has moderate temperature and humidity, contact of it with heated water will be effective. The line (b) in Figure 4 illustrates this operation.

(c) humidification by steam injection

This operation will be essentiallly effective for gas having any temperature or humidity, but this is especially effective for low temperature gas, the reason of which appears later. The line (c) in the figure illustrates this operation.

(Low temperature saturated air)

(d) adiabatic humidification

When exhaust gas has low temperature or low humidity, the same method as (a) is applicable. This is shown as the line (d) in Figure 4

(e) dehumidification by contacting with cooling water

When the operation (d) is not available, the direct contact of gas with cooling water will be inevitable. This is shown as the line (e) in the figure.

These typical operations are applied to industrial exhaust gas according to temperature and humidity of the gas in the following section.

Methods to Produce ΔH in Various Industrial Exhaust Gas

The value of ΔH, which represents the quantity of condensable water vapor per unit mass of dry air described before, is important, while the size of grown particles is determined by this value under a given particle number concentration of exhaust gas as shown in eq(6). Some of the representative industrial processes to produce ΔH are discussed according to some classified gas conditions in this section. The property of exhaust gas was regarded the same as that of air in the following discussions. The notations (a)～(e) appears in the following figures indicate the above classification for typical operations.

(High temperature and high humidity exhaust gas)

This is probably the most profitable case to apply the method of particle growth by condensation when cooling water is obtainable. The flow sheet of this process is shown in Figure 5. Gas after adiabatic humidifier is divided into two parts. One part is dehumidified by contacting with cooling water, and is then mixed with the other to produce ΔH or to enlarge the particles in gas at the mixing chamber. This process is named "A". The value of ΔH in this process depends on the temperature T_g and humidity H_g of exhaust gas, and on the temperature of cooling water which is available. The correlation among them was calculated by eqs(1) and (2), and was illustrated on the right upper side of the humidity chart of Figures 6～10 for various ΔH. The mixing ratio

R_h was chosen in any cases as the optimal value shown in Figure 2 in calculation. If one may require the value of $\Delta H = 0.006$ and if the cooling water temperature of 20°C is available, then the exhaust gas conditions must exist at least on the line of 20°C of cooling water in Figure 8, for instance $T_g = 1000$°C and $H_g =$ 0.07 g H_2O/g dry air, $T_g = 100$°C and $H_g = 0.32$ g H_2O/g dry air, and so forth. The temperature of saturated air or the equilibrium temperature after adiabatic humidification, in this case, comes to $T_e = 72.5$°C. It is matter of course that the larger values than $\Delta H = 0.006$ can be obtained if the gas conditions exist in the upper side of the line of 20°C of cooling water in Figure 8.

(Low temperature exhaust gas)

In this case steam injection method is effective, but this method has a fault that it requires saturated steam as a heat and water vapor source. The process is very simple as shown in Figure 11, and this process is named "B". The value of ΔH in this process depends on the steam quantity Q_{st} and on exhaust gas conditions such as T_g and H_g. The correlation among them was calculated by eqs(3) and (4) and was illustrated on the left side of the humidity chart of Figures 6 ~10. As the property of steam, 100°C, 1 ata and unity in dryness fraction were assumed in the calculation. If the same value of ΔH as the above example is required and if the steam quantity of $Q_{st} = 0.1$ kg steam/kg dry air is available, then the exhaust gas conditions must exist at least on the line of $Q_{st} = 0.1$ in Figure 8. The larger values than $\Delta H = 0.006$ can be obtained if the gas conditions exist in the left side of this line. The temperature rise in air was also illustrated in the figure as T_e, in this example $T_e = 37.9$°C. If the saturated air after steam injection has high temperature, the process "A" may be applied successively after steam injection. This is one of the advantages of this process.

(Gas having intermediate conditions)

When exhaust gas has temperature below about 200°C and low humidity,steam injection can be applied after application of adiabatic humidification. This process is shown in Figure 12, and is named process "B'" because of similarity to process "B". The calculated results in this case were illustrated on the humidity chart of Figures 7~10 .

When both hot water and cooling water are available, the following process may be applicable. One part of gas is humidified and at the same time heated by hot water to obtain high temperature saturated air, and the remainder is cooled down by contacting with cooling water to obtain low temperature saturated air. Then they are mixed to produce ΔH. The process is shown in Figure 13, and is named process "A'". The calculated results can not be shown in this case in Figures 6~10 because of one more additional parameter of heated water temperature. The value of ΔH, however, is obtainable for every given condition since the temperatures of points "2" and "3" in Figure 13 can be evaluated from given gas conditions.

Figure 14 illustrates the rough domain in applying the above processes to various exhaust gas conditions.

Utilization of the Above Results

The steps of procedure to utilize the above results for industrial purpose are as follows. The appropriate process is first selected according to the given temperature and humidity of exhaust gas referring to Figures 6~10 and 14. The value of ΔH is next evaluated from Figures 6~10 or from calculation by setting up the quantity of steam, or the temperature of cooling water which is obtainable. Then the volume mean diameter of grown particles, D_{vf}, can be evaluated from eq(6), using the value of ΔH and knowing the particle number concentration of the gas, n_0.

A dust collector after the preconditioned gas should be designed using the value D_{vf} thus obtained. If the value D_{vf}, on the other hand, is first given from the point of performance of a collector installed after particle enlargement, the value ΔH should be first determined from eq(6) knowing the value n_0. Consequently the steam quantity Q_{st} or cooling water temperature will be determined from the figures using the known value ΔH and knowing the gas conditions.

(Example)

$T_g = 30°C$, $H_g = 0.01$ g H_2O/g dry air and $n_0 = 10^8$ particles/g dry air (roughly corresponds to 10^5 particles/cm^3 gas) are given. It is required to enlarge submicron particles in the gas to 5 microns in D_{vf}.

In this case the value of ΔH which is required is found to be 0.006 g H_2O/g dry air from eq(6). The appropriate process in this case is found to be process "B" because of low temperature gas. The required steam quantity Q_{st} (100°C, 1 ata, $x = 1$) is then found to be 0.1 g steam/g dry air from the point of $T_g = 30°C$ and $H_g = 0.01$ in Figure 8.

Experimental

The experimental results on the processes "A'" and "B" were reported in the previous papers (1976; 1977), and so the experiment on the process "A" and "B'" were briefly shown in this section. Figure 15 shows the schematic diagram of the experimental method. The apparatus can be operated in both processes "A" and "B" by opening and closing valves. The mixture of air with combustion gas from gas burner was supplied as a high temperature gas from the bottom of the adiabatic humidifier. The temperature of the gas was several hundreds centigrade degrees for the process "A" and about 200°C for the process "B'". Tobacco smoke ($D_{vi} = 0.85$ micron) and dust particles contained in combustion gas ($D_{vi} \leq 0.1$

micron) were used as submicron dust particles. Total gas flow rate was 180 l/min. In the experiment of process "A", the valves of v_1 and v_2 are adequately opened to obtain a certain mixing ratio R_h keeping v_3 close. In the experiment of process "B'", the valve of v_2 is closed and v_3 is moderately opened to inject a certain amount of steam into the gas. The technique of size measurement of grown particles was the same as that appeared in the previous papers(1975; 1976; 1977). Experimental results were plotted in the same graph as those of the previous papers (1976; 1977), which was shown in Figure 16. The results obtained in the previous works were also collectively plotted in the figure. It will be found in Figure 16 that the all processes "A", "A'", "B" and "B'" are useful for size enlargement of submicron dust particles by condensation.

Conclusion

Application of the phenomena of particle growth by condensation to industrial dust collection was developed. Four typical processes were proposed for the effective application of the phenomena and the procedure of their utilization was shown according to various exhaust gas conditions. The technique for size enlargement of aerosol particles by condensation was found to be essentially applicable to any industrial exhaust gas which contains submicron dust particles in low number concentration, when the appropriate process shown in this paper was selected. The results suggested that the exhaust gas having high temperature and high humidity is especially profitable to apply this technique because any heat source but cooling water is unnecessary. The exhaust gas having low temperature such as 30°C or below, on the other hand, is advantageous in very simple apparatus but is disadvantageous in necessity of steam.

Nomenclature

D_{vi}, D_{vf} = volume mean diameter before and after growth, respectively, cm
H = absolute humidity, g H_2O/g dry air
ΔH = condensable water vapor, g H_2O/g dry air
i = enthalpy, cal/g dry air or g steam
n_0 = particle number concentration, 1/g dry air
$n(r,0)$, $n(r,\infty)$ = particle number having particle radius r before and after growth, particles/g dry air
Q_{st} = quantity of steam injection, g steam/g dry air
r = radius of particle, cm
R_h = mixing ratio, g dry air of high temperature saturated air/g total dry air
T = temperature, °C
x = dryness fraction of steam

Greek Letter

ρ_s = density of condensed liquid, g/cm^3

Subscripts

e = equilibrium state of air
f = final state shown in Figure 1
g = initial state of air
i = initial state
s = saturated
sf = saturated air in final state
sh = high temperature saturated air
sl = low temperature saturated air
st = steam
wf = water in final state

Superscripts

' = wet
" = dry

References

Yoshida, T., Kousaka, Y. and Okuyama, K.,"A New Technique of Particle Size Analysis of Aerosols and Fine Powders Using an Ultramicroscope", Ind. Eng. Chem., Fundam., 14, No.1, 47(1975)

Yoshida, T., Kousaka, Y. and Okuyama, K.,"Growth of Aerosol Particles by Condensation", Ind. Eng. Chem., Fundam., 15, No.1, 37(1976)

Yoshida, T., Kousaka, Y., Okuyama, K. and Nomura, F., "Growth of Aerosol Particles by Steam Injection", J. Chem. Eng. Japan(in contribution)

Captions of figures

Figure 1 Change in humidity and temperature due to condensation

Figure 2 Condensable water vapor ΔH at various mixing conditions

Figure 3 Condensable water vapor ΔH against quantity of steam injection Q_{st}

Figure 4 Typical operations to obtain high and low temperature saturated gases

Figure 5 Illustration of process "A"

Figure 6 Application of processes "A" and "B" to various exhaust gas conditions($\Delta H = 0.002$)

Figure 7 Application of processes "A", "B" and "B'" to various exhaust gas conditions($\Delta H = 0.004$)

Figure 8 Application of processes "A", "B" and "B'" to various exhaust gas conditions($\Delta H = 0.006$)

Figure 9 Application of processes "A", "B" and "B'" to various exhaust gas conditions($\Delta H = 0.008$)

Figure 10 Application of processes "A", "B" and "B'" to various exhaust gas conditions($\Delta H = 0.010$)

Figure 11 Illustration of process "B"

Figure 12 Illustration of process "B'"

Figure 13 Illustration of process "A'"

Figure 14 Effective application of process "A", "A'", "B" and "B'" to various exhaust gas conditions

Figure 15 Schematic diagram of experimental apparatus

Figure 16 Relation between grown particle diameter D_{vf} and condensable water vapor per single particle

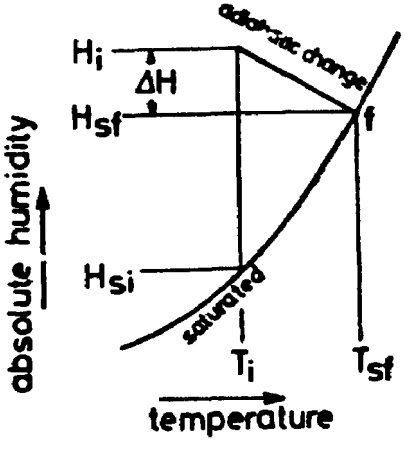

Figure 1 Change in humidity and temperature due to condensation

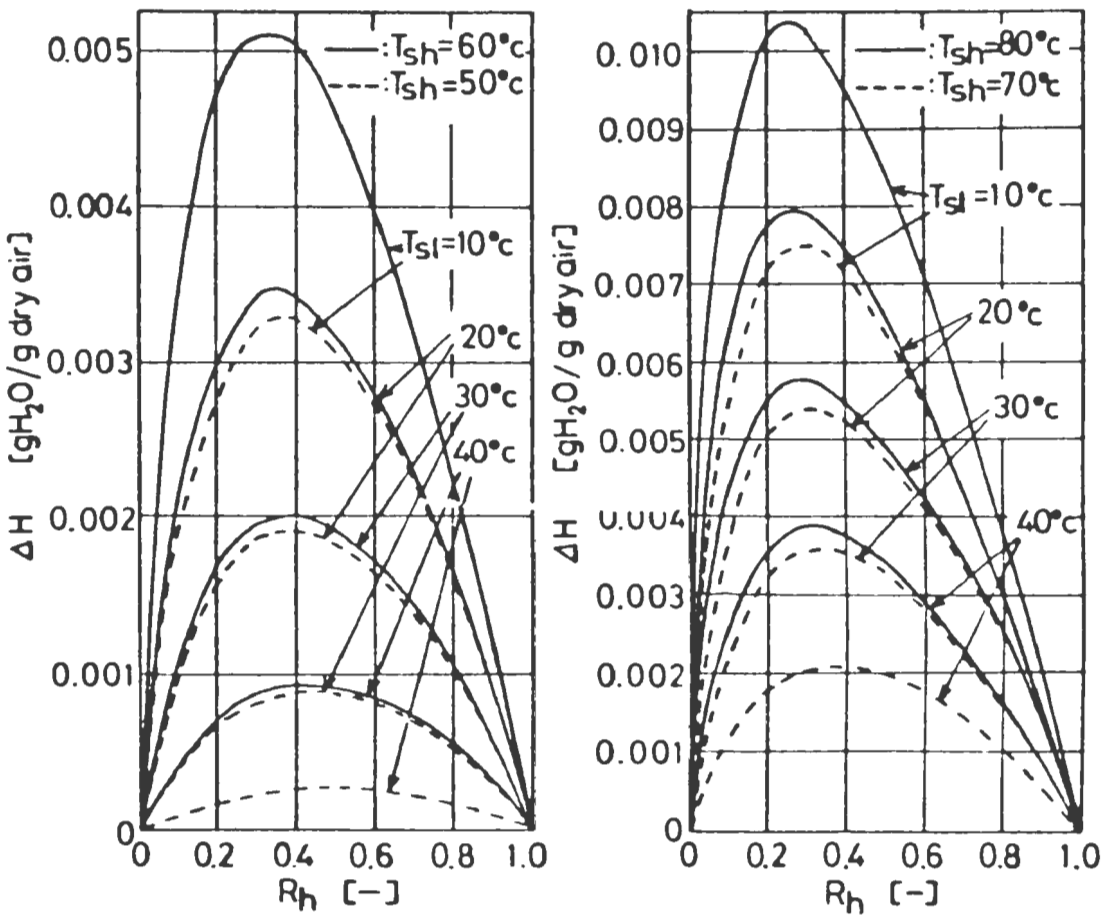

Figure 2 Condensable water vapor ΔH at various mixing conditions

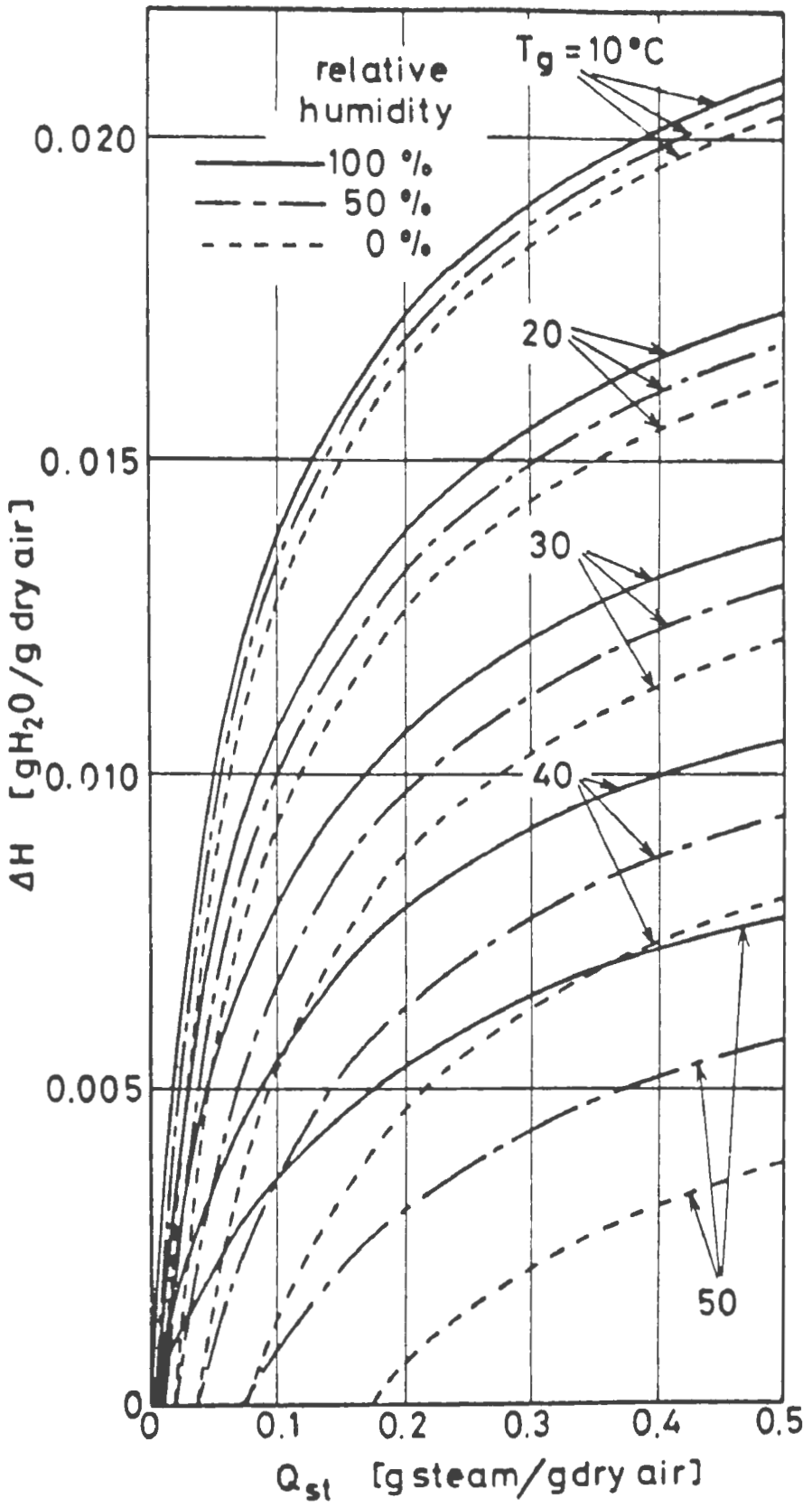

Figure 3 Condensable water vapor ΔH against quantity of steam injection Q_{st}

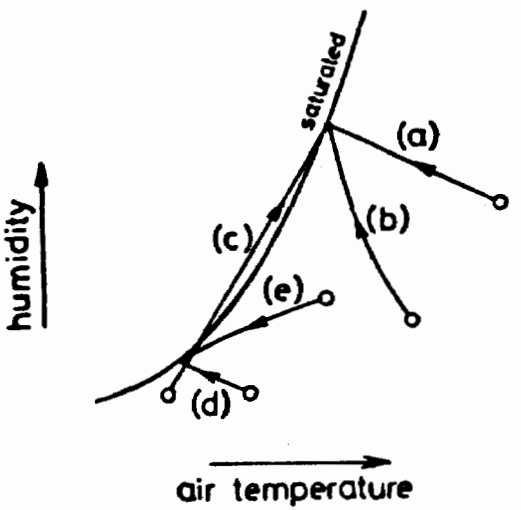

Figure 4 Typical operations to obtain high and low temperature saturated gases

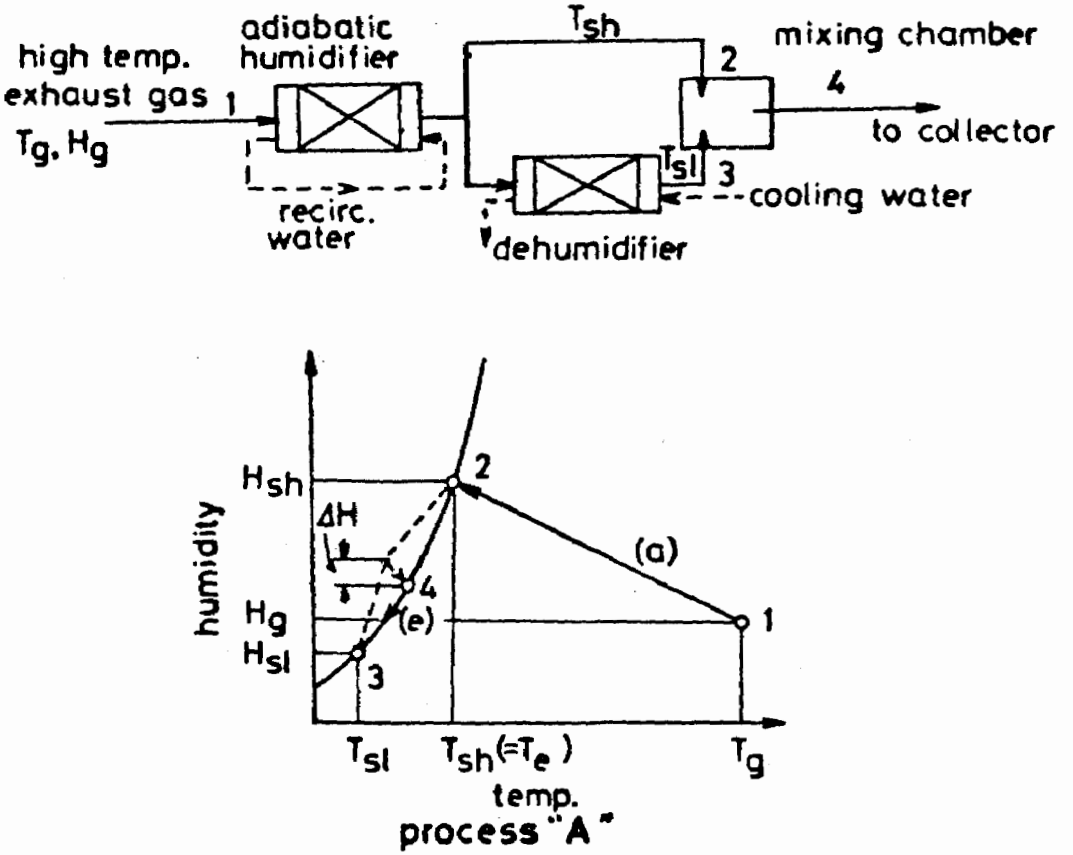

Figure 5 Illustration of process "A"

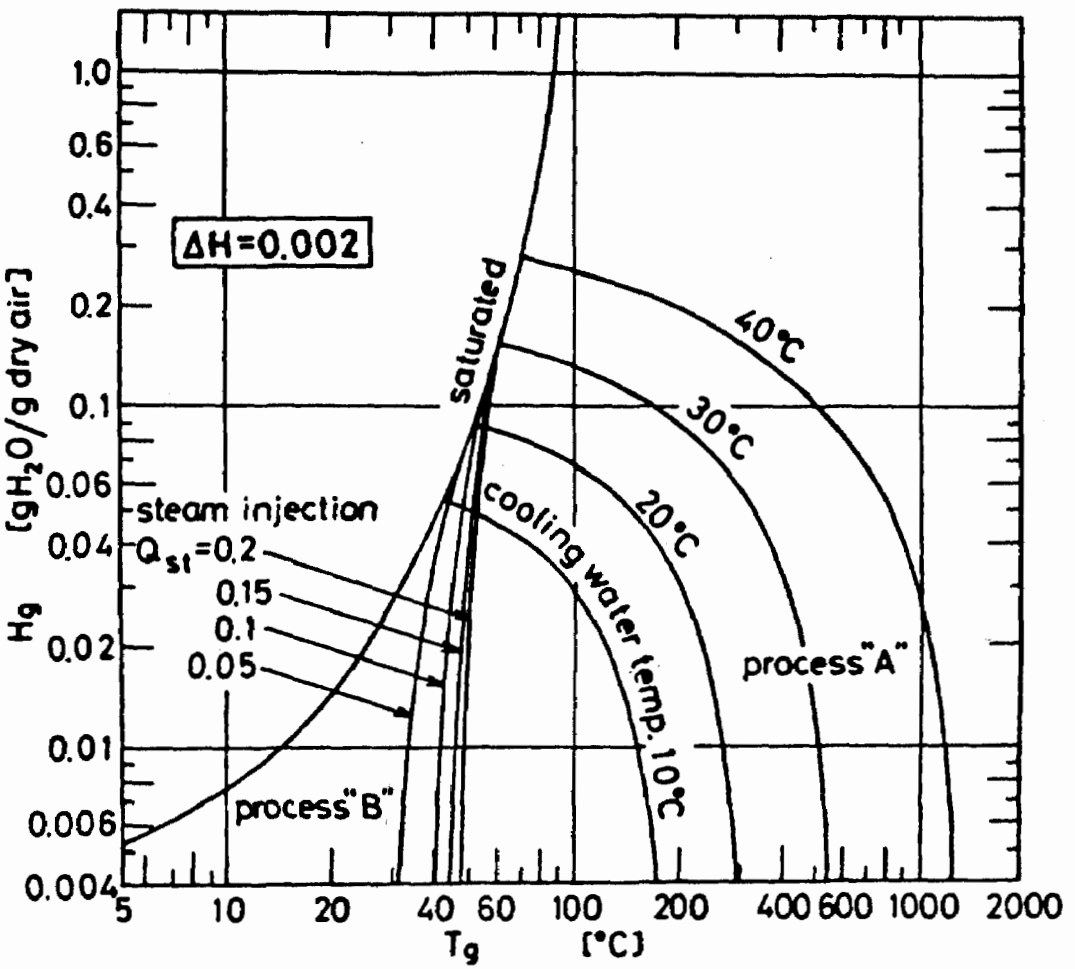

Figure 6 Application of processes "A" and "B" to various exhaust gas conditions($\Delta H = 0.002$)

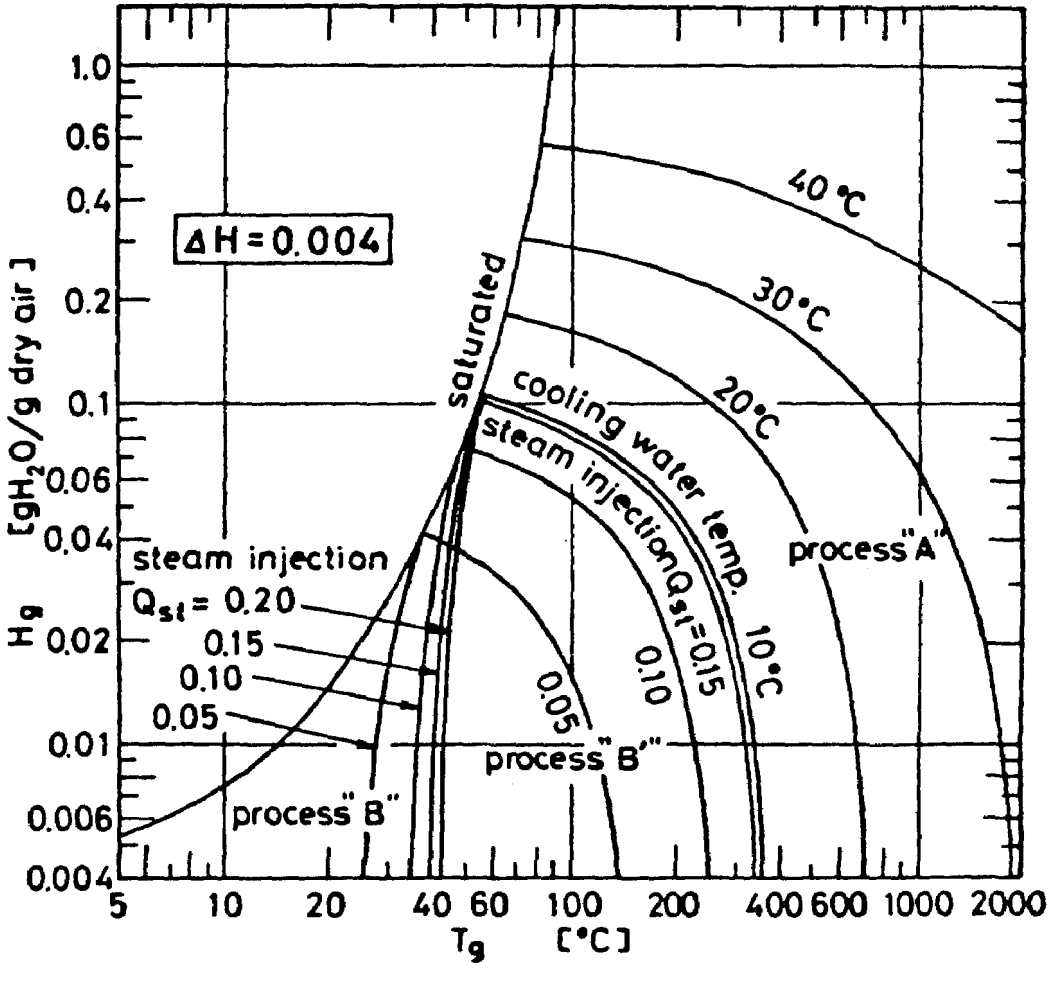

Figure 7 Application of processes "A", "B" and "B'" to various exhaust gas conditions ($\Delta H = 0.004$)

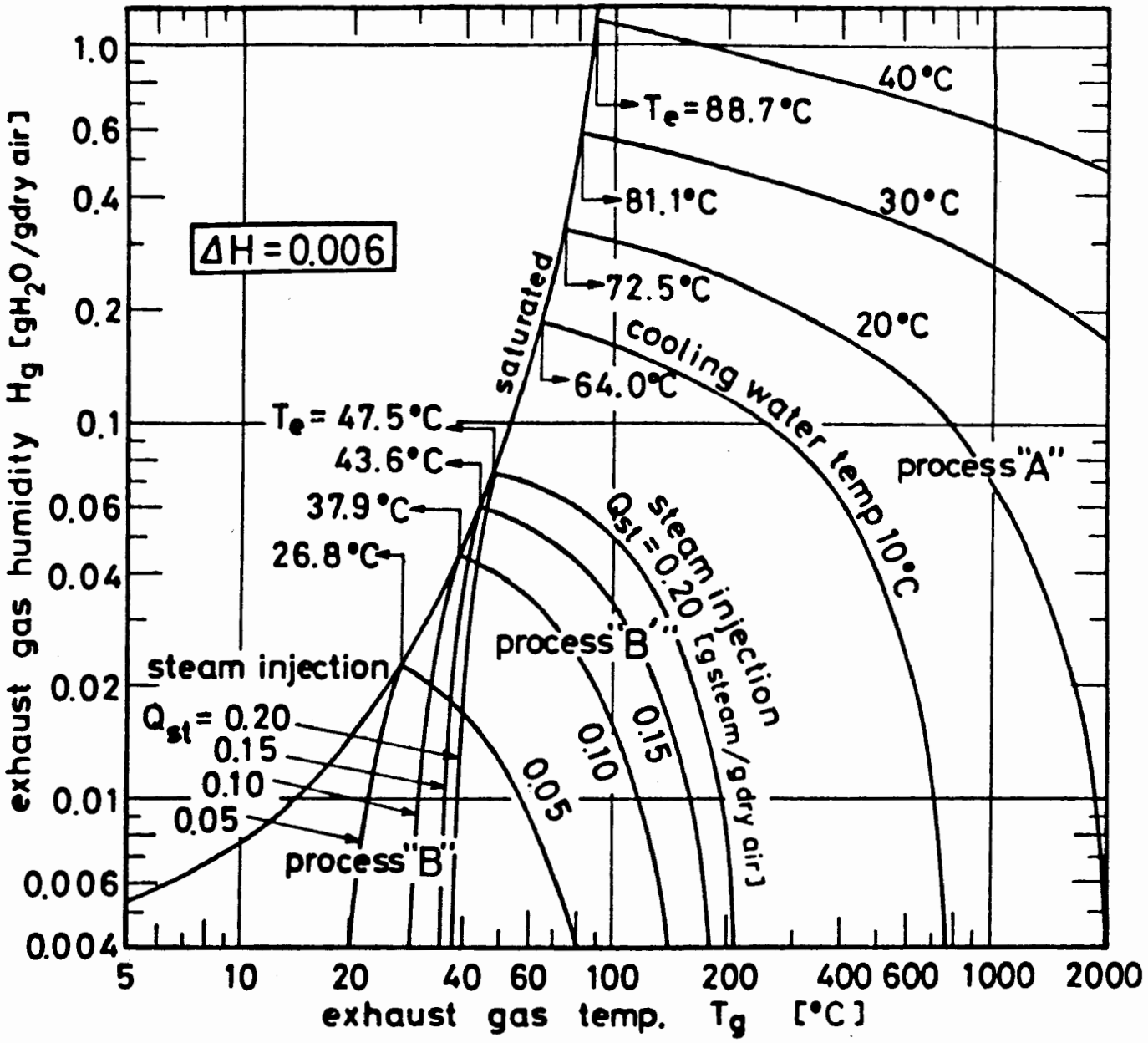

Figure 8 Application of processes "A", "B" and "B'" to various exhaust gas conditions ($\Delta H = 0.006$)

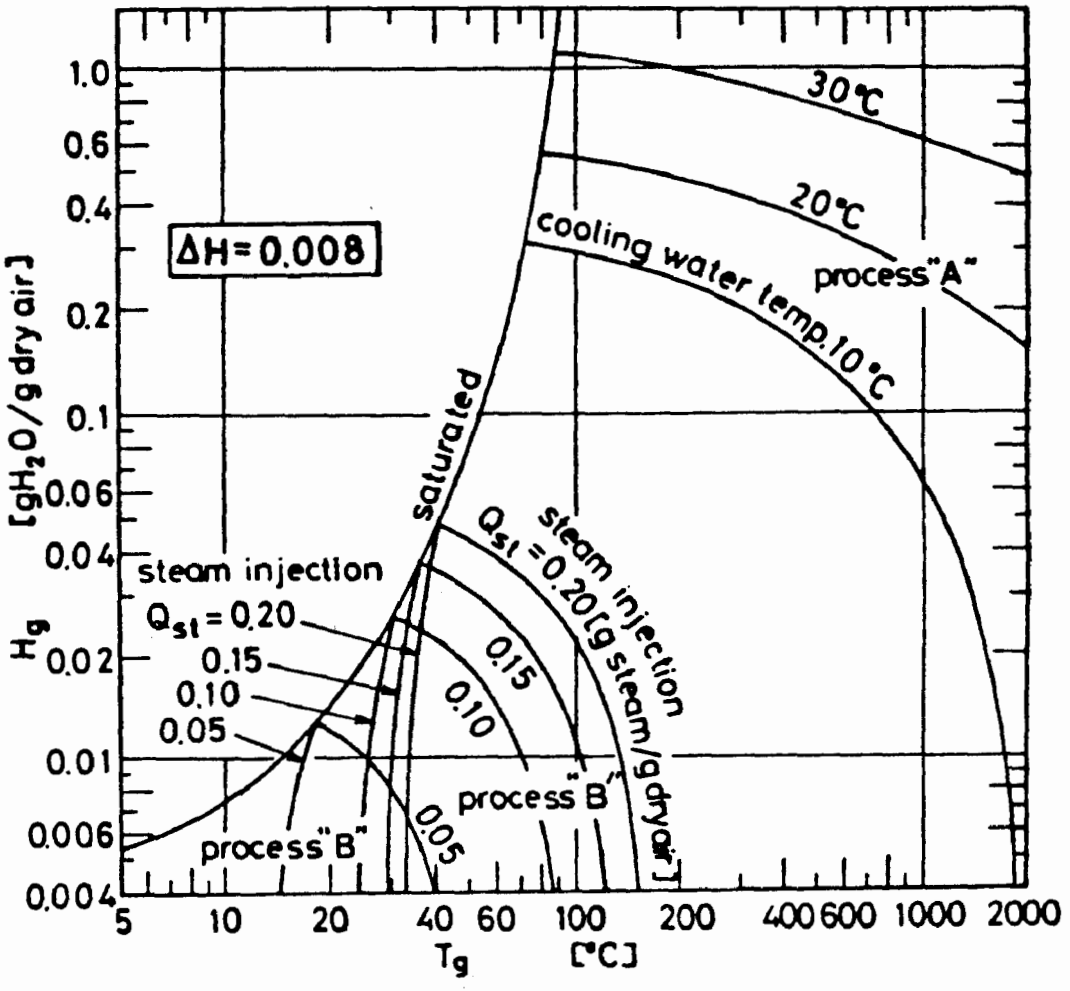

Figure 9 Application of processes "A", "B" and "B'" to various exhaust gas conditions (ΔH = 0.008)

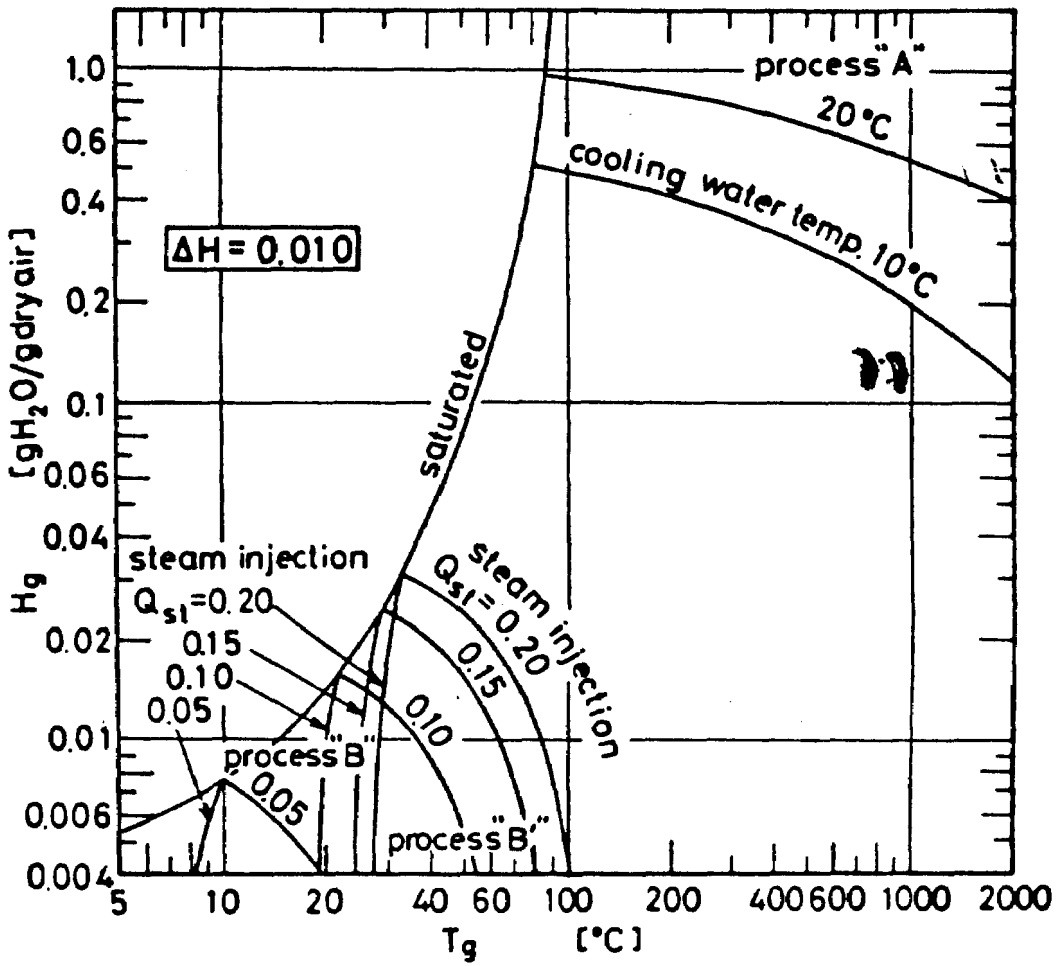

Figure 10 Application of processes "A", "B" and "B'" to various exhaust gas conditions ($\Delta H = 0.010$)

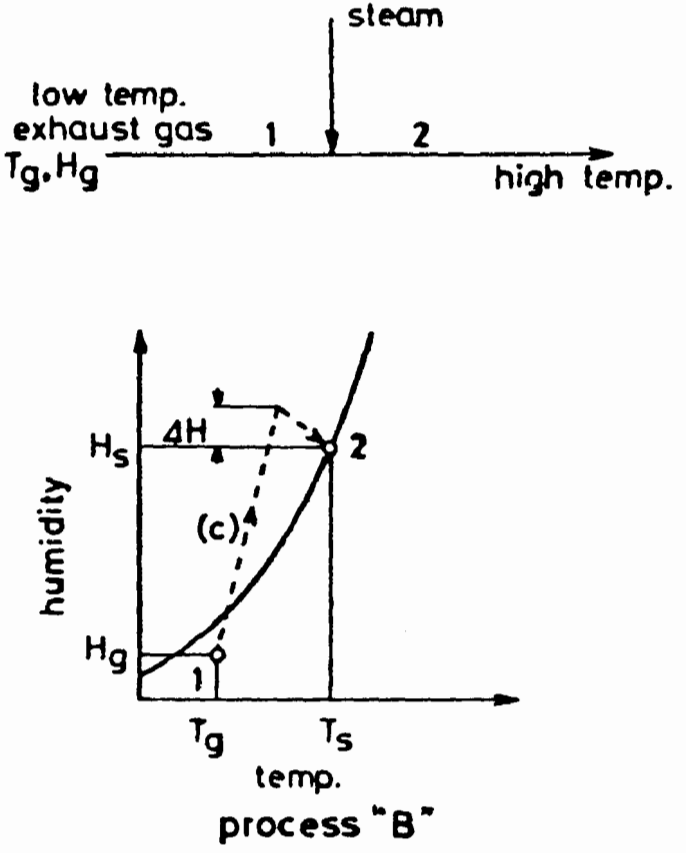

Figure 11 Illustration of process "B"

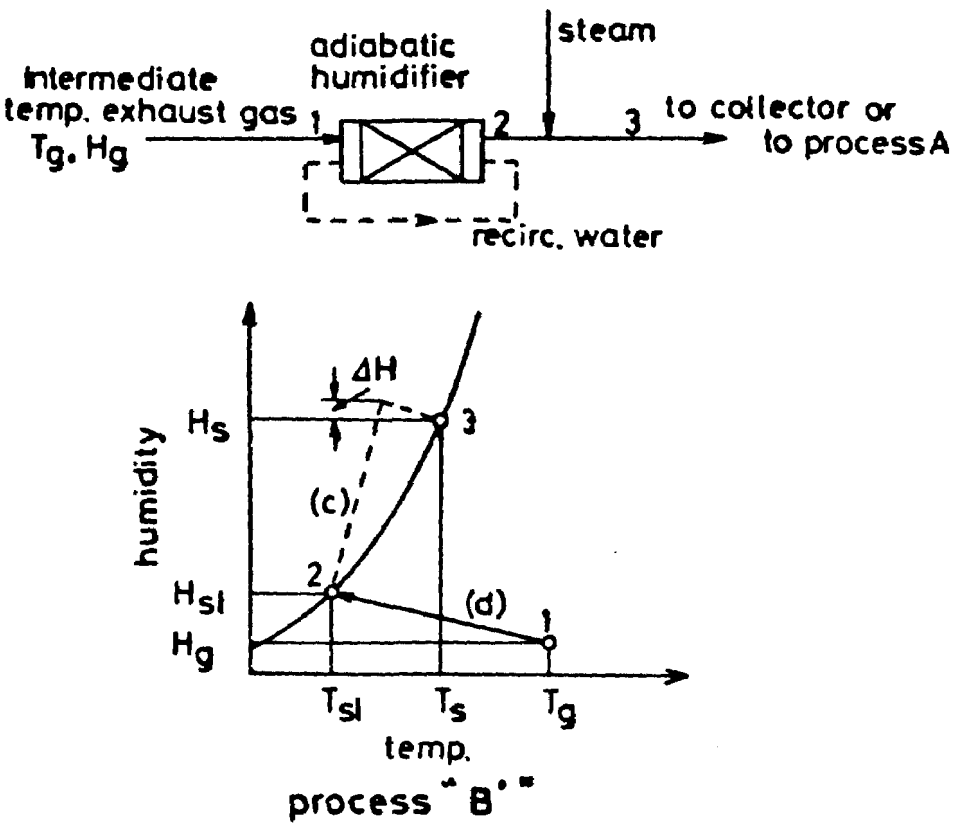

Figure 12 Illustration of process "B'"

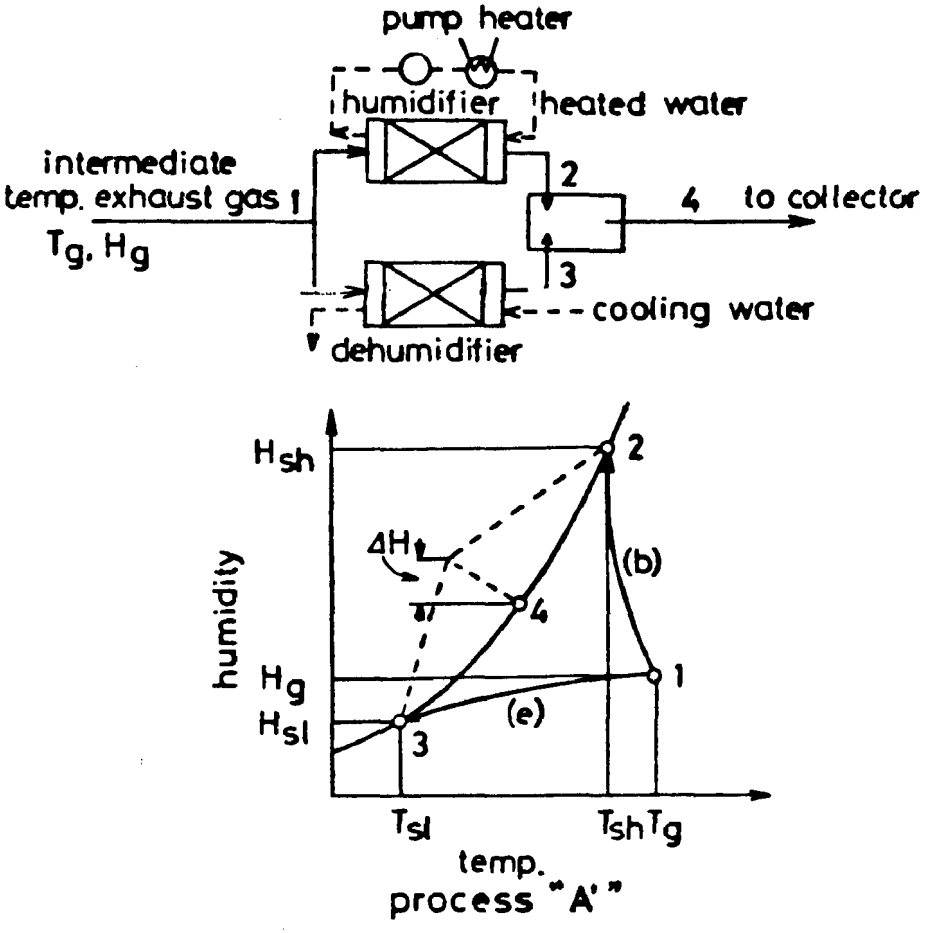

Figure 13 Illustration of process "A'"

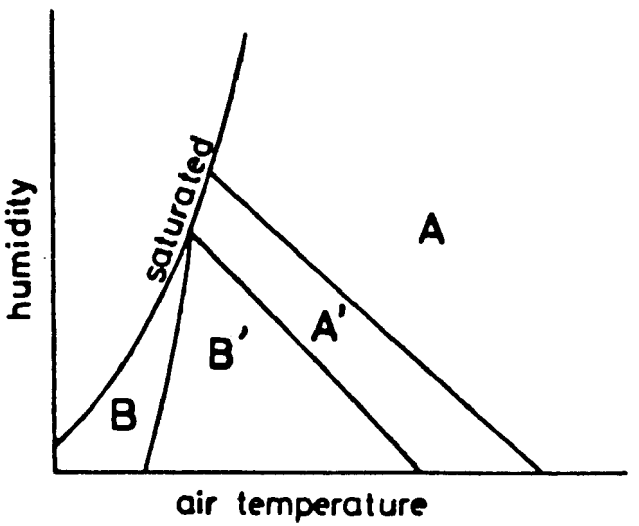

Figure 14 Effective application of process "A", "A'", "B" and "B'" to various exhaust gas conditions

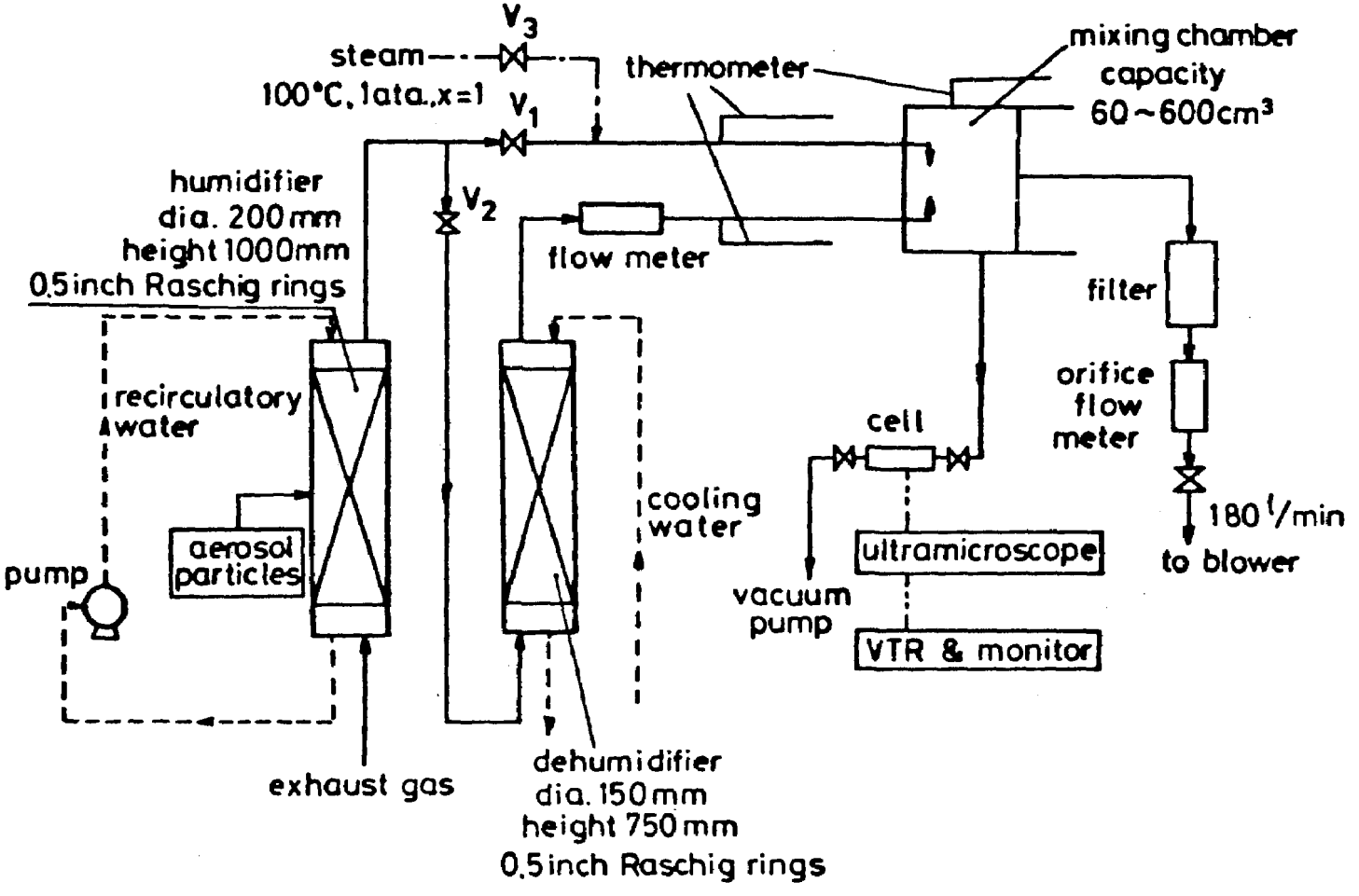

Figure 15 Schematic diagram of experimental apparatus

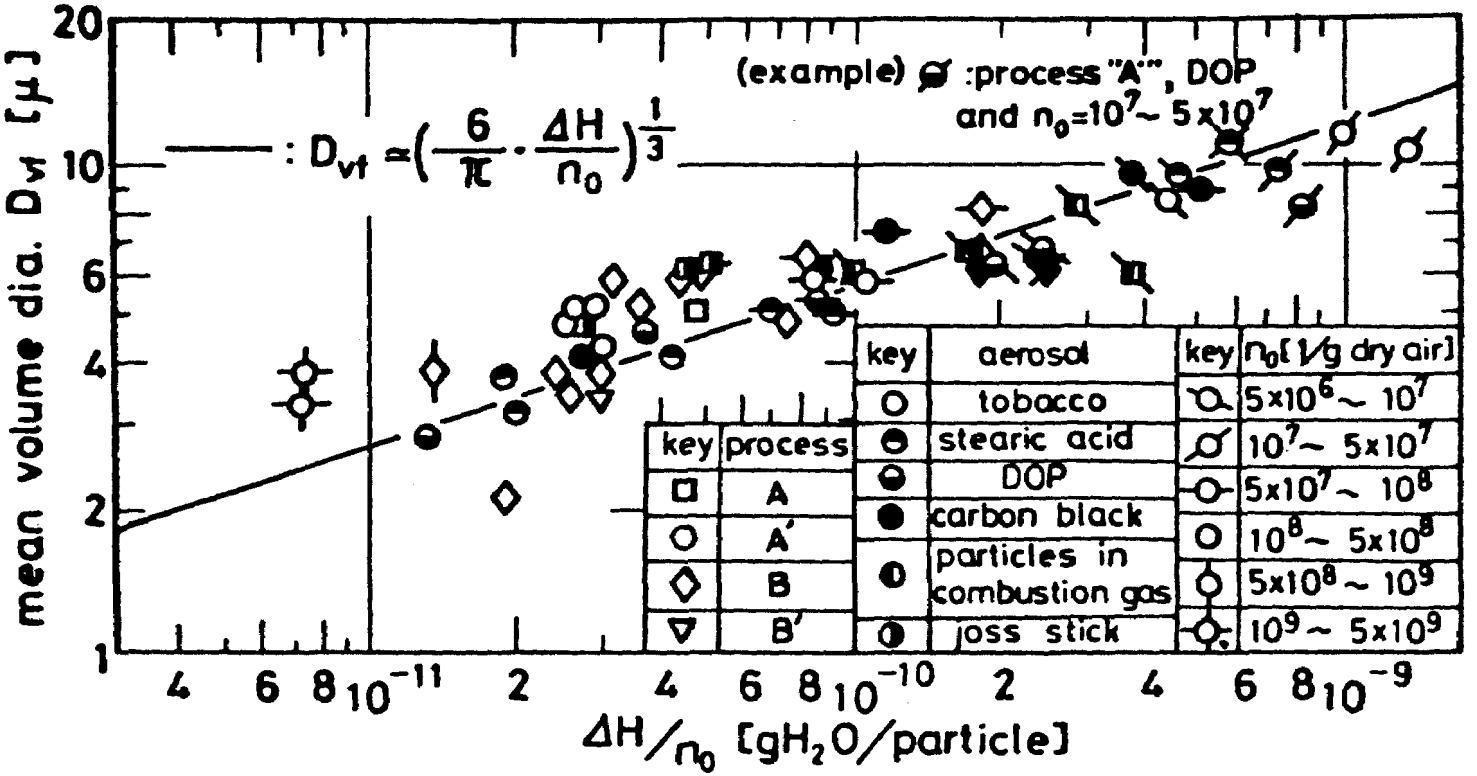

Figure 16 Relation between grown particle diameter D_{vf} and condensable water vapor per single particle

APPENDIX J

MITSUBISHI HEAVY INDUSTRIES, LTD.

The Latest Dust Collecting Technique

October 1976

MITSUBISHI HEAVY INDUSTRIES, LTD.
5-1, Marunouchi 2-chome, Chiyoda-ku, Tokyo 100, Japan

©by Mitsubishi Heavy Industries, Ltd.
(Reproduced by permission)

The Latest Dust Collecting Technique

Yasuo Saito* Koji Tashiro* Shigenori Komura*
Naoji Tachibana** Kazuo Matsui** Katsutoshi Yada**

The electrostatic precipitator is well known as the most efficient and most economical dust collector for a large amount of gas volume and high performance and its role is becoming more and more important with the aggravation of environmental pollution.

The precipitator is now confronted with various problems requiring immediate solution:

(1) Difficulty of collecting dust of submicron and/or high-resistivity.

(2) Capability of maintaining stable perofrmance over a long period.

(3) Structural reliability against a large quantity of gas treated.

(4) Applicability to desulfurizing and denitrating processes.

This paper introduces our company's views on these problems.

1. Introduction

Mitsubishi Heavy Industries has supplied more than 1000 units of dust collectors to many industrial fields since this item was added to their lines of production in 1960. These dust collectors have treated a total of some 200 million Nm^3/h of flue gases till now. At the beginning, the dust collectors were used as attached facilities in works and plants but gradually came to be regarded as indispensable facilities for industries. On the other hand, users' requirements also became severer, calling for the following performances:

(1) To be able to effect designed performance surely.

(2) To be capable of maintaining designed performance for a long time.

(3) To have a stable performance against changes in conditions.

(4) To have long intervals between servicings for easy inspect and repair.

In other words, they came to demand the same or even higher performances than those of the master plants. Our company is attaching the greatest importance to the electric precipitator (abbreviated as EP hereinafter) for the time being and most of the precipitators manufactured and supplied by our company hitherto are EPs.

EPs are generally superior to other types of dust collectors in that they have a very high dust collecting efficiency and that they require less power charge, maintenance and depreciation costs. On the other hand, EPs, which treat dust-containing gases electrically, are susceptible to the effect of the physical and chemical properties of treated gases and dust and therefore, involve much of an empirical engineering element. That is to say, the element which governs dust collecting performance is what is generally called the intensity variable having a "dispersion" which cannot be specified with a simple scale, and the resultant dust collecting efficiency cannot be free from probability variation and their performance guaranty can only be made by a certain reliability.

With the increasing demand for high dust collecting efficiency in recent years, high-performance EPs which can collect dust to such a high degree that flue gases become invisible have been commonly equipped. Such high-performance EPs, however, are susceptible to the effect of probability variation as mentioned above in many cases and this problem is drawing a particular attention of the circles concerned. A simple increase of their sizes cannot be said to be a practical method of solution if equipment economy is taken into account and it is necessary to study, by making analysis of the results of actual operation, a method of grasping the element which governs the dust collecting efficiency of EP accurately. It has also been made clear theoretically that the larger is the volume of past data, the higher performance reliability is obtainable with a smaller risk*. One of the technical aims of our company will also be placed on this point for the time being.

Note: *—S. Masuda et al., Probability Design Method and Its Application to the Guaranty of Performance of Electric Precipitators, Trans. I.E.E.J. 8/73.

In this paper, the authors discuss, in relation to this point, the collection of fine-particle dust contained in flue gas which is rather significant for the small quantity of dust contained and the collection of high-resistivity dust which is comparatively difficult to collect.

With the increase in the size of equipment and its efficiency, any trouble with the equipment came to give a greater effect than ever. As a result, lasting performance and stable continuous operation came to be severely demanded in recent years. EPs with dust-collecting areas of several tens of thousand square meters per unit and several tens of thousand discharging electrodes and attached mechanism have made debut recently. For such large-sized EPs, structural reliability and easy servicea-

*Takasago Technical Institute, Technical Headquarters
**Kobe Shipyard & Engine Works

bility, in particular, are essential conditions for the maintenance of stable performance, for which perfect design which enables quality control to be made thoroughly, effectively and accurately is demanded. In order to ensure the outlet dust burden close to the minimum stably and for a long time besides improving dust collectability on the collecting electrodes, the major function of EP, the improvement of the conventional mechanism for rapping collected dust on the electrodes and the conventional mechanism for preventing reentrainment at the time of rapping are attracting a strong concern of the circles concerned as indispensable factors for the attainment of high performance. In this paper, the authors also touch upon these mechanisms.

On the other hand, flue gas desulfurization or denitration plants are installed as a means to prevent air pollution. An EP is used as equipment for pretreatment, intermediate treatment and after-treatment for such plant and plays a significent role for the attainment of purifying performance and economic design. Consequently, an EP has become indispensable for a total system. In this paper, the authors also discuss its relation with such equipment as a technique for utilizing EP.

2. Measures to realize high grade dust collecting technique

2.1 Grasping of problematical points

As the recent problems of dust collecting technique, measures for fine-particle dust and high-resisti- ty dust collection are proposed. These two problems have aspects which cannot be considered separately. Taking fine-particle dust collection for example, it is necessary to foresee or investigate beforehand electric resistivity in addition to dust burden, particle distribution, bulk density and corona discharge characteristics.

Fine-particle dust is apt to scatter again by rapping or other treatment even after it has been collected. Therefore, it is necessary to take into full consideration that this kind of dust cannot always be collected efficiently. High-resistivity dust is contained in gases emitted from low-sulfur coal-fired boilers, sintering machines in steel mills, cement manufacturing boilers and CO boilers. For these gases, dust collectors fail to attain a high collecting efficiency in many cases due to the back corona action of dust deposited on the collecting electrode. Concerning the back corona phenomenon, realities are being made clear gradually. It is considered that conditioning, improvement of structure, and high-temperature treatment are effective for the phenomenon. Our company is also conducting research on this phenomenon by use of our research facilities shown in Fig. 1.

2.2 Collection of fine-particle dust

In conducting fine-particle dust collection, it is necessary to foresee corona discharge characteristics. This is because there is a fear of current shortage occurring due to the effect of the so-called space charge. Current shortage occurs in the fore chamber of EP, in particular. Our company is coping with the fault by employing various directional barbed wires selectively.

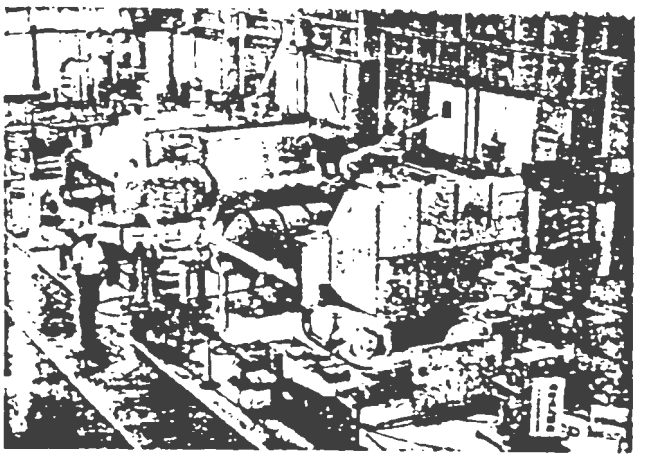

Fig. 1 Dust collection research laboratory

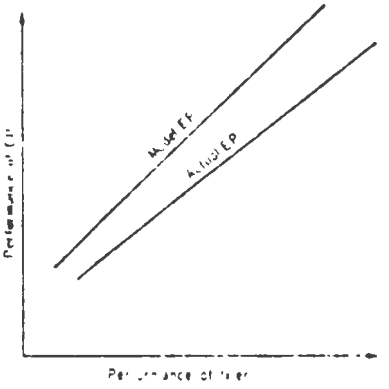

Fig. 2 Relation between the performance of EP and that of filter

What is necessary for the determination of the scale of EP is to grasp the relation between flying grain size and dust collecting rate quantitatively. It is needless to say to point out the importance of recognizing the size of a grain as that of a grain in flight. For example, if it is compared with the size of a grain collected by EP, they do not always agree with each other partly due to the effect of coagulation in the equipment. For this reason, our company developed a special filtering device (patent pending) and conducted measurement at site repeatedly. As the result of statistical analysis of the results of measurement we could obtain the relation between the performance of EP and that of filter (for actual EP and model EP) as shown in Fig. 2. By utilizing this achievement as well, we can increase the reliability of fine-particle dust collection.

What should not be overlooked in fine-particle dust collection is the re-entrainment phenomenon of dust as mentioned above. In case a very high dust collecting performance is demanded, even an instantaneous increase of dust burden due to re-entrainment by rapping becomes a problem. Re-entrainment is a phenomenon that dust once deposited on the collecting electrode comes off due to various reasons and is carried away by gas flow. The

main causes of re-entrainment are as follows:

(1) Rapping
(2) Electric factor
(3) Gas flow
(4) Ionic wind

(1) Rapping produces the largest re-entrainment quantity. As a measure to prevent re-entrainment of dust, our company adopted the damper system as mentioned below, with satisfactory result. (2) Re-entrainment due to electric factor occurs in case of low-resistivity dust with an electric resistivity lower than $10^4\Omega$-cm. Dust collected on the electrode loses its electric charge as soon as it is collected and at the same time, obtains the same electric charge as the collecting electrode by electrostatic induction and flies into the field space reactionally. Dust which flied out into the field space is charged again by the ion emitted from the discharging electrode and goes toward the collecting electrode. This phenomenon is repeated and in the meantime, a portion of the dust escapes out of the equipment without being collected by it. As a countermeasure, it is necessary to design so as to make gas speed low and conceive proper electrode construction and arrangement. (3) Re-entrainment by gas flow occurs in relation to gas speed in case adhesive force between electrode and grain or between grains is small. Re-entrainment in this case is simple separation and conveyance phenomenon by fluid. To prevent this phenomenon, it is necessary to take the following measures: (a) to make gas speed in the equipment low, (b) to make gas speed distribution uniform, (c) to provide the form of the collecting electrode with a pocket characteristic, (d) to maintain the quantity of dust sticking to the collecting electrode at a small level. (4) Re-entrainment is caused by ionic wind (also called corona wind or electric wind) which is generated when ion generated by corona discharge shares its kinetic energy to neutral molecules as it strikes with them on the way of its movement toward the opposite electrode by the action of the electric field, and the ion and neutral molecules move toward the opposite electrode. This phenomenon is shown in Fig. 3 (a) and (b). This ionic wind has a function to carry dust to the opposite electrode but, on the other hand, produces eddy current on the surface of the opposite elctrode, causing collected dust to come off. Particularly, in case of dust with a small apparent specific gravity and weak adhesive power such as the dust discharged from naphtha-fired boilers, it seems that dust collecting efficiency is reduced under the effect of ionic wind. As countermeasures to this, it is necessary to pay consideration to the following points: (a) to reduce gas speed as much as possible, (b) to select discharge electrodes and electrode spacing with consideration to proper ionic wind and (c) proper rapping.

2.3 Collection of high-resistivity dust

High electric resistivity-dust collection must be conducted carefully. This is because when electric resistivity exceeds $10^{11\cdot12}\Omega$-cm, back corona occurs. Back corona is an abnormal discharge phenomenon which occurs in the interior or on the surface of dust layer on the collecting electrode in case the strength of the electric field formed on the dust layer exceeds the electric breakdown field strength due to corona current passing the dust layer. Fig. 4 shows the phenomenon. This phenomenon reduces dust collecting efficiency for the following reasons:

(1) Inverse ion is generated from the collecting electrode side to the corona discharge electrode side, and in consequence, streamer or abnormal current increase occurs easily, causing a sharp decline of applied voltage.
(2) At the same time inverse-polarity ionic wind occurs from the collecting electrode side and fluidly prevents the normal movement of dust to be collected.

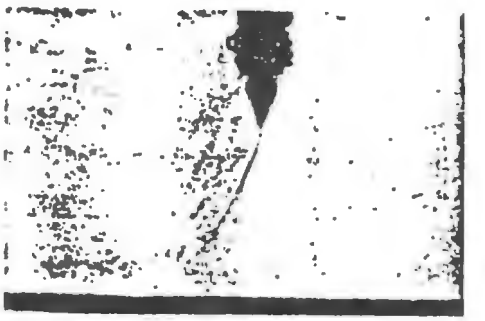

(by courtesy of Dr. Adachi, Assis. Professor of Yamaguchi University)

Fig. 3 (a) Generation of ionic wind

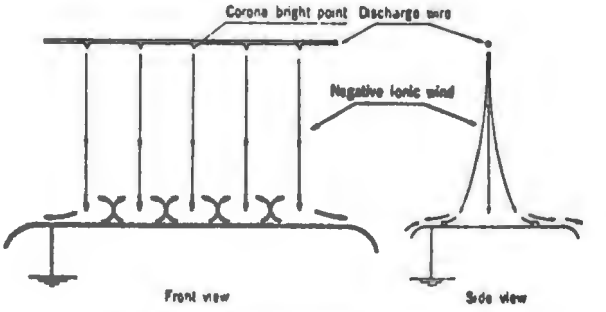

Fig. 3 (b) Flow pattern of ionic wind

(by courtesy of Dr. Masuda, Professor of Tokyo University)

Fig. 4 Appearance of back corona (32 kV, 10μA/cm^2)

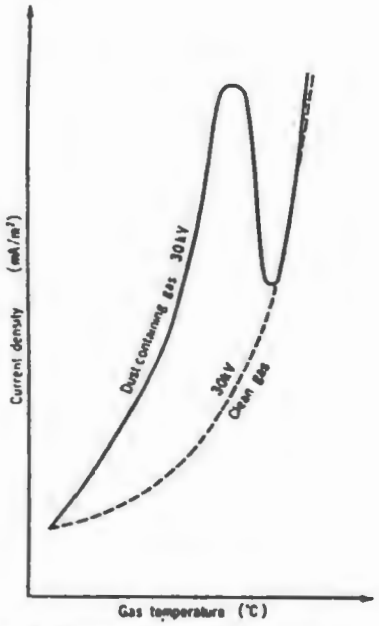

Fig. 5 Relation between gas temperature and current density (fly ash)

(as occurred at a low temperature)

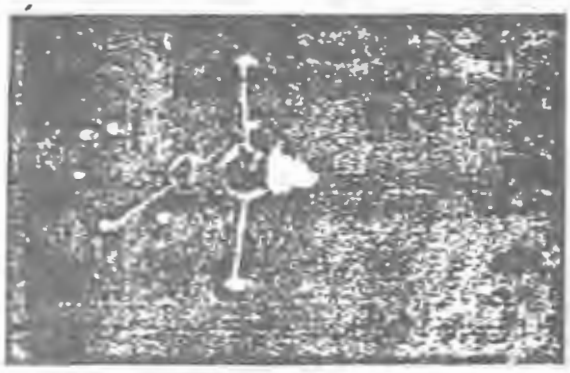

(as occurred at a high temperature)

Fig. 6 Effect of gas temperature on back corona

(3) Inverse-polarity ion from the collecting electrode side reduces or neutralizes the electric charge of dust which was charged by the corona discharge of the discharge electrode and disturbs dust collection by coulomb power electrically.

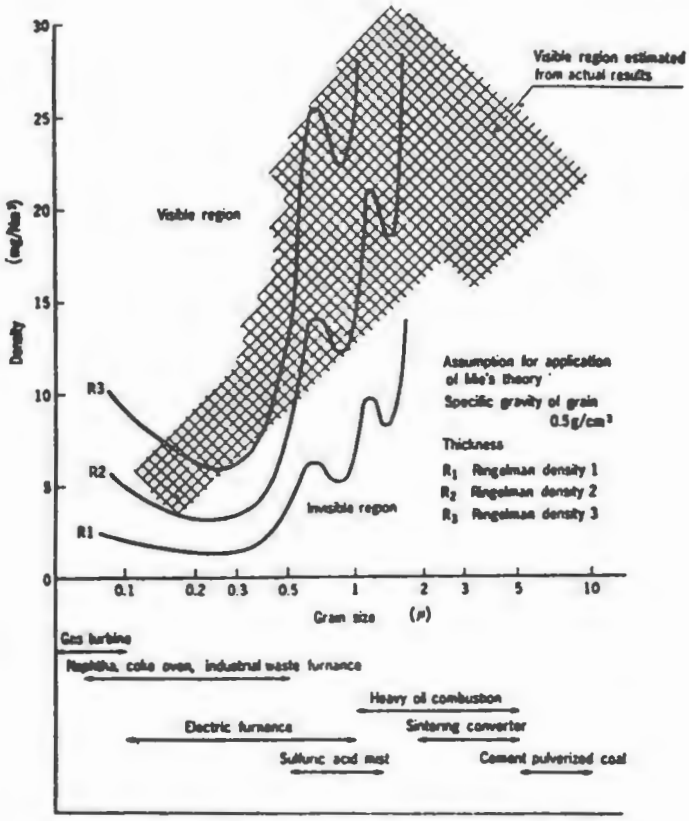

Fig. 7 Permeability based on Mie's theory on scattered light and visible region distribution

As effective methods of collecting high-resistivity dust, various methods are conceivable, one of which is high-temperature dust collecting method. Fig. 5 shows the relation between the gas temperature of high-resistivity fly ash arising from low-sulfur coal-fired boiler and its discharge characteristic. Fig. 6 shows the patterns of back corona at low and high temperatures. As can be understood from Figs. 5 and 6, back corona disappears when temperature is high.

2.4 Smoke density and color

2.4.1 Dust

The color of smoke represents the scattered light of grains visible to the eyes of observers as "smoke". Its thickness varies by the dust content and increases as the sum of the surface areas of grains becomes larger, or in other words, the grain size is smaller. Fig. 7 shows, by applying Mie's theory, isodensity lines corresponding to the Ringelman densities 1, 2 and 3. Also shown in the figure for reference is the visible region which was estimated on the basis of the results of our actual operation. It can be understood from the figure that smoke color varies by grain size even if density is the same. However, as the grain size from the same process is not always the same, special care must be taken for the application of the above data.

2.4.2 Steam and SO_3 mist

As typical visible smokes, steam and SO_3 mist can be mentioned besides dust. Steam and SO_3 mist generate

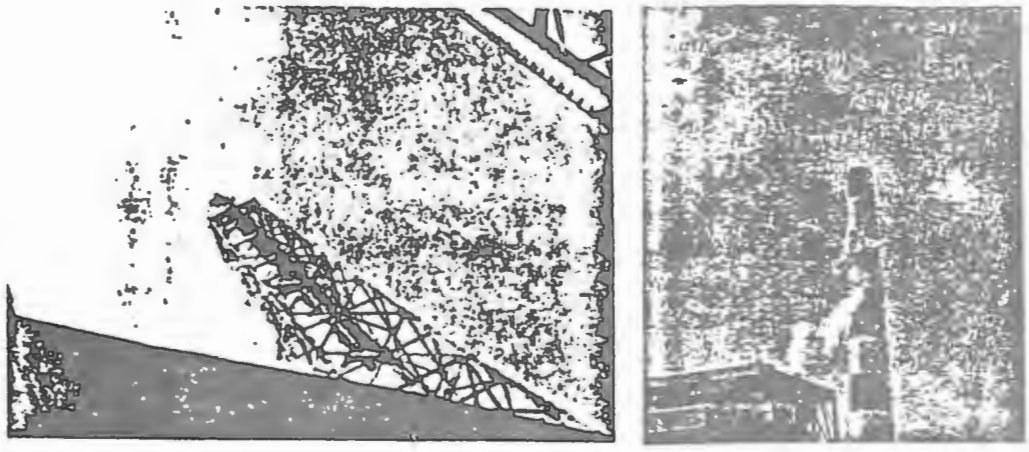

Operating condition:
Plant output 250MW, NH_3, magnesium hydroxide injection,
EP in operation, SO_3 at economizer outlet-15ppm,
Dust at EP outlet 5mg/Nm^3

250MW
Equipped with EP
With NH_3 injection

Fig. 8 Comparison of densities of smoke emitted from heavy oil fired boiler

white plume when they are emitted from stacks and cooled by atmospheric air. In this case too, their condition is affected by the meteorological condition near the exhaust ports of the stacks. That is to say, in case the atmospheric condition is in low-temperature high-humidity condition, steam generates a large volume of white plume. To prevent this, it is necessary to raise exhaust gas temperature, particularly in case atmospheric temperature is low.

Fig. 8 shows a difference in the colors of smokes emitted from SO_3 mist arising from a heavy oil-fired boiler, whether NH_3 is injected into it or nor. From the figures it can be understood that the color of smoke is governed by SO_3 mist rather than dust density.

3. Recent dust collecting techniques and trend of application

3.1 Boilers for utility thermal power plants

3.1.1 EPs for heavy oil (crude oil) fired boilers.

Mitsubishi Heavy Industries completed the world's first fullscale NH_3 injection type EP in 1966 (the injection method is patented by MHI). During the 10 years since, the EP has spread at a rapid pace and almost all of the heavy oil fired boilers in our country are equipped with EPs. At the beginning, EPs with an efficiency of about 80 per cent were adopted as the standard. At present, in response to the severe requirement of less than 10–20 mg/Nm^3 for outlet dust burden, manufacturers are taking such methods as the remodelling of the damper type EP as described below for higher efficiency and the adoption of low-sulfur fuels.

As a recent tendency, the adoption of high-sulfur heavy oil coupled with a full-scale flue gas desulfurization equipment is increasing. In this case, the quantity of dust is larger and moreover, reaction product of NH_3-SO_3 line occupies a greater ratio of its components, giving rise to problems relating to the performance and operation of EP, and making it necessary to improve the NH_3 injecting device, EP and ash treating device in some cases. Study for diversified use of EP is under study. That is to say, for desulfurization and denitration purposes, besides, the conventional low-temperature EPs installed at the air preheater outlet, the high-temperature EPs to be installed before preheaters and wet type EPs to be used after desulfurization are under study.

3.1.2 EPs for coal-fired boilers

Coal-fired boilers are under review. In the past, many coal-fired boilers were used, but for use in new plants, they have many difficulties which cannot be covered by past experience only. The reasons are as follows:

(1) The capacity of one plant is several times as large as that in the past.
(2) It is scheduled to use imported coals and domestic coals jointly. Imported coals are more difficult for EP to collect dust than domestic coals.
(3) Smaller quantity of dust than ever before and a high efficiency over 99 per cent are demanded.

As countermeasures to these, measures adapted to the characteristics of each plant, such as the increase of the size of the conventional EP, the adoption of high temperature EP and the injection of additive are under study.

3.2 Boilers for private power plants and industries

These boilers are mostly fired by heavy oil. With the strengthening of dust exhaust standard in 1971 and the enforcement of the environmental pollution control agreement concluded later, various kinds of dust collectors have come to be installed at a rapid pace. Among various kinds of dust collectors, high-efficiency EPs are showing a steady increase, though there are plants where multiclone (MC) or flue gas-desulfurization equipment is used as substitute.

Difference of the EPs for private power plants and industries from those for utility is that because of the high temperature of exhaust gases NH_3 injection for preventing the corrosion of EP is not necessary and most of them are not injected with NH_3. In case NH_3 is not injected, a greater part of the components of heavy oil dust is carbon, and it has been considered that because of

its low electric resistance, it is difficult to collect with EP. According to the recent results of operation, it has been made clear that this is not true but rather it is easier to collect than NH_3 injected dust, as only unburnt portion of comparatively large grain sizes remains. Even if NH_3 injection aimed at the prevention of corrosion of EP is not necessary, SO_3 cannot be removed unless NH_3 is injected. For this reason, there are cases where NH_3 is injected as a countermeasure to acid smut or to make smokes transparent.

Some of the boilers for private power plants are not yet equipped with EP. There is a movement, however, to impose duty to install EP capable of collecting fine particles, or dust collector having the same or higher performance as equipment standard for the purpose of reducing suspended particulates from the viewpoint of environmental protection. It is expected that sooner or later EPs will be adopted for all boilers for private power plants as they have been adopted for boilers for utility power plants. It is also presumed that new uses of EPs will be developed in relation to desulfurization and denitration.

3.3 Main exhaust gas arising from sintering machines in steel mills

3.3.1 Problematical points in equipment planning

Sintering machine is one of the facilities discharging the largest quantity of exhaust gas in steel mills. Dust is mainly composed of iron content and has a density of around 1 g/Nm^3 generally. Gas contains a considerable amount of SO_2. EPs were adopted comparatively recently in place of the conventional cyclones which were considered insufficient for the prevention of environmental pollution.

Mitsubishi Heavy Industries has turned out 38 units of sintering machines since completing its No. 1 unit in 1967. Its performance and equipment planning involves considerable difficulties and requires sufficient consideration. The important points in equipment planning are as follows:

(1) Working voltage is low because of high electric resistance of dust (performance).
(2) Dust collection is comparatively difficult as the grain size of dust is small (performance).
(3) There is a fear of dust burning, so it is necessary to take a measure to prevent burning (equipment).
(4) Powerful rapping is necessary as a large quantity of dust sticks (equipment).
(5) For large-sized equipment, in particular, study of thermal expansion- and deformation-proof structure is essential (equipment).

3.3.2 Features of our company's planning

Dust contains considerable amounts of metallic and nonmetallic fine particles. Its electric resistivity is $10^{13}\Omega$-cm or higher at normal temperatures (around 150°) and gas moisture content (6–8 vol%). The high resistivity is partly due to the resistivity of the abovementioned fine particles themselves and partly to the fact that SO_3 in gas cannot perform its role as surface resistance reducing agent as it forms gypsum by combining with CaO contained in dust. On the other hand, this gypsum hardens densely by suffering a hysteresis of low temperature – water drop spray – high temperature during the operation of the equipment. This also serves as a factor to increase resistivity.

In case electric resistivity is high, a back corona phenomenon occurs and in consequence, the working voltage drops as already described in 2. Countermeasures to this are as follows:

(1) To reduce resistivity.
(2) To adopt a sufficiently effective dust collecting structure based on new idea even in case electric resistivity is high.

For item (1), various methods are available. However, it is difficult ot find out a practical method for general use because of restrictions from sintering operation and expenses.

For item (2), formation of a strong electric field or a new electric fluid field by utilizing electrode shape and electrode spaced loading system independently or in combination was undertaken. However, its effectiveness is considered not definite in comparison with the conventional EP. At present stage, our company determines the capacity of equipment on the basis of the statistical results of actual operations in the past and by assuming the working voltage on the basis of the characteristic electrode shape and spacing, rapping strength and mechanism and power equipment control system and by use of gas temperature as a parameter, obtaining expected results stably.

In the above, we mainly referred to fine-particle dust. It is clear from the internal condition of the equipment that the fine particles are subject to the effect of re-scattering in the equipment and dust is collected selectively. These fine particles, coupled with the effect of high electric resistance, cause the comparatively low dust collecting performance.

Perceiving the behavior of fine particles in fluid, our company determines the capacity of equipment on the basis of the characteristic mechanism and system and by use of gas temperature and a certain component of dust as parameters. Particularly, it is well known that rapping of attached dust has a great effect on dust collecting efficiency.

Problematical points in equipment planning were enumerated in 3.3.1. They will be discussed later in this paper.

3.3.3 Relation between desulfurization / denitration processes and EP

There is a movement to equip sintering machines with desulfurization and denitration equipment. Here, EPs are also playing a very important role and giving serious effect on the technical and economical aspects of the equipment, which is described in detail in 3.4.

3.4 How to utilize EP for desulfurization and denitration processes

3.4.1 Utilization of EP for desulfurization process

Taking heavy oil fired boilers for example, various combinations are conceivable for desulfurization equipment and EP as shown in Table 1. In the past, combina-

Table 1 Various combinations of desulfurization equipment with EP for heavy oil fired boiler

Case	Combination with EP	Problems
1	(Without EP) Boiler — Desulf. — A, B (After-burner)	Insufficient dust-removing and desulfurizing performance. Formation of acid smut. Generation of white plume by SO_3.
2	(Conventional EP) NH_3 Boiler — Dry EP — Desulf. — A, B	Increase of outlet dust burden due to reaction product carried over from desulfurization process (common to Cases 1 to 3).
3	(EP without NH_3 injection) Boiler — Dry EP — Desulf. — A, B	Insufficient desulfurizing performance. Formation of acid smut. Generation of white plume by SO_3
4	(Dry EP after desulfurization) Boiler — Desulf. — NH_3 — Dry EP — A, B	Pollution of EP by unevaporated mist.
5	(Wet EP) Boiler — Desulf. — Wet EP — A, B	SO_3 at the outlet of desulfurization equipment is in the form of mist, so it can be collected by EP.

Table 2 Desulfurizing and dust-removing performance in case EP and desulfurization equipment are combined

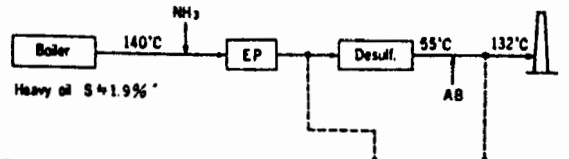

At the time EP efficiency declined	Total quantity of dust (mg/Nm³)		66	9.4
	Amount of $(NH_4)_mSO_4$ in dust (mg/Nm³)		48	5.8
	Dust collecting rate by desulf. equipment (%)	Total dust standard	85	
		$(NH_4)_mSO_4$ content	88	
At the time EP stopped completely	Total quantity of dust (mg/Nm³)		109	57
	Amount of $(NH_4)_mSO_4$ in dust (mg/Nm³)		72	55
	Dust collecting rate in desulf. equipment (%)	Total dust standard	48	
		$(NH_4)_mSO_4$ content	25	

tions 1–3 were most popular. It is desirable for the improvement of the quality of the by-product of the desulfurization process, and soot separation and waste water treating processes to remove dust beforehand by installing a dry type EP before the desulfurization equipment. Apart from this point, it is a basic problem for the determination of the necessity of EP to investigate to what extent desulfurization equipment can play the role of removing dust and SO_3 which is the role of the conventional EP.

3.4.1.1 Dust removing capacity of desulfurization equipment

The gas cooling section and gas absorbing section of the wet type desulfurization equipment widely in use now have a function of a kind of wet type mechanical dust collector. Therefore, the desulfurization equipment displays a considerable performance for dust of comparatively large grain sizes by giving proper pressure loss to it and it is considered that in case it is applied to heavy oil fired boilers, it can remove dust down to 50 mg/Nm³ in outlet dust burden. However, in case a higher dust removing performance than this is required, it is necessary to increase pressure loss to a large extent and for such a case it is rather economical in many cases to install EP if the running expense is taken into account.

On the other hand, in the case an EP is installed before the desulfurization equipment, dust at the inlet of the desulfurization equipment can be collected comparatively well by the effect of charging and coagulation in the EP and therefore, it is possible to make an economical design by combining desulfurization equipment and EP properly. Table 2 compares the performance of desulfurization equipment between a case it is equipped with an EP and another case without EP. The dust removing performance of the desulfurization equipment at the time the EP was completely stopped is very low as compared with that at the time the EP was in operation, and particularly, ammonium sulfate content [$(NH_4)_mSO_4$] collecting efficiency was very low. This is due to the fact that ammonium sulfate content which was created by NH_3 injection became a fine particle of around 1μ in grain size.

3.4.1.2 SO_3 removing capacity of desulfurization equipment

For exhaust gases containing SO_3 such as those emitted from heavy oil fired boilers, it was a general practice to solidify SO_3 in the form of ammonium sulfate content by injecting NH_3 into the gas before removing with EP and thereafter, remove the ammonium sulfate with EP for the purpose of preventing low-temperature corrosion and acid smut formation. As the result, smoke color caused by SO_3 mist became thinner.

In contrast, in case desulfurization equipment only was used (example 1 in Table 1), there was formation of acid smut and even after reheating of the gas with afterburner, white plume (violet) remaining phenomenon was observed, in consequence of which doubts arose as to the SO_3 removing performance of desulfurization equipment. It was confirmed as the result of actual measurement that the SO_3 removing rate of desulfurization equipment is not so high as its SO_2 removing rate.

The reason for the low SO_3 removing rate of desulfurization equipment is presumed to be that when gas is cooled in desulfurization equipment, the greatest portion of SO_3 turns into sulfuric acid mist (H_2SO_4) in the temperature range of 140–120°C and the mist is fine particle smaller than 1μ. While SO_2 gas is diffused and absorbed, this fine H_2SO_4 mist can not be collected in the desulfurization equipment except by the removing action by impact alike in the case of dust. Because of this relation, in case it is necessary to keep the discharged quantity of dust at a sufficiently low level or to remove SO_3, it is essential to use EP jointly. For this reason, case 2 in Table 1 can be said to be the most desirable method as a countermeasure to SO_3.

A method to collect and remove mist and salt generated by desulfurization and denitration equipment by installing a wet type EP after desulfurization (case No. 5) is under study. The features of wet type EP are that it is capable of reducing the density of discharged dust to such a low level that is difficult for dry type EP to attain and that it is effective for coupling with denitration equipment described below, making after-burner unnecessary or reducing operating cost.

3.4.1.3 Relation between denitration process and EP

In the selective catalytic reduction process with ammonia in the dry denitration process, which is in the most advanced stage of technical development, some catalyst is used in a high temperature state of 250 to 400°C generally. In case exhaust gas contains dust or SOx, it is often the case that dust attaches to the catalyst, causing an increase of pressure loss or spoiling of the catalyst, and countermeasure to this is one of the important problems of dry desulfurization process.

Concerning this problem, various studies have been made hitherto, of which the most desirable method is to remove dust completely by installing a dust collector before denitration equipment. This case also involves various technical and economical problems, depending on the operating conditions of the dust collector and it is necessary to investigate these problems for the whole plant.

In order to enable a dust collector to give full play to its functions for pretreatment to desulfurization, it is considered necessary that the dust collector has a high performance enough to reduce dust burden to a low level about 10 mg/Nm^3 lower than the outlet dust burden specified on the basis of the exhaust standard or visible limit. As such high-performance dust collector of this class, EP is most suitable. For this reason, our company is also pushing forward the development of dust collectors for denitration purpose, centering on EP.

Various methods of combination are conceivable for desulfurization equipment or denitration equipment with EP. Basically, they can be squeezed to the following three cases in Table 3. The main problematical points of EP in each case and the present state of our company's development activities are briefly introduced below.

Table 3 Combination of desulfurization equipment, denitration equipment with EP for heavy oil fired boilers

Case	Combination of EP	Value guaranteed by our EP	
		Dust at outlet	SO_3 at outlet
1	Boiler → hot EP (300~400°C) → De NOx → AH → De SOx →	<10mg/Nm^3	Incollectable
2	Boiler → AH (NH$_3$) → dry EP (130~180°C) → De SOx → De NOx →	<10mg	<10mg (in the form of ammonium sulfate)
3	Boiler → AH → De SOx → wet EP (55~60°C) → De NOx →	<1mg/Nm^3	<1mg/Nm^3 (in the form of H_2SO_4 mist)

Case No. 1 Hot EP

In case denitration is performed in the high-temperature section before the air preheater, a hot EP for boiler use which can be used in a high temperature range of 300 to 400°C is necessary. In this case, the problems are as follows:

(1) Increase of gas volume to be treated.
(2) Increase of gas viscosity and decline of dust moving speed.
(3) Fall of electric pressure resistance of gas and drop of working voltage and consequent decline of dust moving speed.
(4) Change of electric resistivity of dust; the change is divided into the favourable change and unfavorable one according to the kind of dust.
(5) To ensure structural strength, it is necessary to pay thorough attention to the selection of materials and stresses capable of withstanding high temperatures and the treatment of thermal expansion and contraction.
(6) Combustible dust such as the dust arising from heavy oil fired boilers is liable to cause ash combustion trouble.

Our company made pursuit of measures to grasp these problematical points quantitatively and their economical treatment by laboratory and pilot test and has recently gained a prospect for their practical application.

Case No. 2 Cold EP

Working conditions for cold EP are the same as those in general use and there is no technical problem at all for elevating its performance as many high-performance cold EP are already in operation under similar working conditions.

Case No. 3 Wet EP

Working conditions for wet EP are the same as those for EP used in conjunction with desulfurization equipment. The largest feature of this system is that it is capable of removing dust to such a low density that cannot be attained by dry type EP and that it is also capable of purifying exhaust gas to be denitrated to a level well comparable with the exhaust gas emitted from gaseous fuel. On the other hand, this system has the following problematical points, for which care must be taken.

(1) There are great differences in the properties of treated gases according to the kind of the preceding desulfurization process.
(2) Perfect corrosion preventing measures are necessary as it produces violent corrosive atmosphere.
(3) Measures to rationalize the method of supplying clean water and disposing of the waste water.
(4) Measures for preventing electric charge trouble of mists carried over from the desulfurization process.

Table 4 shows an example of combination of desul-

Table 4 Combination of desulfurization equipment, denitration equipment and EP (example) for sintering machines

furization and denitration equipment with EP to be used for exhaust gas from sintering machines in a steel mill. This combination type is used for removing dust arising from solid content remaining after mist eliminator treatment to less than 3 mg/Nm^3. The merit of the installation of wet type EP is that it is capable of high-performance dust removing as mentioned above, and thereby increases the effect of the following denitration equipment, and moreover, it can collect mist almost completely, reducing reheating cost remarkably.

Our company conducted pilot tests to grasp the properties of gas after various kinds of desulfurization processes and to confirm the dust collecting characteristics of EP and furthermore, improved the material quality, the methods of cleaning, water treatment and electrode structure. This EP already entered the stage of practical use and actual units are under production for heavy oil fired boilers and sintering machines.

4. Improvement of EP performance – EP with damper

In the case of dry EP, attention must be paid to the re-scattering of dust in the equipment. Concerning rescattering, we referred to in 2.2. Of scattering, rapping scattering is violent. In order to improve dust collecting efficiency by preventing rapping scattering, we developed an EP with damper (patent pending) as described below, which is obtaining excellent result.

Fig. 9 shows a rough sketch of the EP with damper. The interior of the equipment is divided into four sections, for example (A, B, C, D) and each section is independent for gas passage, electrode, charging, and electrode rapping. For dust collection, all sections are made full use of for almost all time zones (all dampers are kept open to the full). During this period, electrode rapping does not take place. With the lapse of preset time depending on the density and property of dust, the dampers at the inlet and exit of section A, for example, are closed to generate electrode rapping only in this section for dust discharge. Besides, as necessity demands, the section A works complementary operations such as charge stopping or quick rapping for the efficiency of dust discharging.

The time of operation of section A is determined beforehand. After finish of the operation of section A, sections B, C and D are operated one after another in the same manner, completing one cycle. These operations are conducted automatically in accordance with a prepared program.

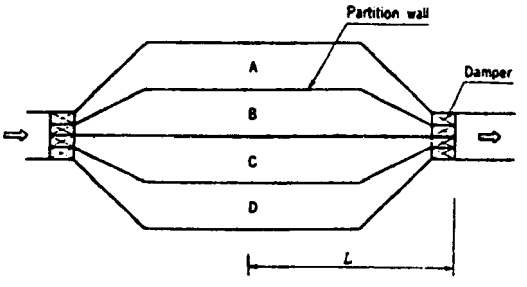

Fig. 9 EP with damper

The locations of the dampers are determined according to dust collecting performance required. For EPs for heavy oil fired boilers, they are installed at the inlet and exit in case outlet dust burden is less than 10 mg/Nm^3 and the partition accuracy of the partition structure of each section is raised.

In case of planning for outlet dust burden exceeding 10 mg/Nm^3, a damper is installed at the exit only. As for the partition of each section, it is enough to partition the L part only. This system makes it possible to perform quick rapping after stopping of charging as mentioned above, and moreover, has a merit to increase the cleanness of electrodes to a great extent and if this merit is taken into account, it can be said to be a noteworthy operation system. Fig. 10 shows the performance of the EP with damper in comparision with that of the EP without damper.

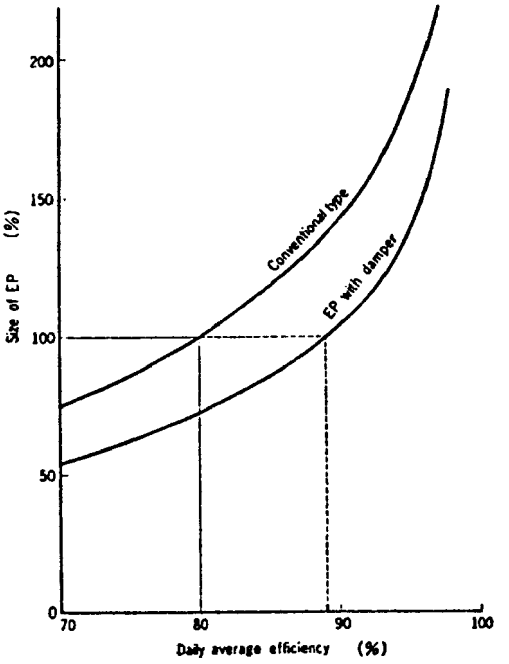

Fig. 10 Relation between dust collecting efficiency and size of EP

5. Reliability of EP

EPs are the best among various kinds of dust collectors now in existence both in performance and a wide range of application. This equipment is always coupled with production facilities directly or indirectly and their working ratios and ease of maintenance are matters of great concern for user. For this reason, it is necessary to pay proper consideration to each condition in the design of the equipment. With the recent progress toward larger air flow rate and higher performance, the capacities of EPs have greatly increased (not a few of our products have a capacity exceeding 15 000 m^3 per unit), and moreover,

they have been improved in heat resistance (up to 400°C) and pressure resistance (up to 2 500 mmAq). On the other hand, EPs have a defect that it is difficult to prevent or control damages as their internal condition cannot be thoroughly inspected during operation and in most cases, damages can only be known through changes in situation.

From this viewpoint, we take up the reliability of this equipment and briefly introduce the main aim of our design of the elements of the equipment and actual products.

5.1 EP casing

The casing of the EP with a capacity exceeding 15 000 m^3 has a surface area as large as 4000 m^2. As it must have strength and rigidity enough to withstand heat and pressure besides various kinds of load including the weight of their internal furnishings, earthquake and wind pressure, it must be built to be a reasonable structural body backed by very strict strength calculation, since it is of comparatively thin steel sheet construction. Furthermore, as thermal expansion and contraction cannot be disregarded, the distance between struts becomes larger than 110 mm maximum in the above example.

Our company entered the actual computarization stage for structural design several years ago and has succeeded in establishing, by using structural analysis programs jointly, reasonable wasteless safe structure designing. For example, a center pillar structure is adopted for large-type high-pressure EPs for higher safety. Thermal expansion and contraction between the casing and the supporting frame is absorbed by a special pin joint or a plain bearing. If the strength of the casing is insufficient, a considerable local deformation will occur (though entire fracture may not occur), causing changes in the arrangement of internal furnishings, particularly electrodes. With this point in mind, our company is making efforts for securing safety and accuracy.

5.2 Collecting electrode

For functional purpose, a collecting electrode is made of thin steel plate and it is necessary to prevent internal temperature difference and deformation caused by impacts due to rapping. The collecting electrode developed by our company is composed of narrow rigid moldings which are combined mutually independently and is free from individual or overall deformation nor irregular interval between each molding.

5.3 Discharging electrode

Generally, this is the part most susceptible to damages and the damage of this part leads to stoppage of the equipment. The discharging electrode developed by our company adopts a short span construction and is stably charged, almost free from chord vibration and disconnection. Consequently, it is not necessary to divide the charging section finely to save the increase in equipment expenses.

5.4 Rapping

The features of our products lie in (1) collecting and discharging electrodes and their supporting mechanisms, (2) method of fixing striking lever and electrodes, (3) striking points and (4) individual rapping and even in case the surface area of the electrode is larger than 70m^2, it can obtain an effective vibration acceleration of about 2000 g near the striking point and several hundred g at the remotest point. Therefore, even adhesive dust comes off from the whole surface easily. The striking hammer is comparatively light in weight and is safe against damage.

Striking noise is small, being 65 phons at a distance of 1 m from the equipment.

5.5 Hopper

The hopper should be designed with emphasis on the prevention of dust bridge and unavailable gas flow. Our company adopted, for the former, an angle of repose, corner plate, downward local cone, through shape, agitator and vibrator according to the property of dust and arranged a large-sized gas cut-off plate for the latter. Recently, we developed a special device (patent pending) to be installed in the hopper for discharging very light, fine-grained adhesive dust. This special device is already in actual use with good results.

5.6 High-voltage insulator

Employing electric dehumidification and blast cleaning systems, this high-voltage insulator is free from damage due to dielectric breakdown, and can be held without damage as it is supported free of thermal expansion and contraction.

5.7 Corrosion and wear

As corrosion preventing measures, we enforce heat retaining and local heating and make severe selection of materials for dry type EP. For sources of corrosion, the best efforts are made for the prevention of outbreak of corrosive atmosphere and for avoiding operation under corrosive atmosphere. For the wet type whose feed water system adopts a closed system recently, various kinds of synthetic nonmetallic materials are used properly to prevent corrosion by feed water.

The largest wear is the wear of the inlet flue by fluid. As a countermeasure to this, we improved the shape of the flue and installed a special current control plate which obtained satisfactory result for the protection of the wall surfaces, also serving for the reduction of ventilation loss.

5.8 Explosion and combusion

The major combustible gas which is liable to explode may be CO. Explosion is a sudden combustion and combustion easily occurs when (1) combustible gas, (2) proper oxygen density and atmospheric temperature and (3) ignition source are present. Our company pays much attention to the following points and takes the following safety measures, which have prevented occurrence of extraordinary accidents in our products.

(1) To check whether oxygen density is lower than the safe oxygen density which is determined by the kind and density of combustible gas contained in mixed gas.
(2) To keep atmospheric temperature off the explosive limits.
(3) To control the combustion of source so as to reduce the maximum value of combustible gas density.
(4) In order to check ignition energy on EP side: to adopt power source equipment which does not gener-

ate high-frequency sparks, glow and arc by controlling voltage by spark detection for each operation, and also of an interlock of CO and O_2 densities and power source equipment. That is, practice of low voltage operation, always, not accompanied by spark.

(5) The special safe structure enabling the largest-surface part of the body of EP to open instantaneously.

Generally, the interlocking operation, which detects combustible gas density and injects inert gas, is apt to be segregated to density and the detected density does not always indicate the maximum density. Besides, in relation to time lag, the interlocking operation cannot be said to be a sufficient preventive measure.

Conditions for dust combustion are the same as those for gas. The neighbourhood of specific dust which emits component gas with the lowest ignition point ignites first and its heat energy burns dust in other parts one after another. Considering that the quantity of dust sticking to the surfaces of the electrodes which are the most important but the weakest parts of EP is responsible for overall combustion, our company enforced electrode damage preventing measures (patent pending) including the above-mentioned measures for preventing explosion. As its result, we could prevent serious accidents till the present.

6. Conclusion

In this paper, the authors took up EP, particularly dry type EP preponderantly and described, concerning the performance and reliability of the equipment, the results of our research and practical application and the technique of combining EP with desulfurization and denitration equipment. It is considered that many technical problems which have greater effect for our company and for a number of researchers on dust collecting techniques from practical engineering viewpoint are still left for solution.

New needs will be developed for EP in future at the request of the nation. We feel great responsibility in our study and solicit continued guidance of the circles concerned.

© by Mitsubishi Heavy Industries, Ltd.
(Reproduced by permission)

TECHNICAL REPORT DATA
(Please read Instructions on the reverse before completing)

1. REPORT NO.	2.	3. RECIPIENT'S ACCESSION NO.
EPA-600/7-78-110a		

4. TITLE AND SUBTITLE	5. REPORT DATE
Electrostatic Precipitator Technology Assessment: Visits in Japan, November 1977	June 1978
	6. PERFORMING ORGANIZATION CODE
7. AUTHOR(S)	8. PERFORMING ORGANIZATION REPORT NO.
Grady B. Nichols	Project 3858-5
9. PERFORMING ORGANIZATION NAME AND ADDRESS	10. PROGRAM ELEMENT NO.
Southern Research Institute 2000 Ninth Avenue, South Birmingham, Alabama 35205	EHE624
	11. CONTRACT/GRANT NO.
	68-02-2610, W.A. 5
12. SPONSORING AGENCY NAME AND ADDRESS	13. TYPE OF REPORT AND PERIOD COVERED
EPA, Office of Research and Development Industrial Environmental Research Laboratory Research Triangle Park, NC 27711	Final; 11/77-4/78
	14. SPONSORING AGENCY CODE
	EPA/600/13

15. SUPPLEMENTARY NOTES IERL-RTP project officer is James H. Abbott, Mail Drop 61, 919/541-2925. EPA-600/7-78-110 is the basic report.

16. ABSTRACT The report gives results of a particulate control technology assessment visit to Japan by a team of U.S. investigators. The visit included discussions with personnel from universities, industries, and other major installations involved with particulate control. Significant research activities were noted in both the academic and industrial sectors related to particulate control and measurements. The report summarizes results of the individual discussions, observations during the tour, and discussions of technical papers. Many valuable technical papers supplied to the U.S. team are reproduced the the Appendix of the report.

17. KEY WORDS AND DOCUMENT ANALYSIS

a. DESCRIPTORS	b. IDENTIFIERS/OPEN ENDED TERMS	c. COSATI Field/Group
Air Pollution	Air Pollution Control	13B
Electrostatic Precipitation	Stationary Sources	13H
Dust	Japan	11G
Measurement	Particulates	14B

18. DISTRIBUTION STATEMENT	19. SECURITY CLASS *(This Report)*	21. NO. OF PAGES
Unlimited	Unclassified	697
	20. SECURITY CLASS *(This page)*	22. PRICE
	Unclassified	

☆U.S. GOVERNMENT PRINTING OFFICE: 1979-640-013/4239 REGION NO. 4